/09000

P - 499

A Progress Report
NASA-LaRC Grant NAG-1-745

January 1, 1992 to June 30, 1992

NASA-UVA LIGHT AEROSPACE ALLOY AND STRUCTURES TECHNOLOGY PROGRAM (LA²ST)

Submitted to:

National Aeronautics and Space Administration
Langley Research Center
Hampton, Virginia   23665

Attention:

Mr. Richard J. Siebels
Grants Officer
MS 126

For Review by:

Mr. Dennis L. Dicus
Grant Monitor
Metallic Materials Branch, MS 188A

Submitted by:

Richard P. Gangloff
Professor

SEAS Report No. UVA/528266/MS93/111
July 1992

DEPARTMENT OF MATERIALS SCIENCE AND ENGINEERING

SCHOOL OF

ENGINEERING
& APPLIED SCIENCE

University of Virginia
Thornton Hall
Charlottesville, VA 22903

UNIVERSITY OF VIRGINIA
School of Engineering and Applied Science

The University of Virginia's School of Engineering and Applied Science has an undergraduate enrollment of approximately 1,500 students with a graduate enrollment of approximately 600. There are 160 faculty members, a majority of whom conduct research in addition to teaching.

Research is a vital part of the educational program and interests parallel academic specialties. These range from the classical engineering disciplines of Chemical, Civil, Electrical, and Mechanical and Aerospace to newer, more specialized fields of Applied Mechanics, Biomedical Engineering, Systems Engineering, Materials Science, Nuclear Engineering and Engineering Physics, Applied Mathematics and Computer Science. Within these disciplines there are well equipped laboratories for conducting highly specialized research. All departments offer the doctorate; Biomedical and Materials Science grant only graduate degrees. In addition, courses in the humanities are offered within the School.

The University of Virginia (which includes approximately 2,000 faculty and a total of full-time student enrollment of about 17,000), also offers professional degrees under the schools of Architecture, Law, Medicine, Nursing, Commerce, Business Administration, and Education. In addition, the College of Arts and Sciences houses departments of Mathematics, Physics, Chemistry and others relevant to the engineering research program. The School of Engineering and Applied Science is an integral part of this University community which provides opportunities for interdisciplinary work in pursuit of the basic goals of education, research, and public service.

A Progress Report

January 1, 1992 to June 30, 1992

NASA-UVA LIGHT AEROSPACE ALLOY AND STRUCTURES TECHNOLOGY PROGRAM (LA²ST)

Submitted to:

National Aeronautics and Space Administration
Langley Research Center
Hampton, Virginia   23665

Attention:

Mr. Richard J. Siebels
Grants Officer
MS 126

For Review by:

Mr. Dennis L. Dicus
Grant Monitor
Metallic Materials Branch, MS 188A

Submitted by:

Richard P. Gangloff
Professor
Department of Materials Science and Engineering
School of Engineering and Applied Science
University of Virginia

Report No. UVA/528266/MS93/110
July 15, 1992
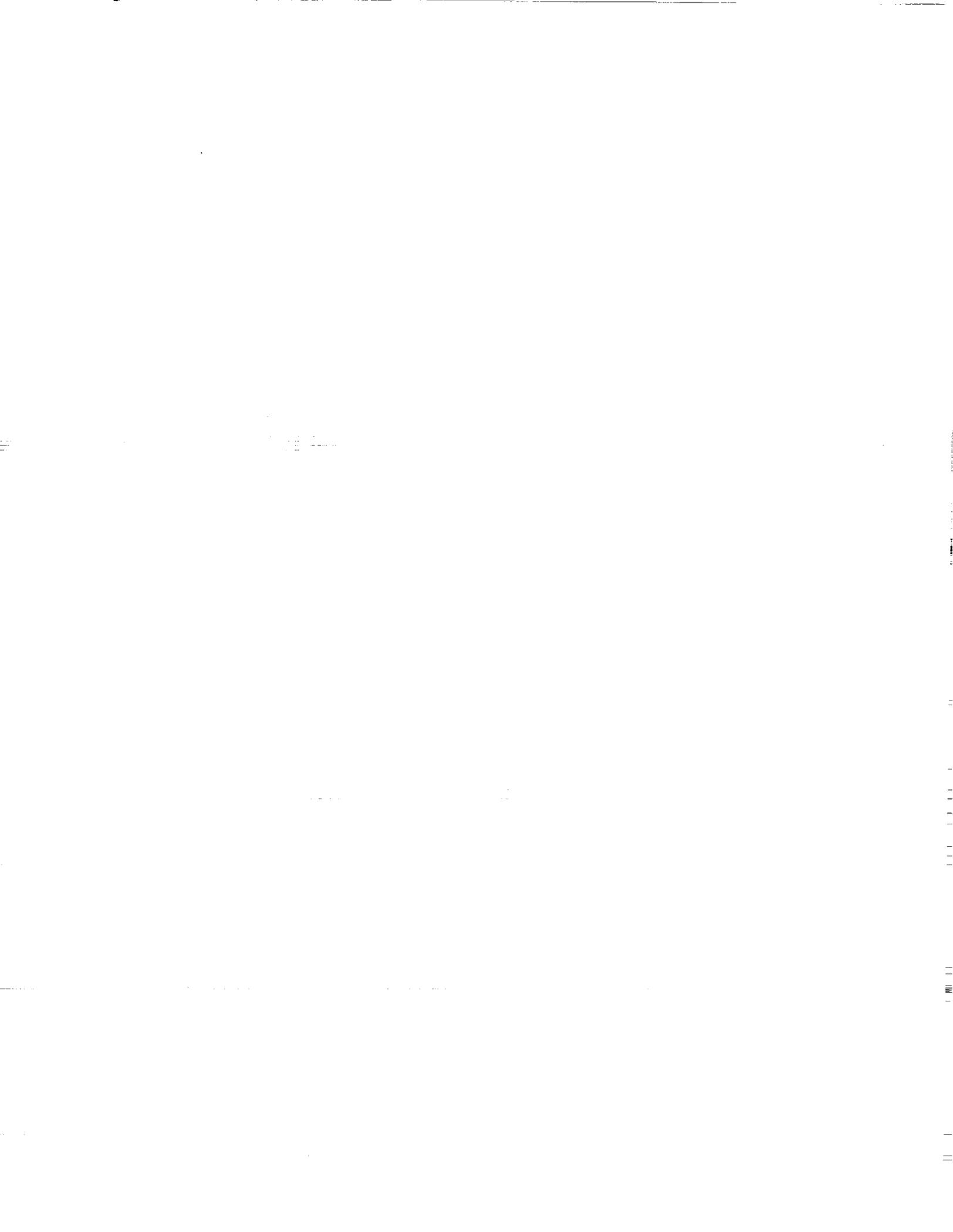
NASA-UVA LIGHT AEROSPACE ALLOY
AND STRUCTURES TECHNOLOGY PROGRAM

LA²ST

Program Director:

Richard P. Gangloff

Co-principal Investigators:

Richard P. Gangloff
John K. Haviland
Carl T. Herakovich
Walter D. Pilkey
Marek-Jerzy Pindera
John R. Scully
Glenn E. Stoner
Earl A. Thornton
Franklin E. Wawner, Jr.
John A. Wert

NASA-LaRC Grant Monitor:

Dennis L. Dicus

TABLE OF CONTENTS

NASA-UVA LIGHT AEROSPACE ALLOY AND STRUCTURES TECHNOLOGY PROGRAM

EXECUTIVE SUMMARY

The NASA-UVa Light Aerospace Alloy and Structures Technology (LA²ST) Program continues to maintain a high level of activity, with projects being conducted by graduate students and faculty advisors in the Departments of Materials Science and Engineering, Civil Engineering and Applied Mechanics, and Mechanical and Aerospace Engineering at the University of Virginia. This work is funded by the NASA-Langley Research Center under Grant NAG-1-745. Here, we report on progress achieved between January 1 and June 30, 1992. These research results were presented at the Third Annual LA²ST Grant Review Meeting held at the Langley Research Center in July of 1992.

The objective of the LA²ST Program is to conduct interdisciplinary graduate student research on the performance of next generation, light weight aerospace alloys, composites and thermal gradient structures in collaboration with Langley researchers. Technical objectives are established for each research project. We aim to produce relevant data and basic understanding of material mechanical response, corrosion behavior, and microstructure; new monolithic and composite alloys; advanced processing methods; new solid and fluid mechanics analyses; measurement advances; and critically, a pool of educated graduate students for aerospace technologies.

The accomplishments presented in this report are as follows.

oo Four research areas are being actively investigated, including: (1) Mechanical and Environmental Degradation Mechanisms in Advanced Light Metals and Composites, (2) Aerospace Materials Science, (3) Mechanics of Materials and Composites for Aerospace Structures, and (4) Thermal Gradient Structures.

oo Sixteen research projects are being conducted by 12 PhD and 3 MS level graduate students, 10 faculty members, and 1 research associate from three departments in the Engineering School at UVa. Each project is planned and executed in conjunction with a specific branch and technical monitor at NASA-LaRC.

oo Two students received the PhD degree in Materials Science and Engineering at UVa, based on research wholly supported by the LA²St Program. Two new graduate students were recruited into the LA²ST Program during this reporting period.

oo Considering undergraduate participation, recruiting efforts were intensified and 7 highly qualified rising seniors were hired for work at NASA-LaRC during the summer of 1992. All students are interested in careers in aerospace materials science and mechanics; the average grade point average for the group is 3.4 (A = 4.0); and represented universities include Duke (2), Georgia Institute of Technology, Harvard (2), University of Missouri, and Virginia Polytechnic Institute. Two undergraduates are participating in faculty directed LA^{2}ST research at UVa.

oo Reporting accomplishments between January and June of 1992 include 7 journal or proceedings publications, 2 PhD dissertations, 1 NASA progress report, and 13 presentations at technical meetings. The LA^{2}ST totals since 1986 are 53 publications (25 archival or journal publications), 8 dissertations or theses, 61 external presentations and 12 NASA progress reports. Since 1986, 23 graduate students, including 22 United States citizens, have been involved with LA^{2}ST research and 8 have received MS or PhD degrees.

oo *Research on environmental fatigue of Al-Li-Cu alloys* successfully produced a range of model recrystallized microstructures by thermomechanical processing of alloy 2090, and determined the fatigue crack growth kinetics and microscopic crack paths for these materials in inert vacuum and aqueous NaCl. The crystallographic orientation of fatigue crack surface facets is being determined by electron backscattering pattern (EBSP) techniques; results to date contradict published orientations defined by less direct methods.   (Project 1)

oo *Research to incorporate environmental effects into fracture mechanics fatigue life prediction codes such as NASA FLAGRO* produced a comprehensive literature review that identified crack growth rate data for aerospace alloys and environments. Empirical curve-fitting, linear superposition and mechanism-based models reasonably predict crack growth rate data, but only for selected cases. Substantial resources are required to quantitatively define environmental effects on component life. Future research will investigate the environmental fatigue behavior of Ti-6Al-4V and Beta 21S in aqueous chloride.   (Project 2)

oo *Research on mechanisms of localized corrosion and environmental fracture in Al-Cu-Li-Mg-Ag alloy X2095 and compositional variations* is focusing on microstructural and electrochemical characterization of X2095 (Weldalite™). Two tempers appear to be susceptible to a rapid, intersubgranular, anodic dissolution based form of SCC under specific polarization conditions in two inhibiting environments.
                    (Project 7)

oo *Research on the effect of zinc additions on the precipitation and stress corrosion cracking behavior of alloy 8090* centers on quantifying stress corrosion cracking resistance through fracture mechanics measurements of da/dt versus applied stress intensity and the threshold K for SCC. The environmental cell for these experiments was designed and built, and testing will begin during the next reporting period.

(Project 8)

oo *Research on hydrogen interactions with Al-Li-Cu alloy 2090 and complimentary model alloys* characterized the mechanical response of hydrogen precharged 2090-T3 in the LT and TL orientations. The experimental results indicate that dissolved hydrogen produces changes in mechanical properties and the fracture path.

(Project 9)

oo *Research on metastable pitting of Al Alloys* demonstrates that electrochemical transients associated with metastable pitting depend on applied potential, halide ion concentration, and exposure time in a deterministic manner. Additional analysis based on techniques of non-linear signal analysis will be pursued. This work is enabled by a NASA Graduate Student Researchers Program Fellowship (Underrepresented Minority Focus).

(Project 9a)

oo *Research on the fracture of Al-Cu-Li-In alloys* is emphasizing fractographic analysis of the microscopic processes that govern ambient and cryogenic fracture toughness. For 2090+In-T6, fracture is intersubgranular for each temperature and stress state due to In-enhanced T_1 precipitation at subboundaries. Four fracture modes are observed for alloy 2090-T8, including high angle boundary delamination, multiple grain shear cracking, single grain slip plane cracking, and intersubgranular cracking. In addition to the well characterized delamination mode, the transgranular processes dominate cracking of 2090-T8 for each temperature and stress state.

(Project 5)

oo *Research on the fracture toughness of Weldalite™* determined the aging response of two alloys at the compositional limits of X2095; 4.0Cu-1.0Li and 4.6Cu-1.6Li (wt%). At room and cryogenic temperatures, σ_{ys} increases and work hardening exponent decreases with aging time (at 143°C) up to 75 hours for each composition. For each aging time and composition; σ_{ys}, work hardening and modulus of elasticity increase; and tensile ductility (% RA) declines, with decreasing tensile test temperature. Modeling predicts that plane strain fracture toughness should accordingly decrease from ambient to cryogenic temperatures.

(Project 6)

oo *Research on elevated temperature fracture of PM Al-Fe-Si-V alloy 8009* was completed during this reporting period and the graduate student attained the PhD degree. This work demonstrates that the fracture toughness of this (and other) PM aluminum alloy decreases with increasing temperature and decreasing loading rate. Causal mechanisms based on delamination and hydrogen embrittlement are eliminated. While dynamic strain aging cannot be ruled out, a likely mechanism for the degradation of fracture resistance is the temperature-strain rate dependent transition from dispersoid-dislocation interactions to silicide particle bypassing by dislocation climb. Dislocations that evade particles accumulate damage at boundary oxides and dispersoid clusters, and enable local matrix shear cracking.

(Project 3)

oo *Research on Ti alloy matrix-SiC fiber reinforced composites* showed a strong thermal cycling-resistance dependence on composite fabrication. Test specimens taken from near the edges of composite panels (and shown by C-scans to be poorly bonded) frequently gave high as-fabricated tensile strength, but after being subjected to thermal cycling, properties were severely degraded. Samples from the interior of the panel did not experience appreciable degradation from thermal cycling. Poorly bonded matrix foils may provide an easy path for oxygen penetration leading to composite delamination. Yttria and calcia coatings were successfully applied to SCS-6 fibers by sol-gel techniques. The coatings are crack free, dense, strongly adherent, and offer protection to the fibers in CP titanium for over 100 hours at 800°C.

(Project 10)

oo *Research on quantifying the spatial distribution and homogeneity of microstructure* was completed and the graduate student received the PhD degree. Most recently, this work applied newly developed methods for analyzing the spatial distribution of particles in materials to the problem of oxide film fragmentation and dispersal in PM aluminum alloys. Results indicate that processing methods involving triaxial deformation and lower working temperatures provide better oxide fragmentation and dispersal than methods involving plane strain deformation at higher temperatures.

(Project 11)

oo *Research on superplastic forming of Weldalite™* demonstrated that microstructure evolution during the initial stages of SPF deformation proceeds the same way in Weldalite™ as in simple Al-Zr-Si alloys studied previously. Modeling of microstructure evolution mechanisms shows that grain boundary sliding is the likely mechanism for the observed evolution of boundary characteristics.

(Project 12)

viii

oo *Research on the deformation of SCS-6/Ti-15-3 metal matrix composite tubulars under biaxial loading* demonstrates that damage induced plasticity results in strong coupling between the axial and torsional response of $[\pm 45]_s$ SCS-6/Ti tubes.

(Project 13)

oo *Research on finite element analysis of the effect of temperature on metallic shell structures* considered buckling of cryogenic tanks and fuselage sections, with emphasis on boundary conditions for analyzing small segments. Exact thermoelastic solutions for thermally loaded straight and curved beams were formulated.

(Project 14)

oo *Research on the thermoviscoplastic behavior* of high temperature alloy panels demonstrated material and geometric nonlinearities. Experiments with instrumented Hastelloy-X panels provided elastic and inelastic temperature and displacement data for thermal buckling. A heat lamp characterization program was initiated. Tensile experiments coupled with Bodner-Partom analyses established the time dependent nonlinear deformation characteristics of Hastelloy-X. Future experiments will investigate 2618 and 8009 aluminum alloys. (Project 15)

INTRODUCTION

Background

In 1986 the Metallic Materials Branch in the Materials Division of the NASA-Langley Research Center initiated sponsorship of graduate student engineering and scientific research in the Department of Materials Science and Engineering at the University of Virginia[1]. This work emphasized the mechanical and corrosion behavior of light aerospace alloys, particularly Al-Li-Cu based compositions, in aggressive aerospace environments[2-4].

In the Fall of 1988, the scope of this program was increased to incorporate research at UVa on the development and processing of advanced aerospace materials[5]. Funding was provided by the Metallic Materials and Mechanics of Materials Branches. In early 1989 the program was further enhanced to include interdisciplinary work on solid mechanics and thermal structures, with funding from several Divisions within the Structures Directorate at NASA-LaRC[6]. The Department of Civil Engineering and the Department of Mechanical and Aerospace Engineering at UVa participated in this expanded program. With this growth, the NASA-UVa Light Aerospace Alloy and Structures Technology Program (LA²ST) was formed within the School of Engineering and Applied Science at UVa.

Since 1989, the LA²ST program has operated with full participation from about 10 faculty and 15 graduate students, as outlined in the last six progress reports[7-12] and three grant renewal proposals[13-15]. Two 2-day Grant Review Meetings were held in June of 1990 and 1991 at the Langley Research Center, with over 25 faculty and graduate students from UVa participating.

In October of 1991, Dean E.A. Starke proposed a substantial enhancement to the base LA²ST Program[16]. The objective of this supplement is to involve UVa faculty with engineering scientists from aluminum alloy producers and airframe manufacturers in a broad research program to develop aluminum alloys and composites for elevated temperature high speed civil transport applications. This research began in January of 1992 and the results are separately reported.

Problem and Needs

Future aerospace structures require high performance light alloys and metal matrix composites with associated processing and fabrication techniques; new structural design methods and concepts with experimental evaluations; component reliability/durability/damage tolerance prediction procedures; and a pool of masters and doctoral level engineers and

scientists. Work on advanced materials and structures must be interdisciplinary and integrated. The thermal and chemical effects of aerospace environments are particularly important to material performance. Nationally, academic efforts in these areas are limited. The NASA-UVa LA^{2}ST Program addresses these needs.

LA^{2}ST Program

As detailed in the original proposal[6] and affirmed in the most recent renewal[15], faculty from the Departments of Materials Science and Engineering, Mechanical and Aerospace Engineering, and Civil Engineering and Applied Mechanics at UVa are participating in the LA^{2}ST research and education program focused on high performance, light weight, aerospace alloys and structures. We aim to develop long term and interdisciplinary collaborations between graduate students, UVa faculty, and NASA-Langley researchers.

Our research efforts are producing basic understanding of materials performance, new monolithic and composite alloys, advanced processing methods, solid and fluid mechanics analyses, and measurement advances. A major product of the LA^{2}ST program is graduate students with interdisciplinary education and research experience in materials science, mechanics and mathematics. These advances should enable various NASA technologies.

The scope of the LA^{2}ST Program is broad. Four research areas are being investigated, including:

oo   Mechanical and Environmental Degradation Mechanisms in Advanced Light Metals and Composites,

oo   Aerospace Materials Science,

oo   Mechanics of Materials and Composites for Aerospace Structures,

oo   Thermal Gradient Structures.

Fifteen specific research projects are ongoing within these four areas and are reported here. These projects currently involve 9 faculty, 1 research associate and 16 graduate students. The majority of the graduate students are at the doctoral level (12 of 16), all are citizens of the United States, and 2 are supported by the NASA Minority Grant Program. In each case the research provides the basis for the thesis or dissertation requirement of

2

graduate studies at the University of Virginia. Each project is developed in conjunction with a specific LaRC researcher. Research is conducted at either UVa or LaRC, and under the guidance of UVa faculty and NASA staff. Participating students and faculty are closely identified with a NASA-LaRC branch.

A primary goal of the LA²ST Program is to foster interdisciplinary research. To this end, many of the research projects share a common focus on the same next generation light alloys and composites, and on light and reusable aerospace structures which will be subjected to aggressive terrestrial and space environments. Emphasis is placed on both cryogenic and elevated temperature conditions, with severe thermal gradients typical of tankage structures.

Organization of Progress Report

This progress report first provides LA²ST Program administrative information including statistics on the productivity of faculty and graduate student participants, a history of current and graduated students, refereed or archival publications, and a list of ongoing projects with NASA and UVa advisors.

Fifteen sections summarize the technical accomplishments of each research project, emphasizing the period from January 1st to June 30, 1992. Each program section contains a brief narrative of objective, recent progress, conclusions and immediate milestones; coupled with a set of visual aids presented at the Third Annual NASA-UVa LA²ST Grant Review Meeting held at NASA-LaRC in July of 1992. The agenda of this meeting is presented in Appendix V.

Appendices document grant-sponsored publications, conference participation and citations of all LA²ST Progress Reports.

References

1. R.P. Gangloff, G.E. Stoner and M.R. Louthan, Jr., "Environment Assisted Degradation Mechanisms in Al-Li Alloys", University of Virginia, Proposal No. MS-NASA/LaRC-3545-87, October, 1986.

2. R.P. Gangloff, G.E. Stoner and R.E. Swanson, "Environment Assisted Degradation Mechanisms in Al-Li Alloys", University of Virginia, Report No. UVA/528266/MS88/101, January, 1988.

3. R.P. Gangloff, G.E. Stoner and R.E. Swanson, "Environment Assisted Degradation Mechanisms in Advanced Light Metals", University of Virginia, Report No. UVA/528266/MS88/102, June, 1988.

4. R.P. Gangloff, G.E. Stoner and R.E. Swanson, "Environment Assisted Degradation Mechanisms in Advanced Light Metals", University of Virginia, Report No. UVA/528266/MS89/103, January, 1989.

5. T.H. Courtney, R.P. Gangloff, G.E. Stoner and H.G.F. Wilsdorf, "The NASA-UVa Light Alloy Technology Program", University of Virginia, Proposal No. MS NASA/LaRC-3937-88, March, 1988.

6. R.P. Gangloff, "NASA-UVa Light Aerospace Alloy and Structures Technology Program", University of Virginia, Proposal No. MS NASA/LaRC-4278-89, January, 1989.

7. R.P. Gangloff, "NASA-UVa Light Aerospace Alloy and Structures Technology Program", University of Virginia, Report No. UVA/528266/MS90/104, August, 1989.

8. R.P. Gangloff, "NASA-UVa Light Aerospace Alloy and Structures Technology Program", University of Virginia, Report No. UVA/528266/MS90/105, December, 1989.

9. R.P. Gangloff, "NASA-UVa Light Aerospace Alloy and Structures Technology Program", UVa Report No. UVA/528266/MS90/106, June, 1990.

10. R.P. Gangloff, "NASA-UVa Light Aerospace Alloy and Structures Technology Program", UVa Report No. UVA/528266/MS91/107, January, 1991.

11. R.P. Gangloff, "NASA-UVa Light Aerospace Alloy and Structures Technology Program", UVa Report No. UVA/528266/MS91/108, July, 1991.

12. R.P. Gangloff, "NASA-UVa Light Aerospace Alloy and Structures Technology Program", UVa Report No. UVA/528266/MS92/109, January, 1992.

13. R.P. Gangloff, "NASA-UVa Light Aerospace Alloy and Structures Technology Program", University of Virginia, Proposal No. MS NASA/LaRC-4512-90, November, 1989.

14. R.P. Gangloff, "NASA-UVa Light Aerospace Alloy and Structures Technology Program", University of Virginia, Proposal No. MS NASA/LaRC-4841-91, September, 1990.

15. R.P. Gangloff, "NASA-UVa Light Aerospace Alloy and Structures Technology Program", University of Virginia, Proposal No. MS NASA/LaRC-5219-92, October, 1991.

16. R.P. Gangloff, E.A. Starke, Jr., J.M. Howe and F.E. Wawner, "NASA-UVa Light Aerospace Alloy and Structures Technology Program: Supplement on Aluminum Based Materials for High Speed Aircraft", University of Virginia, Proposal No. MS NASA/LaRC-5215-92, October, 1991.

SUMMARY STATISTICS

Table I documents the numbers of students and faculty who participated in the LA^{2}ST Program, both during this reporting period and since the program inception in 1986. Academic and research accomplishments are indicated by the degrees awarded, publications and presentations. Specific graduate students and research associates who participated in the LA^{2}ST Program are named in Tables II and III, respectively.

TABLE I: LA^{2}ST Program Statistics

	Current 1/1/92 to 6/30/92	Cumulative 1986 to 6/30/92
PhD Students--UVa:	11	14
--NASA-LaRC:	1	1
MS Students--UVa:	2	4
--NASA:	1	1
--VPI:	0	1
Undergraduates--UVa:	2	6
--NASA-LaRC:	7	11
Faculty--UVa:	10	11
--VPI:	0	1
Research Associates--UVa:	1	4
PhD Awarded:	2	5
MS Awarded:	0	3

TABLE I: LA²ST Program Statistics (continued)

	Current 1/1/92 to 6/30/92	Cumulative 1986 to 6/30/92
Employers--NASA:	0	1
--Federal:	1	2
--University:	0	0
--Industry:	1	2
--Next degree:	0	2
Publications:	7	53
Presentations:	13	61
Dissertations/Theses:	2	8
NASA Reports:	1	12

TABLE II
GRADUATE STUDENT PARTICIPATION IN THE NASA-UVa LA^{2}ST PROGRAM
January, 1992

POS #	GRADUATE STUDENT EMPLOYER	ENTERED PROGRAM	DEGREE COMPLETED	LANGLEY RESIDENCY	RESEARCH TOPIC	UVa/NASA-LaRC ADVISORS
1.	R. S. Piascik NASA-Langley	6/86	Ph.D. 10/89		Damage Localization Mechanisms in Corrosion Fatigue of Aluminum-Lithium Alloys	R. P. Gangloff D. L. Dicus
2.	J. P. Moran NIST	9/88	Ph.D. 12/89		An Investigation of the Localized Corrosion and Stress Corrosion Cracking Behavior of Alloy 2090	G. E. Stoner W. B. Lisagor
3.	R. G. Buchheit Sandia National Laboratories	6/87	Ph.D. 12/90		Measurements and Mechanisms of Localized Aqueous Corrosion in Aluminum-Lithium Alloys	G. E. Stoner D. L. Dicus
4.	D. B. Gundel Ph.D.-UVa	9/88	M.S. 12/90		Investigation of the Reaction Kinetics Between SiC Fibers and Titanium Matrix Composites	F. E. Wawner W. B. Brewer
5.	F. Rivet (VPI)	9/88	M.S. 12/90		Deformation and Fracture of Aluminum-Lithium Alloys: The Effect of Dissolved Hydrogen	R. E. Swanson (VPI) D. L. Dicus
6.	C. Copper Ph.D.-UVa	4/89	M.S. 12/90		Design of Cryogenic Tanks for Space Vehicles	W. D. Pilkey J. K. Haviland D. R. Rummler M.J. Shuart
7.	J. A. Wagner NASA-Langley	6/87	Ph.D.	PhD Research @ LaRC	Temperature Effects on the Deformation and Fracture of Al-Li-Cu-In Alloys	R. P. Gangloff W. B. Lisagor J. C. Newman
8.	W. C. Porr, Jr. David Taylor Naval R&DC	1/88	Ph.D. 6/92		Elevated Temperature Facture of an Advanced Powder Metallurgy Aluminum Alloy	R. P. Gangloff C. E. Harris

TABLE II (continued)

GRADUATE STUDENT PARTICIPATION IN THE NASA-UVa LA^{2}ST PROGRAM

(continued)

POS #	GRADUATE STUDENT EMPLOYER	ENTERED PROGRAM	DEGREE COMPLETED	LANGLEY RESIDENCY	RESEARCH TOPIC	UVa/NASA-LaRC ADVISORS
9.	J. B. Parse Private Consultant	9/88	Ph.D. 6/92		Quantitative Characterization of the Spatial Distribution of Particles in Materials	J. A. Wert D. R. Tenney
10.	D. C. Slavik	9/89	Ph.D.		Environment Enhanced Fatigue of Advanced Aluminum Alloys and Composites	R. P. Gangloff D. L. Dicus
11.	C. L. Lach NASA-Langley	9/89	M.S.	MS Research @LaRC	Effect of Temperature on the Fracture Toughness of Weldalite^{TM} 049	R.P. Gangloff W. B. Lisagor
12.	R. J. Kilmer	11/89	Ph.D.		Effect of Zn Additions on the Environmental Stability of Alloy 8090	G. E. Stoner W. B. Lisagor
13.	M. F. Coyle	12/89	Ph.D.		Visoplastic Response of High Temperature Structures	E. A. Thornton J.H. Starnes
14.	C.J. Lissenden	9/90	Ph.D.		Inelastic Response of Metal Matrix Composites Under Biaxial Loading	C.T. Herakovich M.J. Pindera W.S. Johnson
15.	C. Cooper	1/91	Ph.D.		Shell Structures Analytical Modeling	W. D. Pilkey J. K. Haviland M. Shuart J. Stroud

TABLE II (continued)

GRADUATE STUDENT PARTICIPATION IN THE NASA-UVa LA^{2}ST PROGRAM
(continued)

16.	Douglas Wall	Ph.D.	4/91	Measurements and Mechanisms of Localized Corrosion in Al-Li-Cu Alloys	G. E. Stoner / D. L. Dicus
17.	S. W. Smith	Ph.D.	4/91	Hydrogen Interactions with Al-Li Alloys	J. R. Scully / W. B. Lisagor
18.	D. B. Gundel	Ph.D.	4/91	Effect of Thermal Exposure on the Mechanical Properties of Titanium/SiC Composites	F. E. Wawner / W. B. Brewer
19.	K. McCarthy	MS	5/91	Shell Structures Analytical Modeling	W. D. Pilkey / M. J. Shuart / J. Stroud
20.	M. Lyttle	MS	12/91	Superplasticity in Al-Li-Cu Alloys	J. A. Wert / T. Bayles
21.	T. Johnson (NASA Minority Grantee)	Ph.D.	12/91	Shell Structures Analytical Modeling	W. D. Pilkey / M. J. Shuart / J. Stroud

TABLE III
Post-Doctoral Research Associate Participation
in NASA-UVA LA^{2}ST Program

Pos #	Res. Assoc.	Tenure	Research	Supervisor
1.	Yang Leng	3/89 to 12/91	Elevated Tempera- ture Deformation and Fracture of PM AL Alloys and Composites	R. P. Gangloff
2.	Farshad Mizadeh	7/89 to 12/91	Deformation of Metal Matrix Composites	C. T. Herakovich and Marek-Jerzy Pindera
3.	A.K.Mukhopadhyay	6/91 to 6/92	Aluminum Alloy Development	E. A. Starke, Jr.
4.	Sang-Shik Kim	12/91 to present	Environmental Fatigue Life Prediction	R. P. Gangloff

GRANT PUBLICATIONS (REFEREED JOURNALS AND ARCHIVAL PROCEEDINGS)

The following papers were based on research conducted under LA^{2}ST Program support, and were published in the referred or archival literature.

25. J.B. Parse and J.A. Wert, "A Geometrical Description of Particle Distributions in Materials", Modeling and Simulation in Materials Science and Engineering, in review, 1992.

24. J.B. Parse and J.A. Wert, "Effects of Deformation Processing in the Oxide Particle Distribution in PM Al Alloy Sheet", Metallurgical Transactions, in review, 1992.

23. W.C. Porr, Jr. and R.P. Gangloff, "Elevated Temperature Fracture of RS/PM Alloy 8009: Part I - Fracture Mechanics Behavior", Metall. Trans. A, in review (1992).

22. R.S. Piascik and R.P. Gangloff, "Environmental Fatigue of an Al-Li-Cu Alloy: Part III - Modeling of Crack Tip Hydrogen Damage", Metall. Trans. A, in review (1992).

21. R.S. Piascik and R.P. Gangloff, "Environmental Fatigue of an Al-Li-Cu Alloy: Part II - Microscopic Hydrogen Cracking Processes", Metall. Trans. A, in review (1992).

20. J.A. Wagner and R.P. Gangloff, "Fracture Toughness of Al-Li-Cu-In Alloys", Scripta Metallurgica et Materialia, Vol. 26, pp. 1779-1784 (1992).

19. R.P. Gangloff, R.S. Piascik, D.L. Dicus and J.C. Newman, "Fatigue Crack Propagation in Aerospace Aluminum Alloys", Journal of Aircraft, in review (1992).

18. R.G. Buchheit, Jr., J.P. Moran, F.D. Wall, and G.E. Stoner, "Rapid Anodic Dissolution Based SCC of 2090 (Al-Li-Cu) by Isolated Pit Solutions," Proceedings, Parkins Symposium on Stress Corrosion Cracking, TMS-AIME, Warrendale, PA, in press (1991).

17. R.J. Kilmer, T.J. Witters and G.E. Stoner, "Effect of Zn Additions on the Precipitation Events and Implications to Stress Corrosion Cracking Behavior in Al-Li-Cu-Mg-Zn Alloys", Proceedings of the Sixth International Al-Li Conference, in press (1991).

16. C.J. Lissenden, M-J. Pindera, and C.T. Herakovich, "Stiffness Degradation of SiC/Ti Tubes Subjected to Biaxial Loading with Damage", Int. J. Composites Science and Technology, in press (1991).

15. E.A. Thornton and J.D. Kolenski, "Viscoplastic Response of Structures with Intense Local Heating", Journal of Aerospace Engineering, in press (1991).

14. C.T. Herakovich and J.S. Hidde, "Response of Metal Matrix Composites with Imperfect Bonding", <u>Ultramicroscopy</u>, in press (1991).

13. R.P. Gangloff, D.C. Slavik, R.S. Piascik and R.H. Van Stone, "Direct Current Electrical Potential Measurement of the Growth of Small Fatigue Cracks", in <u>Small Crack Test Methods, ASTM STP 1149</u>, J.M. Larsen and J.E. Allison, eds., ASTM, Philadelphia, PA, pp. 116-168 (1992).

12. R.J. Kilmer and G.E. Stoner, "The Effect of Trace Additions of Zn on the Precipitation Behavior of Alloy 8090 During Artificial Aging", <u>Proceedings, Light Weight Alloys for Aerospace Applications II</u>, E.W. Lee, ed., TMS-AIME, Warrendale, PA, pp. 3-15, 1991.

11. W.C. Porr, Jr., Anthony Reynolds, Yang Leng and R.P. Gangloff, "Elevated Temperature Cracking of RSP Aluminum Alloy 8009: Characterization of the Environmental Effect", <u>Scripta Metallurgica et Materialia</u>, Vol. 25, pp. 2627-2632 (1991).

10. J. Aboudi, J.S. Hidde and C.T. Herakovich, "Thermo-mechanical Response Predictions for Metal Matrix Composites", in <u>Mechanics of Composites at Elevated and Cryogenic Temperatures</u>, S.N. Singhal, W.F. Jones and C.T. Herakovich, eds., ASME AMD, Vol. 118, pp. 1-18 (1991).

9. R.S. Piascik and R.P. Gangloff, "Environmental Fatigue of an Al-Li-Cu Alloy: Part I - Intrinsic Crack Propagation Kinetics in Hydrogenous Environments", <u>Metall. Trans. A</u>, Vol. 22A, pp. 2415-2428 (1991).

8. W.C. Porr, Jr., Y. Leng, and R.P. Gangloff, "Elevated Temperature Fracture Toughness of P/M Al-Fe-V-Si", in <u>Low Density, High Temperature Powder Metallurgy Alloys</u>, W.E. Frazier, M.J. Koczak, and P.W. Lee, eds., TMS-AIME, Warrendale, PA, pp. 129-155 (1991).

7. Yang Leng, William C. Porr, Jr. and Richard P. Gangloff, "Time Dependent Crack Growth in P/M Al-Fe-V-Si at Elevated Temperatures", <u>Scripta Metallurgica et Materialia</u>, Vol. 25, pp. 895-900 (1991).

6. R.J. Kilmer and G.E. Stoner, "Effect of Zn Additions on Precipitation During Aging of Alloy 8090", <u>Scripta Metallurgica et Materialia</u>, Vol. 25, pp. 243-248 (1991).

5. D.B. Gundel and F.E. Wawner, "Interfacial Reaction Kinetics of Coated SiC Fibers", <u>Scripta Metallurgica et Materialia</u>, Vol. 25, pp. 437-441 (1991).

4. R.G. Buchheit, Jr., J.P. Moran and G.E. Stoner, "Localized Corrosion Behavior of Alloy 2090-The Role of Microstructural Heterogeneity", <u>Corrosion</u>, Vol. 46, pp. 610-617 (1990).

3. Y. Leng, W.C. Porr, Jr. and R.P. Gangloff, "Tensile Deformation of 2618 and Al-Fe-Si-V Aluminum Alloys at Elevated Temperatures", <u>Scripta Metallurgica et Materialia</u>, Vol. 24, pp. 2163-2168 (1990).

2. R.P. Gangloff, "Corrosion Fatigue Crack Propagation in Metals", in <u>Environment Induced Cracking of Metals</u>, R.P. Gangloff and M.B. Ives, eds., NACE, Houston, TX, pp. 55-109 (1990).

1. ·R.S. Piascik and R.P. Gangloff, "Aqueous Environment Effects on Intrinsic Corrosion Fatigue Crack Propagation in an Al-Li-Cu Alloy", in <u>Environment Induced Cracking of Metals</u>, R.P. Gangloff and M.B. Ives, eds., NACE, Houston, TX, pp. 233-239 (1990).

COMPLETED PROJECTS

1. DAMAGE LOCALIZATION MECHANISMS IN CORROSION FATIGUE OF
    ALUMINUM-LITHIUM ALLOYS
    Faculty Investigator: R.P. Gangloff
    Graduate Student: Robert S. Piascik
    Degree: PhD
    UVa Department: Materials Science and Engineering
    NASA-LaRC Contact: D. L. Dicus (Metallic Materials)
    Start Date: June, 1986
    Completion Date: November, 1989
    Employment: NASA-Langley Research Center

2. AN INVESTIGATION OF THE LOCALIZED CORROSION AND STRESS
    CORROSION CRACKING BEHAVIOR OF ALLOY 2090 (Al-Li-Cu)
    Faculty Investigator: Glenn E. Stoner
    Graduate Student: James P. Moran
    Degree: PhD
    UVa Department: Materials Science and Engineering
    NASA-LaRC Contact: W.B. Lisagor (Metallic Materials)
    Start Date: September, 1988
    Completion Date: December, 1989
    Co-Sponsor: ALCOA
    Employment: ALCOA Laboratories

3. MECHANISMS OF LOCALIZED CORROSION IN AL-LI-CU ALLOY 2090
    Faculty Investigator: G.E. Stoner
    Graduate Student: R.G. Buchheit
    Degree: PhD
    UVa Department: Materials Science and Engineering
    NASA-LaRC Contact: D.L. Dicus (Metallic Materials)
    Start Date: June, 1987
    Completion Date: December, 1990
    Cosponsor: Alcoa
    Employment: Sandia National Laboratories

4. DEFORMATION AND FRACTURE OF ALUMINUM-LITHIUM ALLOYS: THE
    EFFECT OF DISSOLVED HYDROGEN
    Faculty Investigator: R.E. Swanson (VPI)
    Graduate Student: Frederic C. Rivet
    Degree: MS
    VPI Department: Materials Engineering
    NASA-LaRC Contact: D.L. Dicus (Metallic Materials)
    Start Date: September, 1988
    Completion Date: December, 1990
    Employment: Not determined

PAGE __14__ INTENTIONALLY BLANK

5.   INVESTIGATION OF THE REACTION KINETICS BETWEEN SiC FIBERS AND SELECTIVELY ALLOYED TITANIUM MATRIX COMPOSITES AND DETERMINATION OF THEIR MECHANICAL PROPERTIES
   Faculty Investigator: F.E. Wawner
   Graduate Student: Douglas B. Gundel
   Degree: MS
   UVa Department: Materials Science and Engineering
   NASA-LaRC Contact: D.L. Dicus and W.B. Brewer (Metallic Materials)
   Start Date: January, 1989
   Completion Date: December, 1990
   Employment: Graduate School, University of Virginia; PhD candidate on
                 LA^{2}ST Program; Department of Materials Science

6.   DESIGN OF CRYOGENIC TANKS FOR SPACE VEHICLES
   Faculty Investigators: W.D. Pilkey and J.K. Haviland
   Graduate Student: Charles Copper
   Degree: MS
   UVa Department: Mechanical and Aerospace Engineering
   NASA-LaRC Contact: D.R. Rummler (Structural Mechanics Division), R.C.
                 Davis and M.J. Shuart (Aircraft Structures)
   Start Date: April, 1989
   Completion Date: December, 1990
   Employment: Graduate School, University of Virginia; PhD candidate on NASA-
                 Headquarters sponsored program; Department of Mechanical and
                 Aerospace Engineering

7.   ELEVATED TEMPERATURE FRACTURE OF AN ADVANCED RAPIDLY SOLIDIFIED, POWDER METALLURGY ALUMINUM ALLOY
   Faculty Investigator: R.P. Gangloff
   Graduate Student: William C. Porr, Jr.
   UVa Department: Materials Science and Engineering
   NASA-LaRC Contact: C.E. Harris (Mechanics of Materials)
   Start Date: January, 1988
   Completion Date: June, 1992
   Employment: David Taylor Naval Ship R&D Center

8.   QUANTITATIVE CHARACTERIZATION OF THE SPATIAL DISTRIBUTION OF PARTICLES IN MATERIALS: APPLICATION TO MATERIALS PROCESSING
   Faculty Investigator: John A. Wert
   Graduate Student: Joseph Parse
   UVa Department: Materials Science and Engineering
   NASA-LaRC Contact: D.R. Tenney (Materials Division)
   Start Date: September, 1988
   Completion Date: June, 1992
   Employment: Private Consultant

ADMINISTRATIVE PROGRESS

Faculty Participation

There were no changes in the faculty participants during this reporting period.

Brochure

The brochure prepared in March of 1991 was employed to advertise the LA^{2}ST program during this reporting period. About 150 copies were nationally distributed to stimulate graduate and undergraduate recruitment. All layout, printing and mailing costs were paid by the School of Engineering and Applied Science at UVa.

Student Recruitment

The LA^{2}ST Program continues to recruit the best graduate students entering the participating Departments at UVa, and in sufficient numbers to achieve our education and research objectives. Two graduate students were recruited to join the LA^{2}ST Program in the Summer of 1992. Mr. Mark Mason, a recent BS graduate in Mechanical Engineering from Duke University, will conduct MS research on an environmental fracture program. This work, emphasizing titanium alloys, and will be supervised by Professor Gangloff and monitored by Drs. Piascik and Newman of the Mechanics of Materials Branch. Mr. Michael J. Haynes, a recent BS graduate in Metallurgy and Materials Science from Rensselaer Polytechnic Institute, will conduct MS research on elevated temperature deformation and fracture of advanced aluminum alloys. This work will be supervised by Professor Gangloff and will be defined in the 1993 renewal proposal.

In April of 1990, the LA^{2}ST Program was increased in scope to include undergraduate engineering students[2]. While four students from North Carolina State and California Polytechnic State Universities, worked at NASA-LaRC during the Summer of 1990, there were no qualified applicants for the 1991 program. Efforts to recruit undergraduates for the Summer of 1992 were intensified and entrance criteria were stiffened.

Undergraduate Research Participation

The following 7 undergraduates are being employed at NASA-LaRC under the auspices of our LA^{2}ST Program. Each student is a rising senior in an engineering or science major closely related to aerospace materials and mechanics.

17

STUDENT	UNIVERSITY	MAJOR	GPA (A = 4.0)
Samir Tamer	Duke	Mech. Engr.	3.5
John McEntyre	Georgia Tech.	Matls. Sci.	3.6
Matthew Groves	Univ. of MO	Metall. Engr.	3.6
Deborah Pilkey	Duke	Civil Engr.	3.3
Michael McCormick	VPI	Matls. Sci.	3.0
Stefanie Chiras	Harvard	Engr. Sci.-Mech. Engr.	3.4
Katherine Whitin	Harvard	Engr. Sci.-Mech. Engr.	3.7

Additionally, two undergraduates are being supervised by Professors Wert and Wawner at UVa.

Complementary Programs at UVa

The School of Engineering and Applied Science at UVa has targeted materials and structures research for aerospace applications as an important area for broad future growth. The LA^{2}ST Program is an element of this thrust. Several additional programs are of benefit to LA^{2}ST work.

The Board of Visitors at UVa awarded SEAS an Academic Enhancement Program Grant in the area of Light Thermal Structures. The aim is to use University funds to seed the establishment of a world-class center of excellence which incorporates several SEAS Departments. This program is lead by Professor Thornton and directly benefits NASA.

The Light Metals Center has existed within the Department of Materials Science at UVa for the past several years under the leadership of Professor H.G.F. Wilsdorf, and upon his retirement, by Dean Starke. A Virginia Center for Innovative Technology Development Center in Electrochemical Science and Engineering was established in 1988 with Professor G.E. Stoner as Director. Professors Pilkey, Thornton and Gangloff are conducting research under NASA-Headquarters Grant sponsorship to examine "Advanced Concepts for Metallic

Cryo-thermal Space Structures"[3,4]. Research within this program is complementing LA[2]ST studies.

References

1. R.P. Gangloff, E.A. Starke, Jr., J.M. Howe and F.E. Wawner, "NASA-UVa Light Aerospace Alloy and Structures Technology Program: Supplement on Aluminum Based Materials for High Speed Aircraft", University of Virginia, Proposal No. MS NASA/LaRC-5215-92, October, 1991.

2. R.P. Gangloff, "NASA-UVa Light Aerospace Alloy and Structures Technology Program: A Supplementary Proposal", University of Virginia, Proposal No. MS NASA/LaRC-4677-90, April, 1990.

3. W.P. Pilkey, "Advanced Concepts for Metallic Cryo-thermal Space Structures", University of Virginia Proposal No. MAE-NASA/HQ-4462-90, August, 1989.

4. W.P. Pilkey, "Advanced Concepts for Metallic Cryo-thermal Space Structures", University of Virginia Report No. UVA/528345/MAE91/101, February, 1991.

MECHANICAL AND ENVIRONMENTAL DEGRADATION MECHANISMS IN ADVANCED LIGHT METALS AND COMPOSITES

1. ENVIRONMENTAL FATIGUE CRACK GROWTH AND CRACKING MECHANISMS IN Al-Li-Cu Alloy 2090
   Faculty Investigator: R.P. Gangloff
   Graduate Student: Donald Slavik; PhD Candidate
   UVa Department: Materials Science and Engineering (MS&E)
   NASA-LaRC Contact: D.L. Dicus (Metallic Materials)
   Start Date: September, 1989
   Anticipated Completion Date: December, 1992
   Project #1

2. ENVIRONMENTAL EFFECTS IN FATIGUE LIFE PREDICTION: MODELING CRACK PROPAGATION IN TITANIUM ALLOYS
   Faculty Investigator: R.P. Gangloff
   Graduate Student: Mark Mason; MS Candidate
   Post Doctoral Research Associate: Dr. Sang-Shik Kim
   UVa Department: MS&E
   NASA-LaRC Contact: R.S. Piascik (Mechanics of Materials)
   Start Date: January, 1992
   Anticipated Completion Date: December, 1994
   Project #2

3. ELEVATED TEMPERATURE FRACTURE OF AN ADVANCED RAPIDLY SOLIDIFIED, POWDER METALLURGY ALUMINUM ALLOY
   Faculty Investigator: R.P. Gangloff
   Graduate Student: William C. Porr, Jr.; PhD candidate
   UVa Department: MS&E
   NASA-LaRC Contact: C.E. Harris (Mechanics of Materials)
   Start Date: January, 1988
   Anticipated Completion Date: June, 1992
   Project #3

4. ELEVATED TEMPERATURE DAMAGE TOLERANCE OF ADVANCED POWDER METALLURGY ALUMINUM ALLOYS
   Faculty Investigator: R.P. Gangloff
   Graduate Student: Michael Haynes
   UVa Department: MS&E
   NASA-LaRC Contact: To be determined
   Start Date: September, 1992   (New project not reported here)
   Completion Date: December, 1994
   Project #4

5. CRYOGENIC TEMPERATURE EFFECTS ON THE DEFORMATION AND FRACTURE OF Al-Li-Cu and Al-Li-Cu-In ALLOYS
   Faculty Investigator: R.P. Gangloff
   Graduate Student: John A. Wagner; PhD candidate and NASA-LaRC
                     employee
   UVa Department: MS&E
   NASA-LaRC Contacts: W.B. Lisagor (Metallic Materials) and J.C. Newman
                     (Mechanics of Materials)
   Start Date: June, 1987
   Anticipated Completion Date: May, 1993
   Project #5

6. THE EFFECT OF CRYOGENIC TEMPERATURE ON THE FRACTURE TOUGHNESS OF WELDALITE™
   Faculty Investigator: R.P. Gangloff
   Graduate Student: Cynthia L. Lach; MS candidate and NASA-LaRC employee
   UVa Department: MS&E
   NASA-LaRC Contacts: W.B. Lisagor (Metallic Materials)
   Start Date: August, 1990
   Anticipated Completion Date: May, 1993
   Project #6

7. MECHANISMS OF LOCALIZED CORROSION IN Al-Cu-Li-Mg-Ag ALLOY X2095 AND COMPOSITIONAL VARIATIONS .
   Faculty Investigator: G.E. Stoner
   Graduate Student: Douglas Wall; PhD candidate
   UVa Department: MS&E
   NASA-LaRC Contact: D.L. Dicus (Metallic Materials)
   Start Date: April, 1991
   Completion Date: May, 1994
   Cosponsor: Reynolds Metals Company
   Project #7

8. EFFECTS OF Zn ADDITIONS ON THE PRECIPITATION AND STRESS CORROSION CRACKING BEHAVIOR OF ALLOY 8090

        Faculty Investigator: Glenn E. Stoner
        Graduate Student: Raymond J. Kilmer; PhD candidate
        Department: MS&E
        NASA-LaRC Contact: W.B. Lisagor (Metallic Materials)
        Start Date: September, 1989
        Anticipated Completion Date: December, 1992
        Cosponsor: Alcoa
        Project #8

9. HYDROGEN INTERACTIONS IN ALUMINUM-LITHIUM ALLOY 2090 AND SELECTED COMPLIMENTARY MODEL ALLOYS

        Faculty Investigator: John R. Scully
        Graduate Student: Stephen W. Smith; PhD Candidate
        Department: MS&E
        NASA-LaRC Contact: W.B. Lisagor and D.L. Dicus (Metallic Materials)
        Start Date: April, 1991
        Anticipated Completion Date: To be determined
        Cosponsor: Virginia CIT
        Project #9

10. METASTABLE PITTING OF Al ALLOYS

        Faculty Investigators: John R. Scully and J.L. Hudson
        Graduate Student: Sheldon T. Pride; PhD Candidate
        Department: Chemical Engineering
        NASA-LaRC Contact: D.L. Dicus (Metallic Materials)
        Start Date: September, 1991
        Anticipated Completion Date: To be determined
        Cosponsor: NASA Graduate Student Researchers Program;
                      Underrepresented Minority Emphasis
        Project #9a

AEROSPACE MATERIALS SCIENCE

11. INVESTIGATION OF THE EFFECT OF THERMAL TREATMENT ON THE MECHANICAL PROPERTIES OF Ti-1100/SCS-6 COMPOSITES

        Faculty Investigator: F.E. Wawner
        Graduate Student: Douglas B. Gundel; PhD candidate
        UVa Department: MS&E
        NASA-LaRC Contact: D.L. Dicus and W.B. Brewer (Metallic Materials)
        Start Date: April, 1991
        Anticipated Completion Date: June, 1993
        Project #10

12. QUANTITATIVE CHARACTERIZATION OF THE SPATIAL DISTRIBUTION OF PARTICLES IN MATERIALS: APPLICATION TO MATERIALS PROCESSING
Faculty Investigator: John A. Wert
Graduate Student: Joseph Parse; PhD candidate
UVa Department: Materials Science
NASA-LaRC Contact: D.R. Tenney (Materials Division)
Start Date: September, 1988
Anticipated Completion Date: June, 1992
Project #11

13. PROCESSING AND SUPERPLASTIC PROPERTIES OF WELDALITE™ SHEET
Faculty Investigator: John A. Wert
Graduate Student: Mark Lyttle; MS Candidate
UVa Department: MS&E
NASA-LaRC Contact: T. Bayles (Metallic Materials)
Start Date: September, 1991
Anticipated Completion Date: September, 1993
Project #12

MECHANICS OF MATERIALS FOR AEROSPACE STRUCTURES

14. INELASTIC DEFORMATION OF METAL MATRIX COMPOSITES
Faculty Investigators: Carl T. Herakovich and Marek-Jerzy Pindera
Graduate Student: Mr. Clifford J. Lissenden, PhD Candidate
UVa Department: Civil Engineering and the Applied Mechanics Program
NASA-LaRC Contact: W.S. Johnson (Mechanics of Materials)
Start Date: September, 1990
Anticipated Completion Date: May, 1993
Project #13

THERMAL GRADIENT STRUCTURES

15. EFFECT OF TEMPERATURE ON THE RESPONSE OF METALLIC SHELL
    STRUCTURES
    Faculty Investigators: W.D. Pilkey and J.K. Haviland
    Graduate Student: Karen McCarthy; MS candidate
    Graduate Student: Theodore Johnson; PhD candidate (NASA Minority
                 Grantee)
    Graduate Student: Charles Copper; PhD Candidate
    UVa Department: Mechanical and Aerospace Engineering
    NASA-LaRC Contact: Drs. M.J. Shuart and Jeffrey Stroud (Aircraft
                 Structures)
    Start Date: April, 1991
    Anticipated Completion Date: December, 1992
    Project #14

16. EXPERIMENTAL STUDY OF THE NONLINEAR VISCOPLASTIC RESPONSE
    OF HIGH TEMPERATURE STRUCTURES
    Faculty Investigator: Earl A. Thornton
    Graduate Student: Marshall F. Coyle; PhD candidate
    Undergraduate Student: Ms. Yool Kim
    UVa Department: Mechanical and Aerospace Engineering
    NASA-LaRC Contact: James H. Starnes, Jr. (Aircraft Structures)
    Start Date: January, 1990
    Anticipated Completion Date: To be determined
    Project #15

Research progress, recorded during the period from January 1, 1992 to June 30, 1992, is summarized by Project in the following sections. Each program section contains a brief narrative of objective, recent progress, conclusions and immediate milestones; coupled with the visual aids presented at the Third Annual NASA-UVa LA²ST Grant Review Meeting held at NASA-LaRC in July of 1992 (Appendix V).

Project 1   **Environmental Fatigue Crack Growth and Cracking Mechanisms in Al-Li-Cu Alloy 2090**

Donald C. Slavik and Richard P. Gangloff

Objective

The broad objectives of this PhD research are: (a) to expand the environmental fatigue data base with intrinsic and chemically correct FCP data for Al-Li-Cu alloys, (b) to physically understand intrinsic process zone damage, and (c) to incorporate observations into an environmental fatigue crack growth rate model.

Approach

During this reporting period, we have aimed to understand how alloy texture, microstructure, and environment influence fatigue crack growth rates and microscopic damage mechanisms for AA2090.

Vintage III AA2090 unrecrystallized sheet, unrecrystallized plate, fine grain recrystallized sheet, and coarse grain recrystallized sheet were fabricated utilizing thermo-mechanical processing histories. Fine microstructural details were investigated with a Phillips EM400 transmission electron microscope (TEM). Environmental fatigue crack growth conditions include a high purity 5 μPa pressure vacuum and an aqueous 1 wt% NaCl solution at a constant electrode potential of -840 mV$_{SCE}$. Closed loop computer controlled fatigue crack growth rate experiments at constant K_{max} of 17 MPa$\sqrt{m}$ were utilized to provide intrinsic fatigue crack growth rates.

Global macroscopic textures were determined with X-ray diffraction. Individual grain

and subgrain orientations were established with electron backscattering patterns (EBSP) employing the Dingley method with a submicron beam size. Micro-pole figures were generated by comparing these diffraction patterns with Kikuchi maps. The environmental influence on fracture facet crystallography will be presented. Microscopic damage mechanisms and correlations with intrinsic fatigue crack growth rates will be established.

Current Status

Precipitates, subgrain size, and grain size were characterized with TEM and polarized light optical microscopy. Intrinsic fatigue crack growth rates were measured for the various commercial and model alloys in ultra-high purity vacuum and an aggressive aqueous NaCl environment.

Limited EBSP and micro-pole figures were obtained through collaboration with Drs. S. Miyasato and J. Liu at the ALCOA Technical Center. In collaboration with Professor Wert, we are working to make a similar system operational at UVa. Kikuchi patterns were observed at UVa on a phosphor screen with a low light camera, and image processing hardware. The relationships between the Kikuchi patterns and the micro-pole figures are currently being pursued.

Recent Findings

Tortuous tent-shaped facets are observed for inert environment fatigue cracking for all AA2090 microstructures independent of ΔK. The inert environment fatigue facet crystallography was measured as {100} and {110} for unrecrystallized 2090 plate. This result is completely different from published etch pit results and semiquantitative macroscopic X-ray studies of fatigue facet orientation. These finding are currently being confirmed. The inert environment fatigue crack growth rates were similar for the unrecrystallized and fine grain recrystallized alloy, and were enhanced by 2 times on da/dN for the coarse grain recrystallized microstructures. Mild crack growth rate differences can be related to slip length and crack tip opening displacement differences for the various Al-Li-Cu alloys.

A research effort was undertaken in conjunction with Drs. C.P. Blankenship, Jr. and E.A. Starke, Jr. to understand how the precipitate type influences inert environment fatigue cracking of AA2024, AA2090, AA8090, X2095. Tortuous tent-shaped facets formed in all lithium bearing alloys, independent of the coherent shearable δ' precipitate being present.

This is a major difference from published results which link tortuous {111} facets and localized slip from δ' precipitates. These findings are currently under further study. Fatigue crack growth rates were alloy dependent, varying by 10-fold on da/dN. A cyclic crack tip opening displacement (CCTOD) parameter ($\Delta K/\sqrt{}/(E\,\sigma_y)$) collapsed the data into a single curve for all alloys except X2095. Further work is being performed to determine if the cracking behavior of X2095 is intrinsic, or related to reversible slip and crack closure interactions.

Aqueous NaCl fatigue crack growth rates were established for the various microstructures of AA2090. Intersubgranular cracking and interfacet tearing are observed at high and intermediate ΔK for unrecrystallized AA2090. Flat stepped transgranular facts are observed in unrecrystallized plate and coarse grain recrystallized AA2090 at low ΔK. Based on the backscattered electron channelling work, the facet crystallography was not {100} as suggested by etch pit results. These results will be confirmed.

Fatigue crack growth rates for the unrecrystallized and the fine grain recrystallized microstructures are similar. The fatigue crack growth rates are reduced by 2X on da/dN in the coarse grain recrystallized microstructures. Microscopic cracking mechanisms will be used to explain fatigue crack growth rate trends.

Milestones

Micro-pole figure capabilities from EBSPs and Kikuchi maps will be fully operational at UVa during the next reporting period. Quantitative tilt fractography and the micro-pole figure analysis will be performed for different environmental fatigue crack growth samples to conclusively establish facet crystallography. Mechanistic models that relate to measured facet crystallography will be developed. These results will lead to an accurate interpretation of the microscopic damage modes of AA2090. Damage will be correlated with intrinsic fatigue crack growth rates.

Presentation Graphics Captions

1.   Title.

2.   Literature background.

3.   Environmental fatigue crack growth rate questions for Al-Li-Cu alloys with Vintage III 2090 sheet crack growth rate data.

4. The experimental approach to answer the questions. This slide also provides a general outline for the talk.

5. This slide shows the different AA2090 microstructures produced in this research by controlled thermomechanical processing applied to commercial Vintage III plate alloy. Keller's etch highlights the particles on the high angle grain boundaries for the unrecrystallized alloys. A fine subgrain structure is present in the unrecrystallized alloys. Barker's etch highlights different grain orientations for the recrystallized alloys.

6. Specimen and fatigue crack surface facet orientation for T-plane sections.

7. Tent-shaped facets are observed on the fatigue crack surfaces of Al-Li-Cu alloys, cyclically loaded in vacuum, independent on the presence of the coherent shearable δ' precipitate.

8. Multiple $\{111\}$ systems are oriented for slip; different $\{111\}$ cracking planes can be activated within a single grain and produce a tent facet similar to that developed by cracking across a high angle grain boundary between two variants of the $\{111\}$ texture.

9. Electron backscattered channelling and fracture surface facet orientation measurements indicate that multiple cracking planes form in a single grain, but that the facets are nearly parallel to $\{100\}$ not $\{111\}$.

10. The subgrain structure and fine grain recrystallized microstructure do not influence da/dN for inert vacuum. Fatigue crack growth rates are mildly enhanced for the coarse grain recrystallized microstructure which has the longest slip length and lowest yield stress.

11. Fatigue crack growth rates are observed to be alloy dependent various Al-Cu-Li compositions. The fatigue crack growth rates scale with the yield stress or the cyclic crack tip opening displacement.

12. The conclusions of the inert environmental fatigue crack growth study.

13. Questions associated with aqueous environment sensitive fatigue cracking modes in Al-Li-Cu alloys.

14. SEM characterization of the effect of ΔK (or da/dN) on fatigue fracture surface morphology for Vintage III alloy 2090 sheet (unrecrystallized) in 1% NaCl.

15. SEM characterization of the effect of ΔK (or da/dN) on fatigue fracture surface morphology for Vintage III alloy 2090 plate (unrecrystallized) in 3% NaCl.

16. The T-plane section shows the stepped facet orientation. The polished face micro-pole figure is shown below, and is consistent with the macroscopic X-ray pole figure for this alloy. The facet is not parallel to {100}.

17. Fatigue crack growth rates for each microstructure of alloy 2090 in aqueous 1 wt% NaCl are shown. The inert environment crack growth rates are represented by the solid line for comparison. The fatigue crack growth rates for the unrecrystallized and fine grain recrystallized alloys are similar. These alloys all have an easy boundary crack path for fatigue cracking at high ΔK. The coarse grain recrystallized crack path is transgranular and the crack growth rates are reduced. Different cracking modes lead to different fatigue crack growth rates. It is not understood why the crack growth rates are different in unrecrystallized plate and recrystallized coarse grain microstructures when both crack paths are transgranular. The facet crystallography will be measured which will hopefully clarify this discrepancies.

18. The conclusions of the aqueous environment fatigue crack growth study.

19. Future work.

Environmental Fatigue Crack Growth Rates
and
Cracking Mechanisms for AA2090

D.C. Slavik and R.P. Gangloff
University of Virginia

Unrecrystallized Al-Li-Cu Background

Inert Environment Cracking

o Coherent shearable δ' (Al$_3$Li) localize slip into bands

o Cracking along localized slip bands

   - Facets on {111} planes favored for slip

   - Texture leads to tortuous tent-shaped facets

Environmental Cracking

o H-embrittlement and/or anodically active T$_1$ (Al$_2$CuLi)

o Different fracture mechanism possible

   - Cracking along T$_1$ {111} habit or sub-boundary T$_1$

   - Hydride cracks along {100}

   - Hydrogen decohesion

   - Hydrogen enhanced plasticity

Are these concepts correct?

Environmental Fatigue Crack Growth of Al-Li-Cu

o **Does microstructure influence da/dN?**
  - Grain size
  - Subgrain size
  - Precipitates

o **What are the microscopic cracking mechanisms?**
  - Environmental influence
  - Facet crystallography
  - Texture

o **Do relationships exist between microstructure, cracking mode, and da/dN?**

2090 Sheet
Vintage III

da/dN (mm/cycle) vs ΔK (MPa$-$m$^{1/2}$)

o Vacuum
△ 1wt% NaCl
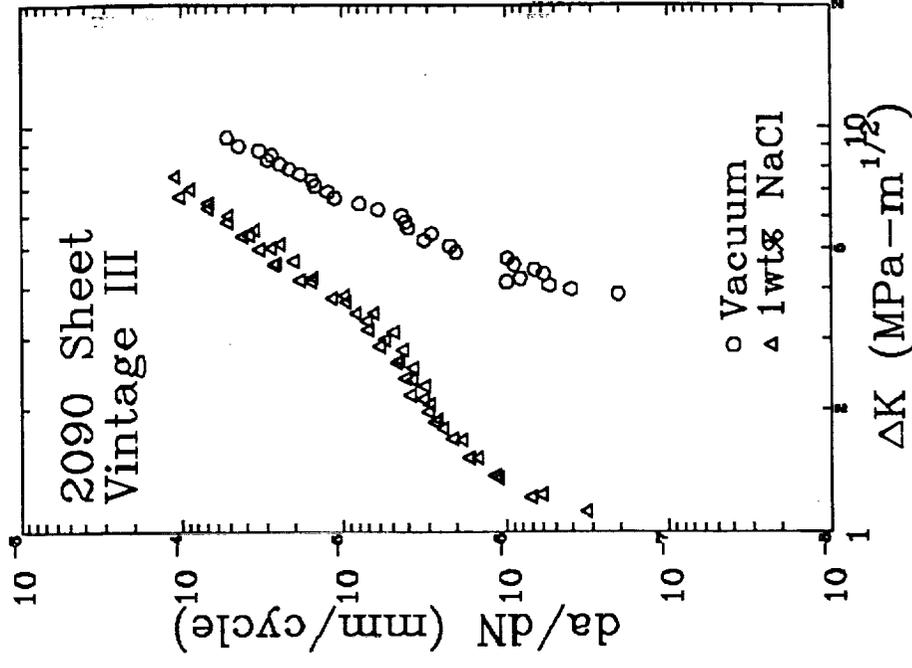
Experimental Approach

o **Alter microstructure with thermo-mechanical processing**
  - Unrecrystallized sheet and plate
  - Fine and coarse grain recrystallized

o **Determine facet orientations**
  - Combined T-plane sections and fractography
  - Quantitative tilt fractography

o **Identify microscopic damage mechanisms**
  - Electron backscattering patterns for crystallography

o **Measure global fatigue crack growth rates**
  - Inert and aggressive environments

o **Relate microscopic damage mechanisms to da/dN**

AA2090 Microstructures (L-Plane)

Unrecrystallized Sheet

Unrecrystallized Plate
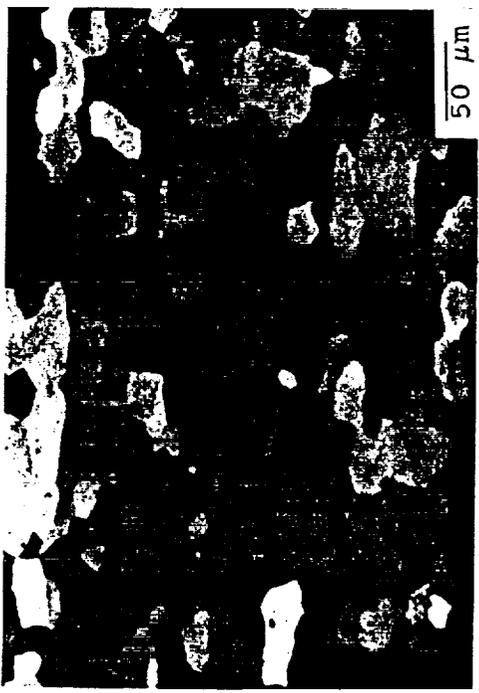
Recrystallized Sheet

Recrystallized Sheet

50 μm
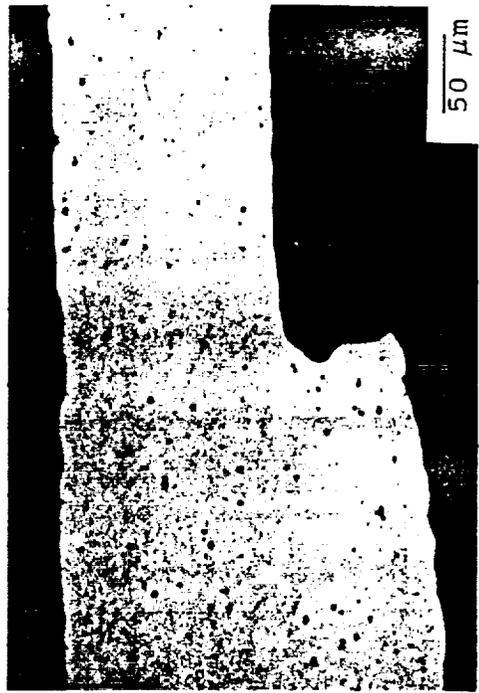
Facet Crystallographic Analysis
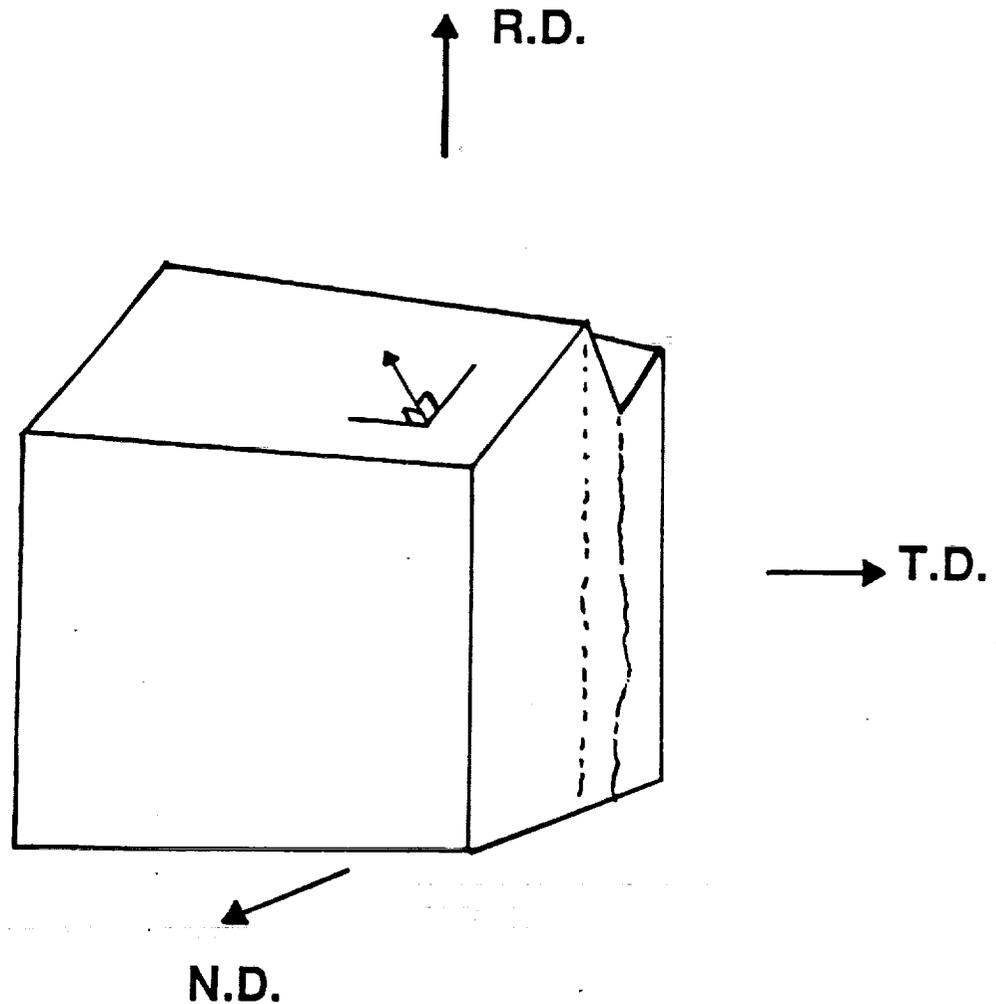
- Facet pole from quantitative multiple tilt fractography
- Grain orientation from electron channeling of polished surface

Inert Environment Cracking Modes

Are tent-shaped facets slip band cracks due to δ' and localized slip?

AA2090 T8E41
(with δ')

X2095 T8
(without δ')

Inert environment facets form independent of δ'

Inert Environment Cracking Modes

Why do the tent-shaped facets form?

Literature suggests {111} persistent slip bands for unrecrystallized alloys

- Facet angles and texture
- Etch pits

{111} Pole Figure

R.D.

T.D.
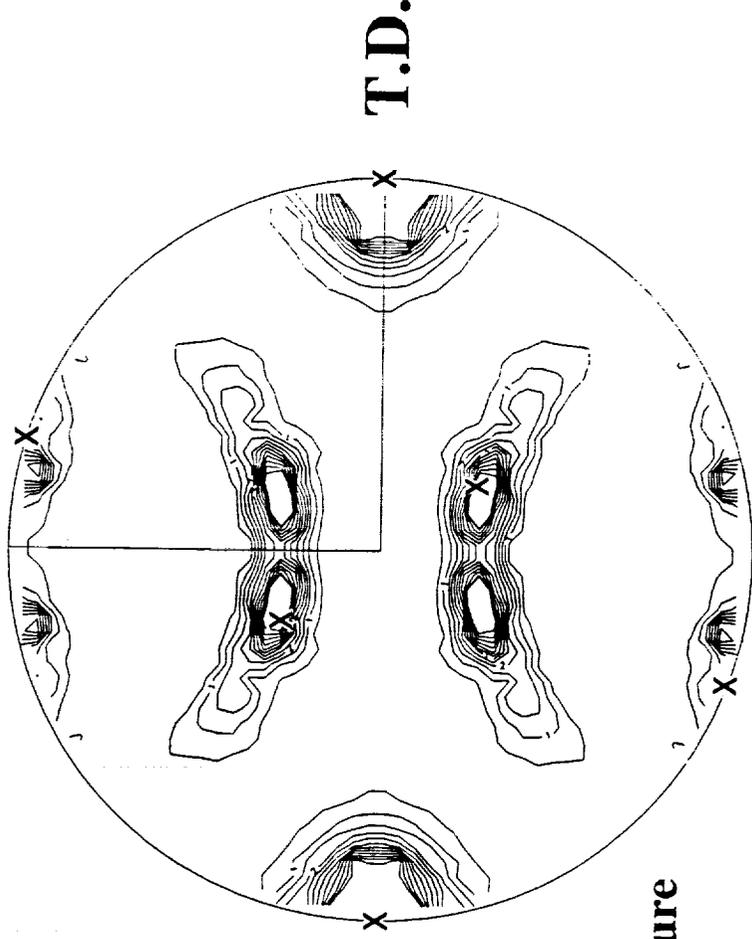
x Single Brass Texture

AA2090 Inert Environment Fatigue Facets
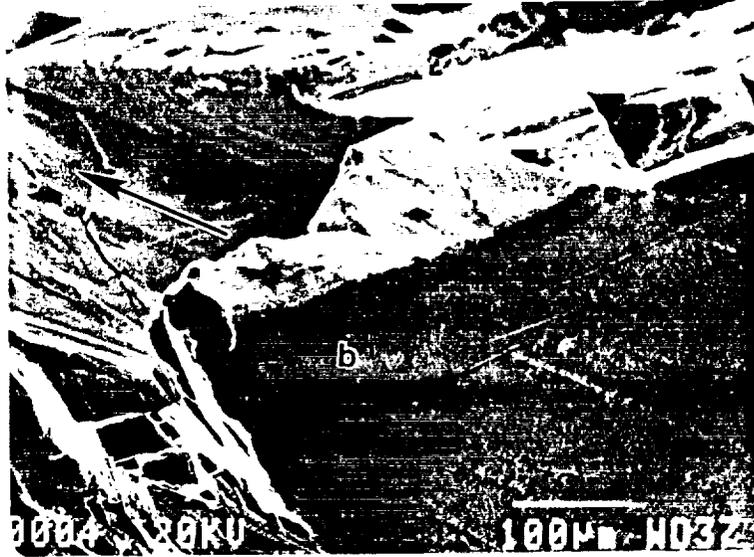
Grain B Micro-Pole Figure

- ● {111} Pole
- ■ {100} Pole
- x Facet Pole

Alloy 2090
Vacuum
$K_{max} = 17 MPa-m^{1/2}$
LT, T/2

□ Plate UnRec (III)
△ Sheet UnRec (III)
○ Sheet Coarse Rec
◇ Sheet Fine Rec

da/dN (mm/cycle)

Stress Intensity Range (MPa-m$^{1/2}$)
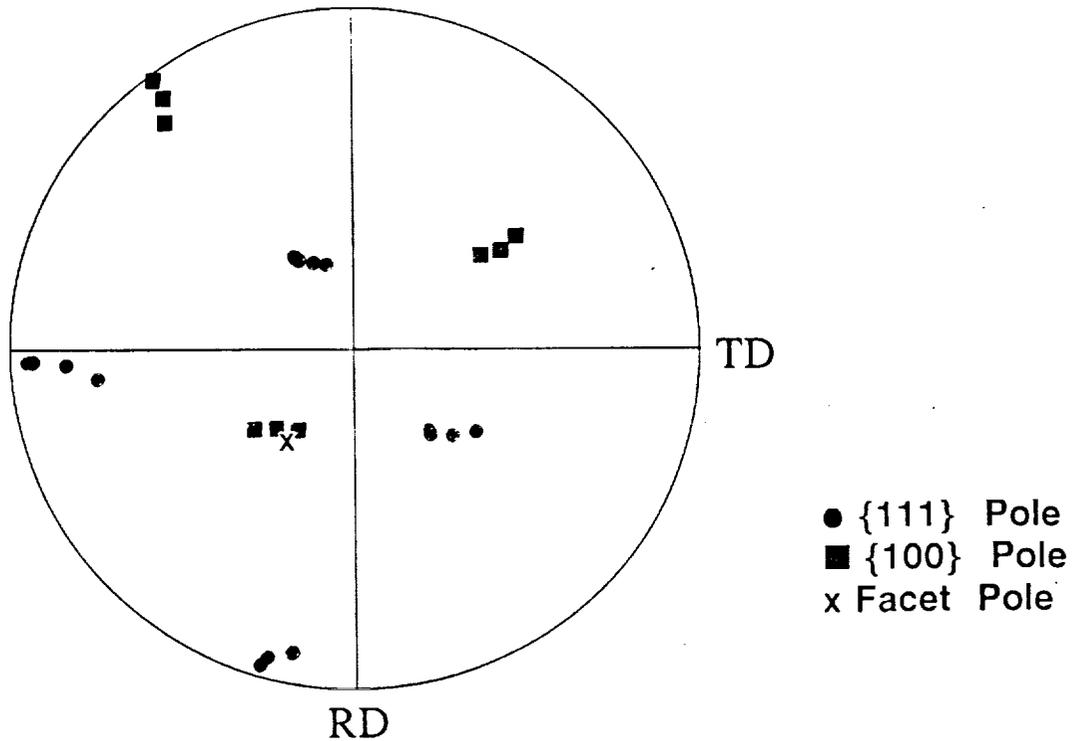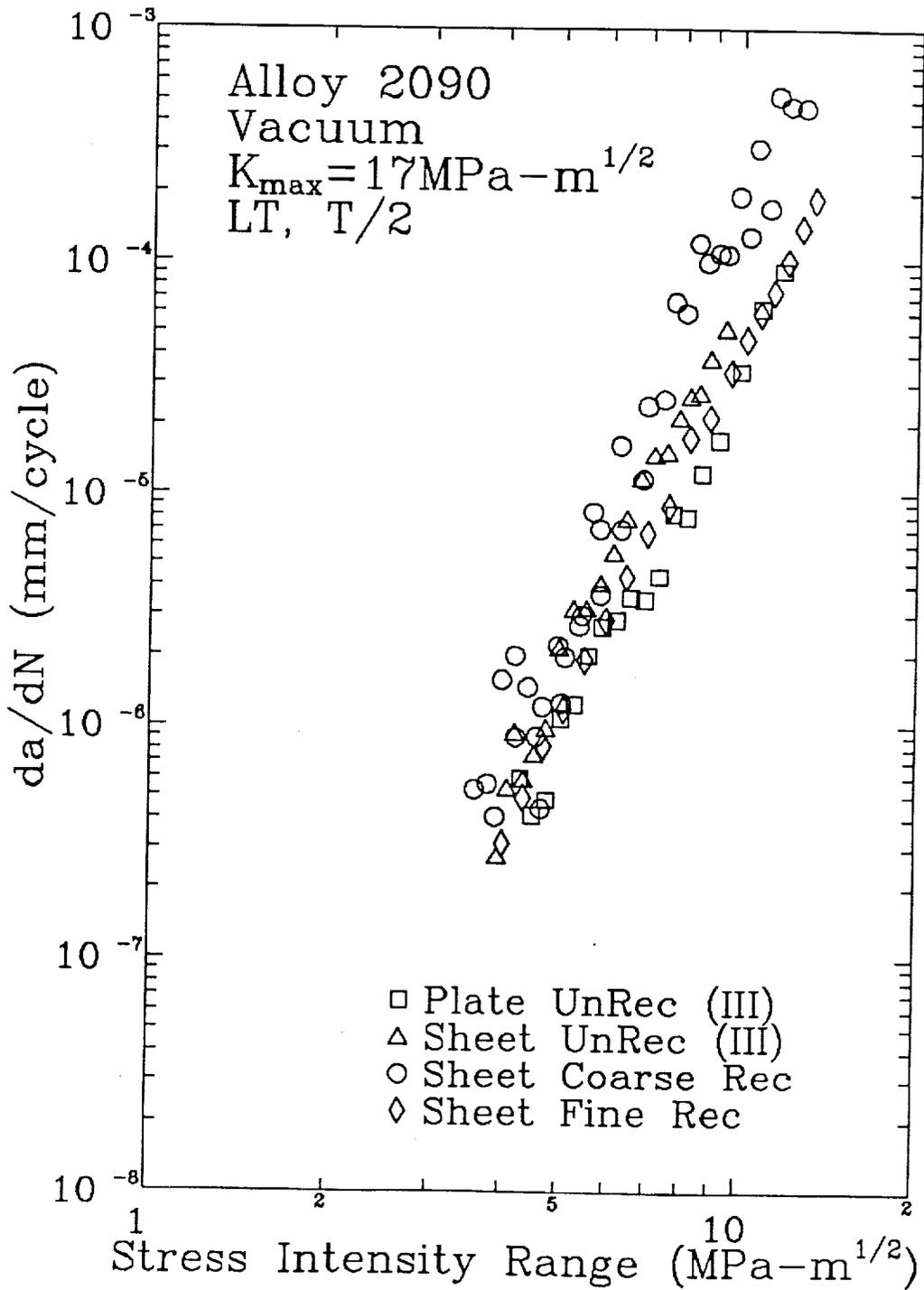
Intrinsic Fatigue Crack Growth Rates:
Aluminum Alloys in Vacuum
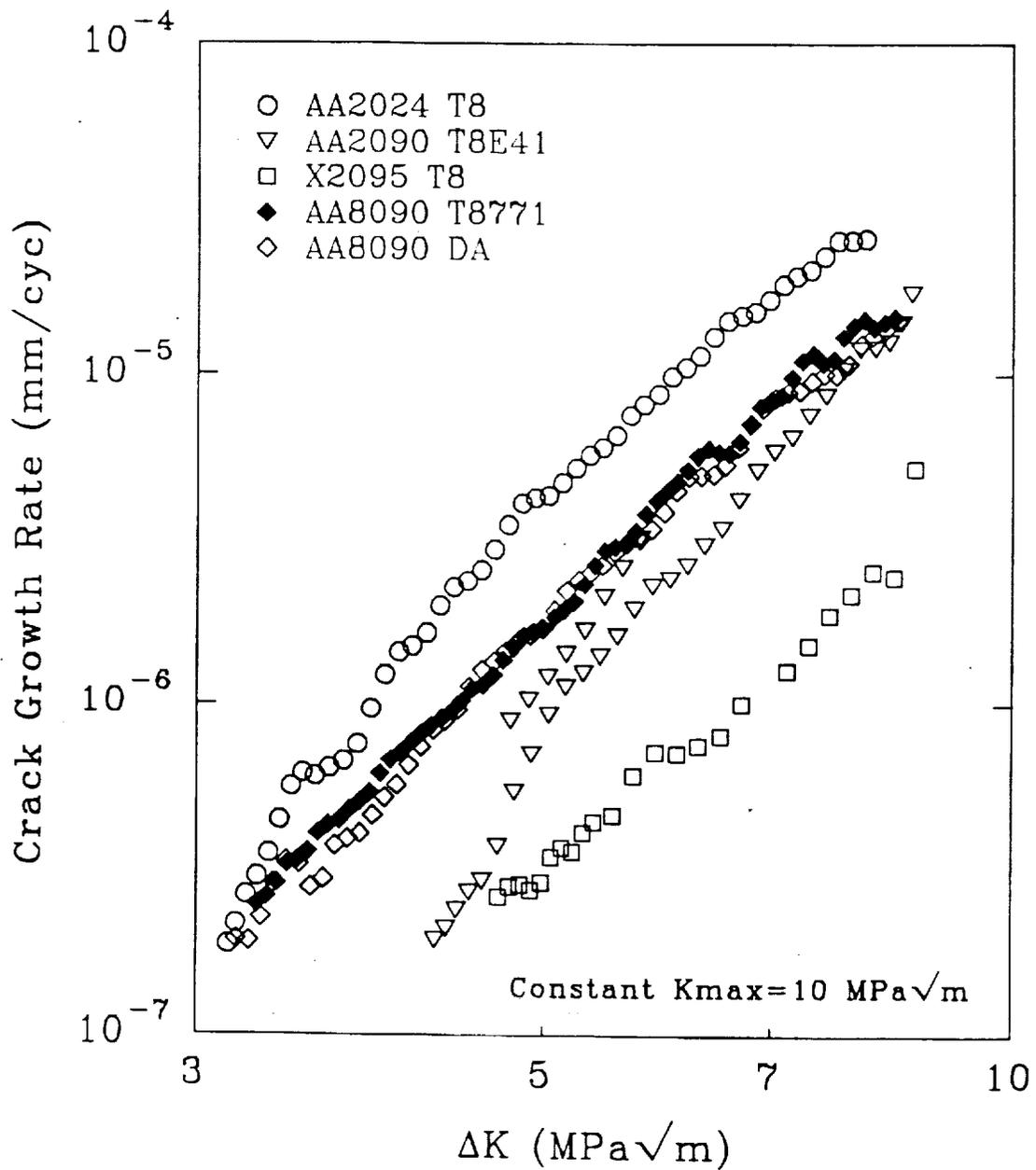
Conclusions

Inert Environment Fatigue Damage

o Tent shaped facets observed for all Al-Li-Cu microstructures

  - Facet size scales with grain size
  - Facet formation independent of δ' precipitates
  - Facets are not along only {111} slip bands

o AA2090 fine grain recrystallized and unrecrystallized da/dN similar

o AA2090 coarse grain recrystallized da/dN enhanced

o Alloy dependent da/dN observed

  - Crack tip opening parameter $\Delta K / \surd / (E \ \sigma_y)$ collapses da/dN
  - Crack closure and reversible slip for X2095

Aqueous Environment Cracking Modes

o What are the cracking modes?

   - Identify ΔK regimes for facet formation

   - Facet crystallography

o Do cracking modes depend on the microstructure?

o Does cracking mode influence da/dN?

Unrecrystallized 2090 Sheet Fractography
Aqueous NaCl

a

b

c
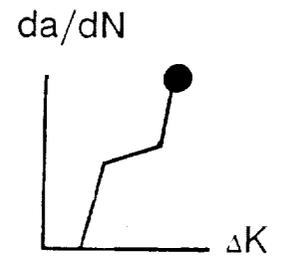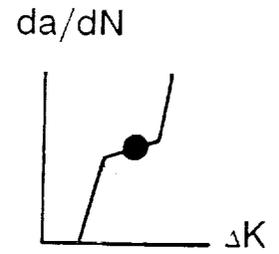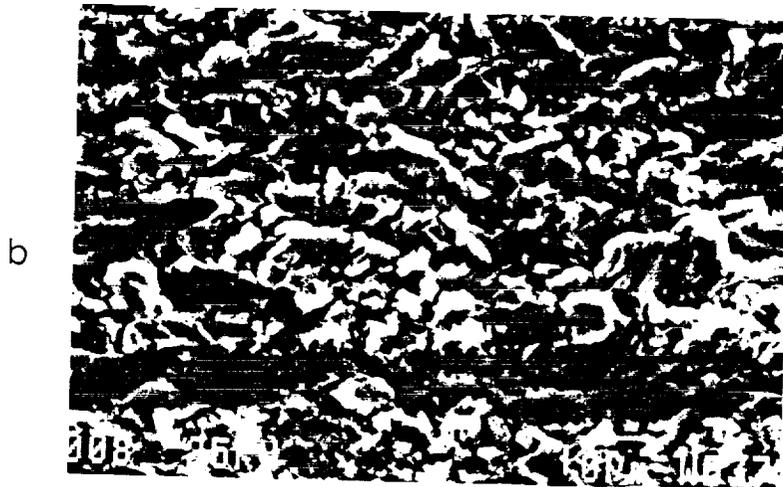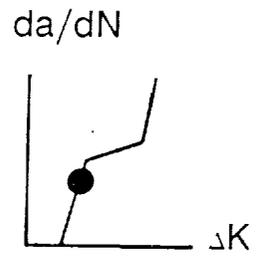
Unrecrystallized 2090 Plate Fractography
Aqueous NaCl
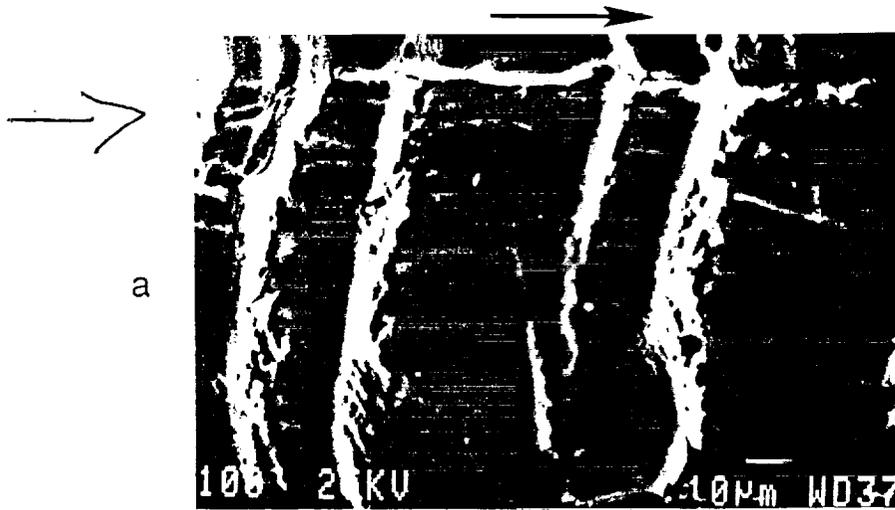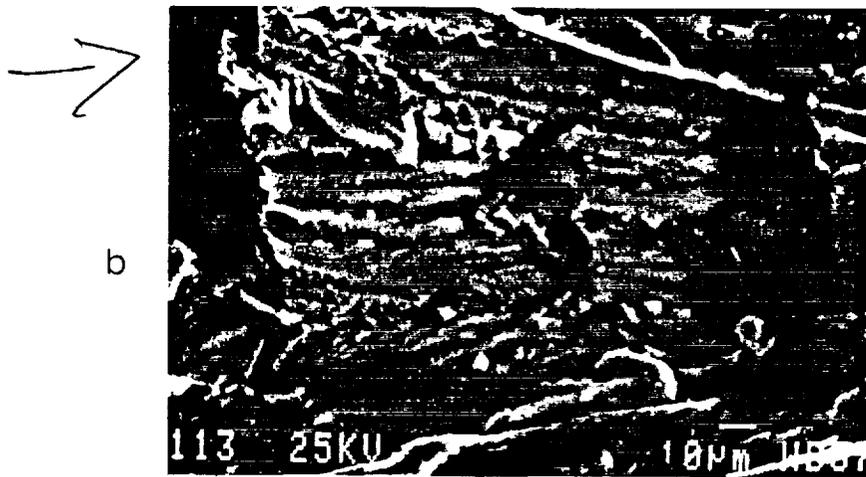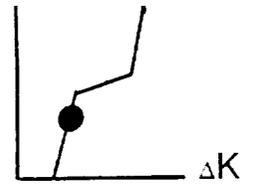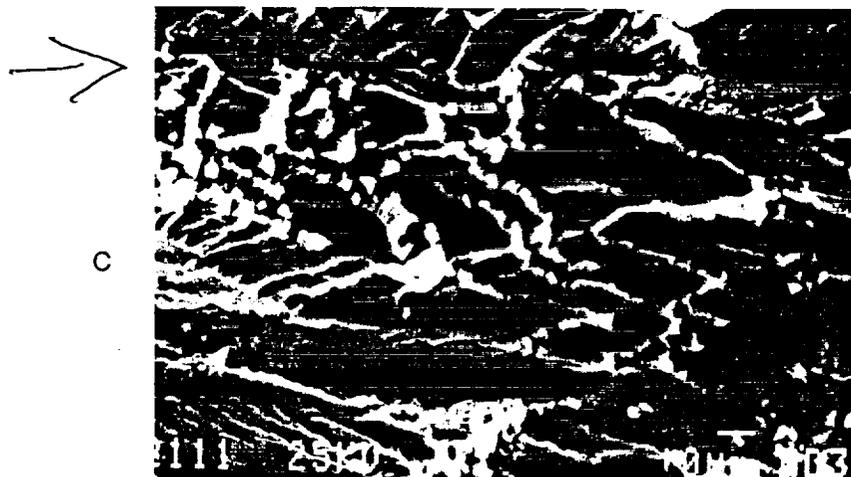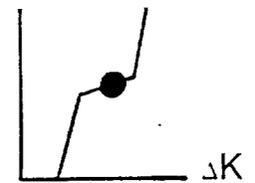
AA2090 Fatigue Facets
Aqueous NaCl Environment
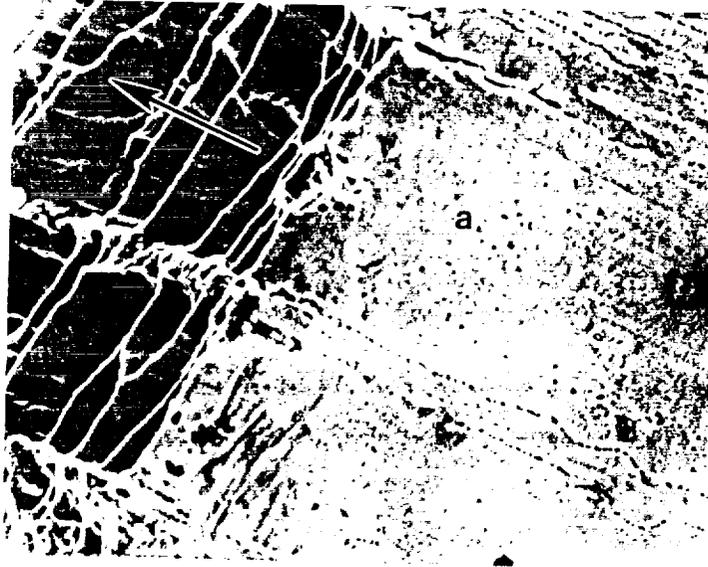
Grain A Micro-Pole Figure

● {111} Pole
■ {100} Pole
x Facet Pole

Alloy 2090
1.0 wt% NaCl
−840 mv SCE
$K_{max}=17MPa-m^{1/2}$
LT, T/2

Vacuum

da/dN (mm/cycle)

10^{-3}

10^{-4}

10^{-5}

10^{-6}

10^{-7}

10^{-8}

□ Plate UnRec (III)
△ Sheet UnRec (III)
○ Sheet Coarse Rec
◇ Sheet Fine Rec

1   2   5   10   2

Stress Intensity Range $(MPa-m^{1/2})$
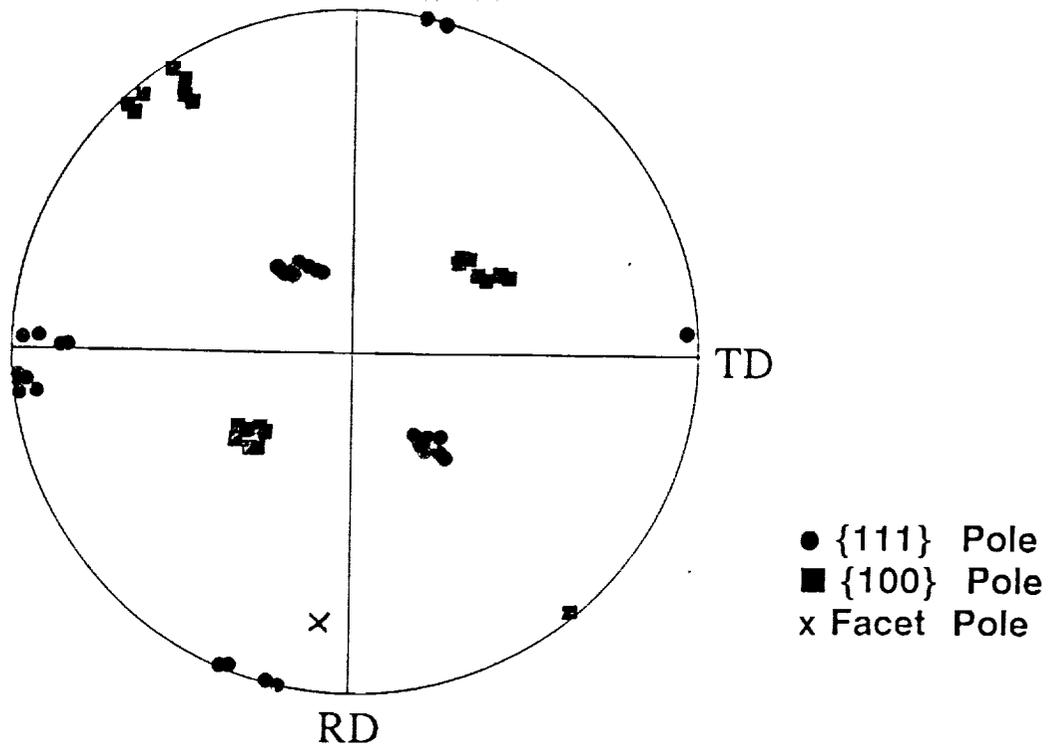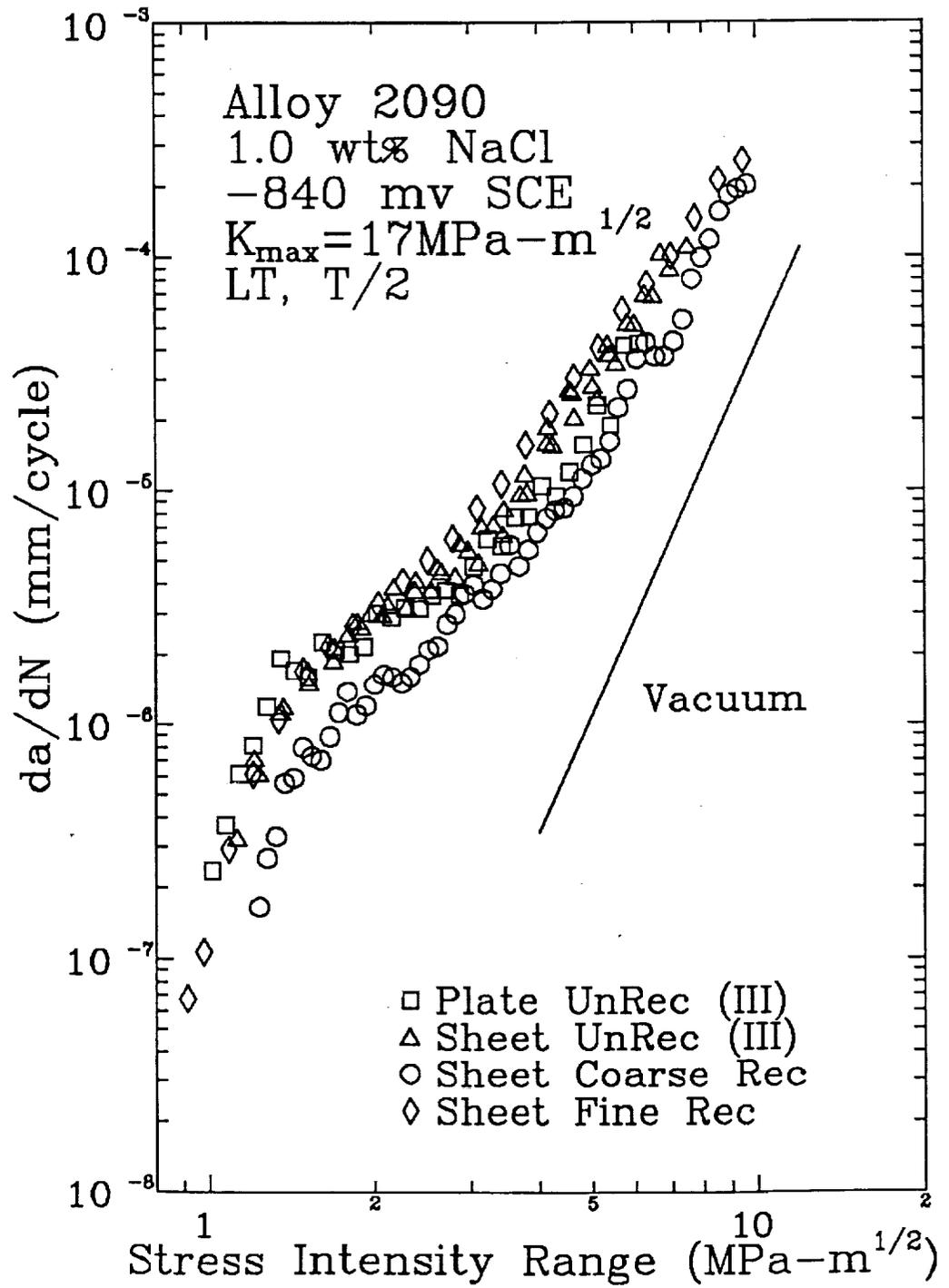
Fatigue Damage Conclusions

Aqueous Environments

o Cracking plane stepped facets observed at low ΔK
 - Facets are not only $\{100\}$

o Similar da/dN for fine grain recrystallized and unrecrystallized

o Reduced da/dN for coarse grain recrystallized

Future Work

o Introduce channeling capability at UVa
- Current patterns from ALCOA Technical Center
- Measure fatigue facet crystallography

o Interpret possible microscopic damage modes
- {111} persistent slip band cracking
- {100} or {110} cracking from alternate slip
- Hydrogen enhanced decohesion
- {100} hydride cracking
- Noncrystallographic cracking
- Subgrain cracking

o Mechanistic understanding of cracking modes

o Correlate damage modes and da/dN trends
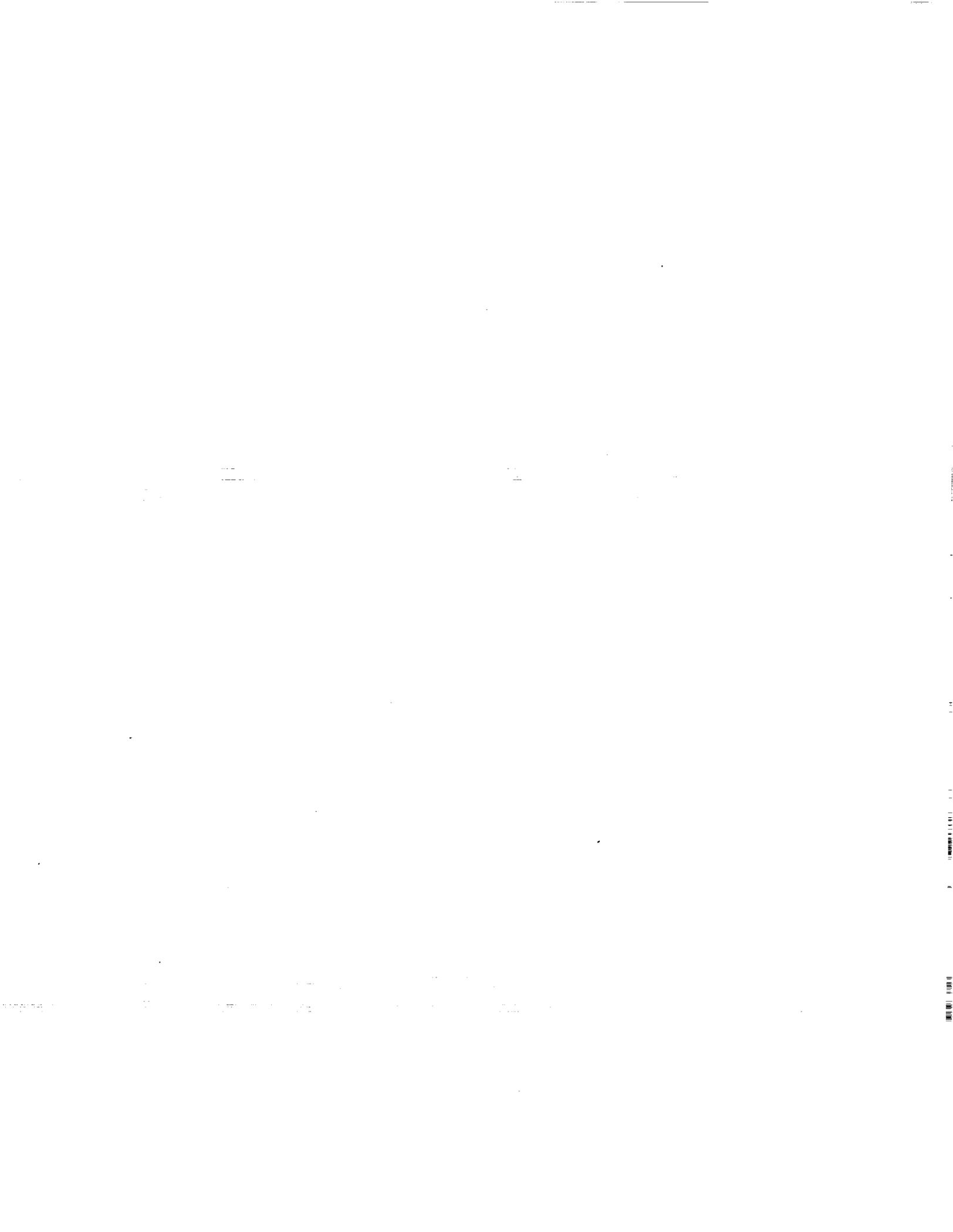
Project 2   Environmental Effects in Fatigue Life Prediction: Modeling Crack Propagation in Titanium Alloys

Richard P. Gangloff and Sang-Shik Kim

Project Objective

The objective of this ongoing research is to enhance the predictive capability of existing damage tolerance fatigue life prediction codes, particularly NASA FLAGRO, by incorporating environmental effects on FCP behavior. Specific goals include to:

oo   Review existing data and modeling methods for environment sensitive fatigue crack propagation in aerospace alloys.

oo   Establish data and mechanistic understanding of crack closure, surface film stability, and microscopic crack tip damage processes for environmental FCP in titanium alloys.

Current Status

A draft copy of an extensive literature review, originally commissioned and supported by Dr. R.G. Forman of the Johnson Space Flight Center, was completed and submitted for evaluation and input by NASA-LaRC and NASA-JSC. A large body of environmental fatigue crack propagation data, particularly relevant to aerospace component applications, is reviewed with emphasis on those variables that govern fatigue crack growth in ferrous, aluminum, nickel and titanium based alloys. A bibliography of over 400 references is assembled. Existing modeling methods that predict environment-enhanced da/dN-ΔK are reviewed. Significant approaches include linear superposition, empirical curve fitting and mechanism-based methods. Those material-environment systems which are adequately described by each method are identified. The application of linear superposition and empirical curve fitting methods for predicting da/dN-ΔK for nickel base superalloys in elevated temperature moist air is demonstrated.

Recent Results

The following conclusions are supported by the literature survey.

oo   Numerous literature data indicate that fatigue crack propagation in most aerospace structural alloys is significantly accelerated by aggressive gaseous and aqueous

environments, especially those capable of producing atomic hydrogen.

oo Fatigue crack growth in corrosive environments is governed by the complex and synergistic interaction of a plethora of chemical, mechanical and material variables.

oo Several quantitative models have been developed for interpolating and predicting environmental fatigue crack growth kinetics for use in life prediction codes through the stress intensity similitude concept. Each approach is encouraging, but limited.

oo Linear superposition is reasonably effective for those materials that are strongly "embrittled" by an aggressive environment. An example is nickel based superalloys in elevated temperature moist air and high strength steels in hydrogen producing gases or electrolytes.

oo Empirical curve fitting is an effective method for interpolating the effects of ΔK, loading frequency and stress ratio on da/dN, however, extensive data are required and no predictive capability exists. This approach was applied to C-Mn steels in marine environments.

oo Mechanistic models for da/dN-ΔK, based on hydrogen embrittlement and anodic dissolution/film rupture/passivation, are in a state of infancy because of the complex and highly localized nature of crack surface reactions and process zone fatigue damage. Such models were employed to predict cracking in stainless steels in nuclear reactor water environments.

oo Many man-years of effort are required to adequately define the environmental effect on fatigue crack propagation for a given material-environment system. When the technological need warrants such an effort, significant results have and can be produced. When a wide range of materials and aggressive environments must be considered, and when resources are limited, it is difficult to adequately incorporate environmental effects into fatigue life prediction codes.

Milestones

The literature review will be revised during the next reporting period and published as a NASA-CR.

A new project will be initiated, according to the 1992 renewal proposal, to investigate environmental fatigue crack propagation in titanium alloys. A new graduate student, Mr. Mark Mason, was recruited in February of 1992 to conduct MS research on this program.

Initially, α/β Ti-6Al-4V (mill annealed and β-quenched) is selected to study mechanisms for environment sensitive fatigue crack closure and crack tip damage. Limited experiments will also be conducted with Beta 21S, a modern β-titanium alloy being considered for High Speed Civil Transport and National Aerospace Plane applications. Aqueous chloride solution is selected to be the initial environment; some experiments will be conducted in ultra-high vacuum, water vapor and methanolic environments to probe mechanisms. During the next year, monotonic load cracking will be performed emphasizing the effect of loading rate, or more precisely crack tip strain rate, on the threshold for the initiation of fatigue precrack growth and on crack growth rates. Essentially, stress intensity based R-curve experiments will be conducted in the various environments. The interest is to obtain threshold and time-based data for use in superposition modeling of environmental fatigue crack propagation. Mr. Mason will conduct these "stress corrosion cracking" experiments.

Fatigue crack propagation experiments will be conducted with the titanium alloys and various environments, including the variables of stress ratio and loading frequency/hold time (limited work, initially). Crack closure will be determined using a compliance technique with a crack opening displacement gauge. The goal is to define the effects of extrinsic crack closure and intrinsic process zone damage on the complex da/dN-ΔK relationships that are likely to be produced by the environmental exposure. These data can be empirically modeled for life prediction applications. Dr. Sang-Shik Kim is responsible for this work and will collaborate with Mr. Mason.

Presentation Graphics Captions

1. Title.

2. Advances that have enabled the fracture mechanics approach to fatigue life prediction in sophisticated computer codes.

3. Curve fit of fatigue crack growth rate data (da/dN-ΔK) employing the modified Forman equation, enhanced by Newman to analytically predict crack closure, for 300M steel in moist air.

4. The strong effect of aqueous chloride environment and stress ratio on fatigue crack propagation in an α/β-titanium alloy; after Bucci.

5. Incorporating environmental effects on FCP into life prediction codes is complex.

6. Objectives.

7. A summary of environmental fatigue crack propagation data for 2000 and 7000 aluminum alloys; after Piascik.

8. Crack propagation threshold values, K_{th}, and corresponding monotonic load crack growth velocities, da/dt, for aerospace alloy-environment systems. Linear superposition is a viable modelling approach for FCP only when fatigue stress intensities are above K_{th} and da/dt is substantial.

9. Effects of heat treatment and chemical environment on K_{th} for α/β Ti-8Al-1Mo-1V; after Czyrklis and Levy.

10. Effects of pH and frequency on the environmental fatigue crack growth behavior of α/β Ti-6Al-6V-2Sn; after Dawson and Pelloux.

11. Effect of loading frequency on the threshold stress intensity range, ΔK_{SCC}, for a strong environmental effect on fatigue crack propagation rate; after Dawson and Pelloux.

12. Effect of environment on the fatigue crack growth behavior of solution treated and aged β/α Beta 21S at high loading frequency; after Hartman-Young and Gangloff.

13. Quantitative models for predicting environmental effects on FCP rate, da/dN. Approaches include linear superposition, empirical curve-fitting and mechanism-based methods.

14. Linear superposition model.

15. Problems associated with the linear superposition model.

16. Empirical curve-fitting models.

17. Problems associated with empirical curve fitting models.

18. Chemical reaction plus process zone damage mechanism-based models.

19. Problems associated with mechanism-based models.

20. Conclusions from the literature review.

Incorporating Environmental Effects in Fatigue Life Prediction

Sang-Shik Kim and Richard P. Gangloff

Mark Mason (August, 1992)

Department of Materials Science and Engineering

University of Virginia

Drs. R.S. Piascik and J.C. Newman

Mechanics of Materials Branch

NASA-Langley Research Center

Advances in Fracture Mechanics

Near-threshold fatigue cracking
Small crack
Crack Closure
Spectrum loading
Advanced Materials

The-state-of-the-art computerized life prediction codes

NASA FLAGRO
NASCRAC
FASTRAN

EXPERIMENTAL DATA
□ R = 0.0
△ R = -1.0
◇ R = 0.5

—— EQN.1 CURVE FIT WITH CRACK CLOSURE

$\frac{S_{max}}{\sigma_o} = 0,$

$\alpha = 2.5$

300M STEEL

MOIST AIR

ΔK_2

ΔK_2

$\Delta K_1 \ (R = 0)$

$$\frac{da}{dN} = \frac{[C(1-R)^m \Delta K^n \{\Delta K - \Delta K_{th}\}]^p}{\{(1-R)K_c - \Delta K\}^q}$$

$$\Delta K_2 = \frac{[1-(S_o/S_{max})_1(1-R_2)]}{[1-(S_o/S_{max})_2(1-R_1)]} \Delta K_1$$

da/dN (IN./CYCLE)

ΔK (KSI $\sqrt{in.}$)

ksi√in.

Ti-8-1-1 Mill anneal
Transverse rolling dir.
Fatigue at room temp.
$R = 0.05$

K_{IEAC}

$f = \frac{1}{2}$ cps

$\frac{1}{2}$ cps

$2\frac{1}{2}$ cps

5 cps

3.5% NaCl

15 cps

50 cps

$R = 0.75$

$\frac{da}{dN}$ (mm/cyc)

in./cyc

4

1

3.5% NaCl
Argon

5 cps

ΔK (MPa√m)
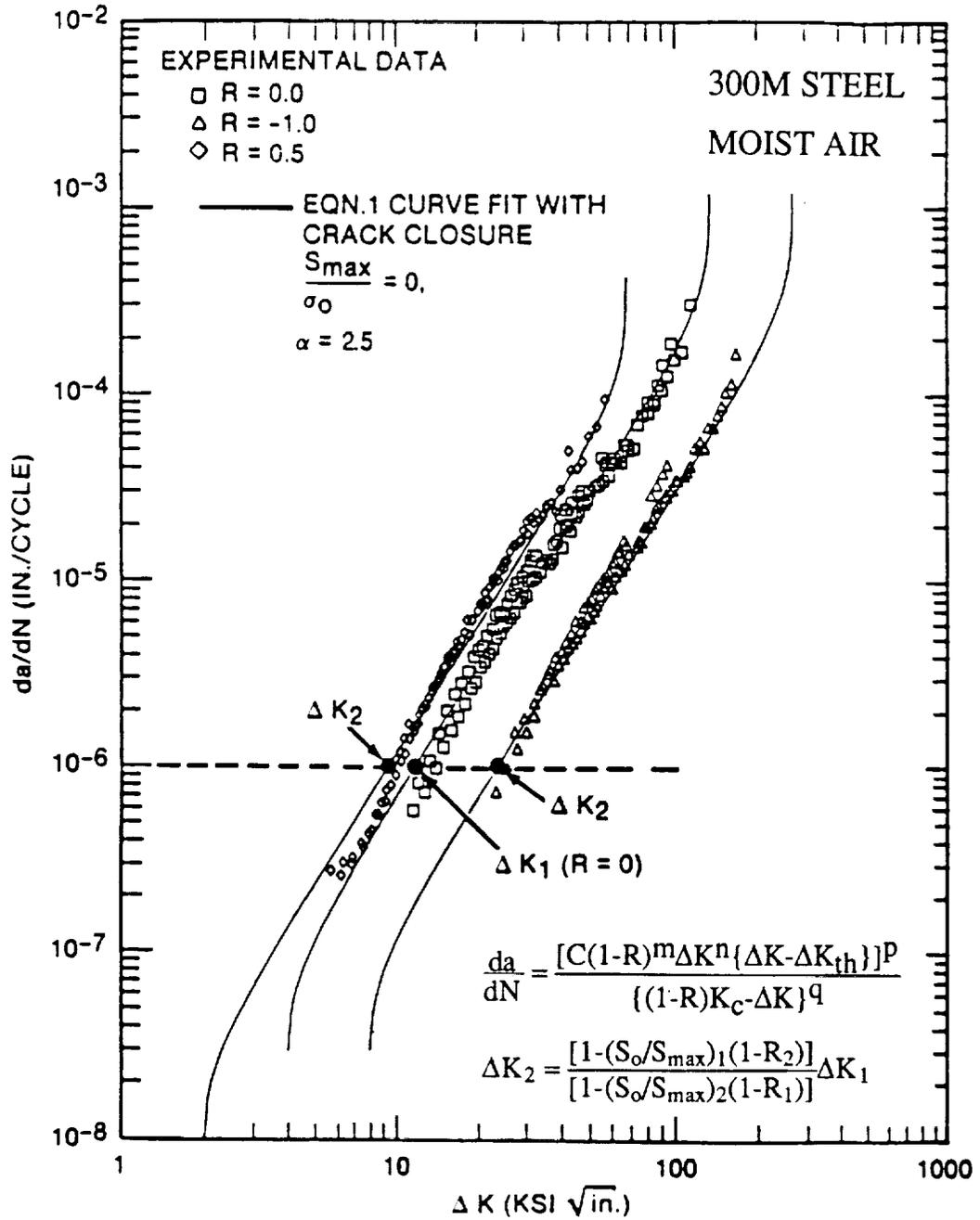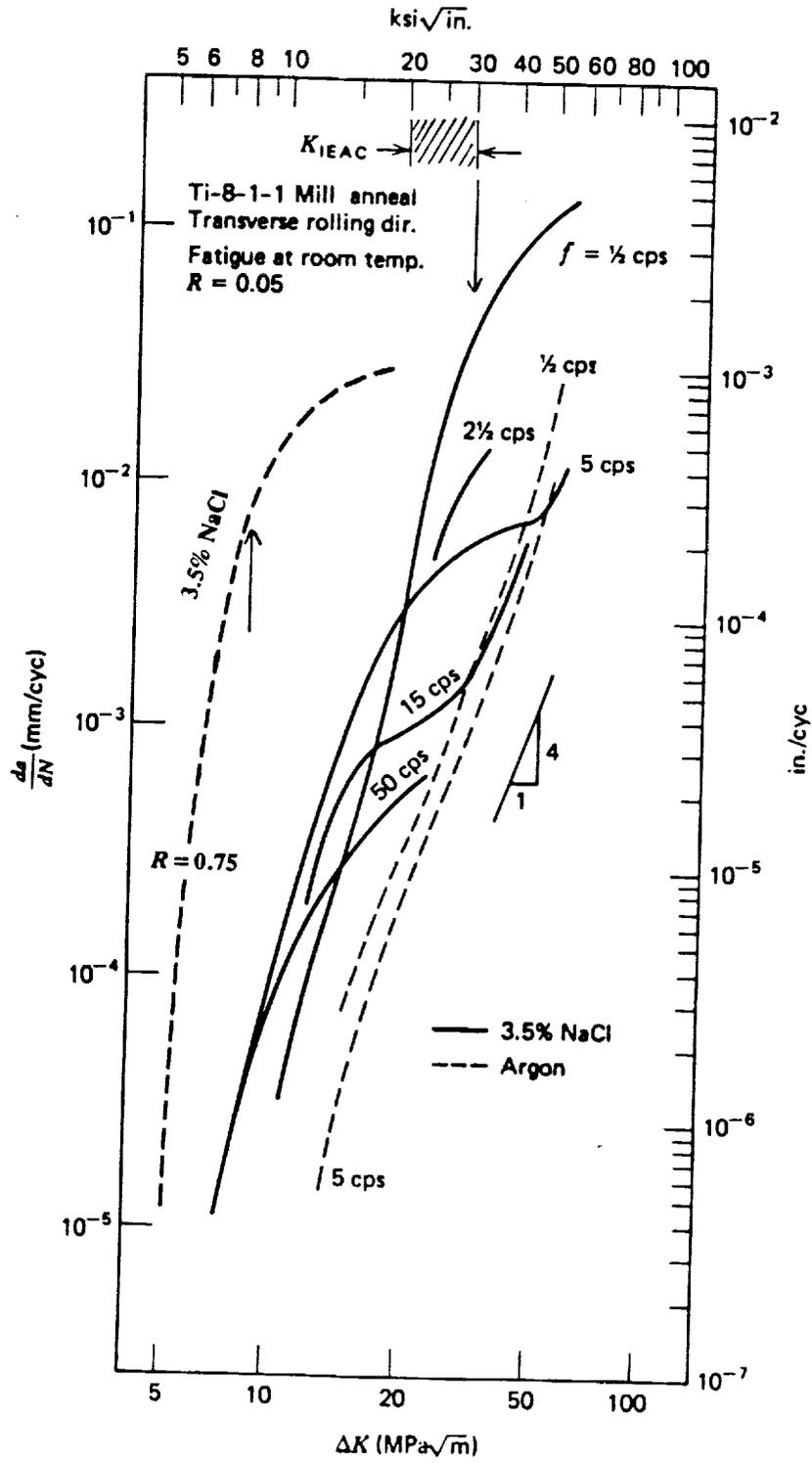
Challenges

Important hydrogen environment effects are not incorporated into life prediction methods.

oo   Multitude variables are important

Mechanical, environment chemistry and metallurgical variables affecting environmental fatigue in aluminum alloys	
stress intensity range	mean stress
crack size and shape	specimen thickness
loading frequency	specimen orientation
loading sequence	loading waveform
solution Cl^-, H^+, O_2, S^{-2}	water vapor pressure
electrode potential	water vapor O_2
alloy microstructure	alloy composition
grain /subgrain size	alloy yield strength
slip morphology	texture
precipitates	temperature

oo   Time dependence

oo   Mechanisms complex: Extrinsic crack closure
                          Intrinsic process zone damage

Objectives

Develop data and mechanistic understanding to quantitatively predict environmental effects on fatigue crack propagation in damage tolerant life codes.

oo Review existing data and modeling methods for aerospace alloys.

oo Establish data and mechanistic understanding of crack closure, surface film stability, and microscopic crack tip damage processes for environmental FCP in titanium alloys.

HIGH STRENGTH ALUMINUM ALLOYS
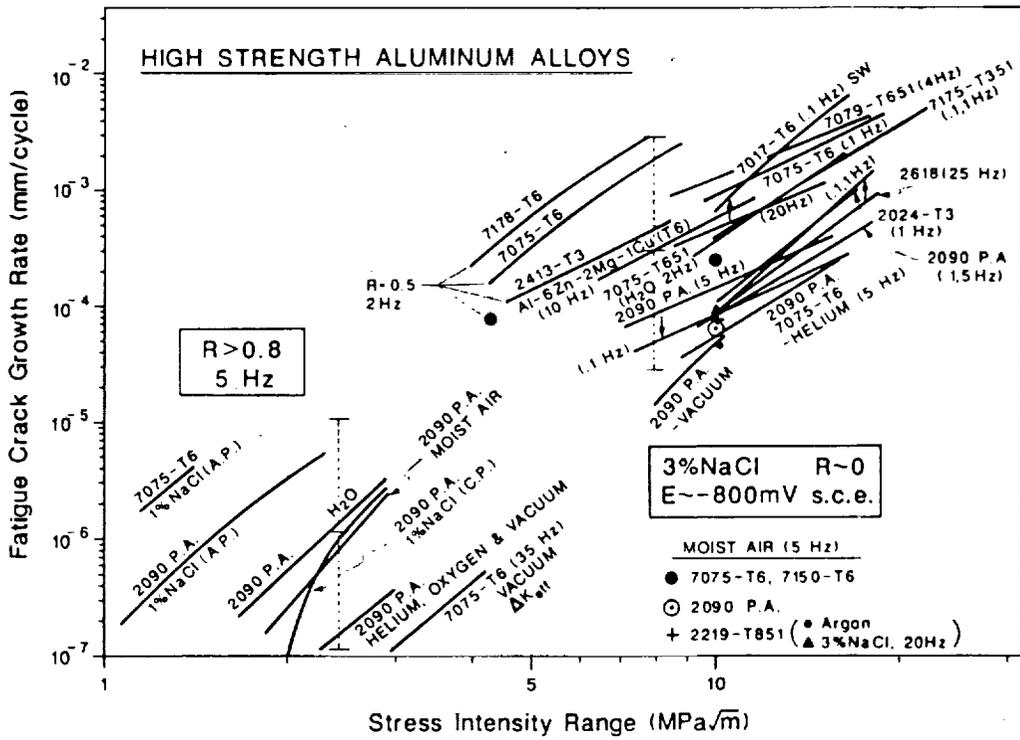
	K_{th} (MPa√m)	da/dt mm/sec
4340/300M in Distilled Water [temperature]	18	10^{-2}
AA 7079 in NaCl [Cl$^-$ concentration]	4	2×10^{-2}
IN718 in High Pressure H_2	30 - 40	—
IN718 at 650°C air vacuum	15 - 25 45	$10^{-4} - 10^{-2}$ $10^{-6} - 10^{-5}$
Ti-8Al-1Mo-1V in NaCl, KI, KCl [electrode potential]	30	10^{-1}
HY130/4340 in NaCl (Low σ_{ys}) [yield strength]	> 75	—
AA 7017, 7075, 2090 in NaCl	6 - 10	4×10^{-5}
Ti-6Al-4V in NaCl	20	10^{-1}
Ti-6Al-6V-2Sn in Methanol/HCl	25	—
Ferritic Steel with Dissolved H [hydrogen content]	25 - 50	$< 10^{-5}$

Ti-8Al-1Mo-1V

MPa√m

ALPHA+BETA-TREATED
STRUCTURE C
ENVIRONMENT

1. Air
2. H₂O
3. 3.5% NaCl
4. 3.5% NaCl+1.0% NaNO₃
5. CH₃OH
6. CH₃OH+0.4% HCl
7. CH₃OH+0.4% HCl+0.5% NaNO₃

BETA-TREATED
STRUCTURE B

MILL-ANNEALED
STRUCTURE A

STRESS INTENSITY, ksi √in.

ΔK. Stress Intensity Range, MN − m$^{-3/2}$

Tl-6Al-6V-2Sn (Mill Anneal)
WR   R • 0.1   t • 0.125"
Haversine Wave Form

○ 0.6M NaCl (pH − 6.4) − 10 Hz
● 0.6M NaCl (pH − 6.4) − 1 Hz
□ 0.6M NaCl + HCl (pH − 1.0) − 10 Hz
■ 0.6M NaCl + HCl (pH − 1.0) − 1 Hz
− −Ambient Air (Lower Limit)

ΔK_{scc} • 14 (pH • 6.4, 1 Hz)

ΔK_{scc} • 13 (pH • 1.0, 1 Hz)

ΔK_{scc} • 10.5 (pH • 6.4, 10 Hz)

ΔK_{scc} • 10 (pH • 1.0, 10 Hz)

Δa/ΔN, Crack Growth Rate, in./cycle

Δa/ΔN, Crack Growth Rate, cm/cycle

ΔK. Stress Intensity Range, ksi − in.$^{1/2}$

Beta 21S

Kmax=25MPa√m
Frequency = 10 Hz

CRACK GROWTH RATE (mm/cycle)

STRESS INTENSITY RANGE (MPa√m)

□ Deaerated 3.5% NaCl
• SEN air
○ CT vaccuum
△ CT air

Quantitative Crack Growth Models

oo Models to interpolate and predict da/dN-(ΔK, R, f, P_{H_2},...) were developed from several perspectives.

  A. Linear Superposition
  B. Empirical Curve Fitting
  C. Mechanism-based

oo Each approach is encouraging, but limited.

A. Linear Superposition

$$da/dN \quad = \quad da/dN_m \quad + \quad da/dN_{SCC}$$

Inert environment
fatigue crack growth rate

Time-based environmental
crack growth rate

$$a/dN_{SCC} = \int_0^{1/\gamma f} [da/dt(K)][K(t)]dt$$

• Determine da/dt(K)

1. Monotonic load experiment

2. Measure effect of τ_H @ K_{max}

$$\log(\frac{da}{dN_e} - \frac{da}{dN_m}) = \log\frac{da}{dt} + \log\tau_H$$

3. Measure effect of f @ ΔK, R

$$(\frac{da}{dN_e} - \frac{da}{dN_m}) = (\frac{da}{dt})[\frac{(1-R)^{(n+1)}}{(n+1)}](\frac{1}{\gamma f})$$

• Determine of K(t)

$$K(t) = K_{min} + \Delta K/[2-\cos(2\pi ft)]$$

• Define γ

Problems

oo   Cyclic loading above K_{th} may affect time-based crack growth.

oo   Terms such as n, γ, and K_{th} are ill-defined.

oo   Cracking above K_{th} is unacceptably rapid; avoided by materials selection.

oo   Environment strongly enhances da/dN at K levels below K_{th}.

Successful Application

oo   Nickel-based superalloys in elevated temperature moist air.

B. Empirical Curve Fitting

oo Hudak et al.

$$\frac{1}{da/dN} = \frac{A_1}{\Delta K^{n_1}} + \frac{A_2}{\Delta K^{n_2}} - \frac{A_2}{[(1-R)K_c]^{n_2}}$$

oo MSE Model

$$da/dN = \exp(B)\,(\Delta K/\Delta K^*)^P\,[\ln(\Delta K/\Delta K^*)]^Q\,[\ln(\Delta K_c/\Delta K)]^D$$

oo SINH Model .

$$\log(da/dN) = C_1 \sinh[C_2(\log\Delta K + C_3)] + C_4$$

Problems

oo Extensive data base required.

oo Limited extrapolative capabilities; particularly long times and chemical environment changes.

Successful Application

oo C-Mn steels in marine environments.

C. Mechanism-Based

$$da/dN = da/dN_m + da/dN_{SCC} + da/dN_{cf}$$

cycle-time dependent
environmental contribution
below K_{th}

oo   Hydrogen Embrittlement Model

oo   Film Rupture and Transient Dissolution Model

	CONTROL PROCESS	da/dN ASSUMPTION	GROWTH RATE PREDICTION
Scott	Crack Tip Cathodic Hydrogen Production	$\dfrac{da}{dN}_{e,\,PLATEAU} \propto i_H$	$A(1/f)\,(\exp(-E/RT))$
Gangloff	Competition Between O_2 and H^+ Reduction	$\dfrac{da}{dN}_{cf} \propto C_H$	$A'\,(V_{max})^{1/2}\exp(\alpha a_0/fV_{max})$
Wei et al.	Molecular Flow Gas Transport	$\dfrac{da}{dN}_{cf} \propto C_H \propto \theta$	$\dfrac{da}{dN}_{cf,SAT}\left(\dfrac{P_0}{f}\right)\Big/\left(\dfrac{P_0}{f}\right)_{SAT}$
	Gas-Metal Reaction	$\dfrac{da}{dN}_{cf} \propto C_H \propto \theta$	$\dfrac{da}{dN}_{cf,SAT}\,(1-\exp(-kP_0/f))$
	Charge Transfer by Transient Reaction	$\dfrac{da}{dN}_{cf} \propto C_H \propto q$	$\dfrac{da}{dN}_{cf,SAT}\,(1-\exp(-\tau/f))$
Holroyd and Hardie	Hydrogen Diffusion in Plastic Zone	$\dfrac{da}{dN}_e \propto \dfrac{\Delta x}{cycle}$	$4(\sqrt{D_H/f}\,)$
Kim et al.	Hydrogen Diffusion in Plastic Zone	$\dfrac{da}{dN}_{cf} \propto \dfrac{\Delta x}{cycle}$	$A''\,(\sqrt{P_0 D_H/f}\,)\,(\exp(-\Delta H/RT))\Delta K^2$
Austin and Walker	Hydrogen Diffusion in Plastic Zone	$\dfrac{da}{dN}_e = \dfrac{da}{dN}_m\,X$	$\dfrac{(\Delta x-s)}{(r_p-s)}\,(\delta_{max}-s)$
			$\dfrac{da}{dN}_{e,\,PLATEAU} = 37.7\,\dfrac{\sigma_{ys}}{E}\,(\sqrt{D_H/f}\,)$

E - Modulus
Δx - Hydrogen penetration distance = $4\sqrt{D_H/f}$
C_H - Hydrogen concentration
C_{H^+} - Hydrogen ion concentration
T - Temperature
θ - Fractional surface coverage
X - Environmental factor

q - Electrochemical charge
σ_{ys} - Yield strength
f - Frequency
i_H - H production rate
a_0, A, A', A'', R - Constants
ΔH - Binding energy of hydrogen to dislocation
s - Striation spacing

τ - Clean surface reaction rate constant
α - Oxygen reduction rate constant
V - Crack mouth opening
P_0 - Nominal gas pressure
D_H - Hydrogen diffusivity
E' - Crack tip electrode potential
k - Reaction rate constant

Conclusions

oo Environmental effects on FCP are broad, important and complex to incorporate in life prediction.

oo FCP rate can be modeled by

1. Linear Superposition
2. Empirical Curve Fitting
3. Chemical reaction + process zone damage mechanism,

but problems exist (eg. time-dependence).

oo Crack closure and small crack-environment interaction are not well understood.

oo **Environmental FCP in titanium alloys not well characterized; provides model system to study mechanisms for environment sensitive crack closure and crack tip damage.**

Environmental Cracking in Ti Alloys

Approach

oo   Materials

Ti-6Al-4V (MA, β-Quenched)

Beta 21S (Ti-15Mo-2.7Nb-3Al-0.2Si-0.15O; STA)

oo   Environments

Vacuum

NaCl/HCl

NaCl/Methanol (limited)

H_2O vapor (limited)

oo   Experiments

Monotonic load crack growth: J(Δa) R-curve; $\dot{\varepsilon}_{CT}$

Fatigue crack propagation: da/dN(ΔK,R)

Fatigue Crack Propagation in Ti Alloys

1. What are contributions of R, ΔK and crack closure to environmental crack growth rate ?

2. What are data for empirical life prediction?

oo R ratio: 0.1, 0.5, 0.7 and constant K_{max}

oo Frequency: 5 Hz

oo Crack closure: Compliance method
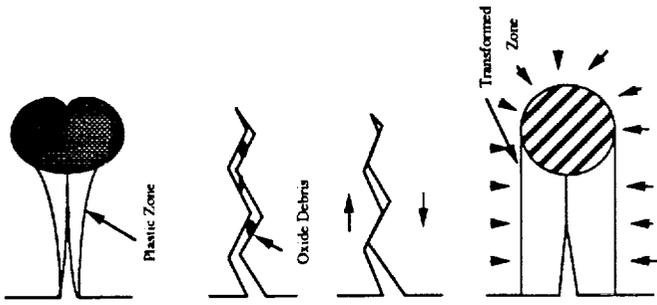
Plasticity-Induced Closure

Oxide-Induced Closure

Roughness-Induced Closure

Phase Transformation-Induced Closure

Plastic Zone

Oxide Debris

Transformed Zone

ELECTROLYTE

OXYGEN DEPLETION
CATION DISSOLUTION,
HYDROLYSIS

H · REDUCTION TO H

WATER REDUCTION TO H

WATER VAPOR

MOLECULAR TRANSPORT
PHYSICAL ADSORPTION H_2O

CHEMICAL REACTION TO
Fe_xO_y · H_2O : H

GASEOUS HYDROGEN

(1) MOLECULAR TRANSPORT

(2) PHYSICAL ADSORPTION H_2

(3) H_2 MIGRATION, DISSOCIATION
TO ATOMIC H

(4) CHEMICAL ADSORPTION

(5) SOLUTION TO LATTICE, TRAP SITES

(6) BULK DIFFUSION TO FPZ

(7) ENHANCED FATIGUE DAMAGE

σ_y, $\Delta\epsilon_P$

$C_{H\sigma}$

C_H

δ

Crack Closure?

ΔK Intrinsic?

R?

ΔK

da/dN

Displacement

Load

Computer

COD Gauge

Load Cell

Environmental Cell

Monotonic Load Cracking in Ti Alloys

1. How are the threshold and rates for crack growth affected by crack tip strain rate?

2. Can monotonic load data be incorporated into a superposition model for da/dN?

    oo   Specimens from fatigue experiments

    oo $J(\Delta a)$ as a function of loading rate; calculation of $\dot{\varepsilon}_{CT}$

    oo   Effect of τ_H and f on da/dN at $K_{max} > K_{th}$

Elevated Temperature Fracture of an Advanced Rapidly Solidified Powder Metallurgy Aluminum Alloy

William C. Porr, Jr. and Richard P. Gangloff

Objective

The goal of this study is to characterize the fracture toughness of advanced powder metallurgy Al-Fe-V-Si alloy 8009 as a function of temperature, loading rate, environment and microstructure. The underlying mechanism for the time-temperature dependence of the fracture toughness of 8009 will be understood from considerations of deformation mechanisms specific to the novel fine grained dispersion strengthened microstructure, greater than equilibrium substitutional solute content from rapid solidification, embrittlement by the moist air environment, and embrittlement by processing originated dissolved hydrogen. The importance of delamination toughening will be assessed.

Status

This project was completed during this reporting period. The graduate student, Mr. William C. Porr, Jr., successfully defended his dissertation and received the PhD degree in Materials Science and Engineering in June, 1992. Two papers are being prepared for journal publication.

Recent Results

Dispersion strengthened aluminum alloys, produced by rapid solidification or mechanical alloying and powder processing, are candidates for next generation aerospace structures that operate at intermediate elevated temperatures. While such alloys exhibit excellent strength and microstructural stability to 400°C, fracture mechanics damage tolerance is degraded at intermediate temperatures and slow loading rates. Research on melt spun and extrusion compacted alloy 8009 (Al-8.5Fe-1.3V-1.7Si wt%; Allied Signal) demonstrates strong reductions in initiation and growth fracture toughness, reduced tensile ductility at various levels of triaxial constraint, increased sustained load crack growth rates, and time-dependent fatigue crack propagation at temperatures near 175°C. Based on high

magnification SEM stereofractography of matching surfaces, the microscopic fracture mode is generally dimpled rupture nucleated by prior particle boundary oxides. The dimple morphology changes from spherical to elliptical in conjunction with decreased fracture resistance.

Proposed mechanisms that govern cracking include time-temperature dependent: (1) prior particle delamination toughening, (2) embrittlement by dissolved hydrogen from processing, (3) hydrogen (or oxygen) environment embrittlement, (4) dynamic strain aging from metastable solute such as Fe, and (5) localized plasticity associated with the 0.5 μm grain size and 30 volume % of silicide dispersoid. Experiments eliminate mechanisms based on delamination and hydrogen embrittlement. While dissolved solute may interact with dislocations, a strain aging mechanism has not been directly demonstrated or quantitatively developed for ultrafine grain size alloys. A new candidate mechanism for the degradation of fracture resistance is the temperature and strain rate dependent transition from dispersoid-dislocation interactions to silicide particle bypassing by dislocation climb. Those dislocations that evade particles localize and accumulate damage at boundary oxides and dispersoid clusters. This fracture mechanism is generic to fine grain size dispersoid strengthened aluminum alloys.

Milestones

No additional work is anticipated on this project. Future work on elevated temperature fatigue and fracture of advanced aluminum alloys will be conducted as described in the ensuing section on Project #4.

Presentation Graphics Captions

1. Title.

2. Program objectives.

3. THE PROBLEM: The deleterious effect of increasing temperature on the plane strain fracture toughness of RS/PM aluminum alloy 8009 (Al-8.5Fe-1.3V-1.7Si; wt%) is compared to the relative temperature insensitivity of K_{IC} for wrought precipitation hardened 2618. For 8009, tearing modules similarly declines with increasing temperature; both K_{IC} and T_R decline with decreasing loading rate.

4. Micromechanical modeling was employed to predict the initiation and growth fracture toughnesses of 8009 employing measured uniaxial and notched tensile properties. Here, we show models developed by Ritchie et al. and Chan.

5. The micromechanically predicted (after Ritchie et al.) and measured temperature dependencies of crack initiation fracture toughness are shown. The result is that fracture toughness decreases with increasing temperature because tensile yield strength, modulus of elasticity and strain to nucleate "local fracture damage" within the crack tip field all decline with increasing temperature. This latter local ductility normally increases with increasing temperature for aluminum alloys such as 2618, and compensates for decreasing σ_{ys} and E.

6. The micromechanically predicted (after Chan) and measured temperature dependencies of crack growth toughness given by the tearing modulus.   .

7. Candidate mechanisms for the reduction in local tensile ductility with increasing temperature and decreasing strain rate for alloys such as 8009.

8. Macrofractographs showing that delamination is severe in extruded 8009 at both ambient and very high temperatures, but does not occur at intermediate temperatures where fracture toughness is low.

9. Macrofractographs showing that plate 8009 only delaminates at the highest temperature. In contrast to extruded 8009, plate material does not exhibit delamination during room temperature fracture.

10. The plane strain crack initiation and growth toughnesses of plate 8009 decrease with increasing temperature. Toughness is isotropic within the rolling plane. The toughness reduction is observed with increasing temperature in spite of the lack of delamination. ·

11. Candidate mechanisms for the reduction in local tensile ductility with increasing temperature and decreasing strain rate for alloys such as 8009.

12. The plane strain fracture toughness of conventionally processed plate 8009, as a function of temperature, compared to the behavior of plate 8009 that was autoclave processed after rolling to reduce the total dissolved hydrogen content. Similar temperature dependent decreases in K_{IC} are observed for each material, indicating that hydrogen in the alloy is not the cause of the deleterious temperature effect. .

13. Candidate mechanisms for the reduction in local tensile ductility with increasing temperature and decreasing strain rate for alloys such as 8009.

14. Scanning electron micrographs of metallographically sectioned notched tensile specimens of extruded 8009: (a) 25°C; strained to 0.188, or 95% of the strain to fracture, and (b) 175°C; strained to 0.104, or 97% of the strain to fracture. Note that microcracks first nucleate at prior ribbon particle surface oxides, but only at very high strains.

15. Schematic representation of the "high toughness" fracture surface topography and void morphology for plate 8009 loaded at 25°C.

16. Schematic representation of the "low toughness" fracture surface topography and void morphology for plate 8009 loaded at 25°C.

17. A summary of the temperature and strain rate dependent evolution of microvoid fracture in 8009. These results are based on extensive high magnification scanning electron fractography, employing stereo pair and matching surface methods.

18. The critical role of dislocation dispersoid interactions in determining plastic flow localization and fracture toughness. The hypothesis is that fracture toughness is reduced at those increased temperatures and/or decreased crack tip strain rates where glide dislocations can climb to evade small silicide dispersoids in 8009 and where plastic deformation is accordingly localized in shear bands in the aluminum matrix.

19. Humphrey and Kalu developed a model to relate the strain rate, temperature and particle size conditions for the transition between dislocation-dispersoid interaction (homogenized slip deformation) and dislocation climb (leading to localized slip).

20. The Humphrey-Kalu model is plotted for typical activation energies for self-diffusion of aluminum. Data indicate the temperature-strain rate-dispersoid size conditions where yield strength and work hardening exponent exhibit inflections in temperature dependence. A single point is plotted to indicate the loading rate (calculated crack tip strain rate)-temperature-dispersoid diameter condition where K_{IC} for 8009 exhibits a sharp reduction with decreasing loading rate at 175°C.

21. Regarding the role of dynamic strain aging due to supersaturated Fe in 8009, recent data show that K_{IC} and T_R significantly decrease with increasing temperature for a developmental aluminum alloy produced by the Exxon Research and Engineering Company. This material is produced by cryogenic ball milling of "pure aluminum" combined with 2 wt% of Al_2O_3 for 5 hours in a liquid nitrogen slurry at -196°C. After consolidation into plate by extrusion at 460°C, the microstructure is reported to consist of 0.5 to 0.7 μm diameter aluminum grains immobilized by alumina particles. Some AlN dispersoids may also be present. We have not examined the microstructure or tensile properties of this alloy. It is unlikely that dynamic strain aging played a critical role in the deformation and fracture of this alloy, however, this

speculation has not been proven. The behavior of this alloy is similar to that of RS/PM 8009 and suggests that the temperature dependence of fracture is generic to fine grain size-dispersoid bearing aluminum alloys.

22.   Conclusions: Phenomenology.

23.   Conclusions: Fracture mechanism.

ELEVATED TEMPERATURE FRACTURE OF RS/PM ALUMINUM ALLOY 8009

W.C. Porr, Jr., Sang-Shik Kim and R.P. Gangloff
Department of Materials Science and Engineering
University of Virginia

LA^{2}ST Grant Review Meeting
July, 1992

OBJECTIVE

APPLICATIONS OF ALLOY 8009 REQUIRE:

- ■ ■ Quantification of elevated
    temperature damage tolerance

- ■ ■ Micromechanical understanding
    of deformation and fracture
    behavior at elevated
    temperatures

    - ■ Metallurgy
        - ultrafine grain
            size
        - fine dispersoids
        - supersaturated
            solute

    - ■ Time dependent deformation

    - ■ Environmental effects

    - ■ Constraint/Delamination
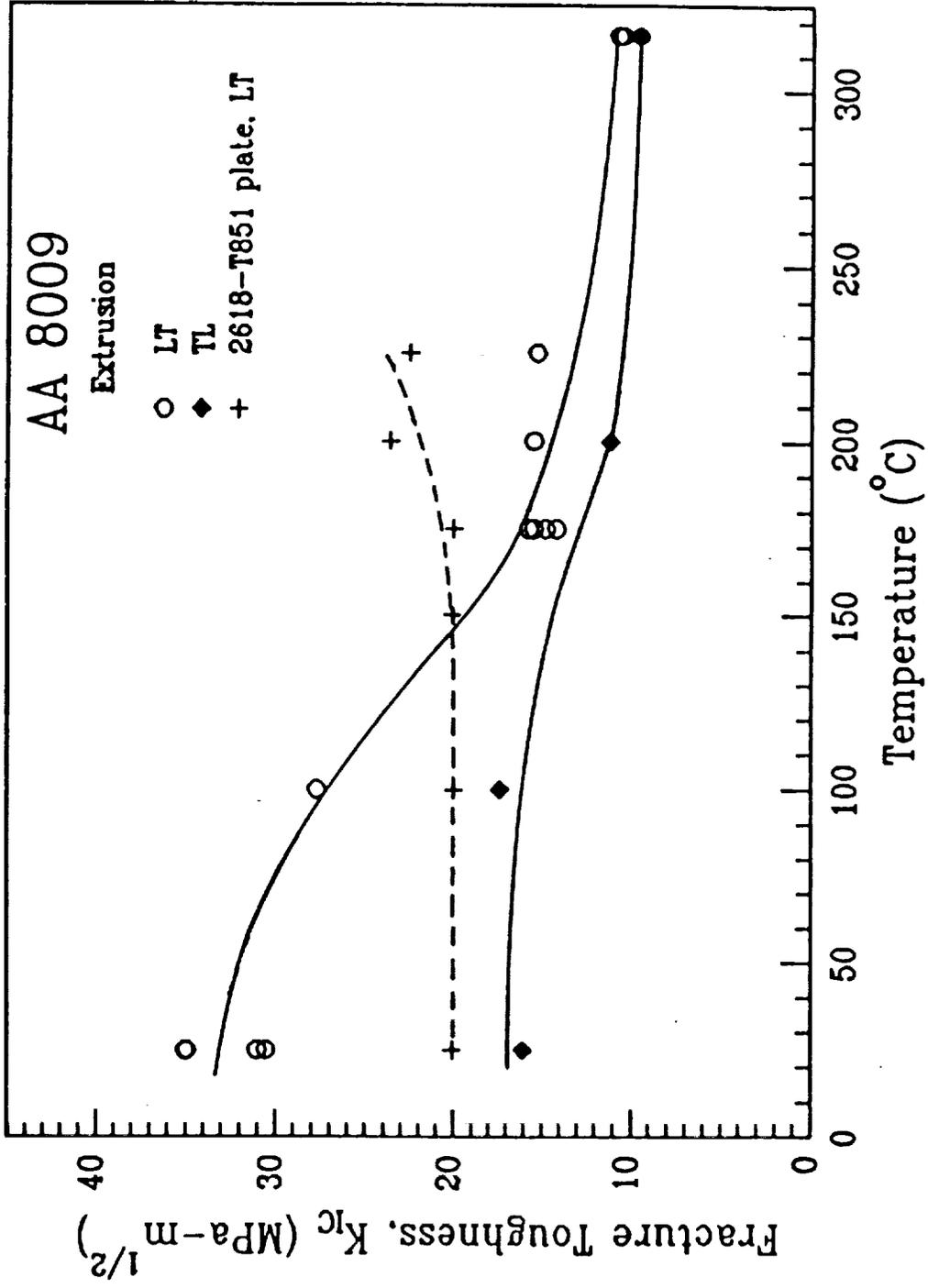
Fracture toughness, K_{IC}, as a function of temperature and specimen orientation for extruded 8009 and plate 2618-T851; displacement rate = 2.54 x 10⁻³ mm/s.

Micromechanical Modelling

- **Can be used to predict fracture toughness and tearing modulus from intrinsic tensile behavior:**

$$K_{IC} = \sqrt{\frac{1}{C_1 \alpha} E \sigma_{ys} l^* \varepsilon_f^*}$$

$$T_R = \frac{\varepsilon_{1f} E}{\sigma_{ys} r \alpha} - \frac{B}{\alpha} \ln\left[\frac{e \varepsilon_{1f} E \lambda}{\sigma_{ys} r \alpha}\right]$$

C-2

AA 8009
Extrusion

Critical Fracture Strain Micromechanical Modelling
□ Predicted
● Measured
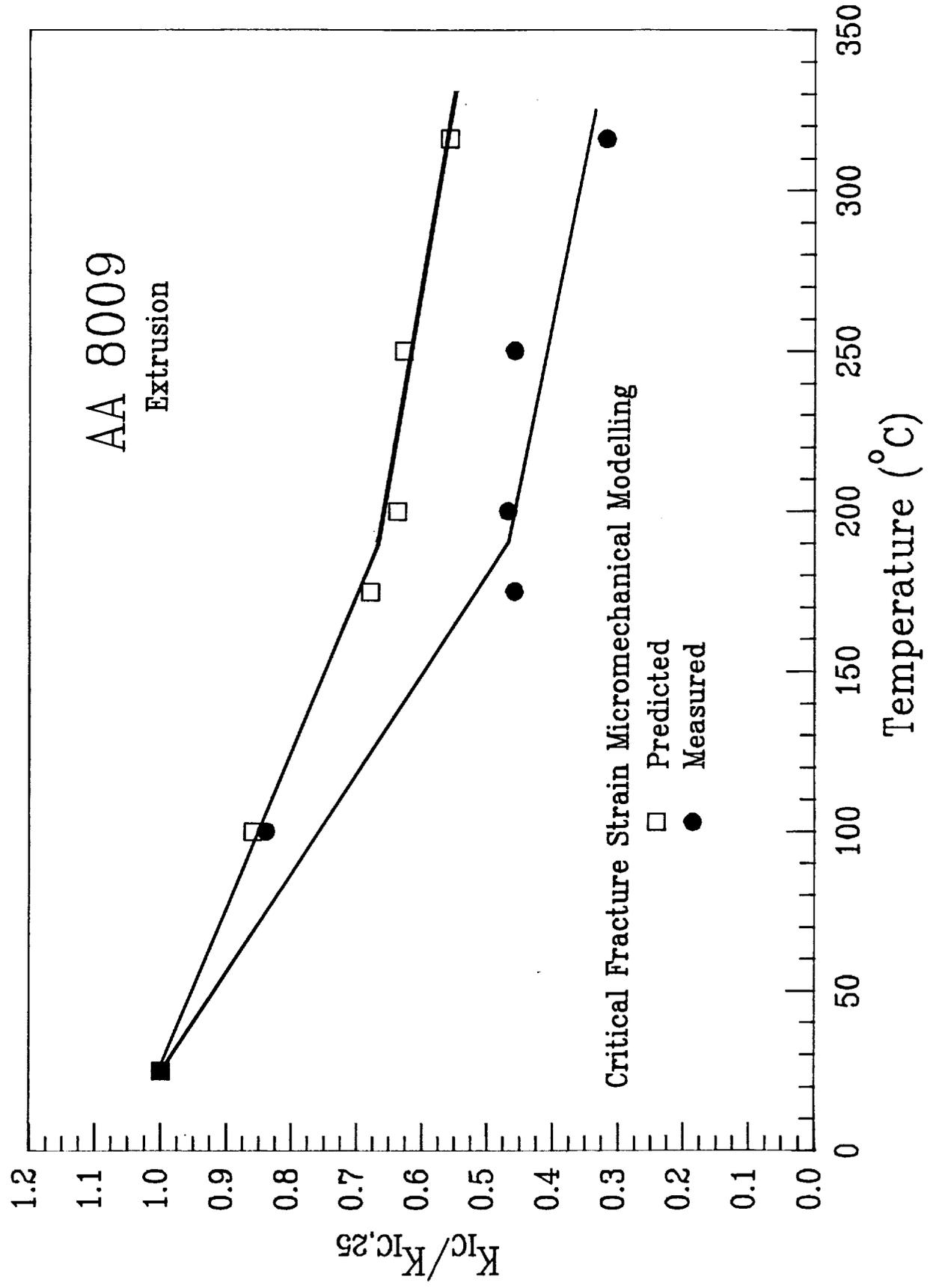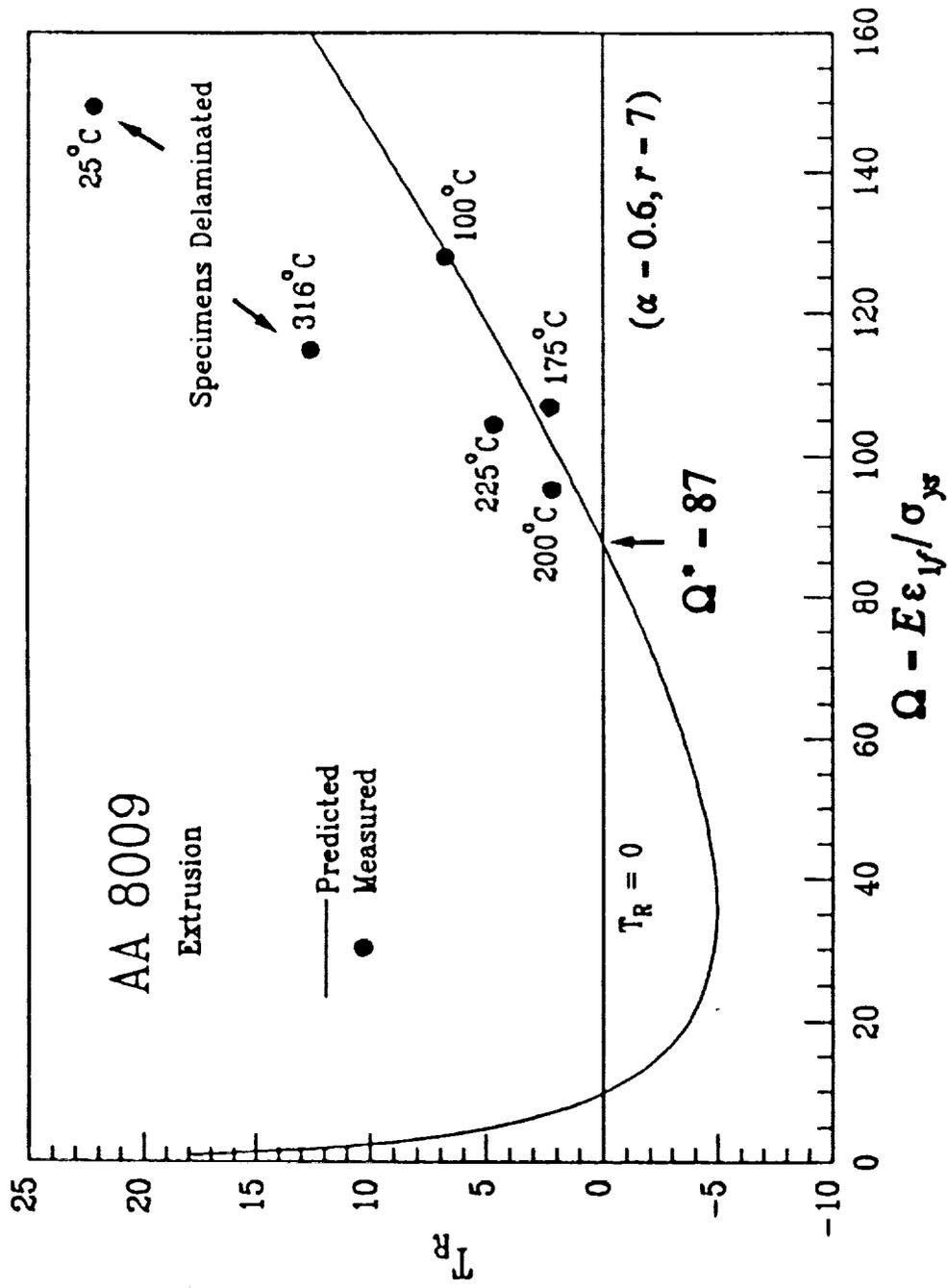
Predicted and measured values of tearing modulus, T_R, as a function of Ω for aluminum alloy 8009. T_R is predicted from Eqn. 20.

POSSIBLE CAUSES

Delamination Toughening

-- Extrinsic

Creep

-- Novel Mechanism Due To Ultra Fine Microstructure

Environment

-- Oxidation
-- Hydrogen Embrittlement

Dynamic Strain Aging

-- Greater than equilibrium substitutional solute concentration
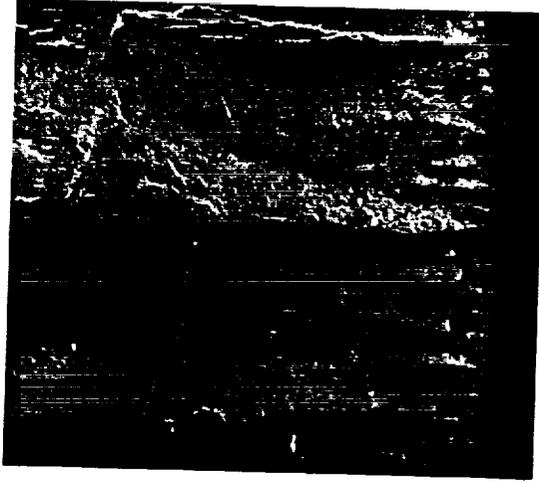
(a) 25 C   (b) 200 C   (c) 316 C

Low magnification SEM photographs of FVS0812 fracture surfaces for different test temperatures.

316° C

175° C

25° C
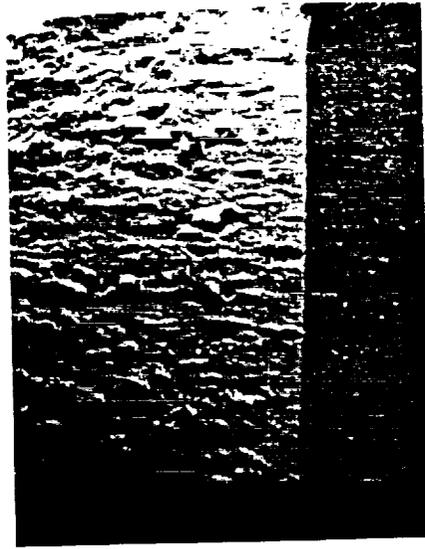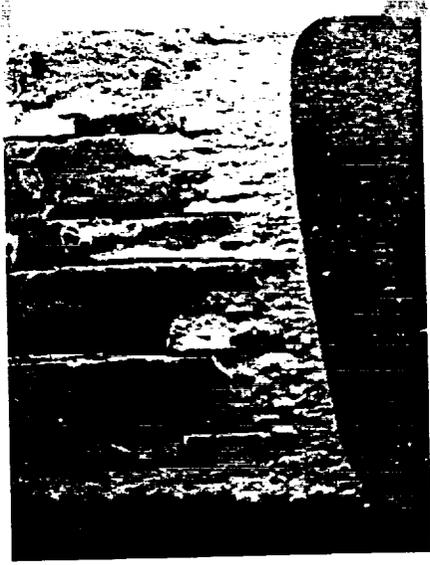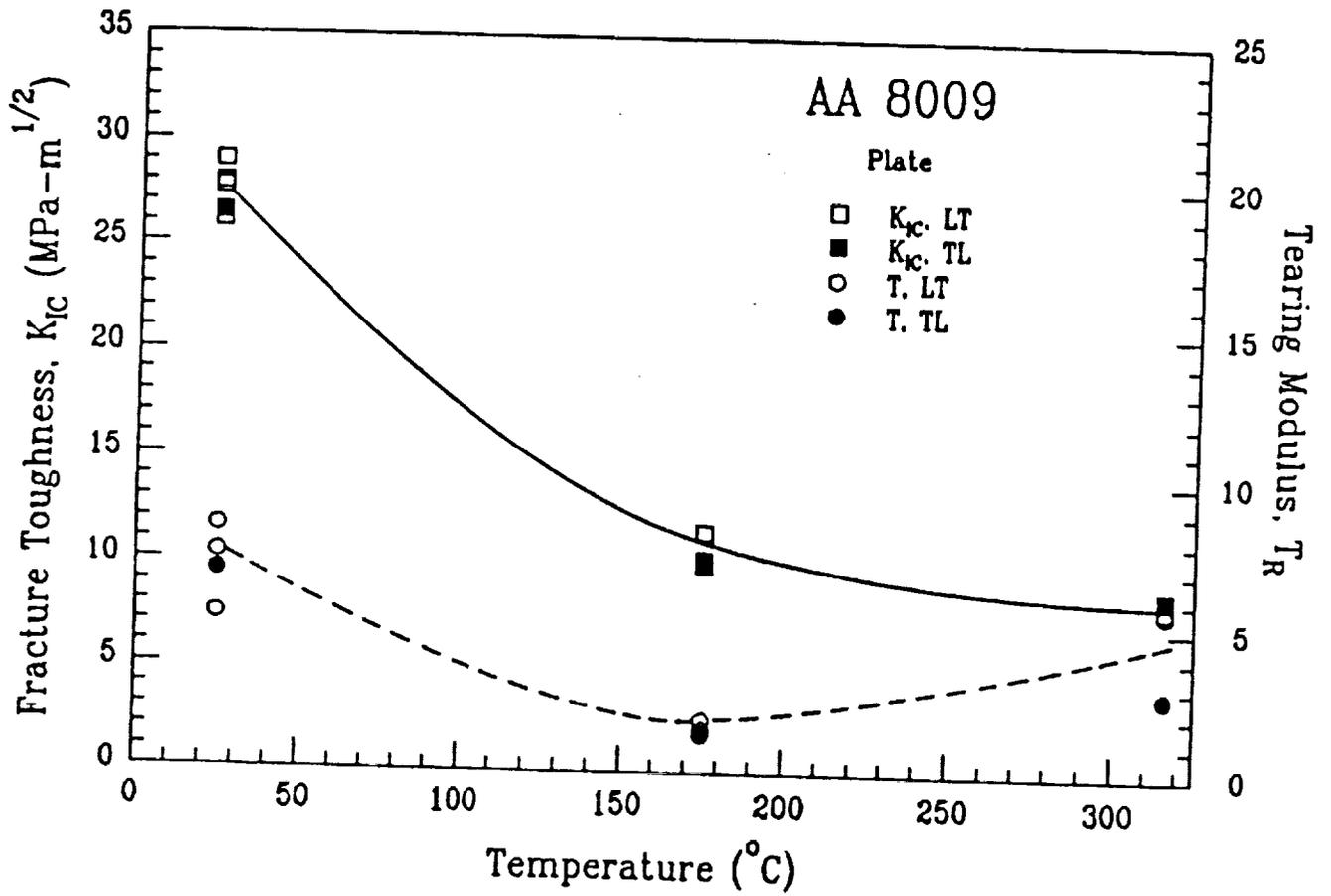
Fracture toughness, K_{IC}, and crack growth toughness, T_R, as a function of temperature and specimen orientation for plate 8009; displacement rate = 2.54 x 10^{-3} mm/s.

POSSIBLE CAUSES

Creep

-- Novel Mechanism Due To Ultra Fine Microstructure

Dynamic Strain Aging

-- Greater than equilibrium substitutional solute concentration

Delamination Toughening

-- Extrinsic

Environment

-- Oxidation
-- Hydrogen Embrittlement

CONVENTIONAL HYDROGEN 8009 PLATE

Test Temperature (°C)	K_{IC} (MPa√m)			
25	26.1	27.7	27.9	29.0
175	10.0	10.2	11.5	
316	8.7			

Air melt spin, Compact, Roll
$C_{H-TOTAL}$ = 4.3 ppm-w

LOW HYDROGEN 8009 PLATE

Test Temperature (°C)	K_{IC} (MPa√m)
25	36.0
175	12.5
316	9.1

Air melt spin, Compact, Roll, Autoclave
$C_{H-TOTAL}$ = 1.0 ppm-w

POSSIBLE CAUSES

Delamination Toughening

-- Extrinsic

Creep

-- Novel Mechanism Due To Ultra Fine Microstructure

Environment

-- Oxidation
-- Hydrogen Embrittlement

Dynamic Strain Aging

-- Greater than equilibrium substitutional solute concentration
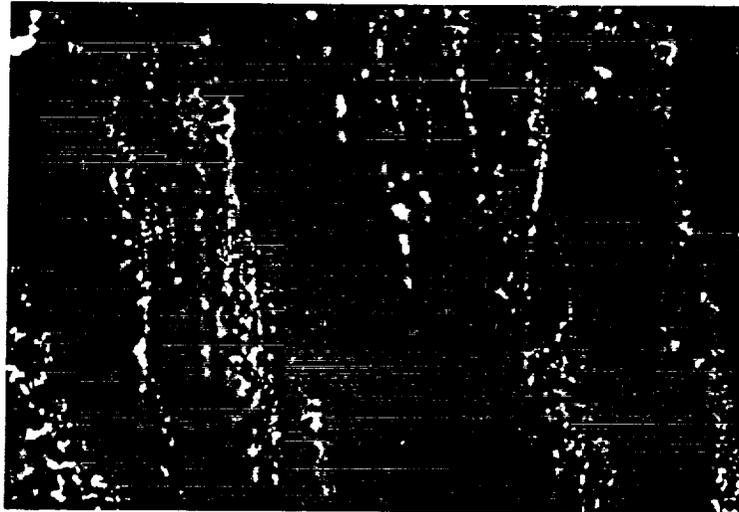
25 microns

25°C
95% Strain to Failure (0.188)
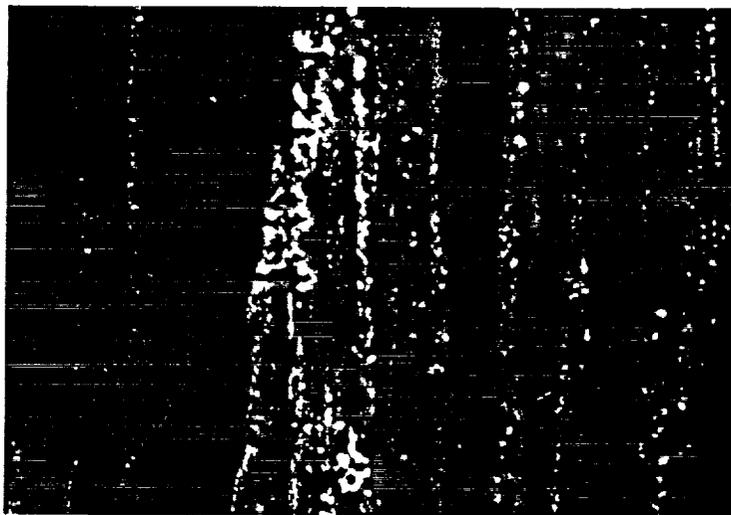
25 microns

175°C
97% Strain to Failure (0.104)
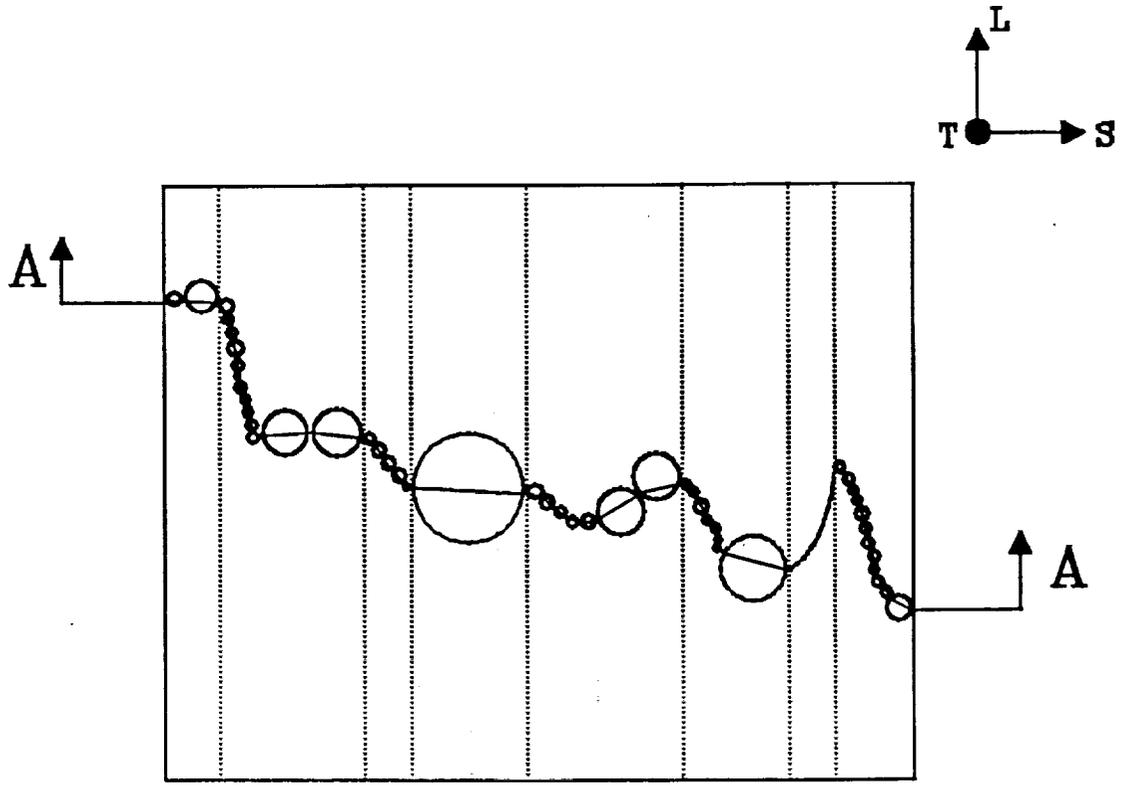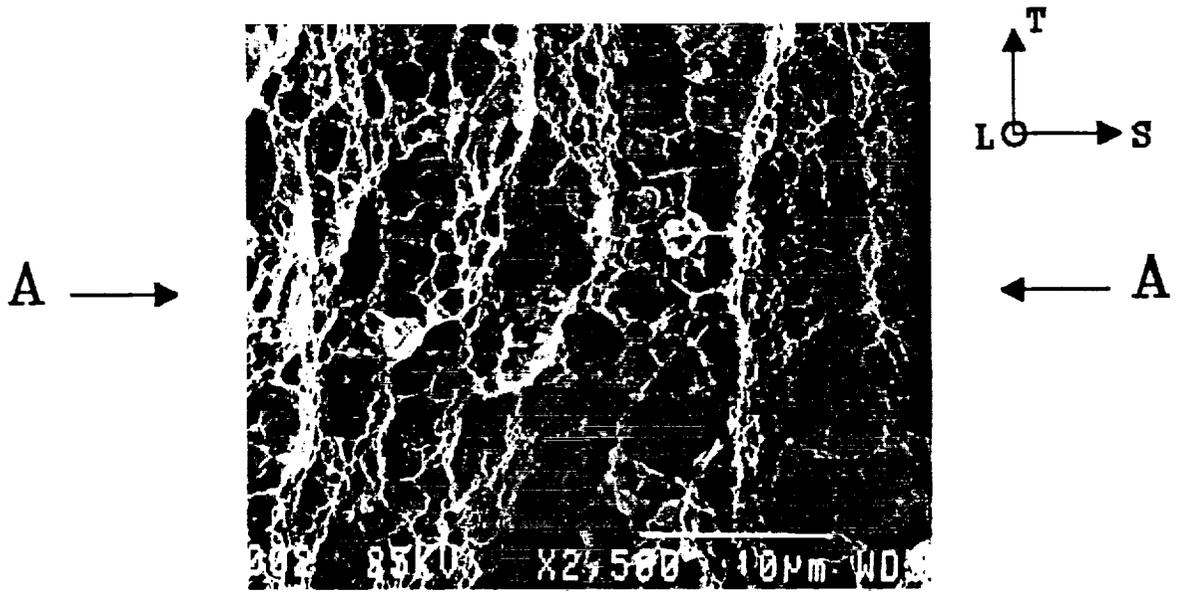
Schematic representation of the "high toughness" fracture surface topography and void morphology for plate 8009 loaded at 25°C; displacement rate = 2.54 x 10⁻³ mm/s.

Schematic representation of the "lowtoughness" fracture surface topography and void morphology for plate 8009 loaded at 175°C; displacement rate = 2.54×10^{-3} mm/s.

Temperature and Strain Rate Dependent Evolution of Fracture in AA 8009

- **Low Temps. and High Strain Rates:**

  - homogeneous dislocation activity
  - voids nucleate first at oxide particles – weak interface
  - with continued strain, voids initiate at dispersoids between oxide voids – void sheeting

- **High Temps. and Low Strain Rates:**

  - dispersoids cease to be barriers to dislocation motion
  - heterogeneous dislocation activity between oxides causes void initiation at low applied strains
  - voids grow rapidly along bands of localized flow resulting in observed shallow morphology

Dislocation Bypassing of Particles

IDEA: With applied strain, dislocations accumulate at nonshearable dispersoids – at elevated temps. or low strain rates, thermally activated climb of dislocations reduces strengthening.

– At some critical strain rate, temperature, and particle size condition, dislocations climb around dispersoids as they arrive; dispersoid strengthening is reduced.

– Evading dislocations allow localized flow between oxide particles and premature void nucleation.

Dislocation–Particle Bypassing Model

- By equating the rate that dislocations arrive at particles with the rate at which they climb around the particles, Humphrey and Kalu predict a critical strain rate for particle bypassing and an associated change in work hardening and deformation behavior:

$$\dot{\varepsilon}_c = \frac{K_1 \exp\left(\dfrac{-Q_v}{RT}\right)}{Td^2} + \frac{K_2 \exp\left(\dfrac{-Q_i}{RT}\right)}{Td^3}$$
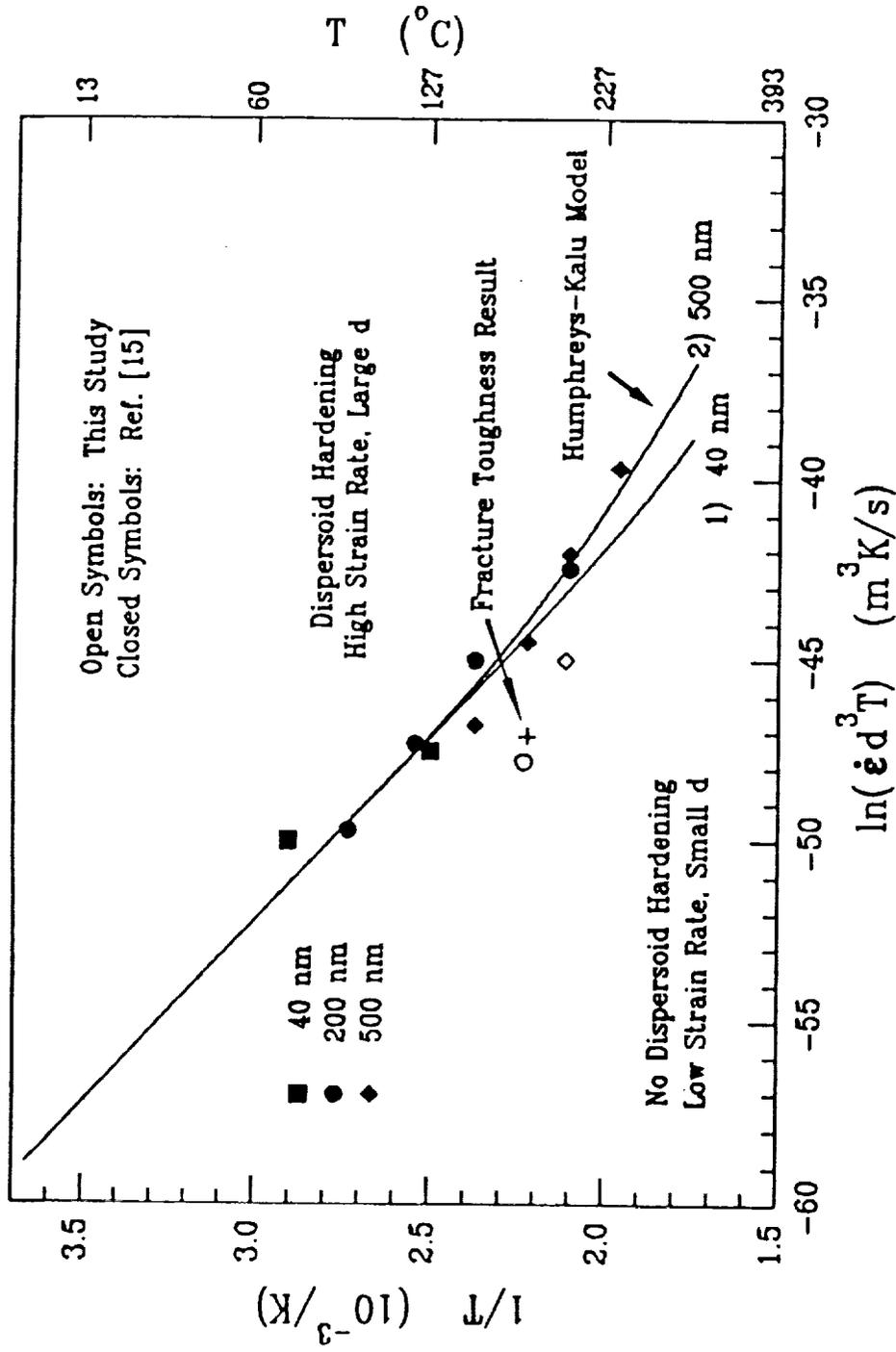
Theoretical transition for climb assisted dispersoid bypassing of dislocations as a function of particle size, temperature, and strain rate, as predicted by Eqn. 22

Exxon DS Aluminum
Disp. Rate = 2.54 x 10⁻³ mm/sec

Exxon DS Aluminum
Disp. Rate = 2.54 x 10⁻³ mm/sec
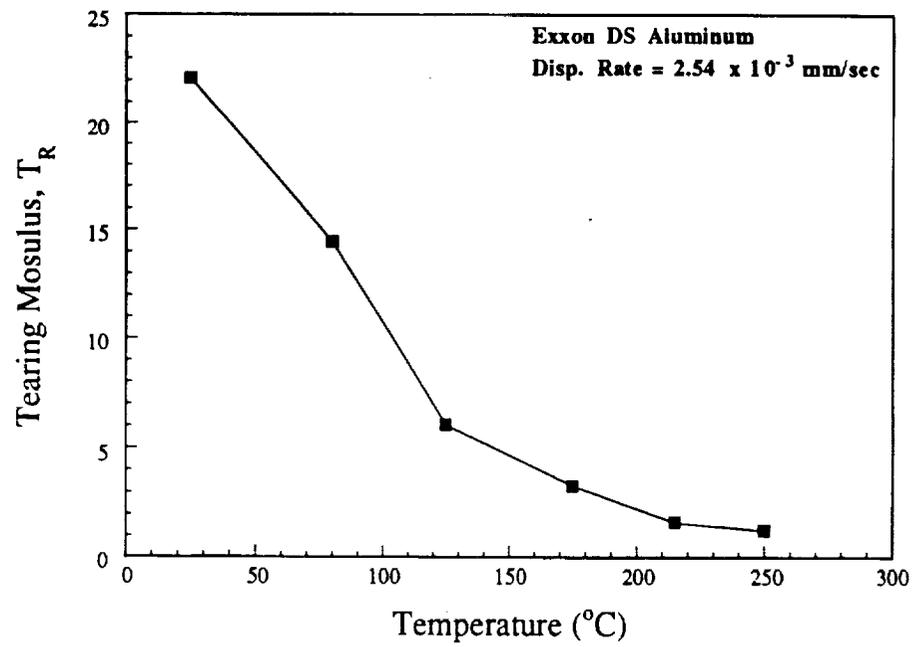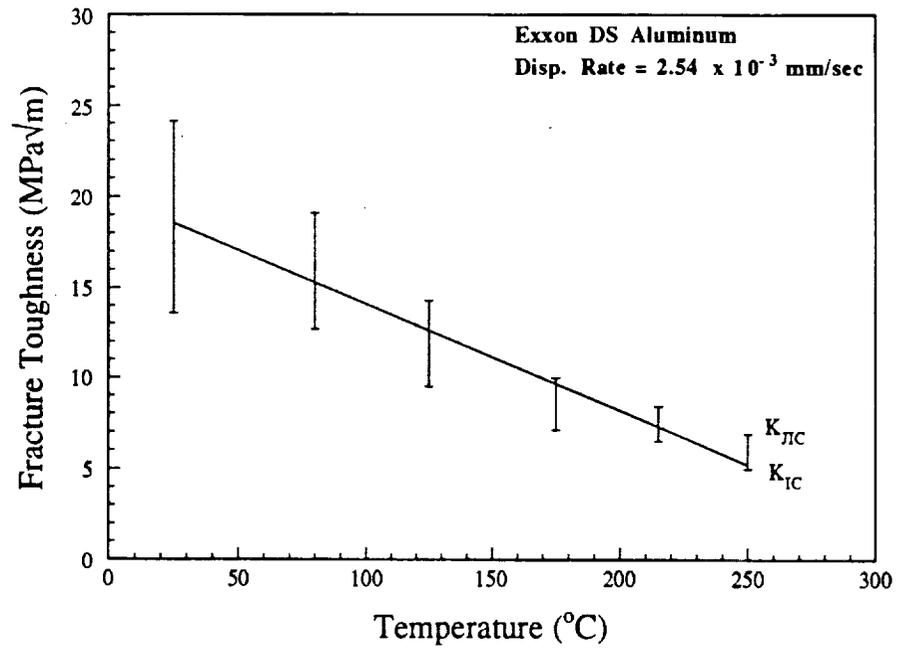
Conclusions: Phenomenology

- Elevated temperature damage tolerance degradation is generic to advanced PM aluminum alloys

- AA 8009 exhibits decreased intrinsic ductility and toughness (K_{Ic},T_R) with increasing temperature

- AA 8009 exhibits decreased fracture toughness with decreased loading rate at 25 and 175°C

- Micromechanical modelling accurately predicts the fracture initiation toughness and crack growth resistance of 8009 with increasing temperature

- Microvoid fracture morphology of 8009 changes with increasing temperature and decreasing loading rate

Conclusions: Mechanism

- The elevated temperature and low loading rate damage tolerance degradation of AA 8009 is not due to:
  - oxidation or hydrogen embrittlement (HE) from moist air
  - HE from strongly trapped internal atomic H
  - changes in delamination toughening

- Damage tolerance degradation from dynamic strain aging is unlikely

- The most likely mechanism for degradation of damage tolerance of AA 8009 is localized plastic flow between oxides and dispersoid clusters, and premature void nucleation, resulting from time-temperature activated dislocation climb negating small dispersoids as dislocation obstacles
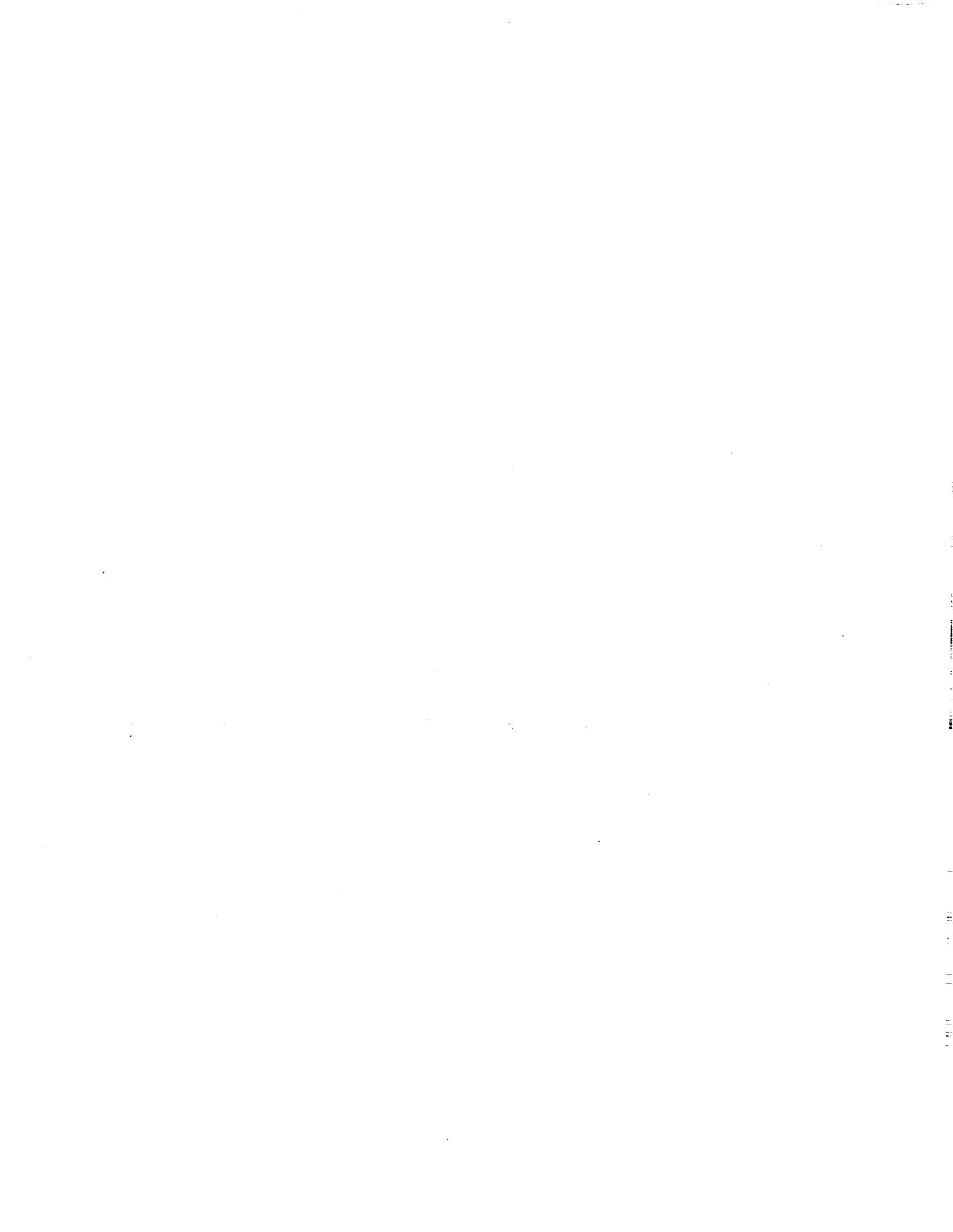
Project 4   Elevated Temperature Damage Tolerance of Advanced Powder Metallurgy Aluminum Alloys

Sang-Shik Kim and Richard P. Gangloff

Objective

The goal of this research is to characterize and model time-dependent and time-cycle-dependent fatigue crack propagation in advanced powder metallurgy aluminum alloys at elevated temperatures. Underlying mechanisms for temperature dependent cracking will be understood from considerations of deformation mechanisms and the influences of microstructure, alloy chemistry and environment.

This is a new program that will begin during the next reporting period. Mr. Michael Haynes was recruited in March of 1992 to conduct MS level research on this topic, commencing in September of 1992. As discussed in the 1992 renewal, this work will extend the results achieved by Porr; Project 3[1].

---

1.   R.P. Gangloff, "NASA-UVa Light Aerospace Alloy and Structures Technology Program", University of Virginia, Proposal No. MS NASA/LaRC-5219-92, October, 1991.

<u>Project 5</u>   Cryogenic Temperature Effects on the Deformation and Fracture of Al-Li-Cu and Al-Li-Cu-In Alloys

John A. Wagner and R.P. Gangloff

<u>Objective</u>

The objective of this PhD research is to characterize and optimize the crack initiation and growth fracture resistance of Al-Cu-Li and Al-Cu-Li-In alloys for cryogenic tank applications. The program aims to understand microscopic fracture mechanisms; as influenced by ambient to cryogenic temperature, stress state and microstructure.

<u>Status</u>

Currently, this work is focusing on the effects of microstructure, temperature and stress state on the fracture of commercial 2090-T81 and experimental 2090+In-T6 plate alloys. Crack growth resistance measurements were obtained, in terms of applied J-integral versus crack extension, for these alloys at ambient and cryogenic temperatures. Two specimen thicknesses were employed to examine cracking under nominal plane strain and plane stress conditions. Fracture surfaces are being analyzed through comparisons with the underlying microstructure to define the physical basis for fracture.

<u>Recent Results</u>

TEM analysis revealed that In additions to 2090 based compositions qualitatively increase the number density of T_1 strengthening phase, however, there is no measurable effect of In on yield strength. J-integral fracture toughness testing of 2090+In-T6 yielded crack initiation and growth toughness that are unacceptably low and fracture was characterized by intersubgranular (ISG) failure. Because of the insensitivity of yield strength to In additions and the low toughness of 2090+In-T6, the present investigation is concentrating on the fracture mode(s) of 2090-T81 under plane stress or plane strain constraint both at 25 and -185°C.

It appears that fracture in 2090-T81 is characterized by four different fracture modes: transgranular cooperative shear (TGS); slip band cracking (SBC); intersubgranular cracking

(ISG); and delamination fracture. Each mechanism is likely to be temperature dependent. The toughness of 2090 increases with increasing thickness and decreasing temperature due to increased levels of delamination fracture and perhaps due to temperature effects on deformation. Work is continuing to determine the mechanisms of fracture associated with transgranular shear, slip band cracking and intersubgranular cracking. A question of particular importance is the crystallographic and localized continuum deformation bases for shear cracking that appears to traverse multiple high angle grains to produce large facets.

Milestones

Future investigations will work toward developing a physical model to describe the evolution of fracture in 2090-T81 at ambient and cryogenic temperatures.

Presentation Graphics Captions

1. Title.

2. Problem statement and program objective.

3. Outline of presentation.

4. Indium additions to 2090 based alloys have been shown to increase the number density of the T_1 strengthening precipitate. However, this table shows that indium additions do not increase the yield strength of Al-Cu-Li alloys in the T6 condition.

5. Both 2090+In-T6 and 2090-T81 show an increase in yield and ultimate strength when tested at -185°C. In comparison to the 2090-T81 which exhibits a modest increase in elongation at -185°C, 2090+In-T6 exhibits a decrease in elongation at the cryogenic temperature.

6. In addition to exhibiting a decrease in elongation at -185°C, 2090+In-T6 also exhibits a decrease in work hardening rate at -185°C.

7. The microstructure of 2090-T81 is unrecrystallized with pancake-shaped grains elongated in the rolling direction. The 2090+In-T6 microstructure is also unrecrystallized, but has copious grain boundary and subgrain boundary precipitation.

8. A comparison of subgrain boundary precipitation in 2090 and 2090+In, each in the T6 condition, illustrates enhanced boundary precipitation in 2090+In after aging at 160°C for 20 hours. The boundary precipitation in 2090+In was apparent after only

3 hours of aging at 160°C.

9. This chart shows the R-curve fracture toughness behavior for both alloys in the plane stress and plane strain conditions. For 12.0 mm thick sidegrooved specimens, 2090-T81 exhibits superior toughness compared to 2090+In-T6. The low toughness of 2090+In-T6 is attributed to intersubgranular (ISG) fracture. For 1.6 mm thick specimens, the R-curve behavior of the two materials is similar, probably due to the absence of delamination toughening in the 2090-T81 in the plane stress condition. It is surprising that similar fracture resistance is recorded for the thin specimens, considering the significant amount of ISG fracture for the In bearing alloy, but not for conventional 2090, as demonstrated in point 12.

10. This metallographic result shows the cross section of a 12.0 mm specimen of 2090-T81 tested at 25°C; note macroscopic transgranular shear (TGS) fracture and grain boundary delamination. This section is normal to the fracture plane and near the point of fracture toughness initiation.

11. Presented is the polished metallographic cross section of a 12.0 mm thick specimen of 2090+In-T6 tested at 25°C; note flat ISG fracture which results in low toughness. This section is normal to the fracture plane and near the point of fracture toughness initiation.

12. Metallographic cross sections of 1.6 mm thick specimens of 2090+In-T6 and 2090-T81 are shown. The fracture of 2090+In-T6 remained ISG, similar to the plane strain case. The 2090-T81 case reveals fracture which was primarily characterized by TGS without delamination. These sections are normal to the fracture plane and near the point of fracture toughness initiation.

13. J-integral R-curves for 2090-T81 (12.0 mm thick) specimens show significantly better crack initiation and growth toughness at cryogenic temperature compared to ambient temperature. The increase in toughness is, at least in part, due to an increased level of delamination at -185°C.

14. Similarly, the R-curve behavior of 2090+In-T6 was enhanced at -185°C and was associated with the occurrence of delaminations which were not apparent at ambient temperature. However, toughness remained low compared to 2090-T81.

15. This is the fracture surface cross section of a 12.0 mm thick specimen of 2090-T81 tested at -185°C. Note, the increased level of delamination fracture compared to specimens tested at 25°C. Also, note the occurrence of TGS fracture which traverses several grains with fracture planes at angles close to those which correspond to planes of maximum shear stress; SBC which appears to occur within individual grains; and ISG fracture which is associated with heavily decorated substructure.

16. These higher magnification metallographic cross sections, and the scanning electron fractographs of the adjacent crack surface, show details of the fracture mode in 2090-T81. The two fractographs exhibit three of the four fracture modes in 2090-T81. Fracture in the left cross section was primarily by TGS in which fracture traversed across several grains. Fracture in the right cross section was by ISG fracture (left side) and by SBC within one grain (right side).

17. The plane stress crack growth resistance of 2090-T81 at -185°C was better than that at 25°C. Since delamination does not occur, this result suggests that temperature affects the intrinsic fracture resistance of alloy 2090. Fractographic analysis is in progress.

18. For 2090+In-T6 under plane stress and without delaminations, the trend of increasing toughness with decreasing temperature is reversed; specimens tested at -185°C exhibit lower toughness compared to those tested 25°C. This trend is consistent with the observed trend of lower work hardening and lower elongation at cryogenic temperatures.

19. Summary.

20. Because of poor fracture toughness behavior and the lack of an increase in yield strength with In additions to 2090 based alloys, future activities will focus on the fracture mechanisms associated with commercially available 2090-T81. Work will include determining the relative proportions of the various fracture modes as a function of stress state and temperature, and examination of the mechanisms for the observed change in fracture mode at -185°C.

FRACTURE OF Al-Li ALLOYS 2090 AND 2090+In AT CRYOGENIC TEMPERATURES

John A. Wagner

LA^{2}ST Program Review

NASA Langley Research Center

July 15-16, 1992

FRACTURE OF 2090 AND 2090+In ALLOYS

Problem

- No systematic investigation conducted to determine the interactive effects of:

  - Temperature
  - Delamination
  - Indium addition
  - Microstructure

  on the fracture of 2090-based alloys

Objective

- Determine the influences of microstructure, stress state and temperature on the occurrence of various fracture mechanisms in Al-Li-Cu-X alloys

FRACTURE OF 2090 AND 2090+In ALLOYS AT CRYOGENIC TEMPERATURES

Outline

- Summary of tensile properties of 2090+In-T6

- Progress on plate material structure/property correlation

- Future direction

2090 + In - T6 TENSILE PROPERTIES

(SHT = 538-560°C, 160°C 72-100 hrs)
2090-T81: σ_{ys} = 559MPa
2090-T6: σ_{ys} = 476MPa

Lab	Ingot Size	Material Condition	σ_{ys}	σ_{ult}
Northrop	160kg	SPF 150%	400MPa	531MPa
		TMTC	407	517
			372	482
Reynolds	14	Sheet	441	510
			448	496
LBL (Bradley)	160	SPF 90%	386	538
		TMTC	386	517
LBL (Verzsconi)	160	SPF Thermal No Strain	365	461
NASA (Wagner)	160	TMTC 12.7mm plate	372	496
			400	559
NASA (Wagner)	14	12.7mm plate	434	517
NASA (Blackburn)	14	12.7mm plate	490	538
Boeing	160			

no data available; but no increase in properties observed

TENSILE PROPERTIES OF 2090 AND 2090+IN
AT 25° AND -185°C

Ultimate
Yield
Elongation

Elongation,
%

2090-T81

2090+In-T6

Strength,
MPa

tp2090

TENSILE PROPERTIES OF 2090 AND 2090+IN AT 25° AND -185°C

tp2090&2090+in
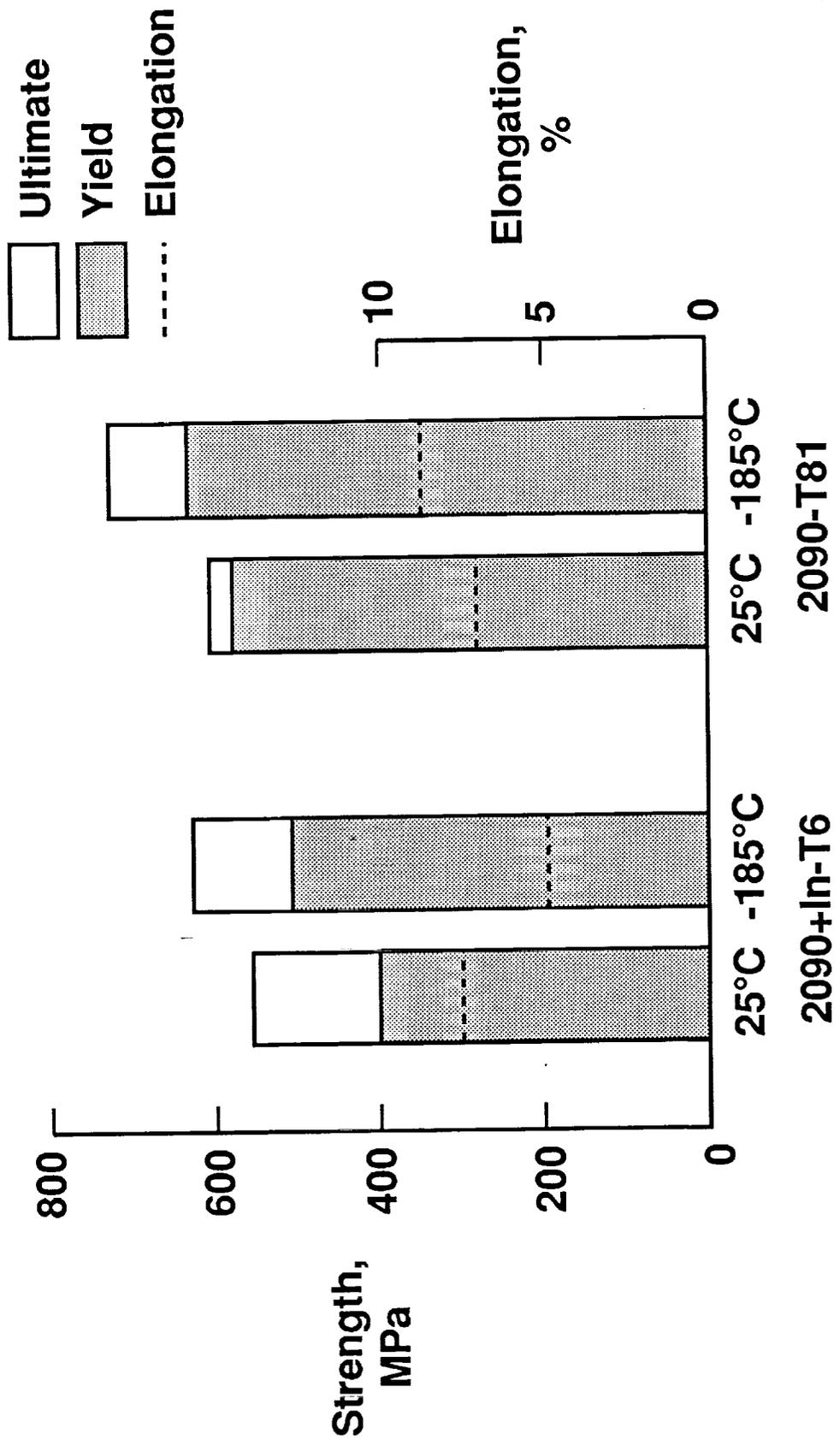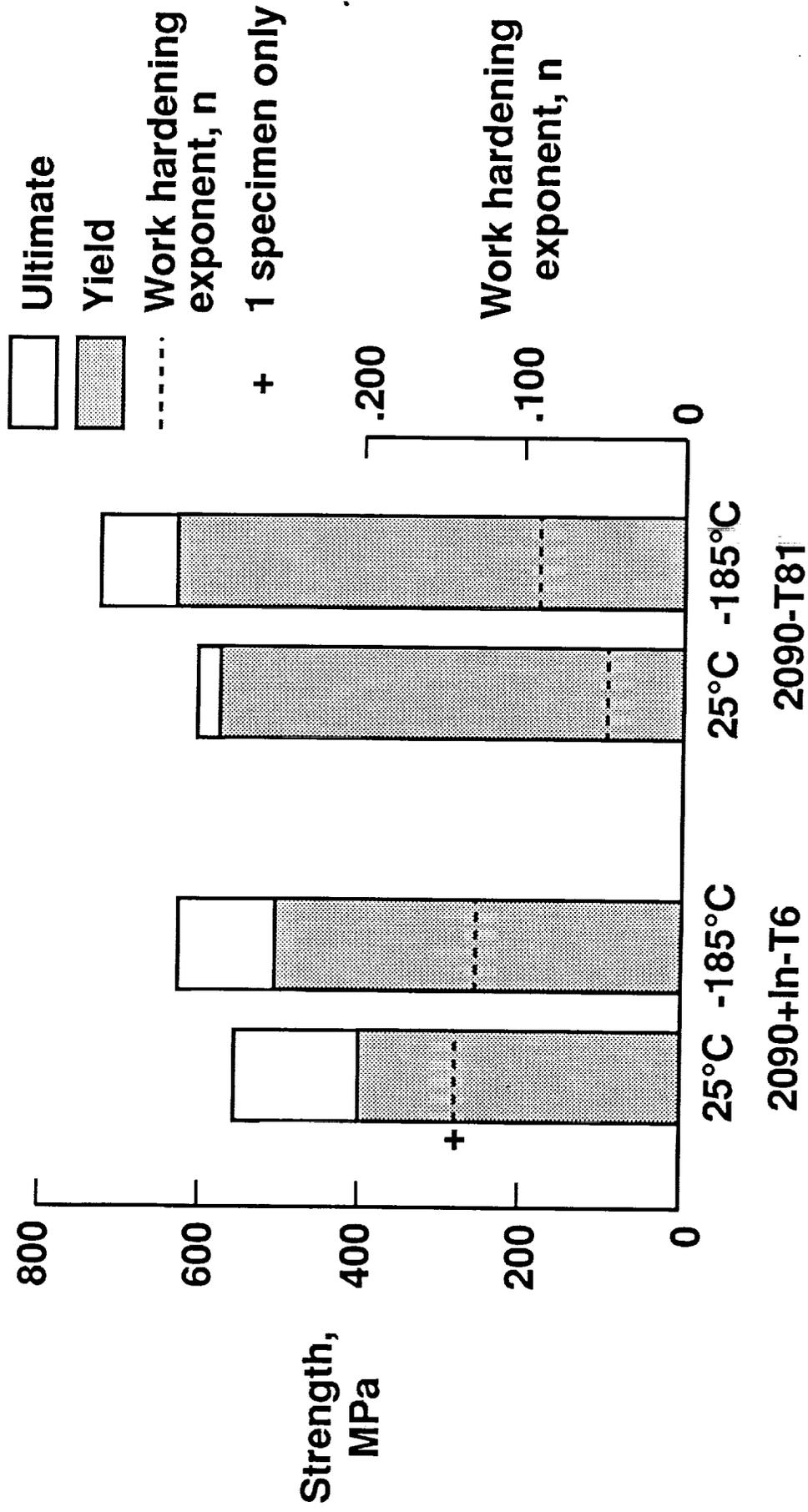
MICROSTRUCTURES OF PLATE ALLOYS
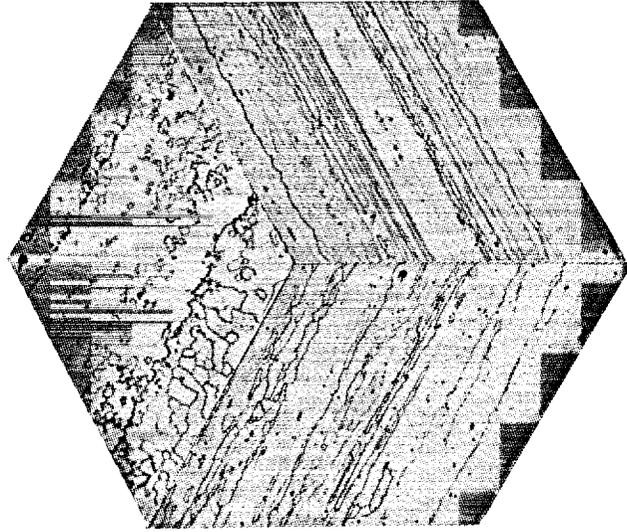
A2090-T81
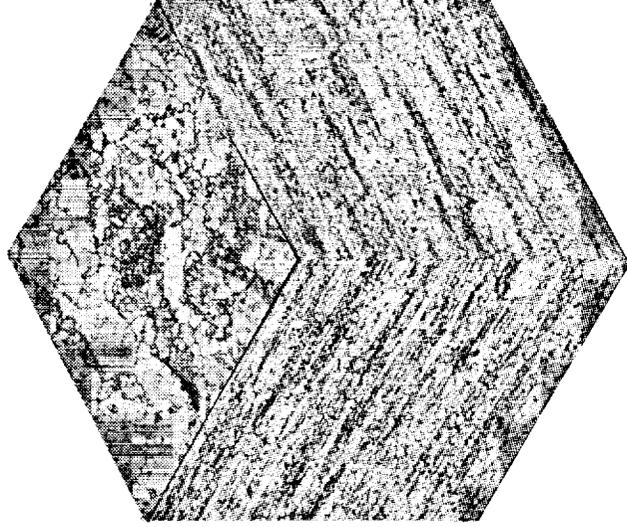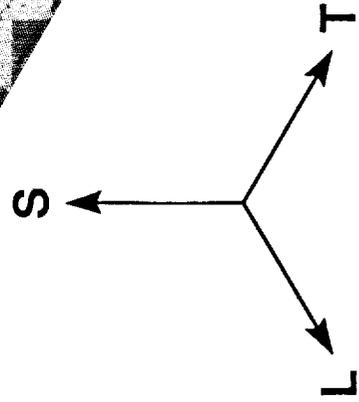
R2090 + In-T6

100μm

COMPARISON OF SUBSTRUCTURE PRECIPITATION OF A2090-T6 AND R2090-T6 AGED 20 HRS AT 160°C
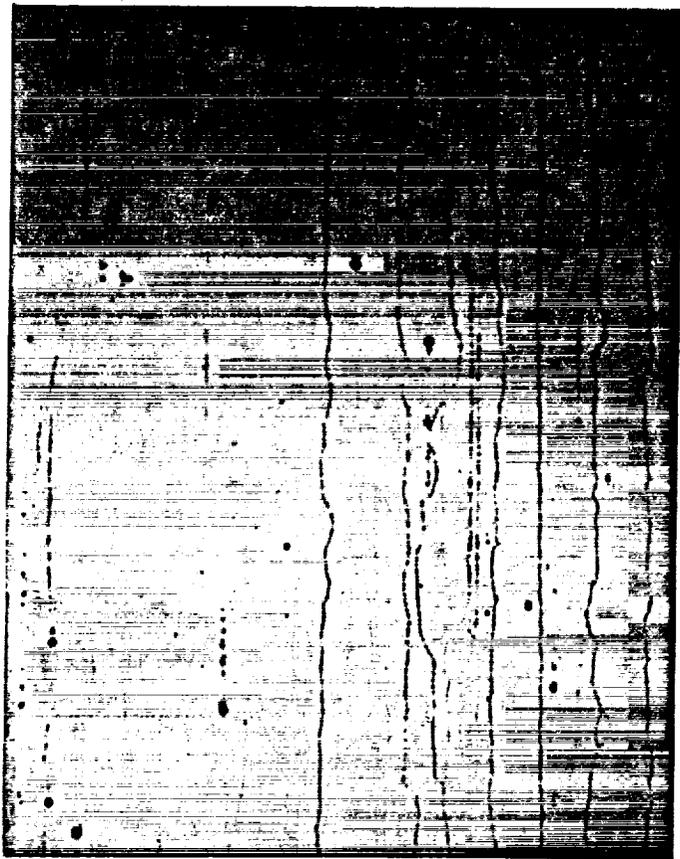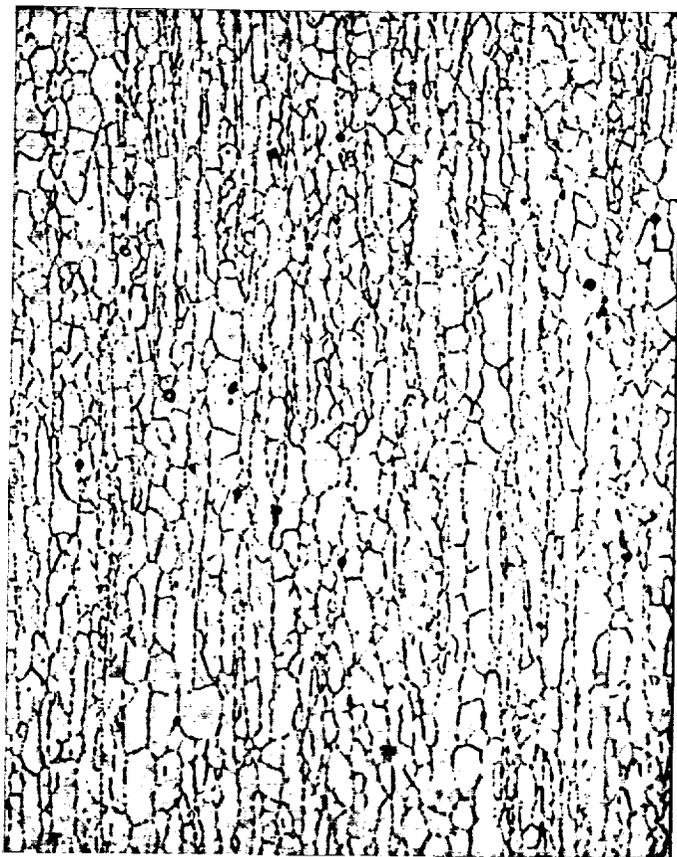
R2090+In-T6

A2090-T6

25μm

R-CURVES OF 1.6MM AND 12MM THICK SPECIMENS AT 25°C

○ 2090+In-T6

● 2090-T81

}1.6mm

12mm

Δa, mm

J, kJ/m^2

2090-T81
T = 25°C

200 μm
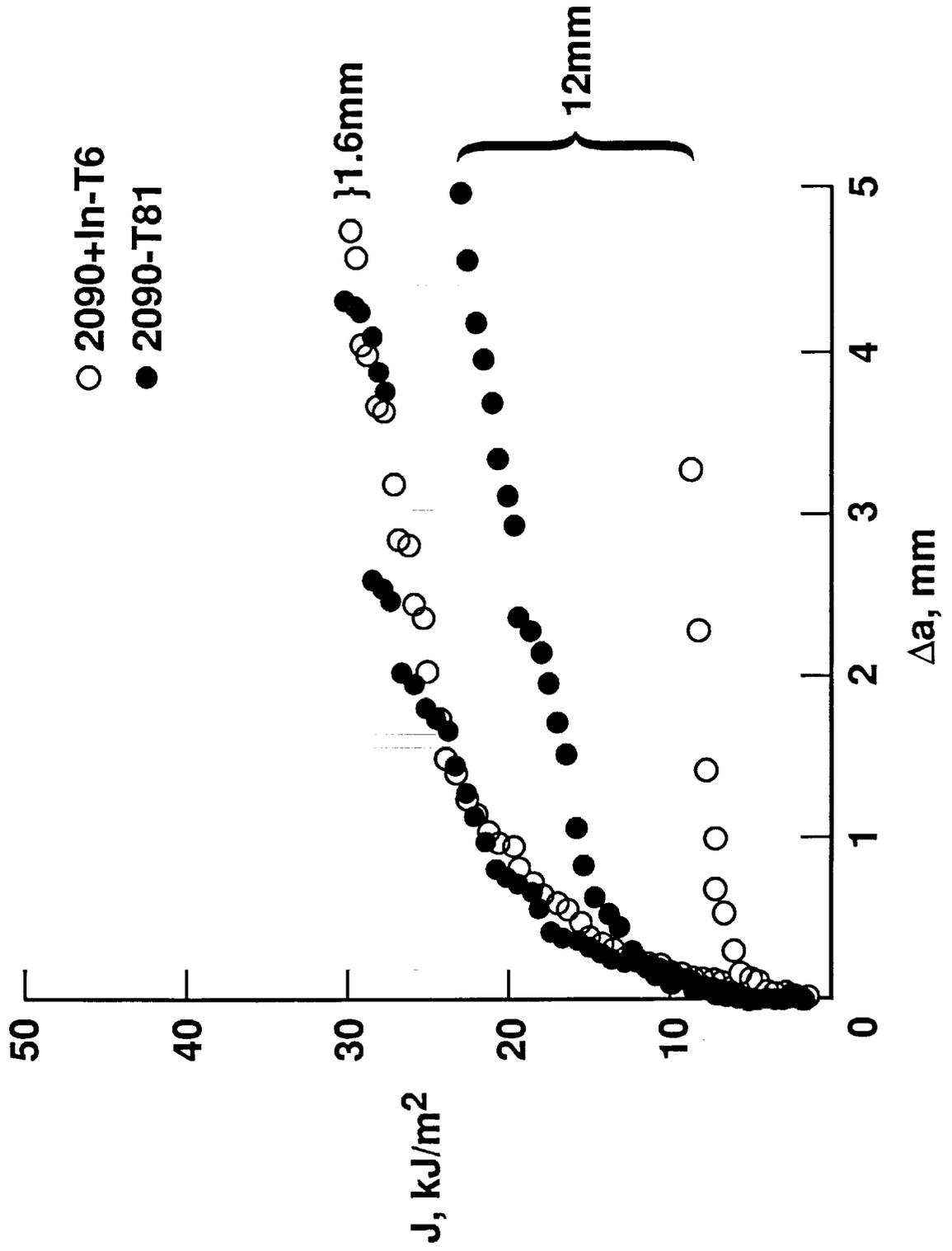
R2090 + In-T6

200 μm
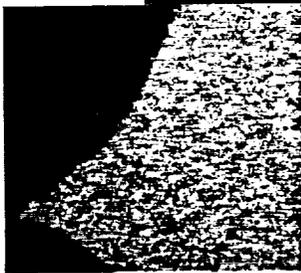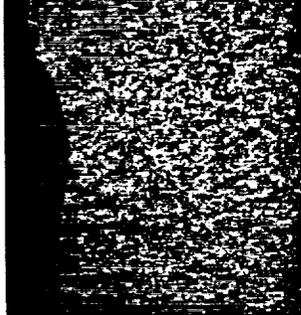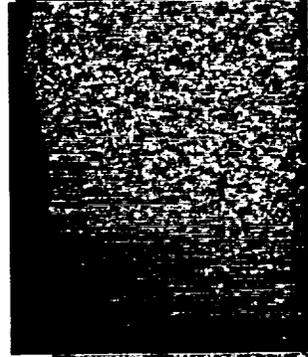
FRACTURE SURFACE CROSS SECTIONS OF 2090+In-T6 AND 2090-T8 TOUGHNESS SPECIMENS AT 25°C

2090-T81

2090+In-T6

400 μm
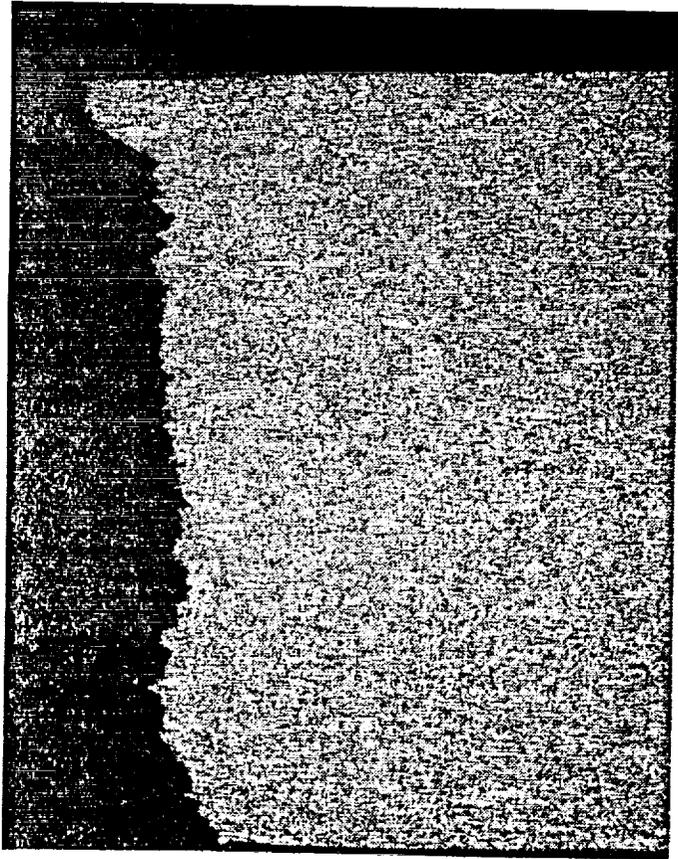
R-CURVE FOR 2090-T81 12MM THICK SPECIMENS
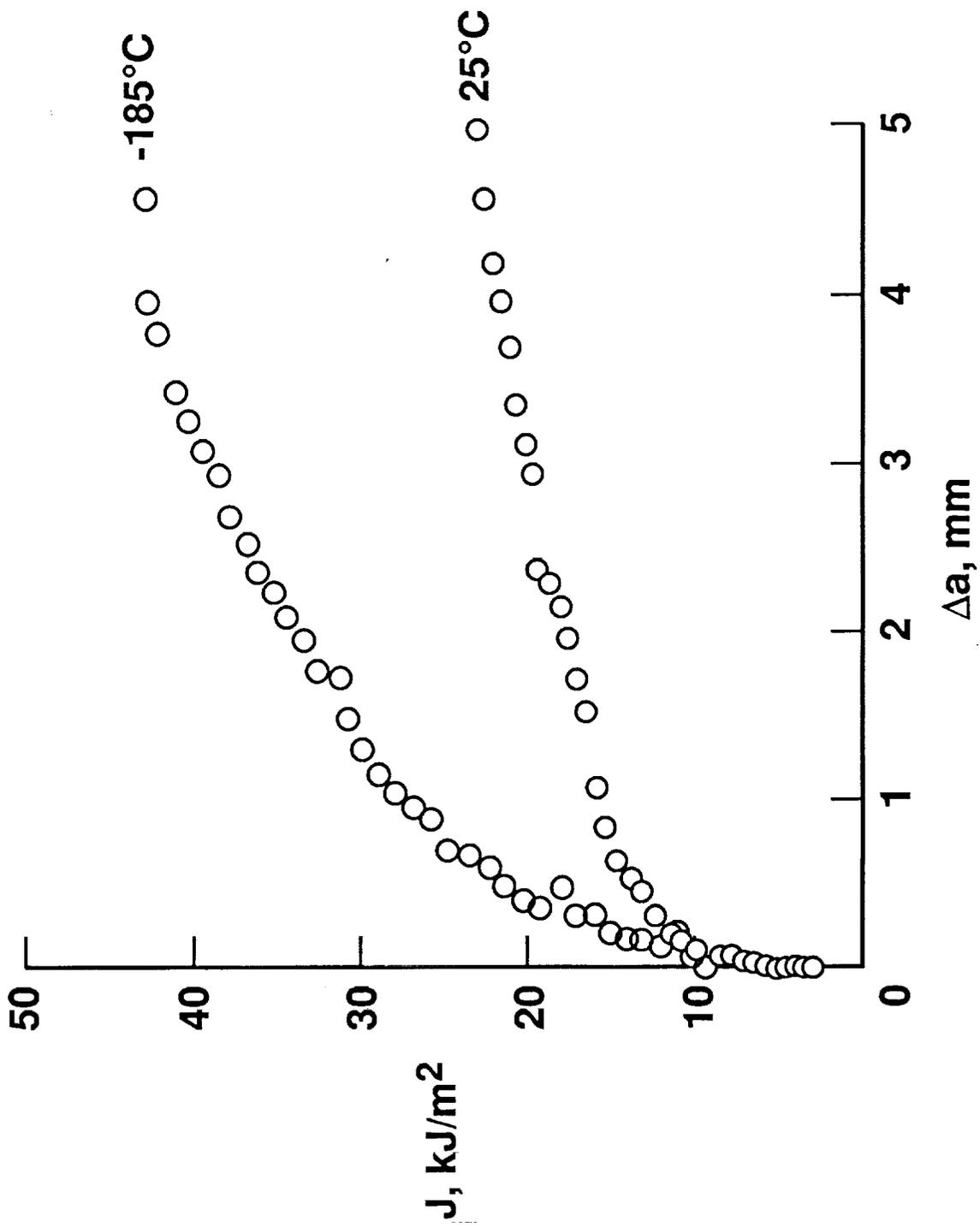
R-CURVE FOR 2090+In-T6 12MM THICK SPECIMENS

2090-T81
T = -185°C

200μm
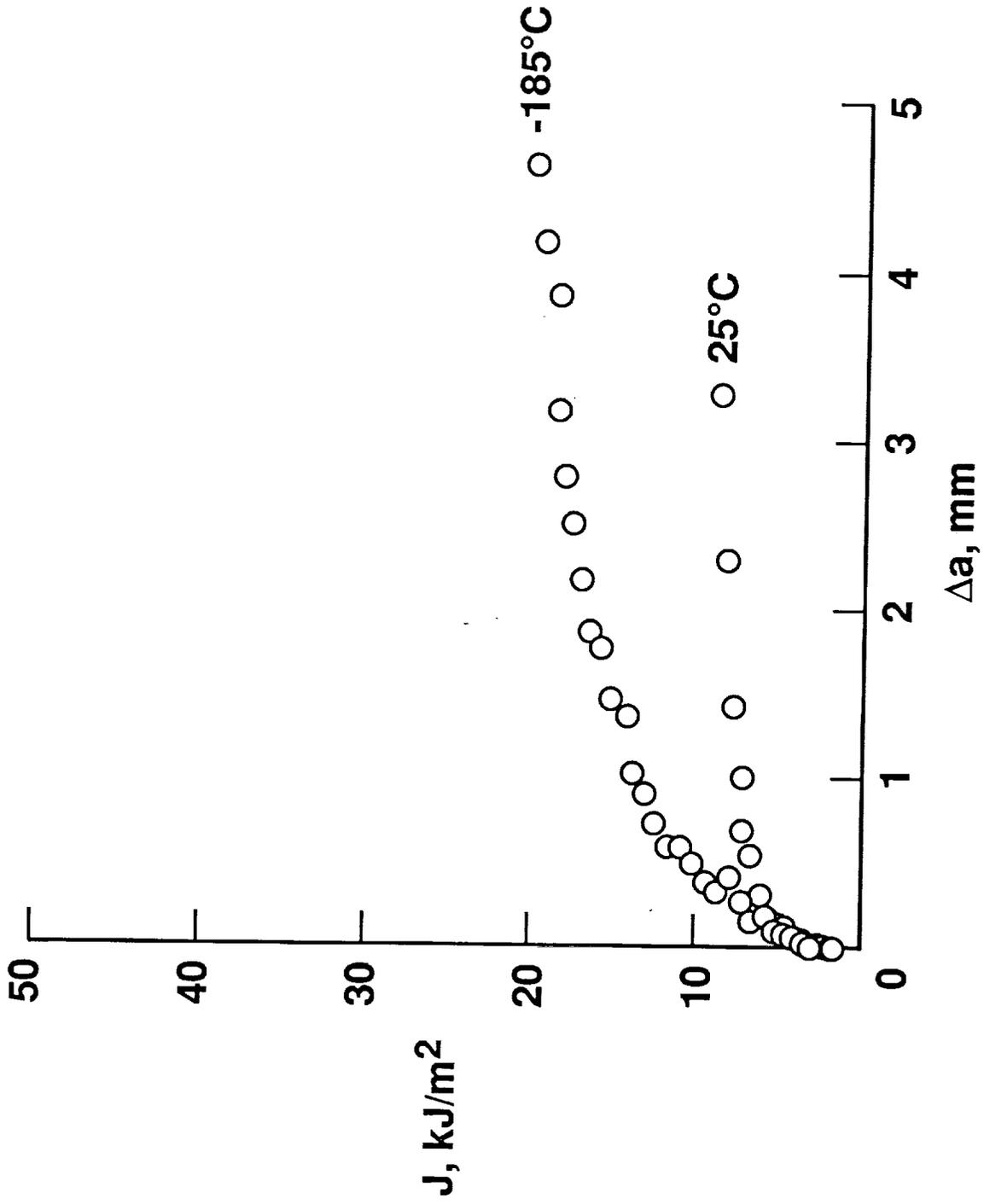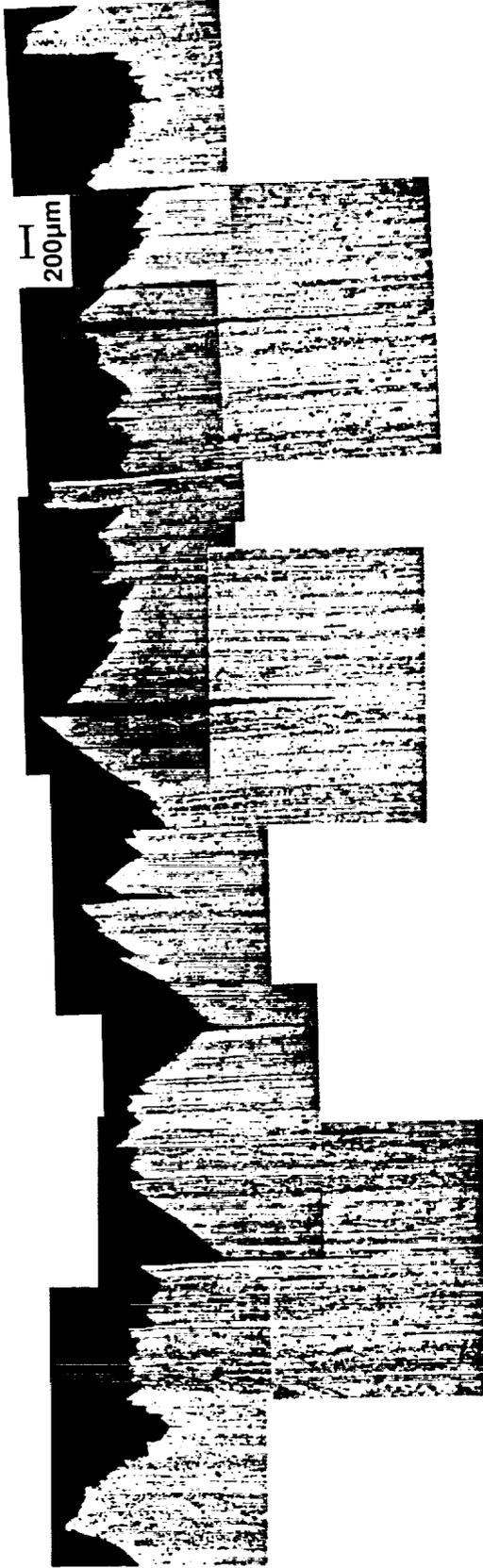
FRACTURE OF 2090-T81 AT -185°C

100μm

40μm
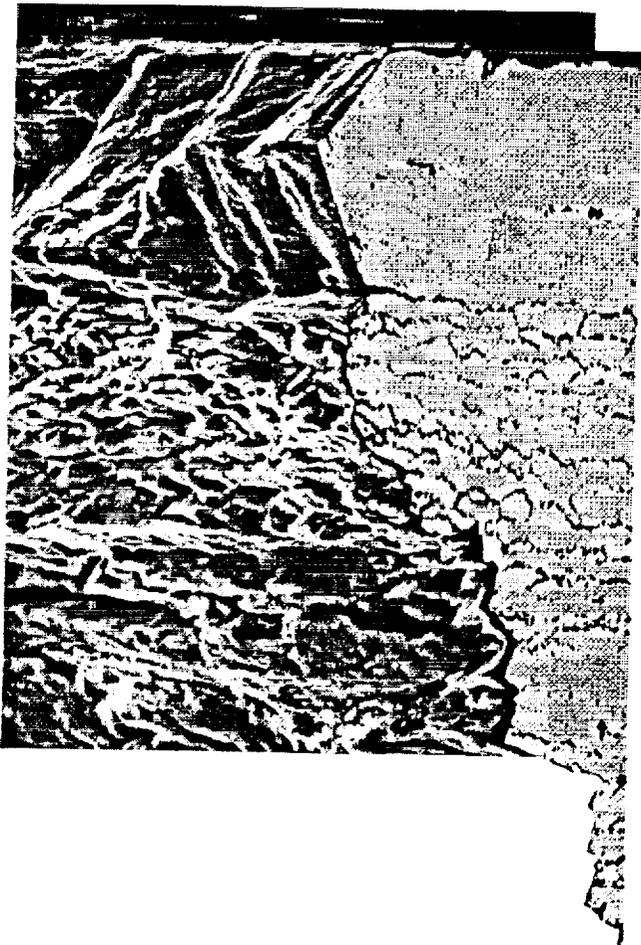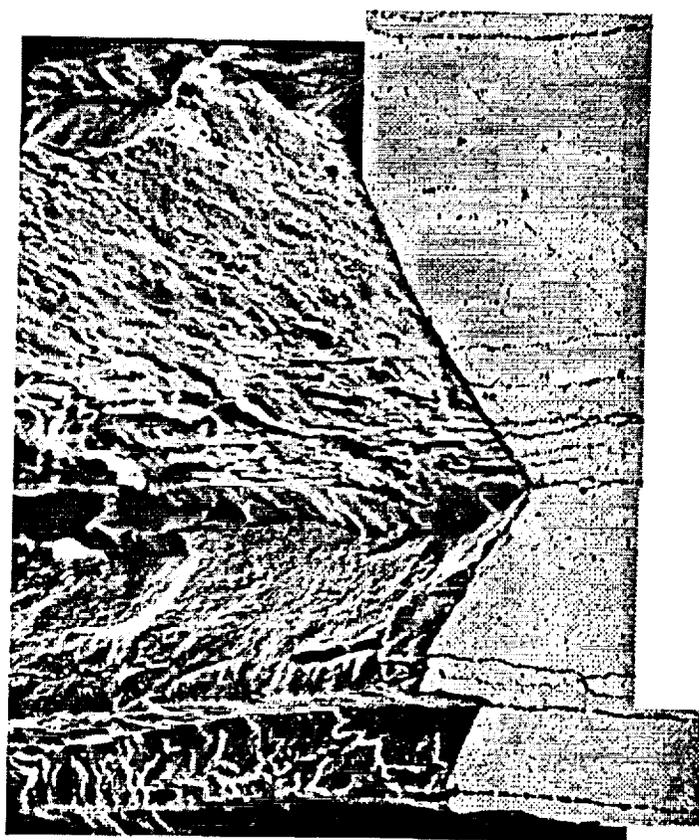
R-CURVE FOR 2090-T81 1.6MM THICK SPECIMENS
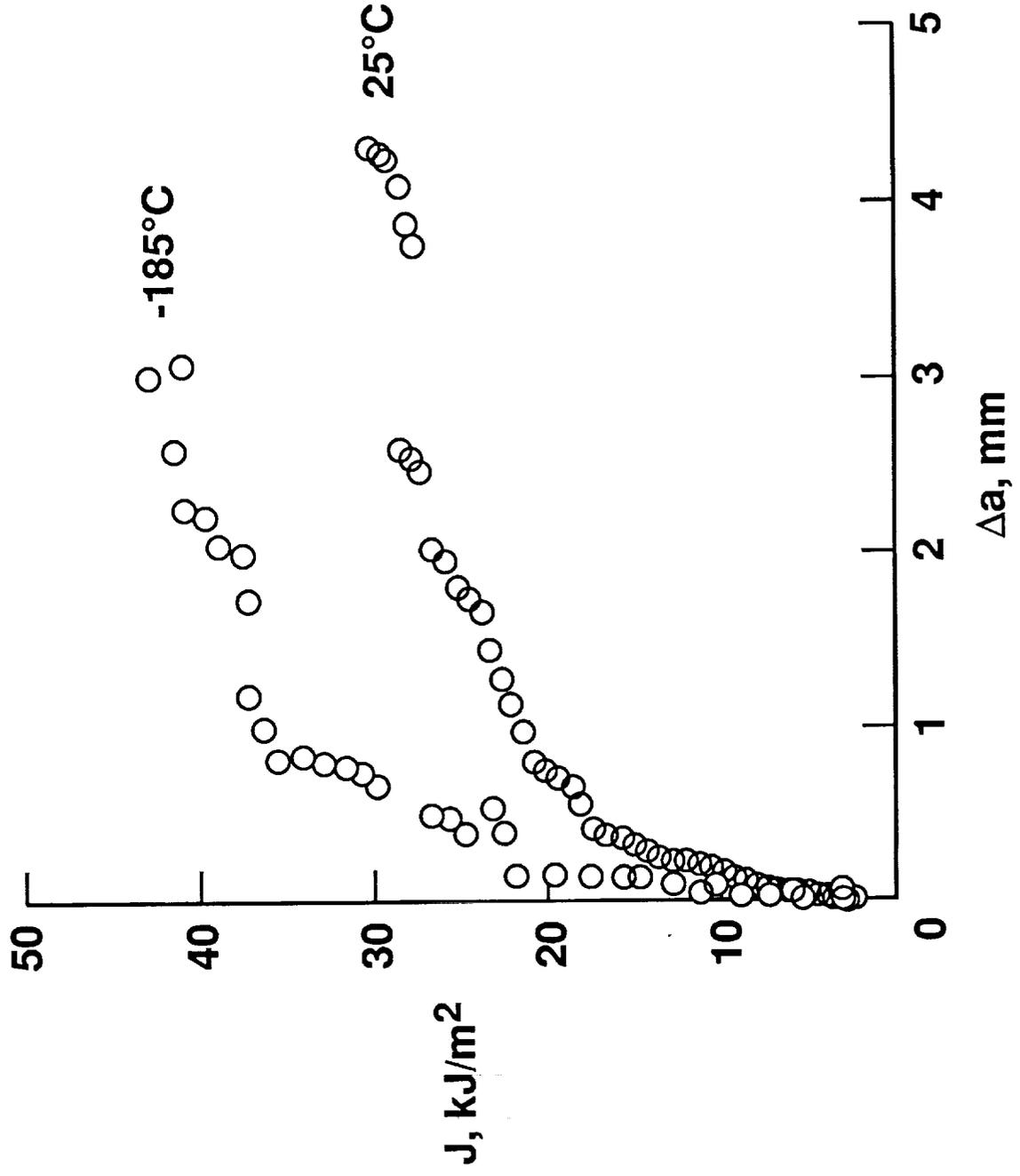
R-CURVE FOR 2090+In-T6 1.6MM THICK SPECIMENS

J, kJ/m²

Δa, mm

25°C

-185°C
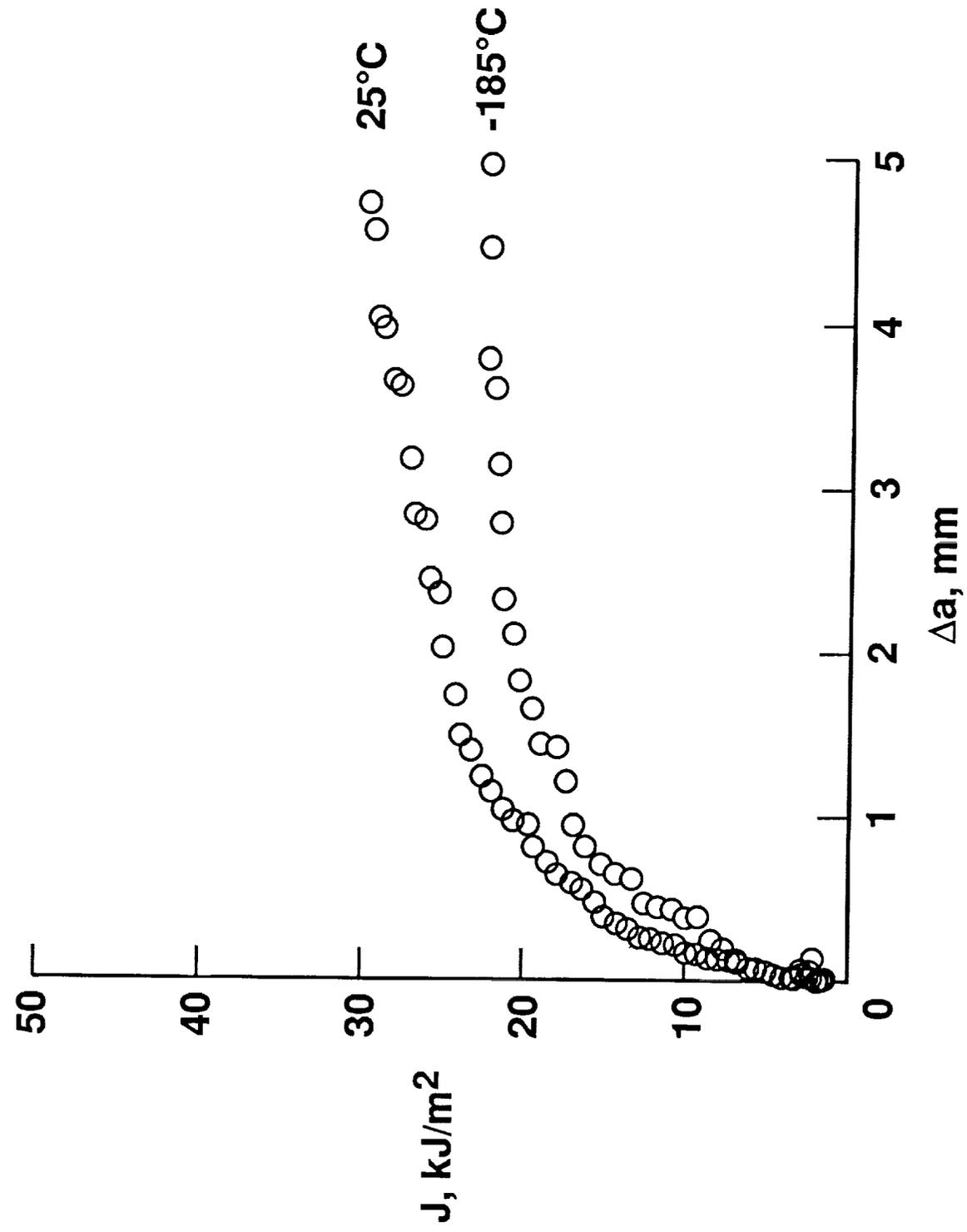
Fracture of 2090 and 2090+In Alloys at Cryogenic Temperatures

SUMMARY

- In additions to 2090-based alloys increase T1 number density with no change in σ_{ys}. The toughness of 2090+In-T6 is low and characterized by intersubgranular fracture.

- Fracture in 2090-T81 characterized by delamination, transgranular shear, and slip band cracking. Increase in toughness at -185°C associated with an increased level of delamination.

- Under plane stress conditions, 2090+In-T6 exhibits a decrease in toughness at cryogenic temperatures consistent with observed decreases in work hardening and elongation at -185°C

Fracture of 2090 and 2090+In Alloys at Cryogenic Temperatures

ISSUES

- Focus future activities on fracture mechanisms associated with 2090-T81

- Quantify the relative proportions of various fracture modes as a function of stress states and temperature

- Examine the mechanisms to account for the observed change in fracture mode of 2090-T81 at -185°C

Project 6   **The Effect of Cryogenic Temperature on the Fracture Toughness of Weldalite™ 049**

Cynthia L. Lach and Richard P. Gangloff

Objective

The objective of this research is to characterize the uncertain effect of temperature on the deformation and fracture behavior of Weldalite™ from cryogenic to elevated temperatures. We will measure fracture resistance and emphasize the determination of fracture mechanisms, including slip plane cracking, high angle boundary delamination, subgrain boundary cracking, and microvoid coalescence.

Status

Two Weldalite™ X2095 compositions were selected for study to examine the limits of the Li and Cu levels for the alloy designated X2095. Specifically, a high Li-Cu alloy (Al-4.64Cu-1.53Li-0.34Ag-0.37Mg-0.17Zr; wt%) and a low copper alloy (Al-4.04Cu-1.00Li-0.37Ag-0.36Mg-0.15Zr; wt%) were chosen for evaluation. Fracture toughness will be investigated as a function of aging temperature and test temperature. Crack growth resistance data will be measured in terms of applied J-integral versus crack extension. All materials have been obtained, and X-ray texture measurements and aging hardening experiments were conducted during this reporting period. Specimens were prepared for fracture toughness experimentation.

Recent Results

Texture analysis was conducted at the midplane (12.7 mm thick plate) for both X2095 variants. The analysis revealed that each composition is textured, typical of rolling producing unrecrystallized microstructures.

A 143°C aging study of the X2095 variants was conducted with times from 1 to 100 hours. The X2095 variants did not overage within the 100 hour time frame. Uniaxial tensile deformation behavior of the two X2095 variants was characterized for the four aging conditions at 25°C and -185°C. The yield and ultimate strengths increased with increasing aging time, and increasing Cu and Li levels. At both test temperatures, as the aging time

51

increased, yield strength increased with a corresponding reduction in work hardening. Increased yield strength and work hardening was observed for each alloy with decreasing temperature to cryogenic levels. The 4.0Cu-1.0Li alloy, aged for 30 hours, exhibited comparable tensile properties to the 4.6Cu-1.5Li alloy aged for 20 hours. To investigate the effect of various strength levels on the fracture toughness of X2095, aging times of 10, 20, 30 and 72 hours were selected.

Preliminary fracture toughness tests were conducted at 25°C for the 4.6Cu-1.5Li alloy; toughness values were low compared to literature results. While large copper bearing phases formed during solution treatment of the high Cu alloy are suspected to degrade fracture toughness, the contributions of high yield strength and low work hardening are undefined.

Milestones

Presently, this work is concentrating on determining the effects of aging condition and temperature on the fracture toughness and fracture mechanisms of the X2095 variants. J-integral specimens of both alloy variants are currently being fatigue precracked. The goal of these experiments is to characterize the crack initiation and growth resistance, and associated microscopic fracture modes, for Weldalite™ X2095. Both K_{IC}, from J at the onset of crack growth, and the tearing modulus from $dJ/d\Delta a$ will be measured with the 3.9 mm thick C(T) specimen. The R-curve will be determined for each of the two Weldalite™ X2095 compositional variants; aged at 143°C for 10, 20, 30, and 72 hours; to determine the interactive effects of yield strength, work hardening, subgrain boundary T_1 and δ' precipitation (for the high Li alloy).

Followup work will determine the effect of temperature (-185°C to 143°C) on the fracture behavior of the X2095 (4.0Cu-1.0Li) alloy for a single aging condition. The effect of CT specimen thickness on the R-curve will also be determined.

Presentation Graphics Captions

1. Title.

2. Issues.

3. Objective.

4. Approach.

5&6. {111} pole figures for the X2095 variants. Texture analysis was conducted at T/2 (midplane) of the 12.7 mm thick plate material. The analysis revealed highly textured alloys with unrecrystallized microstructures.

7. The chemistry range of X2095 is shown on the phase diagram in terms of wt% Cu and wt% Li. The triangles mark the composition of the low copper alloy (4.0Cu-1.0Li) and the high copper alloy (4.6Cu-1.5Li). For the low copper alloy, one does not expect much of the primary phase (T_1 and/or T_B) to be present. However, for the high copper alloy, the 1.5 wt% Li puts it in a region where one would expect significant primary phase. This expectation is confirmed by metallographic analysis; Figure 8. The composition of 2219 (filled circle) is shown in the upper left hand corner, while alloy 2090 (filled square) is shown in the lower right hand corner.

8&9. The as-received X2095 microstructure cubes at 100X and 400X show the amount and relative size of the primary phase present in each chemistry. The high copper alloy (4.6Cu-1.5Li) contains 5.7 volume percent of primary phases that are approximately 15 to 50 μm in size.

10. An aging study was conducted at 143°C for the two X2095 alloy variants treated at times between 1 and 100 hours. Based on hardness, neither alloy overaged within the 100 hour time frame. The high copper alloy (4.6Cu-1.5Li) had higher hardness values. The aging kinetics of both X2095 variants were similar. Aging times of 10, 20, 30 and 72 hours were selected to determine the interactive effects of yield strength, work hardening, subgrain boundary T_1, and δ' precipitation (for the high Li alloy).

11&12. The effect of aging time and test temperature on yield strength and work hardening is shown on these two plots for each variant of X2095. The yield strength increased with increasing aging times, and increasing Cu and Li levels. At both test temperatures, as the aging time increased the yield strength increased with a corresponding reduction in the work hardening exponent from a power-law hardening relationship. An increase in yield strength and work hardening was observed in the cryogenic tensile tests.

13. This plot depicts the effect of alloy composition, test temperature and age condition on the total elongation to fracture. Elongation generally decreases with increasing aging time. Notably, for the 20 hour aging time, elongation increases with decreasing temperature for the high Cu variant, but not for low Cu/Li X2095.

14. Tensile data for the 4.0Cu-1.0Li alloy aged at 30 hours exhibit comparable properties to the 4.6Cu-1.5Li alloy aged for 20 hours. For each case, ductility decreases with decreasing temperature, from ambient to cryogenic, and in contradiction to the elongation results. If one assumes that plane strain fracture toughness is proportional to the square root of the product of yield strength, elastic modulus and local strain to initiate fracture damage; then K_{IC} is predicted to decrease with decreasing temperature for each composition of X2095. (This prediction is based on the hydrostatic stress modified critical strain model for initiation fracture toughness proposed by Ritchie and coworkers. Local strain to initiate fracture damage under plane strain constraint is proportional to -ln(1-RA).) The effect of temperature on fracture toughness will be measured during the next reporting period.

15. Fracture toughness tests were run for two thicknesses of compact tension specimen, 3.9 and 11.7 mm, for the 4.6Cu-1.5Li alloy aged at 143°C for 24 and 72 hours. Plane strain fracture toughnesses K_{IC} were determined by the thin specimen R-curve method (18.8 and 23.7 MPa√m for 24 and 72 hours, respectively), and with thick sidegrooved CT specimens (15.3 and 20.3 MPa√m for 24 and 72 hours, respectively). The origin of this systematic difference is unknown. Fracture toughness decreases with increasing aging time.

16. Future plans.

17. Summary.

EFFECTS OF TEMPERATURE AND MICROSTRUCTURE ON THE FRACTURE OF X2095

C. L. LACH

LA^{2}ST Program Review

NASA Langley Research Center

July 15-16, 1992

FRACTURE TOUGHNESS ISSUES X2095

- HIGH VOLUME FRACTION OF LARGE PRIMARY CU-RICH PHASES

- SUBGRAIN BOUNDARY T_1 PRECIPITATES IN UNRECRYSTALLIZED MICROSTRUCTURE

- HIGH YIELD STRENGTH AND LOW WORK HARDENING

- SLIP LOCALIZATION AND SLIP PLANE CRACKING (LOW CU/HIGH LI)

- HIGH ANGLE GRAIN BOUNDARY DELAMINATION

OBJECTIVE

To characterize the effect of temperature and alloy composition on the deformation and fracture behavior of X2095 from elevated to cryogenic temperatures

APPROACH

- Examine limits of Cu/Li levels X2095 and vary aging to cover strength and work hardening extremes

- Measure crack growth fracture toughness resistance as a function of aging at 25°C and -185°C

- Measure crack growth fracture toughness resistance as a function of temperature (-185°C to 143°) for one aging condition

- Characterize the fracture surface appearance

- Characterize the effect of thickness and relate to literature

(111) POLE FIGURE FOR X2095-T8 (4.0CU 1.0LI)

MIDPLANE T/2

BRASS = 26.34 COPPER = 8.51

H= 1 K= 1 L= 1

Plot Levels:

2.7%		0.75	
4.5%		1.25	
7.2%		2.000	
10.9%		3.00	
14.5%		4.00	
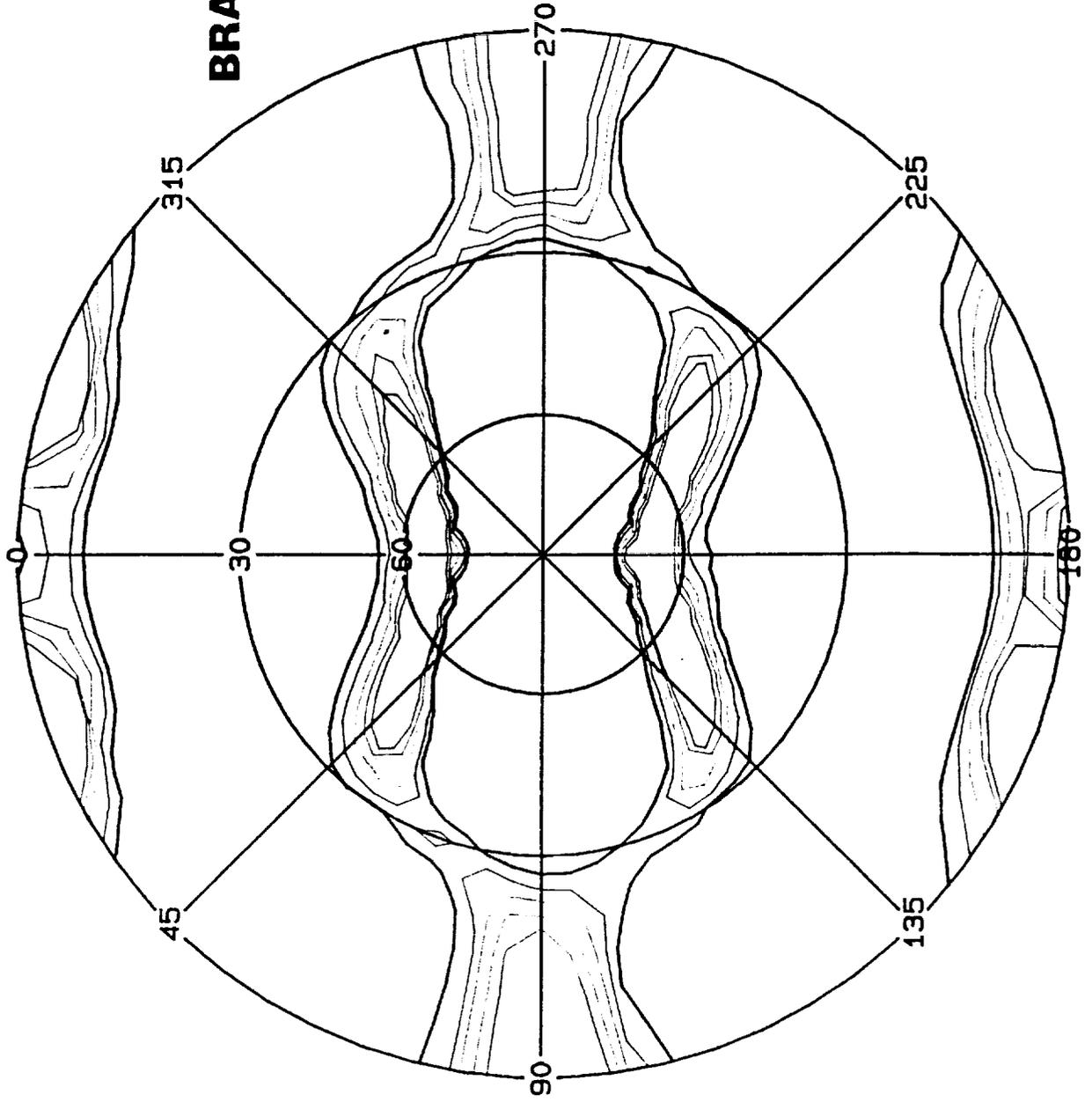
(111) POLE FIGURE FOR X2095-T8 (4.6CU 1.5LI)
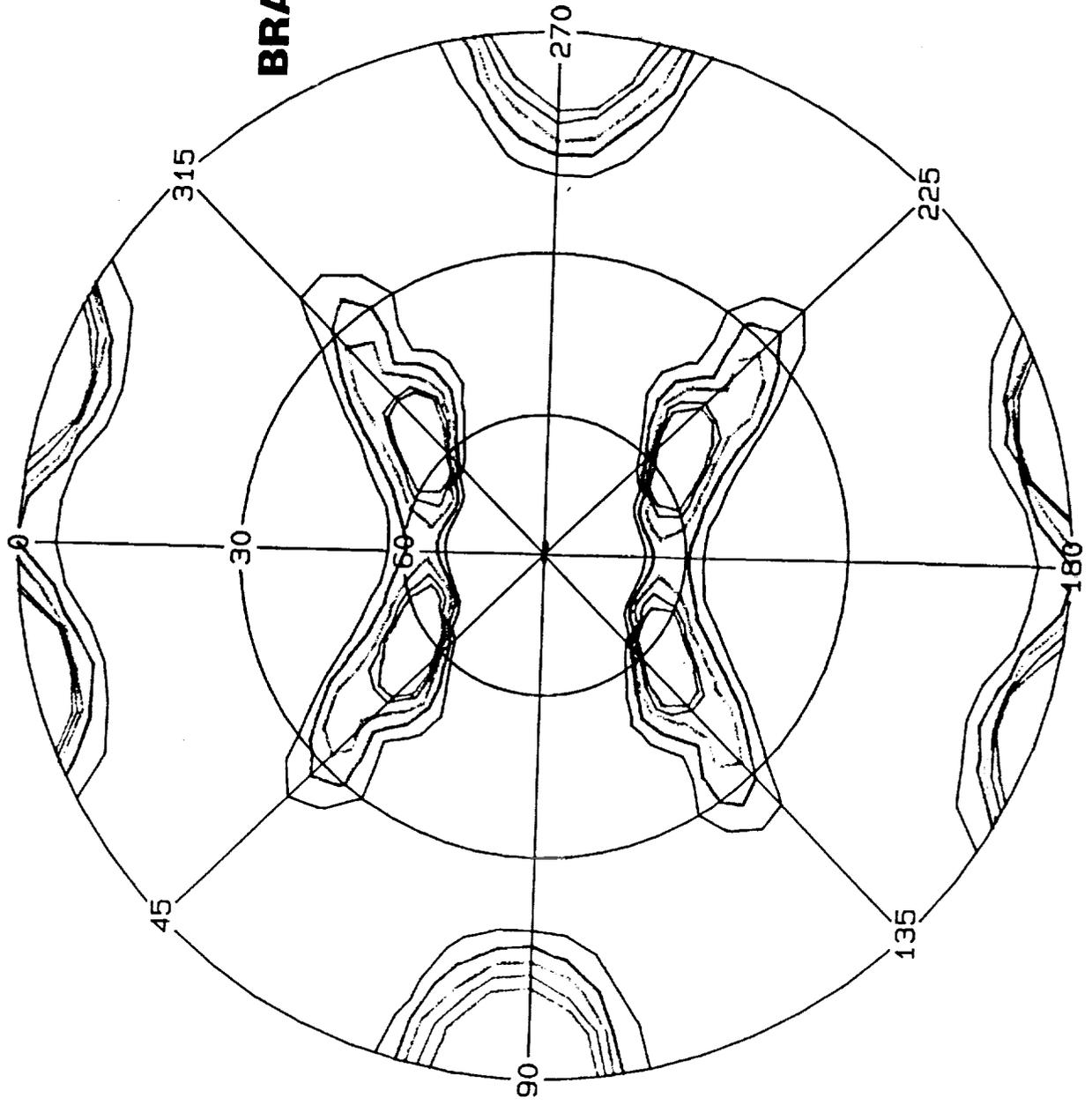
MIDPLANE T/2

BRASS = 39.04 COPPER = 5.37

H= 1 K= 1 L= 1

Plot Levels:

2.6%	0.75
4.4%	1.25
7.0%	2.00
10.5%	3.00
14.0%	4.00

CHEMISTRY OF X2095 VARIANTS

COPPER (wt%)

LITHIUM (wt%)

Area	Phases
1	Al+θ
2	Al+TB
3	Al+T₁
4	Al+T₂

— Phase boundaries at 500°C

--- Phase boundaries at 350°C
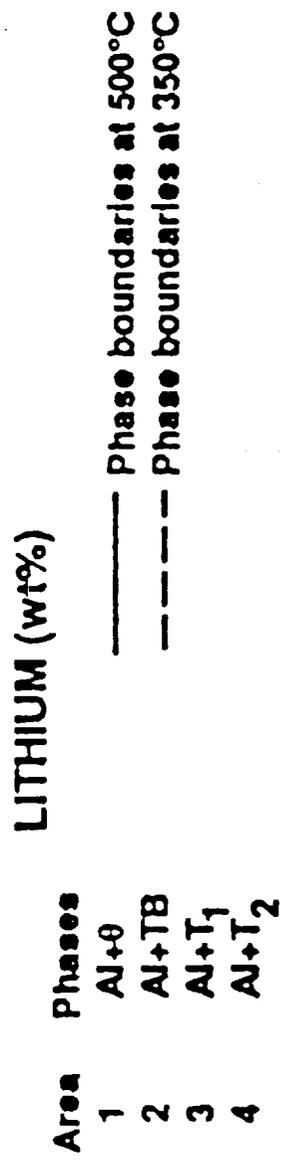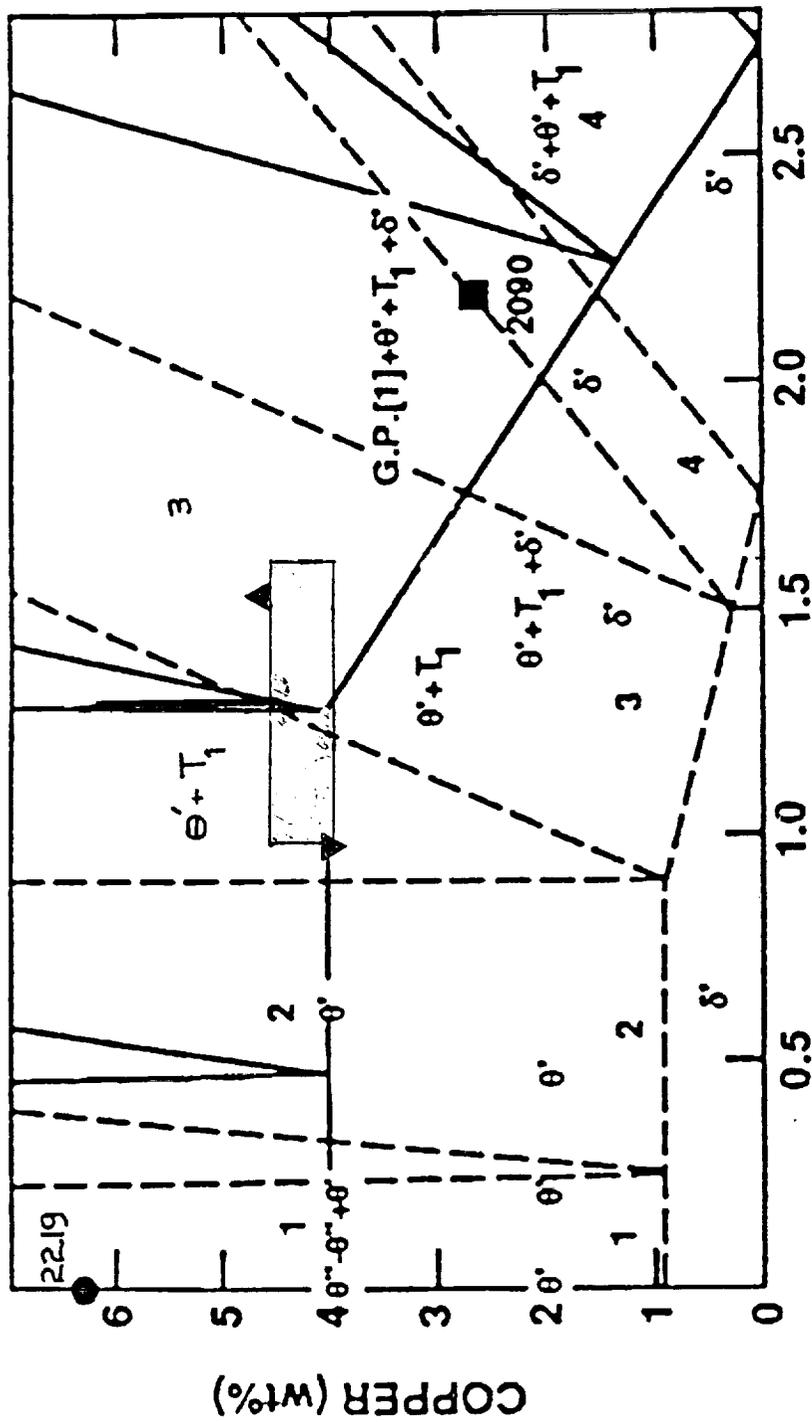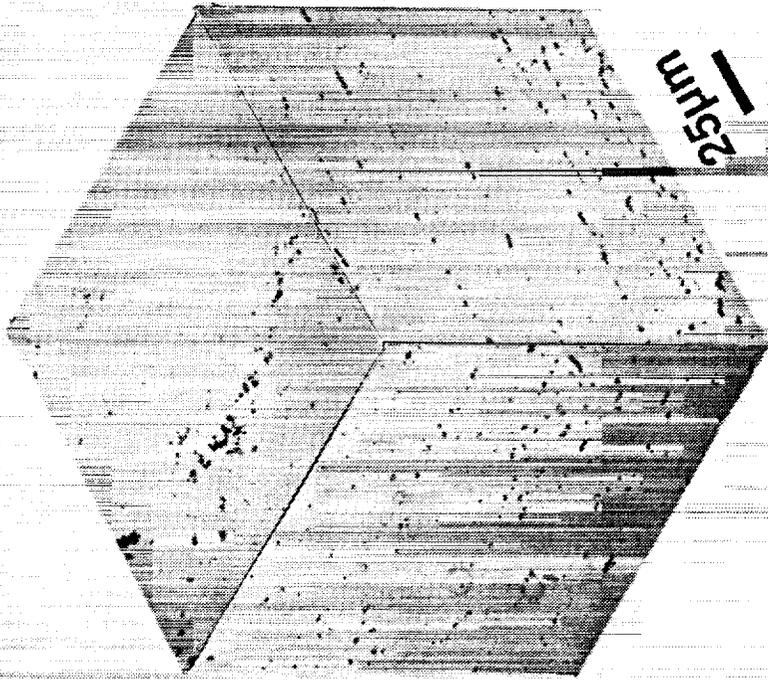
AS RECEIVED WELDALITE™ X2095

X2095
(4.6Cu 1.5Li)

X2095
(4.0Cu 1.0Li)

25μm

25μm

S

L

T

AS RECEIVED WELDALITE™ X2095

100μm

100μm

S

L

T
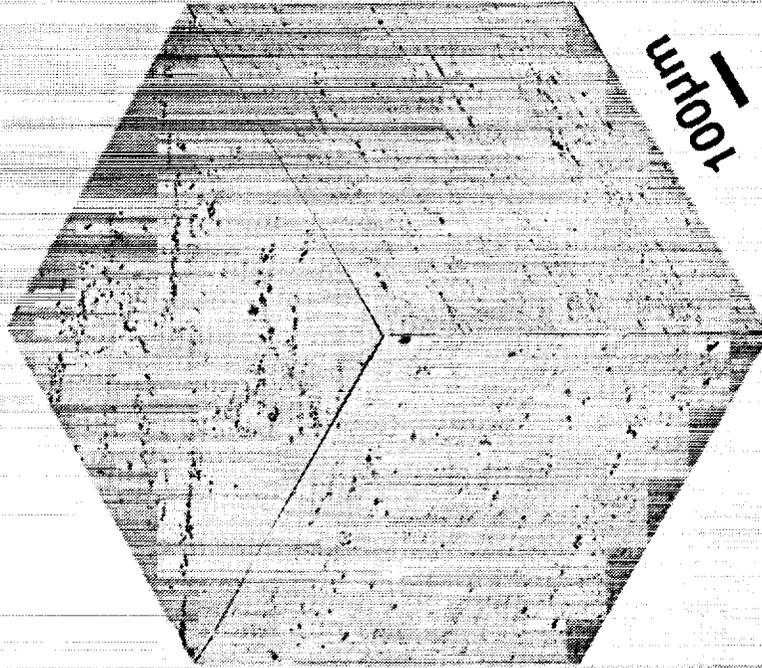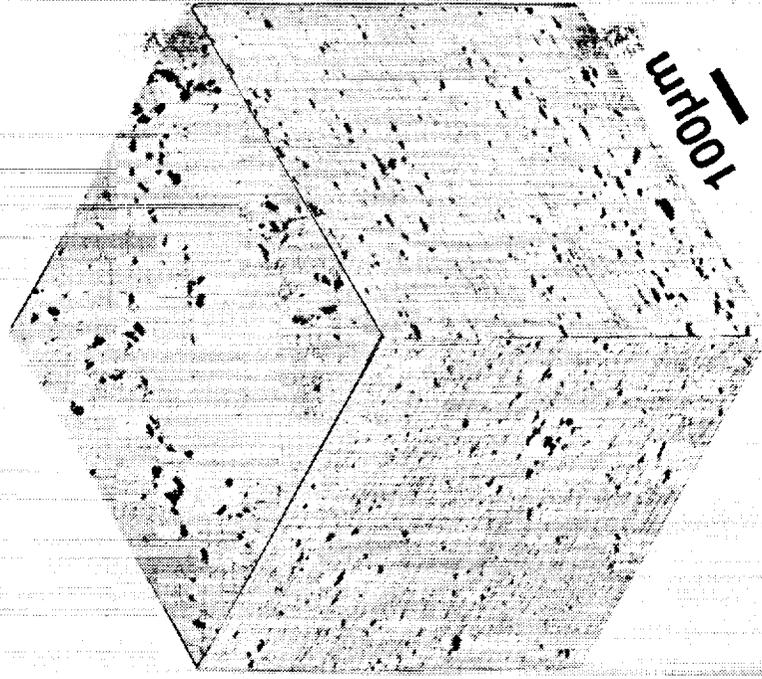
X2095
(4.0Cu 1.0Li)
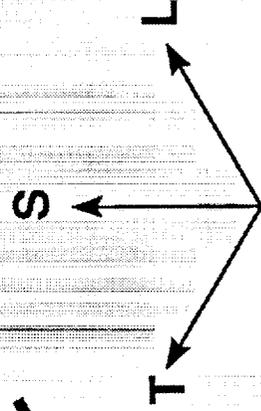
X2095
(4.6Cu 1.5Li)

143°C Aging Response of X2095

Time, hr

Hardness, Rockwell B

Legend:
□ 4.0Cu1.0Li
● 4.6Cu1.5Li
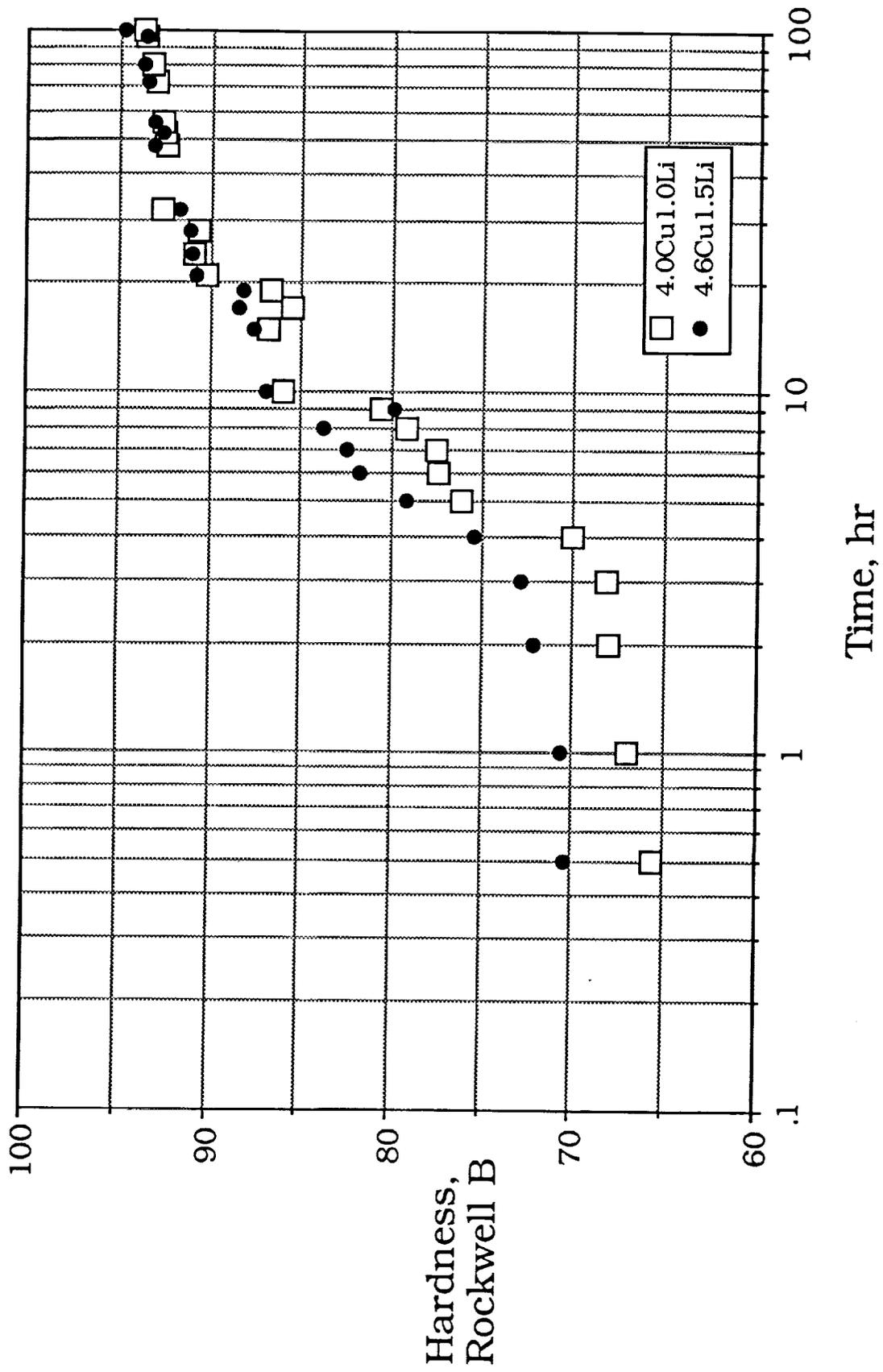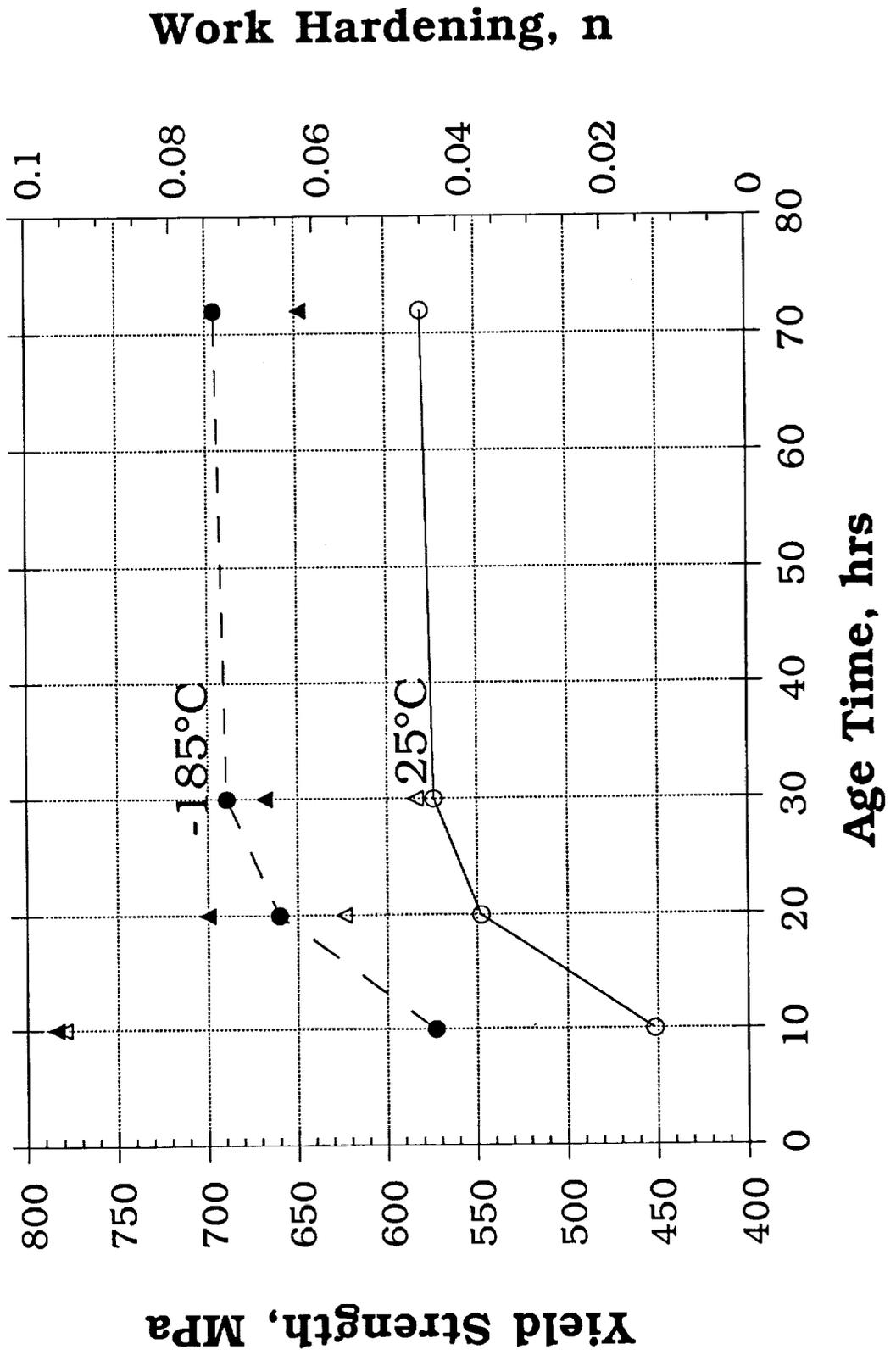
X2095 (4.0Cu1.0Li)

X2095 (4.6Cu1.5Li)
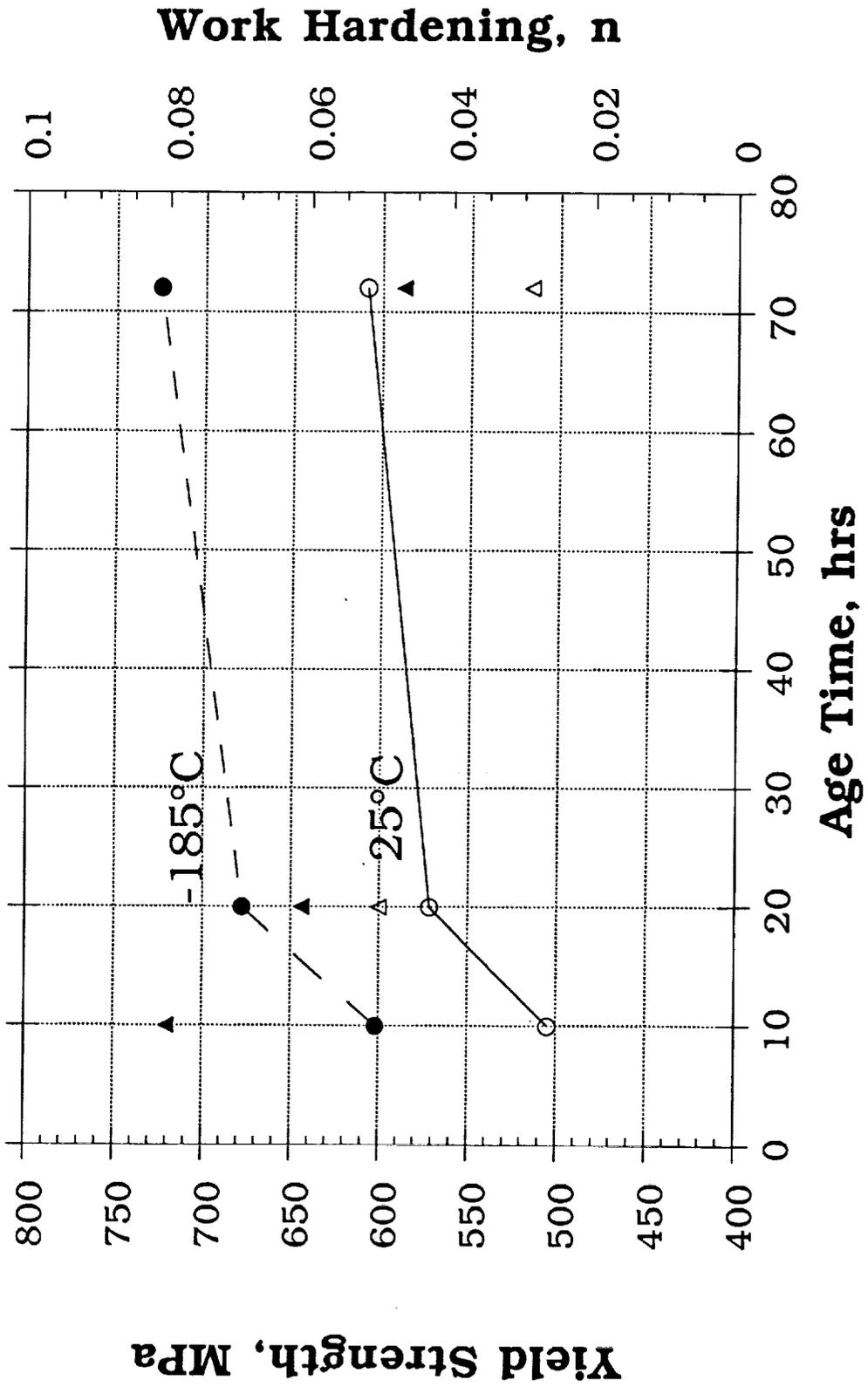
EFFECT OF ALLOY COMPOSITION AND AGE ON THE DUCTILITY

Legend:
- ○ 4.0Cu1.0Li @ 25°C
- ● 4.0Cu1.0Li @ -185°C
- □ 4.6Cu1.5Li @ 25°C
- ■ 4.6Cu1.5Li @ -185°C

X-axis: Aging Time, hrs

Y-axis: % Elongation to Fracture
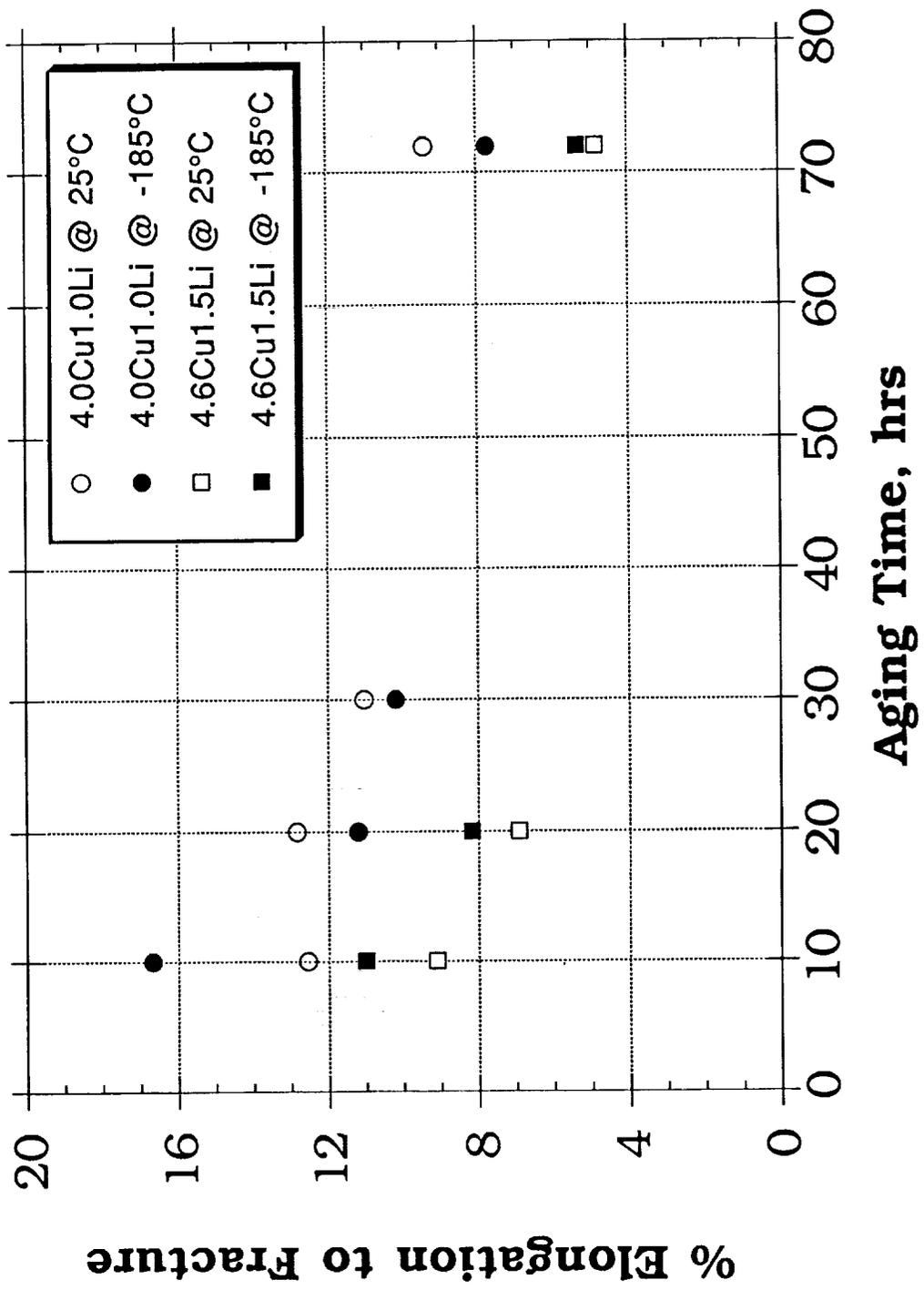
Mechanical Property Comparison of the Lean and Rich X2095 Variants

X2095(4.0Cu1.0Li) 143°C for 30 hours

Temp., °C	Yield Strength, MPa	Ultimate Strength, MPa	% Elongation	Reduction of Area	Elastic Modulus, GPa	Work Hardening, n
25	574.2	595.1	11.1	36.2	72.7	0.05
-185	689.4	747.0	10.2	26.9	83.4	0.07

X2095(4.6Cu1.5Li) 143°C for 20 hours

Temp., °C	Yield Strength, MPa	Ultimate Strength, MPa	% Elongation	Reduction of Area	Elastic Modulus, GPa	Work Hardening, n
25	571.8	598.0	6.9	27.5	75.6	0.05
-185	677.9	727.7	8.2	12.2	83.8	0.06

FRACTURE TOUGHNESS OF X2095(4.6Cu1.5Li)

Thickness (B), mm	Fracture Toughness (KIC), MPa√m	
	143°C Age for 24 hrs	143°C Age for 72hrs
3.9	23.7	18.8
11.7	20.3	15.3

Weldalite
CT (W=50.8 mm, B=3.9 mm)
+ 145°C / 24 hrs
□ 145°C / 72 hrs
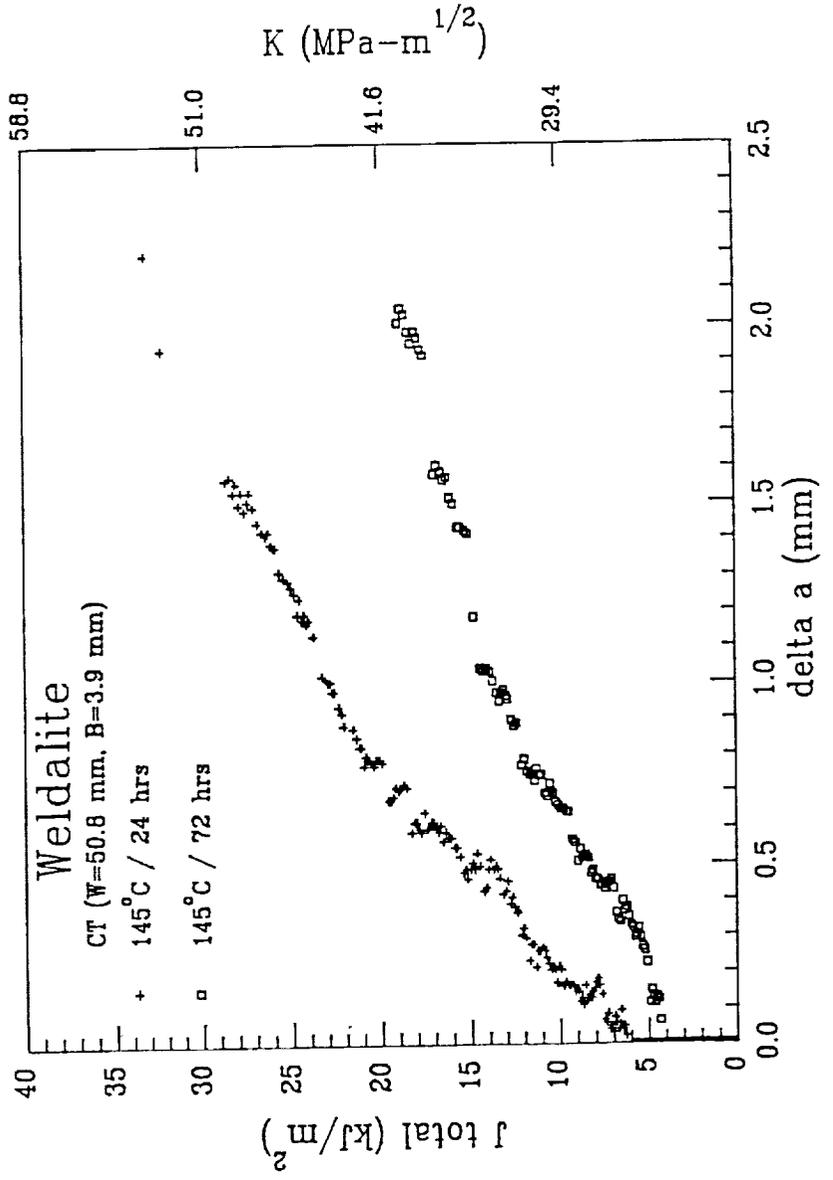
FUTURE PLANS

- Determine the effect of 143°C age at 25°C and -185°C for the lean and rich X2095 variants

- Determine the effect of temperature, -185°C to 143°C, on the fracture behavior of X2095(4.0Cu1.0Li), for a single aging condition

- Determine the effect of CT specimen thickness on the R-curve characterization; compare to literature

SUMMARY

143°C Aging Study

· Identified four aging conditions that cover the extremes of yield strength and work hardening
· The alloy did not overage in 100 hours
· Strength increased with increasing aging time and increasing Cu Li levels

25°C and -185°C Tensile Tests

· Quantified the effect of aging on the yield strength and work hardening (YS ↑ n ↓ ; as aging time ↑)
· Characterized the effect of temperature on the yield strength and work hardening (YS & n ↑ ; temperature ↓)

Preliminary Fracture Toughness Tests

· Test technique works
· Toughness of the rich(4.6Cu1.5Li) X2095 variant is low compared to literature
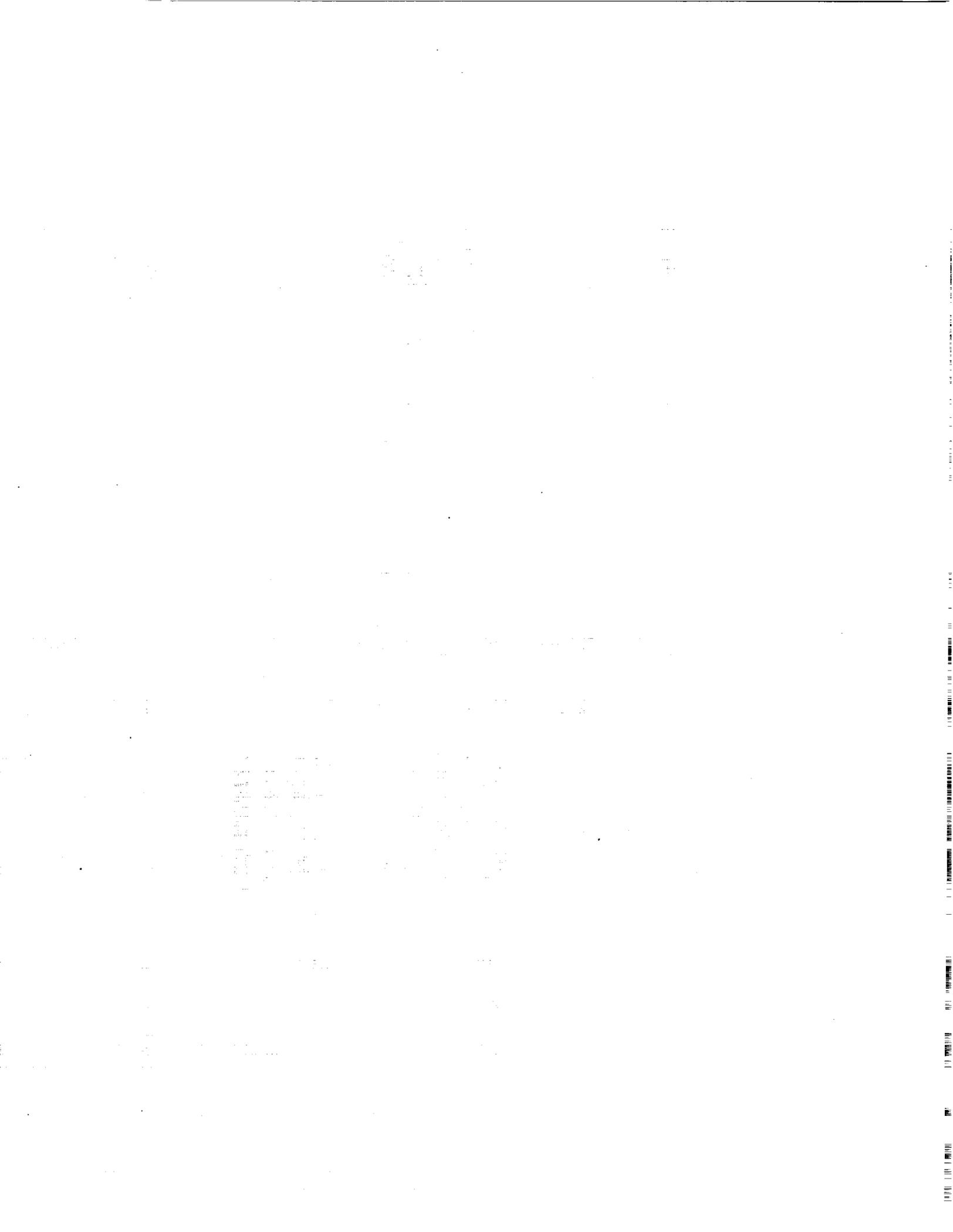
<u>Project 7</u> **Mechanisms of Localized Corrosion in Al-Li-Cu-Mg-Ag Alloy X2095 and Compositional Variations**

F. Douglas Wall and Glenn E. Stoner

Objectives

The overall goal of this research project is to determine the roles of microstructure and electrochemistry in the failure of advanced aluminum alloy X2095. The current focus of the project is to elucidate the roles of size and distribution of the active precipitate phase T_1 (Al_2CuLi) in stress-corrosion cracking (SCC) susceptibility.

Current Status

Initial studies of the electrochemistry of the primary research material X2095, an Al-4.0 Cu-1.0 Li alloy with Ag and Mg additions, have been performed for comparison with the large data base available on alloy 2090. Constant load smooth bar SCC experiments in various environments have provided some information on the SCC behavior of this alloy but have not proven discriminating enough to separate relative susceptibilities of the tempers under investigation. In the near future, work will involve a more quantitative in situ fracture mechanics test to study SCC performance.

Recent Findings

The electrochemical characteristics of bulk X2095 have been evaluated and are comparable to alloy 2090 in chloride, chloride/chromate and chloride/lithium carbonate environments. In general, the matrix phase is passivated in the presence of the inhibiting ion over a wide range of potentials; whereas the primary strengthening phase T_1 shows very little variation in electrochemical behavior in the presence or absence of the inhibiting species. Thus, in the inhibiting environments a potential window exists in which the secondary phase is highly active while the surrounding matrix remains passive. This window is defined by the breakaway (E_{BR}) potentials of the matrix and precipitate phase. Studies on 2090 have shown that mechanically stressed samples polarized within this window fail rapidly while samples polarized cathodic to this window have not shown any failures.[1-3]

Smooth bar constant load time-to-failure (TTF) experiments performed on X2095 in the chromate and carbonate environments have shown that samples polarized cathodic to $E_{BR,T1}$ do not fail or show signs of corrosion (i < 1 μA/cm^2) after five days of testing; however, samples polarized anodic to $E_{BR,T1}$ and cathodic to $E_{BR,\alpha-Al}$ exhibit large corrosion currents (i > 5000 μA/cm^2) and fail within five to ten hours of being polarized. Initial SEM studies of the fracture surface indicate intergranular attack.

In the chloride/chromate environment, samples that are polarized 40 mV cathodic to the E_{BR} of bulk T_1 and then mechanically damaged via scratching with a glass rod show high current densities and rapid times to failure. Samples that are not scratched do not fail at this potential. The discrepancy between the potential where a scratch results in localized attack and the potential where attack occurs without mechanical damage may be indicative of the driving force necessary for propagation vs initiation. Interestingly, the potential where the alloy becomes susceptible to mechanical damage as a means of initiating SCC is 10 mV more cathodic for the peak-aged vs the under aged temper. Neither a physical nor a chemical explanation for this discrepancy has been proposed.

Combinations of potential and applied stress have been found which result in the high current densities usually associated with rapid TTF but do not result in specimen failure. Instead the specimen locally corrodes for a few hours at high current densities then returns to a passive condition. These preliminary results indicate that a potential drop may be responsible for turning off the SCC process for the specific test conditions. It may also be possible that corrosion product is sealing off the SCC crack.

TEM has been performed on under aged and peak aged X2095 as well as 2090 in the T8 condition to gain a qualitative feel for the differences in the microstructures. Although only a sampling of the microstructures has been obtained it appears as though large enough differences exist to allow quantification of the size and distribution of the T_1 precipitate phase.

To this point alloy X2095 has been evaluated with techniques that show it is susceptible to rapid failure via SCC in the same conditions previously found for 2090. However, times to failure for both tempers of X2095 and 2090-T8 have not distinguished the materials in terms of relative susceptibility. Likewise, differences in microstructures have not been quantified. The near term goals of this project will be to gain quantitative information in both of these areas.

Future Work

The primary goal for the next six to eight months of this research project is to quantify the number and size distributions of T_1 precipitates in the three microstructures currently under investigation and determine if there exists a correlation between this information and relative SCC behavior. The microstructural analysis will be performed primarily using TEM. To differentiate the SCC behavior of the three microstructures, experiments will be undertaken to measure crack growth rates as a function of applied stress. The specifics of the test apparatus and procedure can be found in the report by Ray Kilmer also in these proceedings.

References

[1]   F.D. Wall, "Correlation Between Stress-Corrosion Cracking and Electrochemical Behavior for Alloy 2090 Aluminum," Senior Thesis, University of Virginia, May, 1990.

[2]   R.G. Buchheit, F.D. Wall, G.E. Stoner, J.P. Moran, "The Effect of Applied Potential in Constant Load SCC Testing of 2090 in Cl^- and Cl^-/Au_4^- Environments", ECS Fall meeting, Seattle, WA, Oct., 1990.

[3]   R.G. Buchheit, F.D. Wall, G.E. Stoner, J.P. Moran, "Subgrain Boundary Precipitation and Stress Corrosion Cracking in Alloy 2090", CORROSION/91, Cincinnati, OH, March, 1991.

Mechanisms of Localized Corrosion in Alloys 2090 and X2095

F. D. Wall
G. E. Stoner

Department of Materials Science and Engineering
University of Virginia
Charlottesville, Virginia 22901

OUTLINE OF PRESENTATION

I. Objectives

II. Materials

III. Background

IV. Preliminary research

V. Future work

OBJECTIVES

Overall: Determine the roles of microstructure and environment in the SCC behavior of aluminum alloy X2095.

Recent: Evaluate the susceptibility of alloy X2095 to rapid SCC failure.

Future: Over the next six to eight months search for a correlation between distribution and size of T_1 precipitates and SCC behavior.

MATERIALS UNDER INVESTIGATION

Primary material : aluminum alloy X2095
  composition : Al-4 Cu-1 Li-0.25 Mg-0.25 Ag
  tempers   : 20 hrs at 290°F, 36 hrs at 290°F

Comparison matl : aluminum alloy 2090
  composition : Al-2 Li-2.5 Cu
  temper   : T8

Microstructural considerations:
  (1) X2095 does not contain δ'
  (2) T_1 size
  (3) T_1 distribution/density on SGB's

BACKGROUND - THE RAPID FAILURE CRITERIA

The criteria for rapid failure due to SCC for alloy 2090 requires that:

A potential and environment are selected such that the SGB phase T_1 is highly active while the matrix remains passive.

The criteria is not satisfied in NaCl solution because:

The E_{BR} values for α-Al and T_1 are equal; therefore, either both are active or both passive.

The criteria can be met by:

(1) Adding an inhibiting ion to the solution which shifts the E_{BR} of α-Al in the noble direction but does not similarly shift the E_{BR} of T_1 then

(2) Polarizing the sample such that $E_{BR,T1} < E_{appl} < E_{BR,\alpha\text{-}Al}$ and

(3) Loading the sample in the S-T or L-T direction to 60% YS.

These conditions can be satisfied in:

(1) $NaCl + Na_2CrO_4$

(2) $NaCl + Li_2CO_3$

PRELIMINARY RESEARCH - SOME QUESTIONS

(1) Is alloy X2095 susceptible to rapid SCC failure?

(2) If so, what is the nature of the failure?

(3) Can the materials under investigation be ranked in SCC susceptibility using the constant load-rapid failure test?

(4) Are there conditions which will cause cessation of SCC once it has begun?

(5) What effect does satisfying the rapid failure criteria during a mechanical test have on the material properties?

(6) Can the microstructures of the research materials be differentiated?

The electrochemical behavior of alloy X2095 in both tempers was documented for test environments of 0.6M NaCl, 0.1M NaCl + 0.1M Na_2CrO_4, and 0.6M NaCl + 0.1M Li_2CO_3. As shown, the breakaway potential of the bulk alloy is dramatically shifted in the noble direction in the inhibiting environments. Past research has shown that the electrochemical behavior of the T_1 phase is not very sensitive to the addition of the inhibiting ions. Thus, a potential window exists wherein the criteria for rapid SCC can be satisfied.

Effect of inhibiting ions on E_{BR} values of the bulk alloys and SGB phase T_1. All values are mV vs SCE.

material	0.6M NaCl	0.1M NaCl+ 0.1M Na_2CrO_4	0.6M NaCl+ 0.1M Li_2CO_3
X2095-A	-690	-60	-580
X2095-B	-670	-230	-590
T_1	-723	-540	-720

The graph demonstrates the radical change in response for samples polarized cathodic and anodic to the E_{BR} potential for T_1. The samples polarized cathodic to $E_{BR,T1}$ did not fail after a week of exposure, nor did any show signs of localized attack. The current densities measured were less than 1 $\mu A/cm^2$. Samples of each temper polarized anodic to $E_{BR,T1}$ all failed in less than ten hours. The lack of separation in the times to failure suggests that this test lacks the resolution to discern relative SCC susceptibilities. All samples were loaded to 60% of YS.

The time-to-failure response of the two X2095 tempers as a function of applied potential in the NaCl + Na$_2$CrO$_4$ environment.
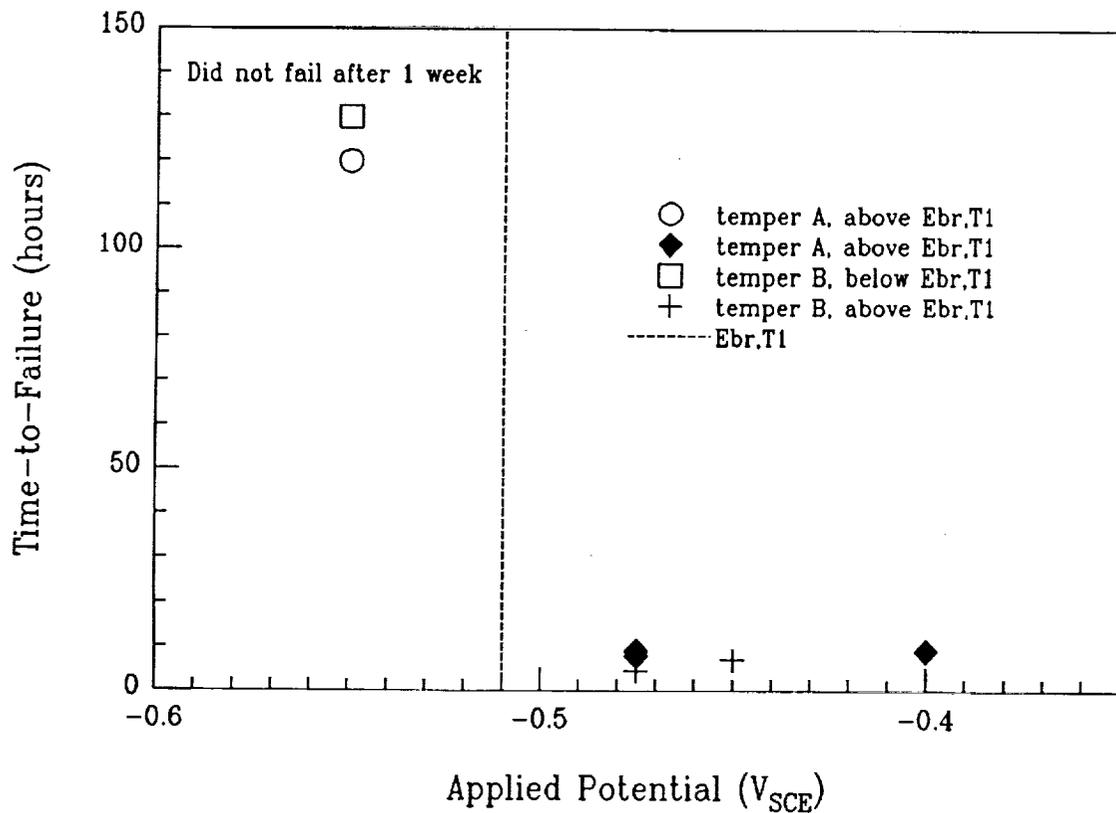
This graph indicates the current response of a mechanically loaded (60%YS) S-T smooth bar tensile sample polarized within the potential window for susceptibility to rapid SCC in the chloride/ chromate environment. Note, even though the current is very high (approx 6 mA/cm^2) the corrosion occurring is highly localized with much of the sample surface remaining passive. Also note that during this test, a considerable amount of H$_2$ gas is released from the corrosion sites and is easily observed with the naked eye.

Current vs time response for an S-T X2095-B sample polarized anodic to $E_{BR,T1}$ in the chloride/chromate environment.
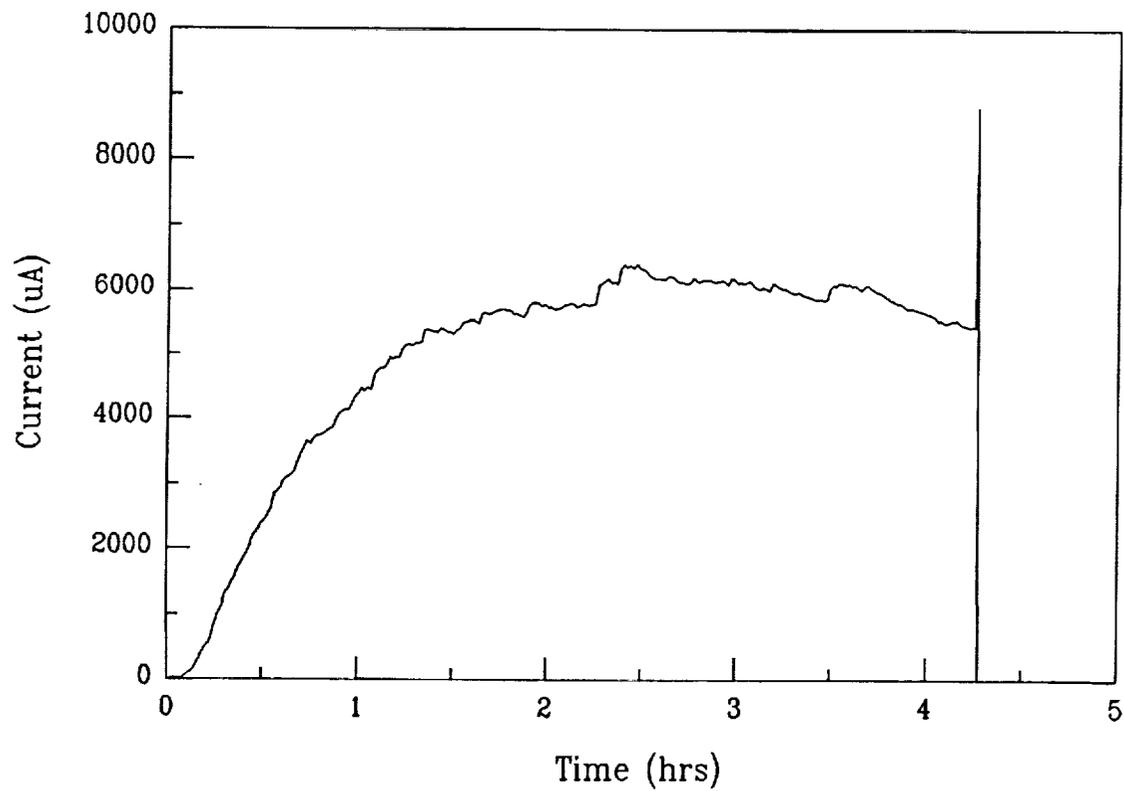
The SEM micrographs on the next few pages demonstrate the fractography associated with a sample polarized above $E_{BR,T1}$ in the chloride/chromate environment and loaded to 60%YS. Note that at the edge of the pit initiating corrosion the intersubgranular nature of the attack. This type of attack suggests that the SGB's serve as an active path for localized corrosion.

Rapid failure mode of X2095-B in Cl$^-$/CrO$_4^{2-}$

Rapid failure mode of X2095-B in Cl⁻/CrO₄²⁻
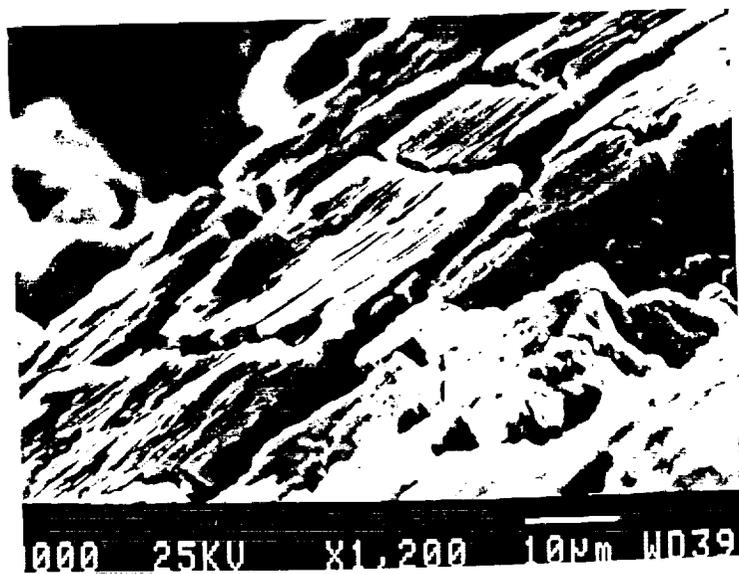
Rapid failure mode of X2095-B in Cl^-/CrO_4^{2-}
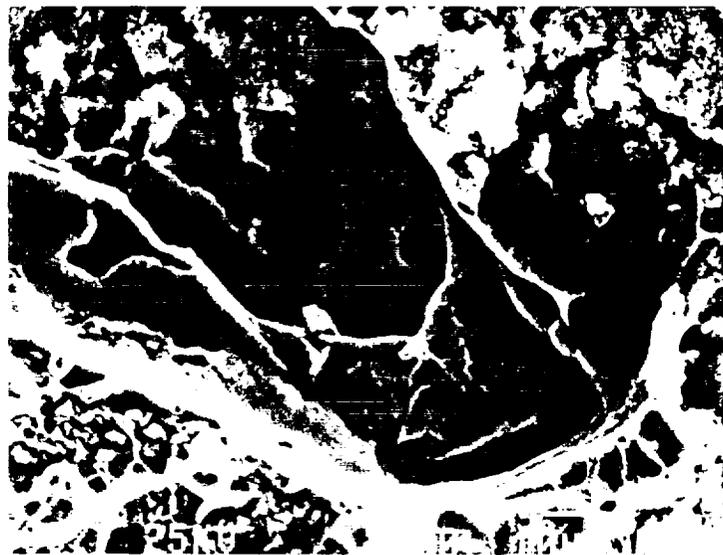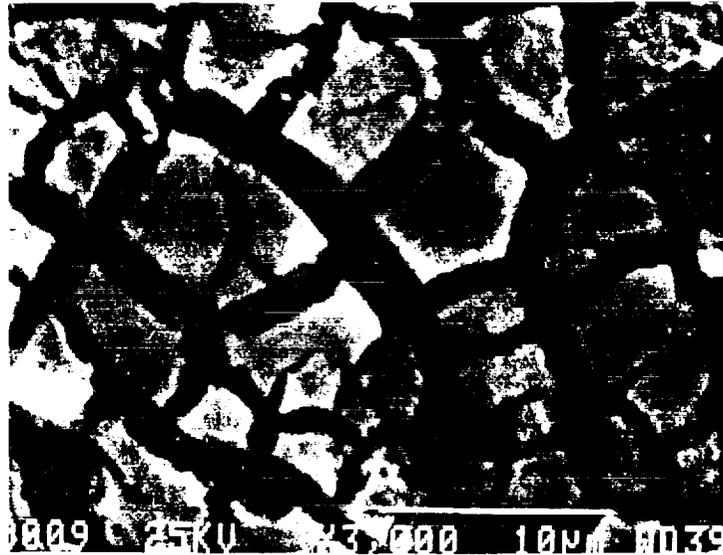
Rapid failure mode of X2095-B in Cl⁻/CrO₄²⁻

This data is from a sample polarized cathodic to the E_{BR} value for a bulk ingot of T_1 and loaded to 60%YS. For the first five days the sample did not show any signs of localized corrosion with a corresponding corrosion current of approximately 1 μA/cm^2. After five days the sample was mechanically damaged by making a small scratch on the surface using a sharp glass rod. Subsequently, the sample corroded locally and failed. The fact that samples held at this potential without mechanical damage do not corrode suggests that the driving force for propagation vs initiation may be different in this environment.

Current vs time response for an S-T X2095-B sample polarized to -550 mV$_{SCE}$ in the chloride/chromate environment. At 130 hours the sample was scratched with a glass rod.
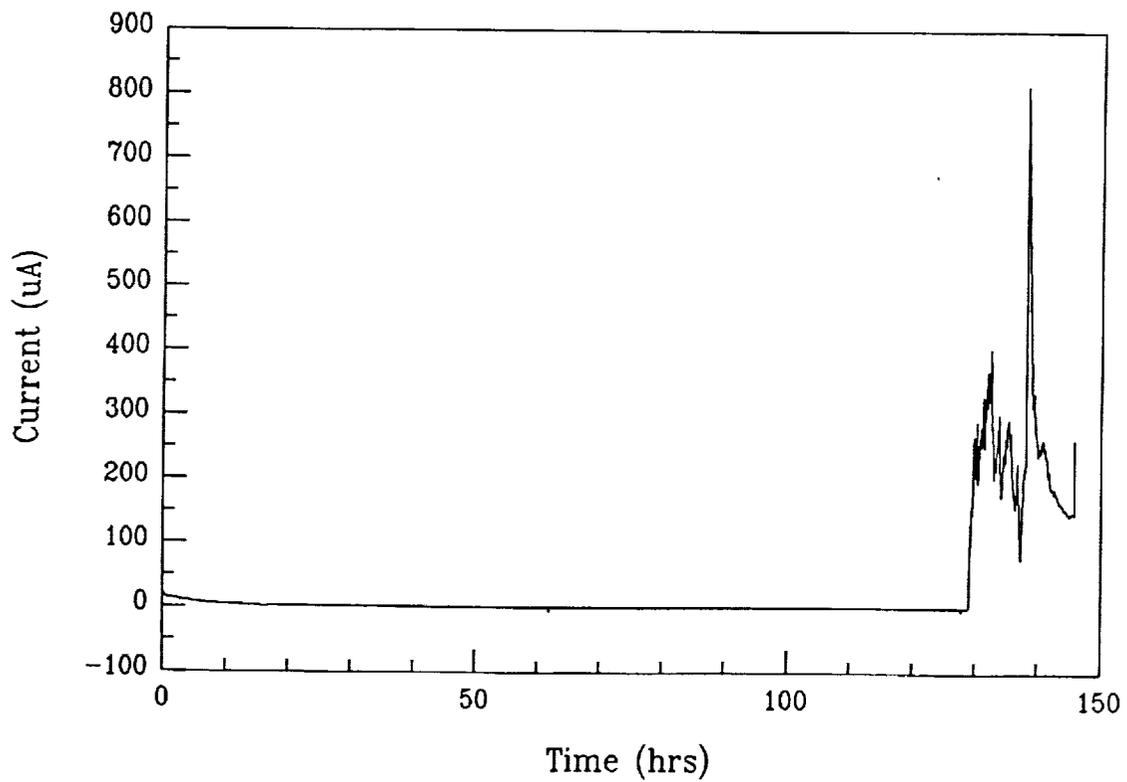
The following page is the result of an experiment intended to determine if there exists a critical potential where a scratched sample changes from a stable system to a propagating SCC crack. This data yields two results. First, at -570 mV_{SCE} the scratched sample does not corrode contrary to the result at -550 mV_{SCE}. Thus, a sharp transition (less than or equal to 20 mV) exists between susceptibility to scratching and immunity. The second piece of information involves the current "spikes" seen for scratches at -660 and -665 mV_{SCE}. At these potentials the scratch event resulted in the "normal" corrosion processes to initiate; however, the current soon subsided and the sample became stable once again. It is possible that this potential range is extremely close to the critical potential required for crack propagation, and that after a small crack has grown, an IR potential drop down the crack results in the crack tip being on the passive (cathodic) side of the critical potential. This is only one possible explanation, however, and further experimentation needs to be performed to fully assess the phenomenon.

Current vs time and potential vs time data for a sample of S-T X2095-B polarized and scratched at several successive potentials in the chloride/chromate environment.
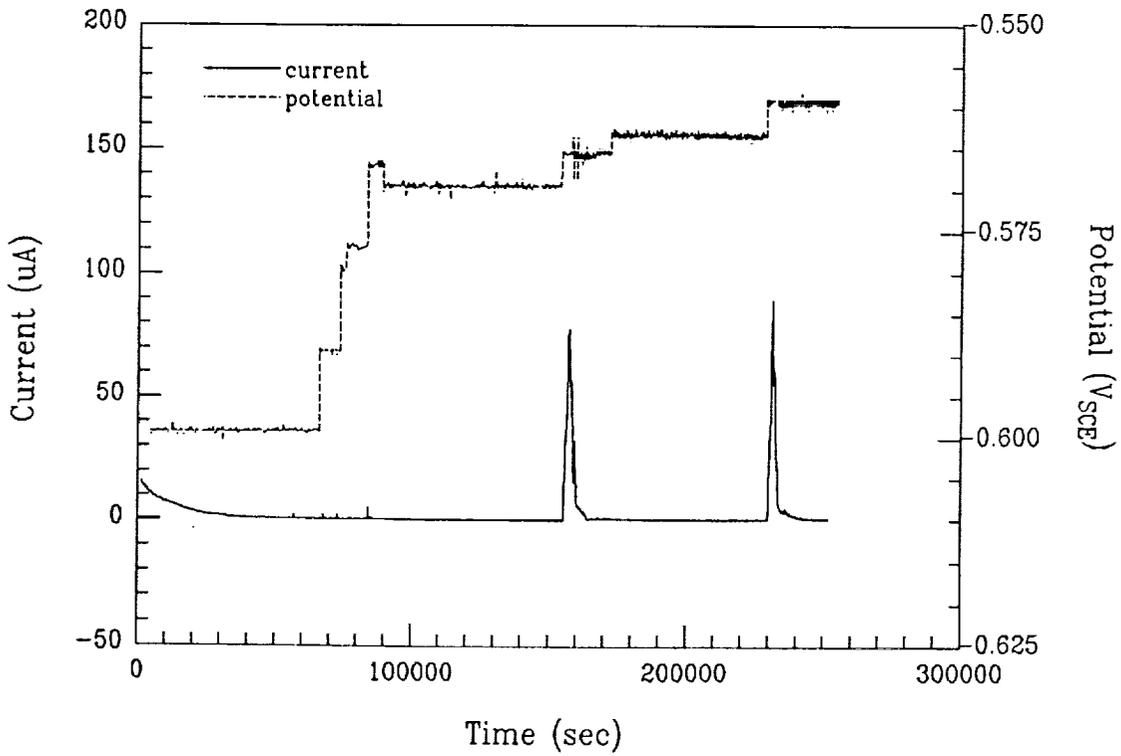
This experiment demonstrates the effect of using a lower stress level during a scratch test in the chloride/chromate environment. The sample was loaded to 25%YS instead of 60%YS. The sample exhibited the localized corrosion processes seen for samples loaded at higher stress levels for the first 28 hours. Then the current returned to the pre-scratched level and remained stable for over 45 hours. This result suggests that the stress level plays an important role in the SCC process.

Current vs time response for an S-T X2095-B sample loaded to 25% of YS, polarized to -550 mV$_{SCE}$ and scratched with a glass rod.
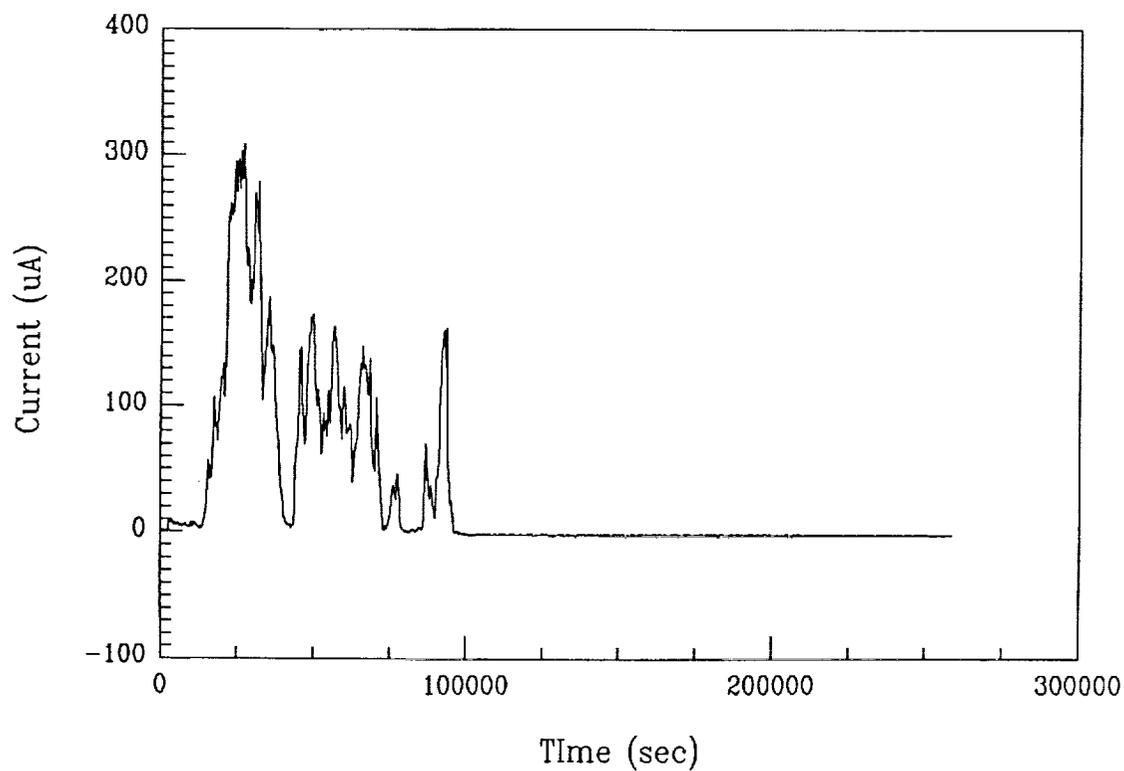
Slow strain rate (SSRT) testing was performed in the chloride/chromate environment to determine the effect of satisfying the condition for rapid failure on the mechanical properties of the material. Note that there is a total loss of properties when the sample is polarized anodic to the E_{BR} value of bulk T_1. The sample polarized cathodic to the E_{BR} value of bulk T_1 but still in the potential region associated with the scratching experiment showed a large loss in ductility. This sample did not show a significant corrosion current until after plastic deformation began.

Stress-strain curves for samples strained at 1.18e-6/sec in the chloride/chromate environment at various potentials.

Stress (KSI) vs % Strain

Legend:
- open circuit
- −0.650 V SCE
- −0.540 V SCE
- −0.475 V SCE
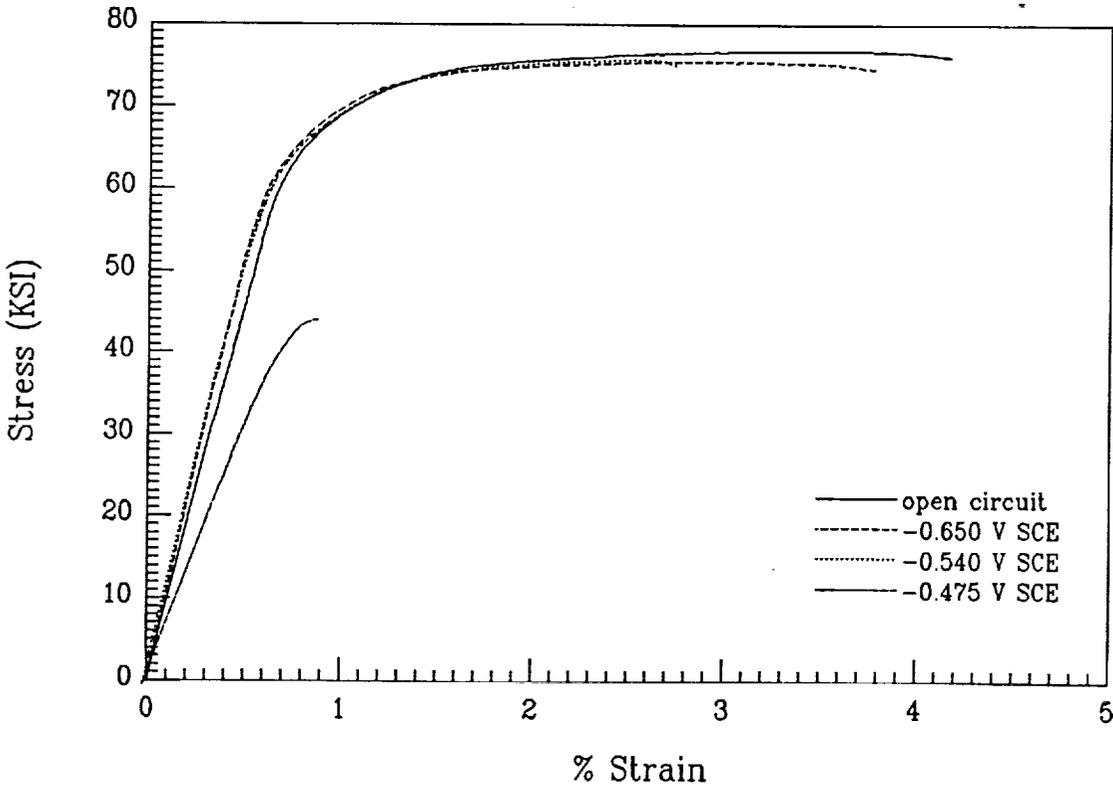
The following TEM micrographs are samples of the microstructures intended for extensive study in this research project. Qualitative comparison of the T_1 size and distribution in the various microstructures suggests that a quantitative comparison should be possible that will distinguish the materials from one another.

TEM of X2095-A

0.5μm
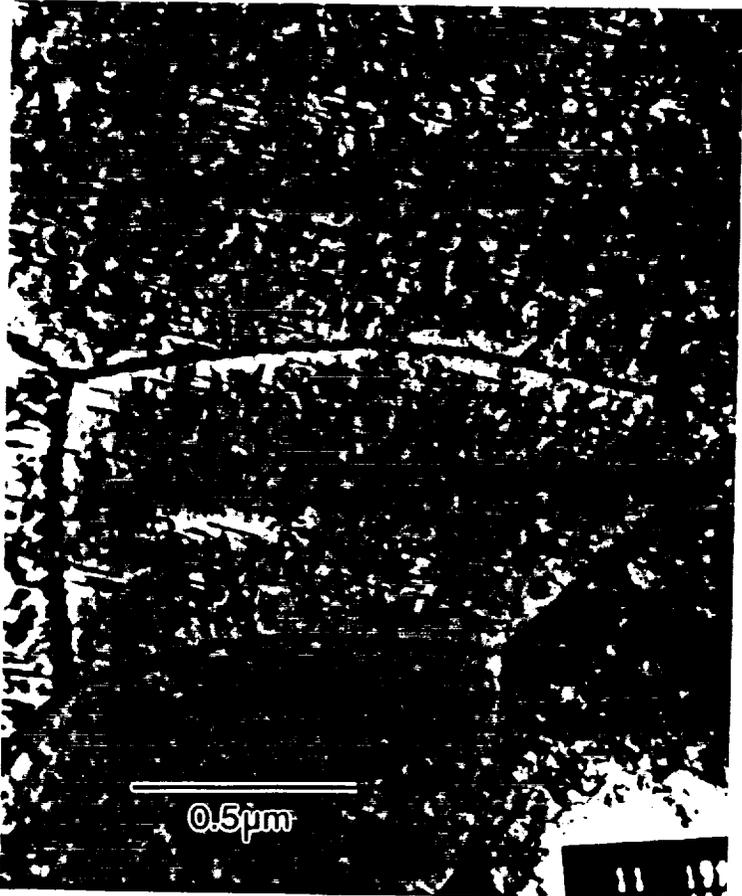
TEM of X2095-A

TEM of X2095-B

0.1μm

TEM of X2095-B

0.5μm
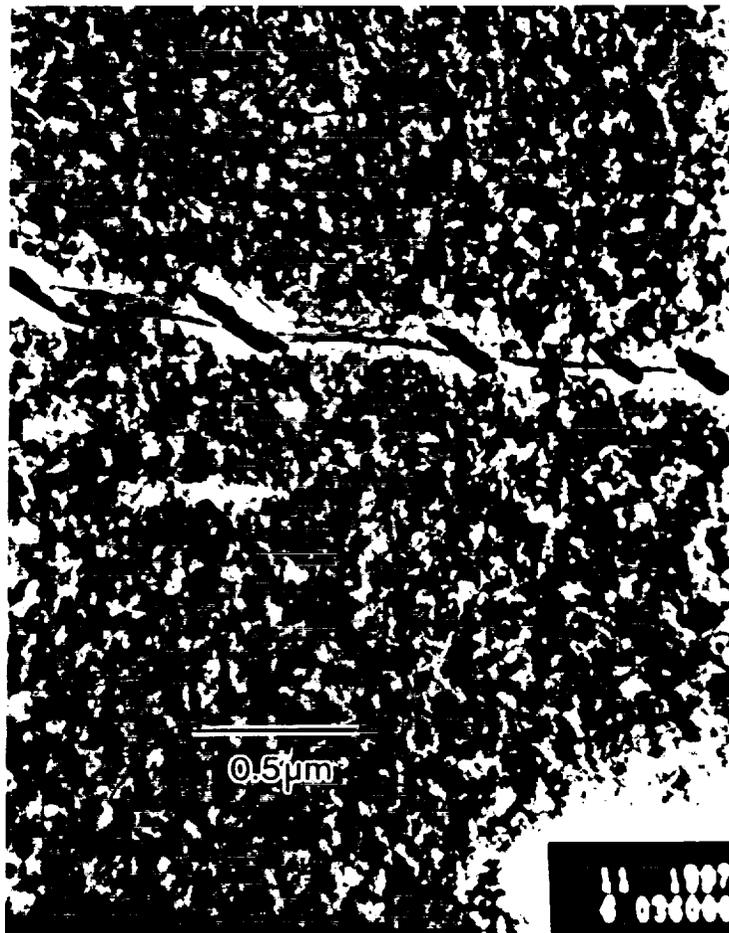
C-3

PRELIMINARY RESEARCH - CONCLUSIONS

(1) X2095 (both A and B tempers) is susceptible to rapid failure when: $E_{BR,T1} < E_{appl} < E_{BR,\alpha-Al}$.

(2) The SCC of X2095 displays evidence of an intergranular crack path in the S-T orientation.

(3) The constant load-smooth bar technique is not sensitive enough to rank relative SCC susceptibility.

(4) Conditions can be generated in which SCC propagation will cease after initiating, possibly due to a potential drop mechanism.

(5) During SSRT, satisfying the criteria for rapid SCC results in complete loss of mechanical properties.

(6) Initial TEM observations indicate that the microstructures of the research materials may be qualitatively distinguished from one another.

FUTURE WORK

Using TEM, determine microstructural differences in the research alloys in terms of:

Fractional coverage of SGB's by T_1.

Relative sizes of average T_1 precipitates.

T_1 spacing on SGB's.

Homogeneity/heterogeneity of T_1 on boundaries vs in grain interiors.

Correlate the microstructural information to SCC susceptibility by:

Finding a less aggressive environment/potential combination which still satisfies the rapid failure criterion, then

Using the environment to control SCC in a rigid fracture mechanics test, acquire da/dt vs applied K information.

Mech. Prop. of X2095-A: 290°F for 20 hrs (S. No. 65662)

	UTS(ksi)	TYS(ksi)	EL(%)	Kic (Ksi√in)
at T/2				
L	86.4	83.2	10.0	
LT	82.4	76.4	10.0	
at T/4				
L	78.3	75.1	12.0	
LT	77.5	70.0	12.0	30.2
at T/8				
L	80.5	76.9	16.0	

Mech. Prop. of X2095-B: 290°F for 36 hrs (S. No. 65663)

	UTS(ksi)	TYS(ksi)	EL(%)	Kic (Ksi√in)
at T/2				
L	88.9	86.5	8.0	
LT	87.6	82.9	6.0	
ST	84.9	71.4	5.5	21.2
at T/4				
L	82.8	80.1	10.5	35.8
LT	83.8	78.0	7.0	24.6
at T/8				
L	--	--	--	--
LT	83.8	73.3	10.0	
ST	85.8	75.1	4.0	

<u>Project 8</u> **The Effects of Zinc Additions on the Precipitation and Stress Corrosion Cracking Behavior of Alloy 8090**

Raymond J. Kilmer and G.E. Stoner

<u>Objectives</u>

The objectives of this PhD research are to document and characterize the effects of Zn additions on the microstructure of alloy 8090 under different aging conditions, and to correlate SCC behavioral changes with changes in alloy composition and microstructure. Emphasis will be placed on optimizing SCC behavior and alloy density.

The Effect of Zn Additions to the Microstructure and SCC Behavior of 8090 and 8090-type alloys.

R.J. Kilmer

G.E. Stoner

Outline

Background:

    * Why?

Results to Date:

    * Microstructural characterization

    * Initial SCC testing

    * Polarization work...initial implications

Research in progress and future work:

    * Separate SCC initiation and propagation issues

        • constant displacement rate (CMOD) test

            • precracked C-T samples

            • NaCl + Na_2CrO_4 environment

    * Assess and rank the electrochemical activities of pertinent microstructural features

        • TEM of corroded foils

        • Polarization testing

        • Scanning auger

    * Investigate the relative susceptibilities of specific tempers to hydrogen embrittlement

        • measure elongations with and without charging using technique developed by Smith and Scully

Background:

- Alloy 8090 (Al-Li-Cu-Mg-Zr) is a lightweight high strength alloy designed for use in aerospace applications. Like other Al-Li alloys the S-T properties, particularly toughness and SCC resistance, are prohibitively poor.

- Zn additions to alloy 8090 and near 8090 alloys have been found to dramatically extend the lifetimes of alternately immersed S-T loaded tensile bars (per ASTM G44 and G49)

- Furthermore, Zn additions have been previously shown to have a profound effect on precipitation in this system

- The objective of this research is to document the effects Zn additions have on the precipitation in a number of Al-Li-Cu-Mg-(Zn)-Zr alloys and correlate these microstructural changes with a change in SCC resistance

Results to Date:

Microstructural Characterization:

Alloy 8090 (Al-2.45Li-1.2Cu-0.7Mg-0.1Zr)

<u>Matrix:</u>

δ' (Al$_3$Li)..............spherical, homogeneously nucleated

S' (Al$_2$CuMg).........needle shaped, heterogeneously nucleated

T$_1$ (Al$_2$CuLi)..........plate shaped, heterogeneously nucleated

<u>Boundaries:</u>

T$_2$ (Al$_6$CuLi$_3$).........globular, grain and subgrain boundaries

S' (Al$_2$CuMg).........subgrain boundaries

T$_1$ (Al$_2$CuLi)..........subgrain boundaries

<u>Zn additions</u> to alloy 8090 decrease the solubility of Li, Cu and Mg in Al and depending on the relative amount of solute present

<u>Matrix:</u>

- increased v/o ....δ' (Al$_3$Li)
- ....S' (Al$_2$CuMg)

<u>Boundaries:</u>

- Predominant boundary phase changes from T$_2$ to T (Mg$_{32}$(Al,Cu,Zn)$_{49}$) as Zn content increases

Microstructure:

- Zn additions (from 0.2 to 1.36 w/o) dramatically influence precipitation
- Characterization methods:
  - TEM with CBED, EDS and SAD
  - DSC and solution potential measurements

Alloy A
- **Low Zn (¯0.2 w/o), low solute (L̲i̲ + Cu + Mg = 3.94 w/o) Sheet**
  - decreased boundary precipitation wrt 8090 baseline
  - S' not qualitatively affected

Alloy B
- **Low Zn (¯0.2 w/o), high solute (L̲i̲ + Cu + Mg = 4.32 w/o) Plate**
  - enhanced boundary precipitation wrt 8090 baseline
  - little apparent change in matrix precipitation
  - improved S-T TYS, UTS and % el. values

Alloy C
- **Medium Zn (¯0.6 w/o), low solute (L̲i̲ + Cu + Mg = 3.60 w/o) Sheet**
  - boundary precipitation less than 8090 baseline (fewer δ'-FZ's)
  - S' enhanced

Alloy D
- **High Zn ($\geq$ 1.0 w/o), low solute (Li + Cu + Mg = 3.68 w/o) Sheet**
  - coarse intermetallic T phase precipitates on grain and subgrain boundaries upon artificial aging
  - S' enhanced

Alloy E
- **High Zn ($\geq$ 1.0 w/o), high solute (Li + Cu + Mg = 4.26 w/o) Plate**

Alloy F
        (Li + Cu + Mg = 4.42 w/o)

Alloy G
        (Li + Cu + Mg = 4.44 w/o)

- coarse T phase evident on grain boundaries at T3 condition *(inappropriate SHT practice employed)*
- S' enhanced
- TYS, UTS improved, % el. and K_{IC} degraded with magnitude of degradation dependent on Mg content and total solute supersaturation
- δ (AlLi) promoted with Zn additions (seen only at grain interiors)

Compositions of alloys employed in microstructural characterization:

Alloy	Product	Li	Cu	Mg	Zn	Zr
A	Sheet	2.27	1.07	0.60	0.21	0.10
B	Plate	2.45	1.20	0.67	0.20	0.10
C	Sheet	1.91	1.07	0.62	0.58	0.10
D	Sheet	2.09	1.00	0.59	1.07	0.10
E	Plate	2.54	1.23	0.49	1.00	0.12
F	Plate	2.53	1.22	0.67	1.36	0.12
G	Plate	2.47	1.23	0.74	0.99	0.12
H	Plate (B)	2.55	1.16	0.69	0.02	0.12
I	Sheet (B)	2.44	1.06	0.63	::::	0.10

Note: (B) denotes baseline alloy

SCC Testing

- Alternate immersion time to failure testing in aqueous chloride (3.5 w/o NaCl) environment was employed to initially assess the alloys SCC resistance as a function of aging time at 160°C.

Alloy	Temper (hrs at 160°C)	Exposure Stress					
		138 MPa		207 MPa		276 MPa	
		F/N	Days	F/N	Days	F/N	Days
F	1	3/3	2,2,3	3/3	2,2,2	N/A	
	5	2/3	2,3	3/3	1,1,2	N/A	
	20	0/3	- - -	0/3	- - -	N/A	
	40	0/3	- - -	0/3	- - -	N/A	
	60	0/3	- - -	N/A		0/3	- - -
	80	0/3	- - -	N/A		0/3	- - -
	100	0/3	- - -	N/A		1/3*	- - -
E	1	2/3	3,10	3/3	2,2,2	N/A	
	5	3/3	1,1,2	3/3	1,1,2	N/A	
	20	0/3	- - -	2/3	2,3,9	N/A	
	40	0/3	- - -	0/3	- - -	N/A	
	60	0/3	- - -	N/A		0/3	- - -
	80	0/3	- - -	N/A		0/3	- - -
	100	0/3	- - -	N/A		0/3	- - -
G	1	3/3	2,3,3	3/3	3,4,17	N/A	
	5	3/3	2,2,3	3/3	1,2,2	N/A	
	20	1/3	17	2/3	9,17	N/A	
	40	0/3	- - -	0/3	- - -	N/A	
	60	0/3	- - -	N/A		0/3	- - -
	80	0/3	- - -	N/A		0/3	- - -
	100	0/3	- - -	N/A		0/3	- - -
H	1	3/3	4,5,17	3/3	4,6,7	N/A	
	5	3/3	3,3,5	3/3	1,2,3	N/A	
	20	2/3	3,4	3/3	2,2,2	N/A	
	40	2/3	3,5	3/3	3,3,4	N/A	
	60	1/3	4	N/A		3/3	2,2,2
	80	2/3	3,6	N/A		3/3	2,3,3
	100	3/3	2,2,3	N/A		3/3	1,1,1

* Indicates sample fractured at threads
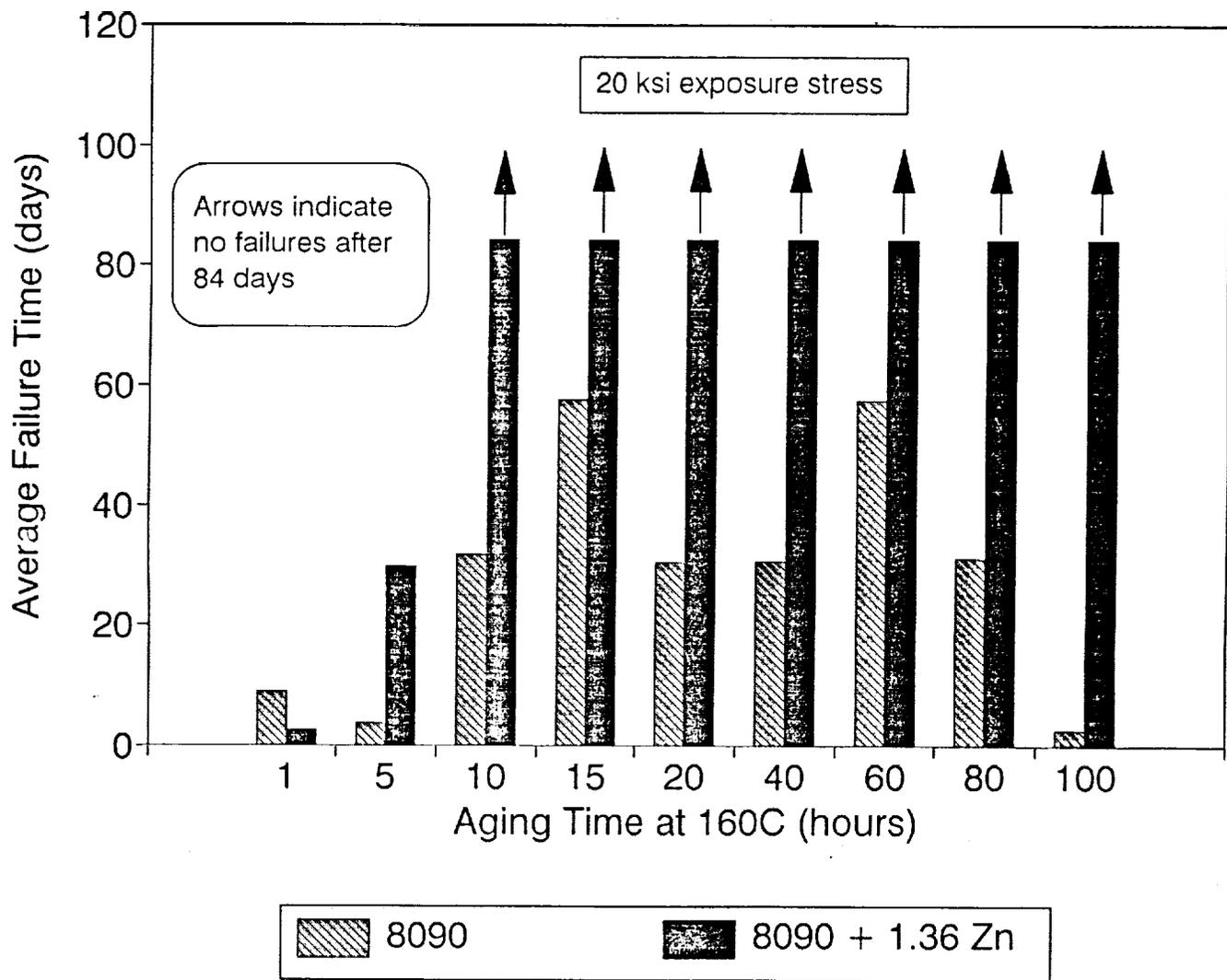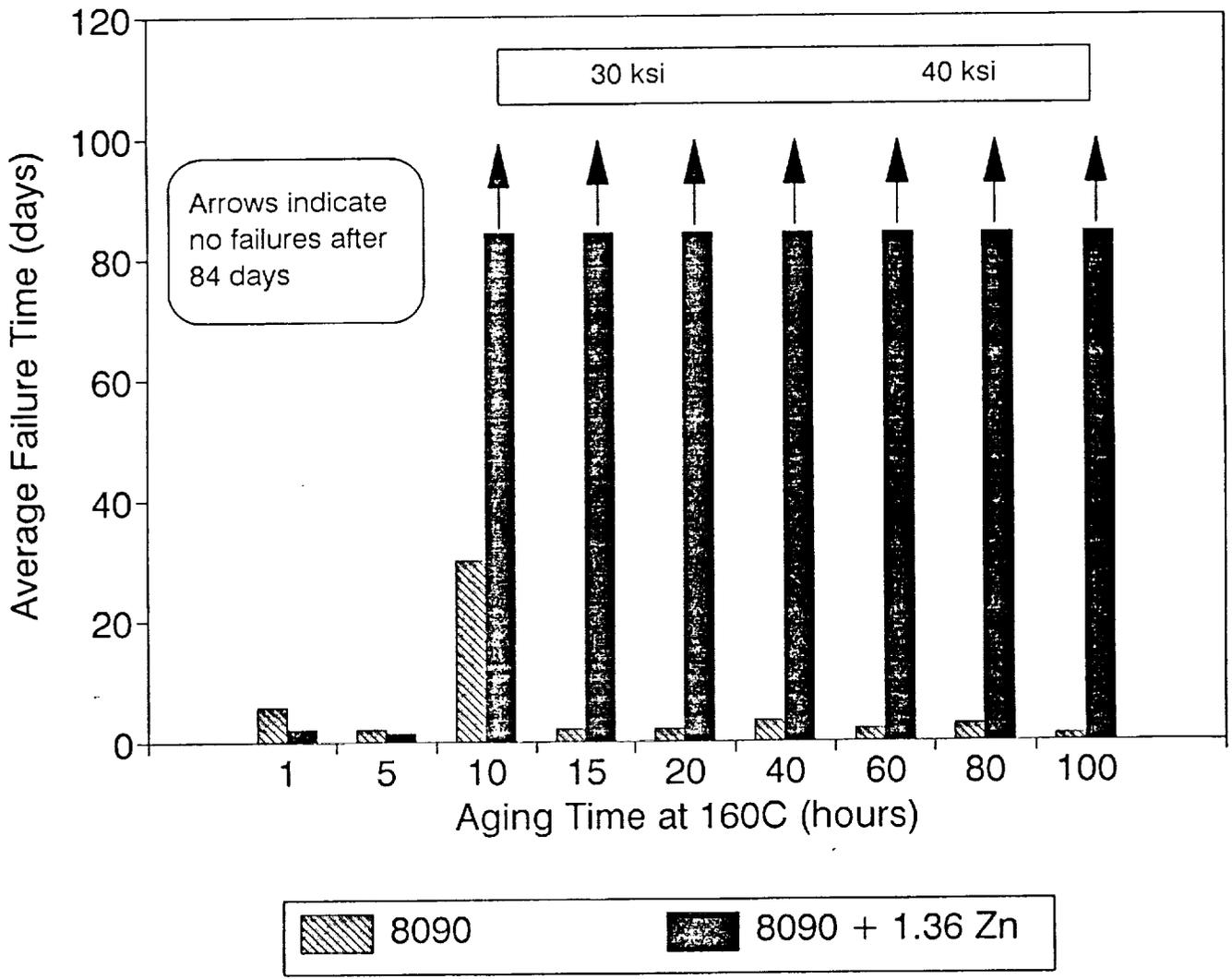
Work in progress

How do Zn additions alter SCC behavior? Is the improvement initiation or propagation related?

Smooth tensile samples lump both initiation and propagation events. A more quantitative measure of SCC propagation utilizes pre-cracked samples to eliminate initiation. To quantify SCC behavior a constant displacement rate technique will be employed on C-T specimens in a chloride/chromate environment. da/dt vs. applied stress intensity will be determined from which K_{init} and the plateau da/dt will be measured for a given displacement rate. 0.1 w/o Na_2CrO_4 will be added to avoid corrosion product and closure problems.

Clevice

Reference
Electrode

Overflow

Displacement
Guage

NaCl / Na CrO Solution Inlet
         2   4

Reference
Electrode

O-ring

Solution
Outlet

Compact Tension
Specimen
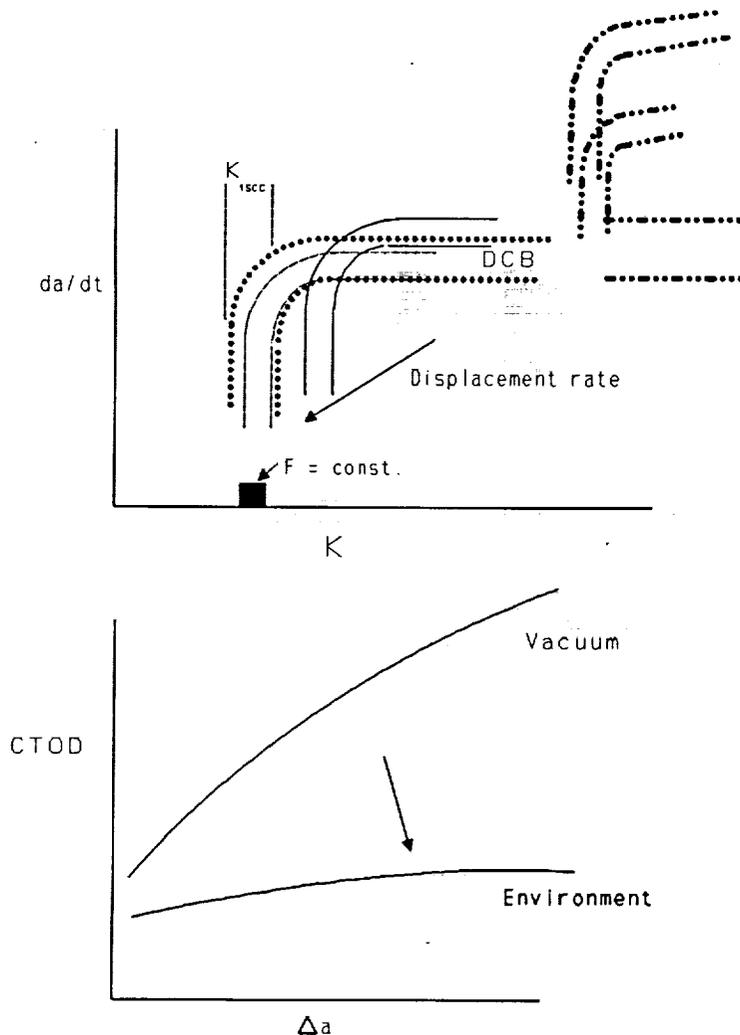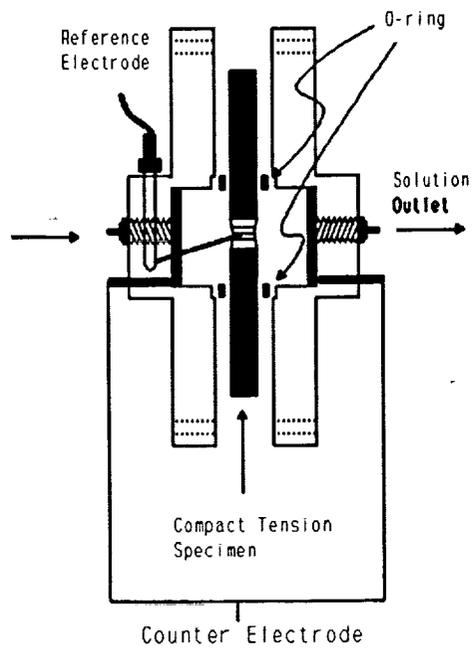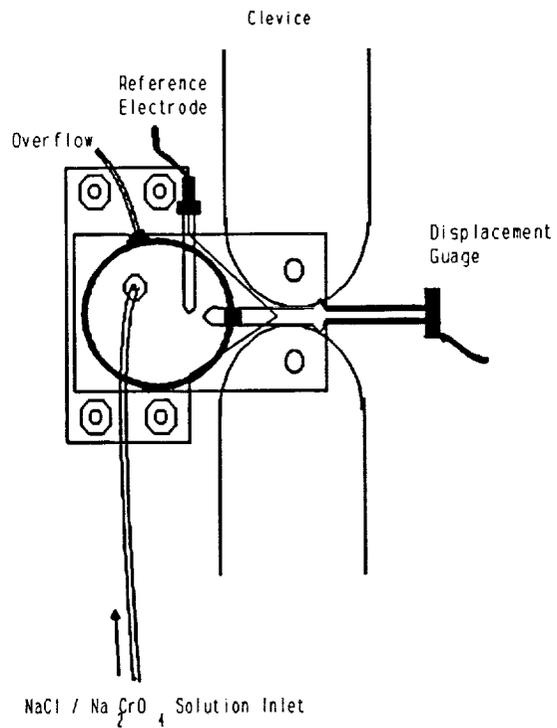
Counter Electrode

Microscopically, how do Zn additions alter electrochemical behavior?

Assess and rank the electrochemical activities of pertinent microstructural features

- TEM of corroded foils to examine the electrochemical behavior of boundary precipitates (anodic, cathodic) and compare with baseline 8090
- Energy dispersive spectroscopy (EDS) will be employed to measure an average Zn/Cu ratio in the boundary phases before and after SCC transition time
- Polarization testing
- Investigate solute profiles adjacent to boundaries via scanning auger spectroscopy

Does Zn change susceptibility to hydrogen embrittlement?

Investigate the relative susceptibilities of SCC susceptible and SCC resistant tempers to hydrogen embrittlement

- elongations will be measured before and after charging with hydrogen as a rough measure of the susceptibility of the alloys to hydrogen embrittlement in the SCC susceptible and SCC resistant tempers
- method used for charging will allow for separation of dissolution effects

Graph 1 (top):
e (vertical axis)

w/o Hydrogen

w/ Hydrogen

} Δe

SCC Susceptible   SCC Resistant

Aging Time

Graph 2 (middle):
e (vertical axis)

w/o Hydrogen

w/ Hydrogen

} Δe

SCC Susceptible   SCC Resistant

Aging Time

Graph 3 (bottom):
e (vertical axis)

w/o Hydrogen

w/ Hydrogen

} Δe

SCC Susceptible   SCC Resistant
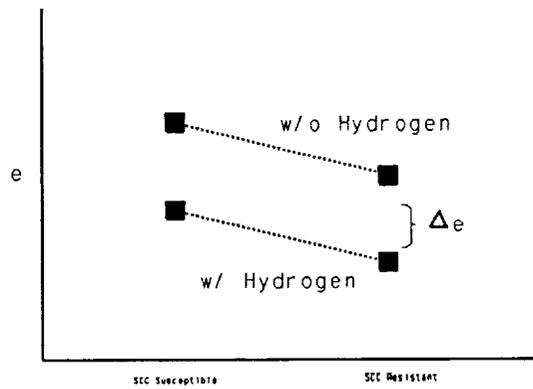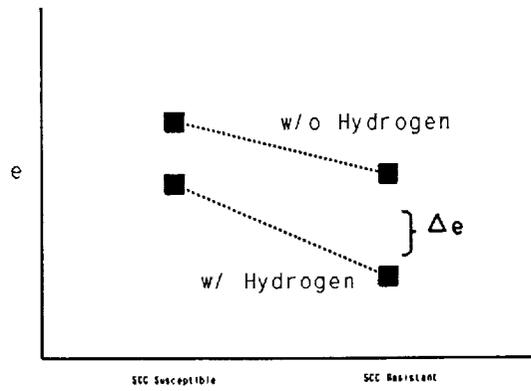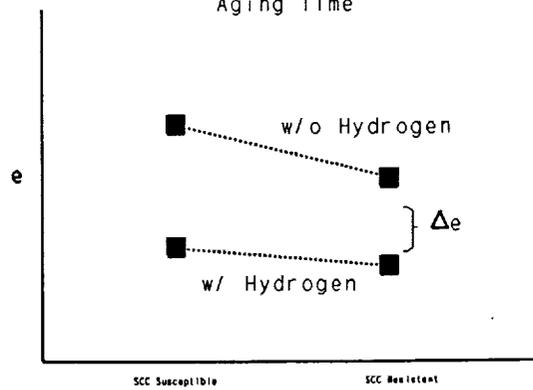
Aging Time

• Possible test result scenerios for hydrogen susceptibility experiments

Recrystallized Alloys

A series of recrystallized 2090 (Al-Li-Cu) alloys was fabricated to examine the effect of grain size on SCC behavior.

Background:

The primary stress corrosion crack pathway in Al-Li-Cu-X alloys is somewhat ambiguous. SCC fracture surfaces display both intergranular and intersubgranular features. When stressed in S-T orientation, SCC failure times are significantly shorter than when stressed L-T orientation suggesting a high angle boundary phenomenon. Intersubgranular path in both orientations is continuous but intergranular path varies markedly due to anisotropic morphology caused by rolling. Recrystallized structures are devoid of subgrains and subgrain boundaries making the ideal candidates for testing the effect of grain boundary and grain boundary anisotropy on SCC resistance.

Fabrication:

Evaluation:

- L-T orientation will be evaluated in four recrystallized Al-Li-Cu alloys
- J-Integral fracture mechanics will be employed to provide a measure of the toughnesses of the alloys
- Tensile tests will determine the TYS, UTS and % el. and fracture surfaces evaluated
- SCC evaluation will involve both TTF testing as well as generating v - K curves from C-T test assembly

Recrystallized Al-Li-Cu-X Alloys
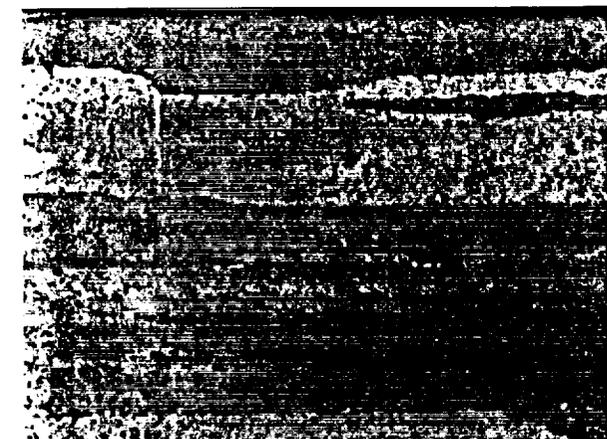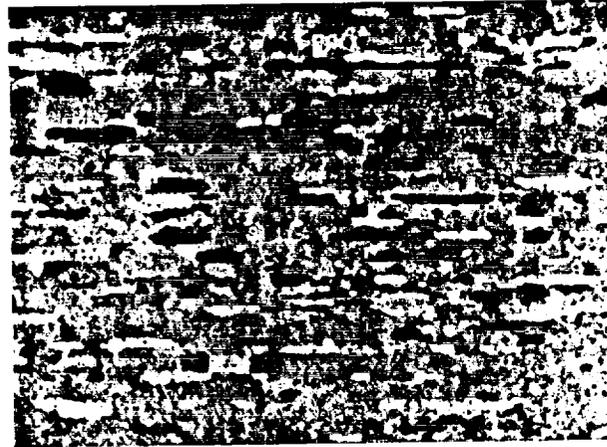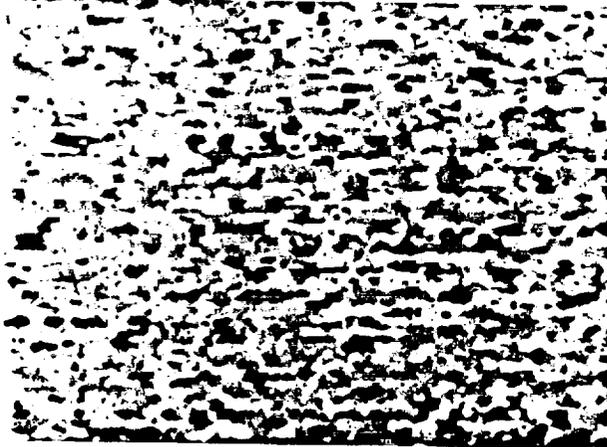
200μm
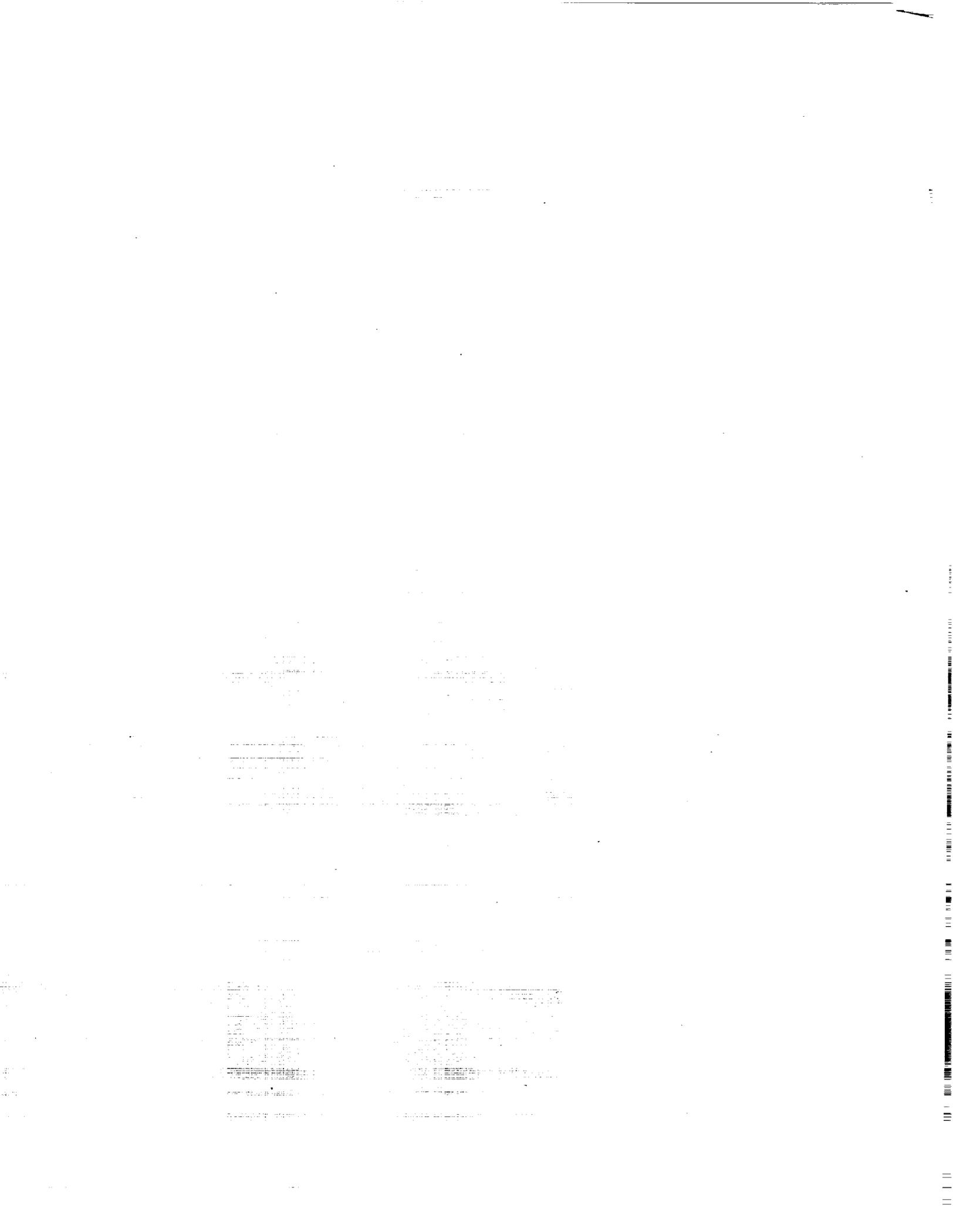
Project 9   **Hydrogen Interactions in Aluminum-Lithium Alloy 2090 and Selected Complimentary Model Alloys**

S.W. Smith and J.R. Scully

Objective

The role that hydrogen plays in the environmentally assisted cracking of aluminum-lithium alloys has not been fully established. This issue must be addressed since hydrogen environmentally assisted cracking (HEAC) is an important issue concerning alloys intended for utilization in advanced aerospace applications. To date the hydrogen absorption, internal transport, trapping and resultant effects on mechanical properties have not been characterized for these alloys.

We seek to develop a fundamental understanding of the effects dissolved and trapped hydrogen have on the mechanical properties of selected Al-Li-Cu-X alloys. In order to reach this goal we will study the behavior of alloy 2090. We have established three major goals in this study. We propose to (a) distinguish HEAC form aqueous dissolution controlled EAC, (b) correlate hydrogen induced EAC with mobile and trapped hydrogen concentrations, and (c) identify significant trap sites and hydride phases (if any do exist). The ultimate goal of this project is to develop deterministic models which define the effect of absorbed hydrogen on the mechanical properties of aluminum lithium alloys.

Current Status

The research to be conducted has been separated into three major phases. They are in general organized into the areas of: (a) hydrogen analyses of electrochemically charged samples, (b) examination of mechanical properties under the influence of absorbed hydrogen, and (c) correlation of hydrogen analyses results with mechanical properties. Throughout the last reporting period research has been centered around determining how absorbed hydrogen effects the mechanical properties of alloy 2090 in the underaged condition. In order to evaluate the mechanical properties, a testing procedure has been developed in which it is possible to perform mechanical testing in a dry environment in order to remove any dissolution effects. This procedure consists of the sputter etch removal of the native oxide

coating from flat tensile bars, and the subsequent deposition of a thin nickel film to protect the alloy. This nickel coated tensile bar can then be hydrogen charged electrochemically in a solution in which the nickel will not suffer from any dissolution effects. Upon completing the electrochemical charging of the mechanical specimen, it is removed from solution, and the nickel coating is polished away. Mechanical testing is then performed in a dry argon environment. EAC studies performed on 2090 alloy in the past has not been able to clearly separate aqueous dissolution from hydrogen effects, however, in using this testing procedure one can clearly evaluate the influence of hydrogen on the mechanical properties of an alloy, independent of any aqueous dissolution effects. In this way, deterministic models can be developed between hydrogen concentration and embrittlement.

Recent Findings

The mechanical tests that have been performed to date clearly show absorbed hydrogen has a deleterious effect on the mechanical properties of alloy 2090 in the underaged (T3) condition. This has been shown by a loss in mechanical properties, elongation to failure, reduction in area and fracture energy, in both the LT and TL orientations. In addition to the evaluation of the mechanical properties, fractographic analysis has shown that there is a change in fracture path with the addition of absorbed hydrogen. For smooth tensile bars, hydrogen is shown to affect the shear fracture process. In notched samples a fracture mode change occurs from a ductile shear process to intersubgranular.

Milestones

Additional mechanical tests will be performed in the next 6 month time frame. In an attempt to obtain higher hydrogen concentrations in the test specimens, potentiostatic charging will be performed at larger cathodic overpotentials and the use of hydrogen recombination poisons during cathodic charging will be evaluated. In addition to studying 2090 in the underaged condition, work will be performed on this alloy in the peak aged condition (T8). Throughout the next reporting period hydrogen analysis through the use of thermal desorption spectroscopy (TDS) will be performed. The TDS system that was purchased in the last reporting period, has been constructed and the system environment should be adequate to begin hydrogen analysis very shortly. In addition to these two types of analyses, fracture specimens will be used in order to perform J-integral R curves to try to clearly evaluate the

62

fracture mode present with the addition of absorbed hydrogen and to define the affect of hydrogen on fracture thresholds.

Presentation Graphics Captions

1. Composite optical micrograph of 2090 - T3 alloy being used.

2. Composite optical micrograph of 7075 - T6 alloy being used.

3. Schematic representation of hydrogen reduction reaction during the film rupture process at a crack tip.

4. Hydrogen partial pressures for scratched electrode tests in buffered 0.5 M Na_2SO_4. The open symbols represent open circuit measurement for the various materials, while the closed symbols represent the minimum potential obtained during a mechanical scratch test. The minimum potential is a measurement of the maximum obtainable hydrogen fugacity during a film rupture event.

5a. Cathodic overpotential (with respect to the reversible potential for hydrogen reduction) vs log of the hydrogen fugacity. For every 30 mV increase in overpotential the fugacity will be increase by an order of magnitude.

5b. Hydrogen concentration in a metal vs the square root of the hydrogen fugacity.

6a. Drawing of an aluminum alloy that has been charged with hydrogen with the assistance of a nickel coating. The native oxide is sputter etched prior to deposition of the coating.

6b. Representation of an environmental test of an aluminum alloy with its native oxide intact.

7. Flowchart outlining the procedures performed during mechanical tests.

8. Overlay of the Pourbaix diagrams for nickel and aluminum. These diagrams are used to determine charging conditions that can be used to avoid any dissolution. Charging is performed in the regions where nickel is noble and aluminum is passive. The phase stability regions for aluminum are studied since the thin nickel coating being used does posses some defects.

9. Hydrogen concentrations obtained at various charging current densities for a nickel coated aluminum specimen. The data presented in this report are for specimens that have been potentiostatically charged at -1 V vs. SCE, which results in a current density of 19.5 μm/cm^2.

10. Tensile data for 7075-T6-LT specimens, that were coated with a thin palladium coating and then galvanostatically charged. Due to adhesion problems encountered with the palladium films, the charging was limited to a period of 24 hours. After charging specimens were stored in dry air for various periods of time in an attempt to create a more uniform hydrogen distribution in these specimens.

11. Tensile data for 2090-T3-LT specimens, that were coated with nickel and then potentiostatically charged for various times. The charging was performed at -1 V_{SCE} in a Na$_2$SO$_4$ solution buffered to a pH of 7. The testing was done at a constant extension rate in a dry Ar environment.

12. Data representing the change in mechanical properties for several 2090-T3-LT specimens, some of which are shown in Fig. 11. The values shown for the elongation to failure were calculated by taking the elongation to failure obtained by a specimen charged for a particular time and dividing it by the elongation to failure obtained for a specimen that was not electrochemically charged. The data for the reduction in area were calculated by taking the percentage reduction in area for a charged specimen and dividing it by the value obtained for a specimen that has not been charged.

13. Schematic of a hydrogen concentration profile for a charged aluminum specimen. These curves were obtain by assuming $D_H = 1 \times 10^{-9}$ cm^2/sec.

14. Data comparing the ratio for the reduction in area for 2090-T3-LT specimens that have been charged and then test at two different strain rates. This data clearly shows that there is a strain rate effect associated with the reported loss in properties.

15. Loss in mechanical property data for charged 2090-T3 specimens in the TL orientation.

16. Tensile data for charged 2090-T3-LT specimens that have been notched with a diamond wafering blade prior to mechanical testing. This procedure was done in order to see how a stress concentration (blunt notch) would effect the observed properties.

17. Change in threshold stress and fracture energy for charged 2090-T3-LT specimens that have been pre-notched. The threshold stress information presented is a ratio of the threshold stress for a charged specimen divided by that obtained for an uncharged

specimen. The fracture energy data is a ratio of the fracture energy of a charged specimen divided by the fracture energy of an uncharged specimen.

18. SEM micrograph of the fracture surface for a tensile specimen of 2090-T3 in the LT orientation. Specimen has not been hydrogen charged. Mechanical test was performed at a strain rate of 2.5×10^{-6} sec^{-1}, in a dry argon environment. Micrograph taken near center of fracture surface.

19. SEM micrograph of the fracture surface for a tensile specimen of 2090-T3 in the LT orientation. Specimen electrochemically charged in 0.25 M Na_2SO_4 solution buffered to a pH of 7 for 25 days at -1 V_{SCE}. Mechanical test was performed at a strain rate of 2.5×10^{-6} sec^{-1}, in a dry argon environment. Micrograph taken near center of fracture surface.

20. SEM micrograph of the fracture surface for a tensile specimen of 2090-T3 in the TL orientation. Specimen was not hydrogen charged. Mechanical test was performed at a strain rate of 2.5×10^{-6} sec^{-1}, in a dry argon environment. Micrograph taken near center of fracture surface.

21. SEM micrograph of the fracture surface for a tensile specimen of 2090-T3 in the TL orientation. Specimen was hydrogen charged in 0.25 M Na_2SO_4 buffered to a pH of 7 for 19 days at -1 V_{SCE}. Mechanical test was performed at a strain rate of 2.5×10^{-6} sec^{-1}, in a dry argon environment. Micrograph taken near center of fracture surface.

22. SEM micrograph of the fracture surface for a tensile specimen of 2090-T3 in the LT orientation. Specimen was notched normal to the tensile axis, prior to mechanical testing, with a diamond wafering blade. Specimen was hydrogen charged in 0.25 M Na_2SO_4 buffered to a pH of 7 for 26 days at -1 V_{SCE}. Mechanical test was performed at a strain rate of $2.5 \times ^{-6}$ sec^{-1}, in a dry argon environment. Micrograph taken near center of fracture surface.

23. Schematic of the thermal desorption spectroscopy system constructed at UVa. The components are numbered as follows: 1) turbo molecular pump with diaphragm backing pump 2) valve 3) six way cross 4) ionization gauge 5) titanium chip gettering pump 6) quadrupole mass spectrometer 7) gate valve 8) four way cross 9) ionization gauge 10) valve 11) flex bellows 12) convectron gauge 13) tribodyn mechanical pump 14) vent valve 15) flex bellows 16) quartz specimen chamber 17) programmable tube furnace.

Hydrogen Interactions in Aluminum-Lithium Alloy 2090 and Selected Complementary Model Alloys

Stephen W. Smith

and

John R. Scully

University of Virginia

Department of Materials Science and Engineering

Center for Electrochemical Sciences and Engineering

Charlottesville, VA 22903

Objective

We seek to develop a fundamental understanding of the effects dissolved and trapped hydrogen have on the mechanical properties of selected Al-Li-Cu-X alloys. In order to reach this goal work will be centered around three major areas: 1) distinguish hydrogen induced EAC from aqueous dissolution controlled EAC, 2) correlate hydrogen induced EAC with mobile and trapped hydrogen concentrations, and 3) identify significant trap sites and hydride phases (if any).

Alloy Microstructure

precipitation sequence:

2090 (Al-Li-Cu alloys)

$$\alpha_{ss} \Rightarrow \alpha_m + GP \Rightarrow \alpha_m + \theta'' \Rightarrow \alpha_m + \theta' \Rightarrow \alpha_m + \theta$$

$$\alpha_{ss} \Rightarrow \alpha_m + \delta'$$

$$\alpha_{ss} \Rightarrow \alpha_e + T_1$$
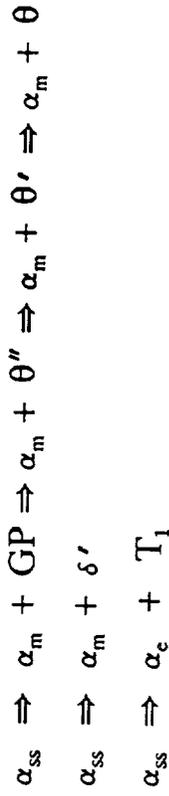
7075 (Al-Cu-Mg-Zn alloys)

$$\alpha_{ss} \Rightarrow GP \Rightarrow \eta' \Rightarrow \eta \Rightarrow T$$

$$\alpha_{ss} \Rightarrow GP \Rightarrow T' \Rightarrow T$$

where:

α_{ss} - supersaturated solid solution

α_m - metastable matrix phase

α_e - equilibrium matrix phase

δ - AlLi   (equilibrium phase, incoherent)

δ' - Al$_3$Li   (metastable, coherent)

T - Al$_6$CuMg$_4$ (incoherent)

T$_1$ - Al$_2$CuLi   (coherent)

η' - MgZn$_2$ (coherent)

θ' - CuAl$_2$ (coherent)

Alloy Properties

composition (wt. %):

Alloy	Li	Cu	Mg	Zn	Fe	Si	Zr	Mn	Cr	Ti
2090	2.15	2.56		0.02	0.05	0.04	0.12			
7075		1.2-2.0	2.1-2.9	5.1-6.1	0.7	0.5		0.3	.18-0.4	0.2

typical tensile properties at 75°F:

property	2090 - T3	7075 - T6
Ultimate tensile strength (ksi)	44	76
Yield strength (ksi)	37	67
Elongation (%)	16	11
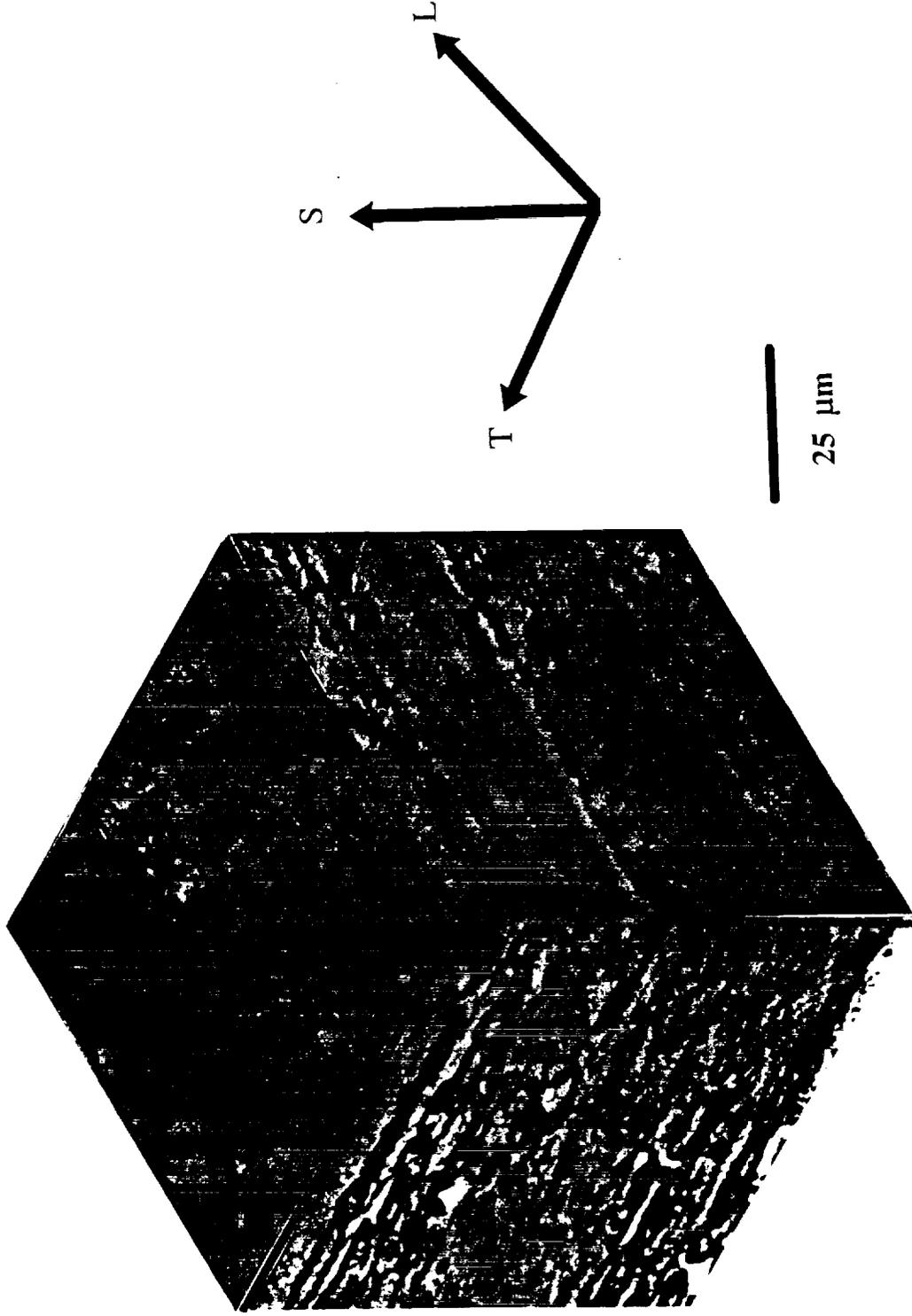
Figure 1. Optical micrograph for alloy 2090-T3.
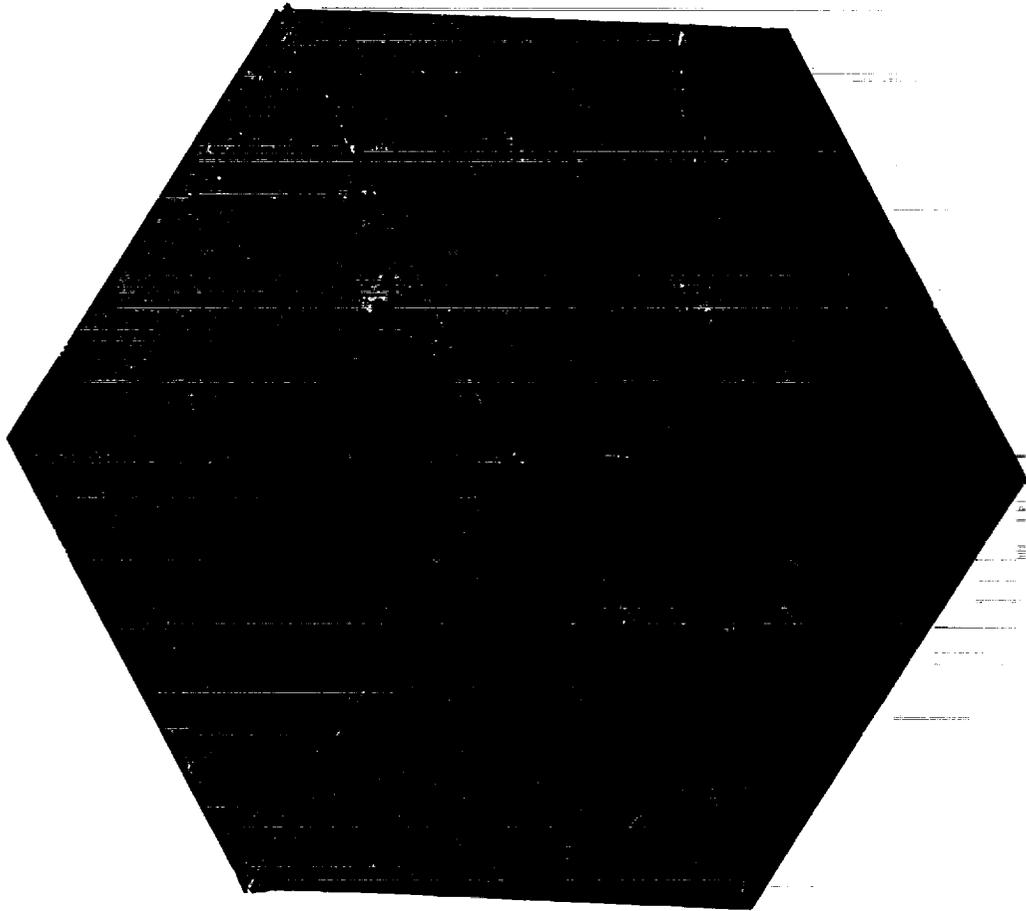
Figure 2. Optical micrograph for alloy 7075-T6.

L

S

T

50 µm

Figure 3. Hydrogen Production at a Crack Tip for an Aluminum Alloy
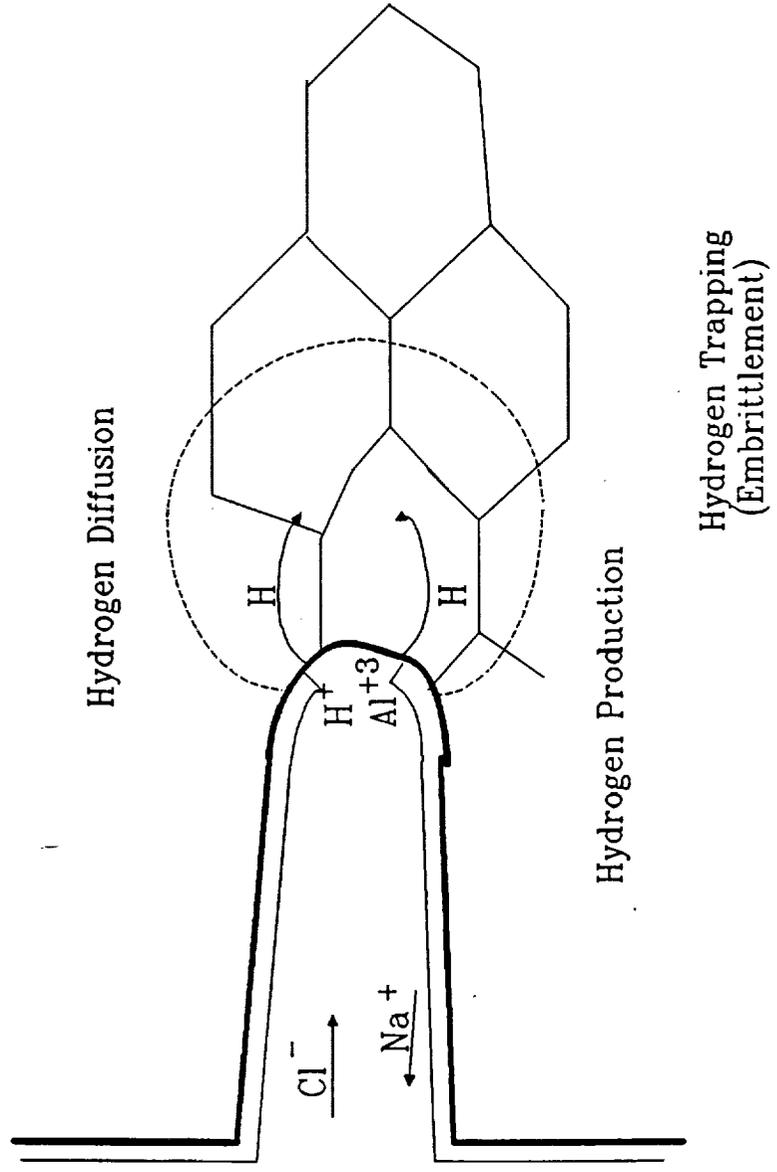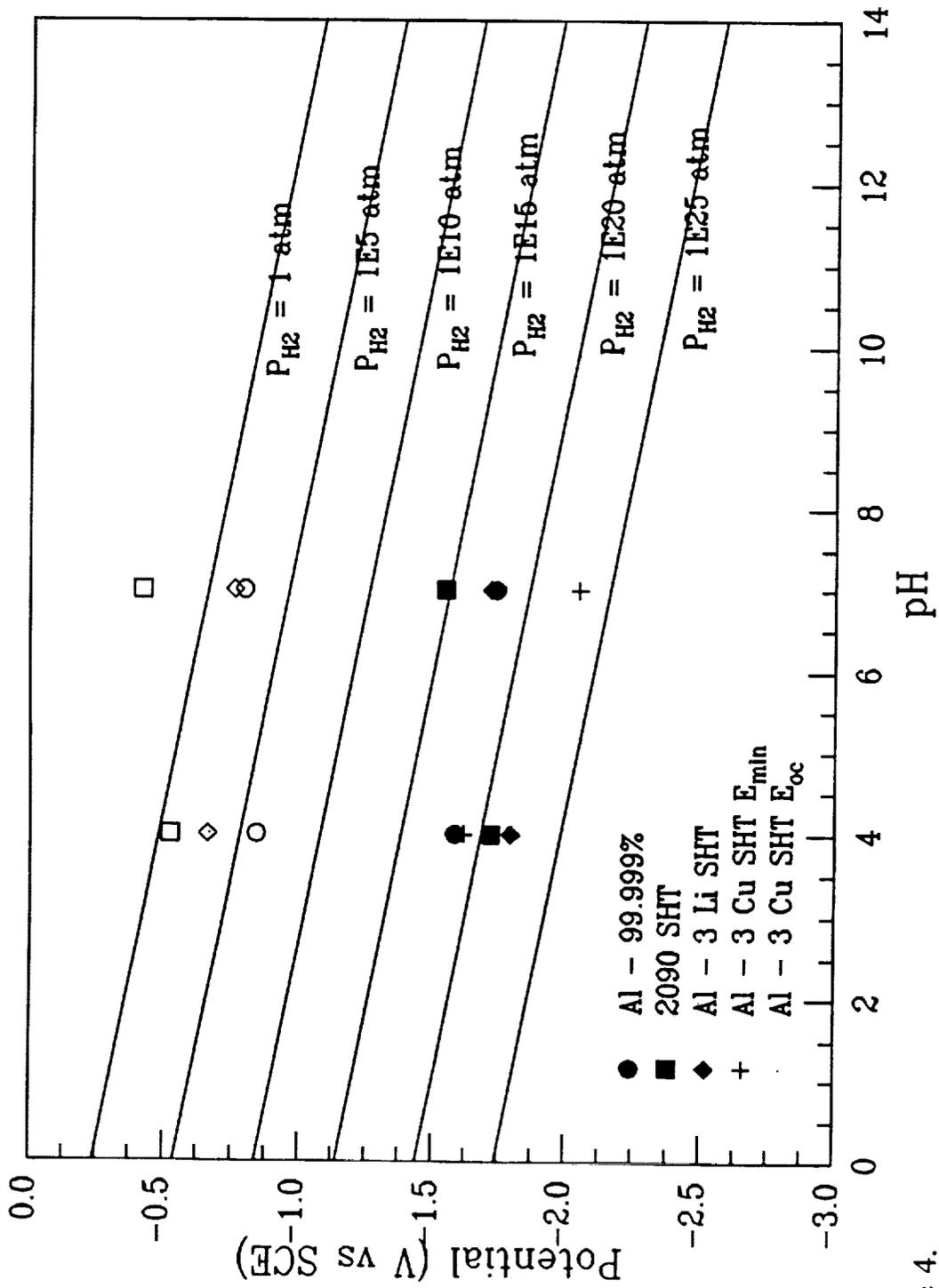
Figure 4.

Hydrogen partial pressures for scratched electrode test in 0.5 M Na$_2$SO$_4$. ●, ■, ◆, and + are E$_{min}$ after scratching. ○, □, ◇, and · are E$_{oc}$ measurements.

Electrochemical Production of Hydrogen

for fast discharge, slow recombination:

$$H^+ \; + \; e^- \; + \; M \; \rightleftharpoons \; M\text{-}H_{ads}$$

$$\log\left(\frac{\eta}{30mV}\right) = f_{H_2}$$

Figure 5a, 5b.

η (mV) versus $\log f_{H_2}$ (atm)

c_H versus $f_{H_2}^{1/2}$
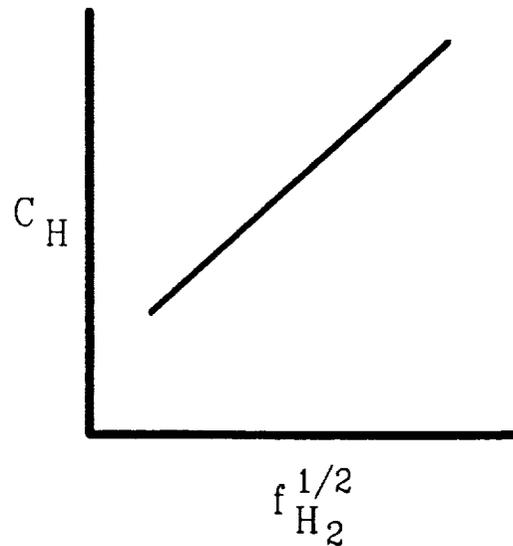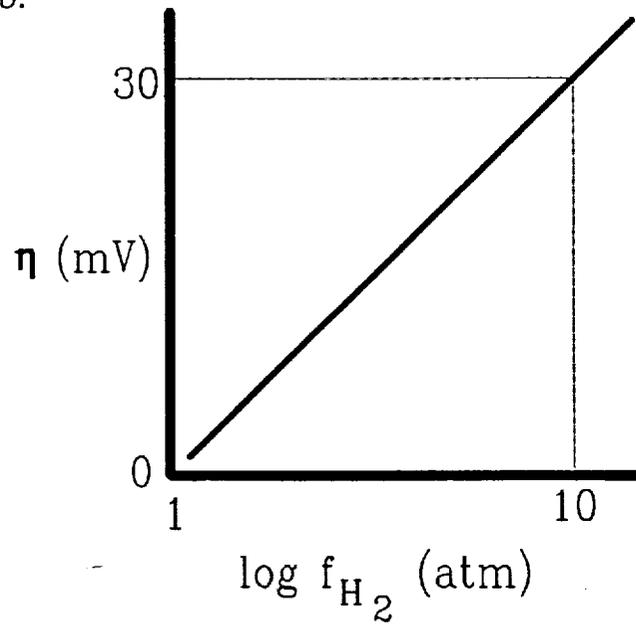
Advantages to Using Nickel Coatings

- Can remove Al_2O_3 layer, which impedes hydrogen diffusion. D_H (Al_2O_3) = 10^{-17} - 10^{-45} cm^2 sec^{-1}.

- Surface of specimen will not be affected by cathodic charging.

- Can distinguish between aqueous and hydrogen effects.
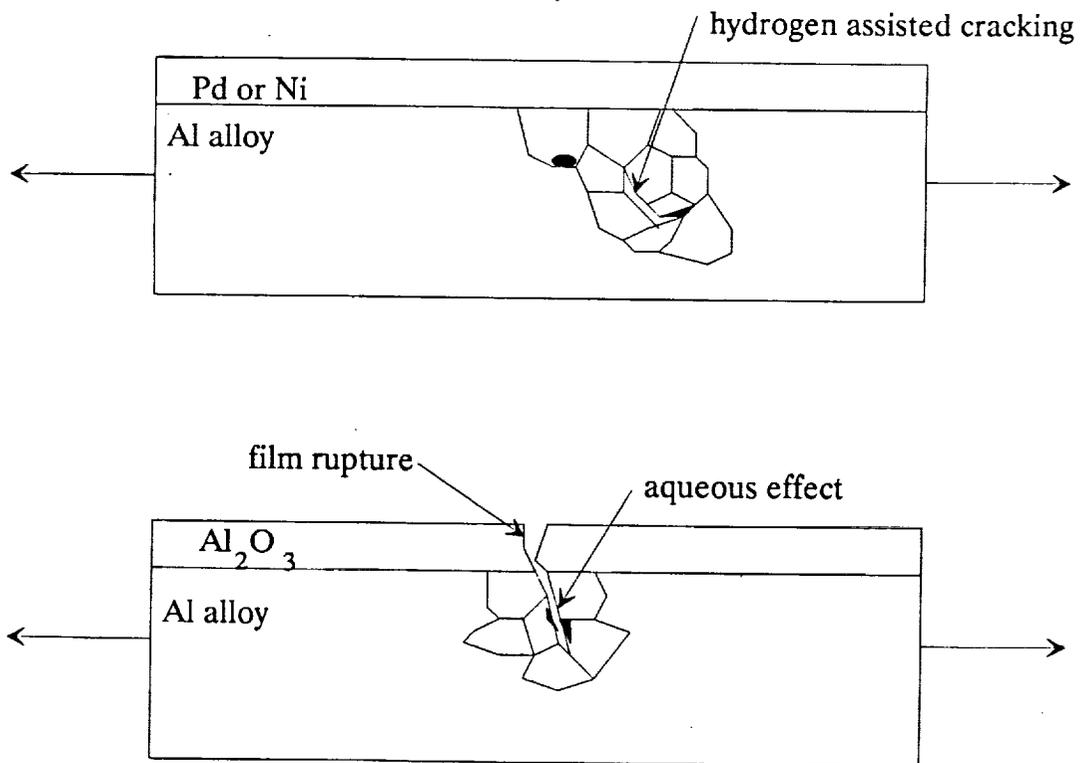
Figure 6a,6b.   Schematic representation of environmental testing with and without a protective matal film.

Figure 7. Mechanical Testing Procedure

Flowchart:

Heat Treat Polish → Oxide removal by sputter etch → deposit Ni coating → Pre-charge with H, remove, repolish surface → Tensile Test (CERT) Dry Ar

Pre-charge with H, remove, repolish surface —
variables:
- cathodic potential, C_H
- Time, C_H dist.
- pH
- H recombination poison

Tensile Test (CERT) Dry Ar —
variables:
- strain rate (10^3 , 10^{-6})
- stress concentration
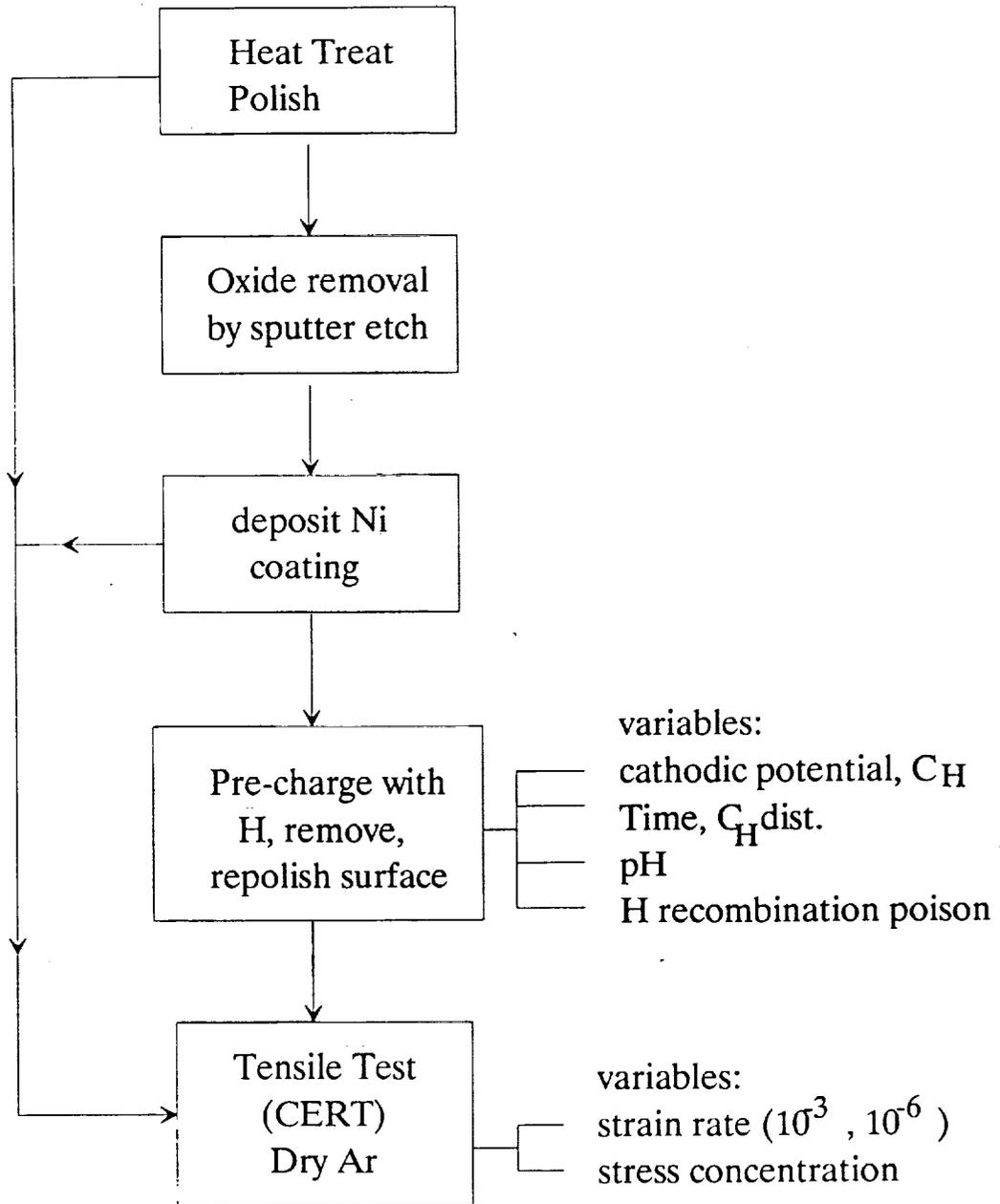
Figure 8. POTENTIAL–pH EQUILIBRIUM DIAGRAM FOR NICKEL AND ALUMINUM IN WATER AT 25°C

Figure 9.   Hydrogen Solubility in Aluminum
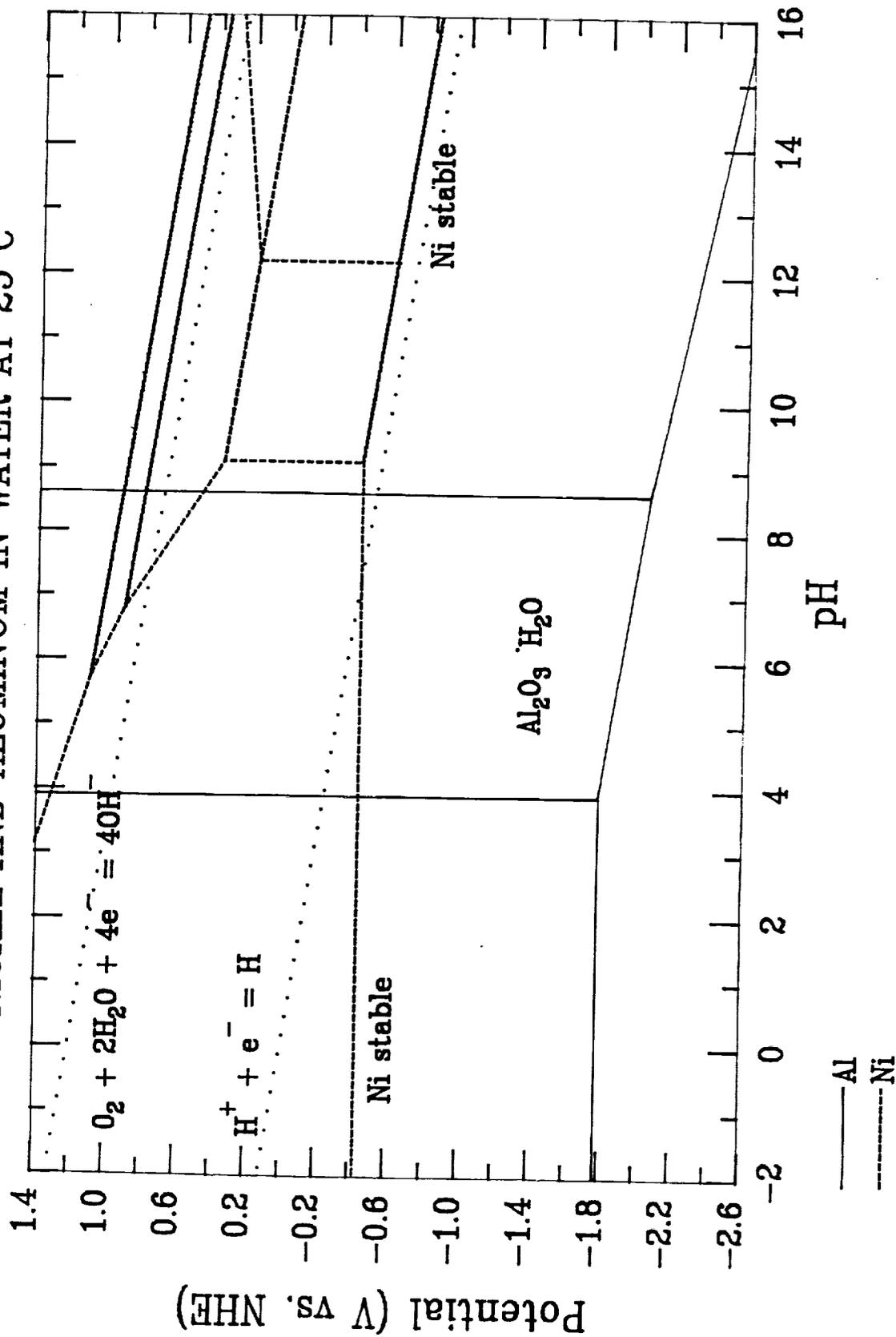
from Youngchang, Heyun and Latanisition
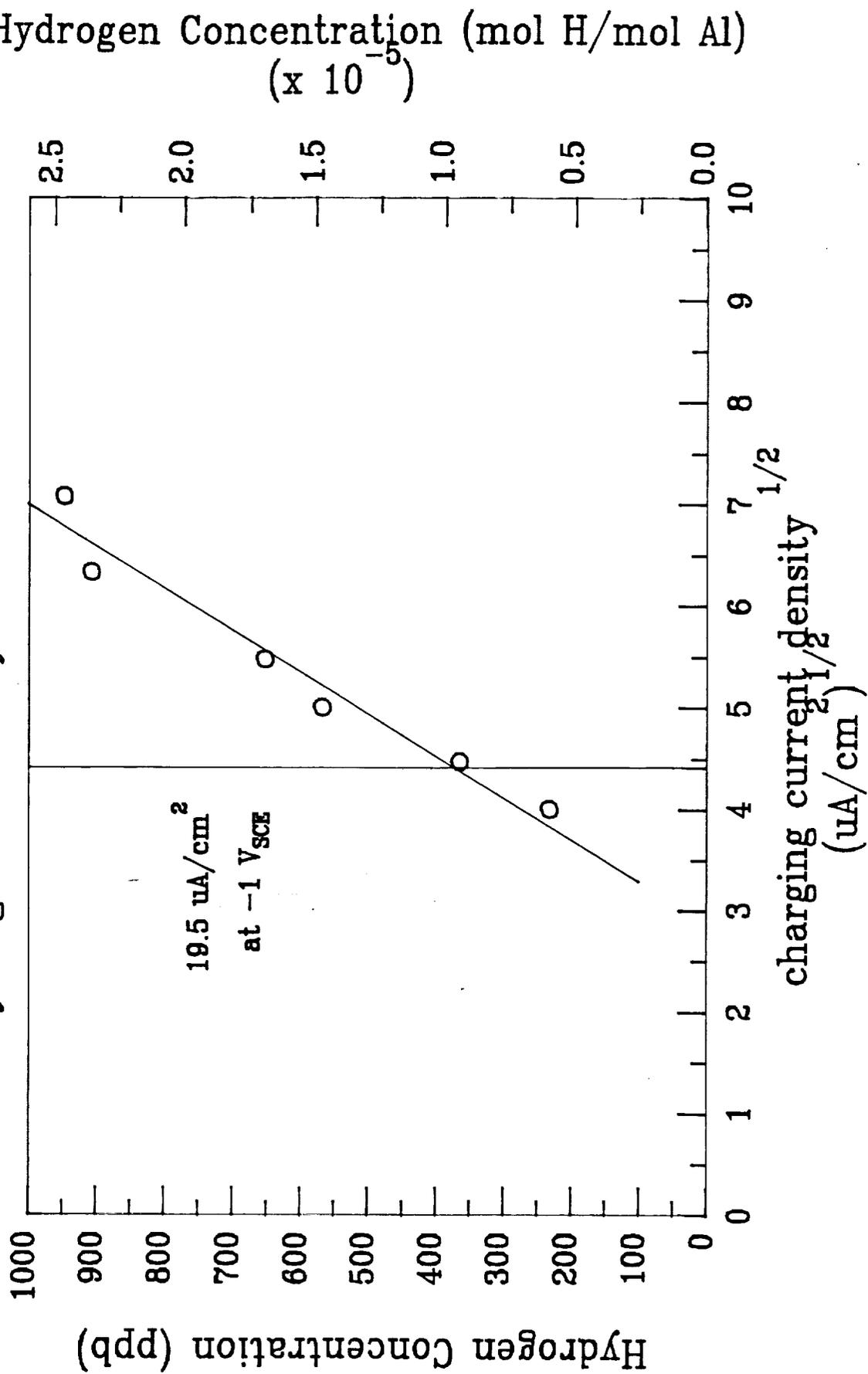
Figure 10. Tensile data for 7075-T6-LT tested in dry Ar

Pd coating used for charging
Charged in 0.1N NaOH for 24 hrs.
and stored for various times
strain rate 3×10^{-3} sec^{-1}

———— no H charging
·············· stored for 3 days
– – – – stored for 15 days

Strain (%)

Stress (ksi)
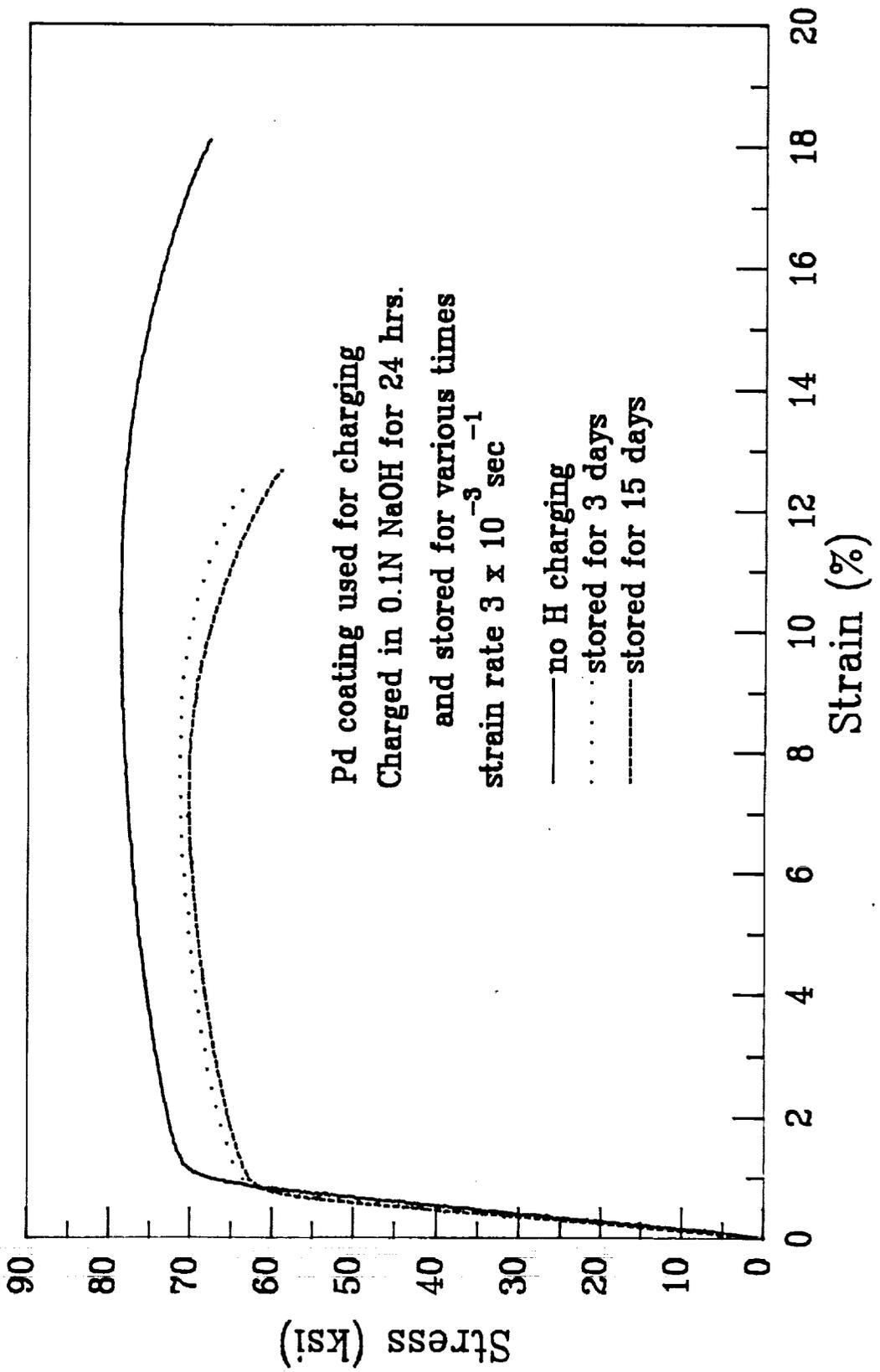
Figure 11. Tensile data for 2090-T3-LT tested in dry Ar

Ni coating used for charging
specimens charged at $-1\ V_{SCE}$

in pH 7 solution

strain rate $2.5 \times 10^{-6}\ sec^{-1}$

——— no H charging

·········· charged for 14.1 days

——— charged for 28.56 days
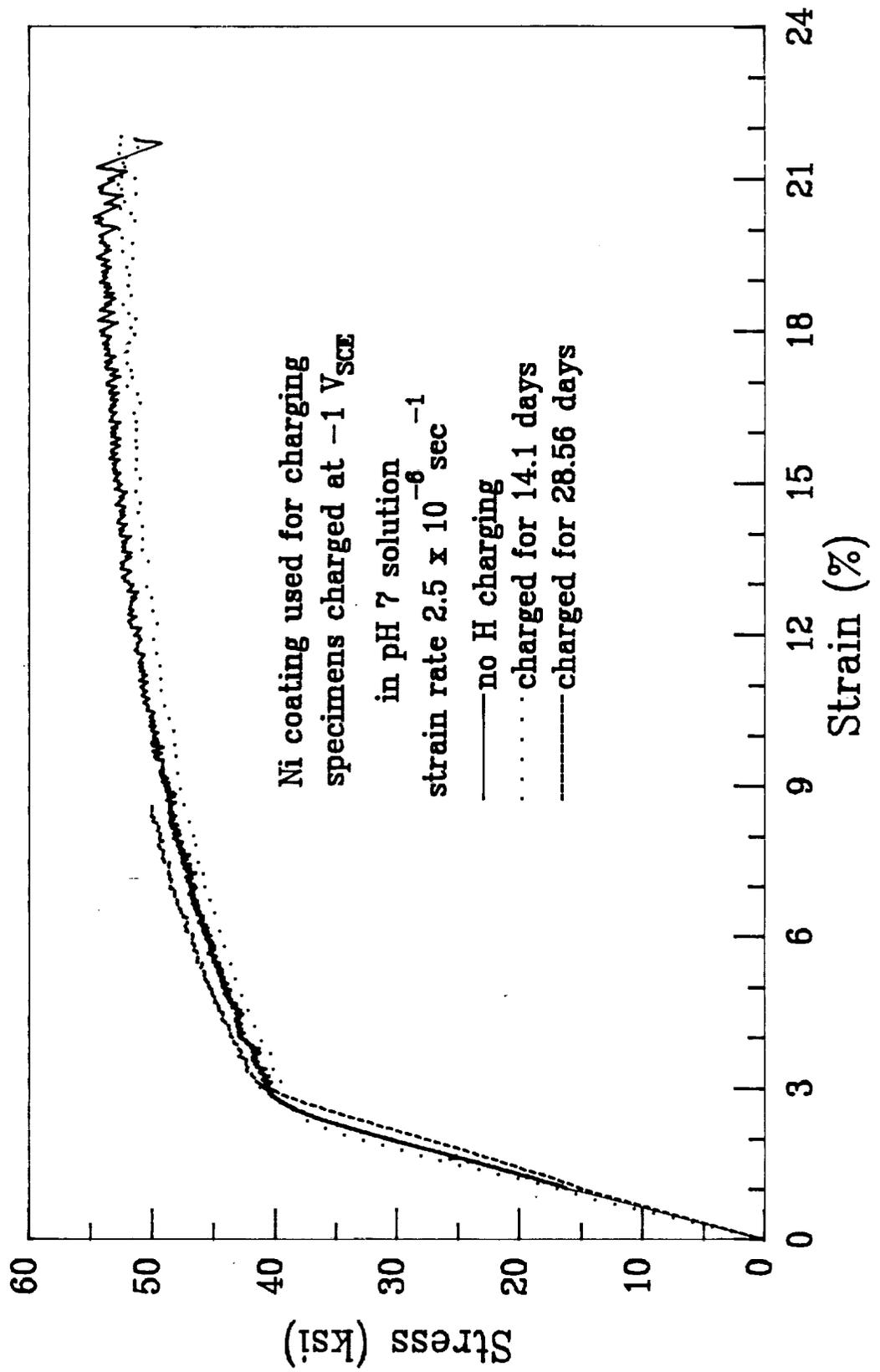
Figure 12. 2090-T3-LT hydrogen charged and tested in dry Ar
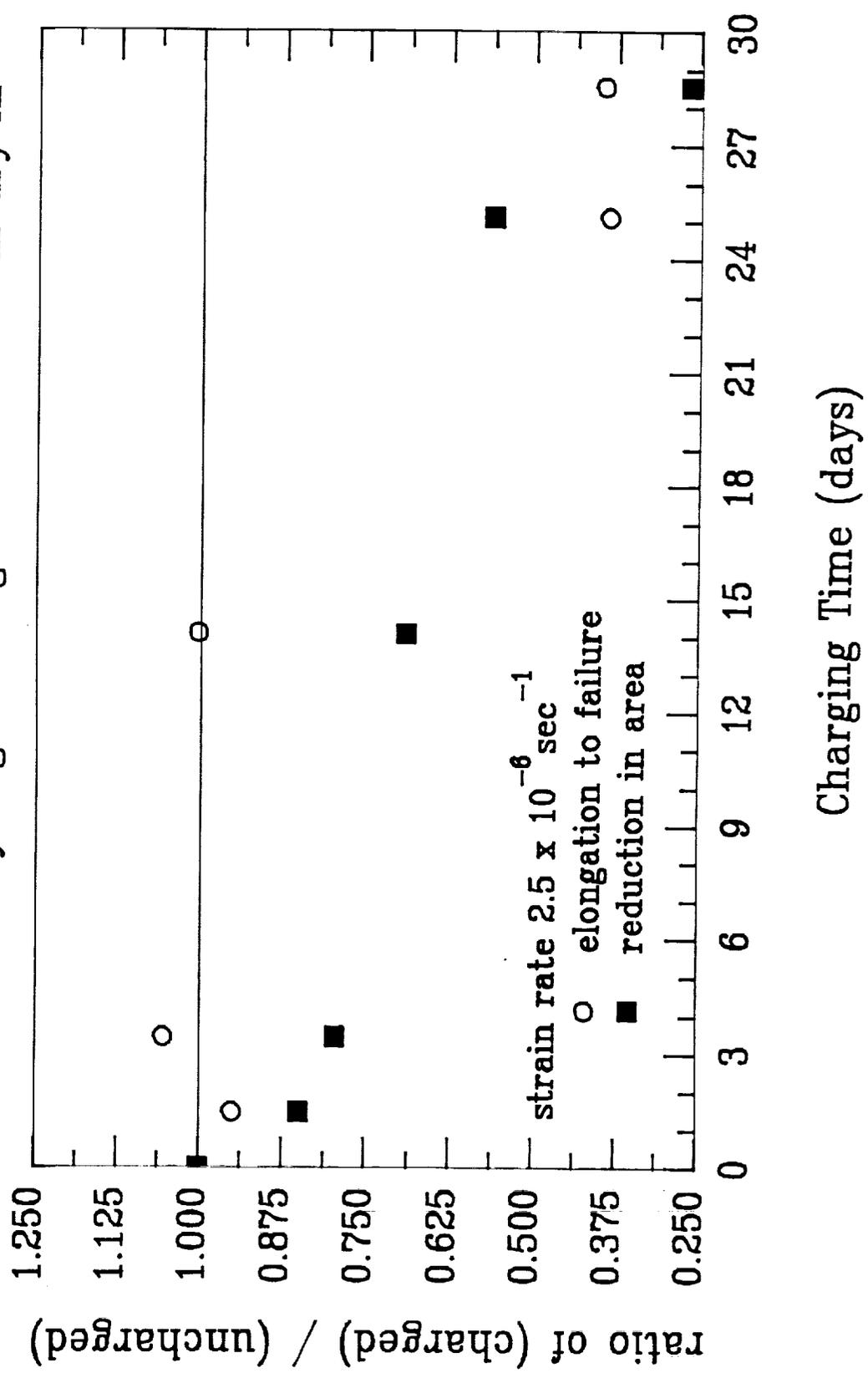
Figure 13.

Hydrogen Concentration Profile
for Charged Specimen

—————— charged for 24 hrs.,
------------ charged for 24 hrs., strored for 24 hrs.
·············· charged for 24 hrs., stored for 2 weeks
— — — charged for 2 weeks

$\dfrac{C_t}{C_o}$

1

0
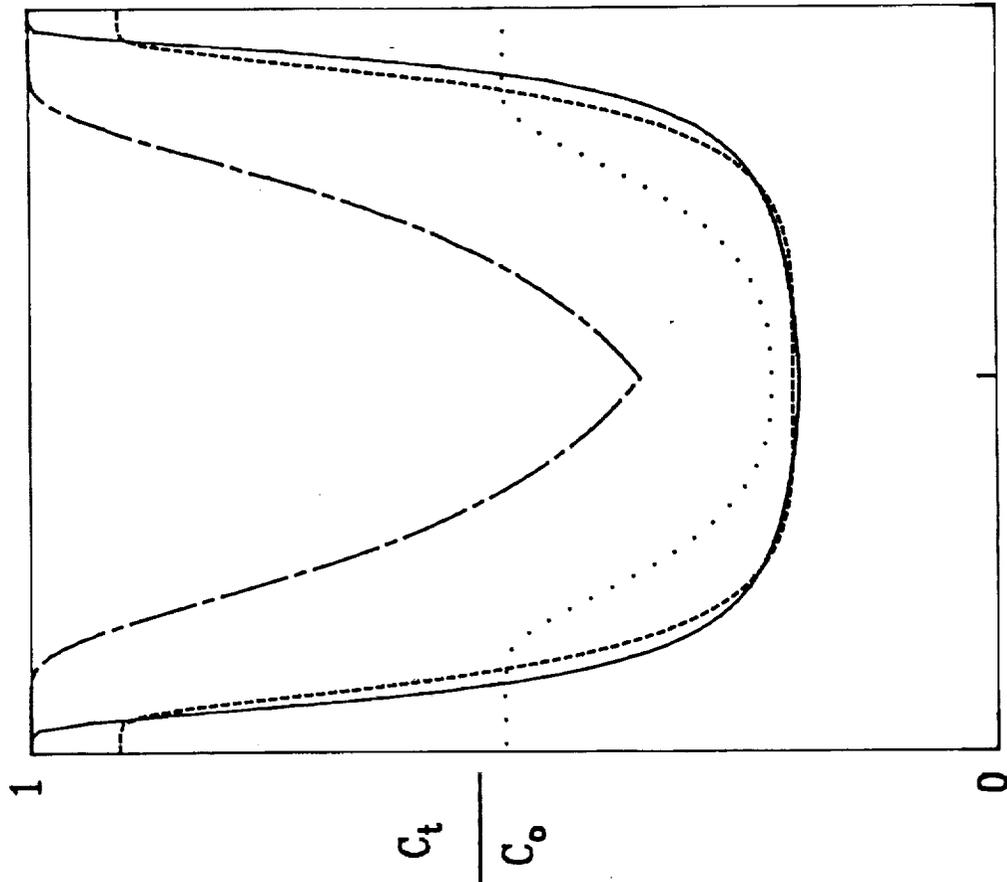
x = 0   x = 1/2 L   x = L

Specimen thickness

Figure 14. 2090-T3-LT hydrogen charged and tested in dry Ar
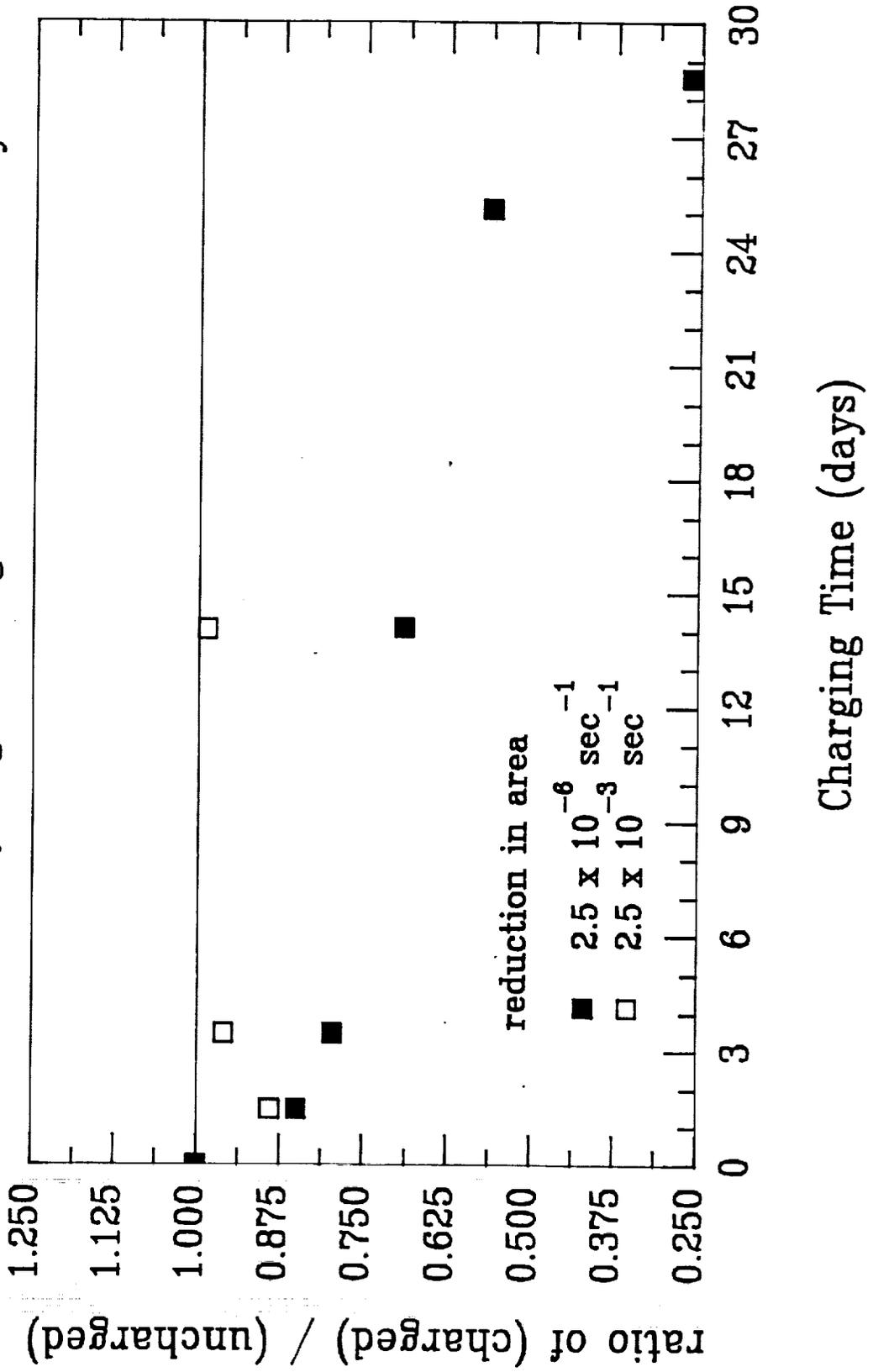
Figure 15. 2090-T3-TL hydrogen charged and tested in dry Ar
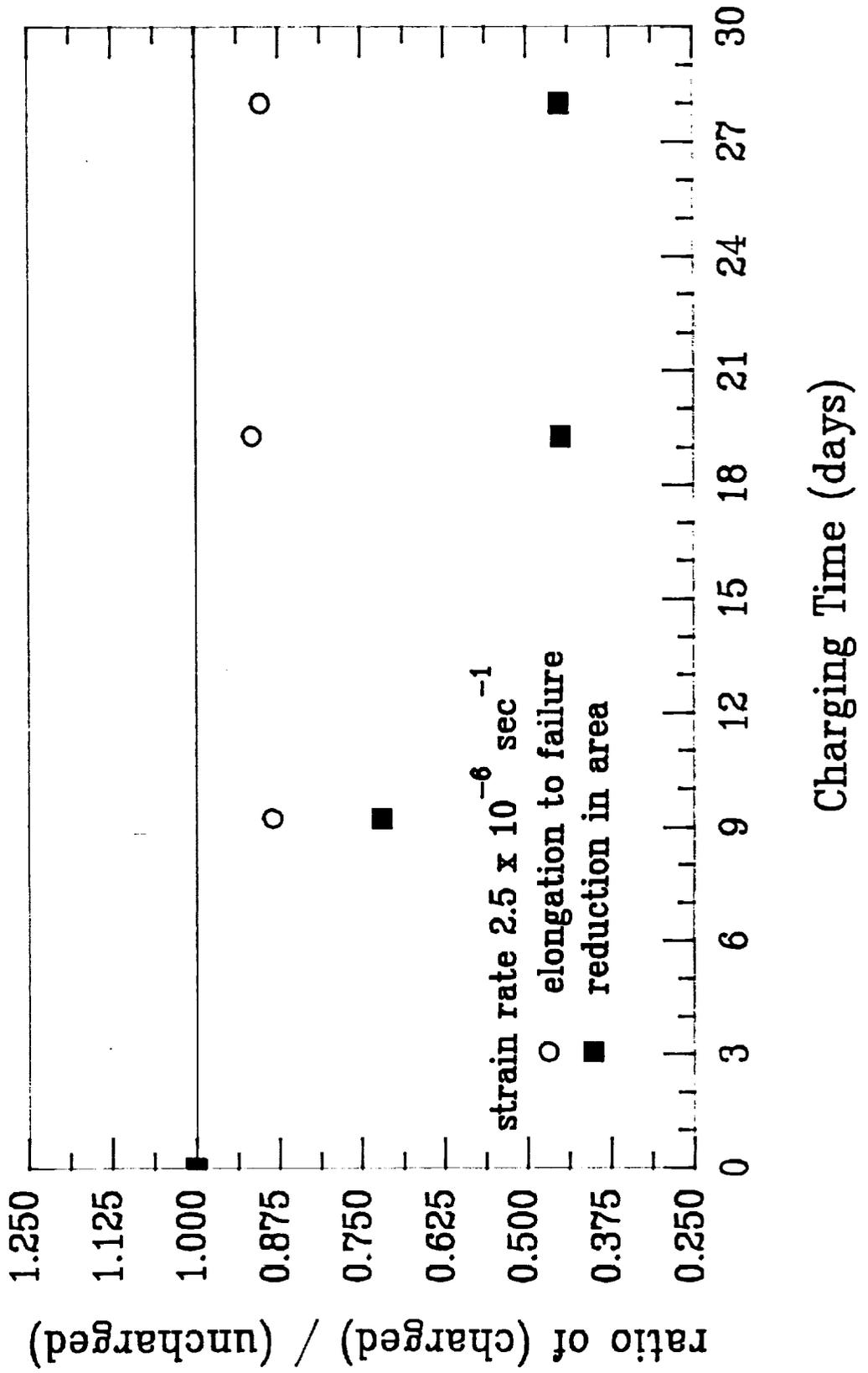
Figure 16. Tensile data for 2090-T3-TL tested in dry Ar

Notched specimens
Ni coating used for charging
specimens charged at -1 V_{SCE}
in pH 7 solution
strain rate 2.5 x 10^{-6} sec^{-1}

—— no H charging
· · · · charged for 8.444 days
— — charged for 26.62 days
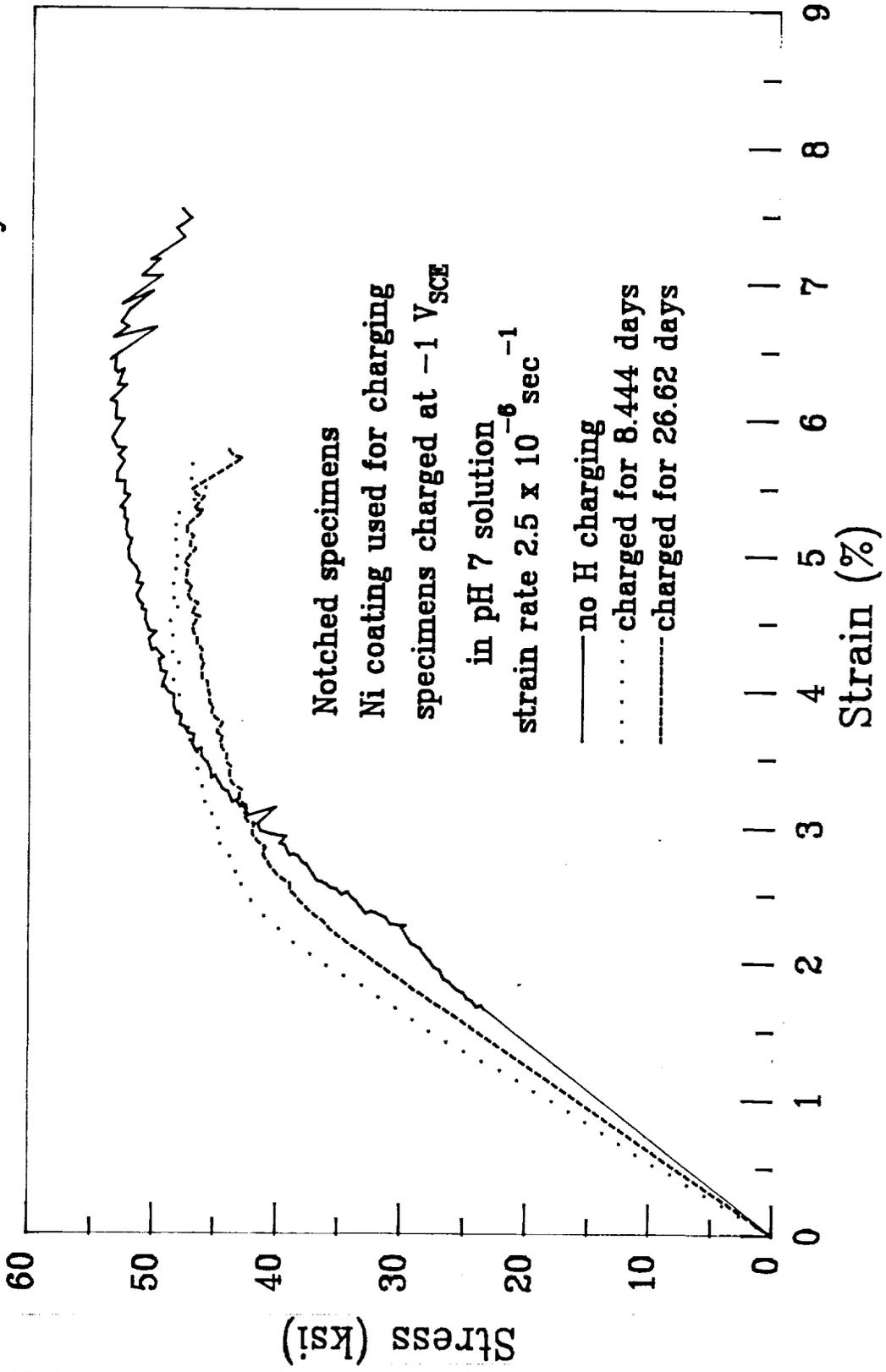
Figure 17. 2090–T3–LT hydrogen charged and tested in dry Ar
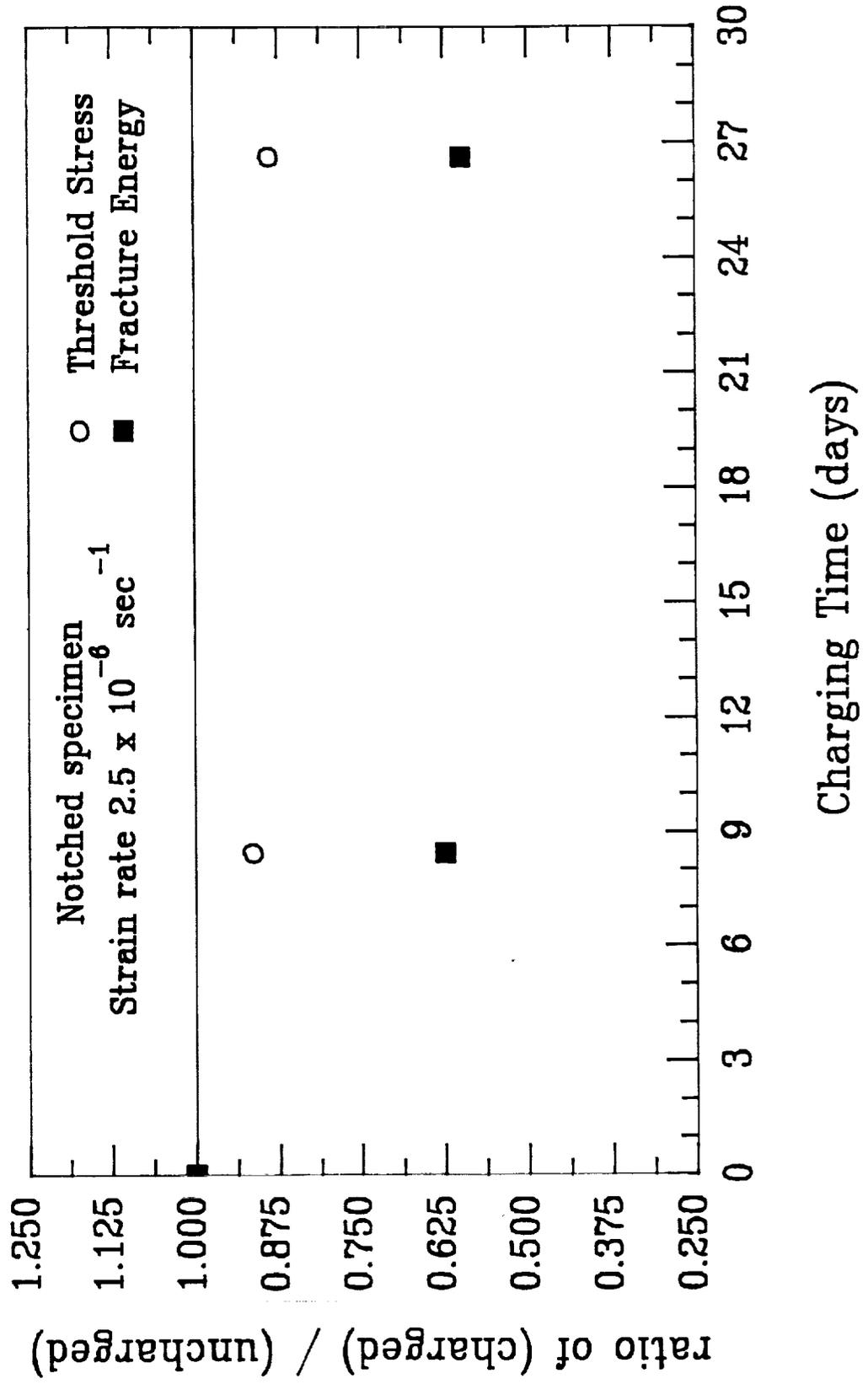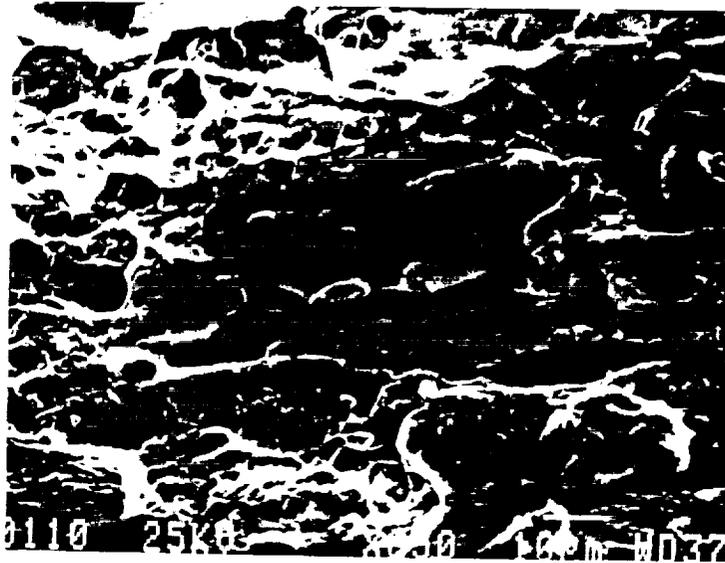
Figure 18.   SEM micrograph for 2090-T3-LT, no hydrogen charging, tested in dry argon.
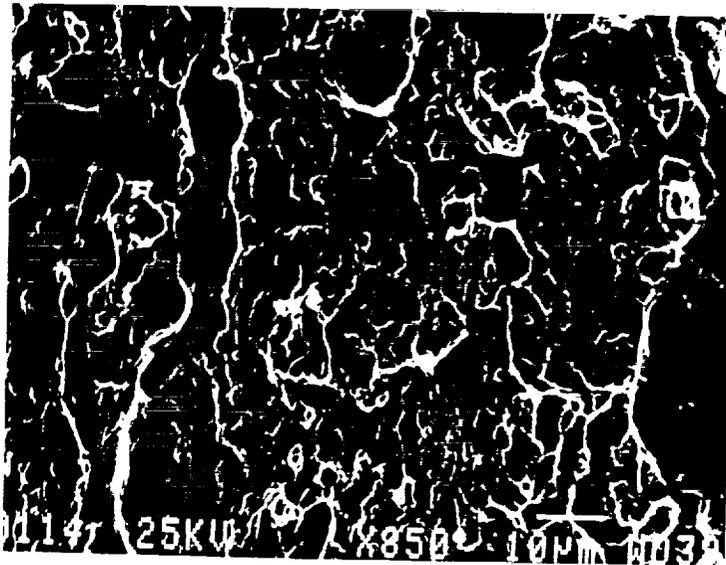
Figure 19.   SEM micrograph for 2090-T3-LT, charged for 25 days at -1V$_{SCE}$, tested in dry argon.

Figure 20.   SEM micrograph for 2090-T3-TL, no hydrogen charging, tested in dry argon.
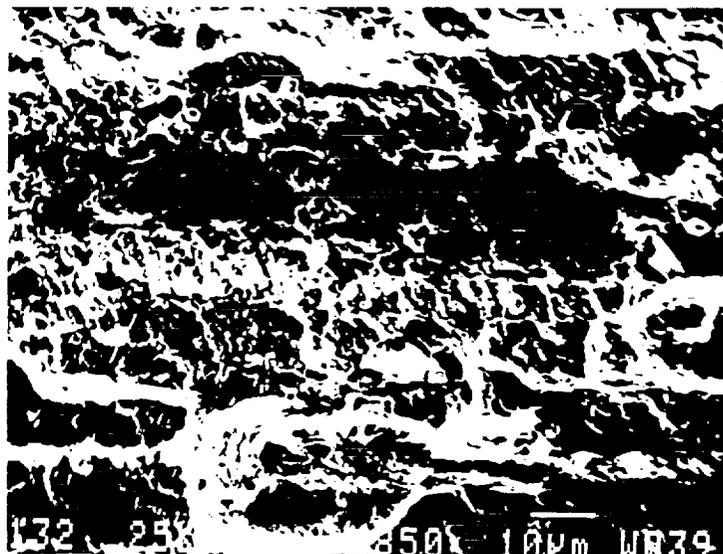
Figure 21.   SEM micrograph for 2090-T3-TL, charged for 19 days at $-1V_{SCE}$, tested in dry argon.
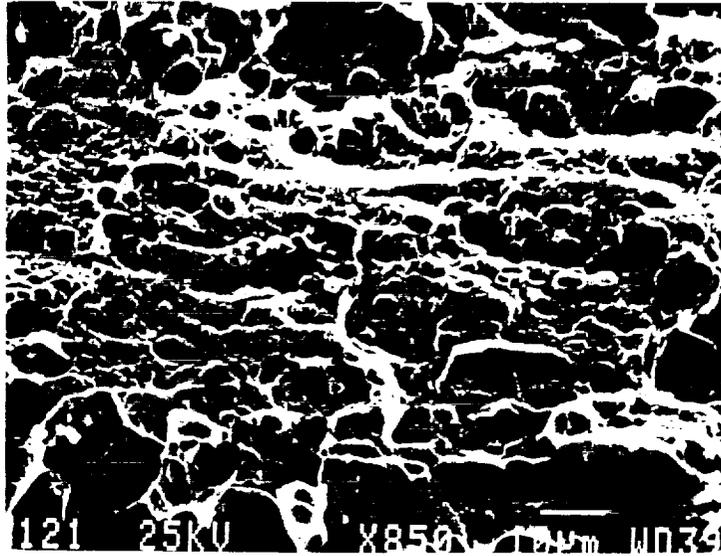
Figure 22.   SEM micrograph for 2090-T3-LT, charged for 26 days at -1V$_{SCE}$, notched with a wafering blade, and tested in dry argon.

Summary of Fractographic Information for 2090-T3

orientation	charging condition	specimen design	macroscopic observation	microscopic observation
LT	None	smooth flat tensile	fracture 45° to tensile axis	transgranular shear
LT	-1V$_{SCE}$ for 25 days	smooth flat tensile	fracture 45° to tensile axis	hydrogen effected transgranular shear
TL	None.	smooth flat tensile	fracture 45° to tensile axis	transgranular shear
TL	-1V$_{SCE}$ for 19 days	smooth flat tensile	fracture 45° to tensile axis	intersubgranular
LT	None	notched flat tensile	fracture 45° to tensile axis	transgranular shear
LT	-1V$_{SCE}$ for 26 days	notched flat tensile	fracture normal to tensile axis	mixed: intersubgranular transgranular shear

Summary: Influence of Internal Hydrogen on Mechanical Properties

- Sputter deposited Ni coatings provide an effective means for facilitating hydrogen entry into Al alloys.

- Hydrogen EAC (HEAC) can be unambiguously separated from dissolution assisted EAC, using these methods.

- Hydrogen charging periods of > 14 days are required to produce hydrogen EAC, consistent with diffusion controlled hydrogen ingress.

- Hydrogen charging produces a change in fracture path for both TL and LT oriented 2090-T3 alloys relative to tests in dry air.

- A mechanical strain rate effect is observed for pre-charged 2090-T3 in the LT orientation. This suggests dynamic hydrogen redistribution to fracture process zones, or in the case of macroscopically shear fracture, dynamic hydrogen interaction with dislocations.

Hydrogen Analysis

Fracture Stress lowered due to intrinsic hydrogen effects:

$$\sigma_f^* - \sigma_{fo}^* - \alpha_i X_i^{\frac{1}{2}} - \alpha_H C_o e^{(\frac{\sigma_H \overline{V_H}}{RT})} - \alpha_H^* C_{TRAP}$$

or:

$$\sigma_f^* - \sigma_{f_o}^* - \{g.b.impurity\,effect\} - \{Hconc.effect\} - \{Htrap\}$$

Trapping:

$$C_{TRAP} - C_o \exp(-\frac{E_B}{RT})$$

$E_B \Rightarrow$ trap binding energy

$E_B < 0$

$$C_{TRAP} - kp^{\overline{2}}(-\frac{\Delta H_s + E_B}{RT})$$

Diffusion in a lattice containing traps:

$$D_{APP} - \frac{D_L}{(1 + \frac{N_{TRAP}}{N_L}k)}$$

$$where: k - \exp(-\frac{E_B}{RT})$$

Figure 23. Design of Thermal Desorption Spectroscopy System
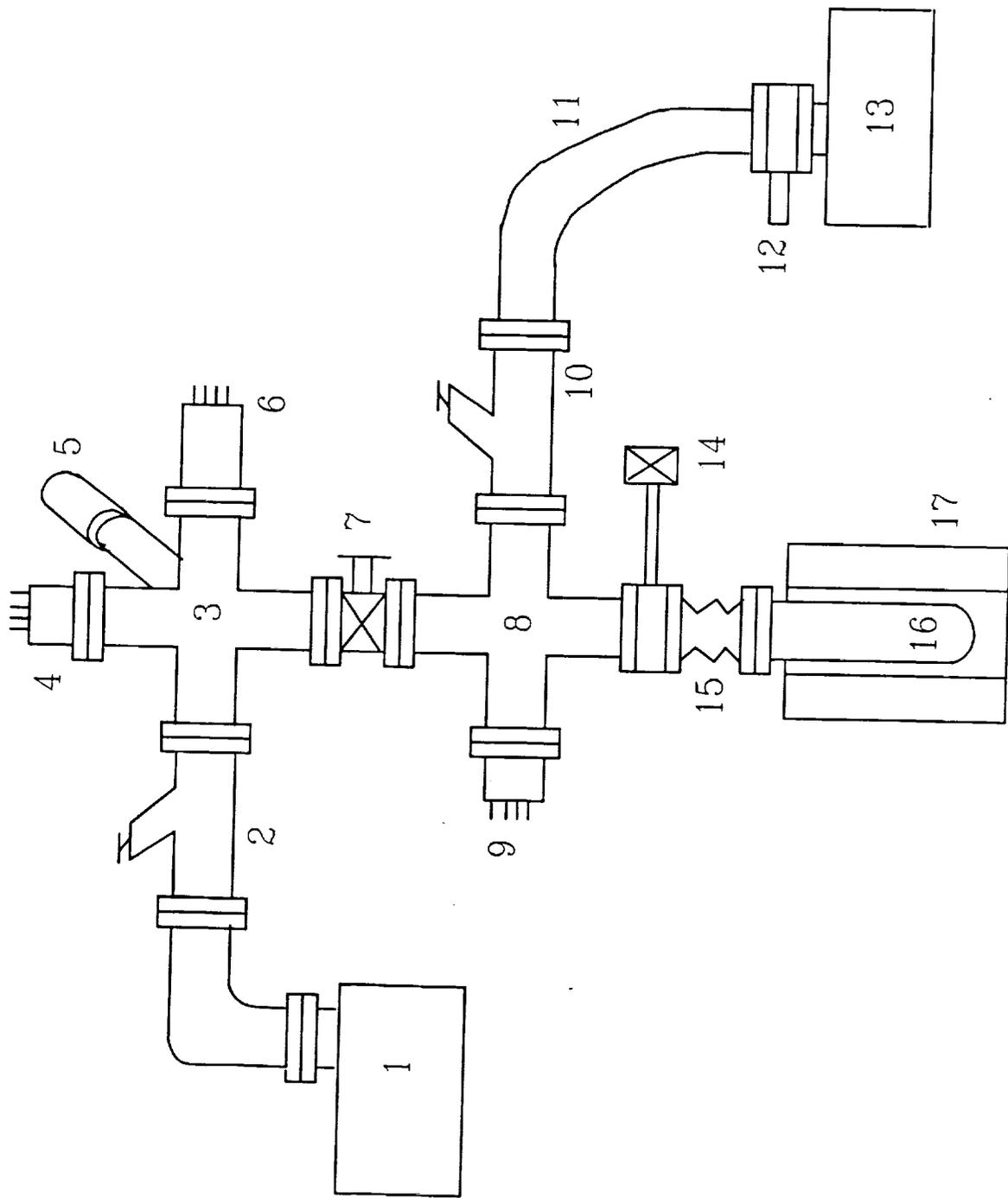
Future Work

- Additional mechanical testing of 2090-T3 and 2090-T8 conditions using a palladium and or nickel coating to aid in cathodic charging.

  Vary potential to obtain higher hydrogen concentrations
  Use hydrogen recombination poisons (sodium arsenite).

- Fractographic analysis to aid in the determination of fracture path present in charged specimens.

- Use TDS to determine how hydrogen is incorporated in Al-Li-Cu-X alloys and significant constituent phases.
  - 1,2,3 dimensional trap sites
  - formation of hydride phases

- Perform permeation measurements to determine hydrogen diffusion rates in aluminum and selected alloys.

- Determine fracture threshold stress intensities as a function of hydrogen charging level and strain rate (J-Integral R curve testing).

- Develop deterministic models which define effect of internal hydrogen on mechanical properties.

Project 9a   Metastable Pitting of Al Alloys

S.T. Pride[1], J.R. Scully and J.L. Hudson[1]

Objective

The goal of this PhD research is to improve the fundamental understanding of pitting nucleation and growth phenomena in Al alloy systems. Emphasis is placed on understanding the electrochemical factors controlling the nucleation, propagation, and repassivation of pit sites in model Al alloys. To accomplish these goals conventional electrochemical methods have been augmented with non-linear signal analysis methods suitable for characterizing electrochemical transients associated with metastable pitting. To date pitting has been investigated on artificially aged Al-Cu alloys.

Introduction

Pitting corrosion of aluminum alloys has a number of detrimental effects on structural materials. These include creation of sites of stress concentration and localized occluded cell chemistry which, in turn, can lead to conditions favorable towards environmentally assisted cracking or fatigue. In the case of aged Al-Cu binary alloys, pitting is induced by galvanic coupling between the θ-Al$_2$Cu phase and the aluminum rich (copper depleted) matrix or grain boundary zone. Most laboratory studies cited in the literature focus on stable pit propagation at high positive potentials. Consequently, little is understood about pit nucleation and the factors responsible for stabilizing pit growth as a result of the galvanic cell formed by microstructural heterogeneities. For instance, factors that control the pit growth process and pit depth as well as govern the transition from metastable to stable pit growth remain unclear. Additionally, little is known about the dynamics of the pit initiation and growth process. Is pit initiation stochastic in nature, or is initiation of metastable pits spatially or temporally dependent on the "progress" of other pit sites? Is the dissolution rate observed in metastable pits fundamentally different than that associated with stable pits, does salt film precipitation stabilize pit growth, or do the differences lie elsewhere? To obtain possible answers to these

---

[1]   Department of Chemical Engineering, University of Virginia, Charlottesville, VA.

PRECEDING PAGE BLANK NOT FILMED

questions various electrochemical techniques will be used to at first examine pure Al, model bulk Al-Cu alloys, and Al-Cu alloy thin films. The dynamic behavior will be studied through analysis of the oscillations in the applied current at constant potential, or alternatively, the open circuit potential. More recently developed electrochemical methods based on the techniques of non-linear dynamics will be employed.

Results

Anodic polarization experiments yielded pitting potentials for pure aluminum (0.25 mm dia., 99.999%) in various halide solutions (Cl⁻, I⁻, and Br⁻) over a range of halide concentrations. Pure Al was used to simulate the Cu depleted grain boundary zone. The aluminum specimen configuration consisted of looped wires to prevent crevice corrosion and associated experimental error. The pitting potentials were found to fit logarithmic functions of concentration for Cl⁻, I⁻, and Br⁻. A "real" distribution of pitting potentials existed at a single halide concentration due to a distribution in the geometric characteristics of pit nucleation sites. In addition, the pitting potentials are used as reference states for characterization of metastable versus stable pitting. It is well known that micro-pits may form at potentials considerably below the pitting potential. Many of these pits readily repassivate. Thus, such metastable pits have a low probability of surviving for long time periods even if their nucleation rate is high. Pits which initiate above the pitting potential have a higher probability of growing for extended periods of time. Two methods are used to investigate this metastable/stable criteria. First, by varying the halide concentration, it is possible to shift the pitting potentials for pure Al relative to the open circuit potential (OCP) of Al-Cu alloys. This shifting of the pitting potentials can be exploited so that the OCP of Al-2%Cu will reside either at or below the pitting potentials of pure Al. Using methods of analysis from nonlinear dynamics on the OCP oscillations, the characteristic voltage responses associated with the formation and repassivation of metastable pits may be obtained. The potential fluctuations recorded reflect the spatial as well as temporal nature of the pitting phenomenon. Preliminary results show that metastable pits form at OCP's that are well below the breakdown potential of pure aluminum in Cl⁻ solutions. Metastable pits life-times vary from approximately 5 to 160 seconds at these potentials. The cumulative number of metastable pits were significantly lower in dilute halide compared to more concentrated solutions. It is unclear whether this is due to the lower halide concentration or due to the

location of OCP of the alloy with respect to the breakdown potential of high purity Al. The rate of metastable pitting events decreases with increasing exposure time for all halide concentrations. These concentration/location effects may be addressed by testing at constant potentials. Such experiments are being conducted now.

Future Work

Future work also includes utilization of the methods of analysis from nonlinear dynamics. In this case, two experimental configurations may be explored. These include current oscillations at constant potential and the galvanic coupling of high purity Al to an θ-Al_2Cu sample through a zero resistance ammeter. This arrangement will allow for both the current and potential fluctuations to be recorded and analyzed. Since the currents associated with the metastable pits are in the 0.01-0.1 μA range, small surface areas (approximately 0.01 cm^2) are used in order to minimize the background current associated with the passive response of the material.

Acknowledgements

METASTABLE PITTING OF Al ALLOYS
IN HALIDE SOLUTIONS

SHELDON PRIDE

ADVISORS:
J.R. SCULLY
J.L. HUDSON

SPONSORS:
DARPA/ONR
NASA-LANGLEY

GOALS

- The objectives of this project is to provide possible answers to the following questions:

  - Is pit initiation stochastic in nature?

  - Or, is initiation of metastable pits spatially or temporally dependent on the "progress" of other pit sites?

  - What governs the transition from metastable to stable pit growth? Do salt films play a role?

  - Is the high dissolution rate observed in metastable pits fundamentally different than that associated with stable pits?

INTRODUCTION

PITTING CRITERIA

- Metastable pitting occurs when pits initiate below the pitting potential. These pits have high probabilities of repassivating.

- Since pits that form at low potentials tend to repassivate, they have a low probability of surviving long enough to become stable pits.

- Pits that initiate above the pitting potential have a high probability of growing.

RELATIONSHIP TO PURE ALUMINUM AND ITS ALLOYS

- Metastable pitting of pure aluminum can be observed by current oscillations when held at potentials below the pitting potential in halide solutions.

- For aluminum alloys pitting is induced by galvanic coupling between precipitates such as $\theta-Al_2Cu$ and the aluminum rich (copper depleted) matrix.

- E_{oc} vs time results will be presented with a bulk Al-2%Cu alloy.

EXPERIMENT METHODS

- The polarization data is needed for the Al rich (Cu depleted) zone at the grain boundaries of Al-2%Cu alloy. Pure Al simulates the Cu depleted zone at the grain boundary.

- Anodic polarizations of 99.999%, 0.25mm dia. aluminum wire loops to determine breakdown potentials of aluminum in various molar Cl⁻, Br⁻, and I⁻.

- Eoc vs time experiments of Al-2%Cu in various molar Cl⁻ to determine the relationship between metastable pitting events and the breakdown potential of pure aluminum.

Reference Electrode Housing

Bubbler

Vent

Vycor tip

Baffle

Pt Counter Electrode

Aluminum Wire Loop
99.999%, 0.25mm dia.
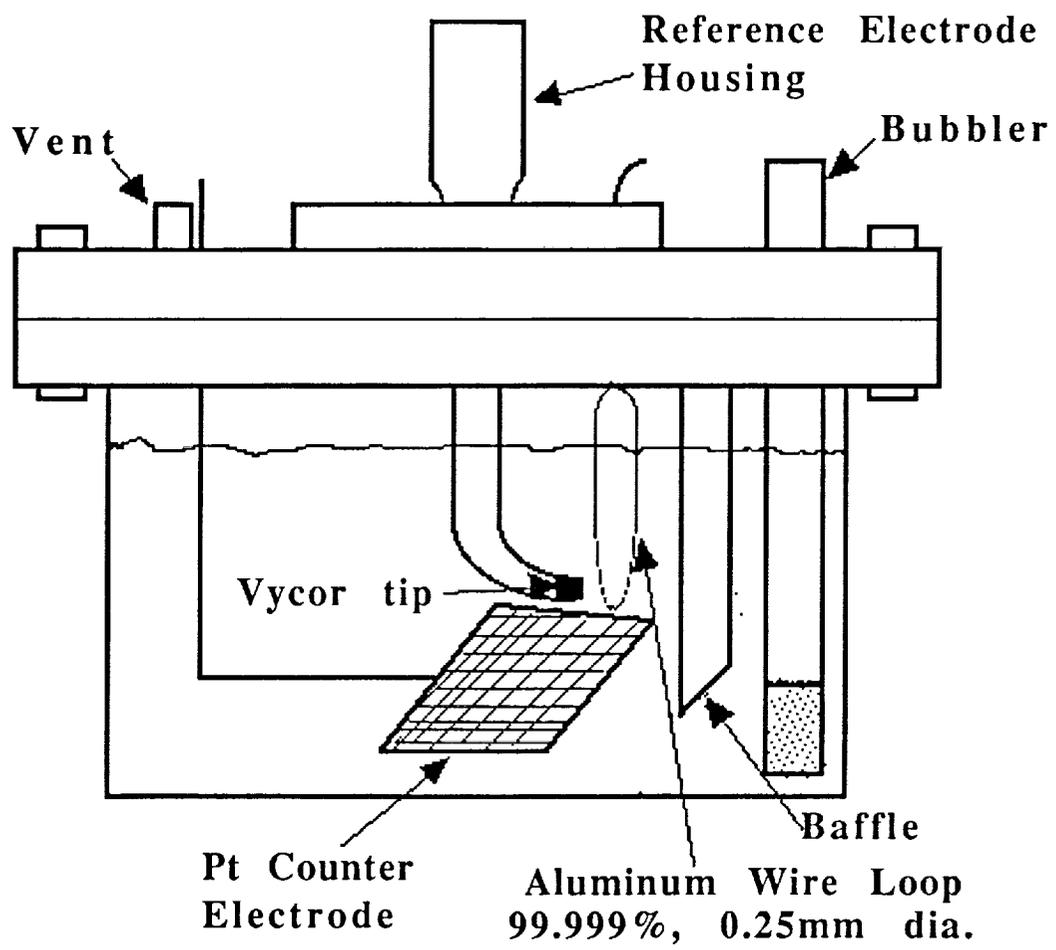
ANODIC POLARIZATIONS OF 99.999% ALUMINUM
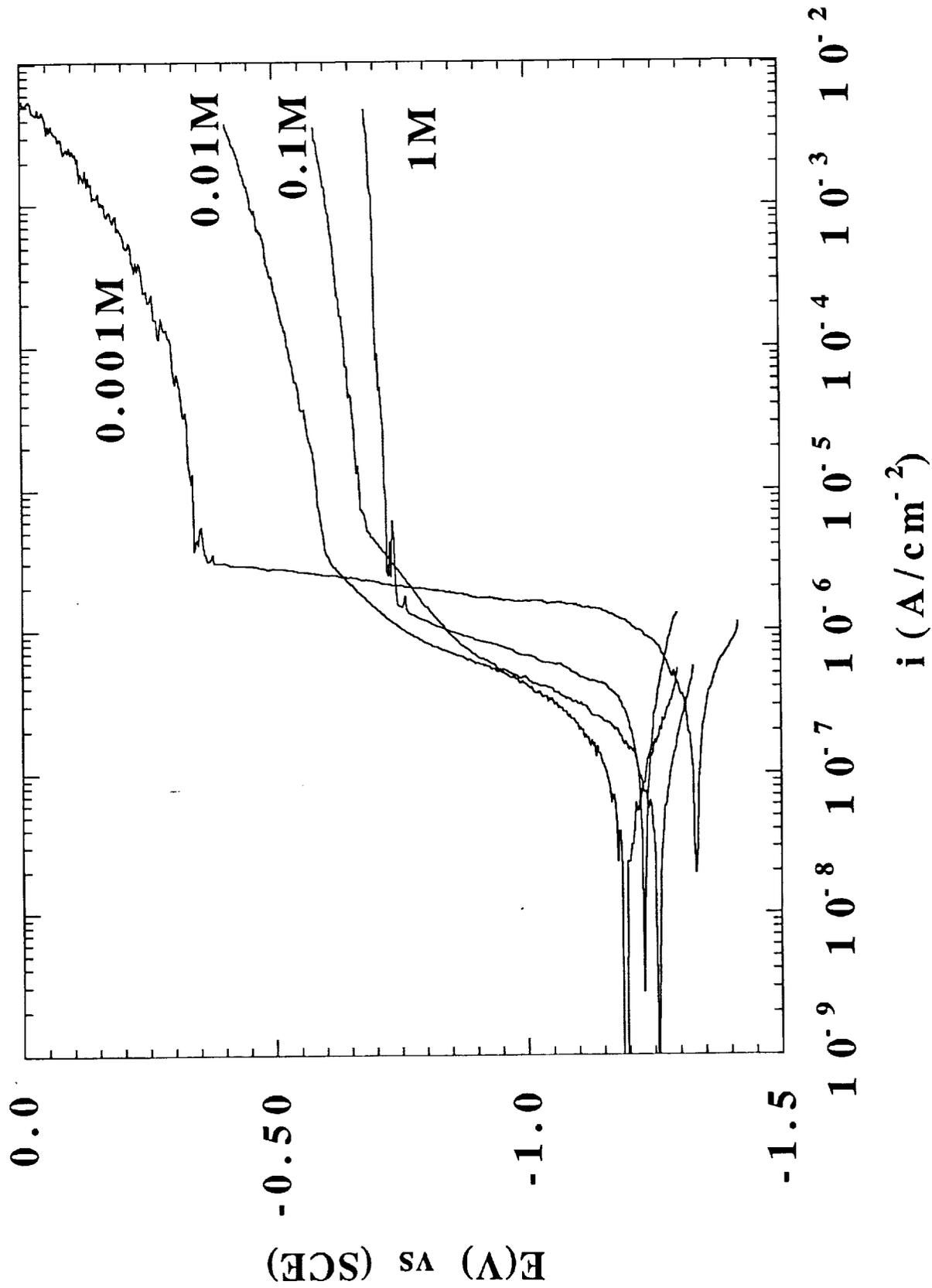
IN Cl⁻ ELECTROLYTES

PITTING POTENTIAL OF 99.999% ALUMINUM AS FUNCTIONS OF MOLAR Cl⁻, Br⁻, AND I⁻
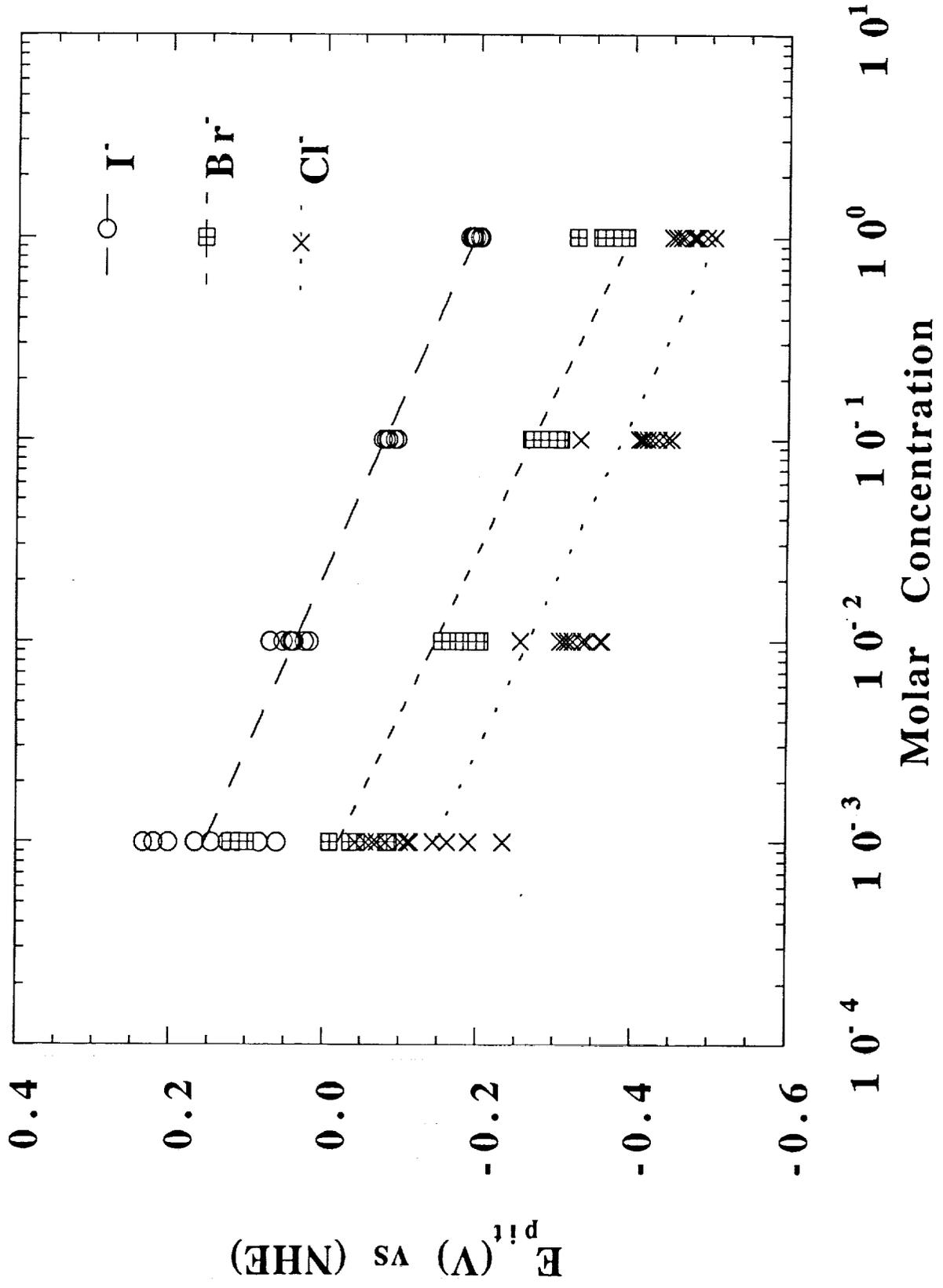
PITTING PROBABILITIES OF 99.999% ALUMINUM
IN Cl⁻ ELECTROLYTES
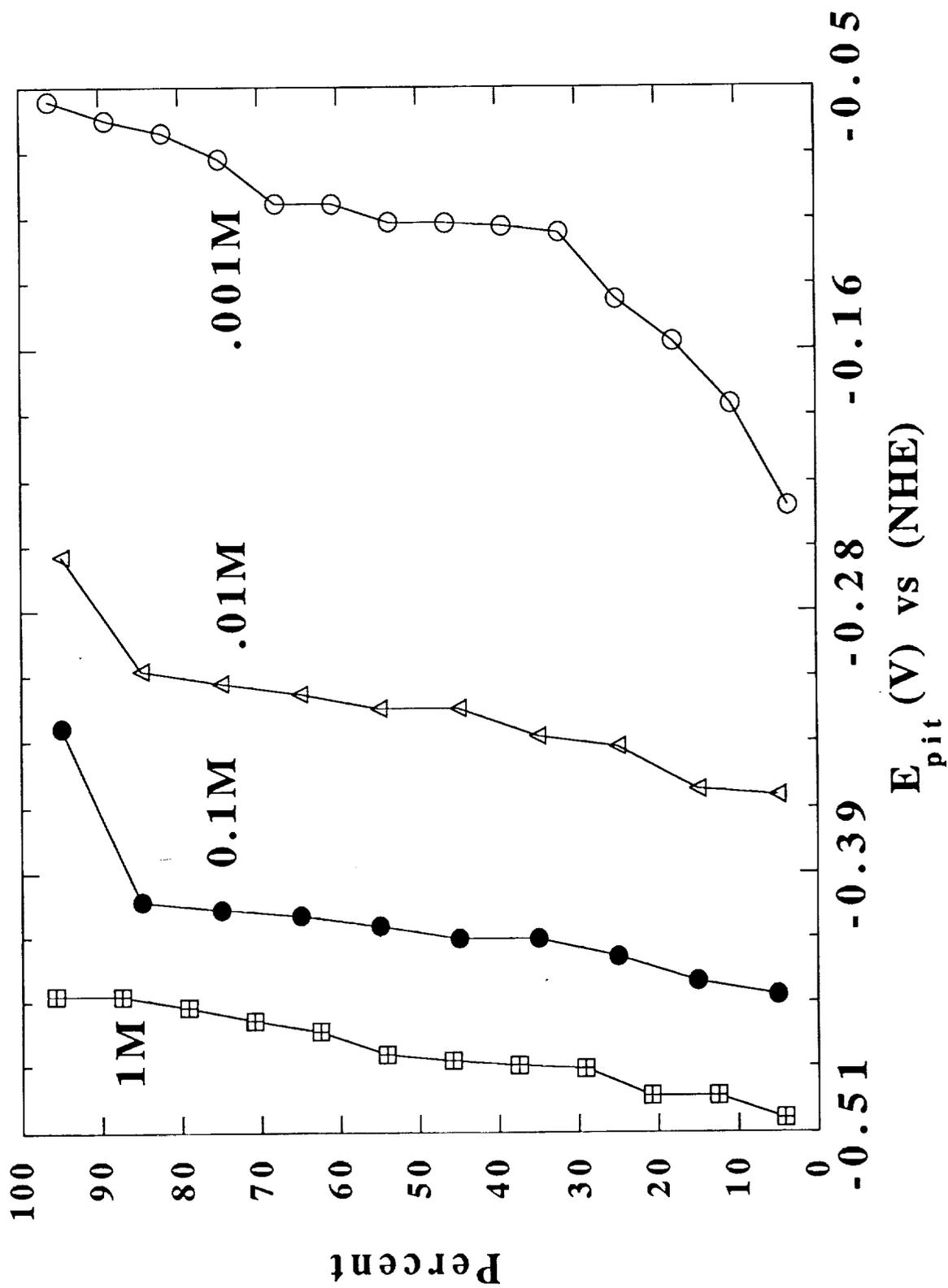
PITTING PROBABILITIES OF 99.999% ALUMINUM

IN 0.001M Cl⁻, Br⁻, AND I⁻ ELECTROLYTES
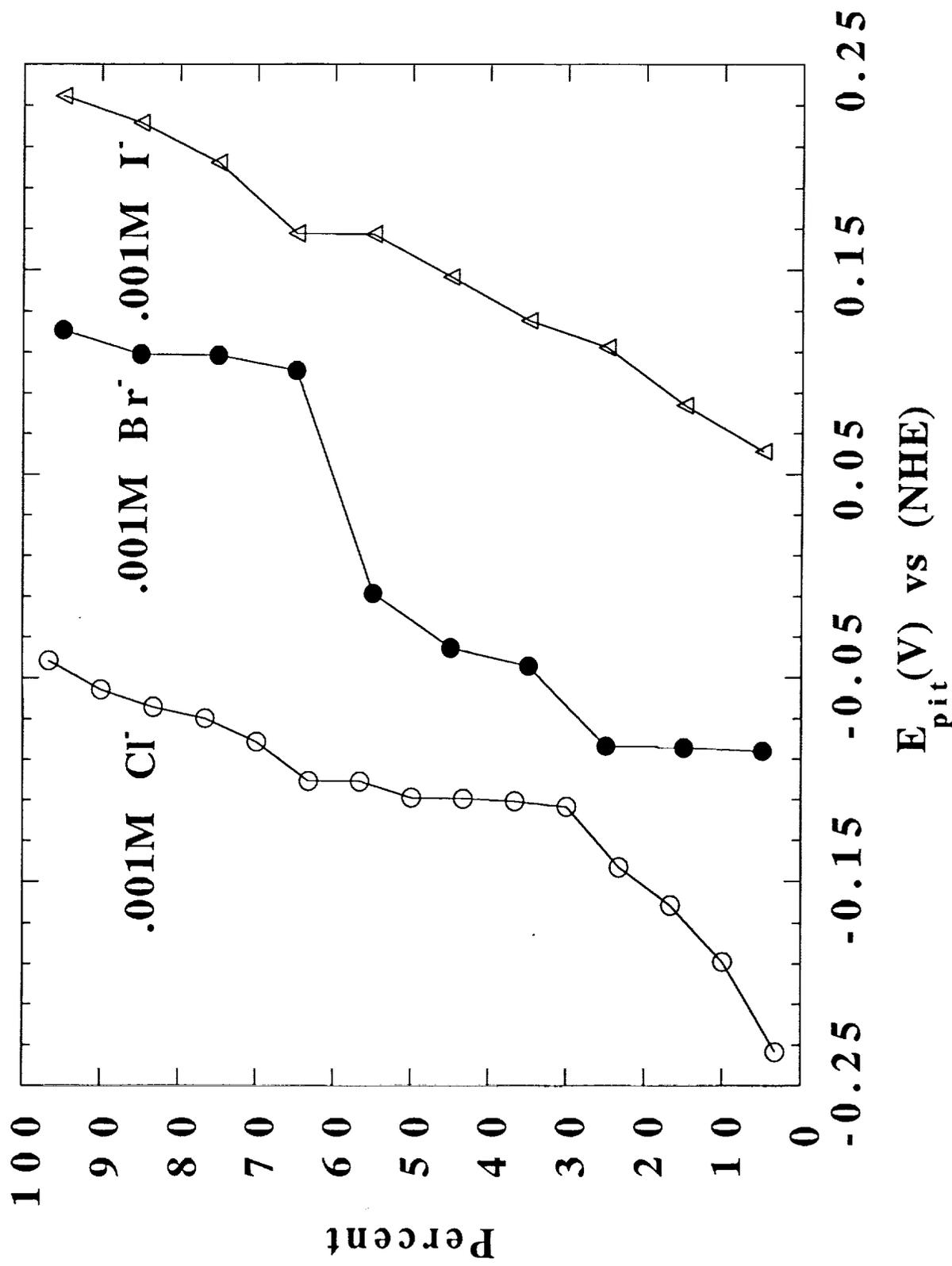
- D. Williams, J. Stewart, and P. Balkwill defined the probability of pitting as:

$$dP_E = \left\{ \exp\left[-(1/v)\int_{E_s}^{E} \Lambda(E)dE \right] \right\} [\Lambda(E)/v]dE$$

v = sweep rate

E_s = start potential for the scan

$\Lambda(E)$ = nucleation frequency for progagating pits

$$\Lambda = \lambda \exp(-\mu\tau_c)$$

λ = nucleation frequency for micropits

μ = probability of repassivation

τ_c = a micropit's critical age for survive

- At low potential only highly occluded sites can nucleate micropits: the current density to sustain the internal pit solution is determined by the size of the opening in pit cover, and is invariably too low to sustain pit growth when the cover collapses.

- At higher potential, micropits nucleate on less occluded sites, with current density high enough render such pits stable against the collapse of any cover.

- D. Williams, J. Stewart, and P. Balkwill derived from the probability equation that · the most probable breakdown potential is:

$$\langle E_b \rangle = E_o + (1/\alpha)\ln(\alpha v / \Lambda_o)$$

$$\alpha \approx 50\,\text{mV}$$

$$\Lambda = \Lambda_o \exp[\alpha(E - E_o)]$$

$$\langle E_b \rangle \propto -\log[Cl^-]$$

$$\Lambda_o \propto [Cl^-]$$

$$\lambda \propto [Cl^-]$$

Al-Cu PHASE DIAGRAM

Weight percent Cu
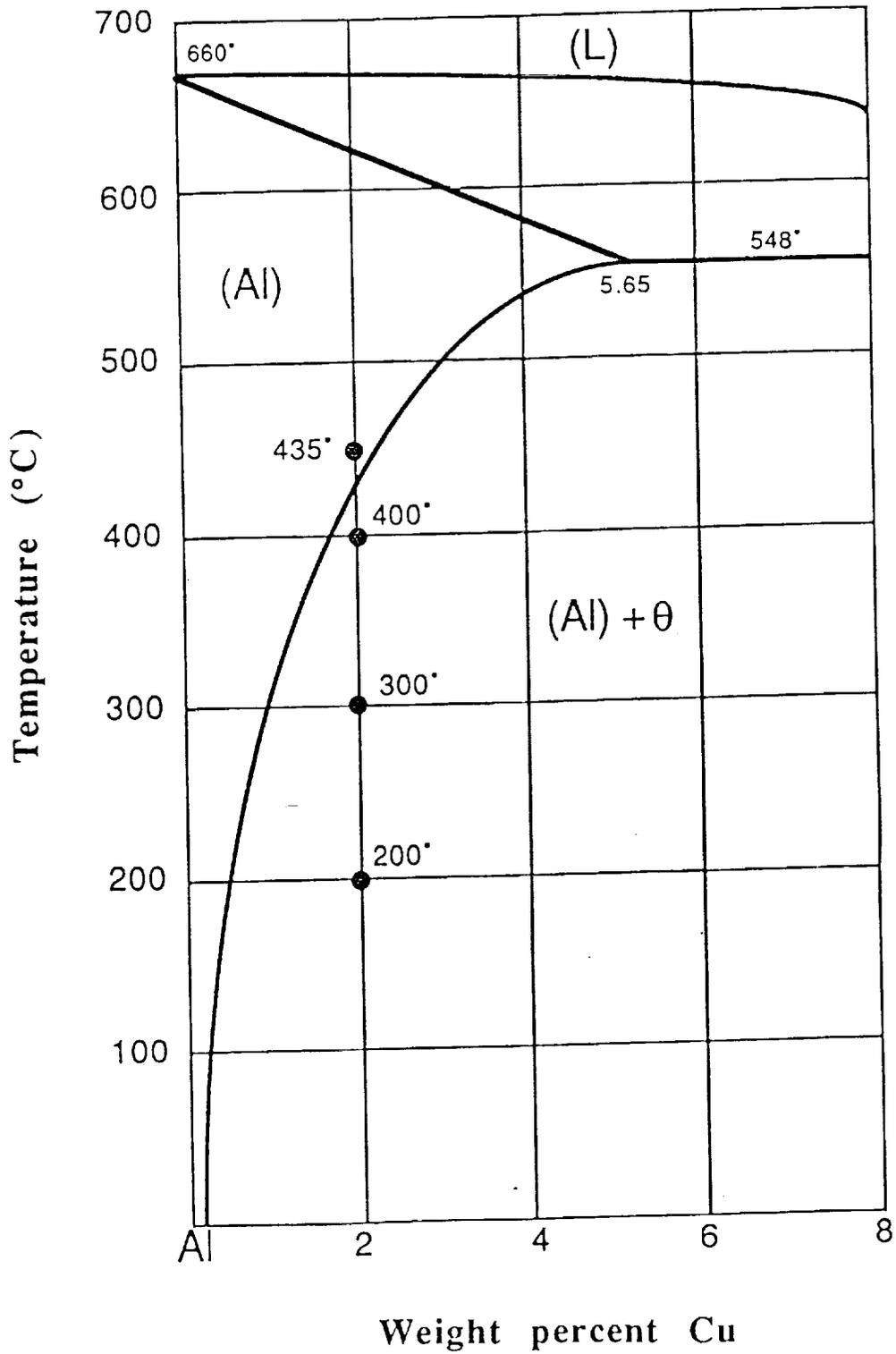
COPPER CONCENTRATION PROFILE ACROSS AN Al-2%Cu GRAIN BOUNDARY (FAST COOL)

Al-2%Cu Annealed Condition

t = 350 nm
d_p = 20 nm

$\dfrac{dT}{dt}$ = 10°C/sec

200 kV

—— Thermokinetic Model
······· Convolution

0.12

Distance from grain boundary (μm)

Cu Concentration (wt %)
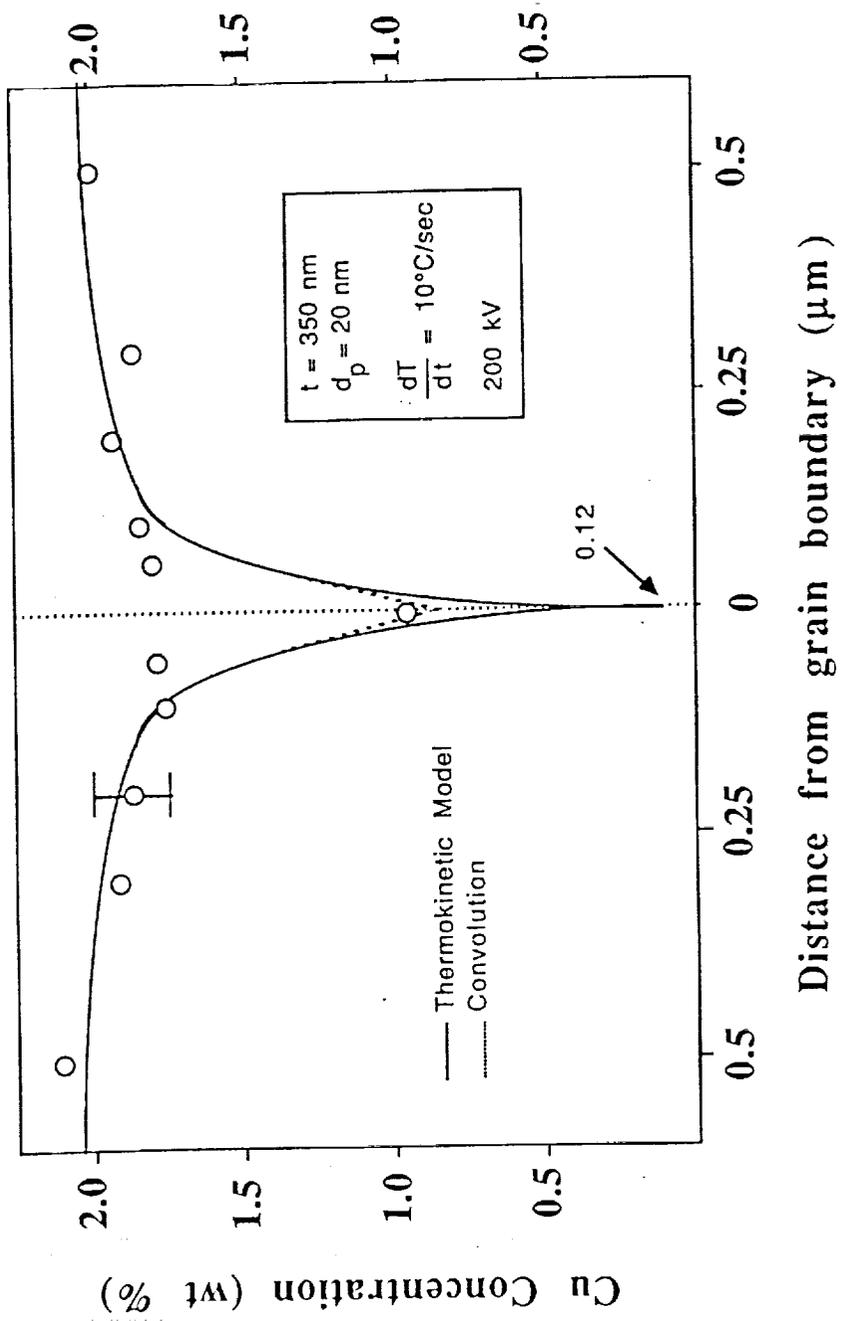
METASTABLE PITTING OF Al-2%Cu IN 0.001M Cl$^-$
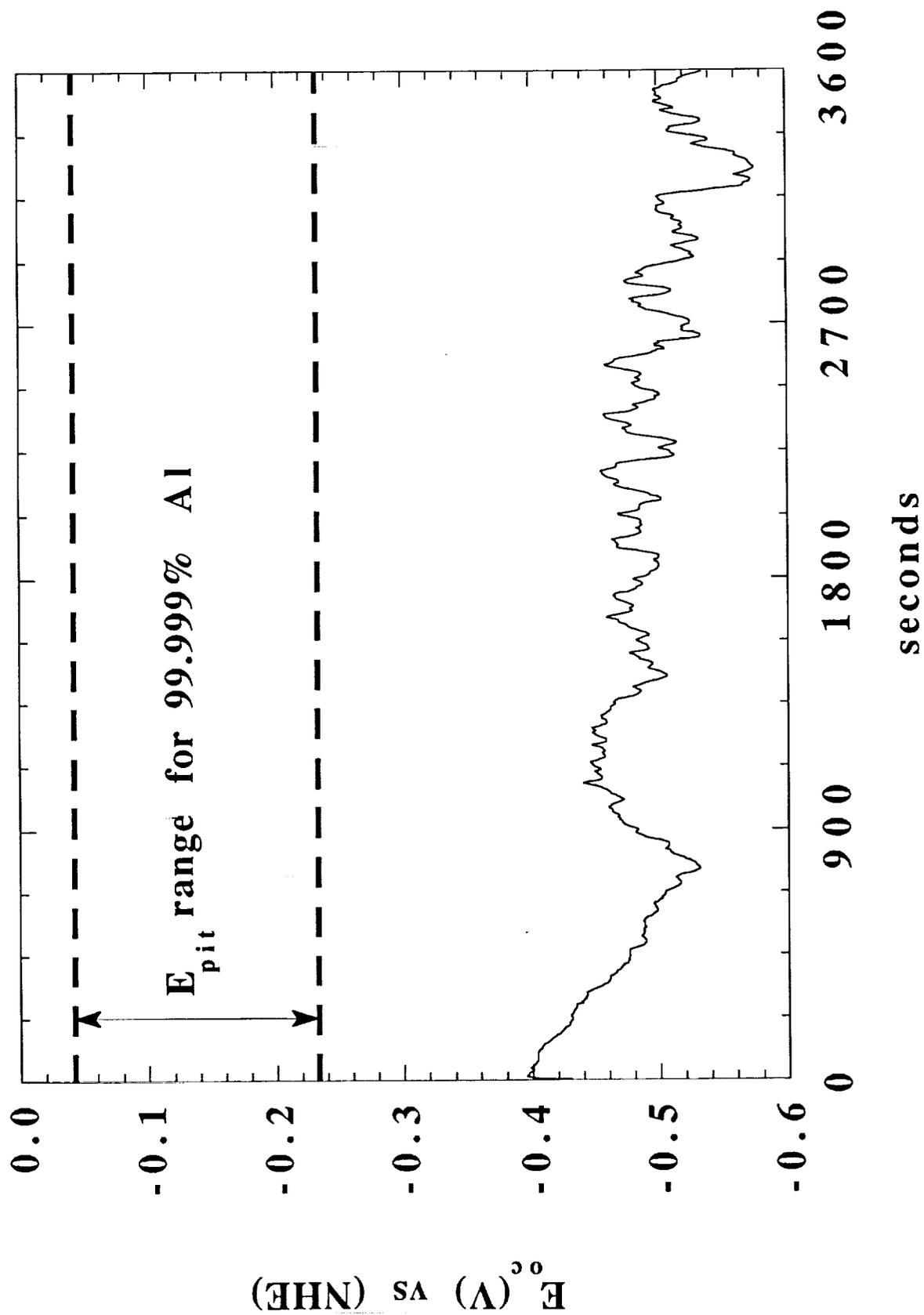
METASTABLE PITTING OF Al-2%Cu in 0.1M Cl$^-$
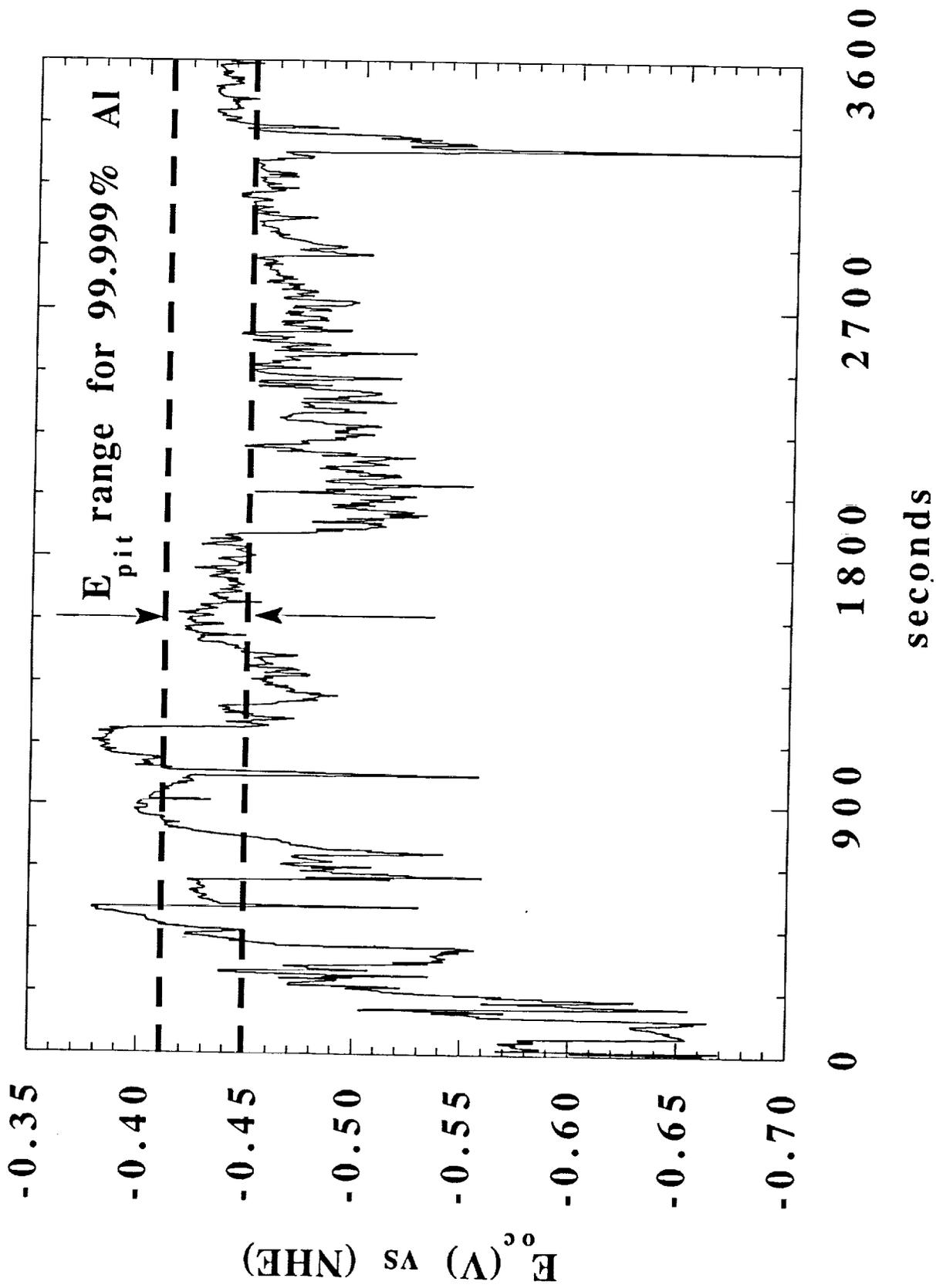
ANODIC POLARIZATIONS OF 99.999% Al WITH
A CATHODIC POLARIZATION OF Al$_2$Cu
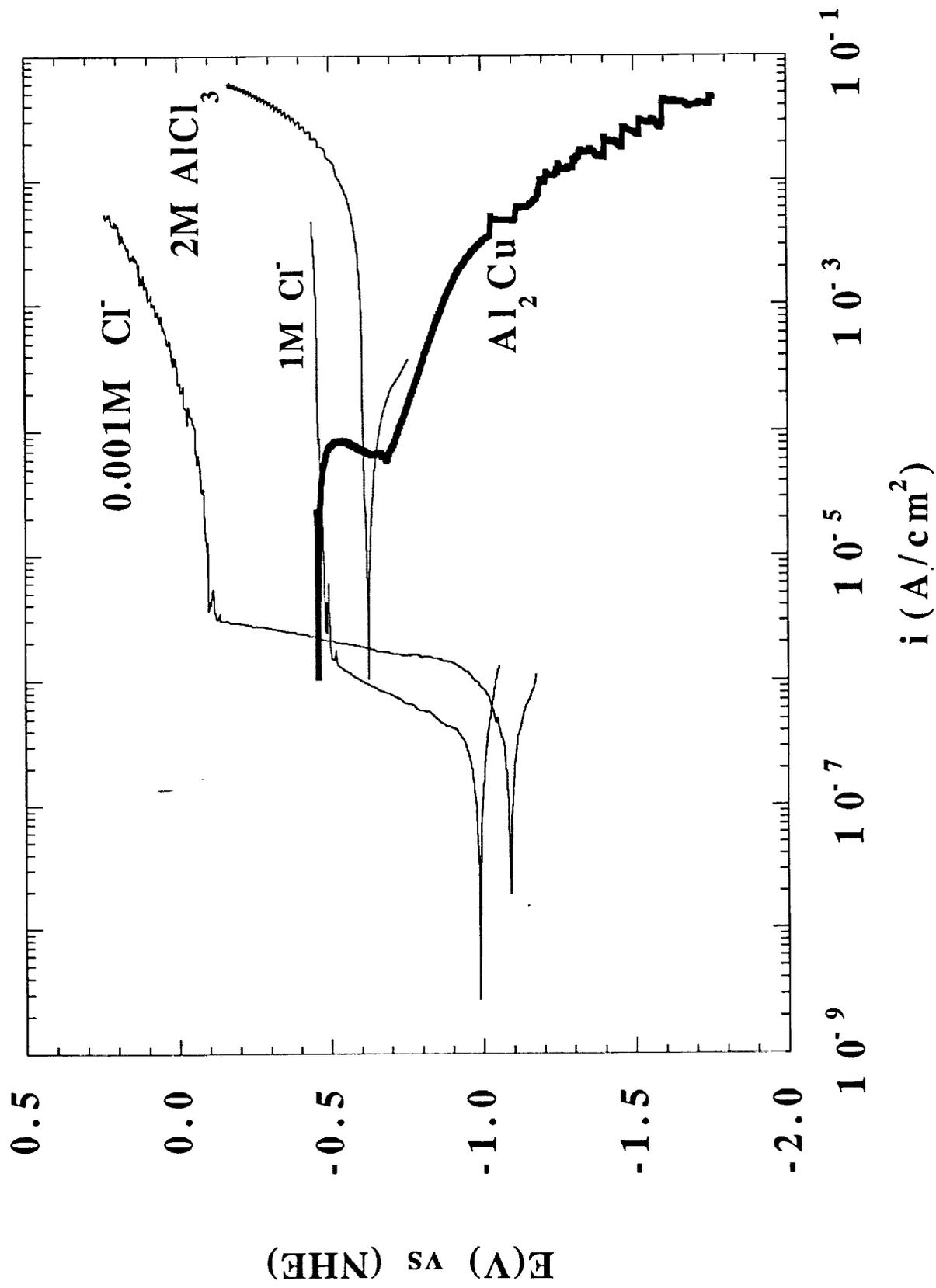
CUMULATIVE NUMBER OF PITTING EVENTS
FOR Al-2%Cu IN Cl⁻ ELECTROLYTES
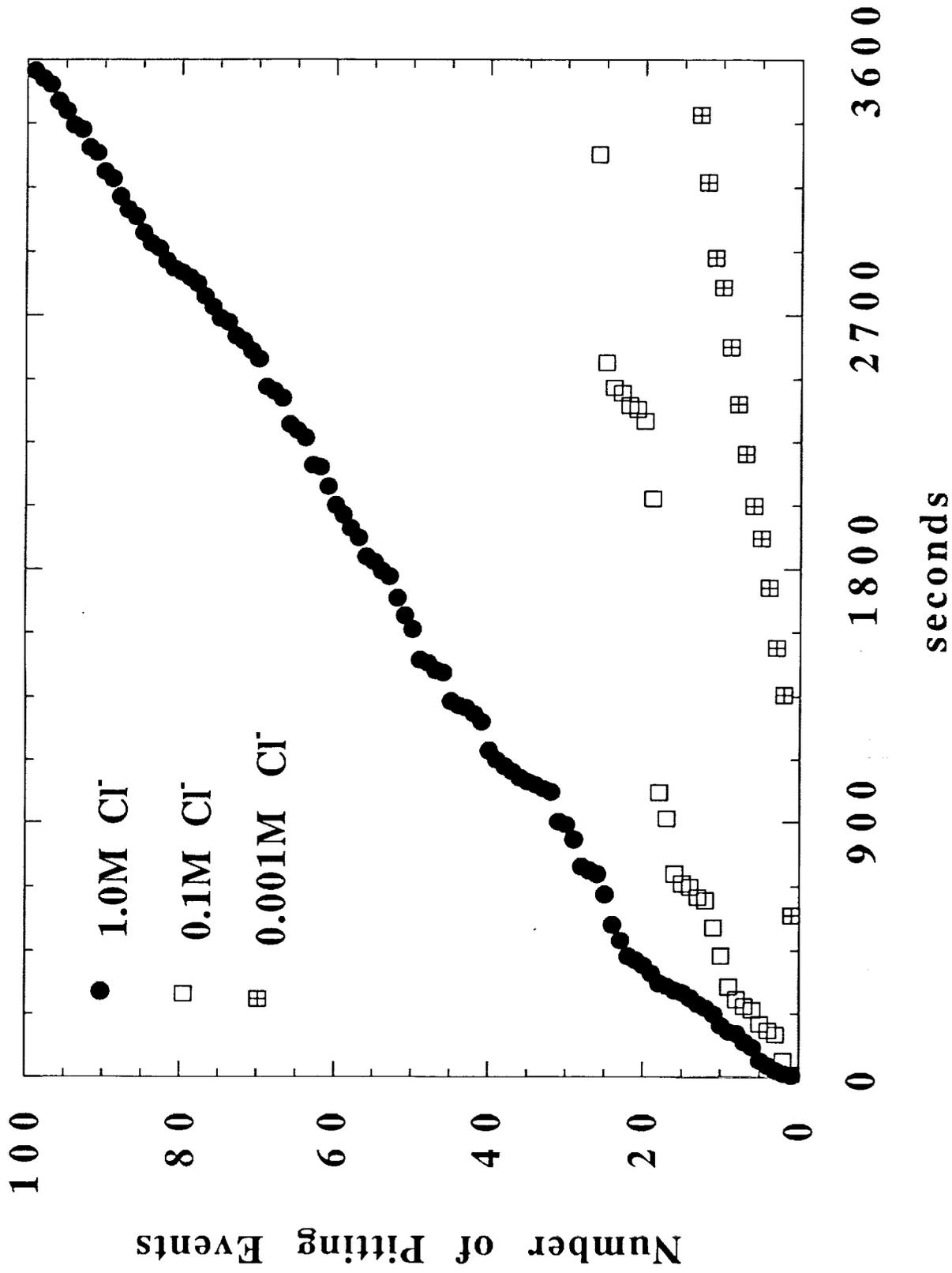
RATE OF CUMULATIVE PITTING EVENTS
FOR Al-2%Cu IN Cl⁻ ELECTROLYTES

Number of Pitting Events/second

seconds

- 1M Cl⁻
□ 0.1M Cl⁻
⊞ 0.001M Cl⁻
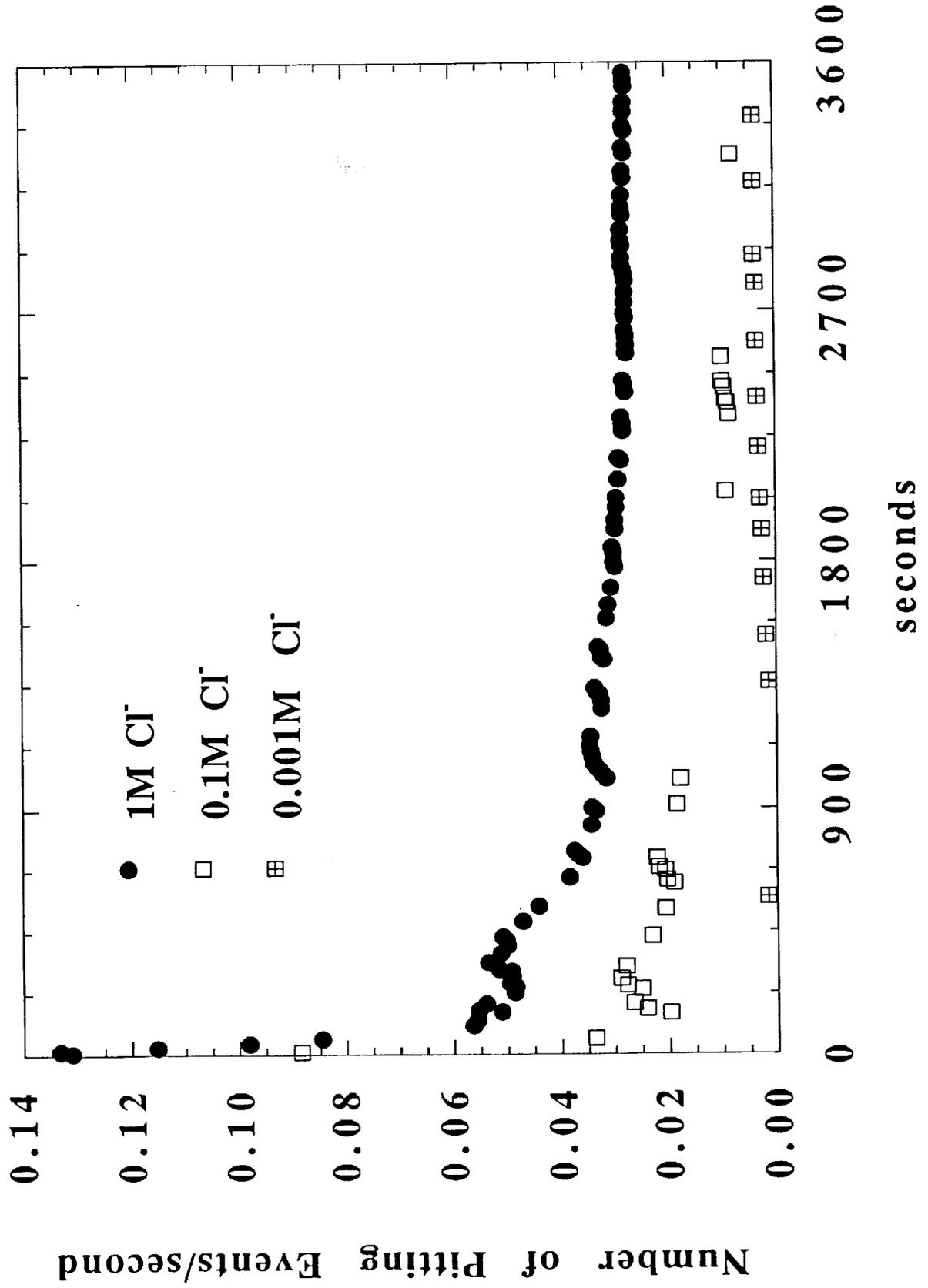
LIFE-TIMES OF PITTING EVENTS
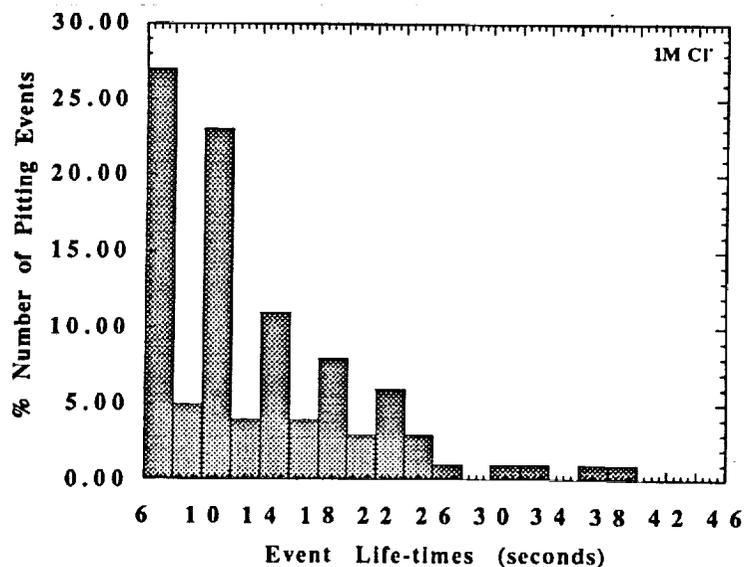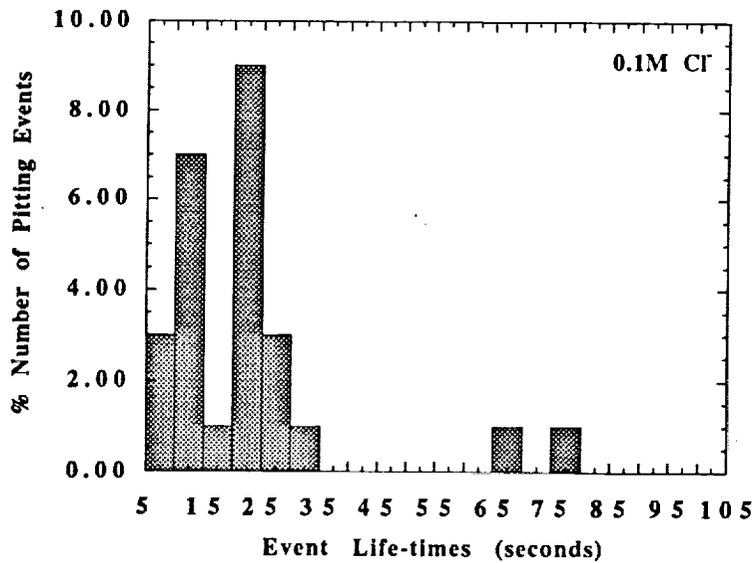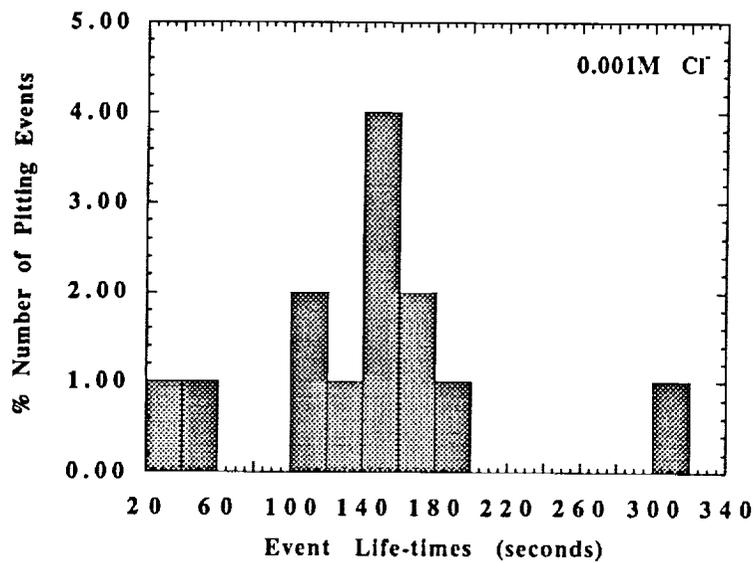
CONCLUSIONS

- The aggressive ranking of the halides may be size dependent.

$$Cl > Br^- > I^- \qquad \text{aggressiveness}$$
$$Cl^- < Br^- < I^- \qquad \text{size}$$
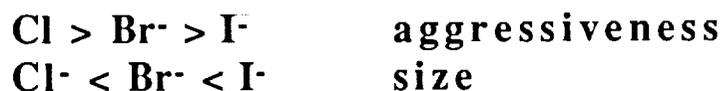
- The pitting potentials can be fitted with logarithmic functions with slopes equal to -0.12.

- The pitting potential has been shown in literature to be a function of nucleation frequency for propagating pits.

- Due to the distribution of potential dependent micropits geometries, there is a "real" distribution of pitting potentials.

- Metastable pits form at potentials well below the breakdown potential.

- The cumulative number of pitting events after a given time is lower in dilute halide compared to concentrated.

- The rate of metastable pitting events decreases with increasing exposure time.

FUTURE WORK

- E_{OC} time series analysis of Al-2%Cι

- Current and potential time series ι
  galvanic coupling between pure Al ι
  with a ZRA.

- Current time series analysis from
  control of pure Al.

Project 10   **Investigation of the Effect of Thermal Treatment on the Mechanical Properties of Ti-1100/SCS-6 Composites**

Douglas B. Gundel and F.E. Wawner

Objective

The overall objective of this research is to characterize the effect of thermal exposure, both isothermal and cyclic, on the mechanical properties of Ti-1100/SCS-6 composites.

Current Status

Work done thus far has primarily focused on the effect of high temperature (700-800°C), short term (1-2 days) cyclic thermal and isothermal exposure on composite microstructure and tensile properties. Thermal cycling studies in air suggest a strong dependence of properties after cycling on the degree of matrix foil to foil bonding achieved during initial composite fabrication. Damage accumulated during cycling included matrix embrittlement, matrix-ply delamination, and fiber-matrix interfacial degradation. The equivalent isothermal exposure caused little damage, and cycling in argon did not degrade the properties.

Other work accomplished involves the development of fiber coatings to slow or stop the fiber-matrix reaction that occurs at high temperatures in these materials. It has been demonstrated that high quality metal oxide coatings can be applied to the fiber by the sol-gel process. The effectiveness of these coatings in Ti-1100 is currently being investigated.

Recent Findings

Initial findings of the effect of thermal cycling to 800°C in air indicated that it was very detrimental to the composite properties. Further investigation, however, shows that the strength of a well-consolidated composite with optimal fiber spacing is only slightly degraded by this treatment. C-scans of the composite panels performed just after fabrication clearly indicate that areas near the panel edges are poorly consolidated. Tensile samples taken from these areas sometimes exhibited low as-fabricated strength, but were always severely degraded after thermal cycling in air (up to 65% loss in strength). Cycling in an argon atmosphere had no effect on any samples, while isothermal exposures designed to give the

samples the same thermal exposure as that experienced by those that were cycled had only a minor effect on strength.

Research into the development of a reaction barrier coating for the fibers has also been undertaken. The sol-gel process has been successfully utilized to coat SCS-6 fibers with yttria and calcia. These coatings have been found to be uniform in thickness, dense, and strongly adherent. Initial results of their effectiveness in CP titanium indicate that the coatings (about 1 μm) stop the reaction during exposures at 800°C for up to 150 hours. Other matrices are currently being investigated.

Milestones

Immediate goals include the optimization of fabrication parameters (or methods) to produce well-consolidated composite panels. After this is achieved further investigations into the effect of thermal exposure can be made. These will include lower temperature, longer term exposures to help determine the temperature range where this composite can be used in service.

The coatings developed thus far by the sol-gel process will be investigated with respect to their ability to protect the underlying fiber. Other potential reaction barriers may also be coated onto the fiber and studied.

Presentation Graphics Captions

1.   Title.

2.   Objective.

3.   Description of composite panels received so far that have been sectioned into longitudinal samples and the thermal exposures that were performed.

4.   Thermal cycling apparatus and temperature vs. time for a typical thermal cycle.

5.   Damage seen on samples taken from the first batch of panels (A and B).

6.   How the panels (C, D and E) were sectioned into tensile samples.

7.   Strength and modulus vs. position in the panel of samples taken from Panel C that were all cycled to 800°C 500 times.

8. Fracture surfaces of a sample from the edge and one from near the center.

9. Tensile strength of samples from Panel C vs. as-fabricated strengths of samples taken from Panel D.

10. Same as 9 but with results of the strengths of isothermally exposed samples from Panel D.

11. C-scans of panels C and D showing regions of poor consolidation.

12. C-scan of new sample -- Panel E.

13. Plot of strength vs. position vs. condition (as-fab. or cycled to 800°C) for samples from Panel E.

14. Fracture surface of samples 8E (cycled) and 9E (as-fabricated).

15. Polished cross-sections of samples 8E and 9E showing the delamination of matrix plies due to cycling in air.

16. Fracture surface of sample 7B showing the ply delamination, matrix embrittlement, and fiber groups.

17. Pictures of the poor fiber distribution of panels A and B and the good distribution of panels C,D and E.

18. Histogram of edge-to-edge fiber spacing of panels A and B vs. panels C,D and E.

19. Plot of the percentage of fibers involved in groups of 1 to 7 in the first and second group of panels received.

20. A comparison of fracture surfaces of samples from the center of panels B and C that were cycled to 800°C.

21. Summary of thermal exposure results.

22. Description of the sol-gel technique employed to coat the fibers with metal oxides.

23. Pictures of the yttria coating on SCS-6 fibers.

24. The dependence of coating thickness on number of dips and alkoxide concentration.

INVESTIGATION OF THE EFFECT OF THERMAL EXPOSURE ON THE MECHANICAL PROPERTIES OF Ti-1100/SCS-6 COMPOSITES

DOUGLAS GUNDEL

F. E. WAWNER

UNIVERSITY OF VIRGINIA, CHARLOTTESVILLE

RESEARCH OBJECTIVE

The objective of this research is to investigate the influence of thermal exposure, both isothermal and cyclic, on the microstructure and mechanical properties of Ti-1100/SiC composites.

Ti-1100/SCS-6 PANELS

- Fabricated at NASA LaRC by VHP'ing

- Longitudinal samples from 5 panels:

  A,B – 27 v/o, 3 x 4 in., 12 samples,
       7 mil foil, brittle surface layer

  C,D – 39 v/o, 3.5 x 3.5 in., 9 samples,
       4 mil foil, no surface layer

  E – same as C,D – processed at
        different time

- Treatments done:
  - Cycled in air 150 to 700C
  - Cycled in air 150 to 800C (Panel C)
  - Cycled in argon 150 to 800C
  - Isothermal Exposure 735C, 26.5h

THERMAL CYCLING APPARATUS
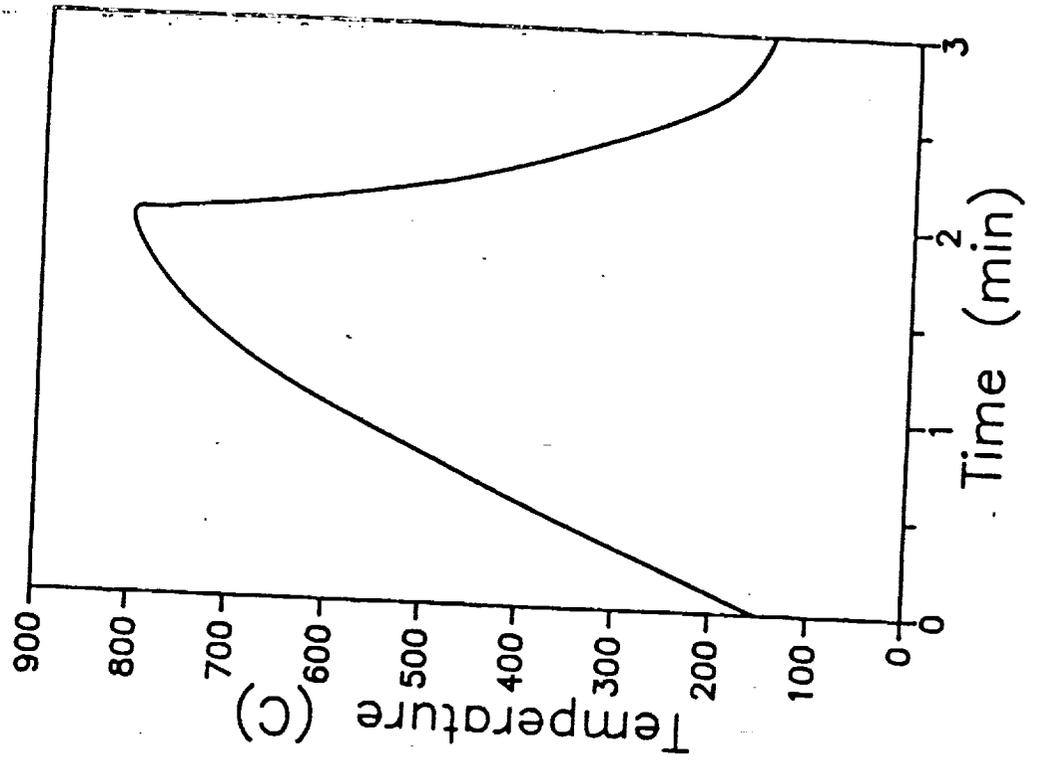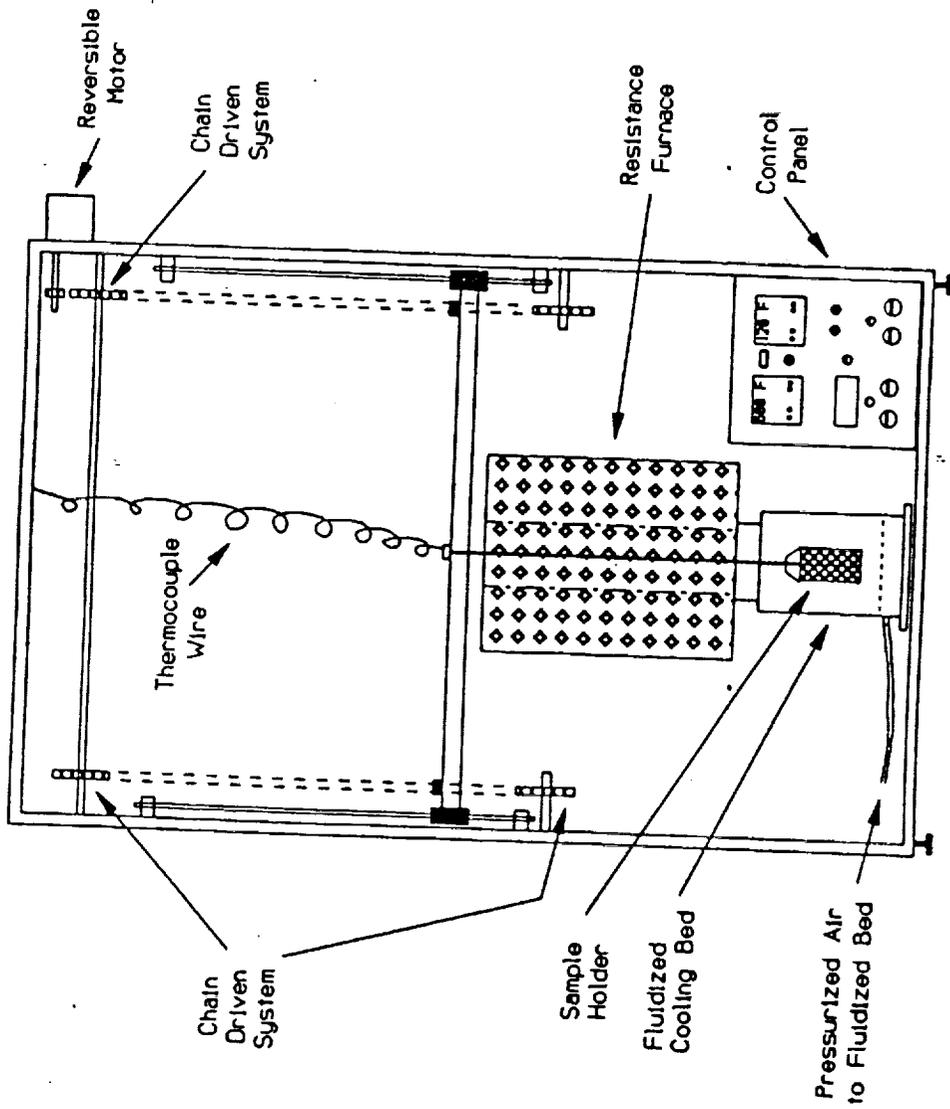
Fracture Surface (Panel A)
Cycled 150-800C 500X
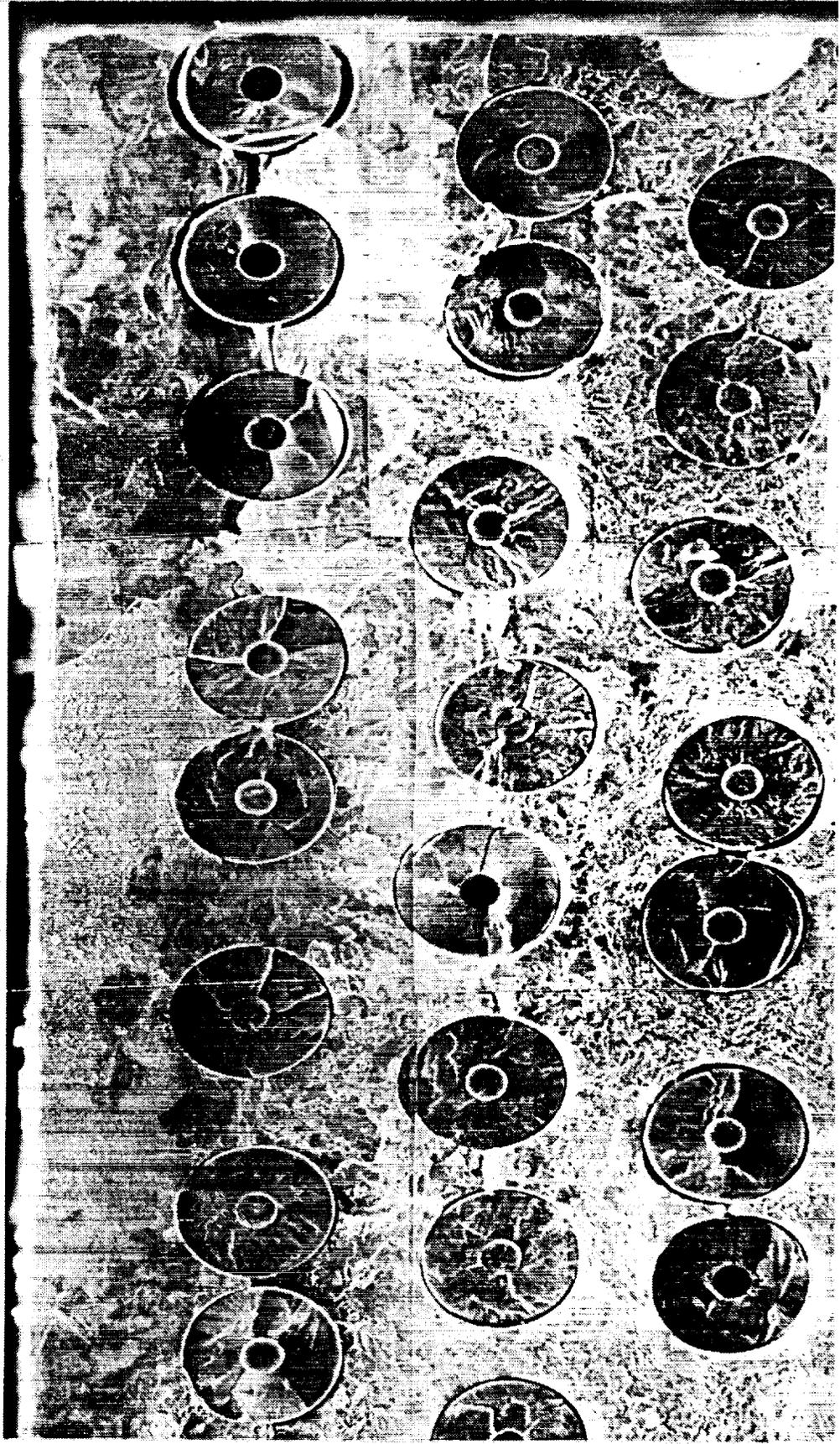
Panel Sectioning Diagram

4.00"

3.00"

1 2 3 4 5 6 7 8 9

.25"
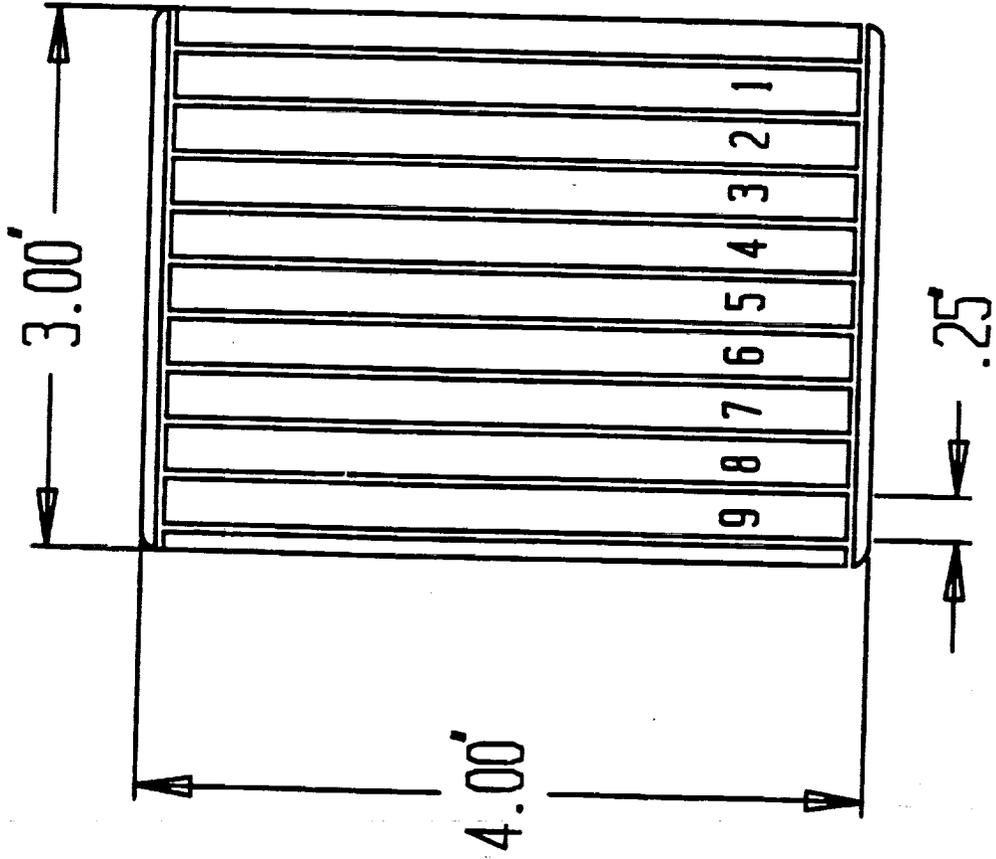
Numbered Samples are 0.25" wide

Tensile Properties vs. Position
Cycled 150-800C 500X (Panel C)
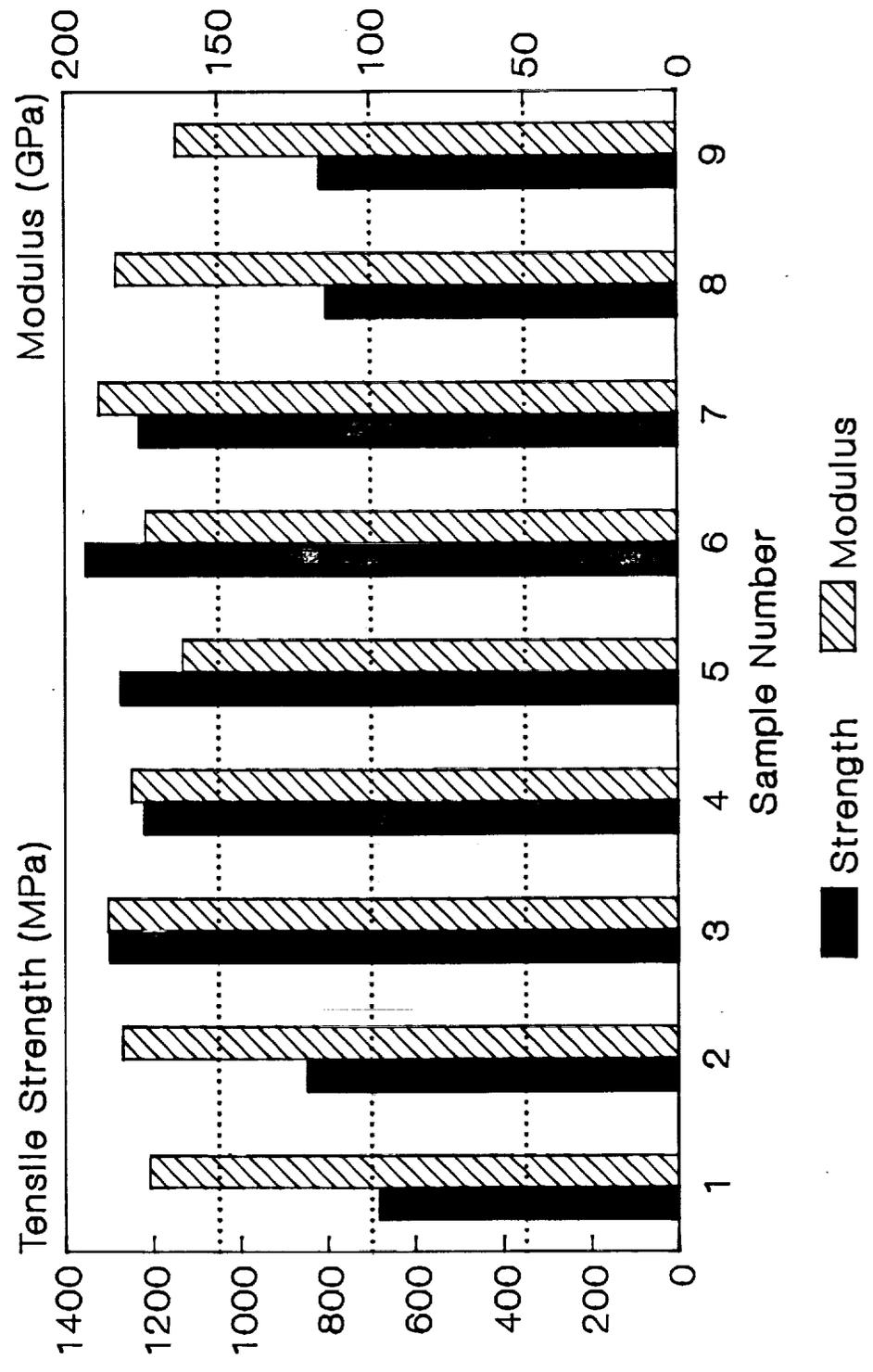
Fracture Surfaces (Panel C)
Cycled 150-800C 500X
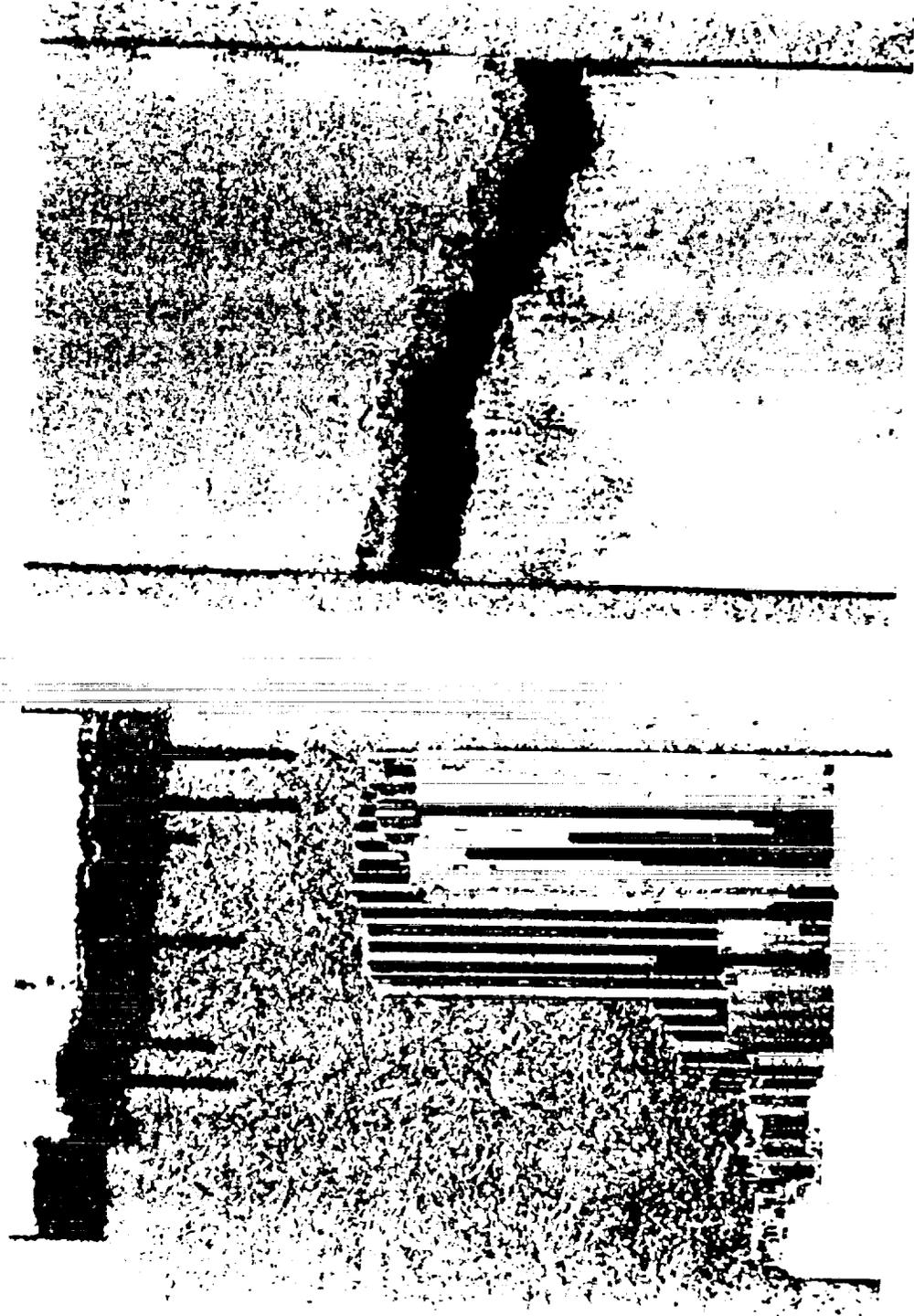
Sample 2C

Sample 6C

Tensile Strength vs. Position

Strength (MPa)

Sample Number

■ Cycled to 800C (C)   ▨ As-fabricated (D)

Tensile Strength vs. Position

Legend: Cycled to 800C (C) ■ | As-fabricated (D) ▨ | Isothermal (D) ▦

Y-axis: Strength (MPa), 0 to 1600

X-axis: Sample Number — 1,9 | 2,8 | 3,7 | 4,6 | 5
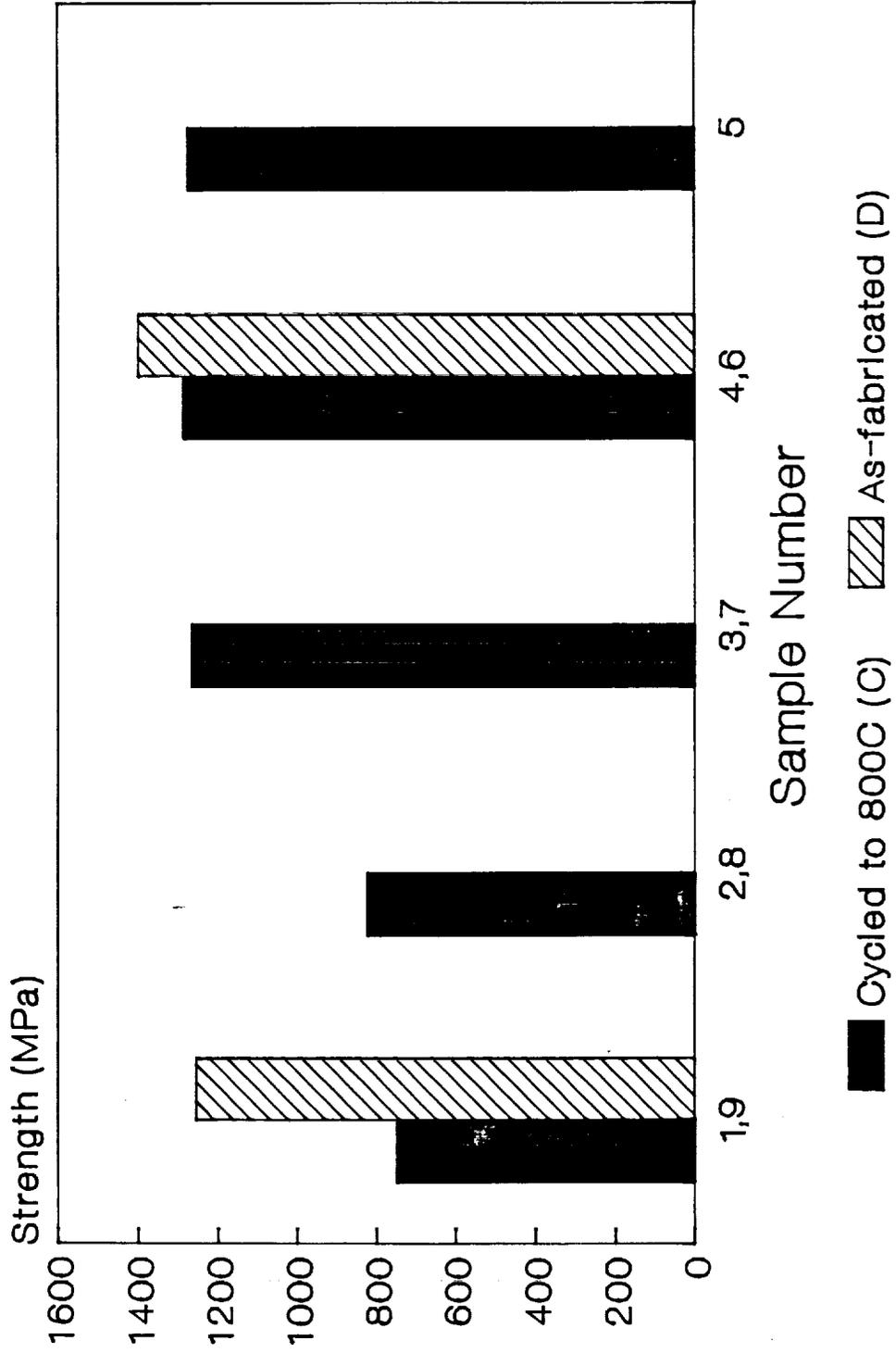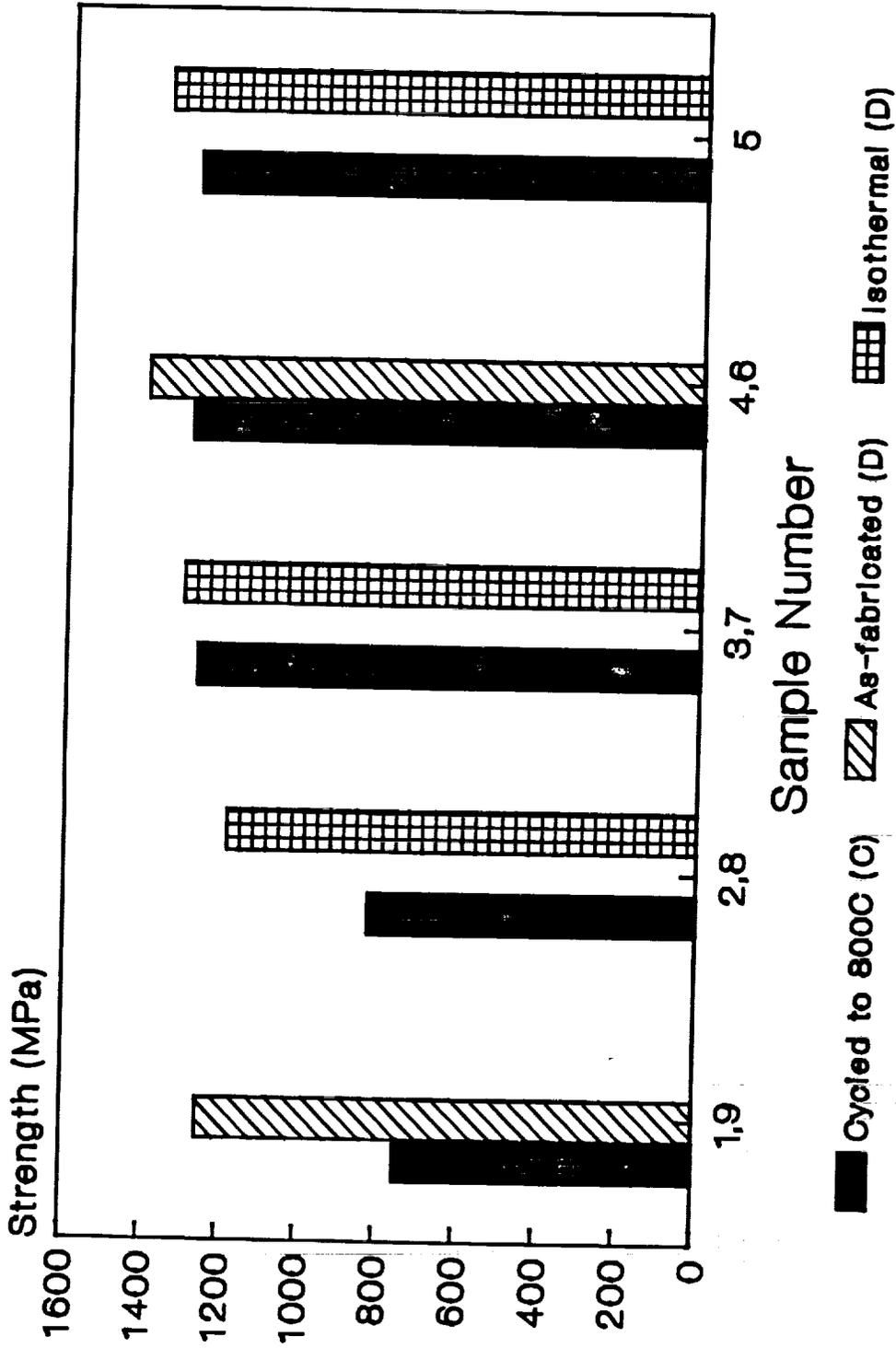
C-Scans of Panels C and D
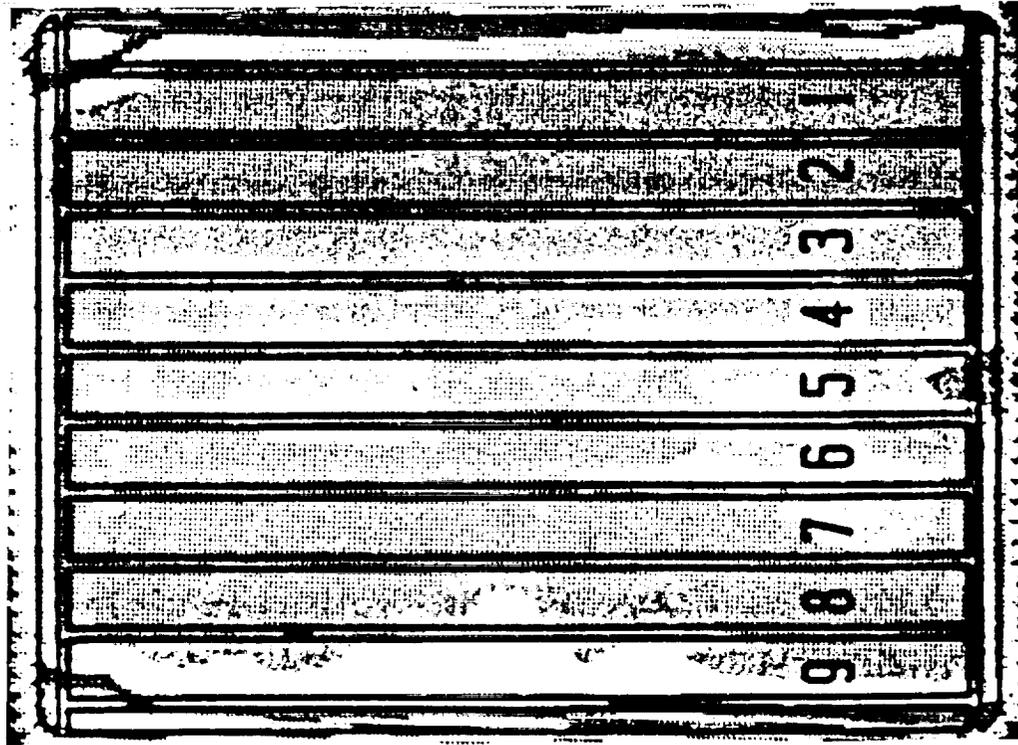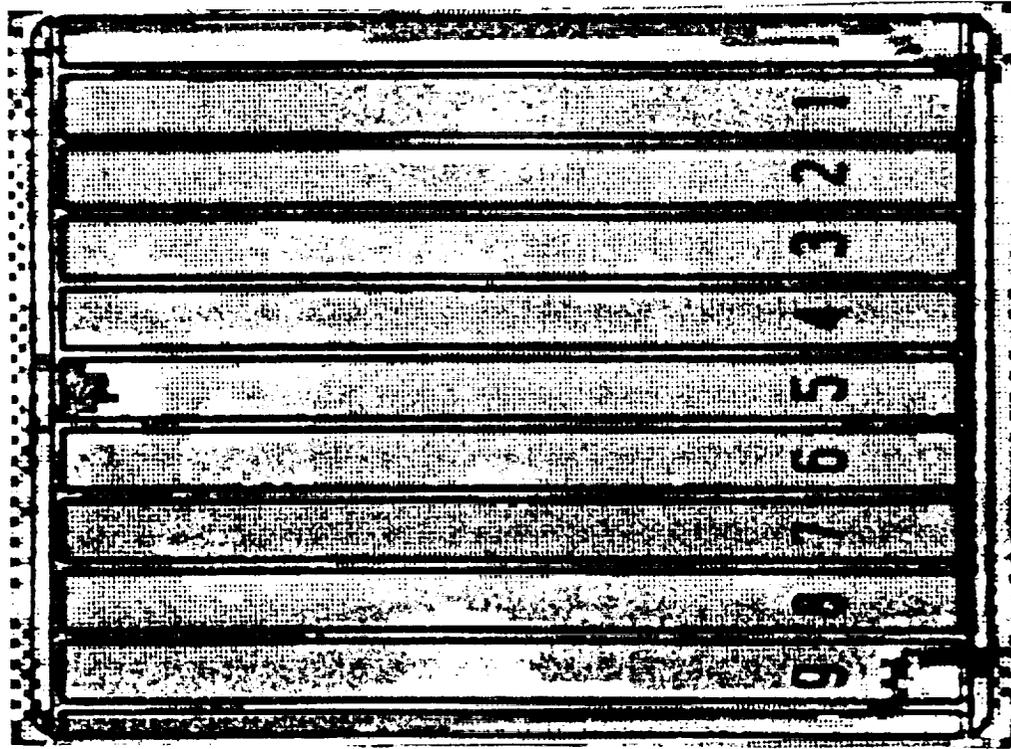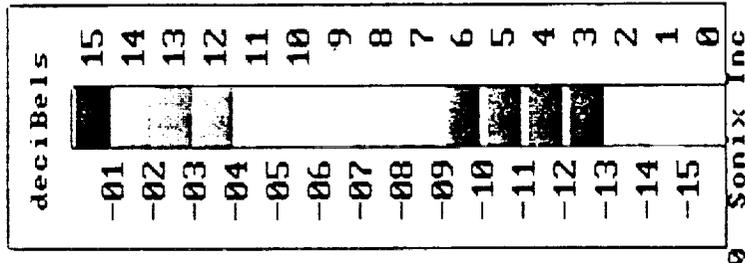
Panel D

Panel C

C—Scan of Panel E
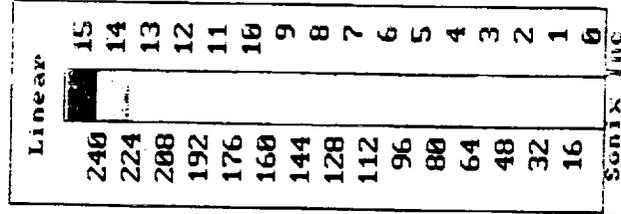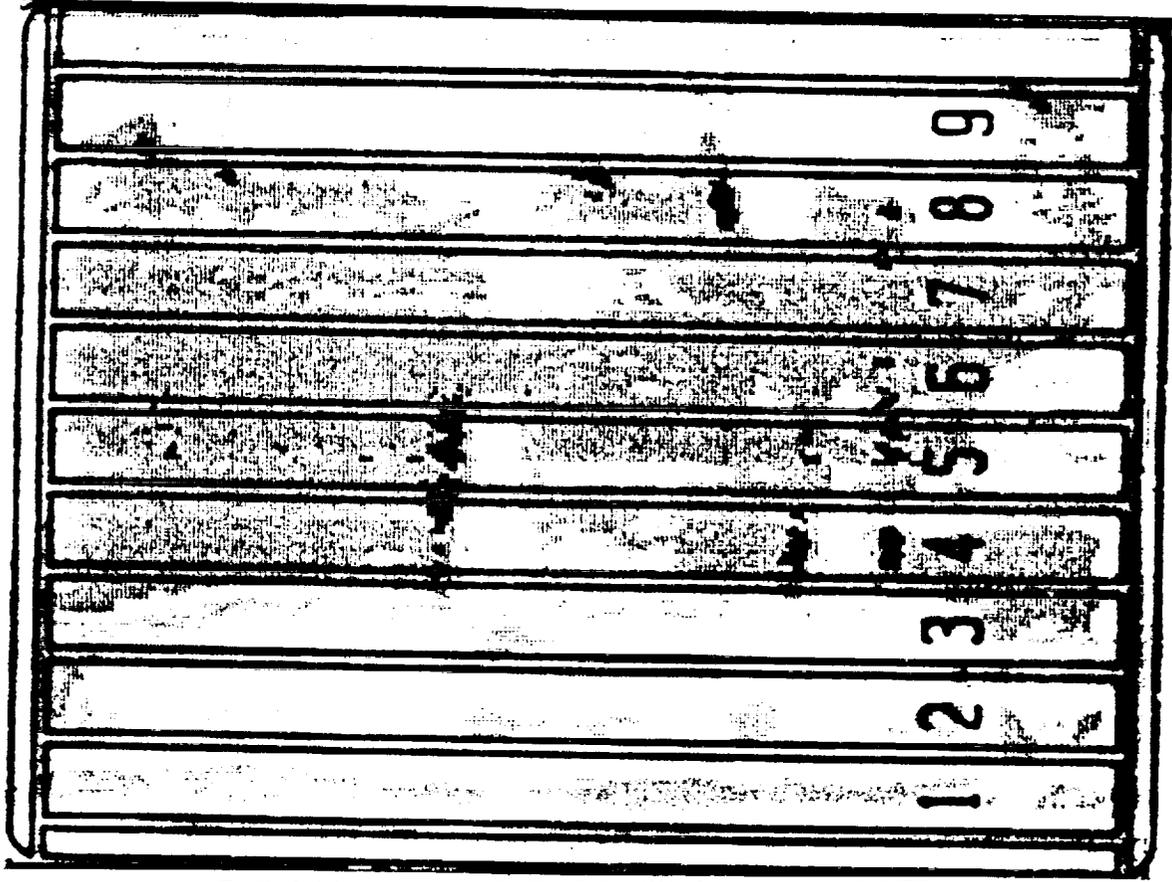
Tensile Strength (Panel E)
Cycled and As–Fabricated

UTS (MPa)

Sample Number

■ As Fabricated ▨ Cycled to 800C
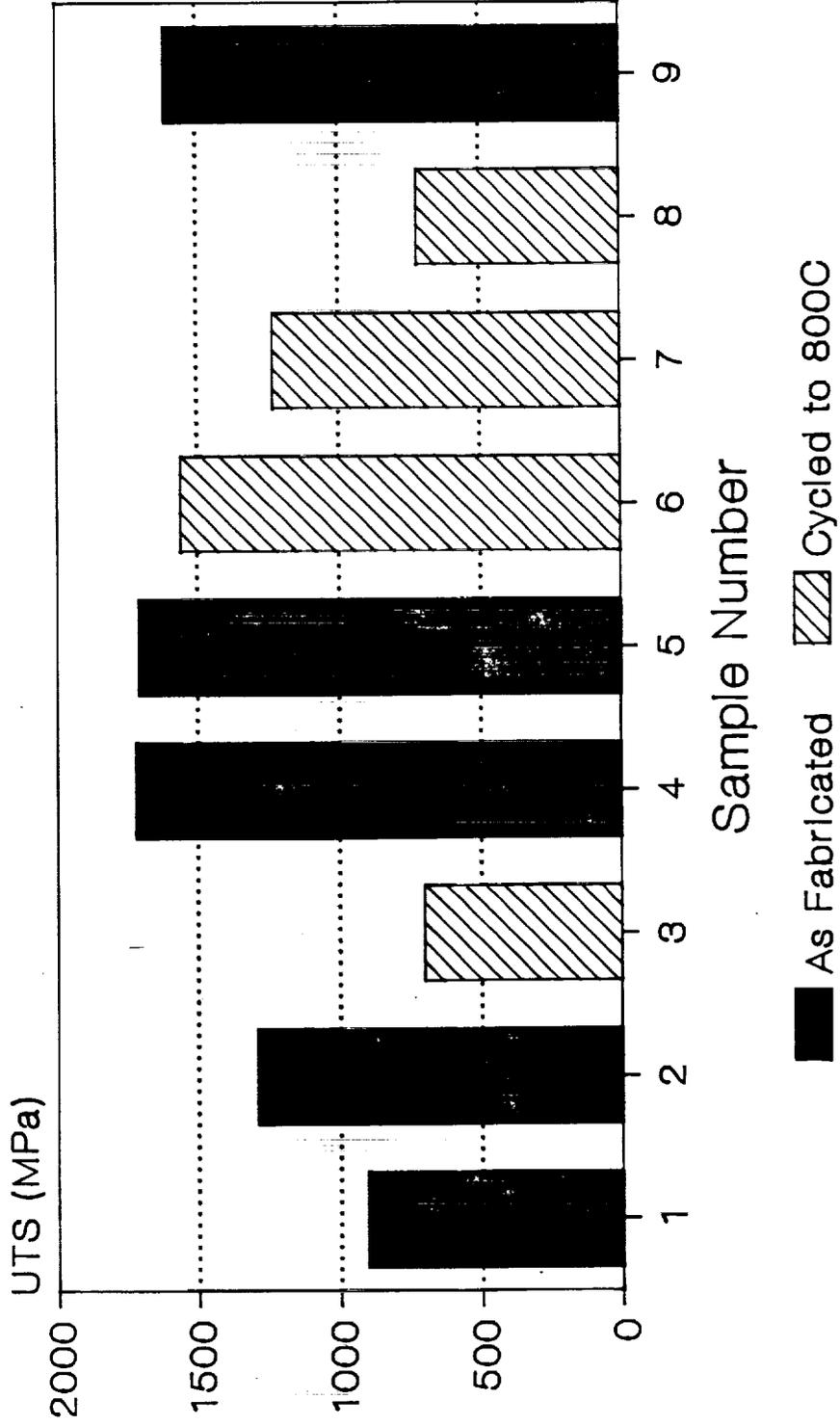
Fracture Surfaces (Panel E)

As-Fab. (9E) vs. Cycled (8E)
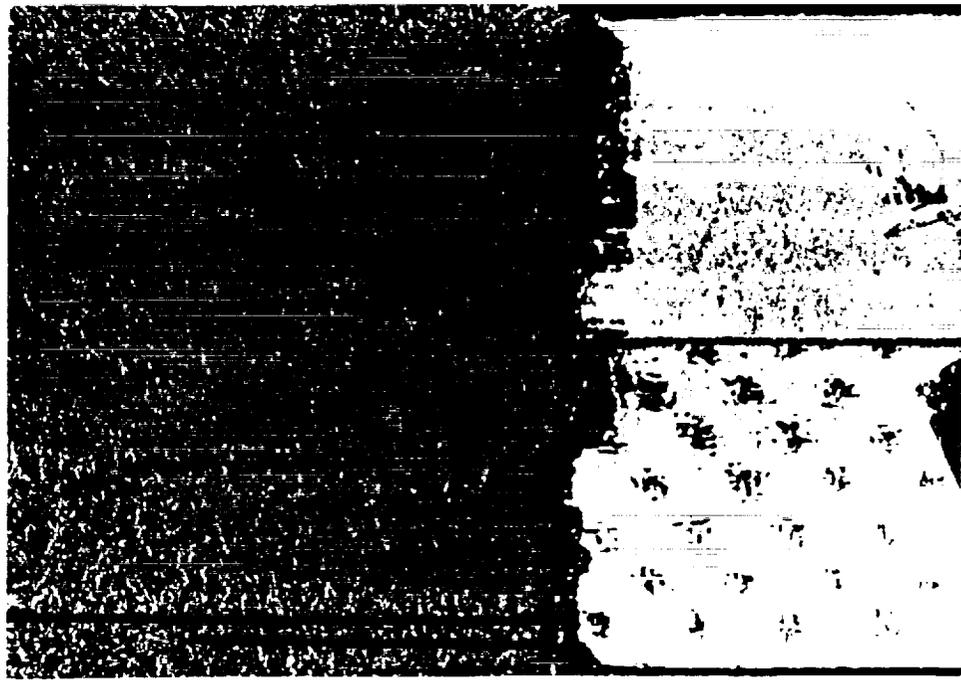
Sample 8E
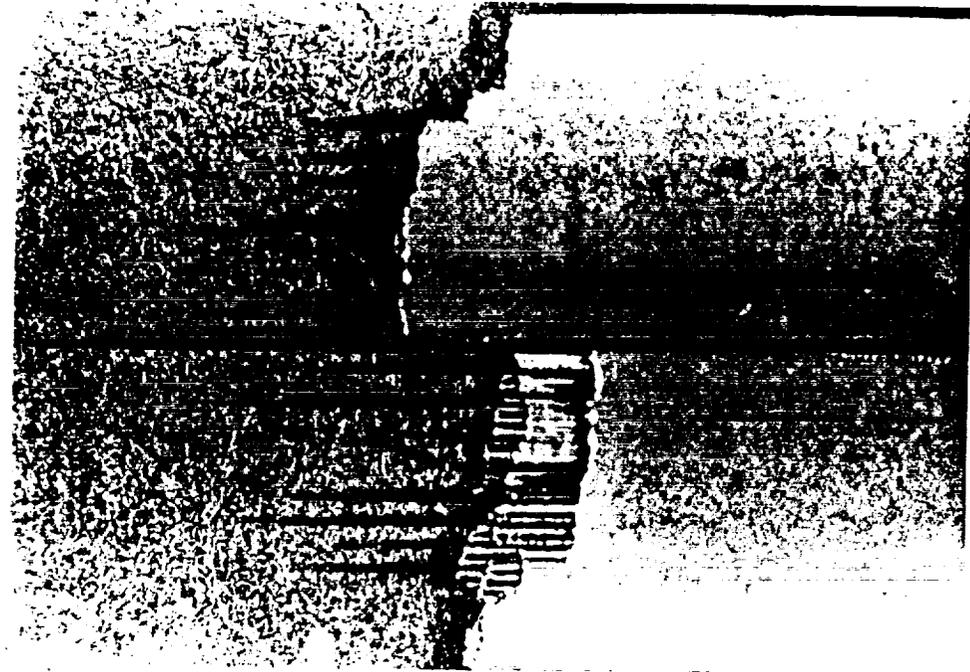
Sample 9E

Fracture Surface (Sample 7B)
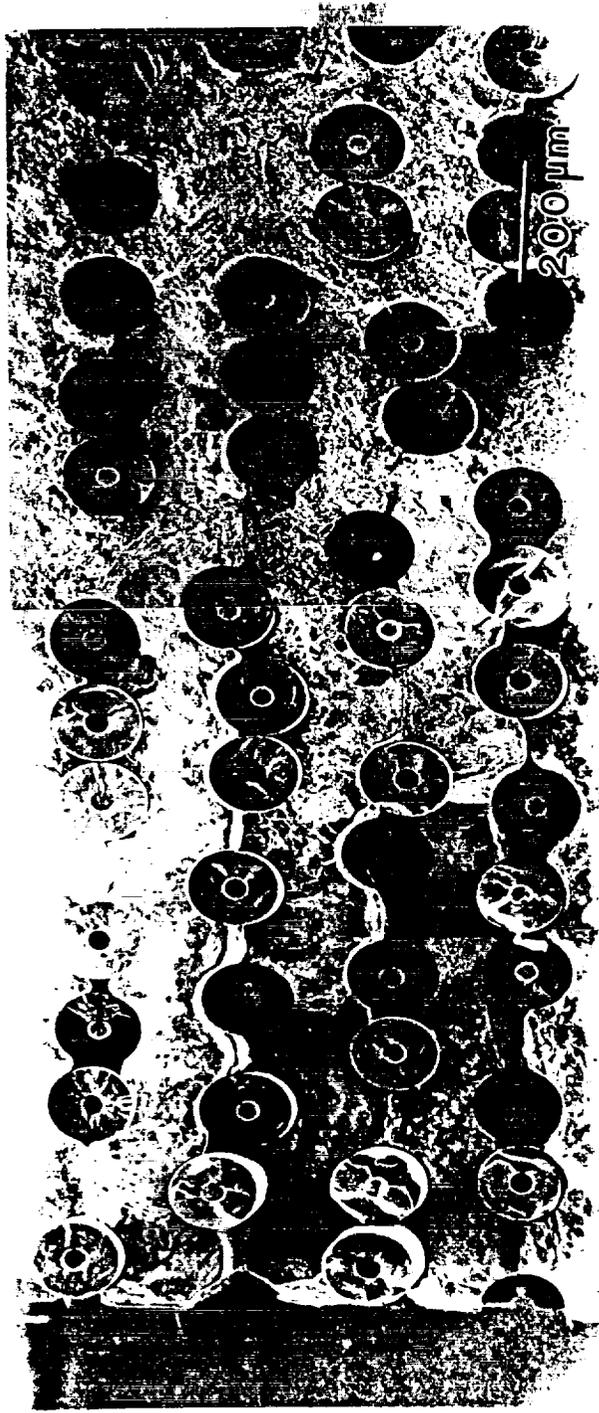
Polished Cross Sections (Panel E)

After Tensile Test
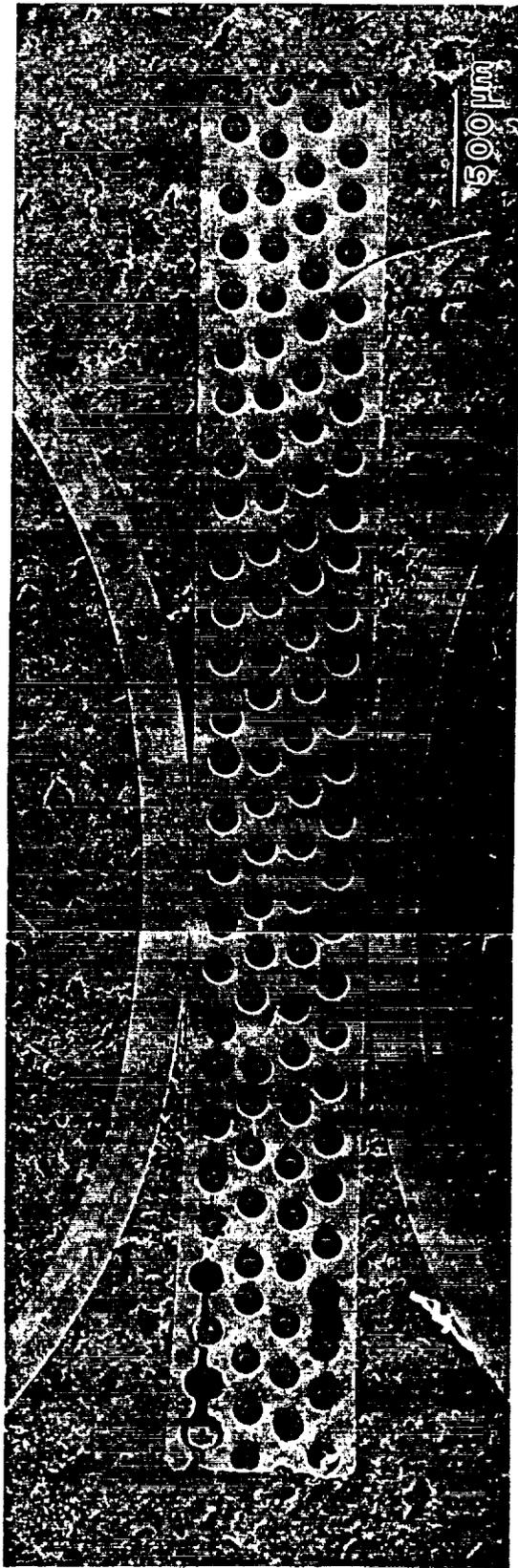
Sample 9E
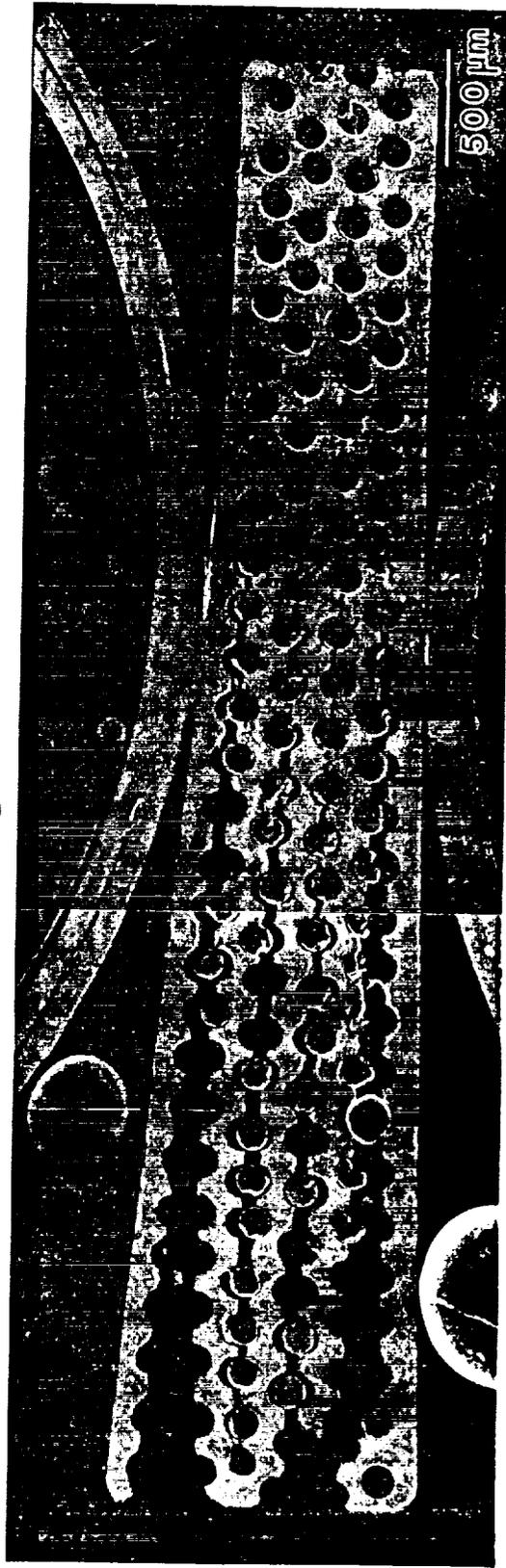
Sample 8:E

C-4

Fiber Spacing

Panels A,B

500 μm

Panels C,D,E

500 μm
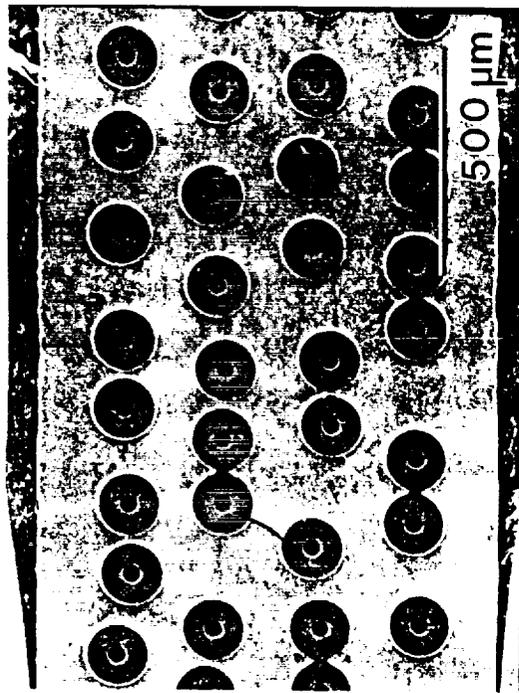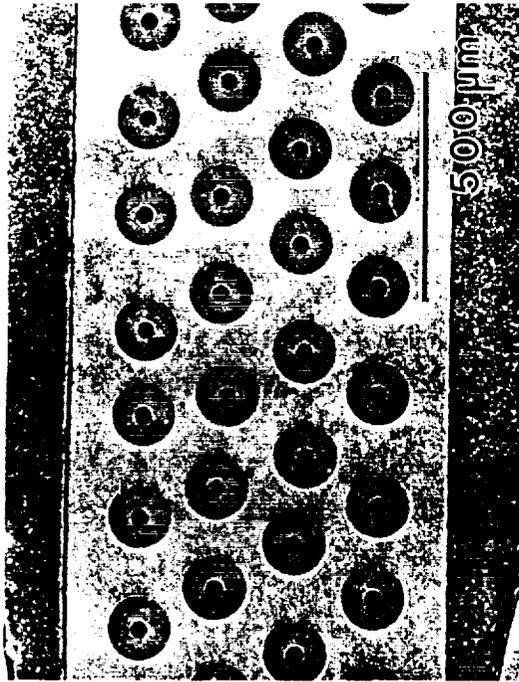
Fiber Spacing Distribution
Panels A,B vs. Panels C,D
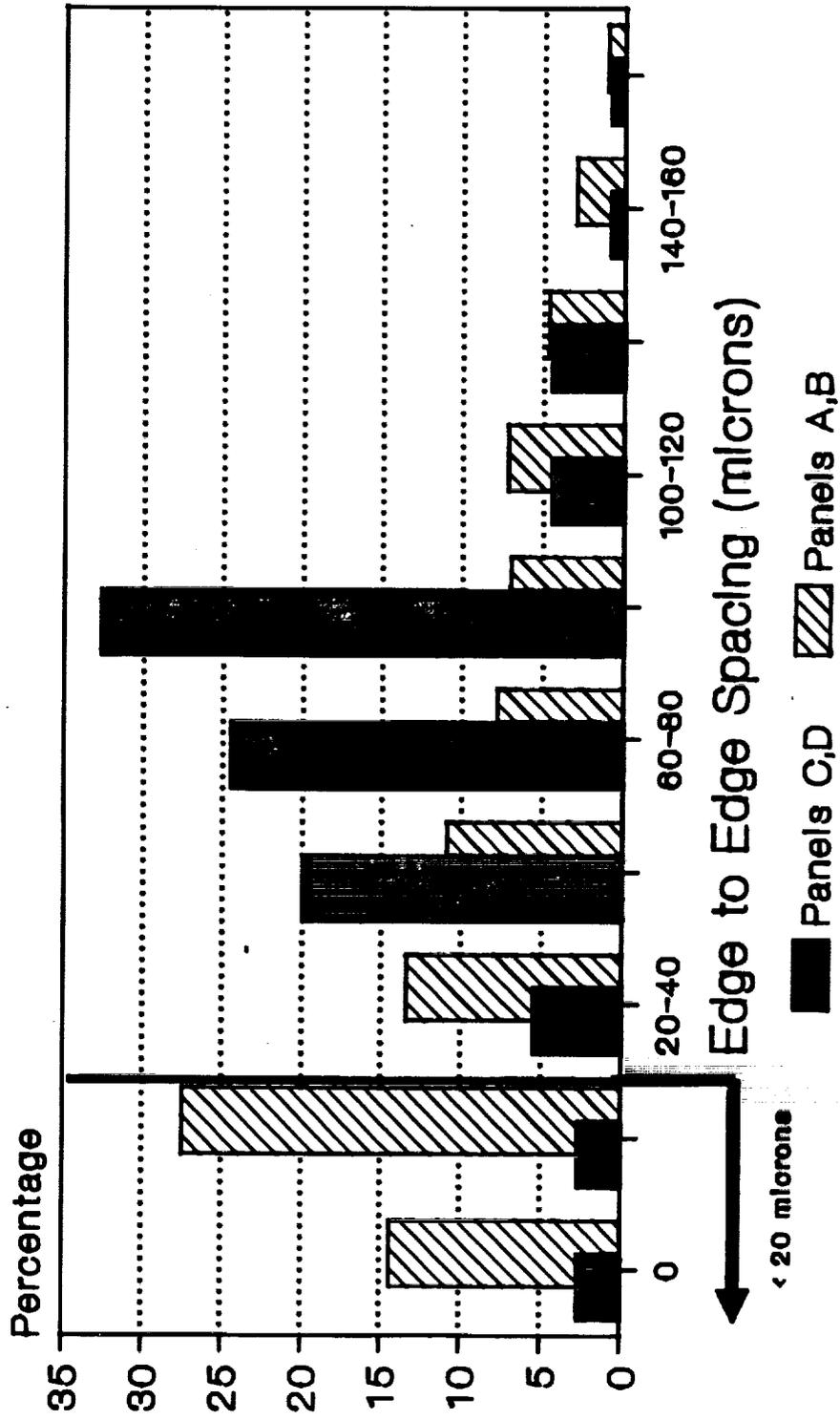
Fiber Distribution Comparison

Percentage of Fibers In Groups

Group Size

■ Panels A,B   ▨ Panels C,D
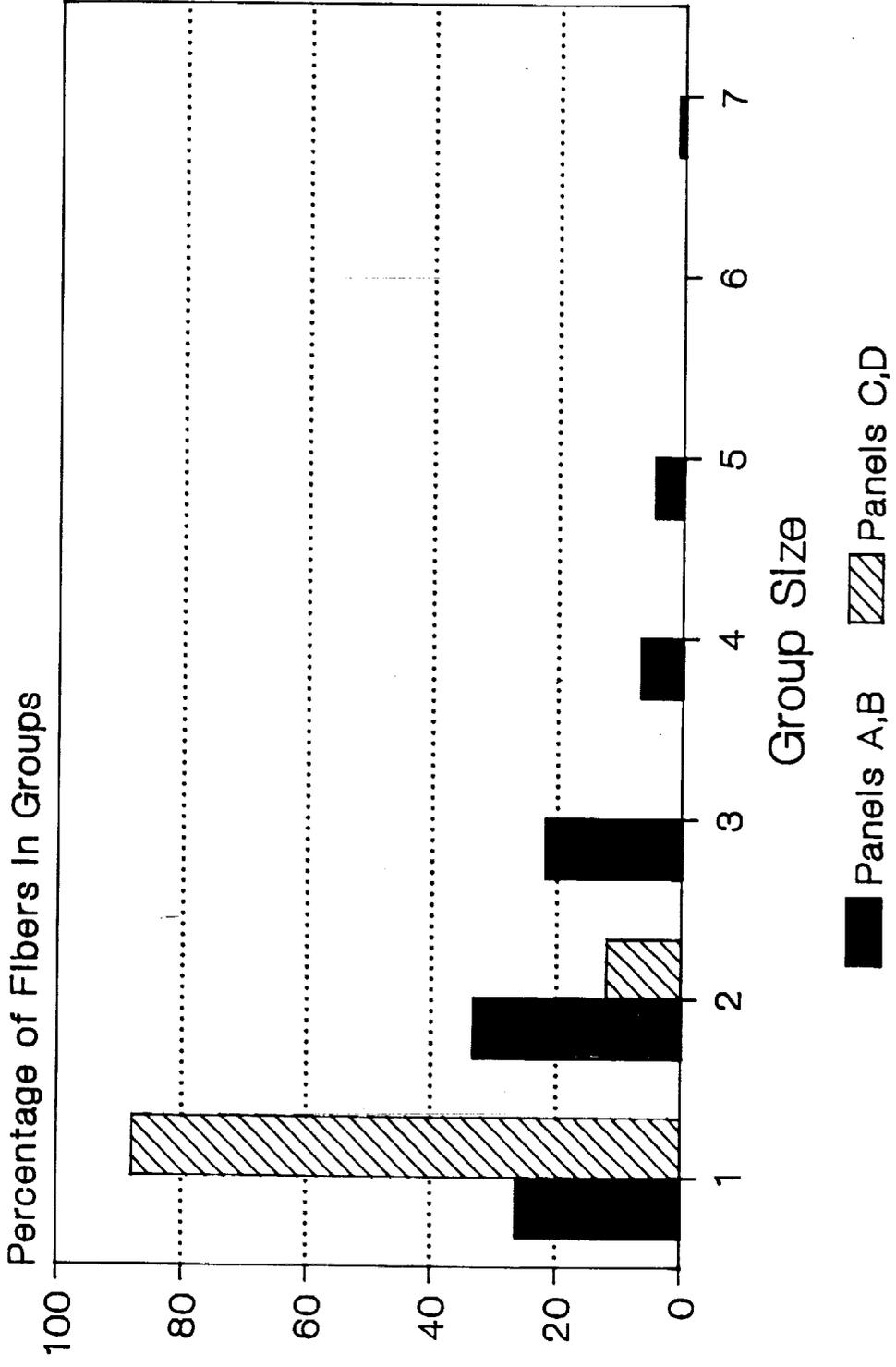
Fracture Surfaces
Cycled 150–800C 500X
Panel B vs. Panel C

Sample 6C
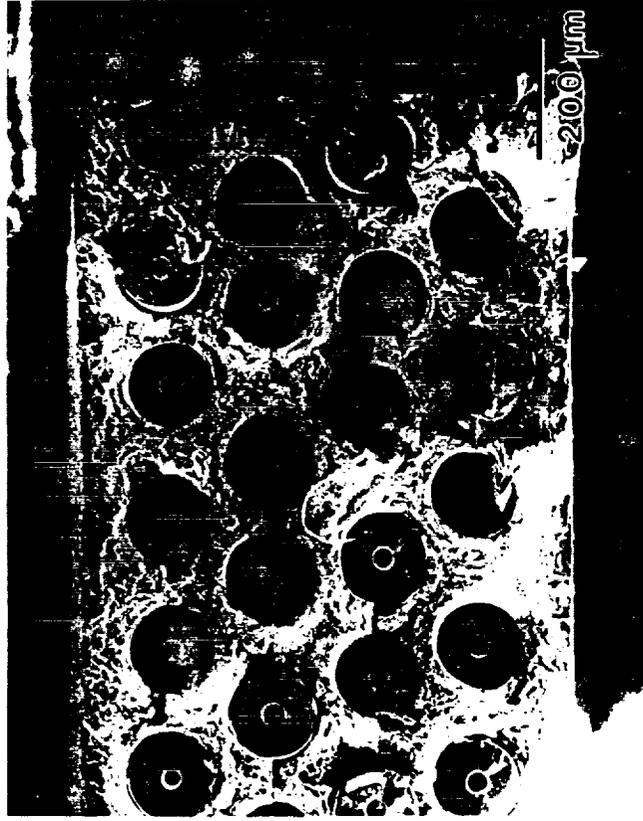
Sample 7B

Summary (Thermal Exposures)

- Argon cycled samples did not exhibit strength degradation.

- Isothermally exposed samples exhibited only slight tensile strength degradation.

- Cycling of well-consolidated samples to 800C only slightly degraded their strength.

- Cycling of samples taken from near the edge of the panels caused dramatic strength losses.

- Damage to the edge samples included matrix embrittlement and matrix ply delamination which lead to fiber-matrix interface degradation and fiber pullout.

- C scans performed just after fabrication indicated poorly consolidated areas of the panels.

- Samples taken from poorly consolidated areas sometimes exhibited low as-fabricated strength but were always severely degraded during thermal cycling.

Sol-Gel Coating of Fibers

- Candidate reaction barrier coatings for fibers in Ti matrices include metal oxides. Yttria has reportedly been successful at slowing the reaction and calcia has been predicted to be stable in Ti alloys and Ti aluminides.

- Sol-Gel techniques are a potentially simple and inexpensive method to produce metal oxide coatings on the fibers.

- Coating Process:
  - *SCS-6* as a substrate (availability)
  - *Metal Alkoxide Precursors:* Yttrium and calcium methoxyethoxide in methoxyethanol (15-20%) were chosen.
  - Steps:
    1. Dilute Precursor
    2. Dip the Fiber
    3. Evaporate solvent and hydrolyze the alkoxide (gel)
    4. Pyrolyze at high temperatures (600-700C)
    5. Repeat many times (10-50) for thick, uniform coating

- The same techniques were used to place the coatings on a quartz substrate and their identity was verified using x-ray diffraction.

Yttria Coating on SCS-6
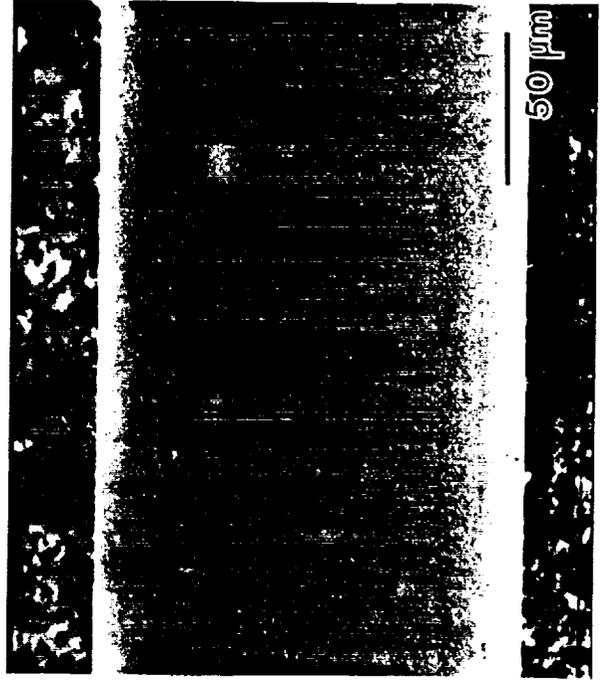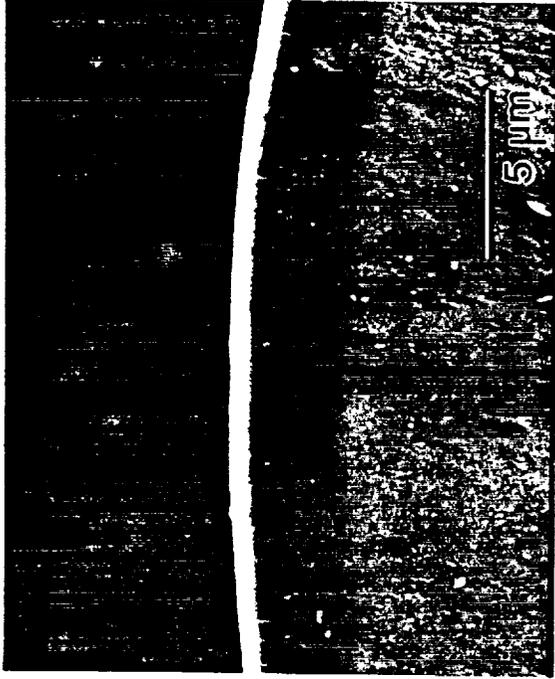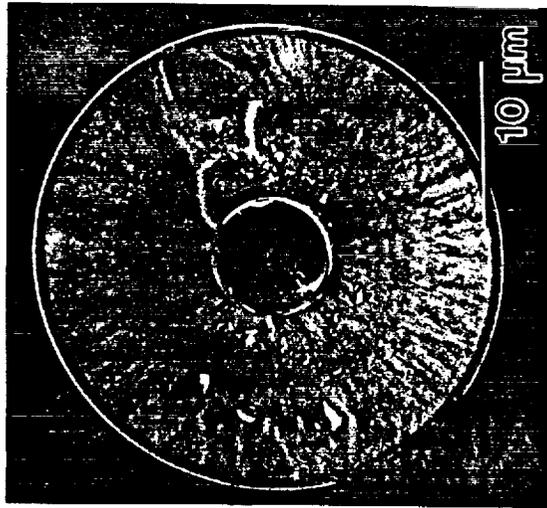
Thickness of Yttria Coating
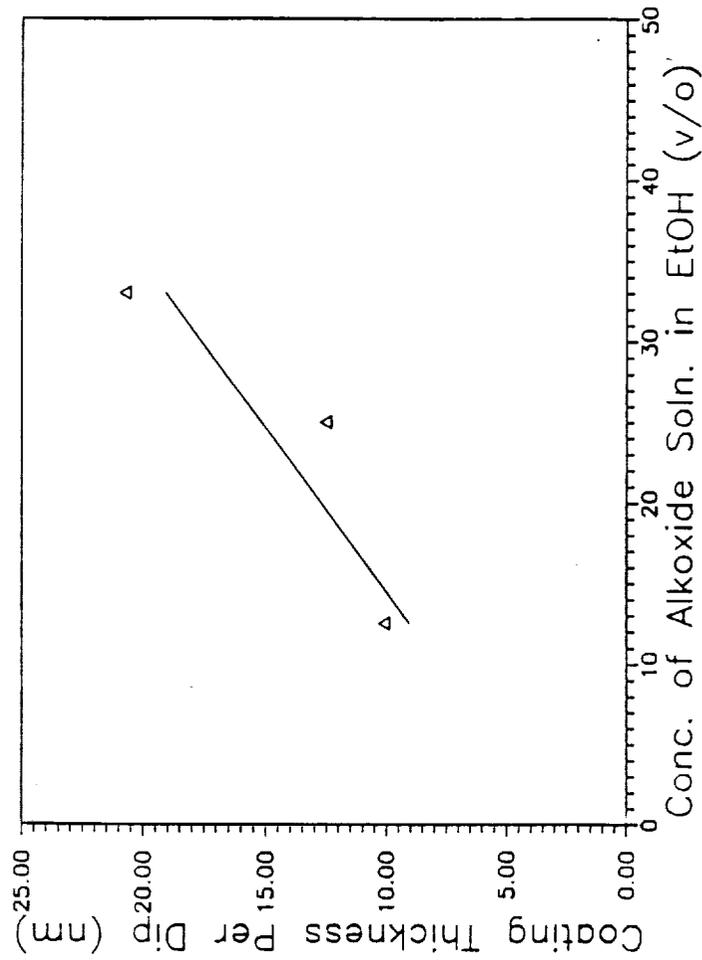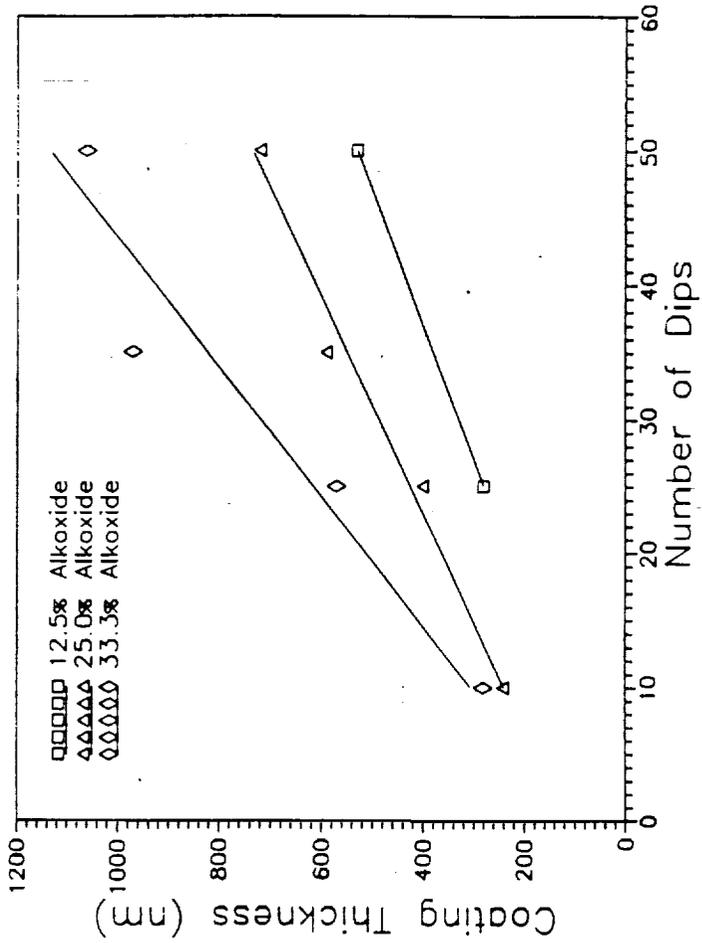
Coated Fibers in CP Titanium
Exposed at 800C for 100h
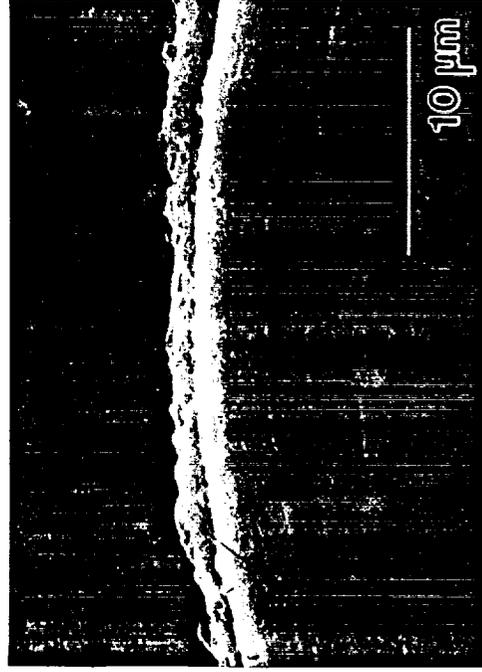
SCS-6
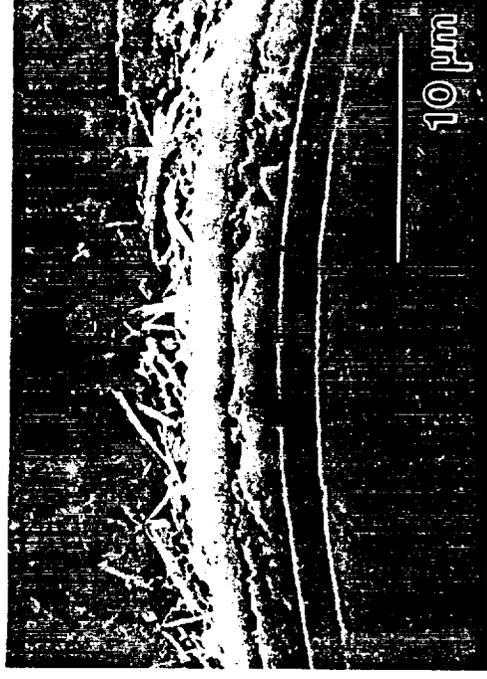
TiB$_2$/SCS-6

Y$_2$O$_3$/SCS-6

CaO/SCS-6

Summary (Sol-Gel Coatings)

- Yttria and calcia have been successfully coated onto SCS-6 fibers by this process.

- The coatings appear to be crack-free, dense and strongly adherent.

- They have been produced up to 1 micron in thickness but thicker layers are possible.

- The coatings offer protection to the underlying fiber from reaction with CP Ti at 800C for times up to at least 100 hours.

Future Work

- Further investigation of the effect of thermal exposures including longer-term, lower temperature treatments to establish a realistic operational temperature range for this material.

- Investigation of long-term environmental effects during exposure.

- Determine the effectiveness of certain metal oxide coatings as reaction barriers in Ti-1100.

Project 11   Quantitative Characterization of the Spatial Distribution of Particles in Materials: Application to Materials Processing

J.B. Parse and J.A. Wert

Objectives

In earlier phases of the present project, the objective was to devise new mathematical methods for microstructural analysis, providing new capabilities for assessing the nature of particle distributions in materials. In the final year of the project, the objective has been to apply the newly developed analysis methods to the problem of fragmentation and dispersal of oxide films in consolidated PM aluminum alloys.

Current Status

This project is complete; the student was awarded a Ph.D. degree in May 1992.

Salient Results

1.   The newly developed analysis procedures are capable of identifying inhomogeneity in the oxide fragment distribution in a consolidated PM aluminum alloy.

2.   Analysis of a variety of hot working processes has revealed that fragmentation and dispersal of oxide films occur gradually during deformation processing.

3.   Triaxial deformation processes (forging + rolling or cross-rolling) fragment and disperse the oxide films more effectively than plane strain deformation processes (rolling).

4.   Deformation processing schedules that include triaxial deformation steps early in the processing schedule appear to more effectively fragment the oxide films.

5.   Reducing the hot working temperature, even for a small strain interval early in the processing schedule, is predicted to more effectively fragment the oxide films.

Presentation Graphics Captions

1. Title. Topics to be presented.

2. Processing Steps For PM Al Alloy Sheet. Provides a description of the processing steps used to produce the PM materials for experimental investigation.

3. Oxide Incorporation In Powder Metallurgy Al Alloys. Illustrates the manner in which oxide films on the surface of powder particles are incorporated into PM products.

4. Objectives of Study. States the objectives of the experimental portion of the research project and gives the alloy composition.

5. Processing Conditions. Summarizes the hot working methods used for deformation processing. The path labels listed in this table are used in subsequent plots and tables.

6. Analysis Steps. Describes the steps used in performing microstructural analysis on each sample.

7. SEM Micrographs of Forged, and Forged + Rolled Materials. Illustrates the variety of oxide fragment distributions obtained in the experimental materials. Notation "L" indicates that the micrograph is normal to the longitudinal direction on the processed sheet; "T" indicates that the micrograph is normal to the long transverse direction on the processed sheet. The short transverse direction is vertical in all micrographs.

8. Typical Analysis Results. Illustrates a few analysis results for 3 hot working conditions. R70 and F50R84 have similar effective strains, but the degree of oxide fragmentation and dispersal is greater for the deformation path that involves triaxial deformation (F50R84) than for the path that involves only plane strain deformation (R70). Higher strain (F50R95) produces further fragmentation and dispersal of the oxide film.

9. Typical Analysis Results: Particle Density. Shows the variation of oxide fragment density as a function of effective strain for all of the deformation paths. The paths providing triaxial strain produce the highest fragment density.

10. Typical Analysis Results: Hermann Plot. Shows the direction associated with each processing step in terms of Disorder/Order and Cluster/Disperse coordinates.

11. Oxide Dispersal Parameter Definition. Schematic diagram that illustrates the definition of oxide fragment length and gap, and how these are combined to give the dispersal parameter.

12. Oxide Fragment Length and Gap Results. Shows oxide fragment size and edge-to-edge gap as functions of effective strain, for all deformation processing paths employed.

13. Oxide Dispersal Parameter Results. Shows the variation of oxide dispersal parameter as a function of effective strain for all processing paths employed. Note that oxide fragment dispersal is improved for paths that incorporate triaxial strain steps (forging + rolling and cross-rolling) compared to plane strain paths (rolling).

14. Summary and Processing Recommendations. A short list that presents salient observations and recommendations for improved oxide fragmentation and dispersal during deformation processing.

Fragmentation and Dispersal of Oxides During Processing of a PM Aluminum Alloy

J.B. Parse[*] and J.A. Wert

Department of Materials Science and Engineering

University of Virginia

[*] Ph.D. May 1992

Topics

- Introduction and Objective
- Alloy and Processing Conditions
- Microstructures
- Analysis Results
- Processing Recommendations

Processing Steps for PM Al Sheet

- **Gas atomize**
- **Classify**
- **Cold press to about 70% of full density**
- **Vacuum degas (753 K) and hot press to full density**
- **Forge, Roll, Forge + Roll, Cross-Roll to fragment and disperse oxide particles**
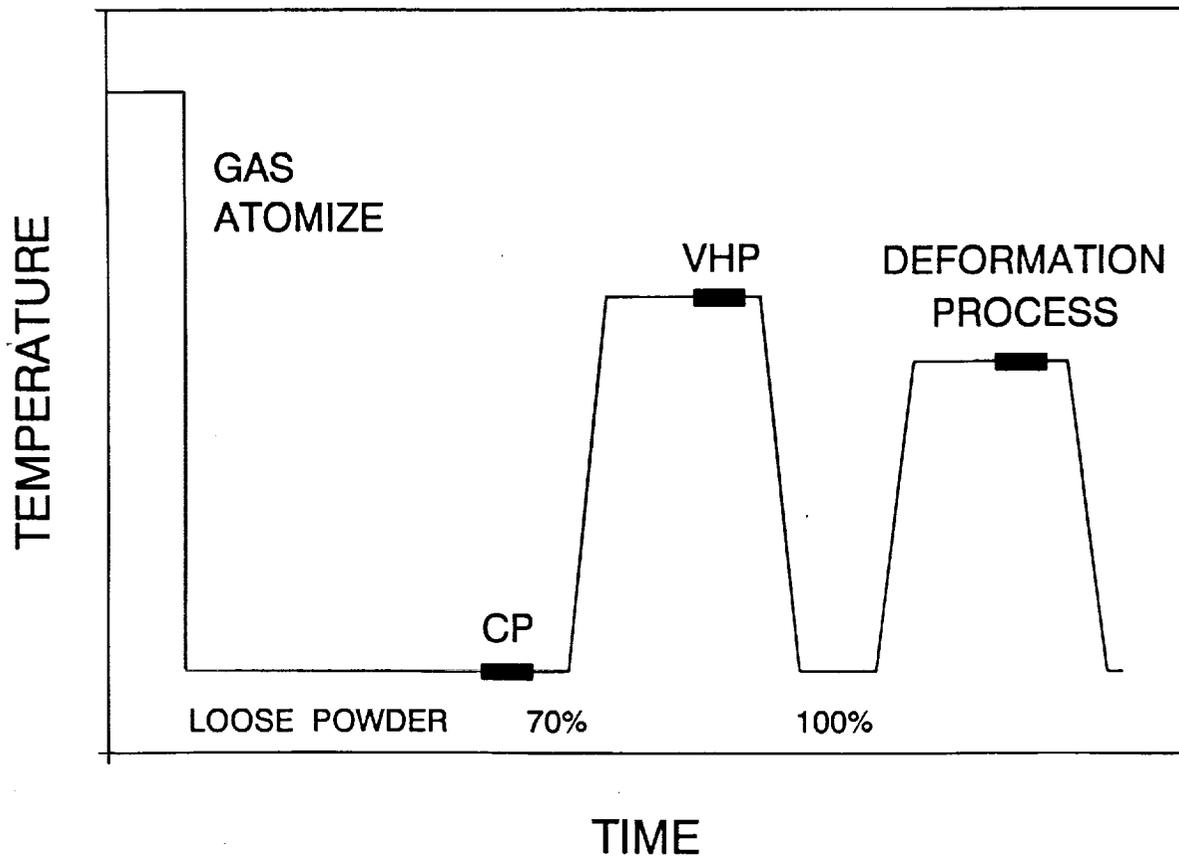
Oxide Incorporation in Powder Metallurgy Al Alloys

- Oxide film forms on Al alloy powders during gas atomization
- Fragmented oxide film is incorporated into consolidated alloy
- Oxide film is hydrated
- Presence of hydrogen in consolidated alloy is deleterious

Vacuum hot pressed billet
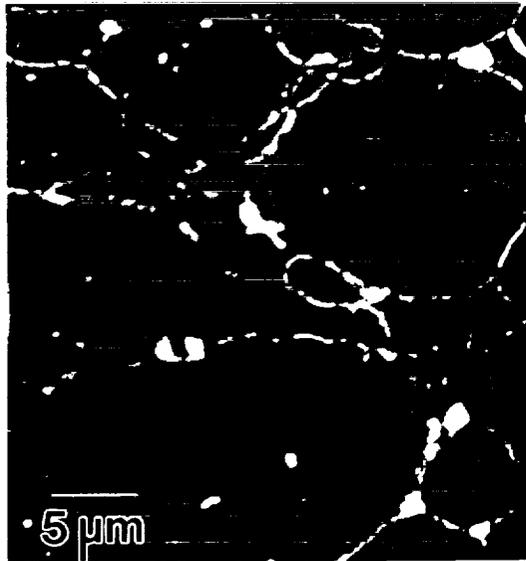
Objectives of Study

- **Determine effectiveness of deformation processing for fragmentation and dispersal of oxide films in a PM Al alloy.**

- **Use newly developed methods for assessing oxide particle distribution**

- **Make recommendations for optimization of processing**

- **Alloy investigated: Al - 2Mn - 1.25Si - 0.3V - 0.1Zr**

Processing Conditions

Deformation Path	Path Label	Total Reduction in Thickness	Total Effective Strain
Direct Rolled	R50	50%	1.46
	R70	70%	1.85
	R95	95%	3.08
Cross-Rolled	XRL95	95%	3.31
Forging	F50	50%	0.65
	F70	70%	1.85
Forged + Rolled	F50R84	84%	1.96
	F50R95	95%	3.26
	F70R95	95%	3.16

Analysis Steps

- **Process PM samples**

- **Mount, polish and electropolish metallographic specimens**

- **SEM micrographs**

- **Record x - y position of each oxide particle in micrograph**

- **Quantitative analysis of particle distributions**
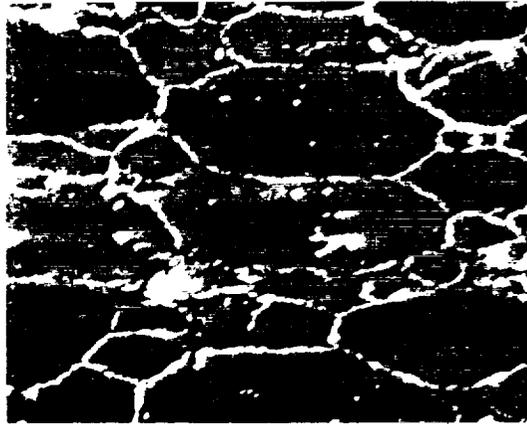
(a) Forged, 50% reduction.   (b) Forged, 70% reduction.

(c) Forged to 50%; rolled to 88% (L).   (d) Forged to 50%; rolled to 88% (T).
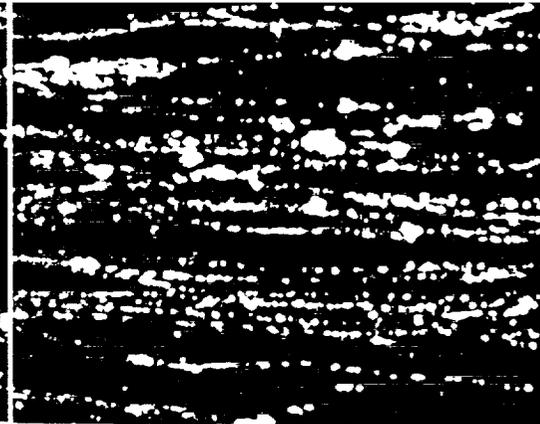
(e) Forged to 70%; rolled to 95% (L).   (f) Forged to 70%; rolled to 95% (T).

10 μm

Figure 17(a-f). SEM micrographs of forged, and forged- and rolled material.

Typical Analysis Results

Deformation State	R70	F50R84	F50R95
Effective Strain	1.85	1.96	3.26
Oxide Fragment Density ($1/\mu m^2$)	0.33	0.39	0.56
Nearest Neighbor Distance (μm)	0.97	0.78	0.84
Horizontal Neighbor Distance (μm)	1.3	1.4	1.4
Vertical Neighbor Distance (μm)	2.1	1.9	1.5

Typical Analysis Results : Particle Density
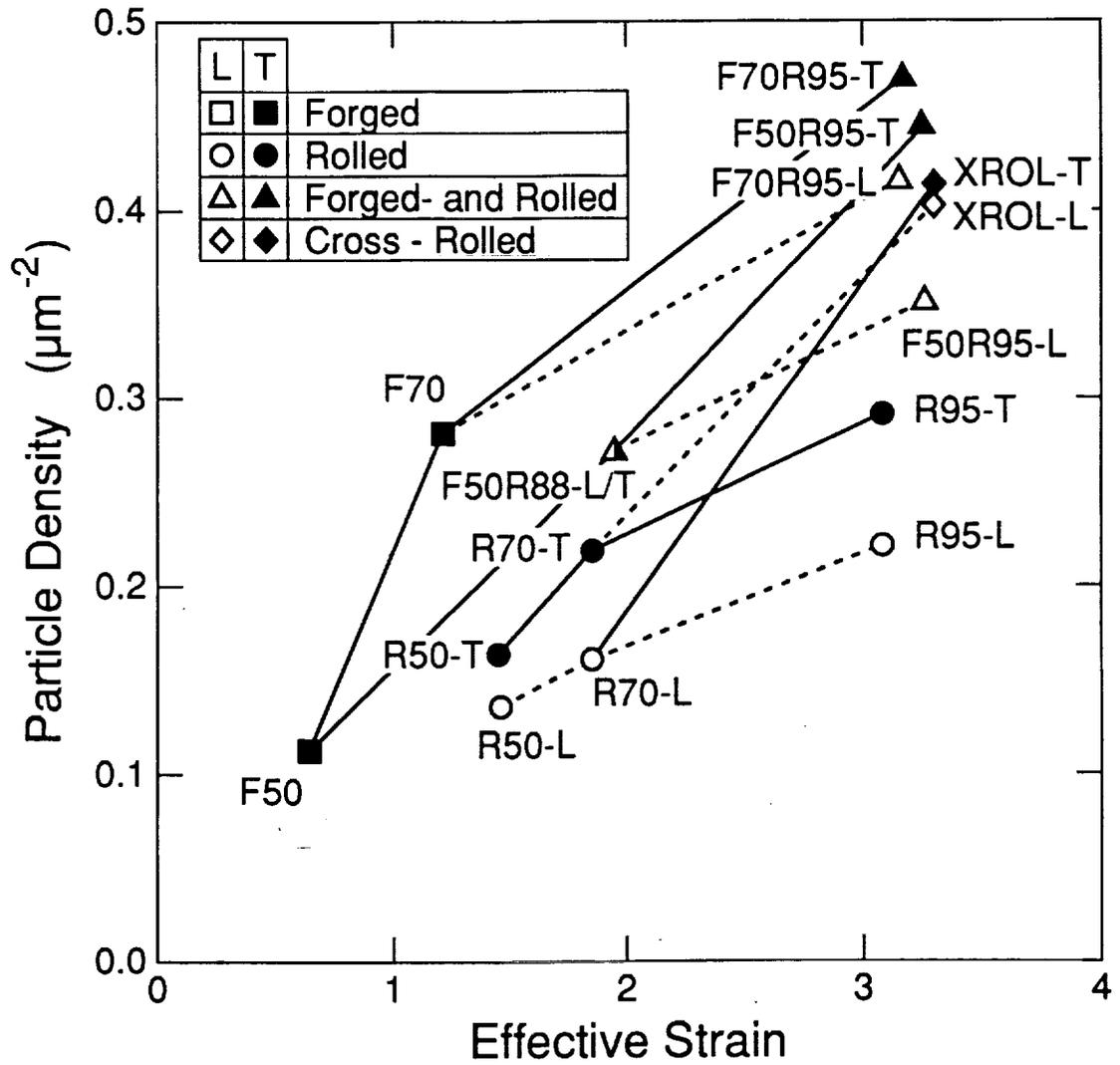
Typical Analysis Results : Hermann Plot
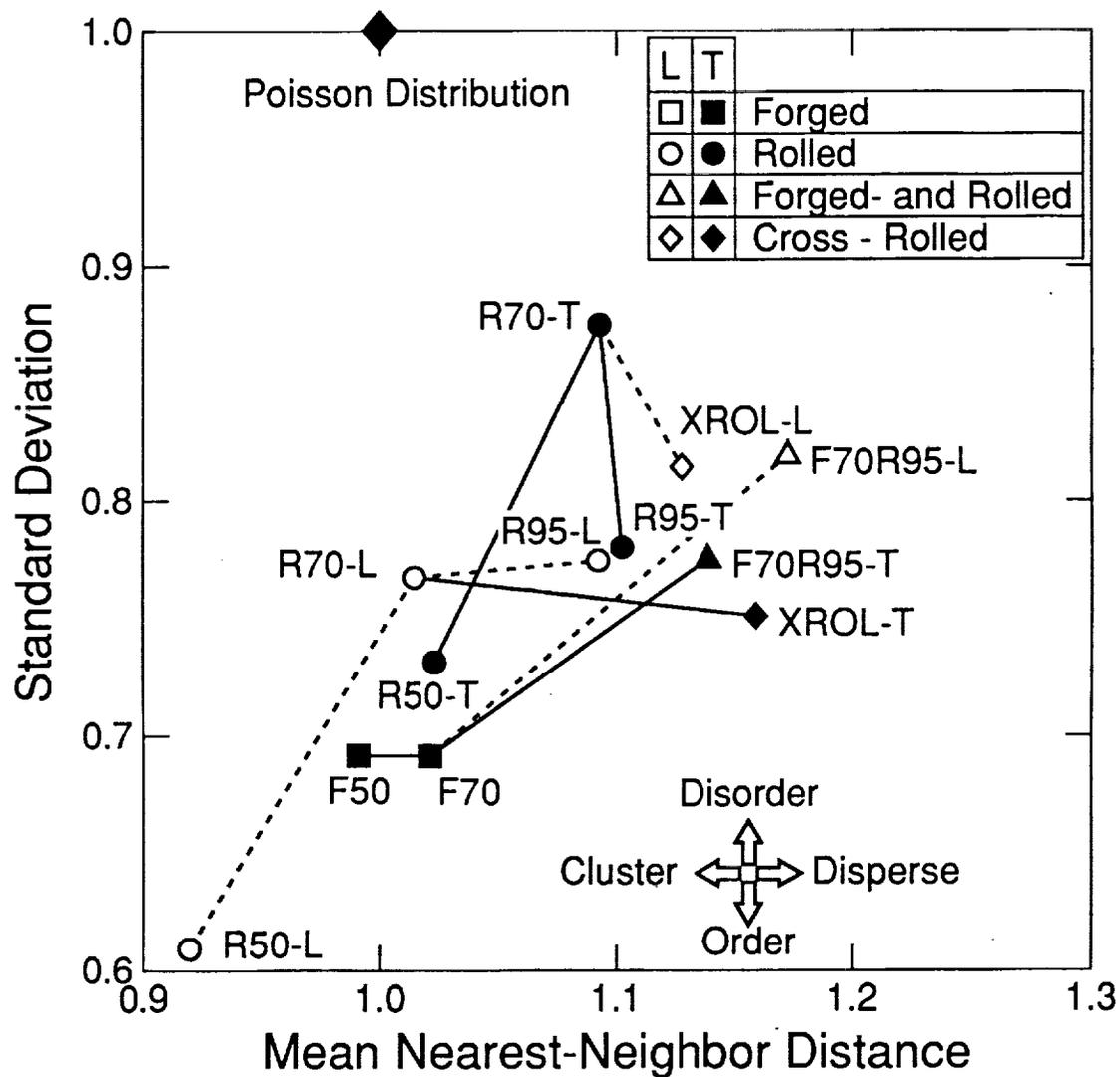
Oxide Dispersal Parameter Definition

- **Original continuous oxide film is broken into fragments**
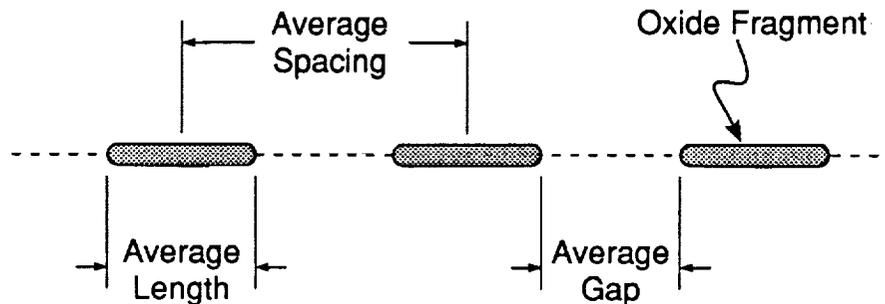
- **Oxide fragment spacing determined from measurements**

- **Oxide fragment length determined by calculation**

- **Gap between oxide fragments = spacing - length**

- **Dispersal parameter defined as gap / length**

Oxide Fragment Length and Gap Results
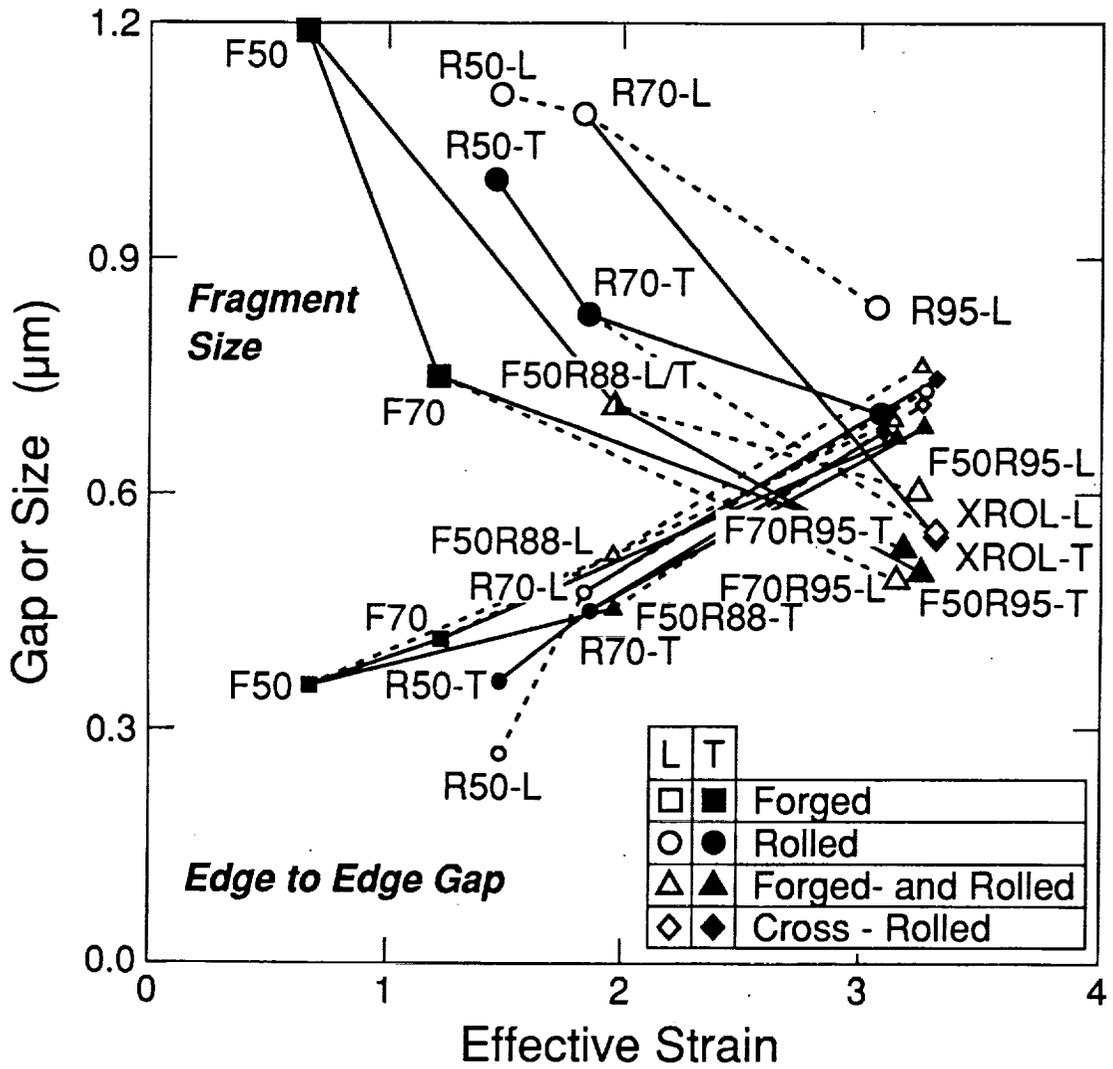
Oxide Dispersal Parameter Results
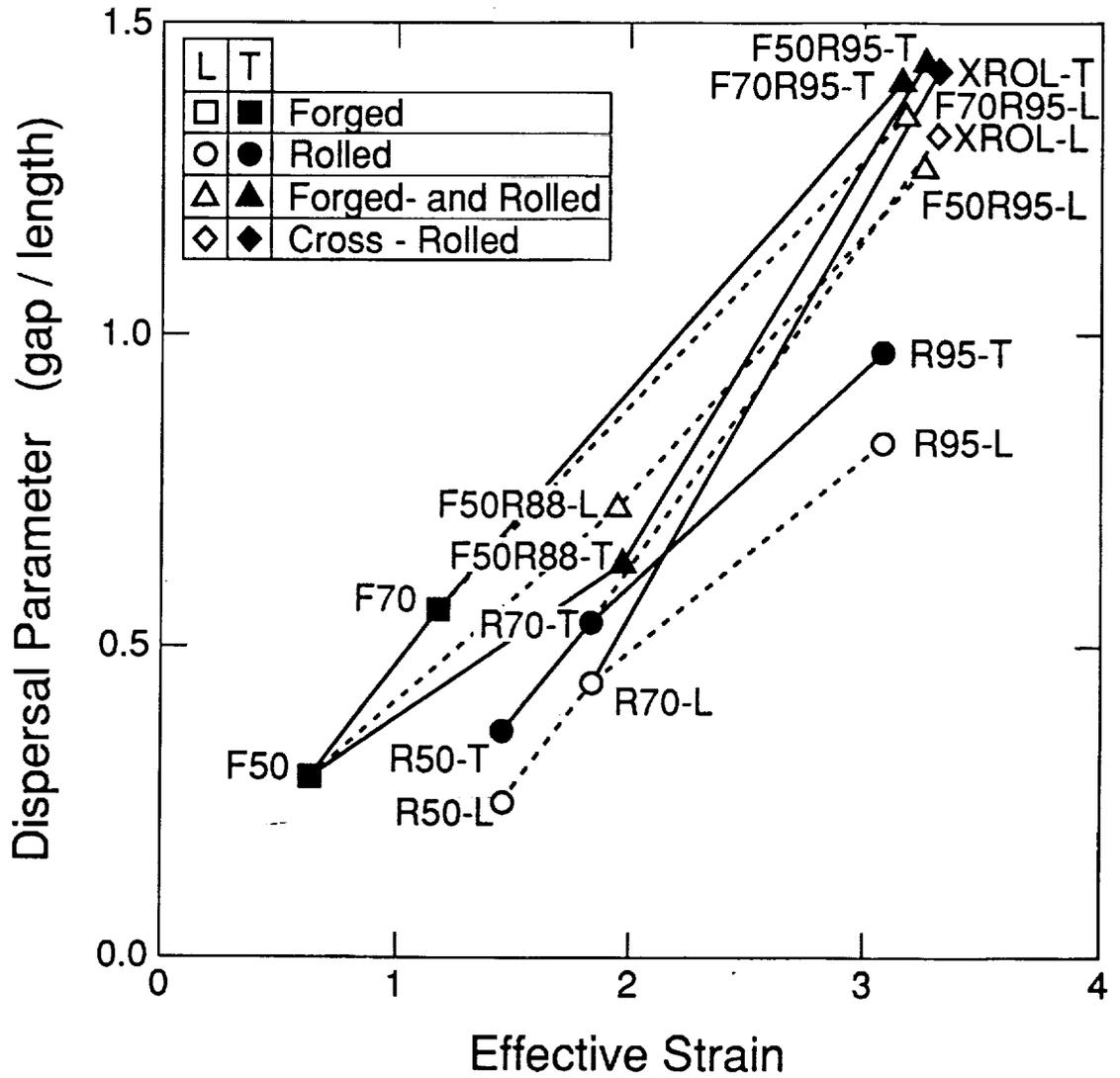
Summary and Processing Recommendations

- Newly developed analysis procedures are capable of identifying inhomogeneity in oxide fragment distribution.

- Fragmentation and dispersal of oxide fragments occur gradually during deformation processing.

- In the alloy investigated, the average oxide fragment length does not decrease below about 0.5 μm, which is attained at an effective strain near 3.

- In the alloy investigated, the edge-to-edge gap between oxide fragments increases monotonically with strain.

- Triaxial deformation processes (forging + rolling or cross-rolling) fragment and disperse the oxide films more effectively than plane strain deformation.

Project 12   Processing and Superplastic Properties of Weldalite™ Sheet

Mark Lyttle and John A. Wert

Objectives

The objective of this research is to identify the mechanisms of microstructural evolution during processing and superplastic forming, with the goal of enhancing the superplastic behavior of Weldalite sheet. Knowledge of the mechanisms of microstructural change can be used to address problems of directionality and variability in the superplastic properties of similar alloys. Modeling of microstructural evolution can provide guidelines to improve processing and superplastic forming of the material.

Current Status

This project is currently in its middle stages. All experimental procedures have been developed and about half of the planned TEM work has been conducted. The initial modeling has been completed and further refinements will be necessary to relate the effect of processing and forming on the microscopic changes and their effect on macroscopic strain.

Important Results

1. Weldalite behaves similarly to other continuously recrystallized superplastic materials. During the period of initial straining the primarily low-angle boundary deformation microstructure transforms into a microstructure containing primarily high-angle boundaries, that facilitate subsequent superplastic extension.

2. Grain rotation processes driven by superplastic straining induce microstructure and texture transformations in Weldalite sheet that are essentially identical to those previously observed in simpler Al-Zr-Si and Al-Cu-Zr-Si alloys.

3. The model of grain boundary slip as the mechanism responsible for the grain structure evolution simulates behavior that corresponds favorably with that observed experimentally.

4. The model of intragranular slip as the mechanism responsible for the grain structure evolution has no discernible correlation with the behavior observed experimentally.

Future Work

1. Most TEM work for uniaxially strained samples should be finished during the summer of 1992.

2. Biaxially strained samples will be prepared using forming facilities at NASA-LaRC, and x-ray texture and limited TEM analyses will be performed on these materials.

3. As more experimental data are accumulated, suitable refinements for the grain rotation models model should be discovered. These refinements will indicate what direction the investigation into the effects of processing should proceed.

Presentation Graphics Captions

1. Title. Topics to be presented.

2. Objectives. States the primary focus of the research and the long term goals for this research.

3. Overview of Superplasticity. Summarizes the principal requirements for superplasticity and describes the process of continuous recrystallization.

4. Continuous Recrystallization. Schematic representation of the change in microstructure during continuous recrystallization from a rolling texture to a texture suitable for superplastic behavior.

5. Composition and Optical Observations. Composition of the alloys used and data on thickness of deformation bands and size of second phase particles.

6. Maximum Elongation Testing. Testing reveals optimal temperature and strain rate range for superplasticity. Schematic stress-strain curve for a superplastic material with experimental strains noted.

7. TEM Grain Misorientation Map for 049 Gauge, Strain = 0.11. TEM micrograph montage at 13000x. Misorientation between adjacent grains indicated by an angle (degrees) on individual grain boundaries. Sample shown contains a relatively high

fraction of low angle grain boundaries.

8. TEM Grain Misorientation Map for 2095 Gauge, Strain = 0.47. Same format as previous slide, but sample contains a relatively low fraction of low angle grain boundaries.

9. Cumulative Distribution Plot of Misorientation in 049. Indicates the fractional distribution of misorientation angles within samples.

10. Micropole Figures for 049 Sample At Various Strains. Shows the location of the <111> poles of individual grains relative to the longitudinal direction (L) and the transverse direction (T).

11. Cumulative Distribution Plot of Misorientation in 2095. Indicates the fractional distribution of misorientation angles within samples.

12. Micropole Figures for 2095 Sample At Various Strains. Shows the location of the <111> poles of individual grains relative to the longitudinal direction (L) and the transverse direction (T).

13. Modeling of Changes in Microstructure During Superplastic Forming. Outlines the procedure used to model the two mechanisms, grain boundary sliding and intragranular slip, that could cause the microstructural evolution during initial straining.

14. Cumulative Distribution Plot Using Rotation Model 1. Indicates the fractional distribution of misorientation angles within samples. Depicts the application of grain boundary sliding model to experimental data from 049 grip section.

15. Comparison of Experimental and Modeled Micropole Figures. Compares the distribution of <111> poles between an 049 sample strained to 0.21 and that generated by applying rotation model 1 on the 049 grip section.

16. Cumulative Distribution Plot Using Slip Model 2. Indicates the fractional distribution of misorientation angles within samples. Depicts the application of intragranular slip model to experimental data from 049 grip section.

17. Conclusions and Future Work. Contains the important experimental results and evaluates the effectiveness of the two models in predicting actual behavior and the capability to recommend better processing methods.

Superplasticity of Weldalite

M.T. Lyttle and J.A. Wert
Department of Materials Science and Engineering
University of Virginia

Topics

- Introduction and Objective
- Conditions for Superplasticity
- Maximum Elongation Tests
- Superplastic Effect on Misorientation
- Modelling of Grain Boundary Rotation
- Summary and Future Work

Objectives

- Observe microstructural evolution during the initial stages of superplastic forming using transmission electron microscopy

- Develop a model to explain the changes in microstructure and examine their impact on the material's superplastic properties

- Recommend processing methods for improving superplastic properties

Overview of Superplasticity

Necessary Characteristics for Superplasticity

- Small Grain Size
- High Angle Grain Boundaries

Continuous Recrystallization

- Initial Structure Contains Mostly Low Angle Boundaries
- Concurrent Straining and Annealing
- Grain Rotations Accumulate
- High Angle Grain Boundaries Result

Summary of Prior Results:
Evolution of the Deformation Microstructure in Al-Zr-Si and Al-Cu-Zr-Si Alloys

- **Deformation Microstructure**
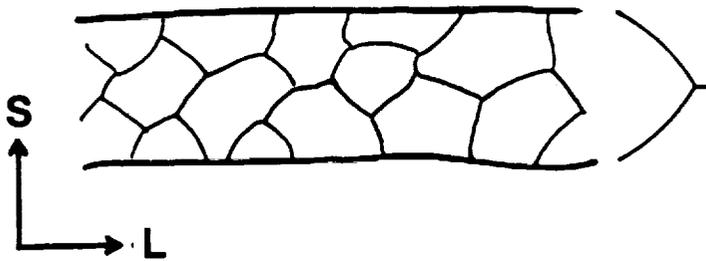
1 variant of the deformation texture

- **Annealed Microstructure**
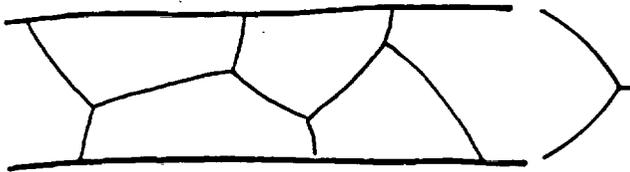
1 variant of the deformation texture

- **Concurrently Strained and Annealed Microstructure**
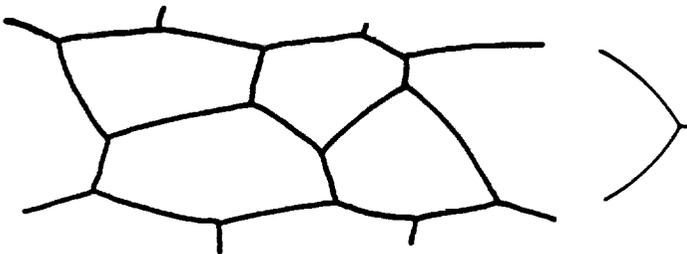
random texture

Composition and Optical Observations

	Cu	Li	Ag	Mg	Zr
x2095	4.49	1.15	.4	.37	.17
049	4.76	1.27	.37	.33	.13

x2095

Average Thickness of Deformation Bands 25 μm

Average Diameter of Particles 4 μm

049

Average Thickness of Deformation Bands 20 μm

Average Diameter of Particles 3 μm

Maximum Elongation Testing

- **Elongations of >800% were observed**
- **Temperature = 500°C**
- **Strain Rate = 6.6×10^{-4} /s**
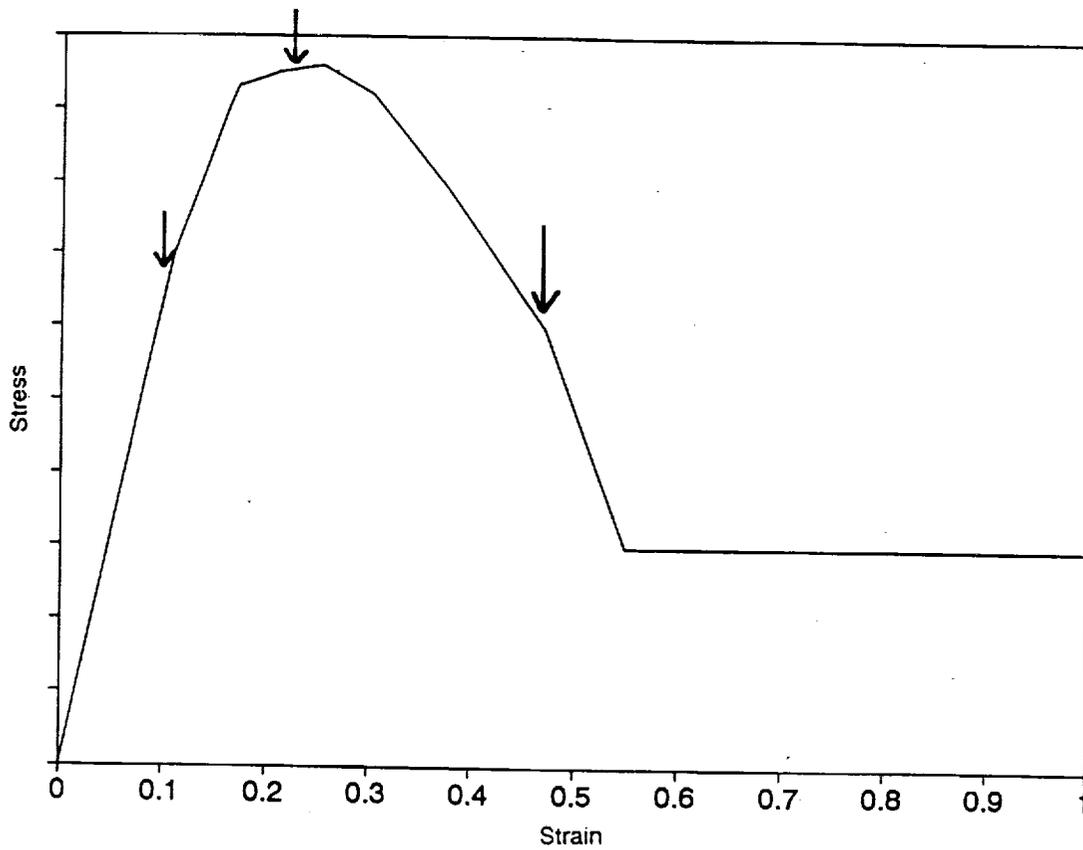
TEM Grain Misorientation Map for 049 Gauge

Strain = 0.11

TEM Grain Misorientation Map for 049 Gauge

Strain = 0.47
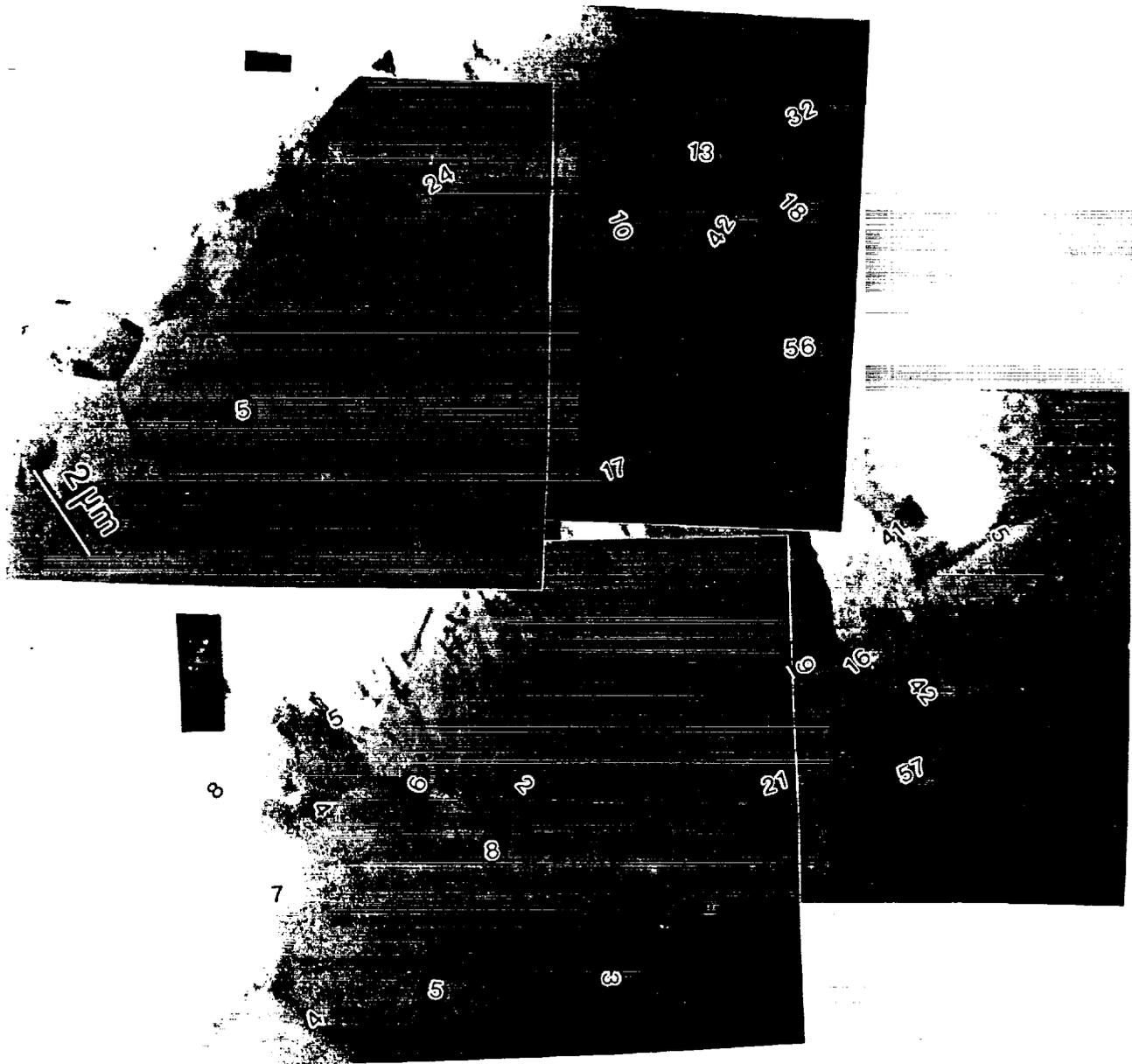
Cumulative Distribution Plot of Misorientation in 049
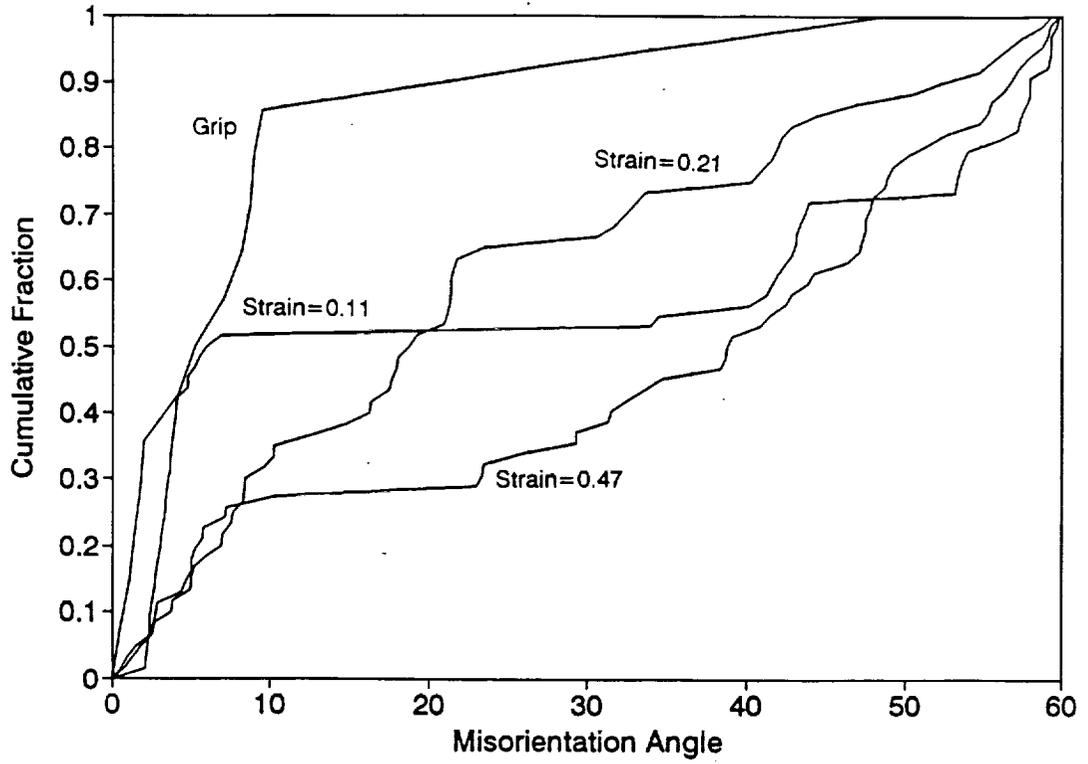
Micropole Figures for 049 Sample At Various Strains
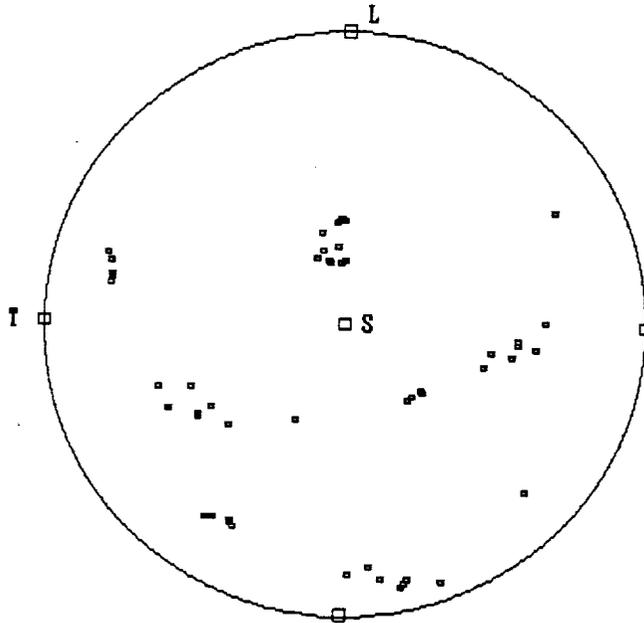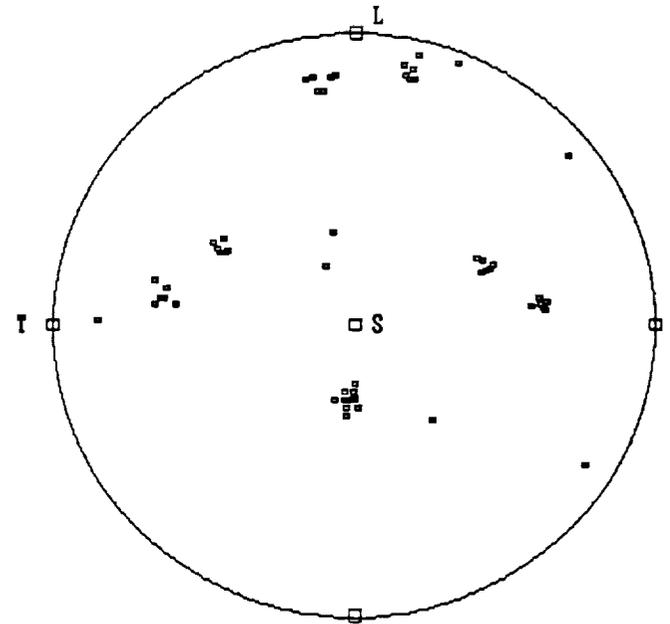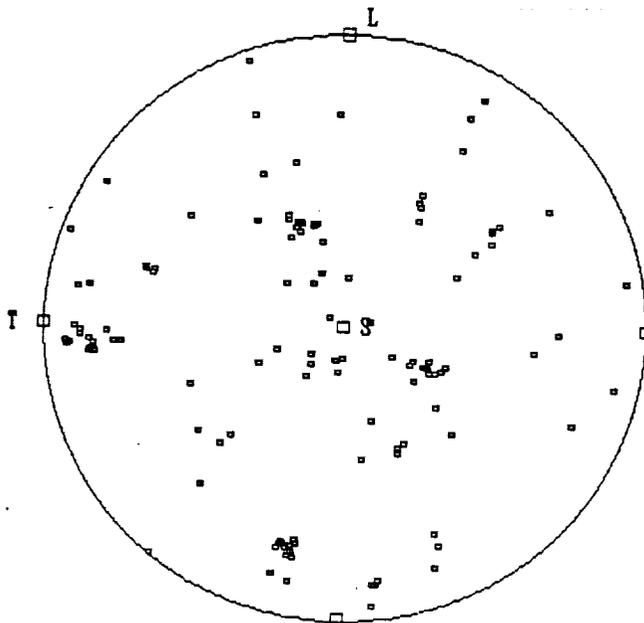
Grip
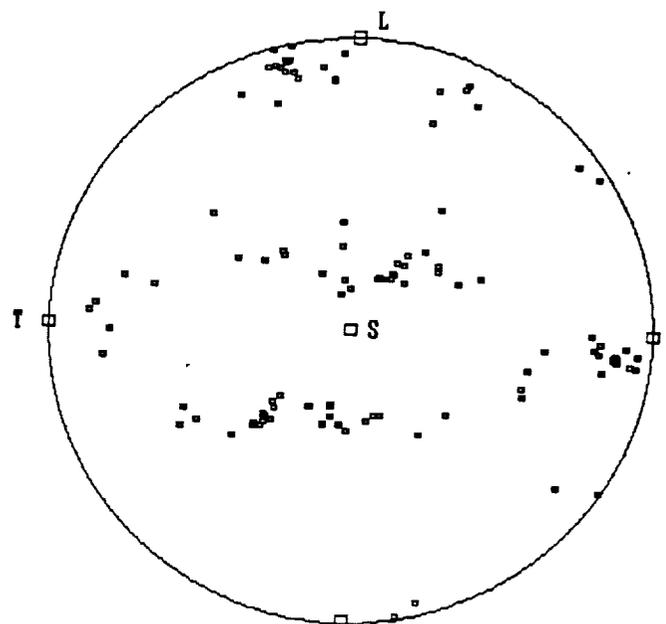
Strain=.11

Strain=.21

Strain=.47

Cumulative Distribution Plot of Misorientation in 2095
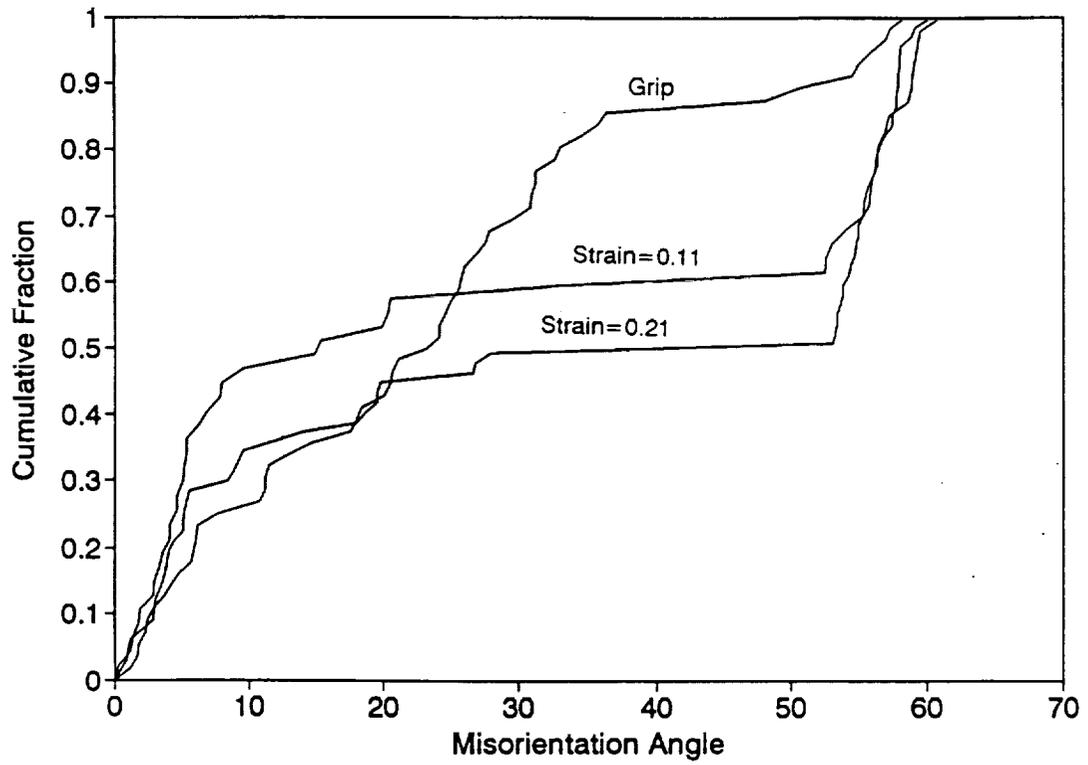
Micropole Figures for 2095 Sample At Various Strains
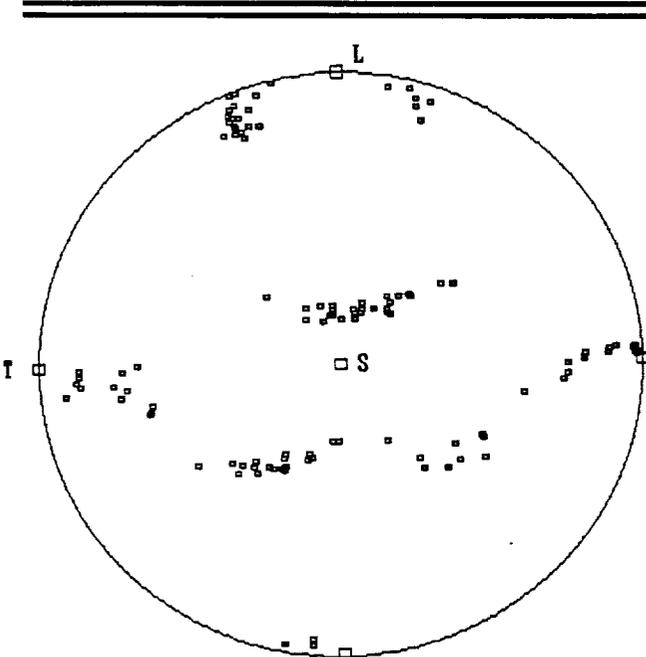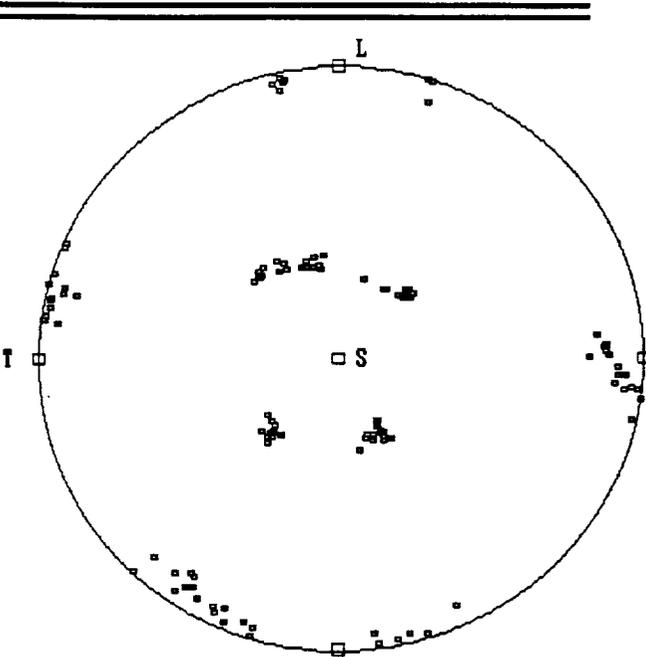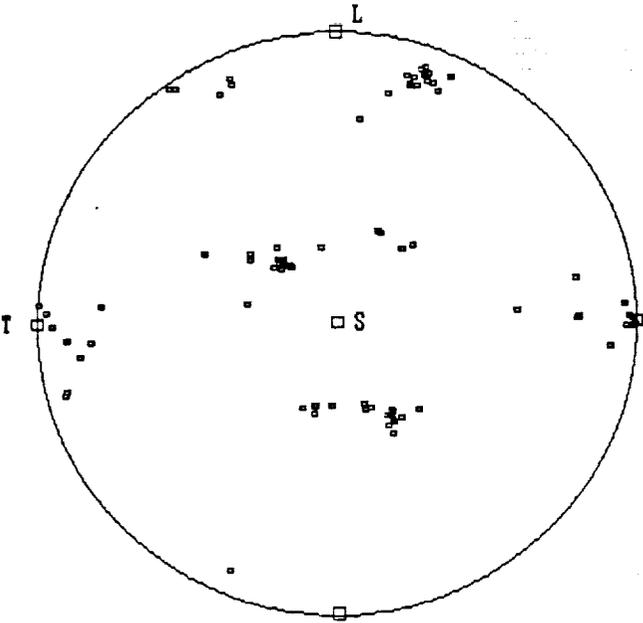
Grip

Strain=.11

Strain=.21

Modelling of Changes in Microstructure During Superplastic Forming

Model 1: Rigid Body Rotation of Grains

- Rotation Occurs by Sliding Along Grain Boundaries
- Use Initial Experimental Data for Grip Sections
- Fix an Arbitrary Angle of Rotation
- Perform Rotation Around Random Axis For Each Grain
- Examine Final Grain Orientation

Model 2: Grain Rotation Caused by Slip Within Grains

- Rotation Occurs by Intragrain Slip
- Use Initial Experimental Data from Grip Sections
- Simple Model Allows Up To Two Slip Systems In Each Grain
- Allow Each Grain To Rotate as a Single Crystal
- Examine Final Grain Orientation

Cumulative Distribution Plot Using Rotation Model 1

049 Grip, Rotations of 5,10,15,20 deg.

Grip

15 deg

10 deg

5 deg

20 deg

Cumulative Fraction

Misorientation Angle
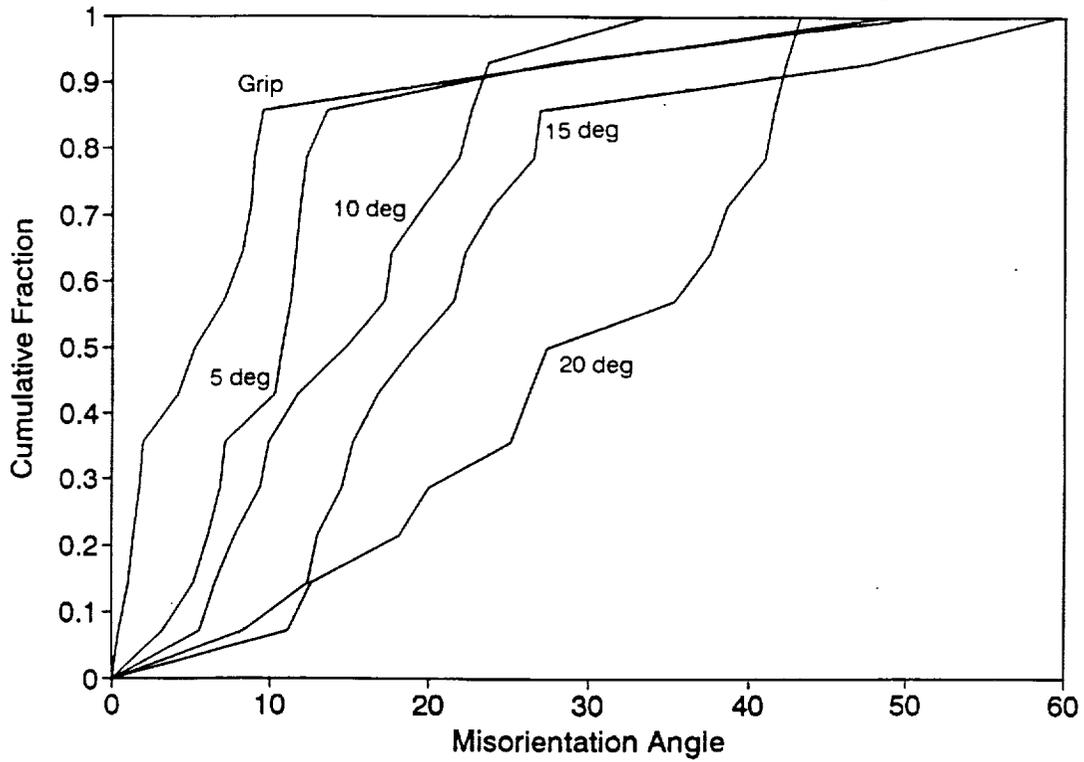
Comparison of Experimental and Modelled Micropole Figures
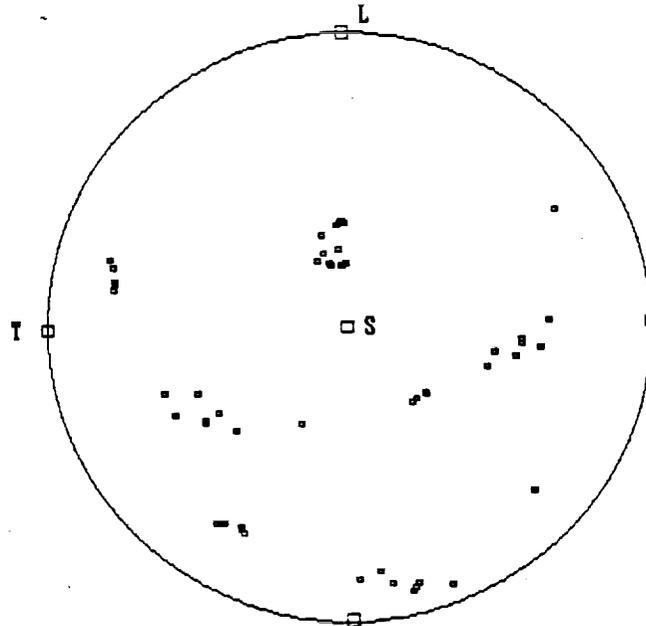
049 Grip
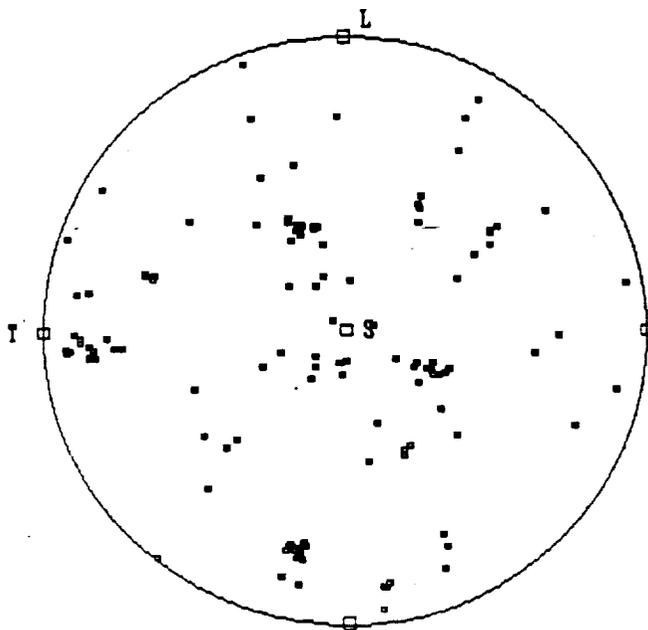
Strain=.21
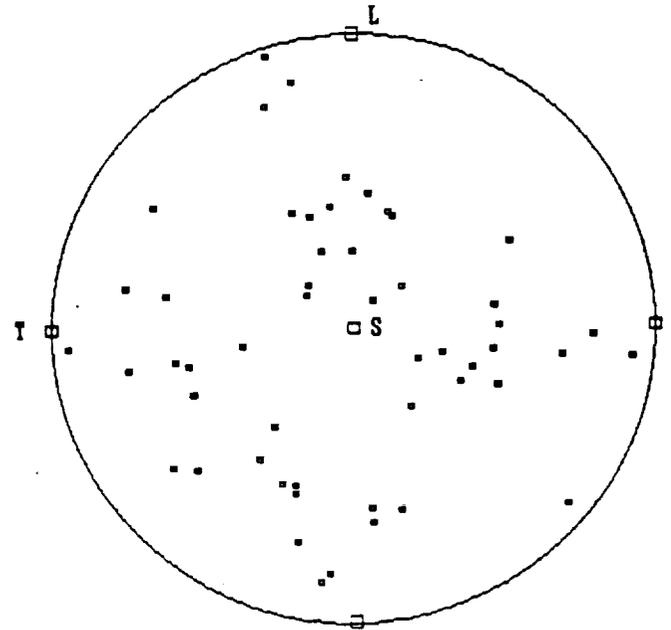
20 degrees Rotation

Cumulative Distribution Plot Using Slip Model 2

049 Grip, Maximum Duplex Slip
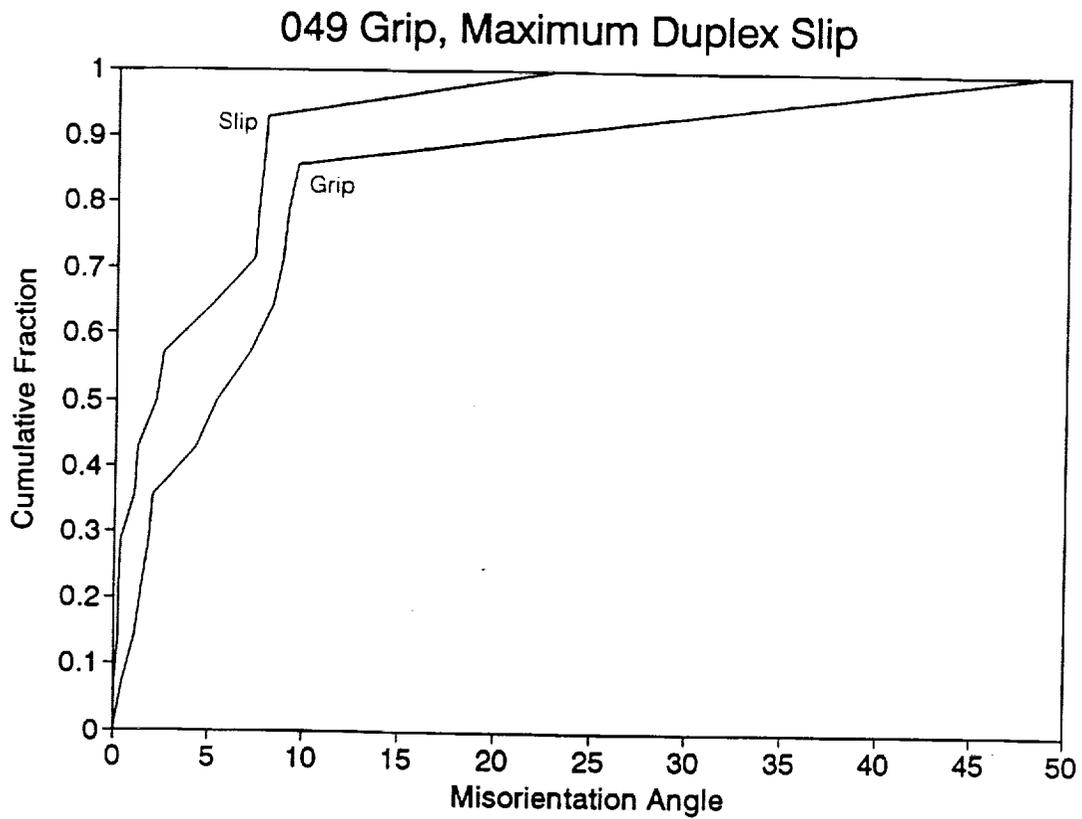
Conclusions and Future Work

- Tensile tests and TEM observations conducted at a variety of strains reveal the change in microstructure during forming

- Behavior predicted by grain boundary sliding model corresponds to experimental results

- Behavior predicted by intragranular slip model does not approximate that observed experimentally

Future Work

- Refine model to include joint contributions of grain boundary sliding and intragranular slip

- Effect of tensile axis orientation on superplastic properties
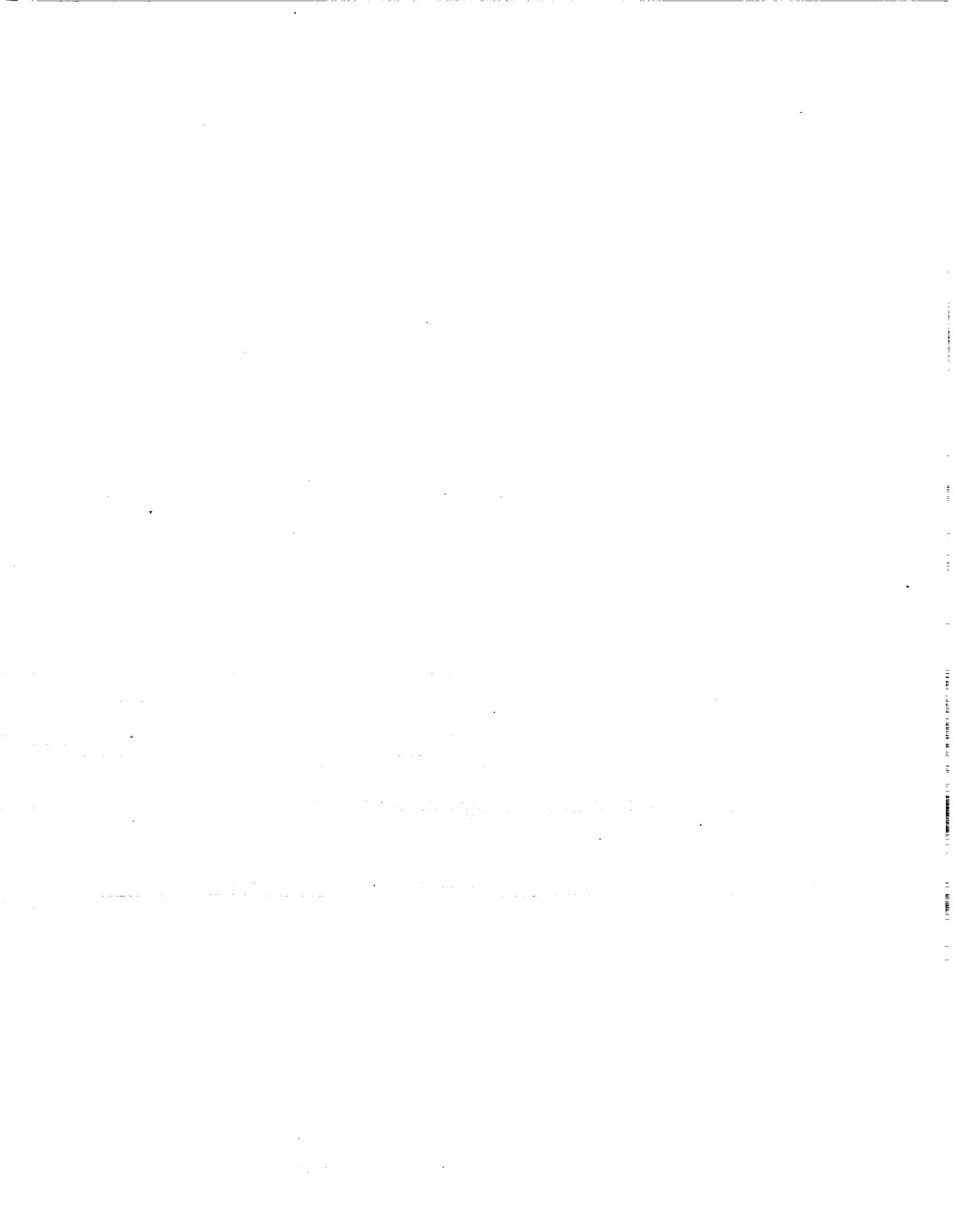
Project 13   Inelastic Deformation of Metal Matrix Composites

C.J. Lissenden, M.-J. Pindera and C.T. Herakovich

Objective

The long term objective of this investigation is to attain a complete understanding of the inelastic response of metal matrix composites subjected to arbitrary, biaxial load histories. The core of the research program is a series of biaxial tests conducted on advanced metal matrix composite systems using a combined axial/torsional load frame. These tests involve primarily tubular specimens and include tension, compression, torsion, internal pressure and combinations thereof in order to critically assess the inelastic response of advanced metal matrix composites in a wide temperature range.

Current Status

To date, a large number of biaxial tests have been conducted on both unidirectional $[0_4]$ and angle-ply $[\pm 45]_s$ silicone carbide/titanium laminated tubes. The loadings include combinations of tension and torsion.   Experimental results have been compared with analytical results obtained from a micromechanical model. The method of cells was used to predict the elastic properties, initial yield surfaces, effect of fiber/matrix debonding and inelastic responses. Damage to the composite has been seen to occur at low stress levels and have deleterious effects on the material response. Some of the effects of damage are: degraded axial and shear stiffnesses, accelerated initiation of matrix yielding and large coupling of inelastic strain components.

Recent Findings

Some material configurations may have an initial imperfect fiber/matrix bond due to the fabrication cool down.

Degradation of the interfacial bond precedes and accelerates yielding of the matrix for certain loadings.

The $[\pm 45]_s$ tubes exhibited a highly nonlinear tensile response due to both damage and plasticity. The axial elastic modulus exhibited damage induced degradation of as much as 50% during cyclic loading to successively higher axial stress levels.

Large axial plastic strains occur during increments of torsional loading at high levels of constant axial stress when damage is present in $[\pm 45]_s$ tubes.

The axial shear response of a $[0_4]$ tube exhibits a sudden loss of shear stiffness believed to be caused by the combined effects of damage and plasticity.

Current analytical models are incapable of quantitatively predicting the inelastic response of MMC subjected to arbitrary biaxial loading.

Milestones

Develop a model to account for damage as well as matrix plasticity in metal matrix composites. A debonding model along the lines of those presented by A. Needleman and V. Tvergaard will be used along with a critical stress criterion for matrix cracking. The model will be implemented using a repeating unit cell elastoplastic finite element analysis.

Experiments will be conducted on $[0_4]$ tubes whereby the tube will be subjected to internal pressure then a torsional load applied. This will enhance the study on the damage mechanisms present, as well as being the first step in verifying the above mentioned model.

Presentation Graphics Captions

1. Title slide: Inelastic Deformation of Metal Matrix Composites.

2. The goal of the study is to develop a model to accurately predict the inelastic deformation of metal matrix composites (MMC).

3. The development of MMC: elastoplastic theories and damage.

4. Types of damage to titanium matrix composites include: fiber/matrix debonding, matrix microcracking and fiber cracking and breakage.

5.   Problem Definition: inelastic response of MMC is due to damage and matrix plasticity. The objective of the study is to develop a (unit cell finite element) model to predict the inelastic deformation of MMC.

6.   The experimental program consists of biaxial tests conducted on [0] and [±45]ₛ SCS-6/Ti-15-3 tubes. Type I tests are consecutively increasing axial tests with a torsional load applied at the maximum axial load. Type II tests are the inverse of Type I tests.

7.   Micromechanical predictions are based on the method of cells with the features indicated.

8.   Fiber and matrix constituent response and properties are presented.

9.   Figures show the predicted influence of the normal and tangential bonding parameters on the elastic properties of a unidirectional composite.

10.   Figure shows the predicted influence of the normal and tangential bonding parameters on the axial and shear moduli of a [±45]ₛ laminate.

11.   Figures show the experimental response of [0₄] tubes to Type I and Type II loadings. The symbol AE refers to acoustic emissions.

12.   Figure shows the experimental response of a [±45]ₛ tube to a full cycle of Type I loading. Notice the accumulation of axial strain during torsional loading. The table gives the maximum stress level applied in each increment.

13.   Figures show the experimental axial and shear responses from Test#18 (shown on previous slide). Notice the permanent shear strain and the large axial strain accumulated during the shear loading stage (B-D).

14.   Figures present a summary of the experimental stiffness degradation data for both [0₄] and [±45]ₛ tubes.

15.   Predicted yield surfaces including residual thermal stresses, for both [0₄] and [±45]ₛ laminates.   Effect of bonding parameters is shown, and some experimentally determined points plotted.

16.   The summary presents the three main thrusts of the project.

17.   Future experiments include the internal pressurization of [0₄] tubes.

18.   Conclusions are presented for the work to date.

INELASTIC DEFORMATION OF METAL MATRIX COMPOSITES

by

C. J. Lissenden

C. T. Herakovich

M.-J. Pindera

Dept. of Civil Engineering and Applied Mechanics

University of Virginia

NASA Technical Monitor

W. S. Johnson

July 16, 1992

UVA
APPLIED
MECHANICS

Goal

- DEVELOP MODEL TO ACCURATELY PREDICT INELASTIC DEFORMATION OF MMC

    — matrix plasticity

    — fiber/matrix debonding

    — matrix microcracking

UVA
APPLIED
MECHANICS

Overview

- Fiber reinforcement of metals

  — MMC

- Elastoplastic theories

  — Dvorak: PHA (Classical)

  — Aboudi: Method of cells (Bodner-Partom)

- Experimental evidence of damage

  — titanium matrix composites

- Development of limited damage models

- Development of a general model

Damage to Titanium MMC

- Interfacial zone damage

  — separation

  — sliding

  — microcracking

- Matrix microcracking

- Fiber cracking and breakage

Fiber/Matrix Separation

Radial Matrix Microcrack

UVA
APPLIED
MECHANICS
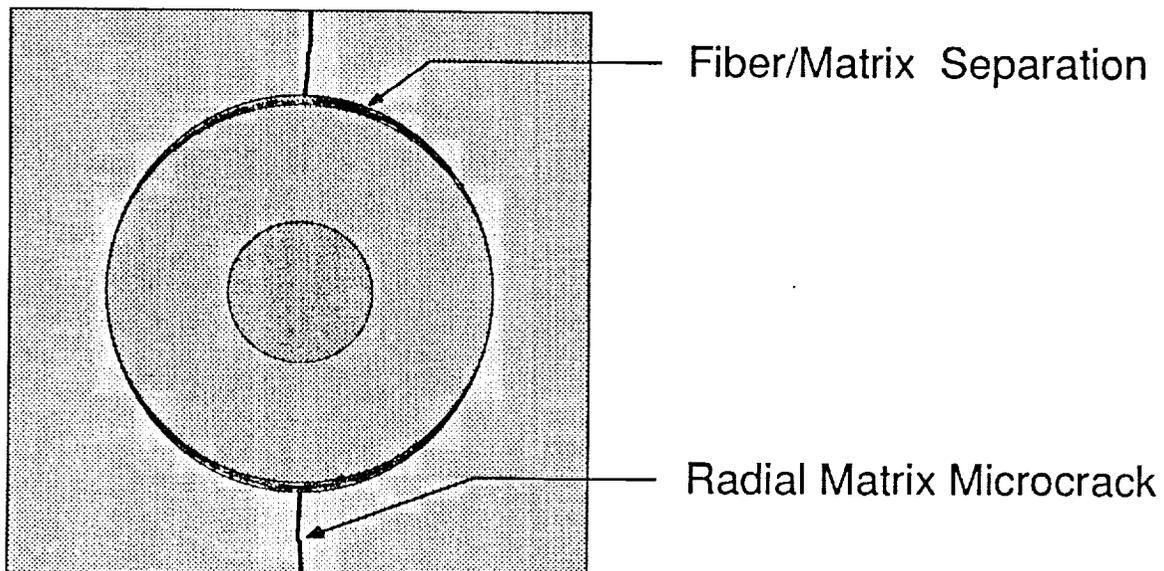
Problem Definition

- Inelastic response of MMC due to

    — matrix plasticity

    — damage

OBJECTIVE

- Delineate effects of damage and plasticity

- Develop predictive model for general loading

    — matrix plasticity

    — interfacial debonding

        • nonlinear   traction/displacement
          relation

    — matrix microcracking

EXPERIMENTAL PROGRAM

UNIT CELL F-E ANALYSIS

UVA
APPLIED
MECHANICS

Work to Date

EXPERIMENTAL PROGRAM - characterize inelastic response of SCS_6/Ti-15-3

- Tubular specimens

[0_4]

$*$ = Strain Gage

[±45]$_s$

- Biaxial loads

Type I Loading

Type II Loading

Work to Date

MICROMECHANICAL PREDICTIONS

- Method of cells

    — Bodner-Partom Plasticity

    — Mises Yield Criterion

    — Flexible Interface model

        • Thin elastic film

        • Tractions proportional to displace-ments

        • R_n and R_t

Doubly Periodic Array

Unit Cell

UVA
APPLIED
MECHANICS
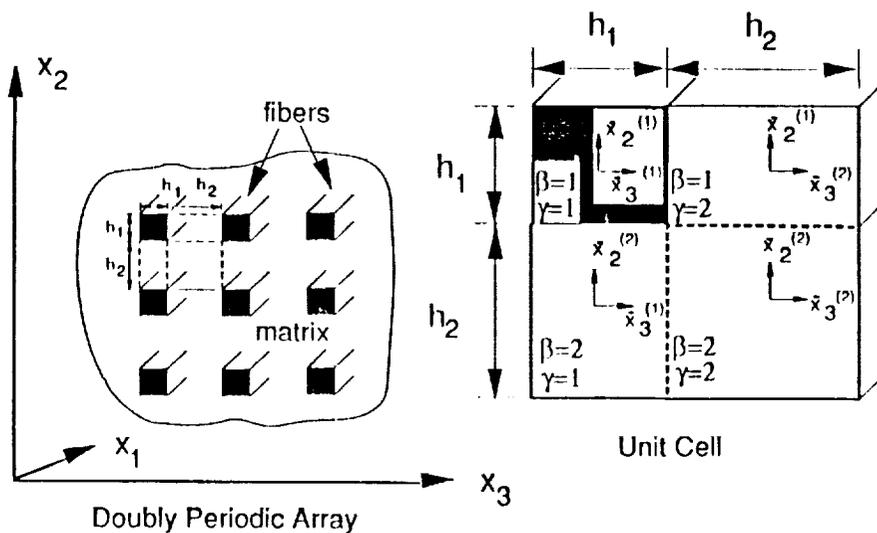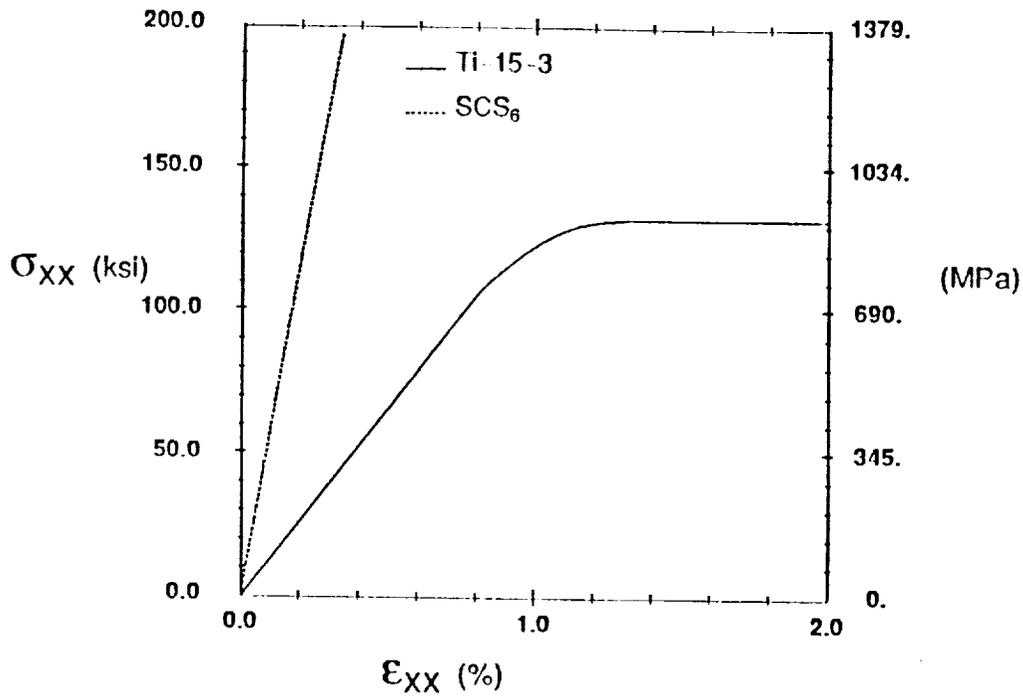
Figure 2: Constituent Properties

Table 1. Constituent Properties

Mat'l	E	G	ν	α	Y
SCS_6	58.0 msi (400.0 GPa)	23.2 msi (160.0 GPa)	0.25	$5.14 \times 10^{-6}{}^{\circ}F^{-1}$ ($2.86 \times 10^{-6}{}^{\circ}C^{-1}$)	----
Ti-15-3	13.2 msi (91.0 GPa)	4.85 msi (33.4 GPa)	0.36	$2.77 \times 10^{-6}{}^{\circ}F^{-1}$ ($1.54 \times 10^{-6}{}^{\circ}C^{-1}$)	110 ksi (758 MPa)

Bodner-Partom Parameters for Ti-15-3

D_0	Z_0	Z_1	m	n	q
$10^4 sec^{-1}$	140 ksi (965 MPa)	170 ksi (1172 MPa)	1700	7	1
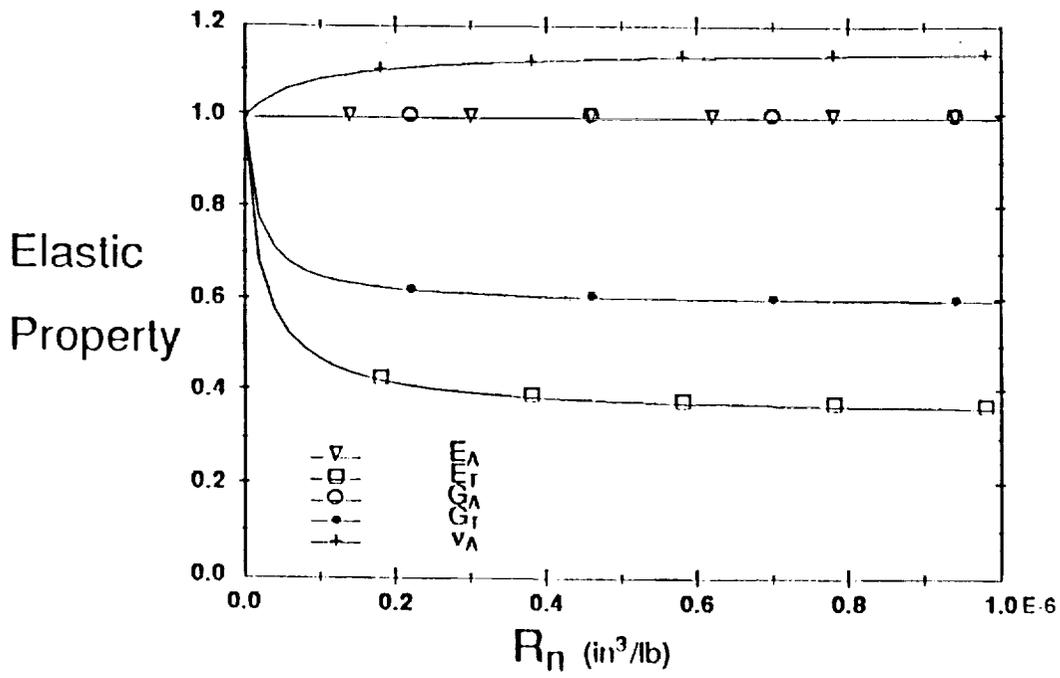
(a) R_n Variation
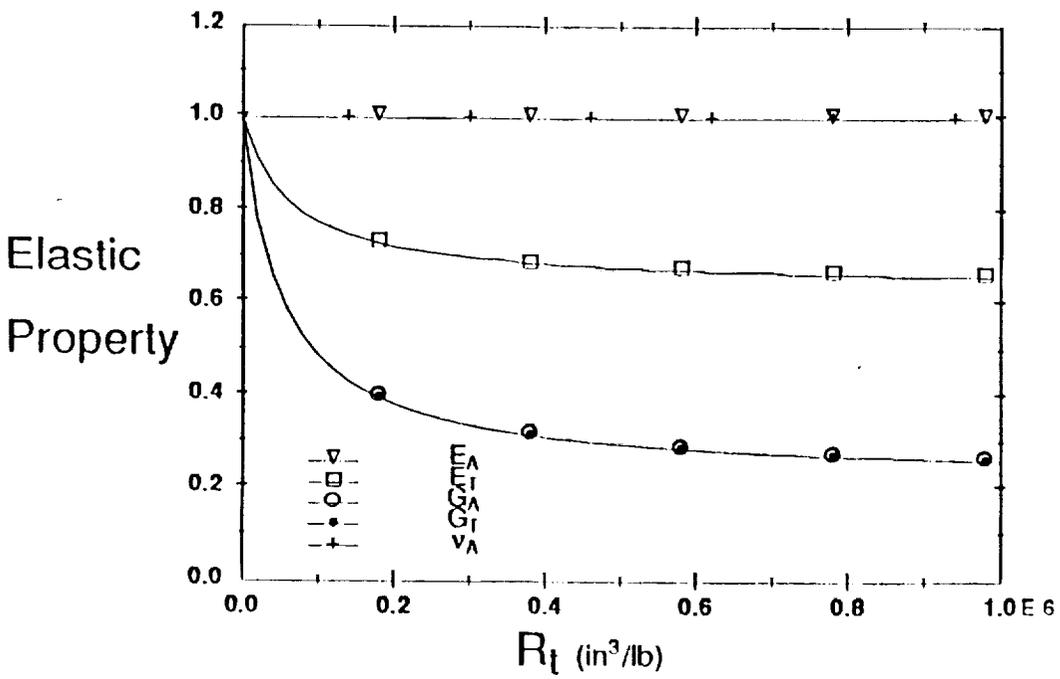
(b) R_t Variation

Figure 3: Variation in Elastic Properties of [0] SCS_6/Ti-15-3
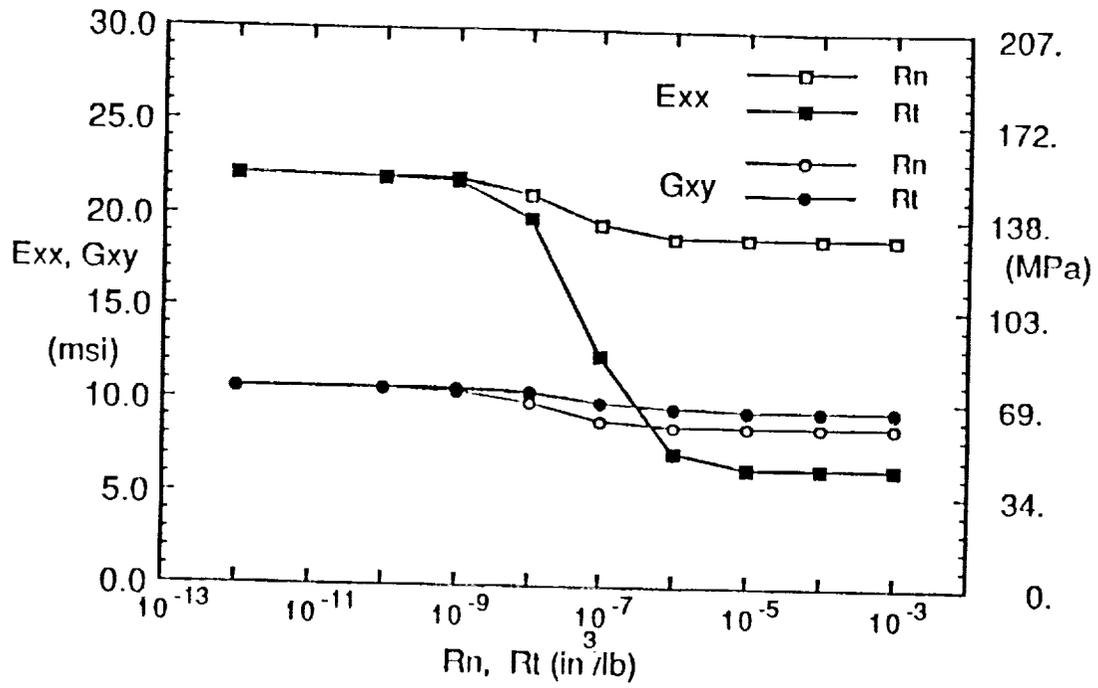
Figure 4: Moduli Variation with Debonding for $[\pm 45]_s$
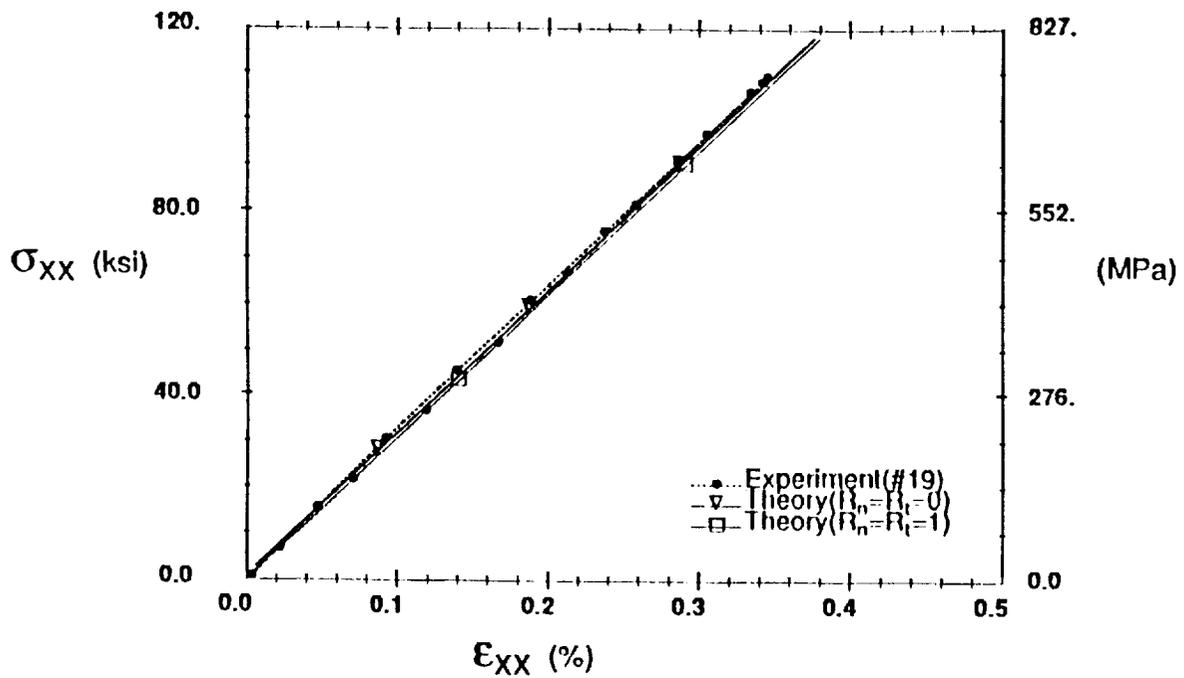
(a) Type I Loading Axial Response
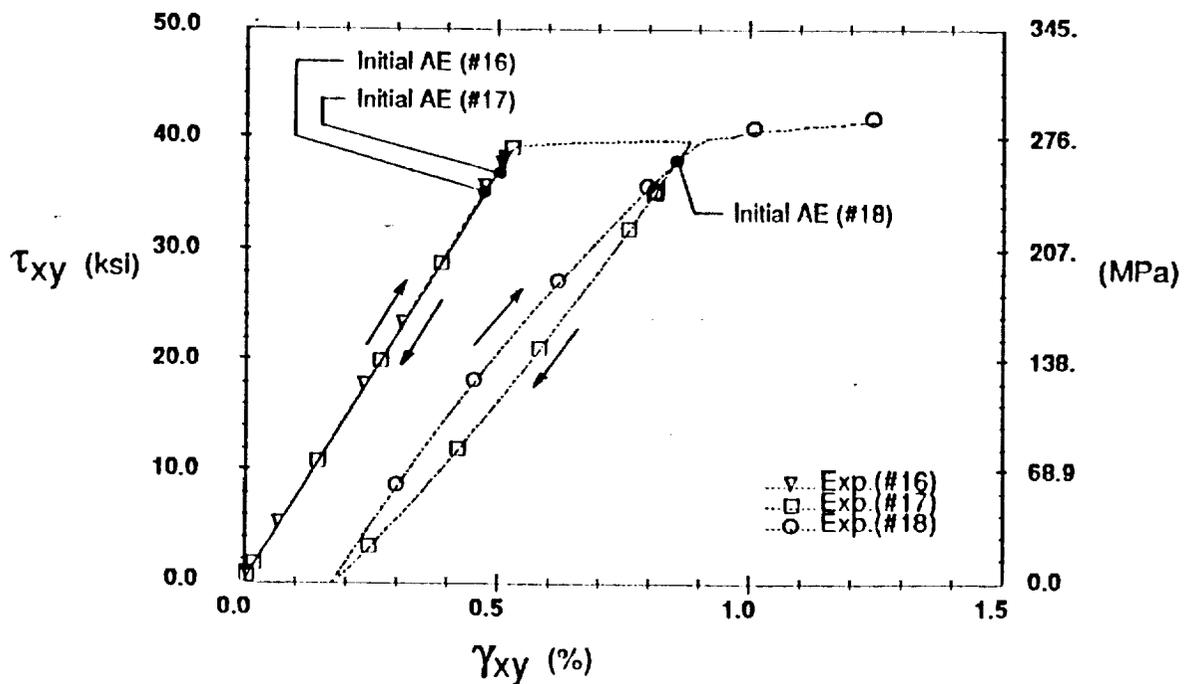
(b) Type II Loading Shear Response

Figure 7: [0_4] Experimental Results
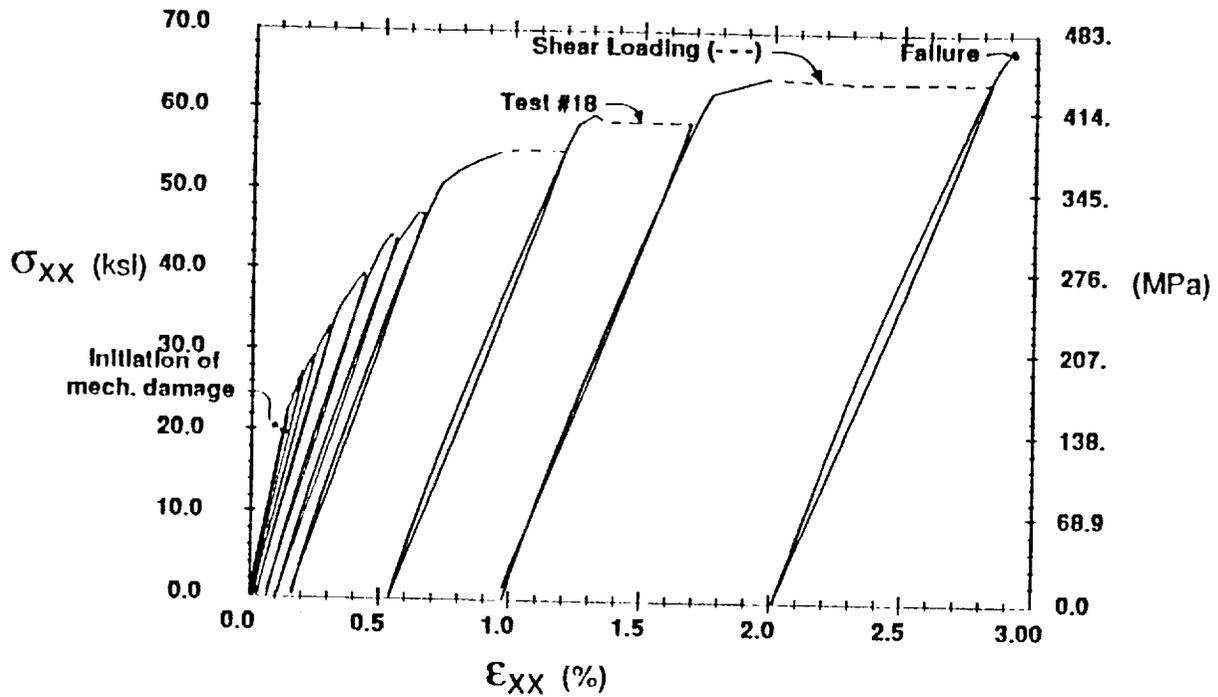
Figure 8: [±45]ₛ Type I Loading Axial Response

The chart shows σ_{XX} (ksi) on the left axis (0.0 to 70.0) and (MPa) on the right axis (0.0 to 483.) versus ε_{XX} (%) on the horizontal axis (0.0 to 3.00). Labels include "Shear Loading (- - -)", "Failure", "Test #18", and "Initiation of mech. damage".

Test #	Max. σ_{xx} (ksi)	Max. τ_{xy} (ksi)		Test #	Max. σ_{xx} (ksi)	Max. τ_{xy} (ksi)
1	3	N/A		11	27	1
2	12	N/A		12	30	2
3	N/A	5		13	33	2
4	N/A	-5		14	40	5
5	8	2		15	44	5
6	12	2		16	48	5
7	8	N/A		17	56	5
8	18	2		18	59	5
9	18	2		19	64	5
10	22	2		20	68	N/A

Table 2. [±45]ₛ Type I Loading History
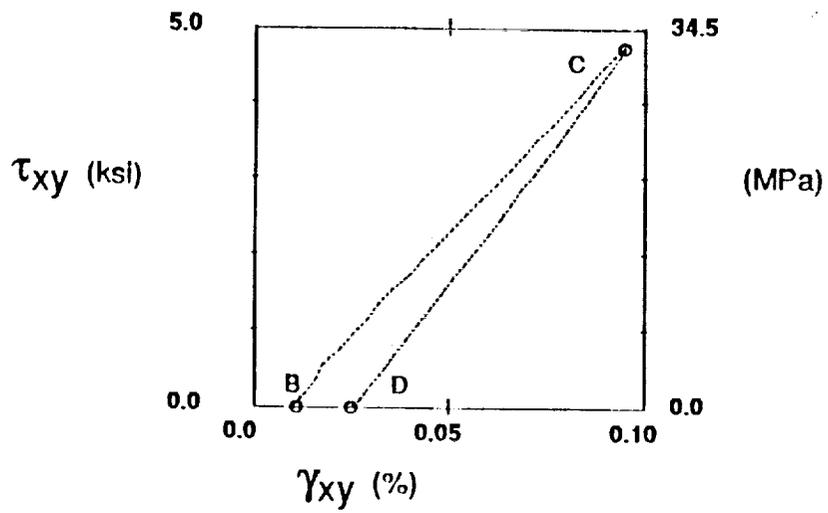
(b) Shear Response
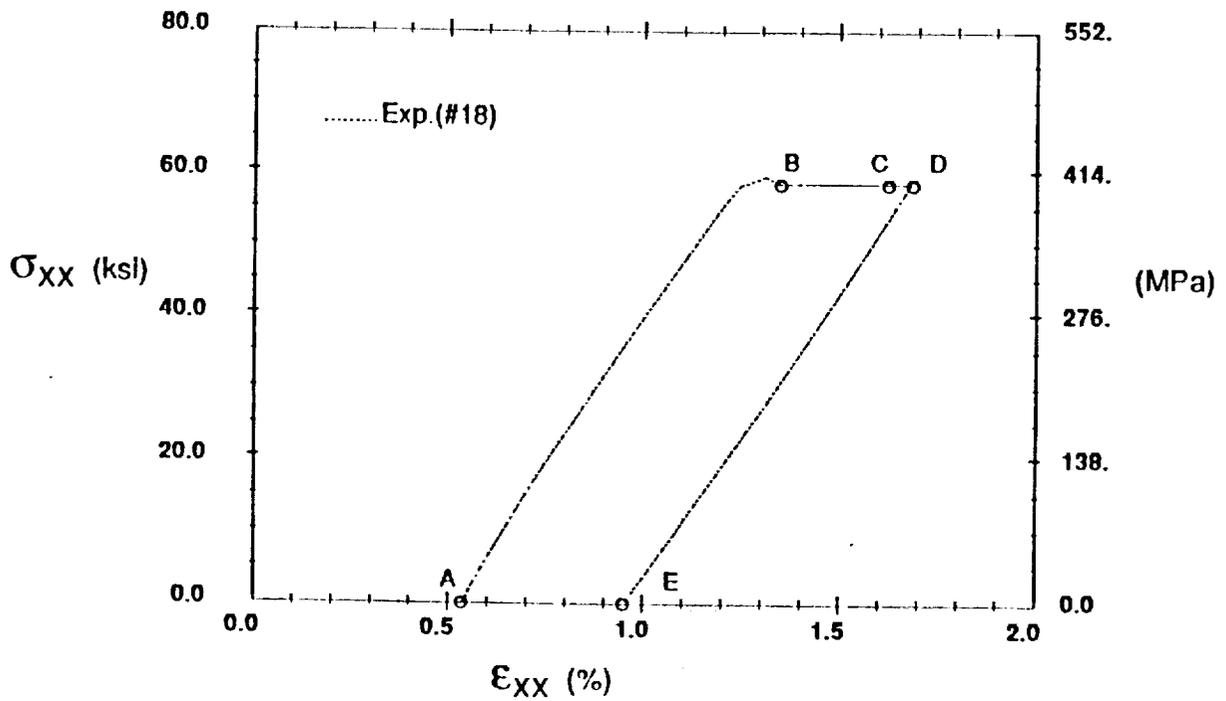
(a) Axial Response

Figure 9: [±45]$_s$ Type I Experimental Results (#18)
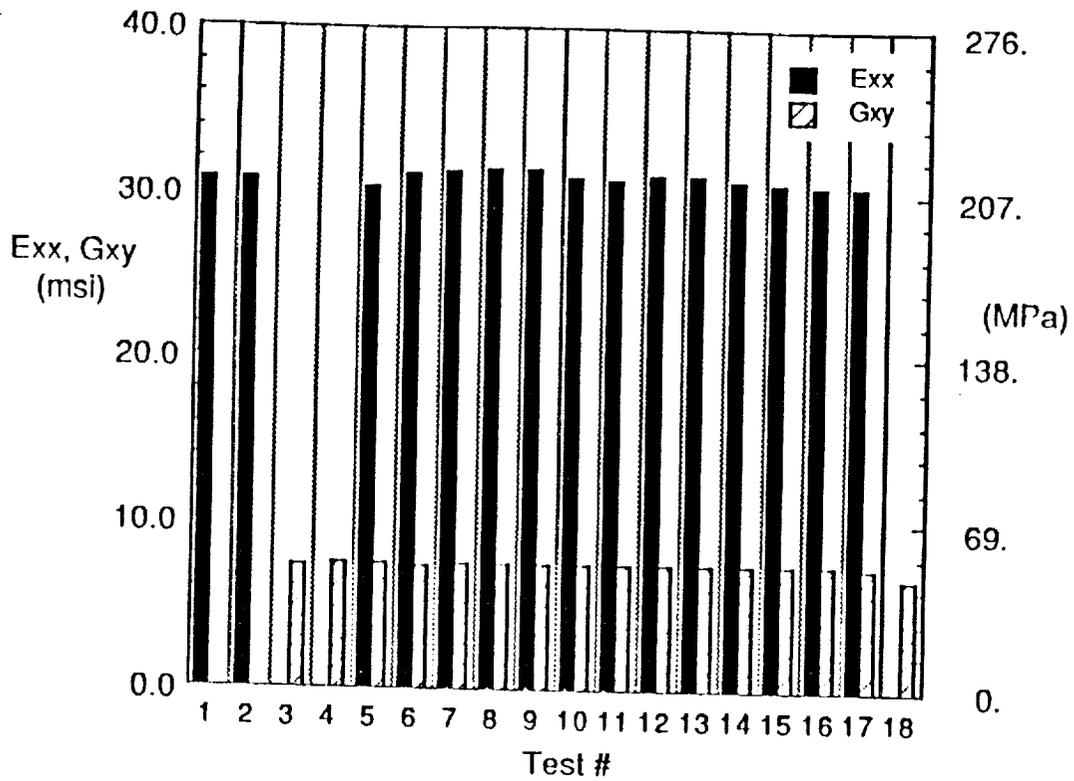
(a) $[0_4]$ Type II Loading
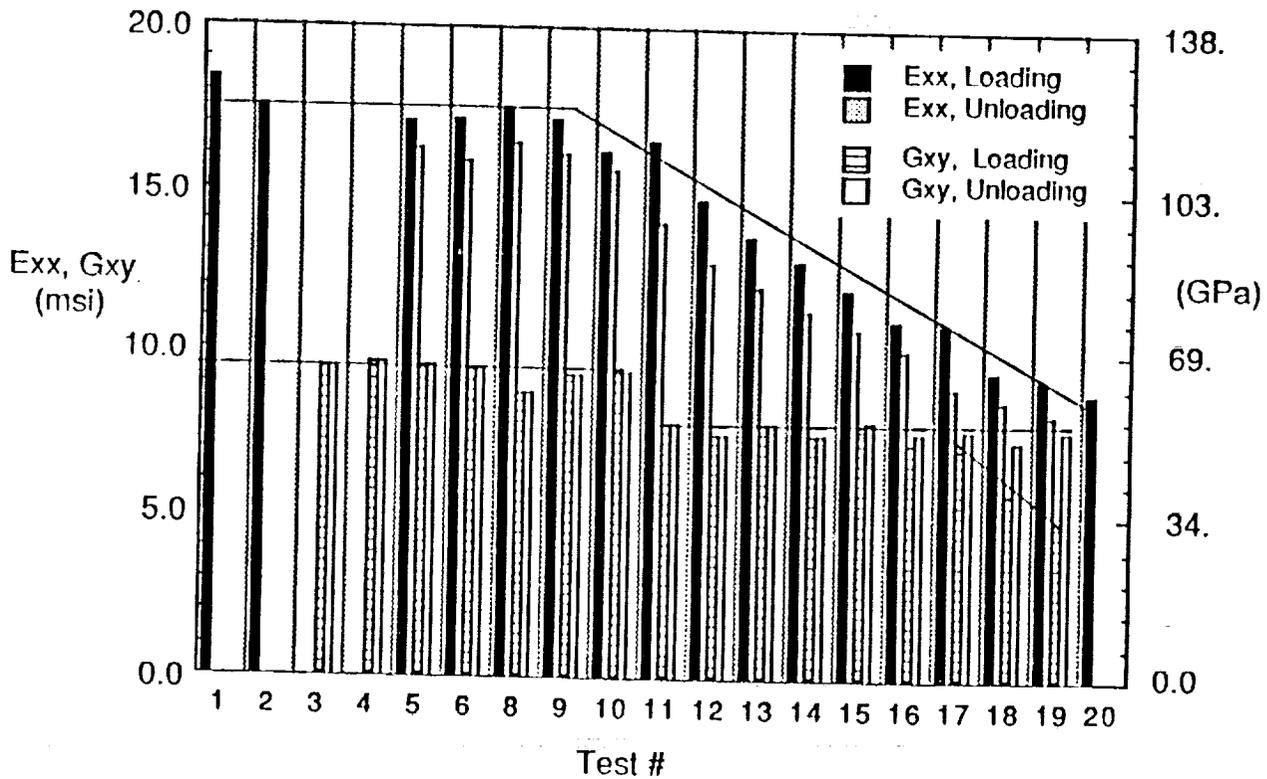
(b) $[\pm 45]_s$ Type I Loading

Figure 11: Experimental Moduli
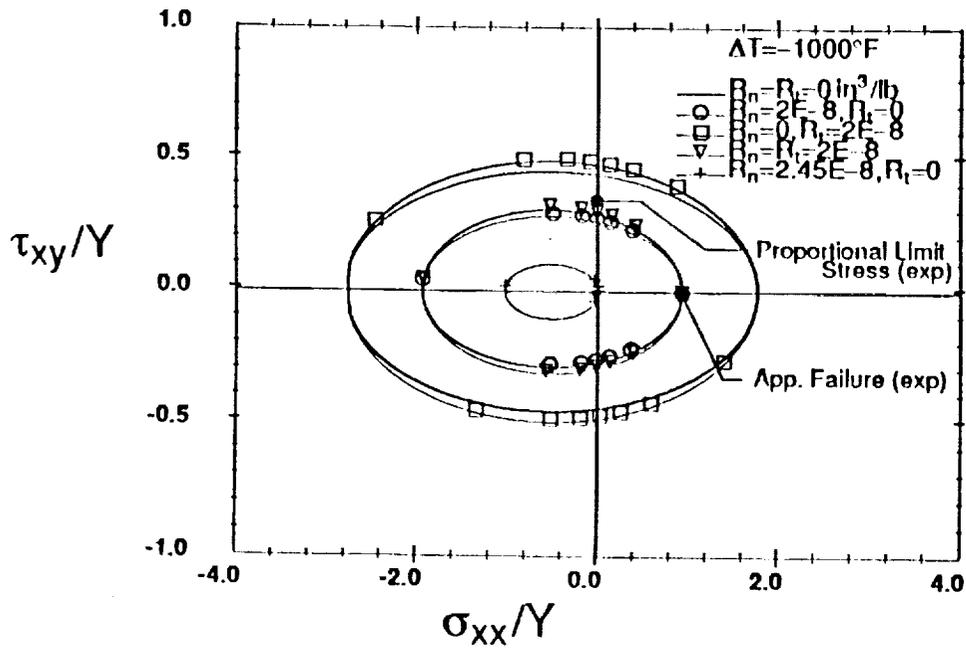
(a) $[0_4]$
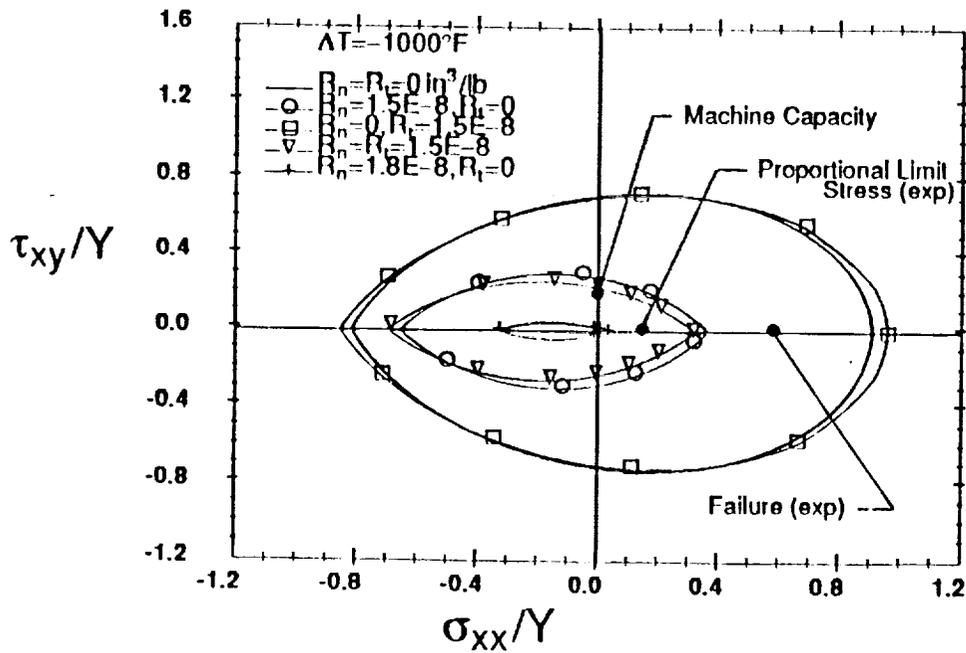
(b) $[\pm 45]_s$

Figure 5: Yield Surfaces

Summary

EXPERIMENTAL CHARACTERIZATION

- Tubular Specimens

  — axial, torsional, and internal pressurization

  — load combinations

MODEL DEVELOPMENT

- Interface Constitutive Equations (ICE)

  — traction/displacement relations

  — general loading/unloading conditions

- Repeating Unit Cell F-E analysis

CORRELATE THEORY/EXPERIMENT

UVA
APPLIED
MECHANICS

Conclusions

[0] LAMINAE

- Sudden loss of shear stiffness accompanied by AE (shear loading)

    — combined damage and plasticity

- Damage degrades shear modulus and accelerates yielding

[±45]$_s$ LAMINATES

- Highly nonlinear tensile response accompanied by AE

    — damage

    — plasticity

- Axial modulus degraded 50%

- Damage accelerated yielding

- Large (coupled) axial plastic strains

UVA
APPLIED
MECHANICS

PRECEDING PAGE BLANK NOT FILMED

Future Experiments

- Internal pressurization of [0₄] tubes

Type III
Loading

PRECEDING PAGE BLANK NOT FILMED
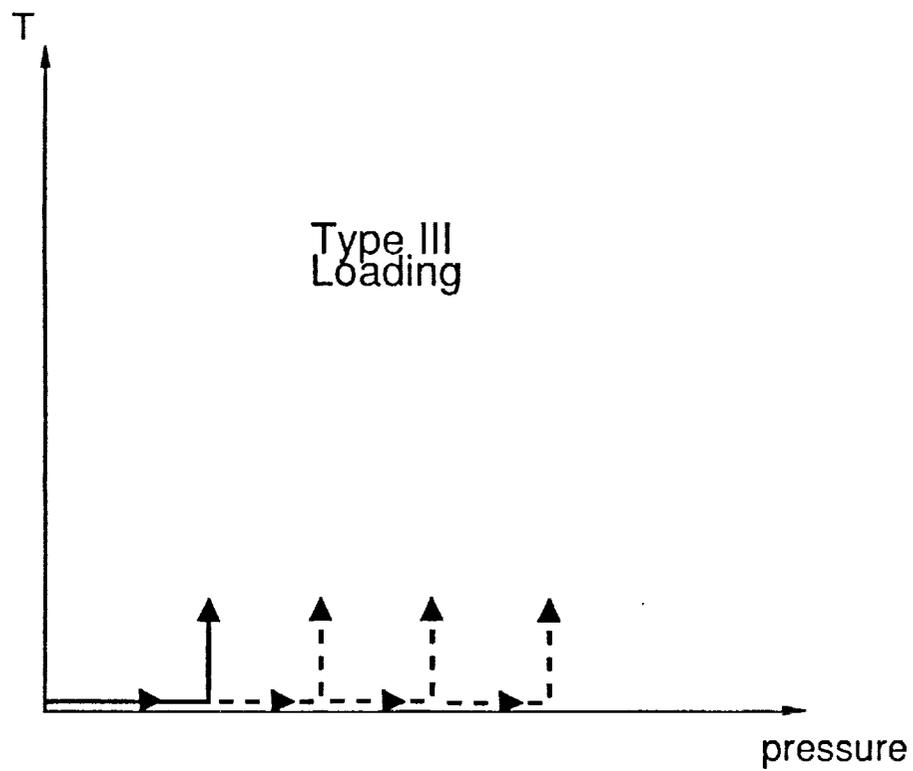
Project 13a   Static and Fatigue Response of SCS-6/β 21S MMC

F. Mirzadeh and C.T. Herakovich

Objective

The objective of this project was to conduct monotonic tension and tension-tension fatigue tests on an SCS-6/β 21S silicon carbide/titanium fibrous composite at room and elevated temperature (480°C) for three laminate configurations and two specimen types.

Status

The project is complete and a final report has been submitted. This report is presented in Appendix III.

Results

oo Laminate stiffness is not affected significantly by temperature.

oo Laminate strength is reduced significantly at elevated temperature.

oo Fatigue life increases at elevated temperature

oo Stiffness degradation during fatigue is reduced at elevated temperature.

oo The [0] laminate exhibits little stiffness degradation during fatigue at either temperature.

oo Extensometers mounted on the specimen are not recommended.

Milestones

No future work is anticipated on this program.

Presentation Graphics Captions

1. Title.

2. Overview--composite, laminates, test conditions, specimen types.

3. Specimens and extensometers.

4. Room and elevated temperature response of [0/90/0] SCS-6/β 21S.

5. Axial modulus as a function of specimen type, temperature and laminate type.

6. Tensile strength as a function of specimen type temperature and laminate type.

7. Initial response with different extensometers.

8. Fatigue response of [0/$\pm$ 45/90/$\pm$ 45/0] SCS-6/β 21S.

9. Fatigue life at room and elevated temperatures.

10. Stiffness degradation during fatigue.

11. Summary.

STATIC & FATIGUE RESPONSE

OF

SCS-6/β 21S MMC

FARSHAD MIRZADEH

CARL T. HERAKOVICH

LA^{2}ST REVIEW

NASA LANGLEY RESEARCH CENTER

JULY 15-16, 1992

UVA
APPLIED
MECHANICS

OVERVIEW

- COMPOSITE:

  — SCS-6 SILICON CARBIDE FIBER

  — β 21S TITANIUM ALLOY MATRIX

- LAMINATES:

  — $[0]_3$, $[0/90/0]$, & $[0/+-45/90/-+45/0]$

- TEST CONDITIONS:

  — MONOTONIC TENSION

  — T-T FATIGUE (1 Hz, R = 0.1)

  — ROOM TEMPERATURE

  — ELEVATED TEMPERATURE (480°C)

- SPECIMEN TYPES:

  — STRAIGHT-SIDED COUPON

  — DOG BONE

UVA
APPLIED
MECHANICS

SCS6/β 21S
Round Robin Specimens

MTS

MTS

Heated Zone

Thermocouple

Room Temperature

High Temperatue
(480 C)

UVA
APPLIED
MECHANICS
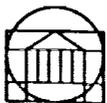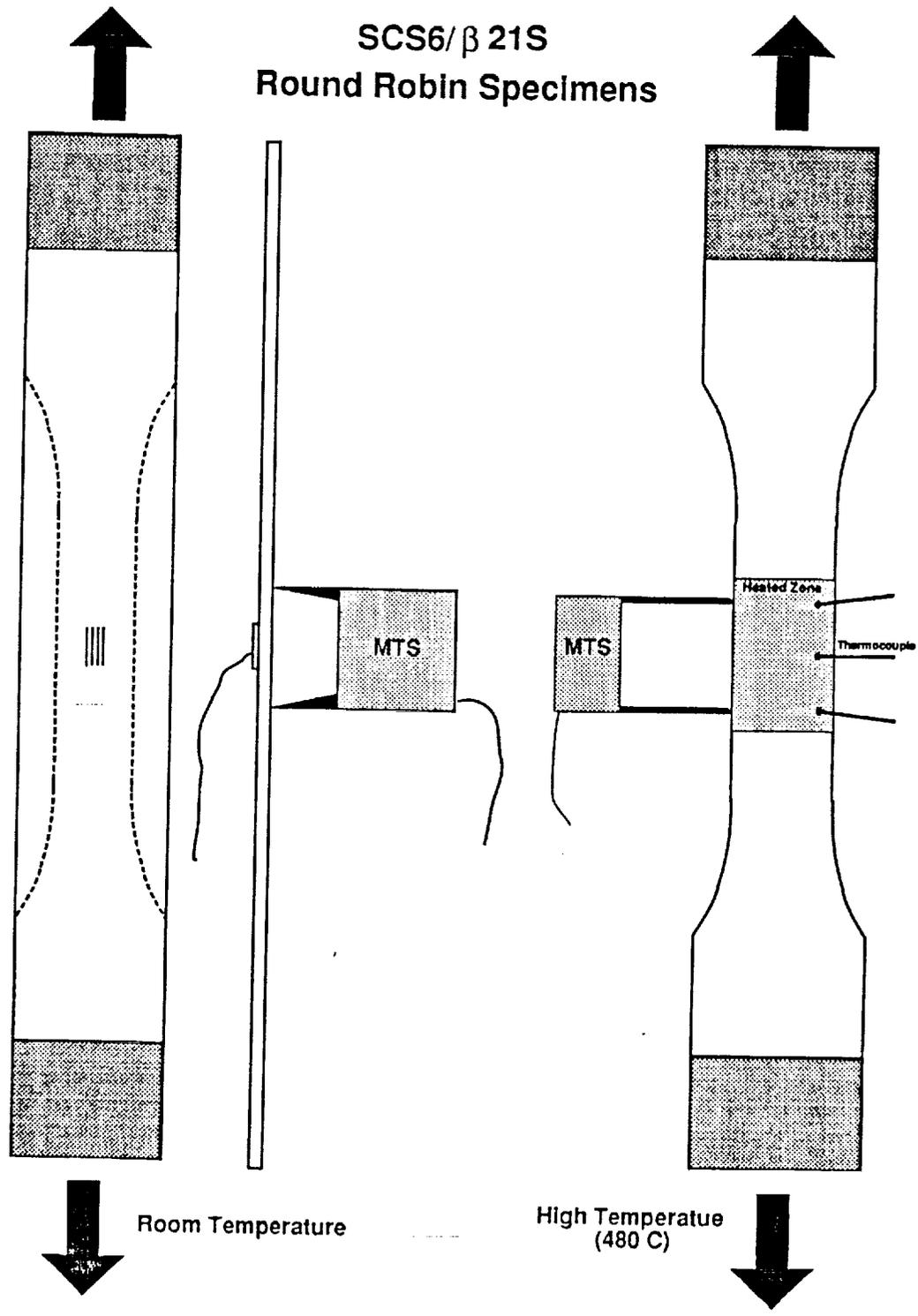
SCS-6/β 21S

Tension Test

—⊘—Specimen#155ST (T=RT) [0,90,0] Ext.
—●—Specimen#155ST (T=RT) [0,90,0] Front Gage

—◆—Specimen#117ST (T=480°C)[0,90,0] Ext.

—§—Specimen#174DB (T=480°C) [0,90,0] Ext.
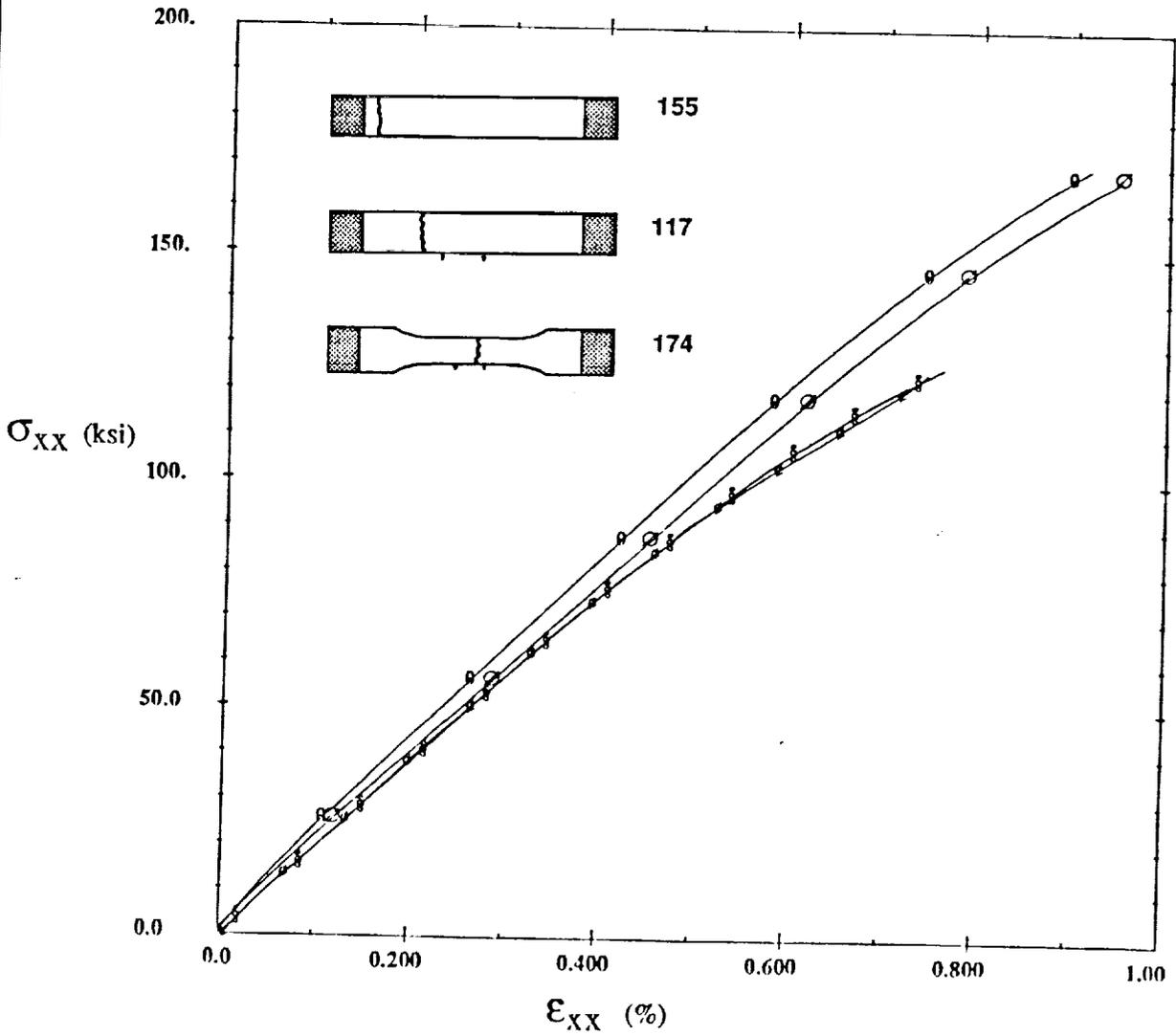
155

117

174

σ_{XX} (ksi)

ε_{XX} (%)

UVA
APPLIED
MECHANICS

SCS-6/β21S MODULUS VARIATIONS

Horizontal bar chart plotting AXIAL MODULUS (GPa) on the x-axis (0, 100, 200) against material configurations grouped as [0/+-45/90/-+45/0], [0/90/0], and [0]. Bars: DB ET, SS ET, DB RT, SS RT, DB ET, SS ET, DB RT, SS RT, DG ET, SS ET, DB RT, SS RT.

AXIAL MODULUS (GPa)
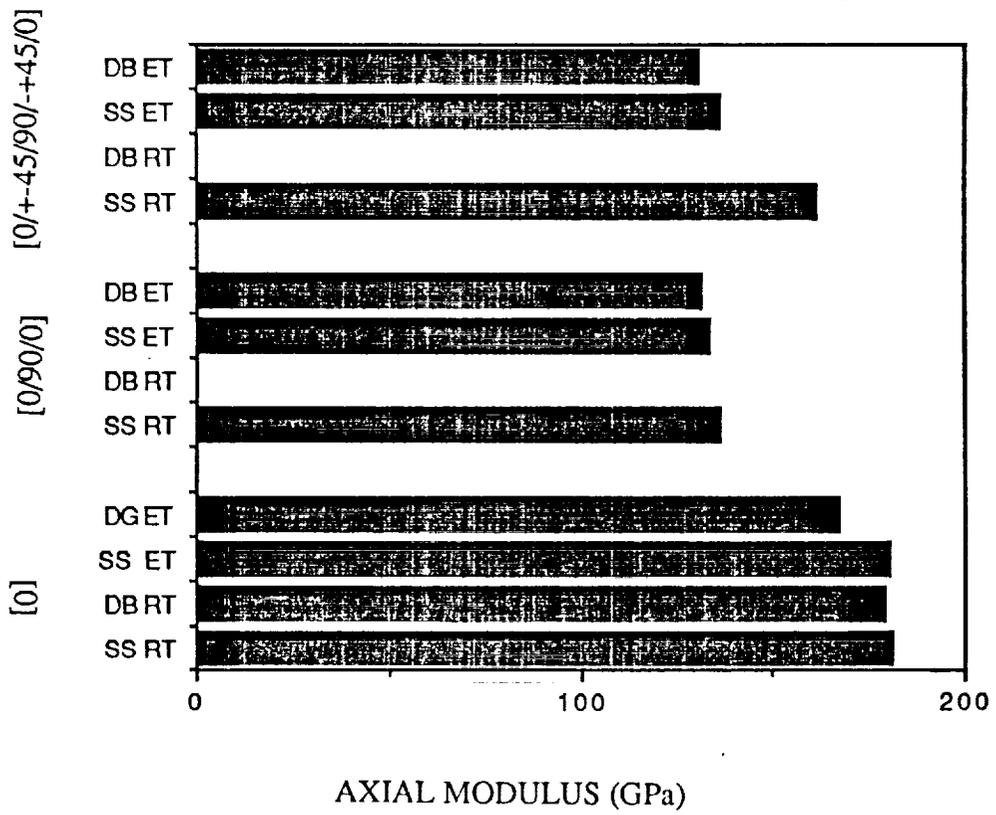
SCS-6/β21S STRENGTH VARIATIONS

AXIAL STRENGTH (MPa)

UVA
APPLIED
MECHANICS
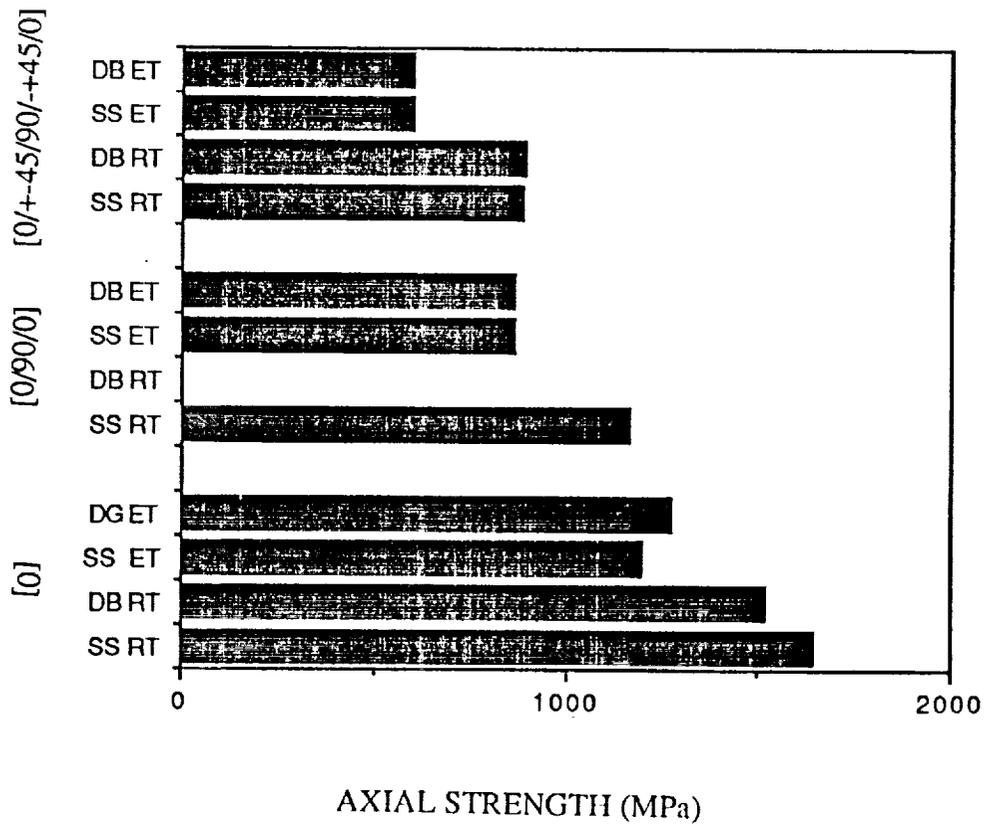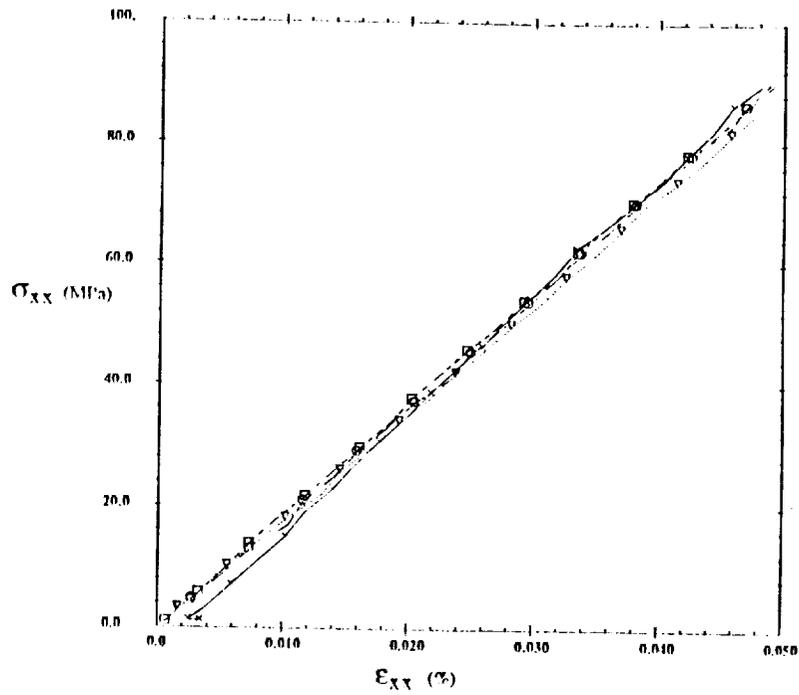
Fig. 5. RT Response of ET [0], SCS-6/β-21S Specimens

Fig. 2. RT Response of RT [0], SCS-6/β-21S Specimens

UVA
APPLIED
MECHANICS
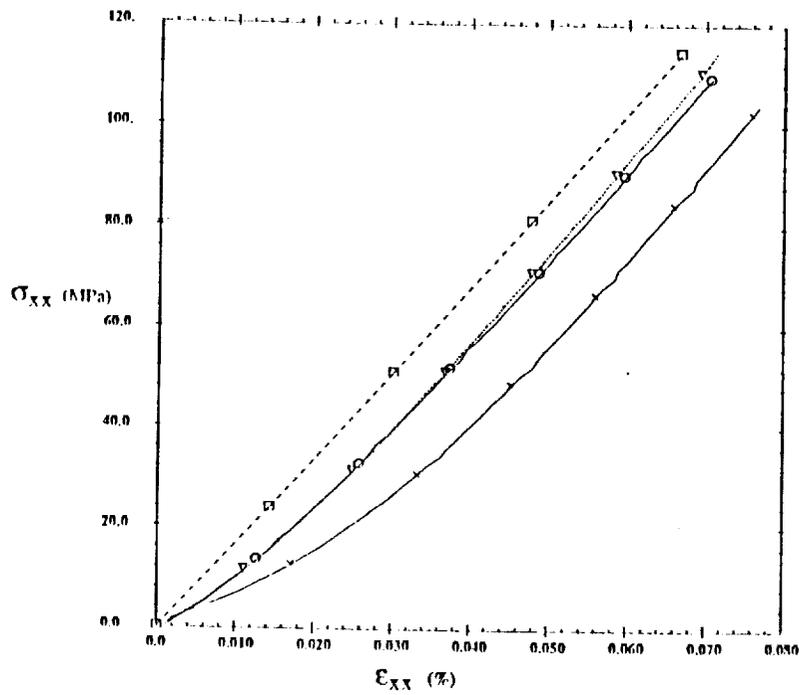
SCS-6/β 21S

Fatigue Test At 480°C

[0/+-45/90/-+45/0] ST #255
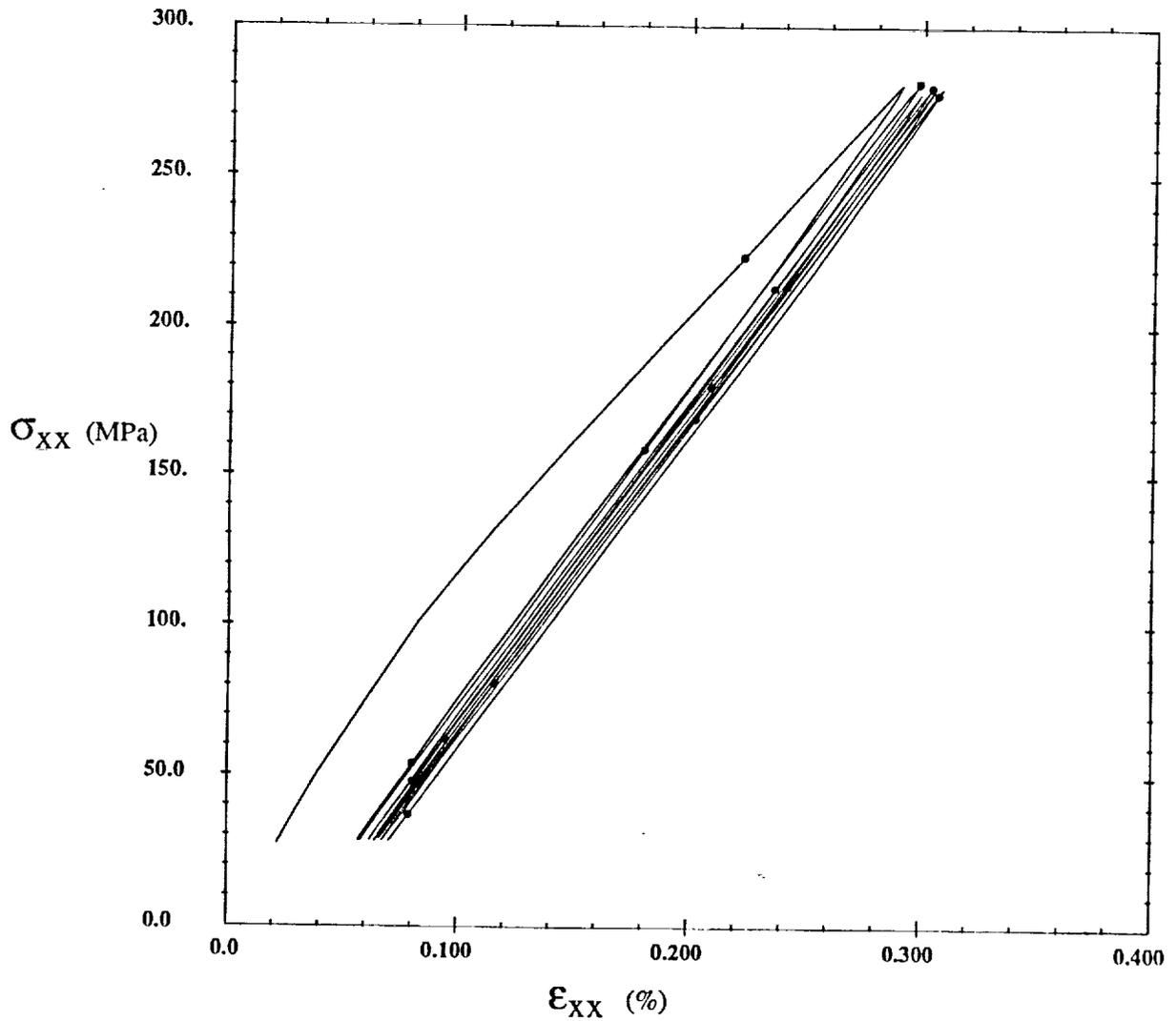
Room Temperature Fatigue
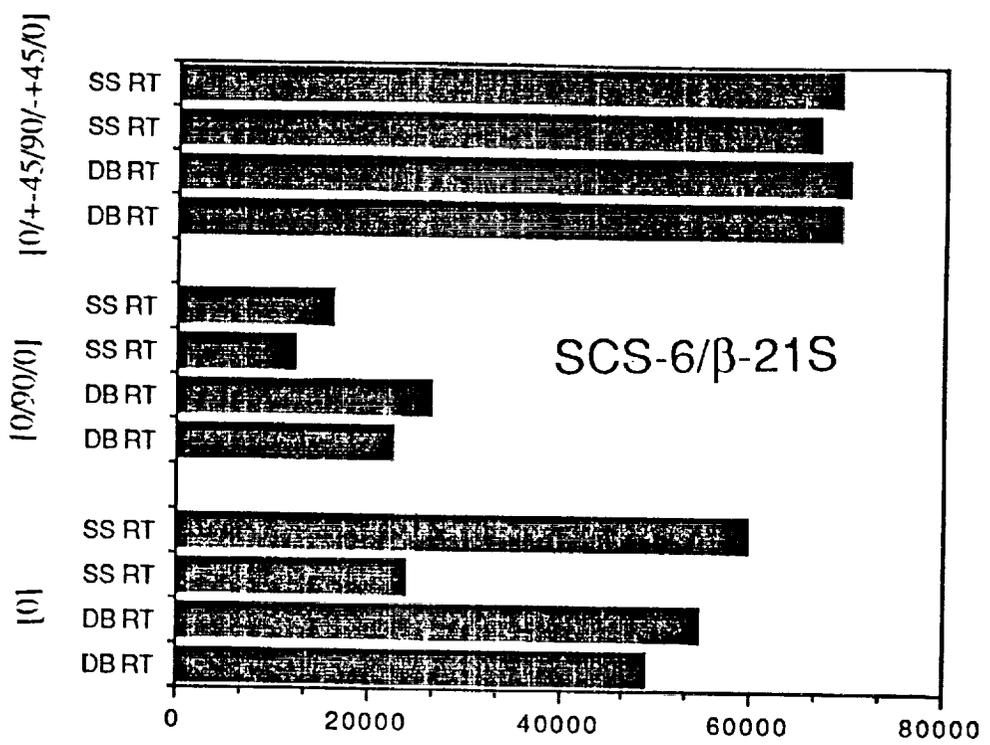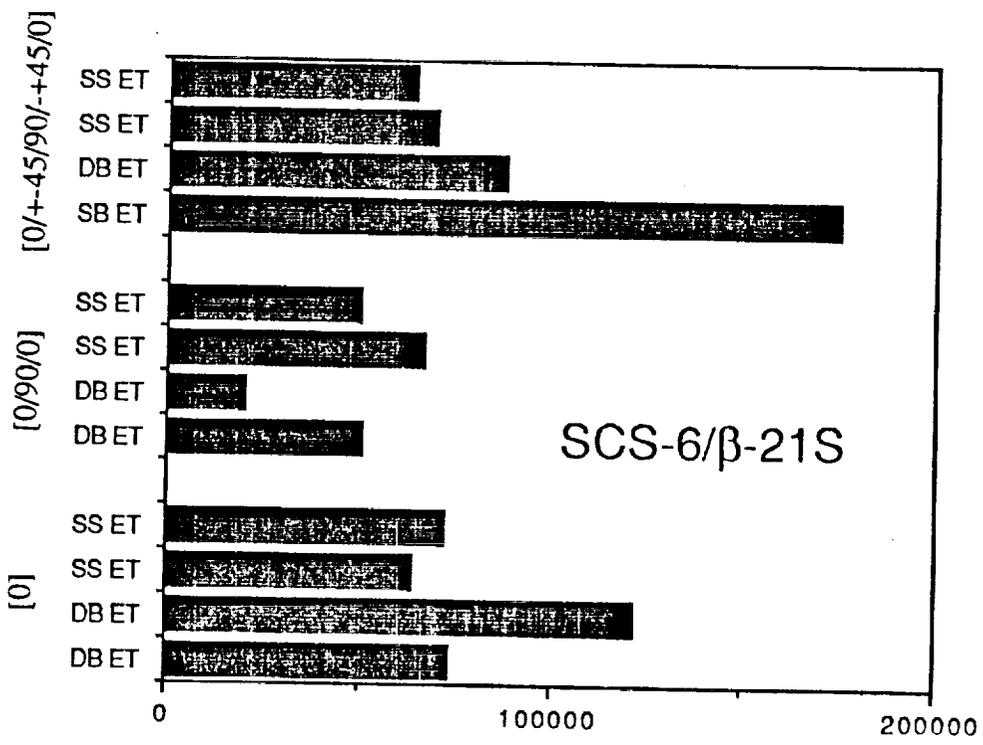
Elevated Temperature Fatigue

SCS-6/β-21S
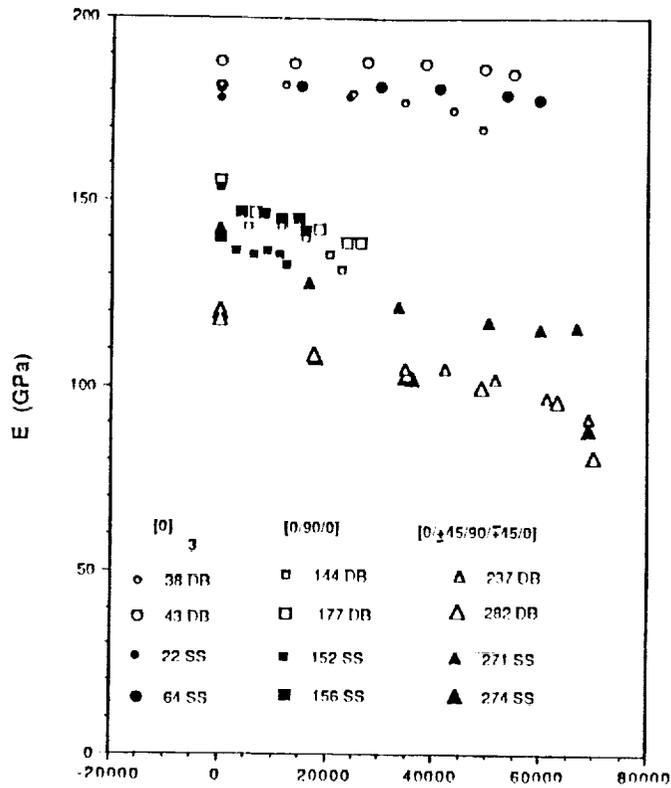
Room Temperature Fatigue
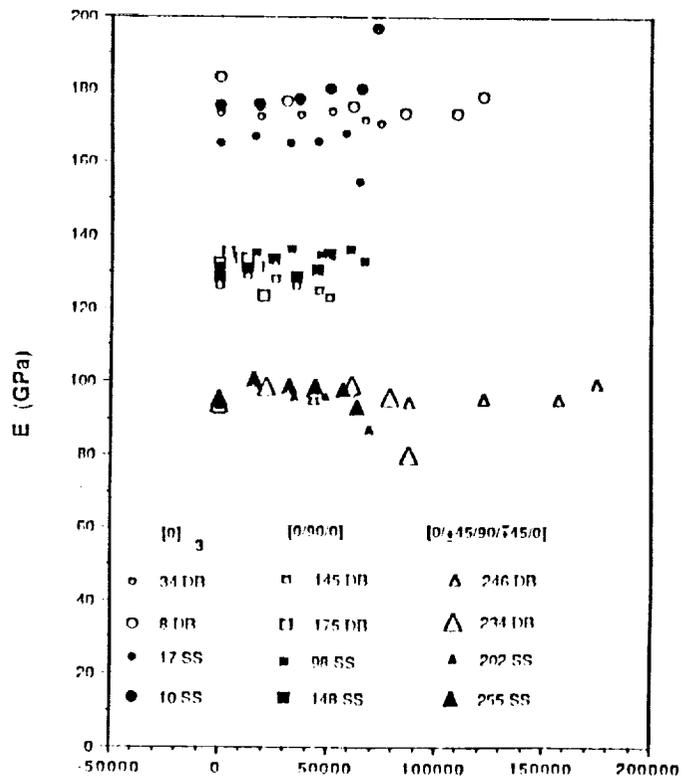
Elevated Temperature Fatigue

SUMMARY

- EXTENSOMETER MOUNTED ON SPECIMEN NOT RECOMMENDED

- STIFFNESS NOT AFFECTED SIGNIFICANTLY BY TEMPERATURE

- STRENGTH REDUCED AT ELEVATED TEMPERATURE

- FATIGUE LIFE INCREASED AT HIGH TEMPERATURE

- STIFFNESS DEGRADATION REDUCED AT HIGH TEMPERATURE

- $[0]_3$ EXHIBITS LITTLE STIFFNESS DEGRADATION

UVA
APPLIED
MECHANICS
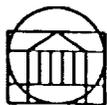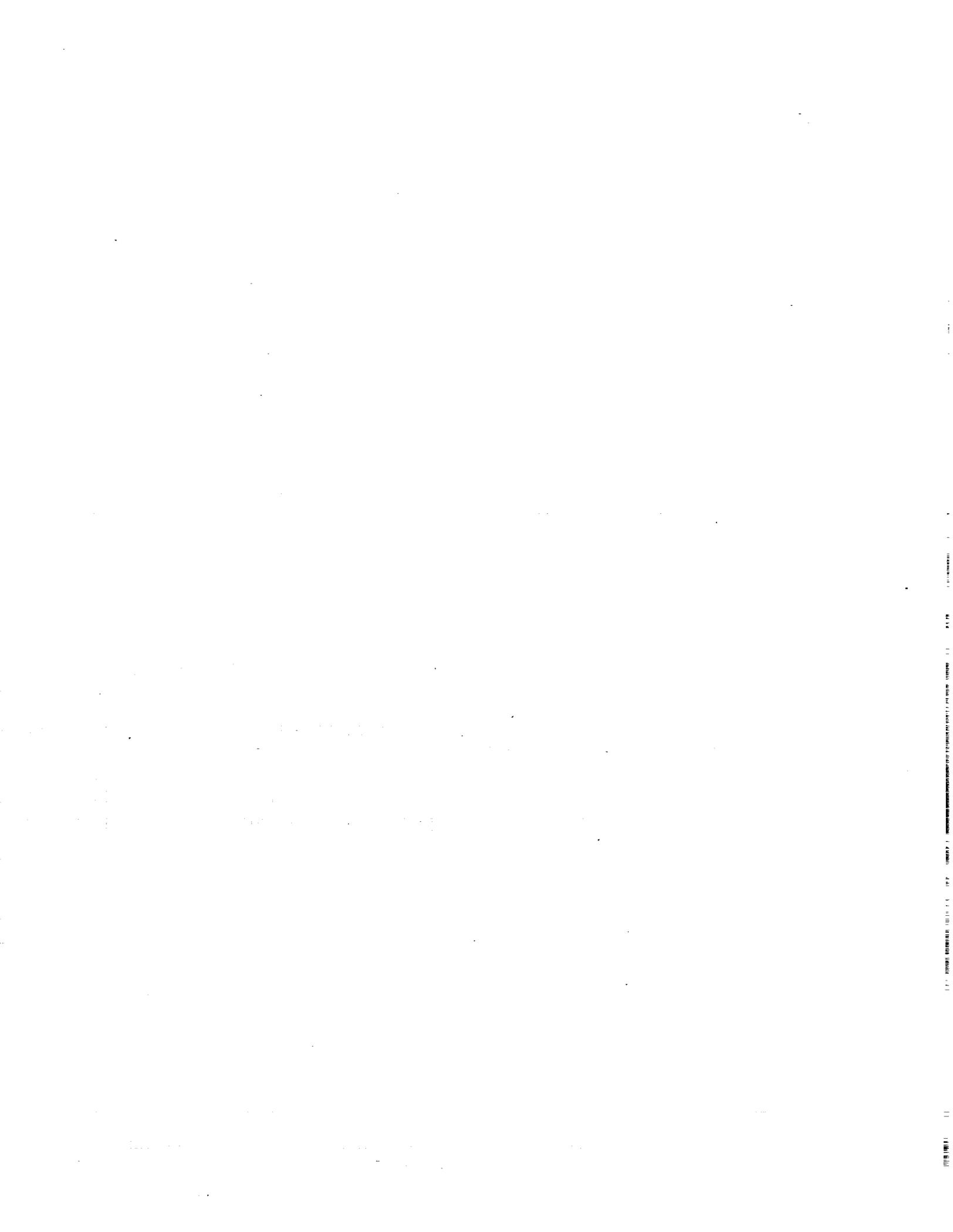
Project 14   Effect of Temperature on the Response of Metallic Shell Structures

C. Copper, K. McCarthy, T. Johnson, W.D. Pilkey and J.K. Haviland

Objectives

The present objective is to investigate thermal problems in shell structures, such as the hydrogen tanks in the Aerospace Plane or the fuselage structures of high speed civil transports. Such thermal problems would arise when a shell is subjected to external heating while the internal walls are maintained at the temperatures of cryogenic fuels in the Aerospace Plane, or when there are severe temperature variations around or along the fuselage of a high speed civil transport. Depending on the particular design, the tank could be load carrying, subject to compression and bending loads. The presence of stiffeners and frames could complicate the problem considerably, especially because they could lead to thermal buckling.

An additional objective, of a program supported by a related NASA grant, is to define a set of test problems which can be used to evaluate the accuracy of structural finite elements with thermal loads. These tests could then be used to choose appropriate elements to be used to analyze a real problem, and to help code developers to identify weaknesses of existing elements.

Finally, we are developing improved formulas for cross-sectional thermal stresses in structural members. Such formulas are tractable now due to the availability of computers to practicing engineers.

PAGE 88 INTENTIONALLY BLANK

CRYOGENIC TANK BUCKLING ANALYSIS

Presented by Karen Marie McCarthy (Graduate Student; UVa)

Dr. W.D. Pilkey (Project Supervisor)
Dr. J.K. Haviland (Consultant)
Dr. M.J. Shuart (NASA Monitor)

Department of Mechanical and Aerospace Engineering
School of Engineering and Applied Science
University of Virginia, Charlottesville, VA 22901

Objectives

To study effects of severe combinations of structural loads and thermal gradients on various combinations of structural arrangements and materials, such as skin and stringer combinations, double skin structures, and composite materials. Typical applications would be to cylindrical and non-cylindrical fuselage sections of high speed civil transports and to cryogenic tanks on the National Aerospace Plane.

Progress During Reporting Period

The EAL structures program at NASA was chosen for analysis, because this permitted temperature gradients through the thickness of the skin. Work to date has been concentrated on a cylindrical tank design with stiffeners. The tank is 240 inches long, 120 inches diameter. Two skin thicknesses were studied, 0.75" and 0.25". Initially it was open ended, but when marked effects were observed at the open ends, hemispherical end caps were added. The tank was cut on two planes of symmetry, leaving a quarter tank resembling a sugar scoop. At first, the quarter skin was divided into 400 panels, later this was increased to 1400 panels as is shown in Fig. 1. Skin temperatures varied from -1000°F internal to +1000°F external. Because the program is linear in temperature, the choice of an inner temperature lower than absolute has no effect. Stresses were shown to be predictable from one-dimensional calculations, that is:

$$\text{Thermal Stress} = \Delta T \; \alpha \; E/(2(1-v))$$

where ΔT is the temperature differential between inner and outer skin surfaces, α is the coefficient of thermal expansion, E is Young' modulus, and v is Poisson's ratio. When ring stiffeners and stringers were added, the cylinder was shown to be subject to thermal buckling. Figure 2 shows the thermal buckling mode for a 0.25" cylinder with 6 frames and 20 stringers. Compression buckling stresses were also calculated. These showed that the unstiffened cylinder buckled at 20.85 ksi, while the stiffened cylinder buckled at 27.46 ksi. In most cases, thermal buckling occurred when the stiffeners and stringers were internal, and maintained at the temperature of the inner skin. Note that predicted thermal stresses depended only on the temperature difference, thus identical thermal stresses resulted from surface temperatures of -1000°F internal and +1000°F external as from 0°F internal and +2000°F external. Other analyses showed that the 0.75" cylinder was well overdesigned, while the effect of a sudden change of thickness from 0.75" to 0.25" was to induce large stresses at the change in thickness. Altogether, eleven configurations were studied.

Current Work

The main conclusion drawn from these studies was that realistic thermal buckling temperatures might be obtained with thinner skins and more stringers. However, with 1400 panels, the runs were getting too large, and there seemed little possibility of making the large increases in numbers of panels that were needed. Accordingly, the structure of Fig. 1 was reduced to a single bay with only one frame, reducing the number of panels to 120 as in Fig. 3. Although the provision of adequate boundary conditions was greatly complicated, almost identical results were obtained for the thermal buckling stress. Figure 4 shows the first thermal buckling mode for comparison with Fig. 2. Using this configuration with different skin thicknesses and stringer spacing, calculations were made for a structure with 0.125" skins and twice as many stringers. The value for ΔT was now 1236°F, a more achievable value, showing that thermal buckling is within the range of possibilities.

Thermal buckling temperatures are shown in the following Table 1.

TABLE 1: Thermal Buckling Temperatures

Configuration	tskin	b/t	ΔT (buck.)	No. of panels
Quarter Cylinder	0.75"	25.13	50,000°F	400
Quarter Cylinder	0.25"	37.70	6074°F	1400
Single Bay	0.25"	37.70	6000°F	120
Single Bay	0.125"	37.70	1236°F	480

In the above table, tskin is the skin thickness, b/t is the ratio of stringer spacing to skin thickness, ΔT (buck.) is the temperature difference at which thermal buckling occurs, and 'No. of panels' is the number of skin panels, which indicates the complexity of the analysis.

Note how close the ΔT for buckling is between the Quarter Cylinder, with 1400 skin panels, and the Single Bay, with 120 skin panels. Also, compare the buckling modes shown in Figs. 2 and 4.

Future Work

The following items are proposed with the intention to uncover the basic phenomena involved. They will include hypothetical structural models rather than actual designs.

(1) Obtain more realistic data on thermal and structural loads.

(2) Study effects of combined structural, pressure, and thermal loads.

(3) Study effects of local changes in skin thickness.

(4) Study effects of taper and of arbitrary cross-sections.

(5) Study effects of imperfection sensitivity.

(6) Study double-walled construction.

(7) Study composite structures.

(8) Use ABACUS program to study behavior beyond the elastic limit.
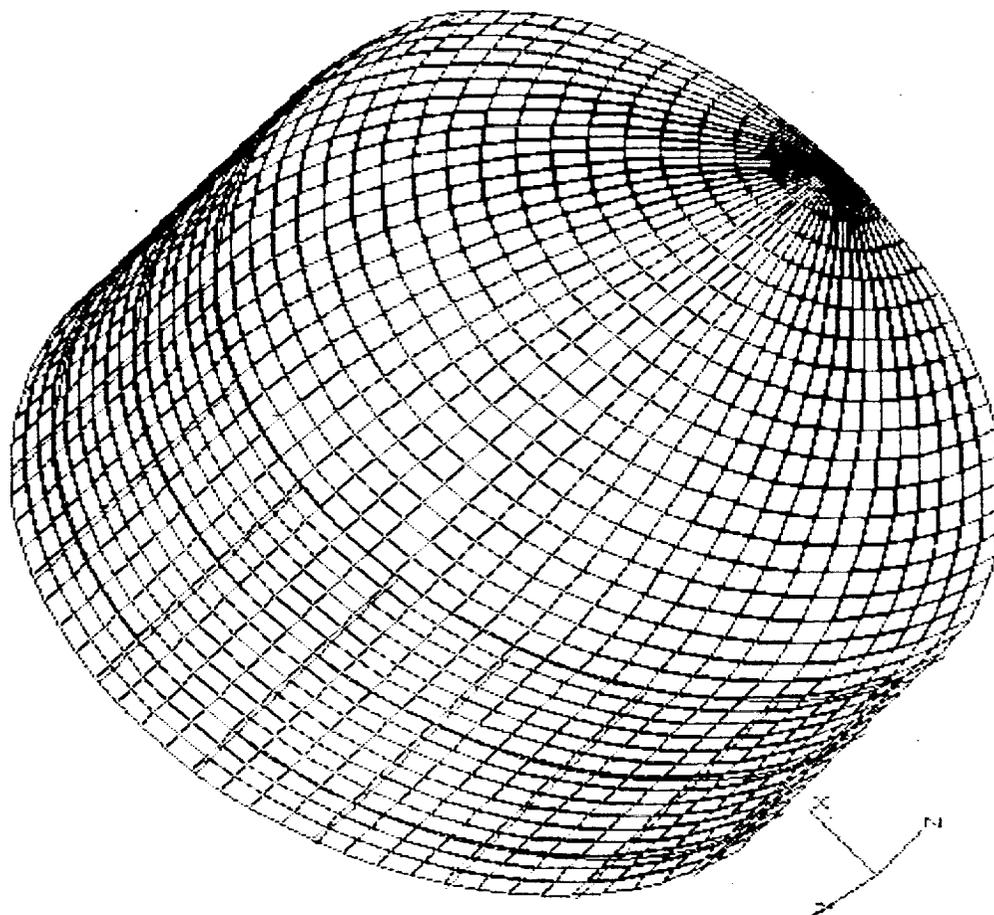
FIGURE 1 QUARTER CYLINDER WITH 0.25" SKINS

TBS1M12
MODE 1
BUCK1

FREQUENCY =

FIGURE 2   THERMAL BUCKLING MODE.   QUARTER CYLINDER.   0.25" SKINS
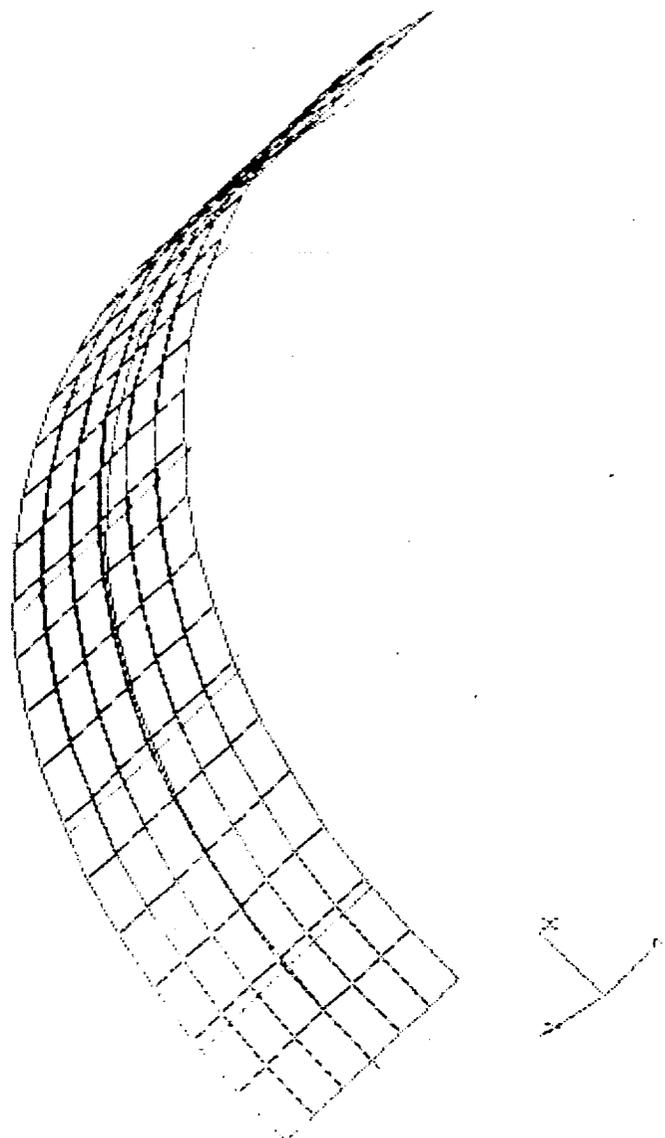
FIGURE 3   SINGLE BAY WITH 0.25" SKINS
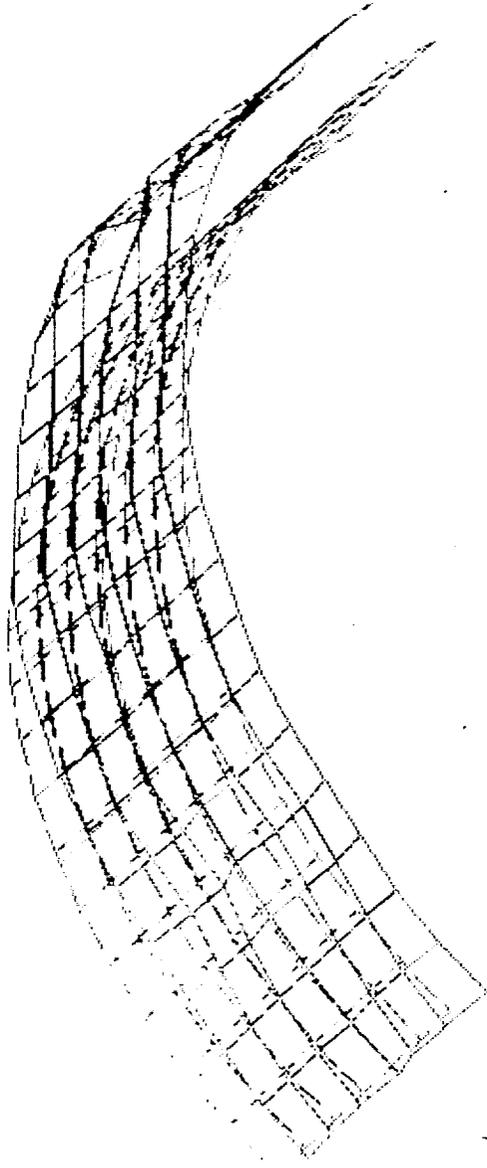
TESSJ19
MODE 1
BUCK1

FREQUENCY = 0.27569E+00 HERTZ

FIGURE 4   THERMAL BUCKLING MODE.   SINGLE BAY.   0.25" SKINS

QUARTER CYLINDER VON MISES STRESS

143561.	
142852.	
142143.	
141434.	
140725.	
140016.	
139306.	
138597.	
137888.	
137179.	
136470.	
135761.	
135051.	
134342.	
133633.	
132924.	
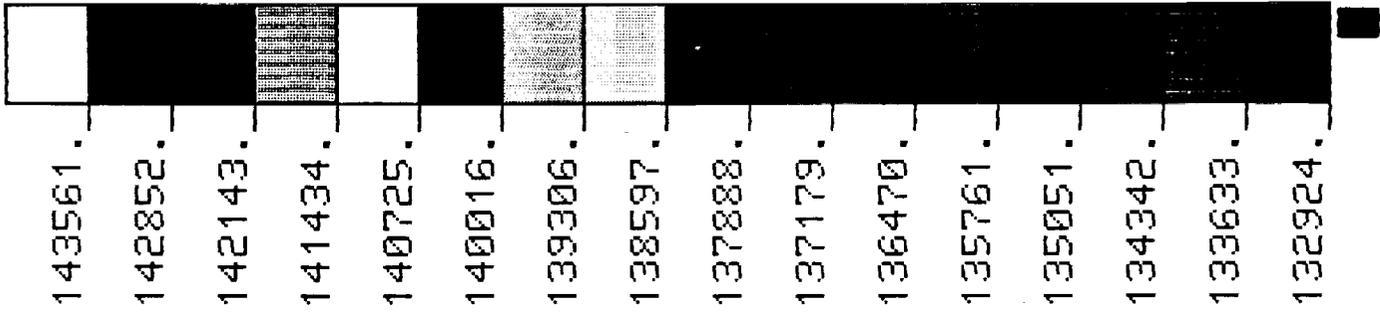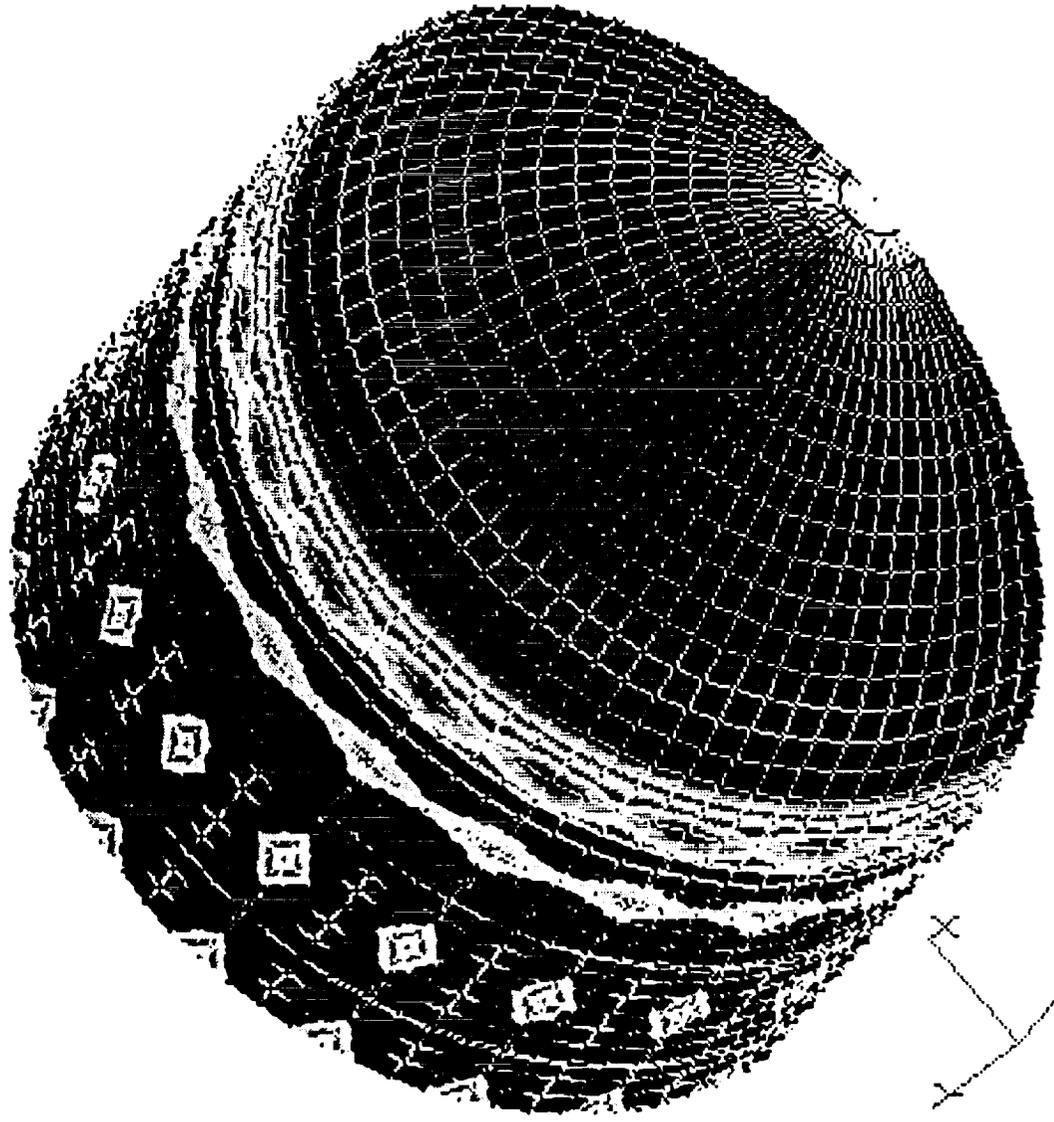
TBS1M12
LOAD SET = 1   LOAD CASE = 1   SURFACE = 3
STRESS

SINGLE BAY VON MISES STRESS
(Wide stringer spacing)
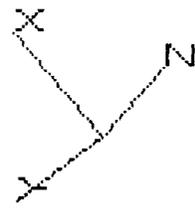
142026.
141433.
140841.
140249.
139656.
139064.
138472.
137879.
137287.
136694.
136102.
135510.
134917.
134325.
133732.
133140.

BS5J19
OAD SET = 1   LOAD CASE = 1   SURFACE = 3
TRESS

SINGLE BAY VON MISES STRESS
(Narrow stringer spacing)

13898.	
13724.	
13550.	
13375.	
13201.	
13027.	
12853.	
12679.	
12505.	
12331.	
12157.	
11983.	
11809.	
11635.	
11461.	
11287.	

BS3JY2
OAD SET = 1   LOAD CASE = 1   SURFACE = 3
TRESSES

THERMAL STRESSES IN CURVED BEAMS

Presented by Charles Copper---Graduate Student; UVa
W.D. Pilkey---PI
M.J. Shuart---NASA Observer

Department of Mechanical and Aerospace Engineering
School of Engineering and Applied Science
University of Virginia, Charlottesville, VA 22901

PAGE 94 INTENTIONALLY BLANK

THERMAL STRESSES IN
CURVED BEAMS

by
Charles Copper

PI
W. D. Pilkey

NASA Observer
Mark J. Shuart

GENERAL PROBLEM
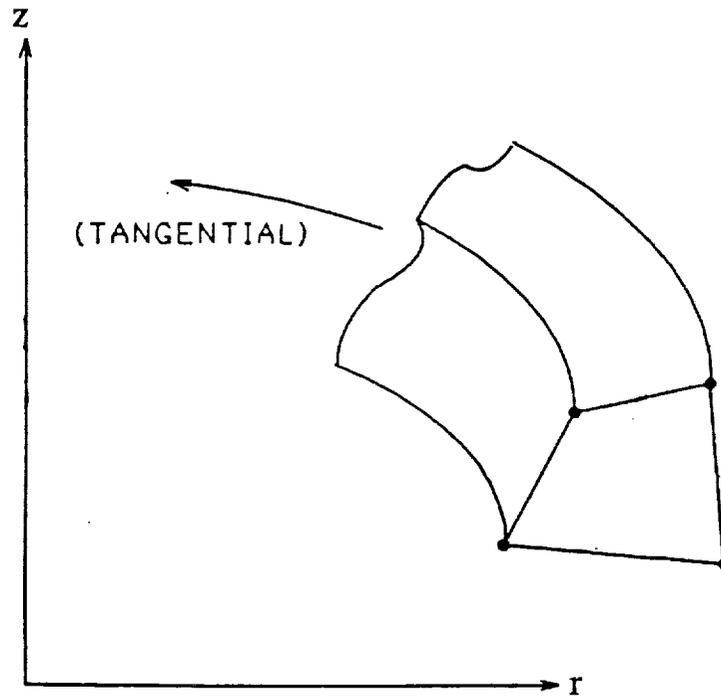
$$T(r,\theta,z) = T_1(r,z) + \theta\, T_2(r,z)$$

where T_1 and T_2 are arbitrary, and the radius of curvature is constant.

FORMULATION OF NORMAL STRESSES
AND THE INPLANE SHEAR

$$\sigma_{rr} = -\phi_{,rrz} + \nu\nabla^2\phi_{,z} - \alpha ET$$

$$\sigma_{\theta\theta} = -\phi_{,rz}/r + \nu\nabla^2\phi_{,z} - \alpha ET$$

$$\sigma_{zz} = -\phi_{,zzz} + (2-\nu)\nabla^2\phi_{,z} + \alpha ET$$

$$\sigma_{rz} = -\phi_{,rzz} + (1-\nu)(\nabla^2\phi)_{,r} + \int\alpha ET_{,r}dz$$

where

$$\nabla^4\phi = -[\alpha E/(1-\nu)]\int\nabla^2 Tdz$$

and

$$\phi_{,\theta\theta} = 0$$

Note: These four stresses are linear in θ.

C-5

FORMULATION OF REMAINING SHEAR STRESSES

$$\sigma_{r\theta} = E\{U_{r,\theta}/r + \Omega_{,r} - \Omega/r\}/(2(1+\nu))$$

$$\sigma_{z\theta} = E\{U_{z,\theta}/r + \Omega_{,z}\}/(2(1+\nu))$$

where

$$\nabla^2\Omega - \Omega/r^2 = - (U_{r,r\theta} \quad U_{z,z\theta} + U_{r,\theta}/r)/r$$
$$- 2(1+\nu)\sigma_{\theta,\theta}/(rE),$$

and
$$\Omega_{,\theta} = 0$$

$$U_r = r(\sigma_{rr} - \nu(\sigma_{zz} + \sigma_{\theta\theta}))/E + r\alpha T$$

$$U_z = \int[\sigma_{zz} - \nu(\sigma_{rr} + \sigma_{\theta\theta})/E + \alpha T]dz$$

Note: These two stresses are constant in θ.

EXAMPLE #1
(Rectangular Cross-Section)

Height = 20 in.
Inner Radius = 100 in.
Outer Radius = 110 in.

Material Properties correspond to Steel

$$T = 100(e^{(10-z)} - 1)/(e^{20} - 1)$$

Stress resultants are zero.

STRESS PLOTS FOR EXAMPLE #1

σ_{rr}

σ_{zz}

$\sigma_{\theta\theta}$
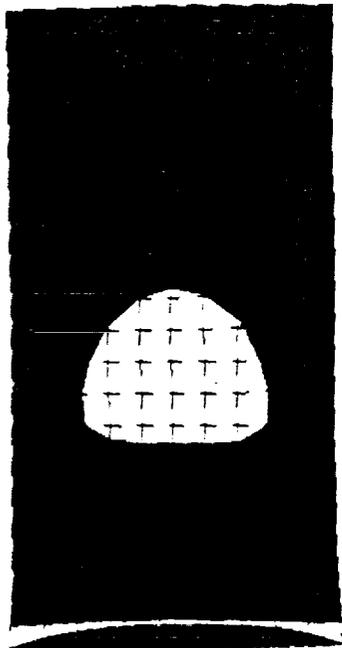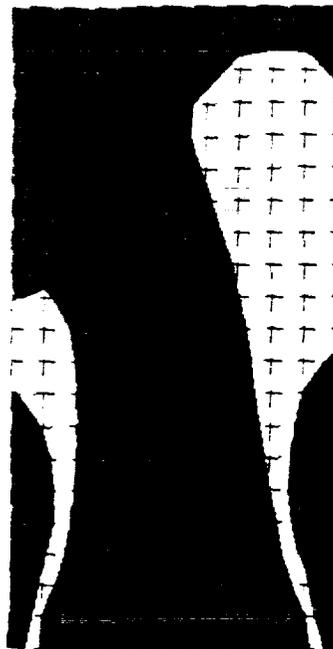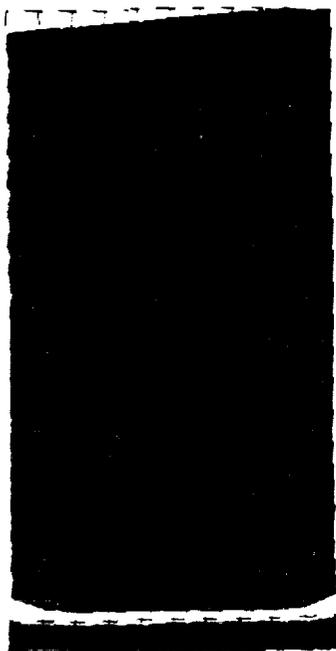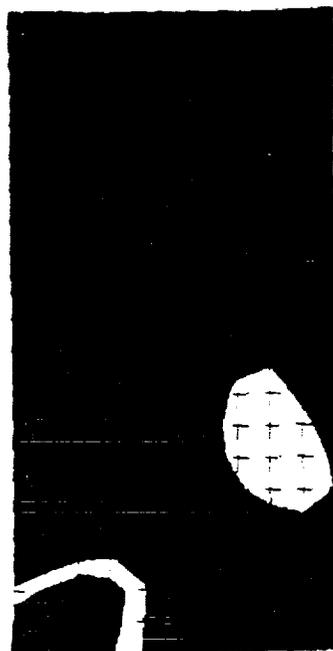
σ_{rz}

EXAMPLE #2
(Rectangular Cross-Section)

Height = 20 in.
Inner Radius = 10,000 in.
Outer Radius = 10,010 in.

Material Properties correspond to Steel

$$T = 100(e^{(10-z)} - 1)/(e^{20} - 1)$$

Stress resultants are zero.

STRESS PLOTS FOR EXAMPLE #2

σ_{rr}

σ_{zz}

$\sigma_{\theta\theta}$
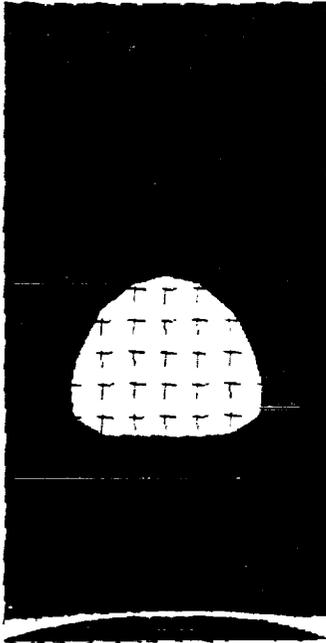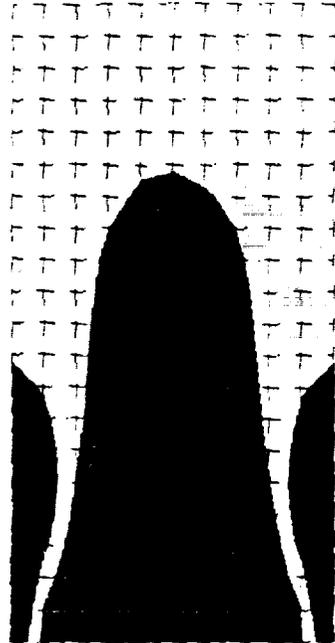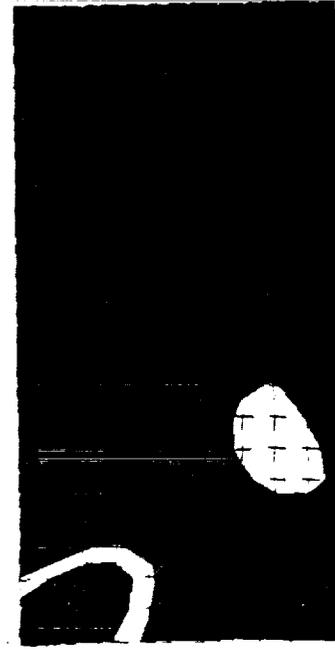
σ_{rz}

Future Work

1) Solution for the remaining 2 shear stresses

2) Compare with existing solutions techniques for a curved beam and a straight beam

ACCURATE THERMAL STRESSES FOR BEAMS

Presented by T.F. Johnson---Graduate Student; UVa
Walter D. Pilkey---UVa Advisor
Jeffery Stroud---NASA Advisor

Department of Mechanical and Aerospace Engineering
School of Engineering and Applied Science
University of Virginia, Charlottesville, VA 22901

Abstract

In this project a general theory of thermoelasticity provides equations for the longitudinal normal stress and shear stresses in beams. The theory takes into account the Poisson effect of lateral and transverse stresses σ_{YY} and σ_{ZZ} on a thermally loaded beam. A previously derived formula for the normal stress that reduces the three-dimensional problem to a two-dimensional one is explained. A new shear formulation is developed by extending the normal stress theory. Stresses from these equations are compared to those obtained from mechanics of materials and a commercial general purpose finite element code. The thermoelastic theory is extended to multi-connected cross-sections.

Recent Findings

A new shear stress formulation was derived. This formulation is currently being programmed. Program NORMAL has provided information on the effects on the longitudinal normal stress due to: beam geometry, temperature distribution, temperature magnitude and material properties of the beam.

Milestones

Complete the shear stress program. Incorporate composites and multi-connected regions in the formulation. Compare the results to those obtained from finite elements.

PRECEDING PAGE BLANK NOT FILMED

PAGE 96 INTENTIONALLY BLANK

Presentation Graphics Captions

1.   Title.

2.   Outline of Talk.

3.   Purpose of Project.

4.   Objectives During Project.

5.   Temperature Distribution and Governing Assumptions.
     The temperature distribution is linear in the x-direction but arbitrary across the cross-section. These assumptions are obtained from the Clebesh-Voight beam assumptions.

6.   Beam Being Analyzed.
     This beam is prismatic. X-direction is the longitudinal axis.

7.   Analogy Between Airy Stress Function and Plate Bending Problem.
     Both equations are biharmonic. The Laplacian of Phi is the last equation that must be calculated. Program NORMAL does this.

8.   Final Normal Stress Equations.

9.   Discussion of Results.
     The following graphs are results are obtained for running program NORMAL with different material properties. The elastic modulus and Poisson's ratio are varied. Each graph looks at a different location on the cross-section.

10. At the Center on the Edge and One Unit Up.

11. At the Center Two Units and Three Units Up.

12. At the Center Four Units Up.
     Two Units from Center on the Edge.

13. Two Units from the Center One and Two Units Up.

14. Two Units from the Center Three and Four Units Up.

15. Shear Strains and Thermal Warping Function.
     The strains are obtained from Hooke's law, for the normal stresses are known. The thermal warping function is obtained from equilibrium.

16. Final Shear Stresses.

17. The Effective Lines.
   In mechanics of materials an effective area is used to calculate the average shear stress across a line in beam's cross-section. The elasticity stresses however, uses a definite integral because it determines the stress at a point in the cross-section.

18. Future Work.

Accurate Thermal Stresses

for

Beams

T. F. Johnson
University of Virginia

Walter Pilkey
UVa Advisor

Jeffery Stroud
LaRC Advisor

July 16, 1992

1. Title Page

OUTLINE

Purpose and Background

Objectives

Normal Stress Formulation

Results

Shear Stress Formulation

Multi-connected Regions and Composites

Comparision of Finite Element Solution
   to Exact Elasticity

2. Outline of Talk

PURPOSE

○ Improve Traditional Formulas for
  Thermal Stresses of Rods, Plates, and Shells

○ Accurate Cross-Sectional
  Thermal Properties for Beams

  Normal Stress $\quad \sigma_{xx}$
  Shear Stresses $\quad \sigma_{xy}, \sigma_{xz}$

○ The Theory Can Be Fully Automated

○ Computationally Feasible

3. Purpose of Project

OBJECTIVES

O Rederive and Implement Normal Stress Theory

O Create and Implement a New Shear Stress Formulation

O Extend the Normal and Shear Stress Theory to
   Multi-connected Regions

O Compare Finite Elements to Elasticity

4. Ojectives During Project

BOLEY'S THEORY

Temperature Distribution

$$T(x,y,z) = T_1(y,z) + xT_2(y,z)$$

Assuming Traction Free Surface

$$\sigma''_{xx} = \sigma''_{xy} = \sigma''_{xz} = \sigma'_{xy} = \sigma'_{xz} = 0$$

Primes (') indicate differentiation wrt x

5. Temperature Distribution and Governing Assumptions

Beam of Arbitrary

Cross-Sectional

Shape
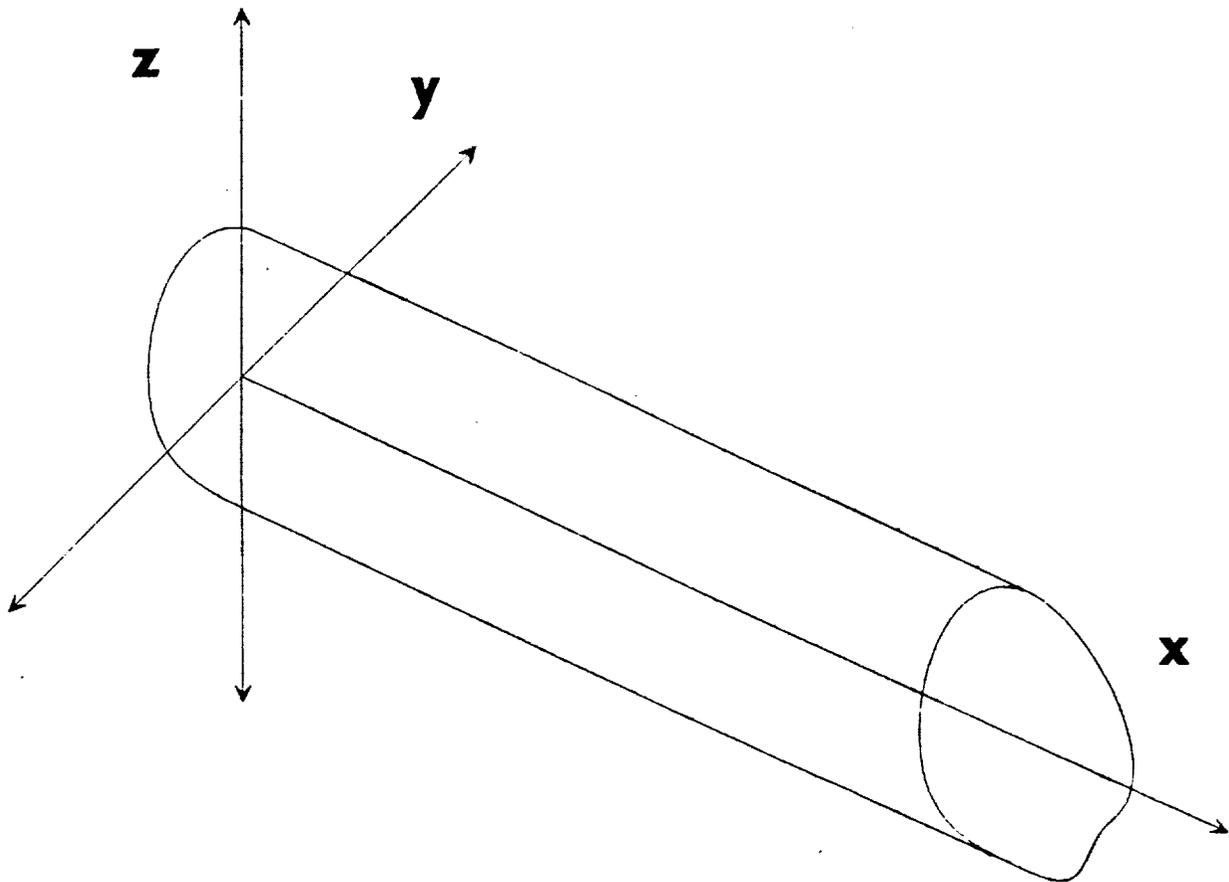
Applied Temperature Distribution:

O Linear in X-Direction

O Arbitrary in Y and Z -Directions

6. Beam Being Analyzed

IMPLEMENTATION

$$\nabla^4 \phi = -\alpha E \nabla^2 T/(1 - \omega) \qquad \nabla^4 w = p/D$$

Surface Free of Tractions   Clamped Plate

$$\phi = 0 \qquad\qquad w = 0$$

$$\phi_{,n} = 0 \qquad\qquad w_{,n} = 0$$

$$\phi_{,i} \quad i = y,z$$

$$\nabla^2 \phi$$

7. Analogy Between Airy's Stress Function
and a Plate Bending Problem

$$\sigma_{xx} = -\alpha ET + \upsilon\nabla^2\phi + C_1(x) + C_2(x)y + C_3(x)z$$

$$C_1(x) = P_T^*/A$$

$$C_2(x) = (I_y M_{Tz}^* - I_{yz} M_{Ty}^*)/(I_y I_z - I_{yz}^2)$$

$$C_3(x) = (I_z M_{Ty}^* - I_{yz} M_{Tz}^*)/(I_y I_z - I_{yz}^2)$$

$$P_T^* = \int_A (\alpha ET - \upsilon\nabla^2\phi)dA$$

$$M_{Ty}^* = \int_A (\alpha ET - \upsilon\nabla^2\phi)zdA$$

$$M_{Tz}^* = \int_A (\alpha ET - \upsilon\nabla^2\phi)ydA$$

8. Final Normal Stress Equations

RESULTS

Temperature Distribution

Temperature Magnitude

Material Properties

Geometry

Poisson's Ratio vs Percentage Diff. (%)

@ Node 6 for Exponential Distribution

Percentage Difference (%) vs Poisson's Ratio
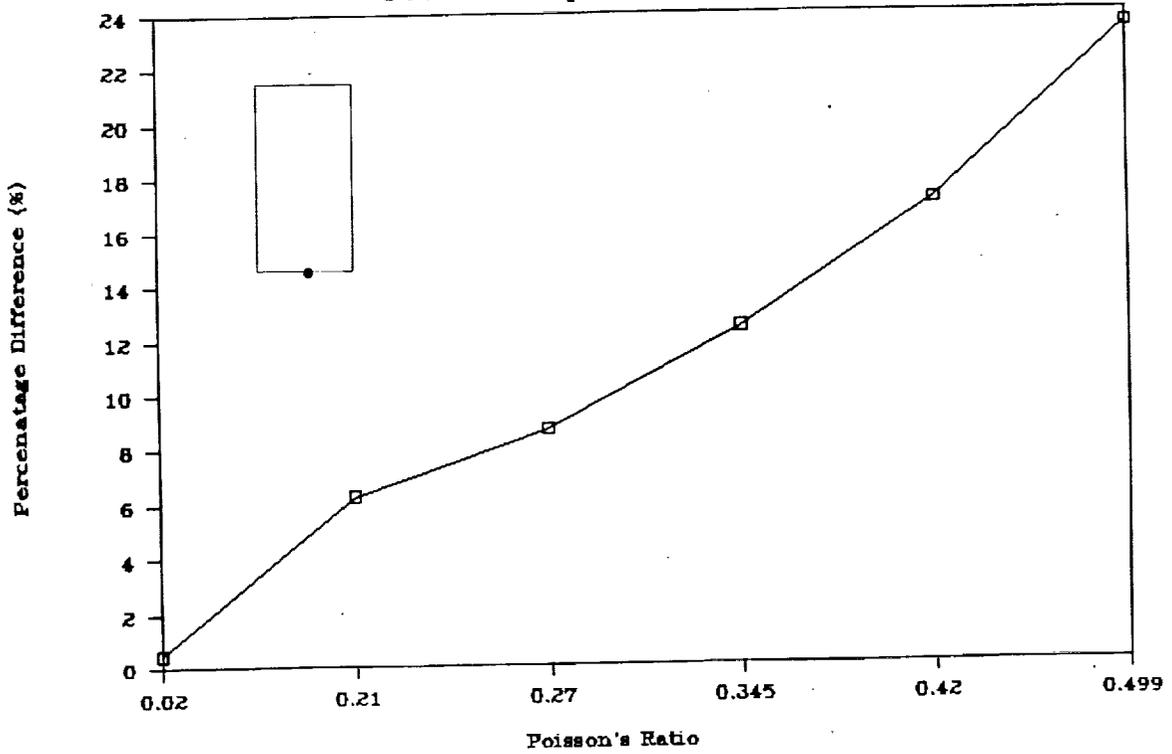
Poisson's Ratio vs. Percentage Diff.

@ Node 17 for Exponential Distribution

Percentage Difference (%) vs Poisson's Ratio
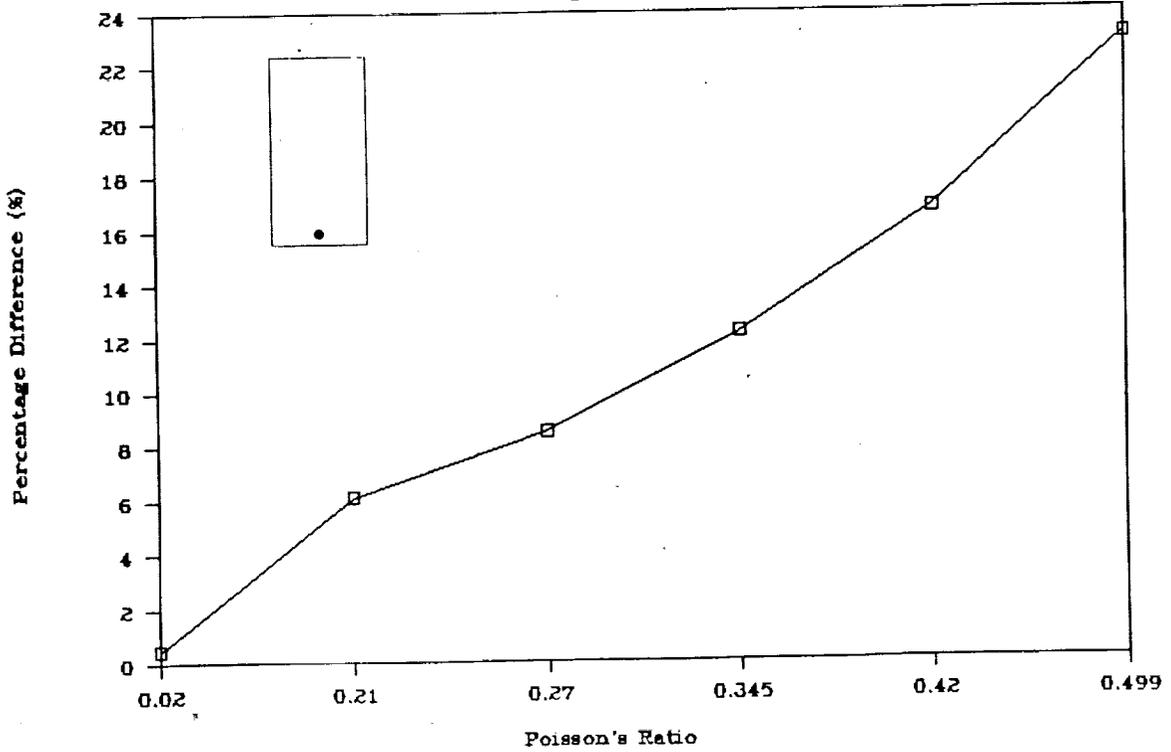
10. At the Center, on the Edge and One Unit Up

Poisson's Ratio vs. Percentage Diff.
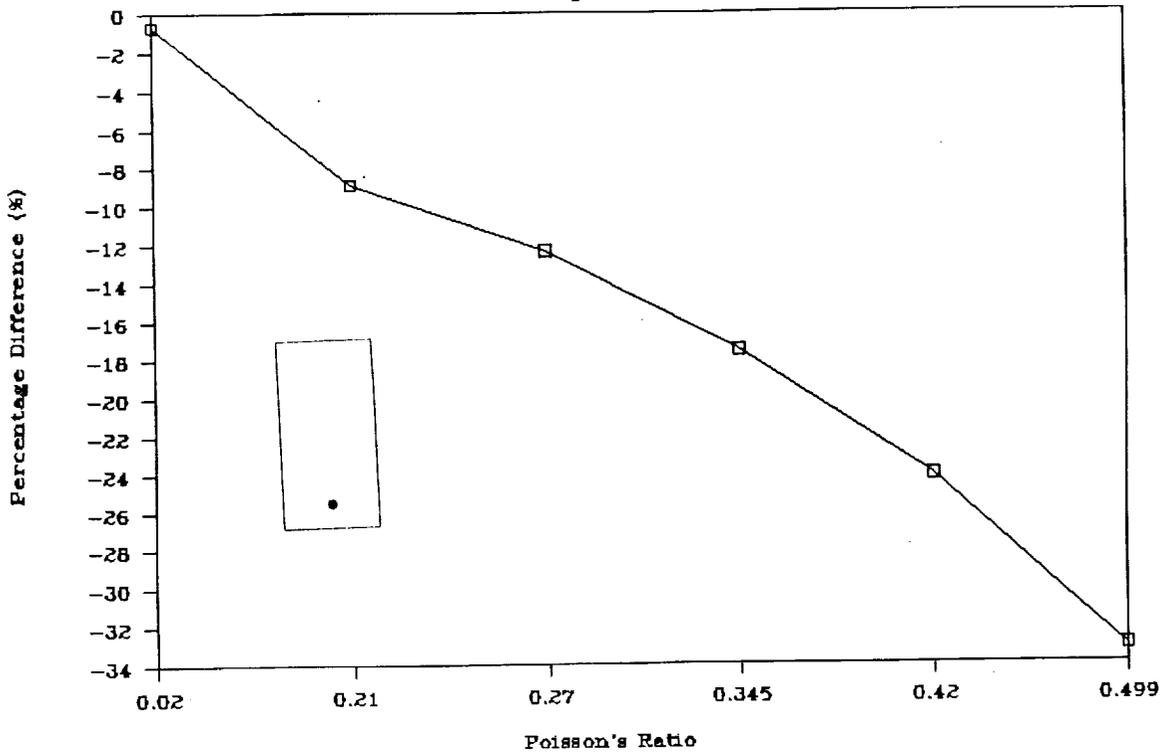
Poisson's Ratio vs. Percentage Diff.
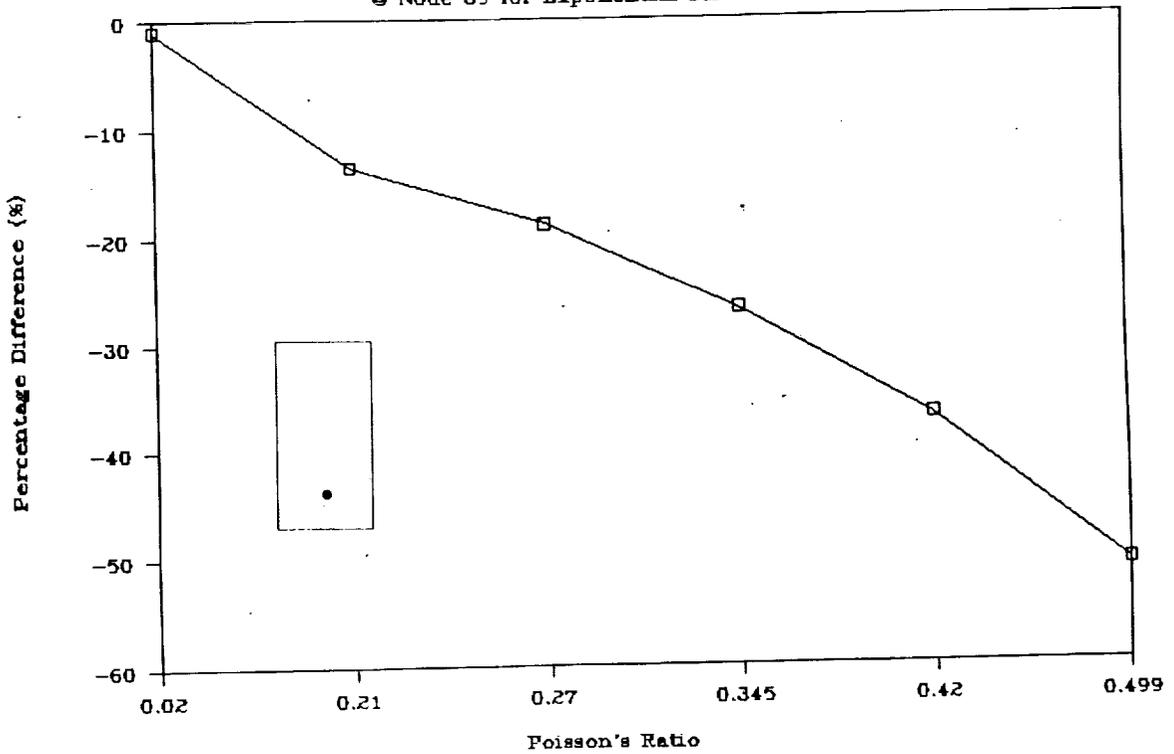
11. At the Center, Two Units and Three Units Up

Poisson's Ratio vs. Percentage Diff.

@ Node 50 for Exponential Distribution
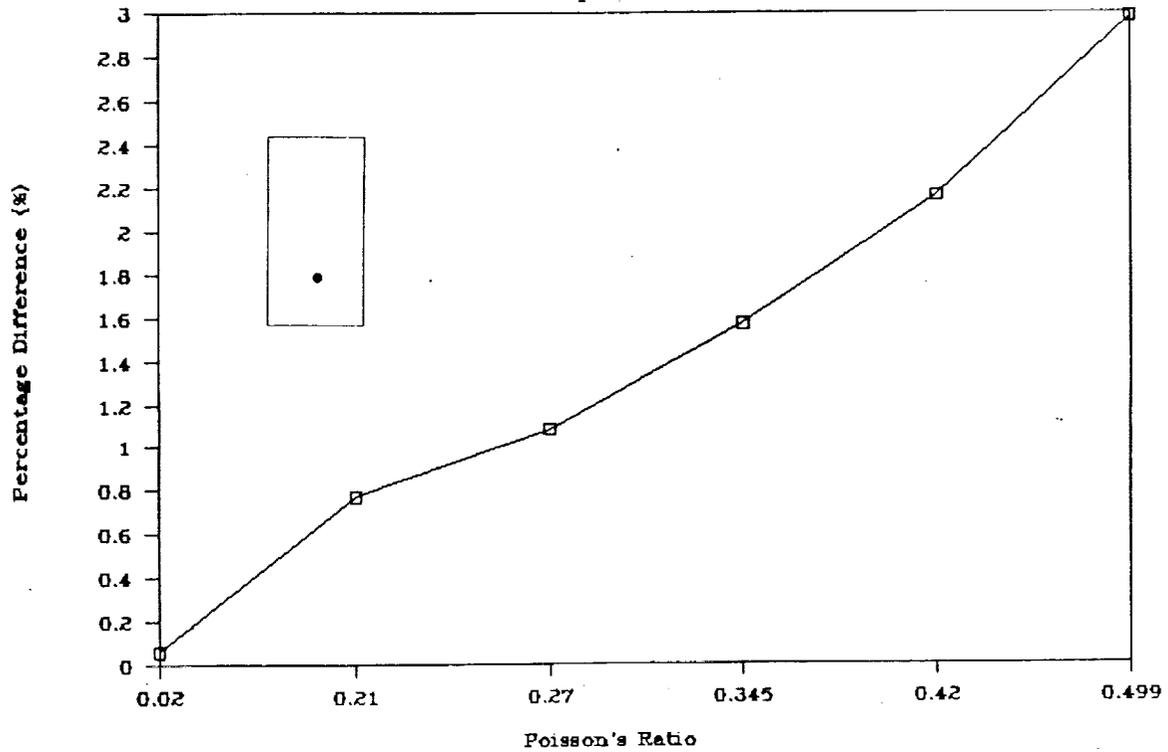
Poisson's Ratio vs. Percentage Diff.

@ Node 4 for Exponential Distribution
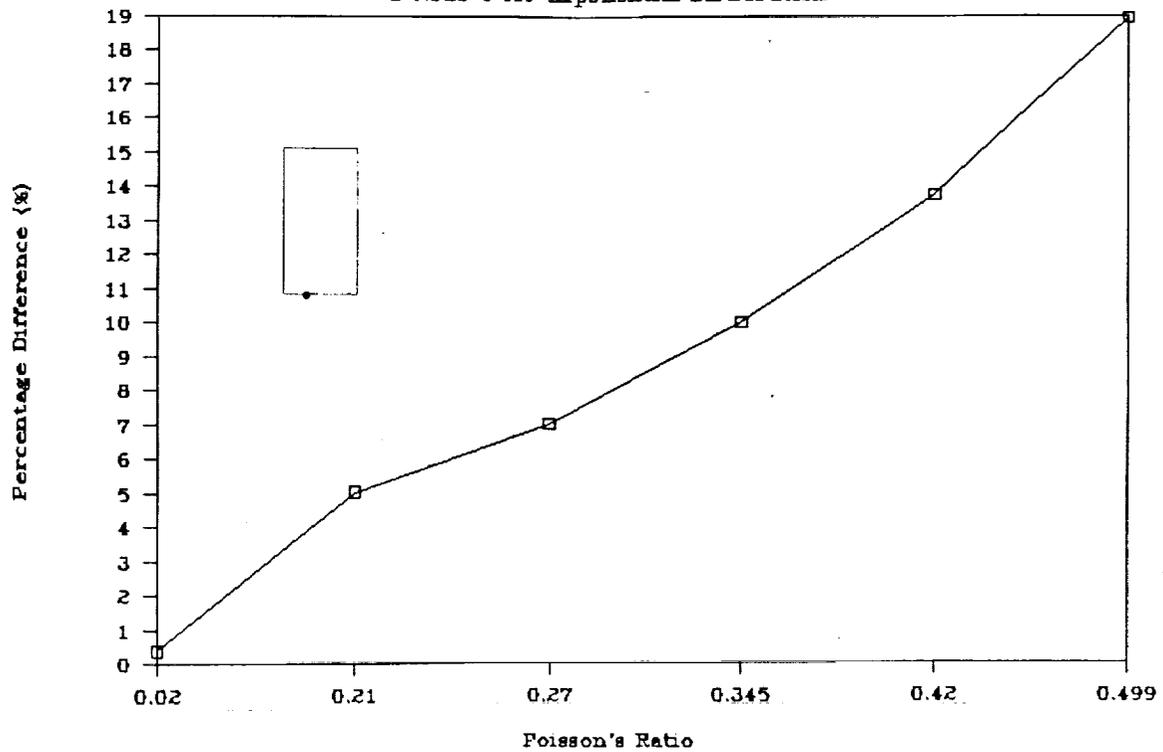
12. At the Center, Four Units Up
Two Units from Center on the Edge

Poisson's Ratio vs. Percentage Diff.

@ Node 15 for Exponential Distribution
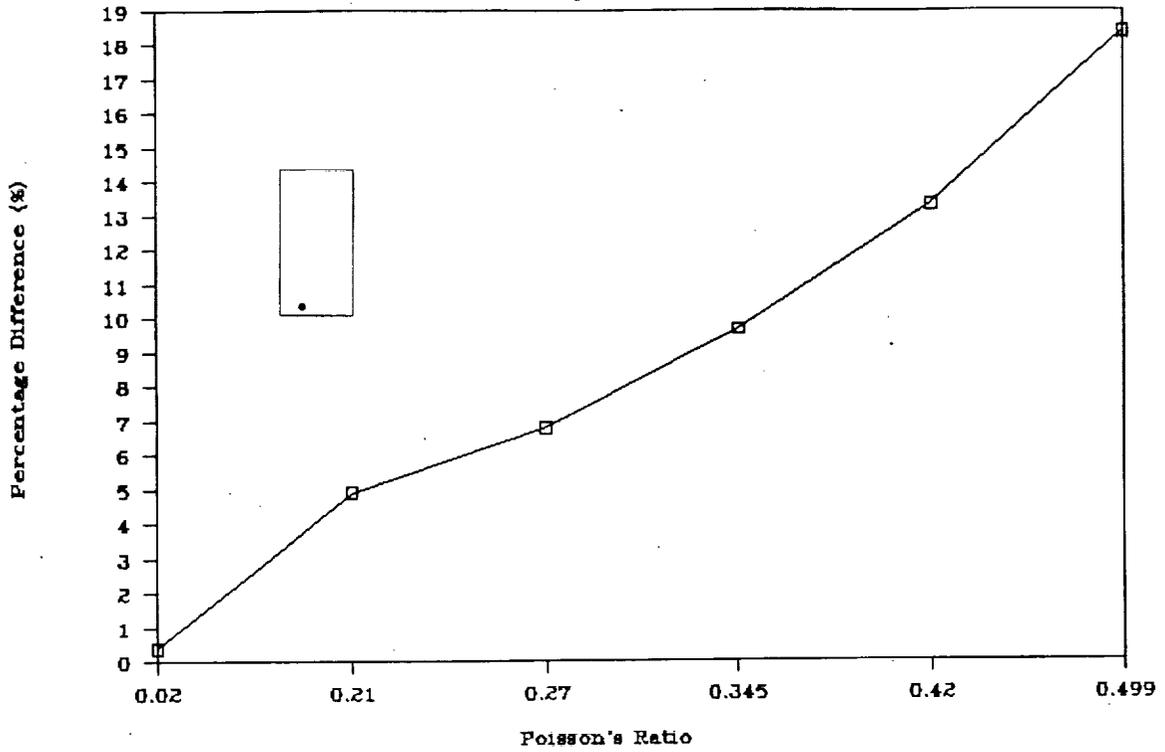
Poisson's Ratio vs. Percentage Diff.

@ Node 26 for Exponential Distribution
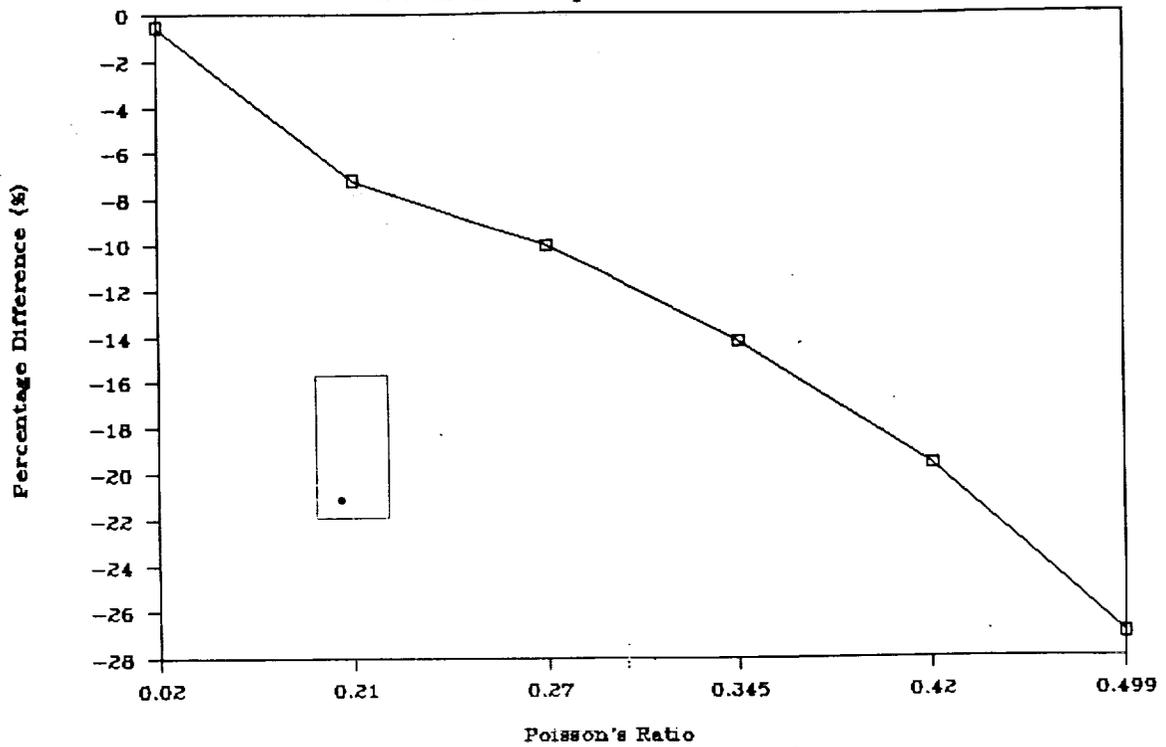
13. Two Units from the Center, One and Two Units Up

Poisson's Ratio vs. Percentage Diff.

@ Node 37 for Exponential Distribution
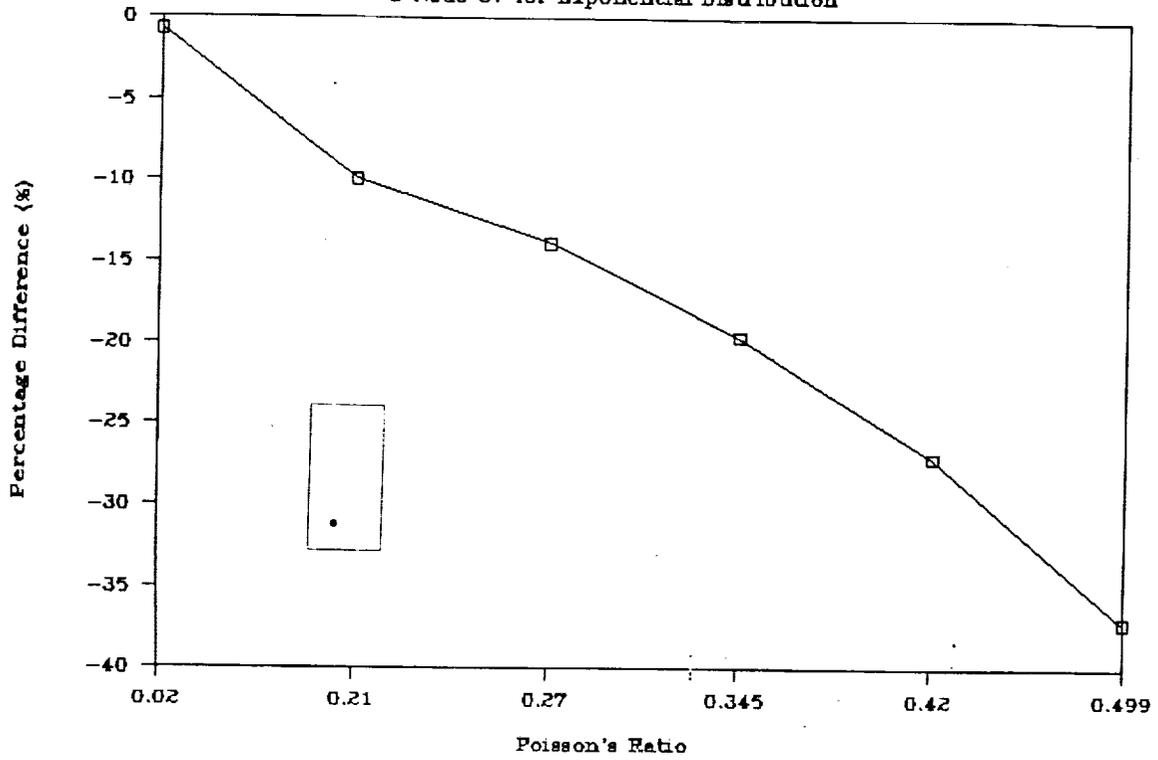
Poisson's Ratio vs. Percentage Diff.

@ Node 48 for Exponential Distribution
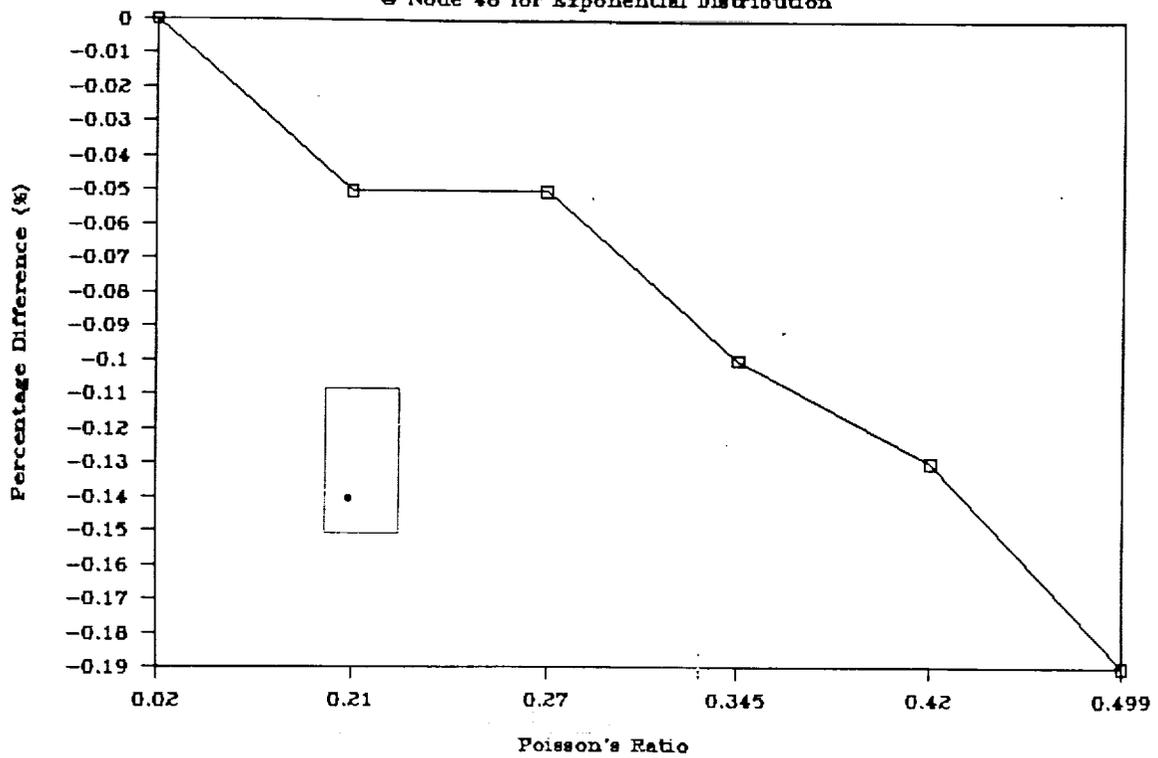
14. Two Units from the Center, Three and Four Units Up

Thermal Shear Stress

Strains

$$\varepsilon_x = \frac{1}{E}\left(C_1 + yC_2 + zC_3\right)$$

$$\varepsilon_y = \frac{1}{E}\left[(1 + v)\alpha ET - v(C_1 + yC_2 + zC_3)\right.$$

$$\left. + \phi,_{zz} - \phi,_{yy} - v^2\nabla^2\phi\right]$$

$$\varepsilon_z = \frac{1}{E}\left[(1 + v)\alpha ET - v(C_1 + yC_2 + zC_3)\right.$$

$$\left. + \phi,_{yy} - \phi,_{zz} - v^2\nabla^2\phi\right]$$

Thermal Warping Function

$$\sigma_{xx,x} + G\gamma_{xy,y} + G\gamma_{xz,z} = 0$$

$$\nabla^2\Omega = -\frac{1}{2}\nabla^2\phi' - \frac{1}{(1 + v)}(C_1' + yC_2' + zC_3')$$

15. Shear Strains and Thermal Warping Function

Stresses

$$\sigma_{xy} = \frac{1}{2} \int_{y_0}^{y_i} \left[(1 - v) \, \phi,'_{zz} - v \, \phi,'_{yy} + \alpha ET' \right] dy$$

$$+ \frac{1}{2(1 + v)} \left[\Omega,_y - yv(C_1' + \frac{1}{2}yC_2' + zC_3') \right]$$

$$\sigma_{xz} = \frac{1}{2} \int_{z_0}^{z_i} \left[(1 - v) \, \phi,'_{yy} - v \, \phi,'_{zz} + \alpha ET' \right] dz$$

$$+ \frac{1}{2(1 + v)} \left[\Omega,_z - zv(C_1' + yC_2' + \frac{1}{2}zC_3') \right]$$

16. Final Shear Stresses
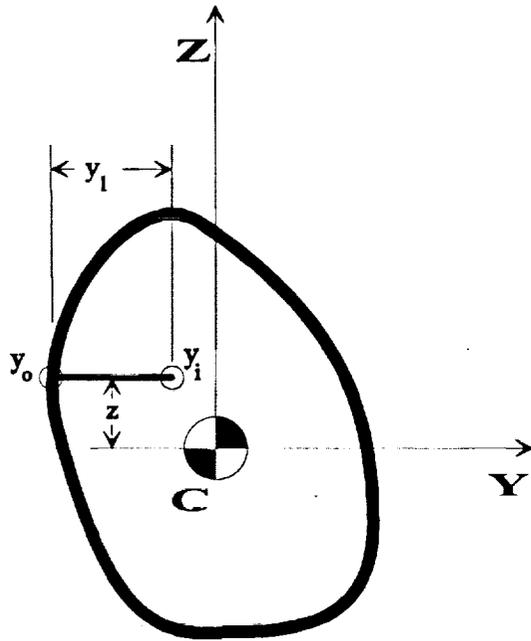
Effective Line in the Y-direction

Fig. 2a
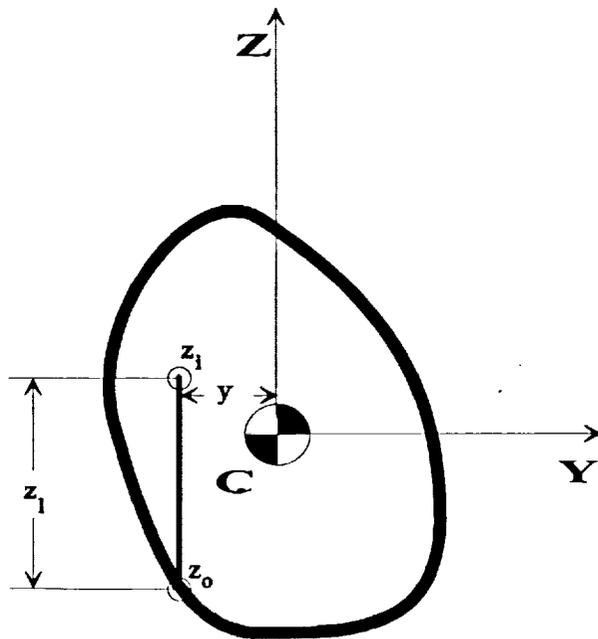
Effective Line in the Z-direction

Fig. 2b

17. The Effective Lines

Multi-connected Regions

Composites

Comparison of Finite Elements To Exact Elasticity

18. Future Work

Project 15   Experimental Study of the Nonlinear Viscoplastic Response of High Temperature Structures

Marshall F. Coyle and E.A. Thornton

Objectives

The basic objective of this research program is to investigate experimentally the viscoplastic response of thermal structures for high speed flight. An additional objective of the experimental program is to provide high quality data for validation of finite element analysis using unified viscoplastic constitutive models.

Status and Recent Results

Recent progress of a research program focused on understanding the thermoviscoplastic behavior of structural panels is described. The program has three tasks: (1) finite element simulations of geometric and nonlinear material behavior, (2) experimental determination of parameters for Bodner-Partom constitutive models of panel materials, and (3) thermal-structural tests of panels subjected to localized heating.

Finite element analysis of nonlinear panel bending is under development. A finite element formulation for elastic panel bending described by the Von Karman equations is described. Numerical results for thermal buckling of panels with initial deformations are presented. Correlation of predicted panel behavior with experimental results is underway. the extension of the finite element analysis to include thermoviscoplastic behavior is underway.

A research task focused on the experimental determination of the constitutive model parameters is in progress. This task will provide data for the panel materials for the range of temperatures and strain rates to be used in the thermal-structural test program. Initial tensile tests for Hastelloy-X have been completed, and material parameters for the Bodner-Partom constitutive model have been determined. Testing is underway to develop material parameters for the aluminum alloy 2618, the Concorde structural material. Test panels of the 8009 aluminum alloy were provided by NASA-LaRc, and material test specimens are currently being manufactured. A test program to determine Bodner-Partom material

parameters for this alloy has been planned.

In the experimental study, rectangular plates are heated transiently by a quartz heat lamp focused on the panel centerline. Parallel edges of the panel are maintained at constant temperature by chill water flow through coolant tubes. The panel is supported at only four points to provide well-defined thermal and structural boundary conditions. A heat lamp characterization study is described, and an empirical formula for the incident surface heat flux is developed. The thermal buckling test procedure is described, and results from two tests are presented.

Temperatures and displacement results for elastic and inelastic tests are presented. The panel exhibited a global buckling response in both tests. In the inelastic test, the panel maximum displacement exceeded two plate thicknesses and significant permanent deformation was induced.

The tests reaffirm that localized heating can cause substantial out-of-plane bending of real panels. The global bending deformations demonstrated were due to in-plane spatial temperature gradients and initial panel warpage. Small initial warpage with compressive membrane thermal forces was sufficient to initiate substantial transverse bending.

Milestones

Future plans include continued development of each of the research tasks. Within the next year, correlations of simulated thermoviscoplastic panel behavior with experimental data will be initiated.

Presentation Abstract

The presentation describes computational and experimental studies of the thermal-structural behavior of thin panels subjected localized heating. Recent progress on three research tasks is described: (1) development of a finite element thermoviscoplastic computational approach, (2) experimental determination of material parameters for Bodner-Partom constitutive models of panel materials, and (3) experimental study of panels subjected to intense local heating. A heat lamp characterization study and thermal buckling tests of Hastelloy-x panels are described. Plans for future research are highlighted.

102

# EXPERIMENTAL AND COMPUTATIONAL STUDIES OF THERMOVISCOPLASTIC PANELS

Earl A. Thornton
Marshall Coyle

Mechanical, Aerospace and Nuclear Engineering
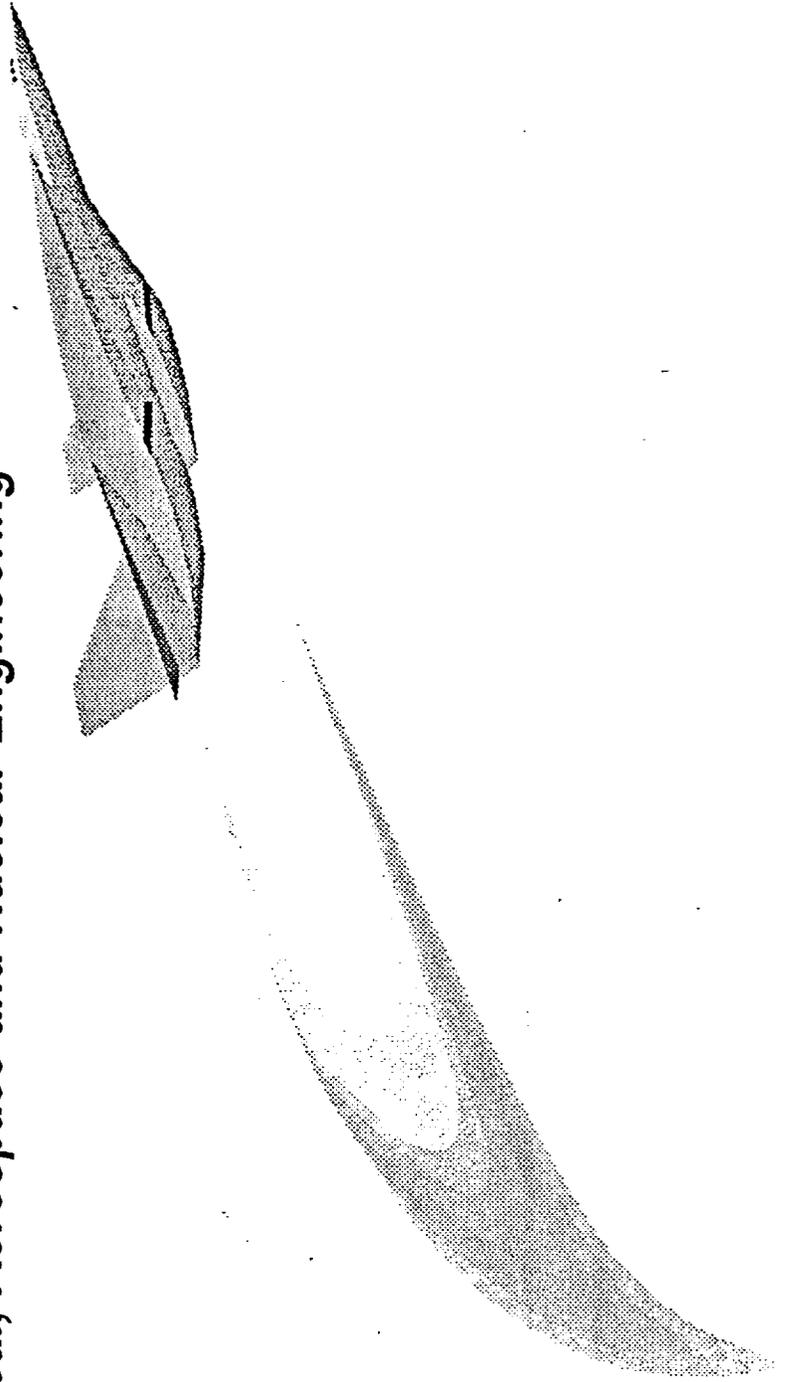
RESEARCH OBJECTIVES

- Investigate Thermoviscoplastic (TVP) response of thin panels subject to intense local heating.

- Evaluate finite element Thermal-Structural analyses with unified TVP constitutive models by comparison with experimental data.
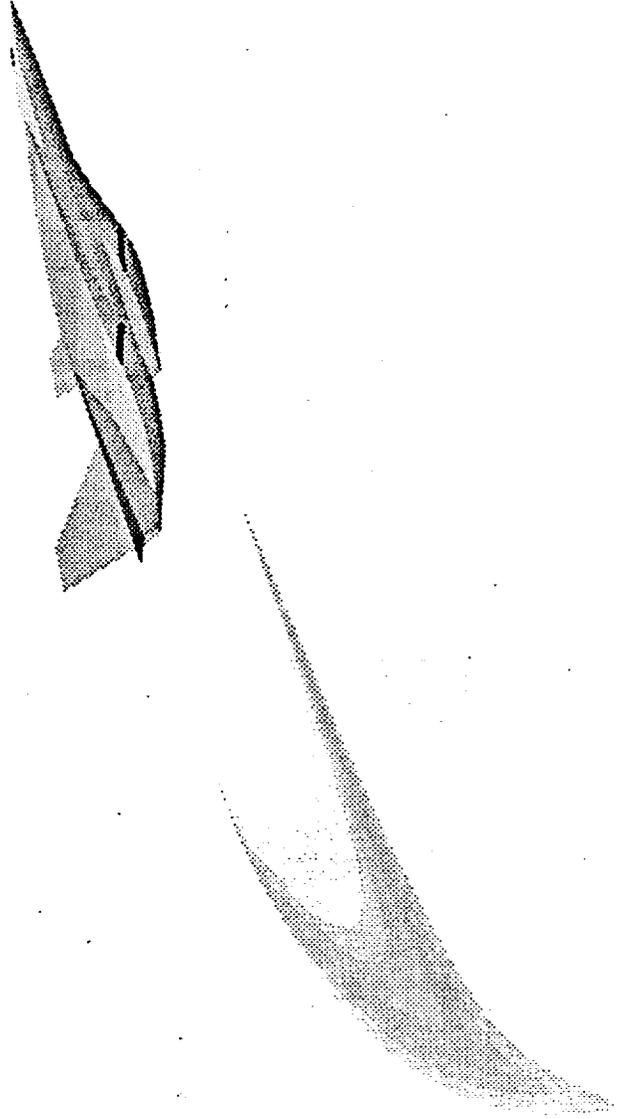
# THERMOVISCOPLASTIC RESEARCH PROGRAM

- FINITE ELEMENT TVP ANALYSIS
  J. D. KOLENSKI

- BODNER-PARTOM CONSTITUTIVE MODELS
  MARK A. ROWLEY

- THERMAL-STRUCTURAL TESTS OF PANELS
  MARSHALL F. COYLE

FINITE ELEMENT ANALYSIS

Computational Plate Analysis

- CST Plane Stress Element & DKT Bending Element
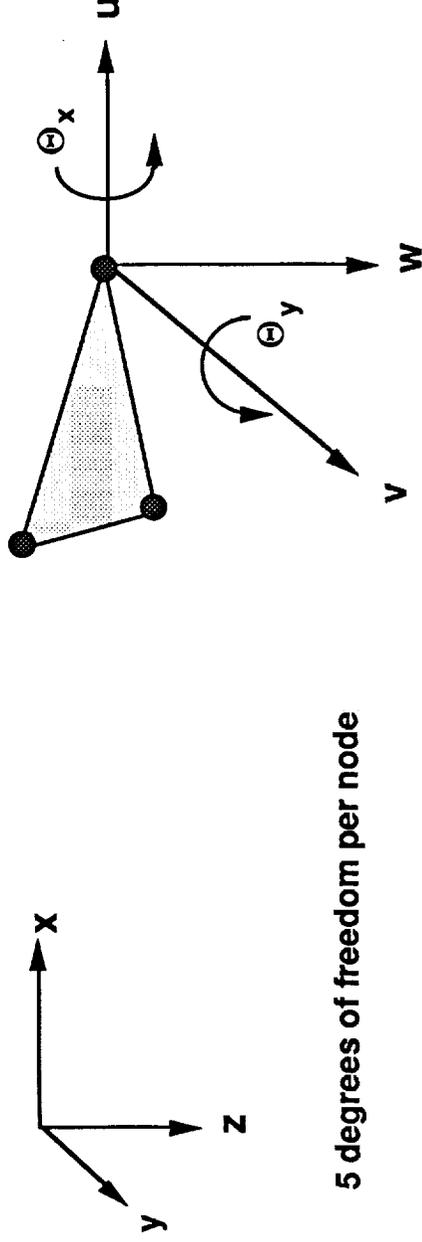
5 degrees of freedom per node

- Prescribed Nodal Temperature Histories

- Quasi-static Response

- Neglects Temperature Gradient Through Thickness

- Temperature Dependent Material Properties

- Newton-Raphson Iterative Equation Solver

Governing Plate Equations

Equilibrium

$$\frac{\partial^2 M_x}{\partial x^2} + 2\frac{\partial^2 M_{xy}}{\partial x \partial y} + \frac{\partial^2 M_y}{\partial y^2} + \frac{\partial}{\partial x}\left(N_x \frac{\partial w}{\partial x}\right) + \frac{\partial}{\partial y}\left(N_{xy}\frac{\partial w}{\partial y}\right) + \frac{\partial}{\partial x}\left(N_{xy}\frac{\partial w}{\partial y}\right) + \frac{\partial}{\partial y}\left(N_y \frac{\partial w}{\partial y}\right) + q = 0$$

$$\frac{\partial N_x}{\partial x} + \frac{\partial N_{xy}}{\partial y} = 0$$

$$\frac{\partial N_{xy}}{\partial x} + \frac{\partial N_y}{\partial y} = 0$$

Strain-Displacement

$$\{\varepsilon_m\} = \begin{Bmatrix} \dfrac{\partial u_0}{\partial x} \\[4pt] \dfrac{\partial v_0}{\partial y} \\[4pt] \dfrac{\partial u_0}{\partial y} + \dfrac{\partial v_0}{\partial x} \end{Bmatrix}$$

$$\{\varepsilon_b\} = z\begin{Bmatrix} -\dfrac{\partial^2 w}{\partial x^2} \\[4pt] -\dfrac{\partial^2 w}{\partial y^2} \\[4pt] -2\dfrac{\partial^2 w}{\partial x \partial y} \end{Bmatrix}$$

$$\{\varepsilon_{nl}\} = \begin{Bmatrix} \dfrac{1}{2}\left(\dfrac{\partial w}{\partial x}\right)^2 \\[4pt] \dfrac{1}{2}\left(\dfrac{\partial w}{\partial y}\right)^2 \\[4pt] \dfrac{\partial w}{\partial x}\dfrac{\partial w}{\partial y} \end{Bmatrix}$$

$$\{\varepsilon\} = \{\varepsilon_m\} + \{\varepsilon_b\} + \{\varepsilon_{nl}\}$$

Stress-Strain

$$\{\sigma\} = \begin{bmatrix} \sigma_x & \sigma_y & \tau_{xy} \end{bmatrix}^T = [E]\{\varepsilon - \varepsilon_0\}$$

von Kármán Plate Theory Finite Element Formulation

$$\begin{bmatrix} [K_m] & \frac{1}{2}[K_{mb}] \\ \frac{1}{2}[K_{mb}]^T & [K_b]+\frac{1}{2}[K_{bl}]+\frac{1}{2}[K_{bnl}]-[K_{bt}] \end{bmatrix} \begin{Bmatrix} \delta_m \\ \delta_b \end{Bmatrix} = \begin{Bmatrix} R_T \\ R_{TM}+R_q \end{Bmatrix}$$

$[K_m] = \int_\Omega [B_m]^T[A][B_m]d\Omega$ **Membrane Stiffness**

$[K_{mb}] = \int_\Omega [B_m]^T[A][C][G]d\Omega$ **Coupling Stiffness**

$[K_b] = \int_\Omega [B_b]^T[D][B_b]d\Omega$ **Bending Stiffness**

$[K_{bl}] = \int_\Omega [G]^T[N_m][G]d\Omega$ **Linear Geometric Stiffness**

$[K_{bnl}] = \int_\Omega [G]^T[C]^T[A][C][G]d\Omega$ **Nonlinear Geometric Stiffness**

$[K_{bt}] = \int_\Omega [G]^T[N_T][G]d\Omega$ **Thermal Bending Stiffness**

$\{R_T\} = \int_\Omega [B_m]^T\{N_T\}d\Omega$ **Thermal Force**

$\{R_{TM}\} = -\int_\Omega [B_b]^T\{M_T\}d\Omega$ **Thermal Moment**

$\{R_q\} = \int_\Omega q\{N\}d\Omega$ **Pressure Load**

Applications of Computational Plate Analysis

Validation Studies

- Classical Small Deflection Plate

- Large Deflection Problems
  - Pressure Loaded Plate (Levy, Clough)
  - Simply Supported Movable & Immovable Edges

Thermal Postbuckling of Plates with Initial Imperfections

- Aluminum Panel
  - Immovable & Movable Edges
  - Varying Initial Plate Imperfection

- Hastelloy-X Panel (UVa Experiment)
  - Point Supported
  - Initial Plate Imperfection
  - Slowly Heated

Validation Problem

Uniform Pressure Load on Simply
Supported Aluminum Plate
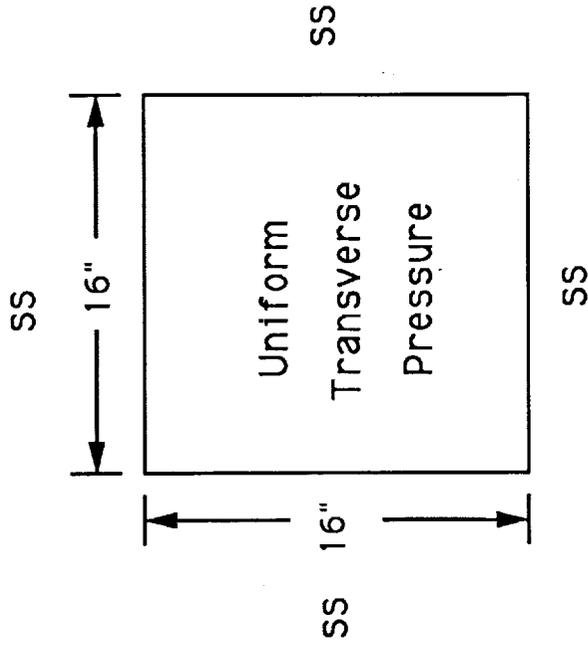
Transverse Deflection of Plate Center
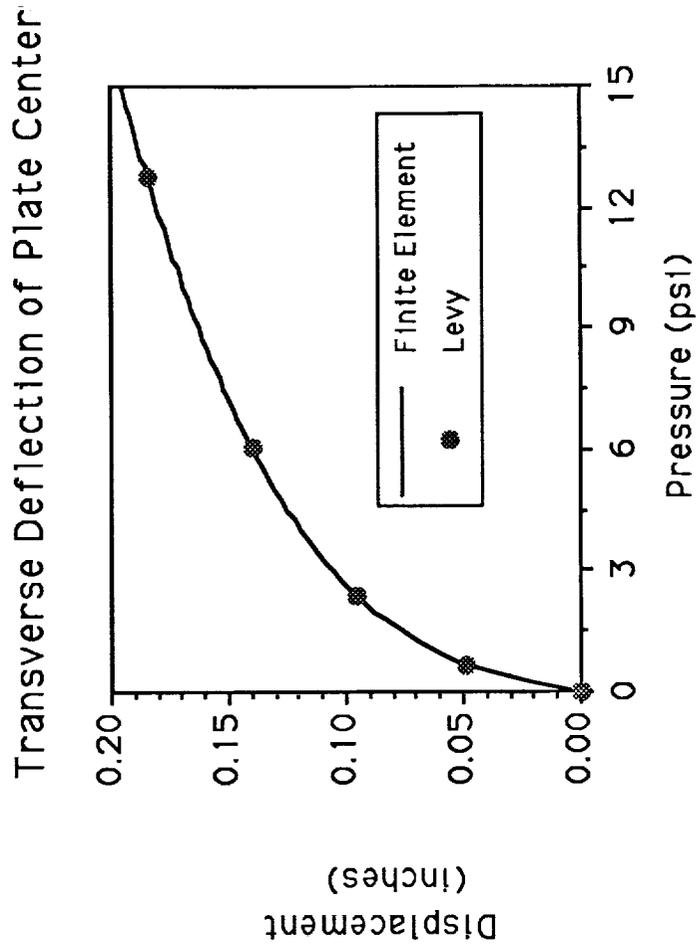
Plate with Immovable Edges and Uniform Temperature
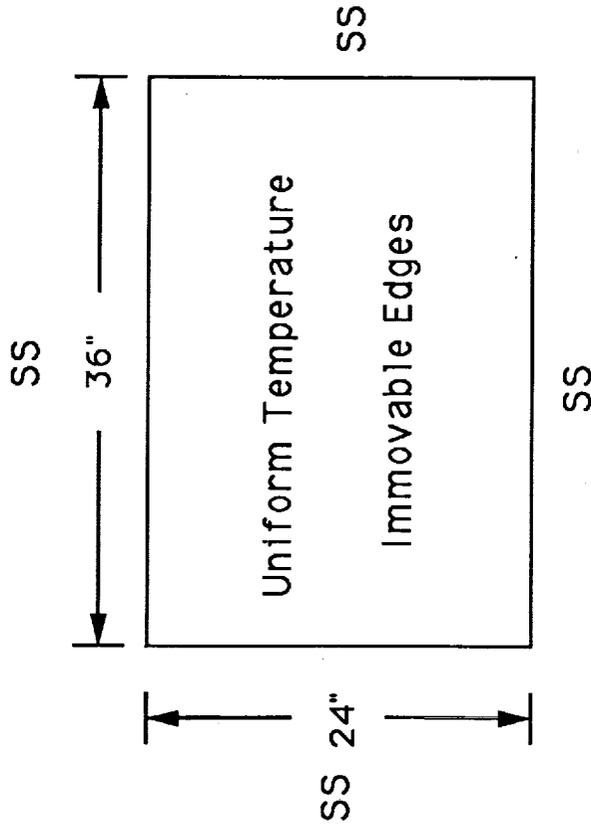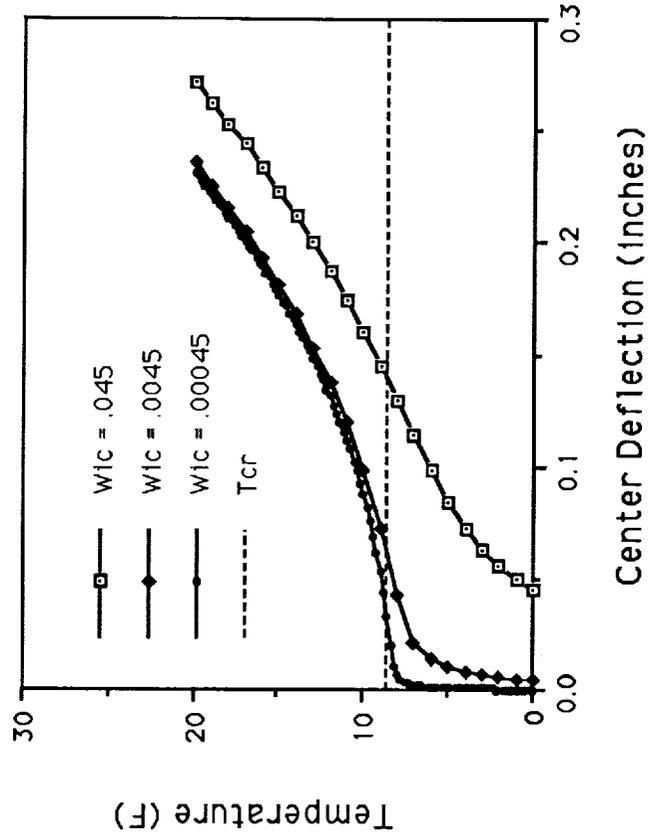
Wic = Initial Transverse
Deflection at Plate Center

SS

SS   36"

Uniform Temperature
Immovable Edges

SS   24"

SS

h   =   0.25   in.
E   = 10.4 E+06 psi.
CTE = 12.7 E-06 in./in.-F
v   =   0.33

Plate with Movable Edges and Linearly Varying Temperature

Finite Element vs. Analytical Solution

T = 0 at Y = +12 in. & -12 in.
Linear Temperature Variation
in Y Direction from Plate
Edges to Plate Center
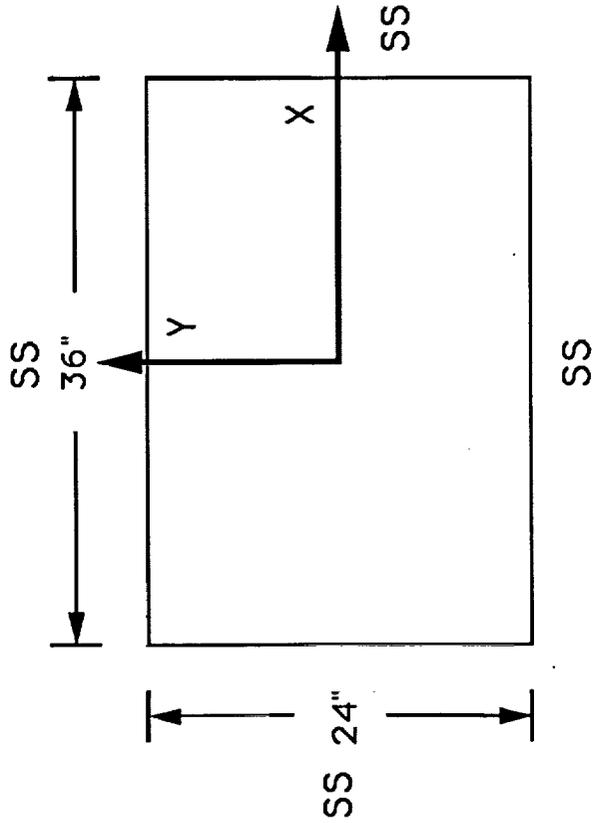
Center Deflection (Inches)

Temperature (F) @ Plate Center

Legend:
— Gossard
□ Finite Element

Initial Plate Imperfection (Wic) = .00045"

SS

SS 36"

SS

SS 24"

X

Y

h   = 0.25   in.
E   = 10.4 E+06 psi.
CTE = 12.7 E-06 in./in.-F
v   = 0.33
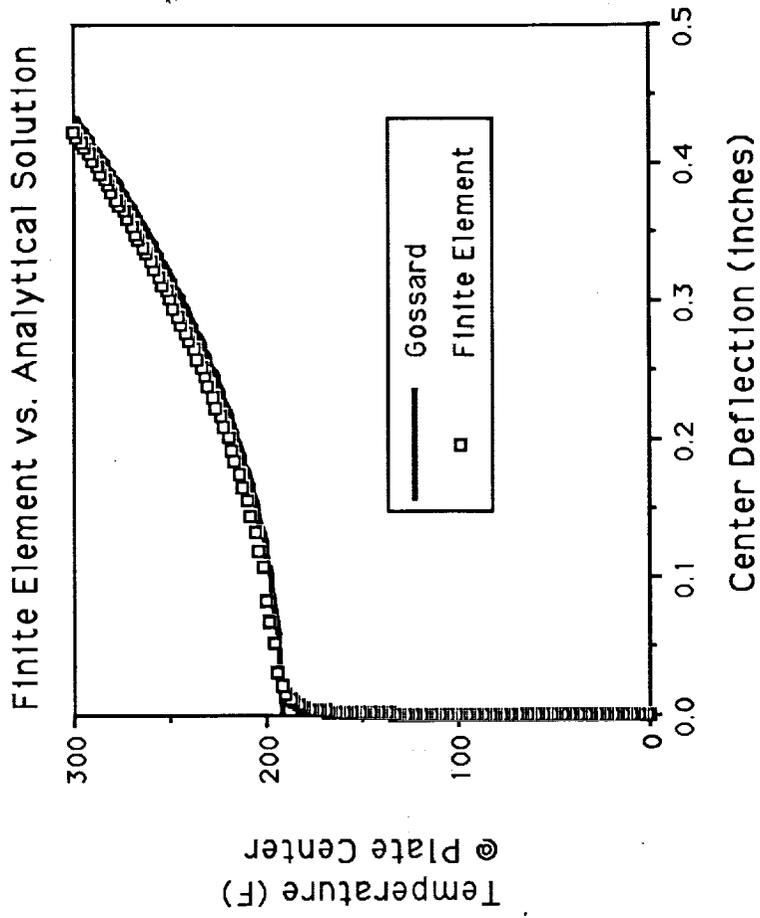
Point Supported Hastelloy-X Plate

Temperature (F) @ Plate Center vs. Center Deflection (inches)

Wlc = 0.003"

plate thickness = 0.125 "

Corner Point Supports

15"

10"
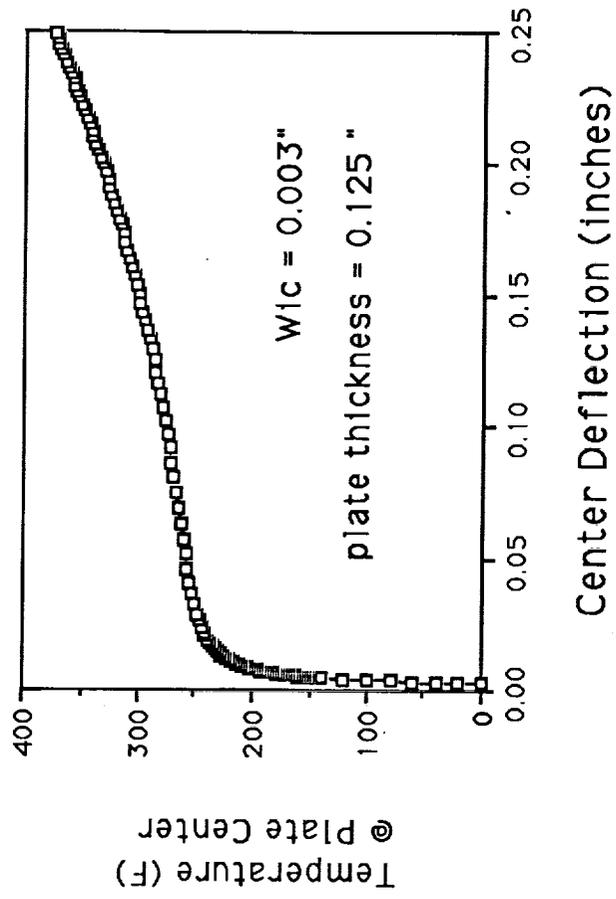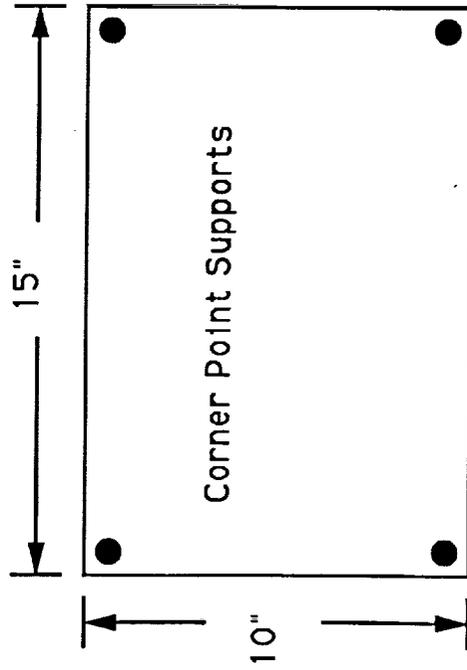
Slowly Heated Hastelloy-X Plate

Stress Variation Through Plate Thickness
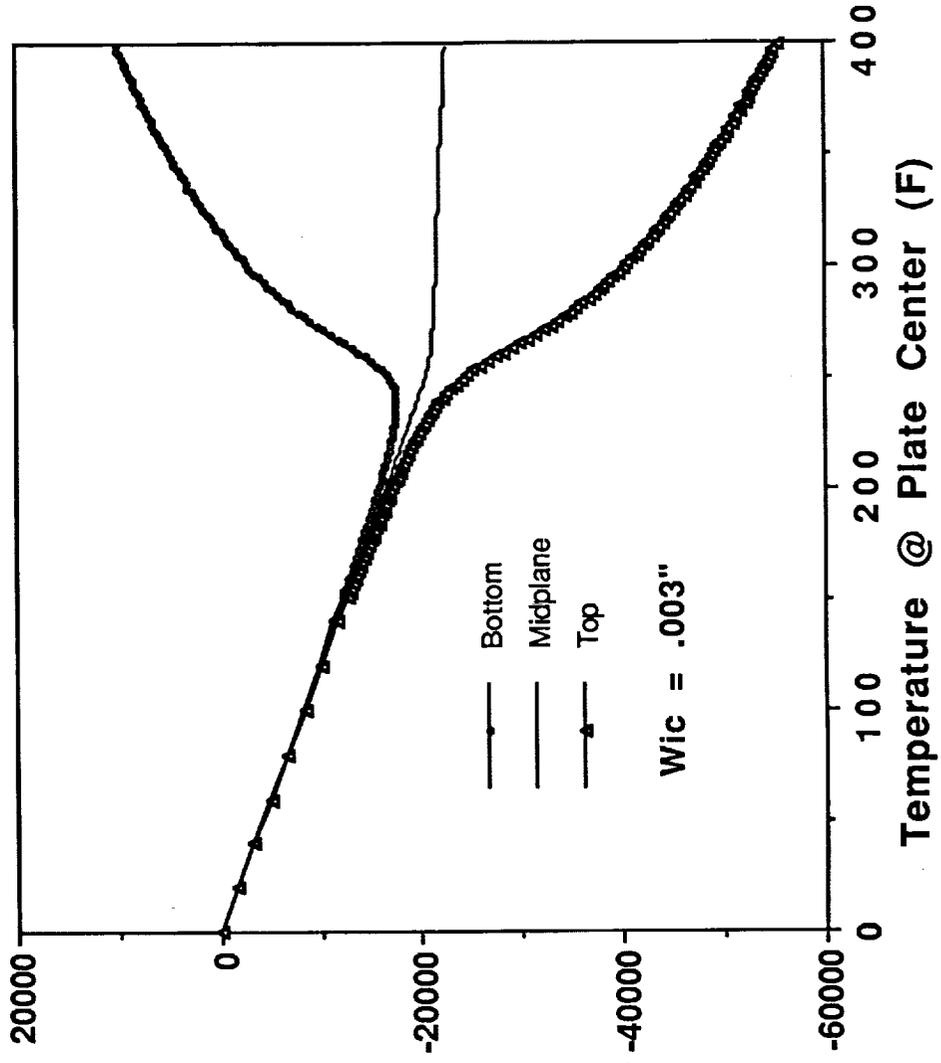
Stress (psi) at
Plate Center

Future Work

- Improved Iterative Solution Algorithm

- Viscoplastic Bending

- Simulation of Elastic and Inelastic Experiments

BODNER–PARTOM CONSTITUTIVE MODELS

Essential Equations for the Bodner Partom Viscoplasticity Model

1. $\dot{\varepsilon}_T = \dot{\varepsilon}_E + \dot{\varepsilon}_P$ (Flow Law)

2. $\dot{\varepsilon}_P = \dfrac{2}{\sqrt{3}} D_0 \left\{ \dfrac{\sigma}{|\sigma|} \right\} \exp\left\{ -\dfrac{1}{2}\left(\dfrac{Z}{\sigma}\right)^{2n} \right\}$ (Kinetic Eqn.)

3. $Z = Z^I + Z^D$ (Evolution Eqns.)

$\dot{Z}^I = m_1\left(Z_1 - Z^I\right)\dot{W}_P - A_1 Z_1 \left\{ \dfrac{\left(Z^I - Z_2\right)}{Z_1} \right\}^{r_1}$

$\dot{Z}^D = m_2\left(Z_3 - Z^D\right)\dot{W}_P - A_2 Z_1 \left\{ \dfrac{\left(Z^D - Z_2\right)}{Z_1} \right\}^{r_2}$

4. $\dot{W}_P = \sigma \cdot \dot{\varepsilon}_P$ (Rate of Plastic Work)

Typical Parameter Determination

Curve Fitting

Uniaxial Tensile Tests

m_1
m_2

Sigma vs Gamma Curve for Hastelloy - X

m_2

1

m_1

1

Gamma (1/psi)

Stress (psi)
(Thousands)

$$\gamma = \frac{1}{\sigma} \frac{d\sigma}{d\varepsilon_P}$$

7th Order Polynomial Curve Fit

Stress (psi)
(Thousands)

Plastic Strain (in/in)

—— Curve Fit   —— Experimental Data
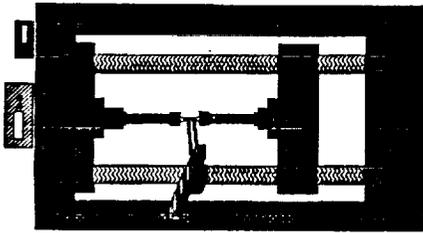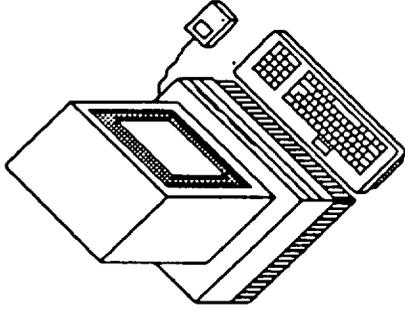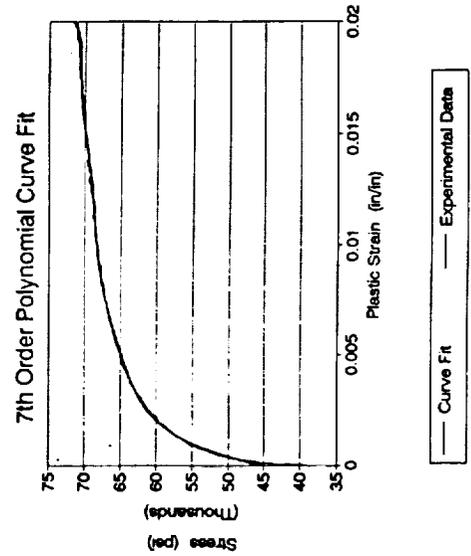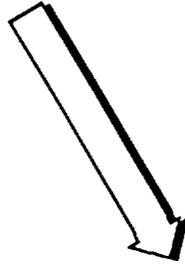
$$\sigma = a_0 + a_1 \varepsilon_P + a_2 (\varepsilon_P)^2 + \ldots$$
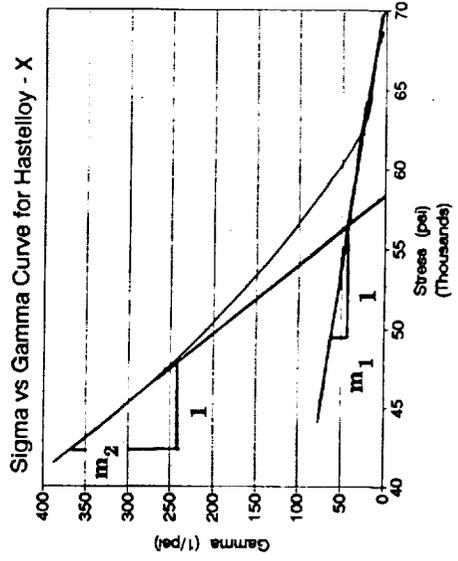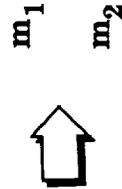
Testing Schedule for Hastelloy - X

TEMPERATURE

STRAIN RATE	25C (77F)	204C (400F)	371C (700F)	537C (1000F)
3.3×10^{-4} (sec^{-1})	3 tests	3	2	2
3.3×10^{-3} (sec^{-1})	2	3	2	2

1. All tests are isothermal, constant strain rate, uniaxial tensile tests performed on an Instron screw driven load frame.

2. Additional tests are planned at a strain rate of 3.3×10^{-5} sec^{-1} for full temperature range.

Temperature Independent Parameters for Hastelloy - X

D_0	Limiting Shear Strain Rate	$10000 \ \text{sec}^{-1}$
m_1	Isotropic Hardening Rate Coeff.	$0.210 \ \text{E-02} \ \text{,psi}^{-1}$
m_2	Directional Hardening Rate Coeff.	$0.223 \ \text{E-01} \ \text{psi}^{-1}$
Z_1	Max. Value of the Isotropic Hardening Variable	$0.332 \ \text{E+06} \ \text{psi}$
Z_3	Max. Value of the Directional Hardening Variable	$0.111 \ \text{E+06} \ \text{psi}$

Temperature Dependent Parameters for Hastelloy - X

	T = 77F	400F	700F	1000F	
n	1.000	0.905	0.850	0.825	Kinetic Parameter
Z_0 (psi)	0.265 E+06	0.240 E+06	0.240E+06	0.240 E+06	Initial Value of Isotropic Hardening Variable
Z_2 (psi)	0.265 E+06	0.240 E+06	0.240E+06	0.240 E+06	Min. Value of Isotropic Hardening Variable
$A_1 = A_2$ (psi)	0.00	0.00	0.00	0.00	Recovery Coeff.
$r_1 = r_2$	0.00	0.00	0.00	0.00	Recovery Exponent

Comparison of Model vs. Experiment

Hastelloy - X   (T=77F)

Hastelloy - X   (T=400F)

Stress (psi) (Thousands)

Strain (in/in)
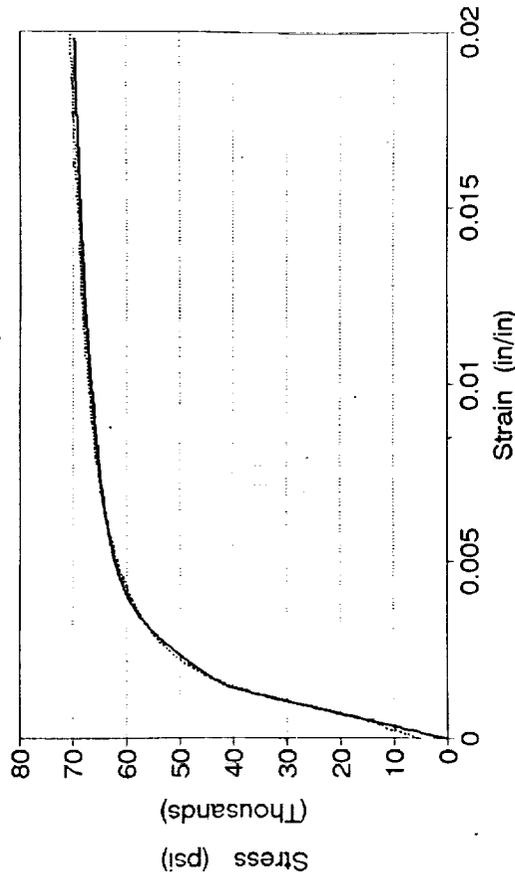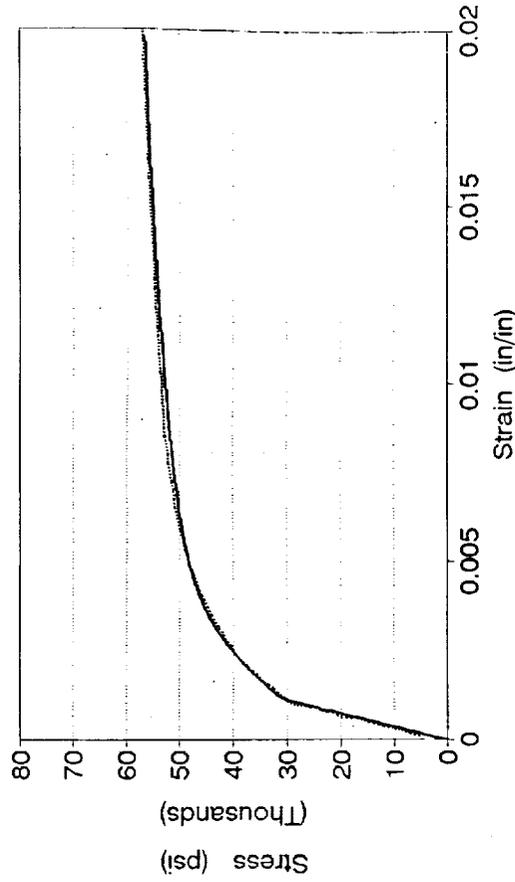
— Model   .... Experiment

Comparison of Model vs. Experiment

Hastelloy - X   (T=700F)
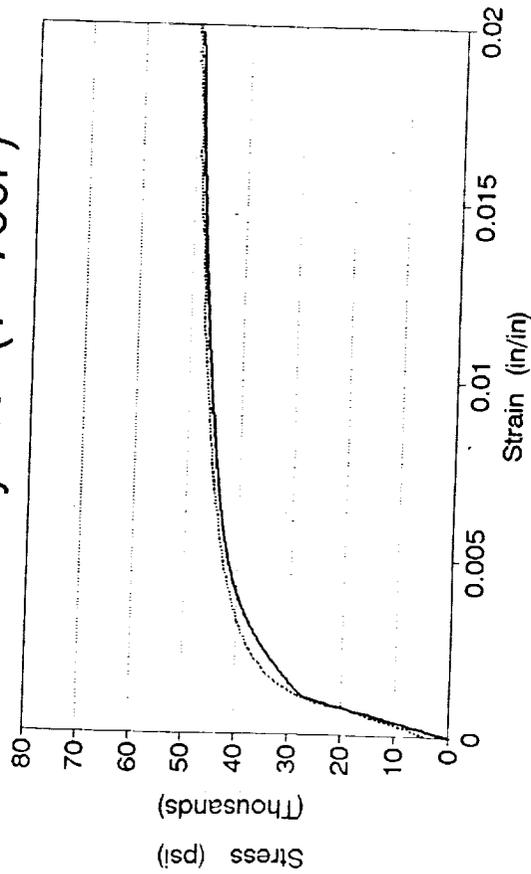
Hastelloy - X   (T=1000F)
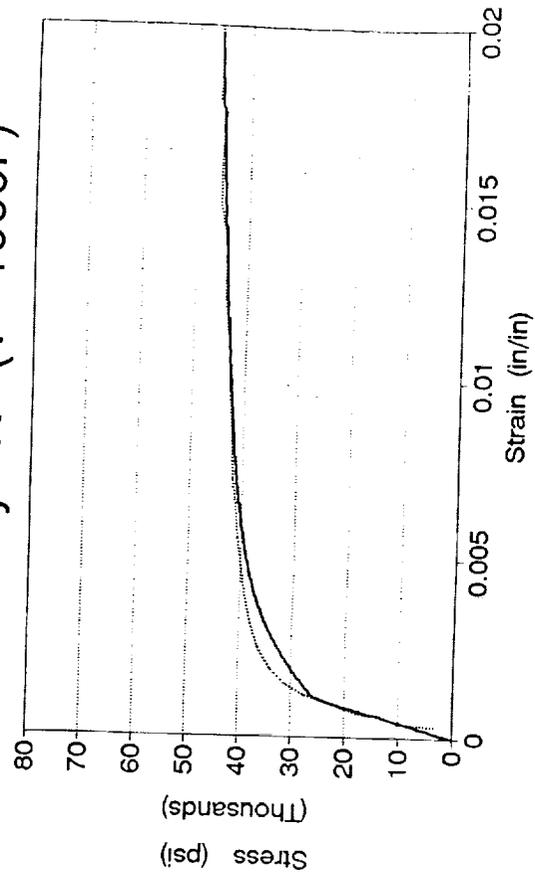
Future Work

1. Plan to test Hastelloy - X at another decade of strain rate.

2. Employment of non - linear least squares technique for establishing model parameters.

3. Currently testing 2618 aluminum and plan to develop model parameters.

4. Plan to test 8009 aluminum and develop model parameters.

Experimental Study of Plate Buckling

Objectives

- Investigate experimentally the nonlinear response of panels subjected to localized heating

- Provide data for validation of finite element thermoviscoplastic analyses

Scope

- Description of experimental program

- Presentation of results

Test Panel Configuration

Quartz Lamp

Test Panel

15 in.

0.125 in.

10 in.
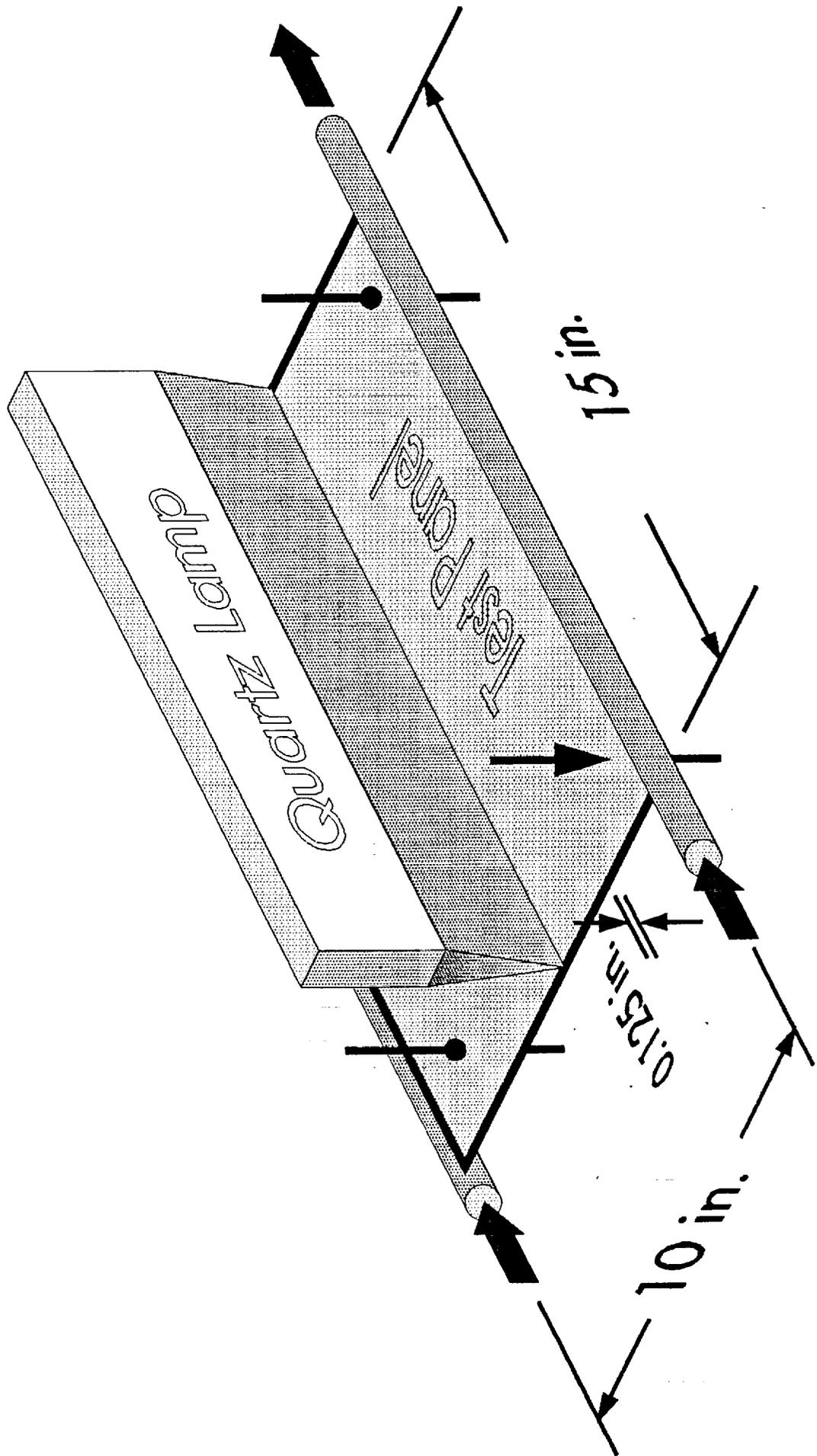
Heat Lamp Performance

Commercial Lamps (Research, Inc.)

- Tungsten filament quartz lamps

- Elliptical reflector concentrates incident flux on nominal width of 0.1 in.

Orientation Tests

- Significant heat flux levels outside of nominal width

- Variations along lamp length

Lamp Characterization Test Schematic
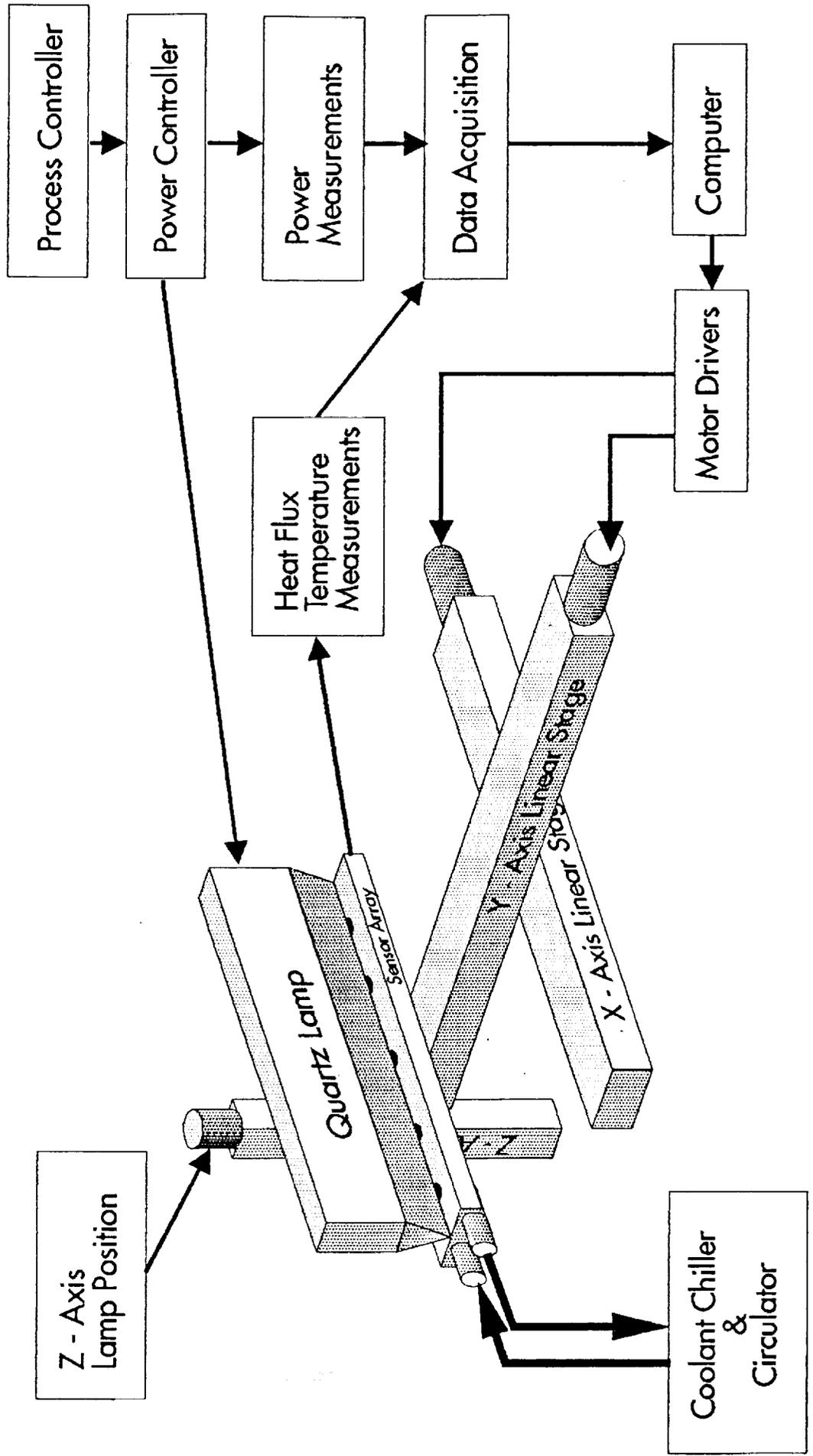
Test Fixture for Lamp Characterization Tests
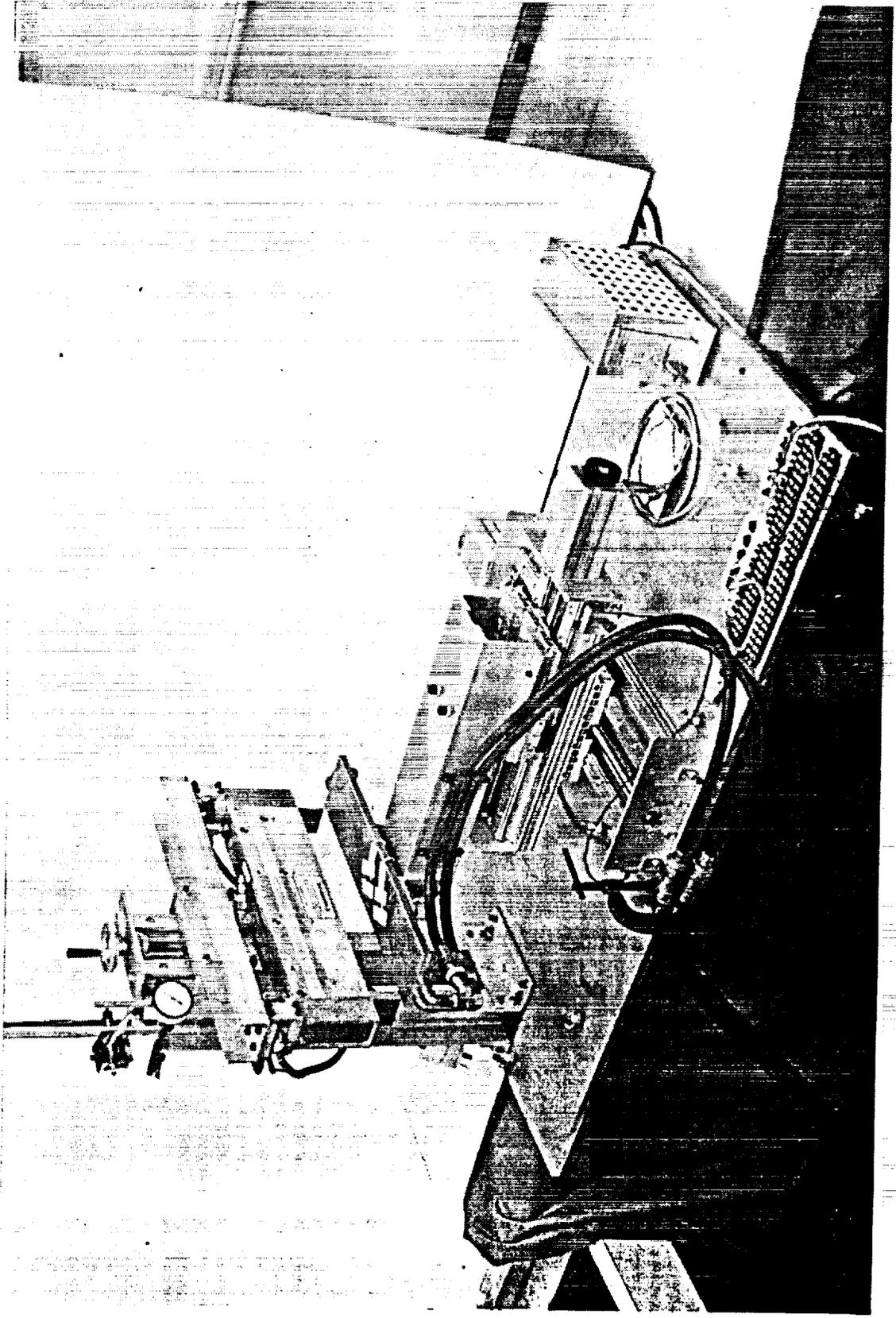
Non-Dimensional Average Heat Flux
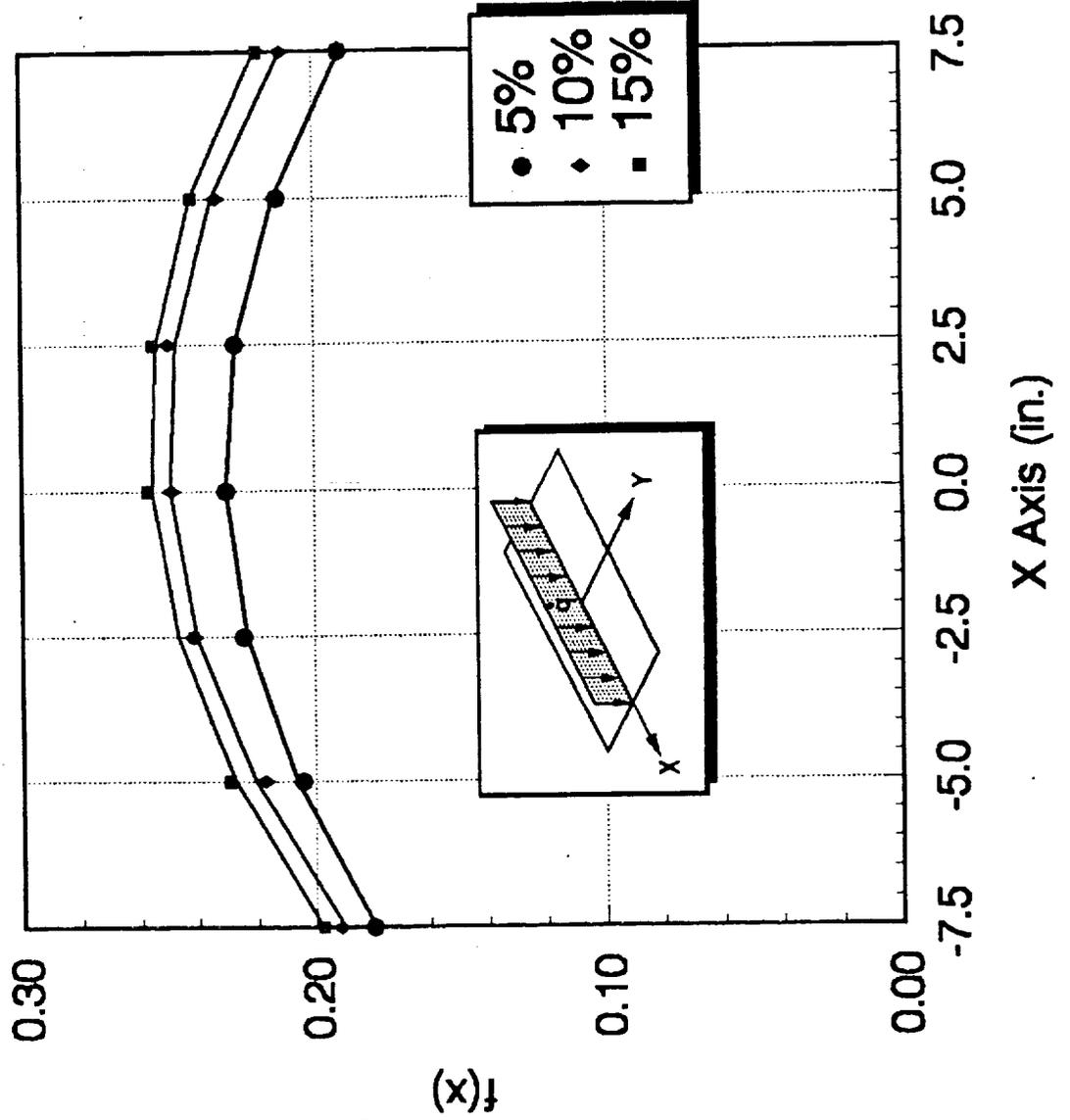
Incident Heat Flux Distributions at X = 0.0

Y Axis (in.)

BTU/ft²-sec

- 5%
- 10%
- 15%
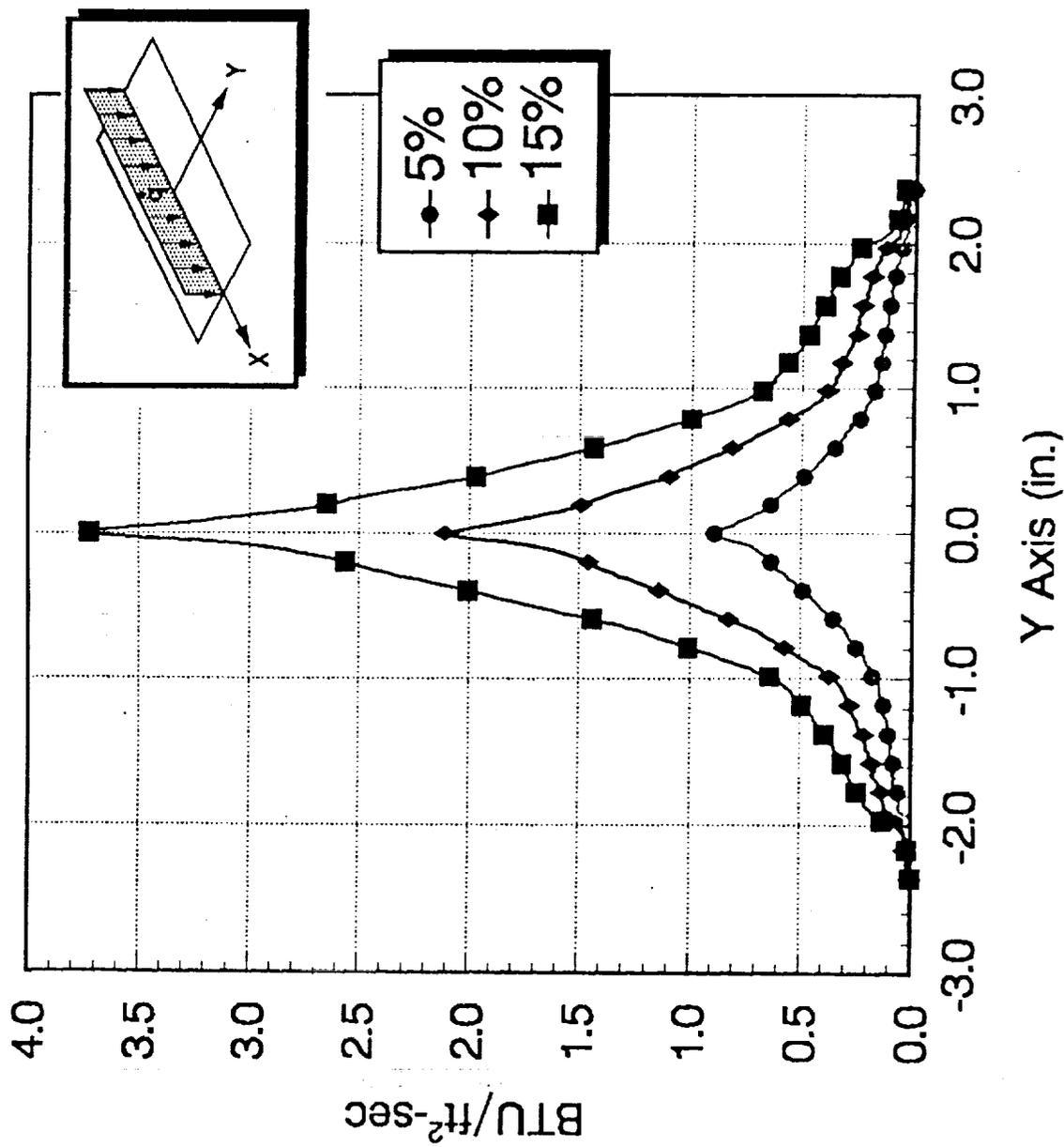
# Lamp Characterization Tests

- Lamp controller sets percent control output P

- First test series showed lamp power and incident flux varied linearly with P

- Second test series established (x,y) spatial variation of incident flux

- Data reduced to a form suitable for thermal analysis

$$q(x,P) = (a_0 + a_1x + a_2x^2) \ (mP + b)$$

$$0 < q < 24 \quad BTU/ft^2\text{-}s$$

where a_0, a_1, a_2, m, and b are given in paper

Panel Buckling Test Schematic
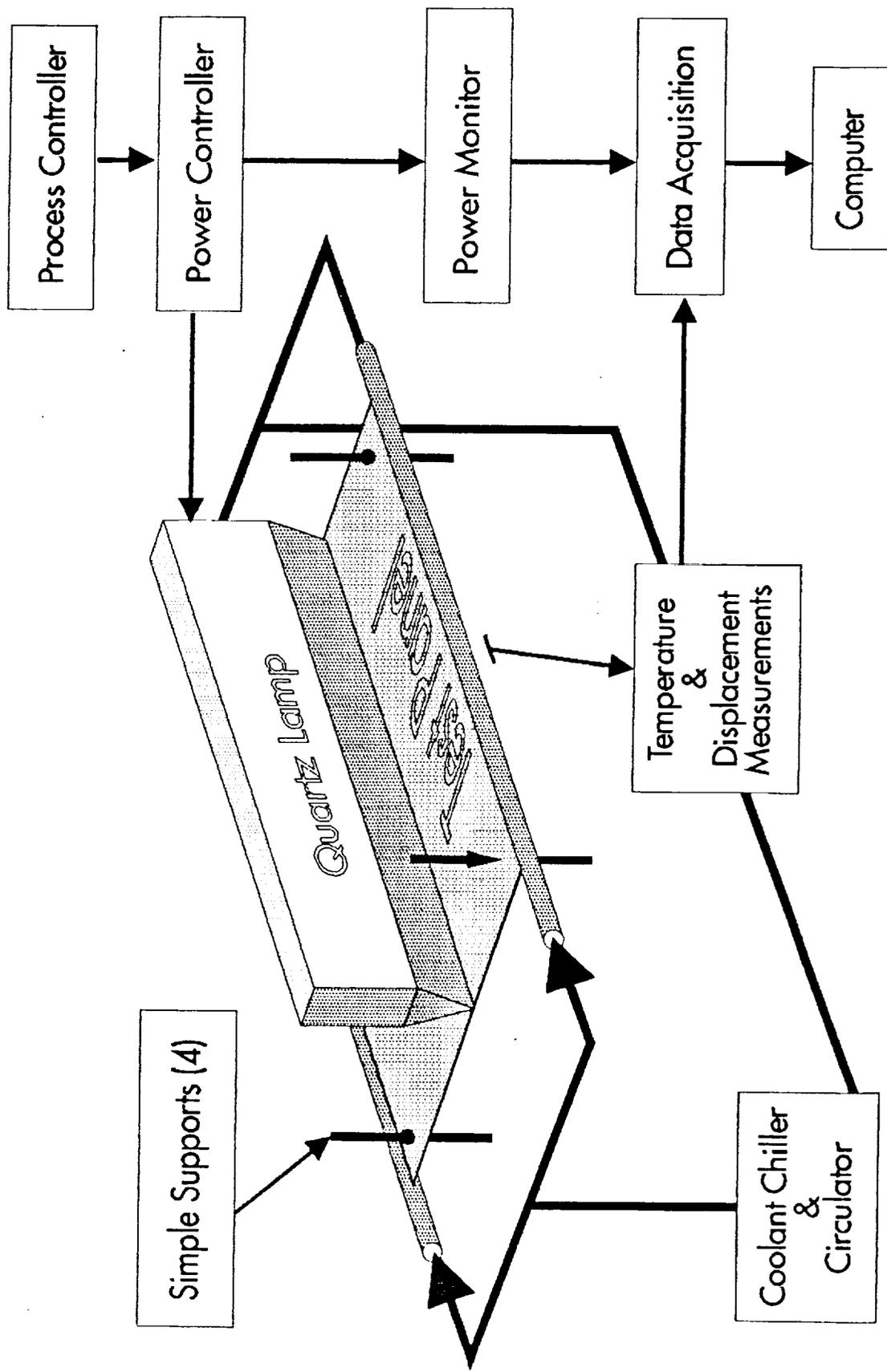
Initial Transverse Deflection
of Hastelloy-X Test Panel
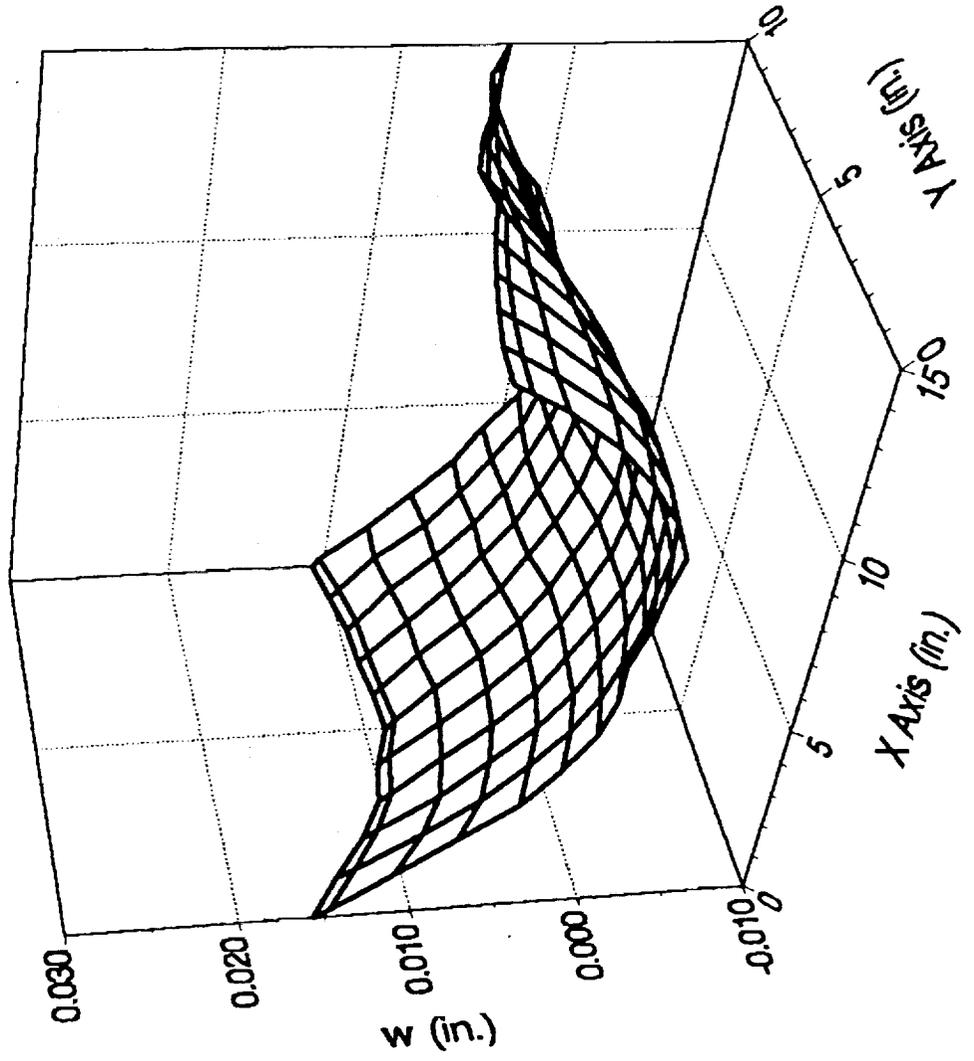
Panel Instrumentation
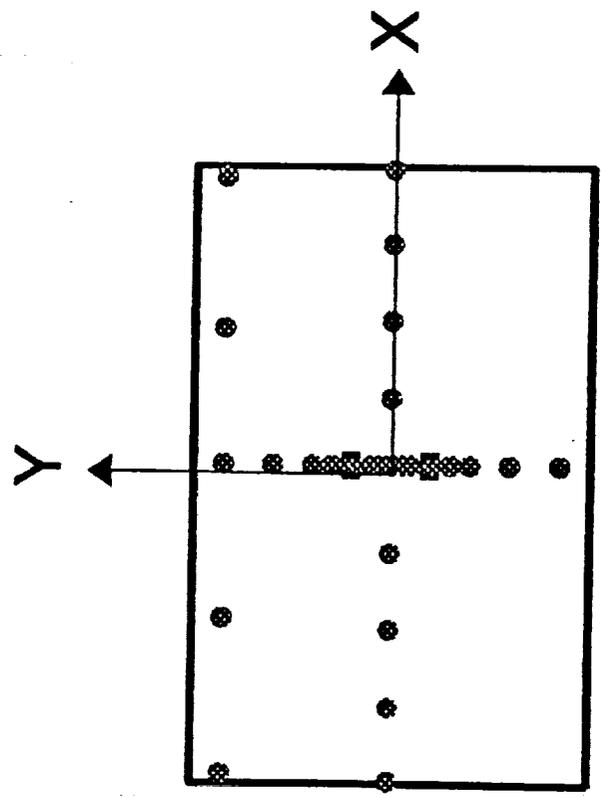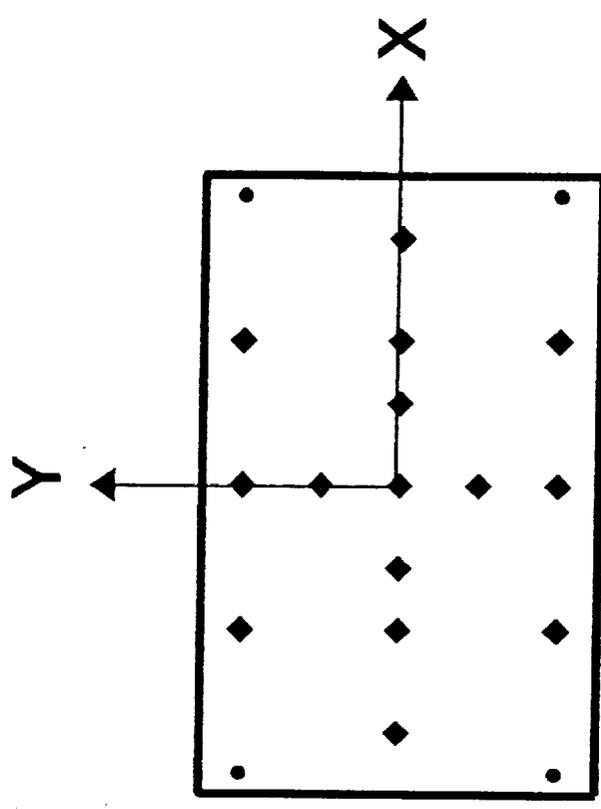
TEST FIXTURE FOR THERMAL-STRUCTURAL TESTS OF PANELS
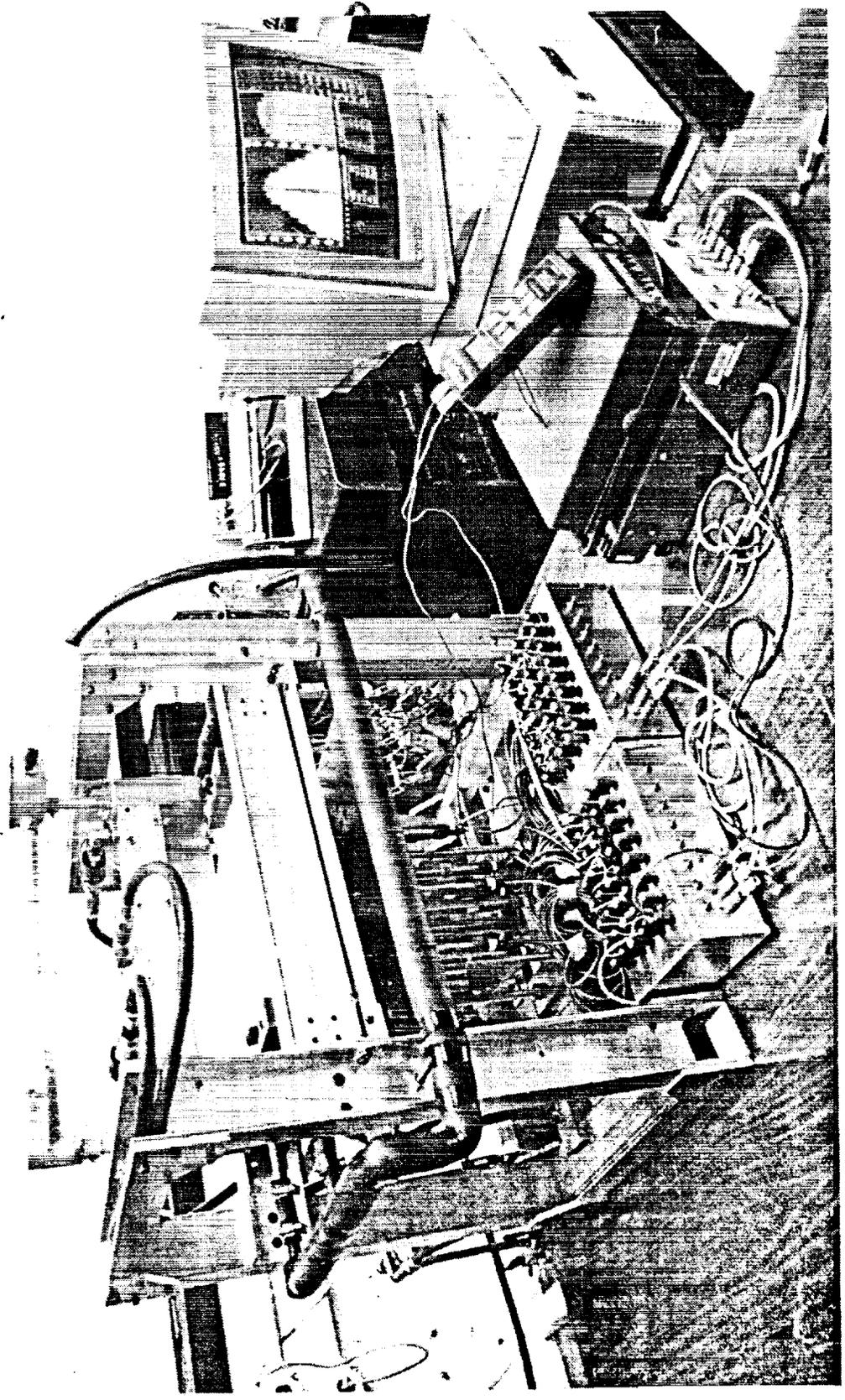
Test Procedure

- Initialize panel temperatures with coolant flow for 30-60 minutes

- Conduct test with lamp at constant P % lamp output

- Shut off lamp when maximum desired panel temperature attained

- Record temperature and displacement data as panel temperatures return to steady state
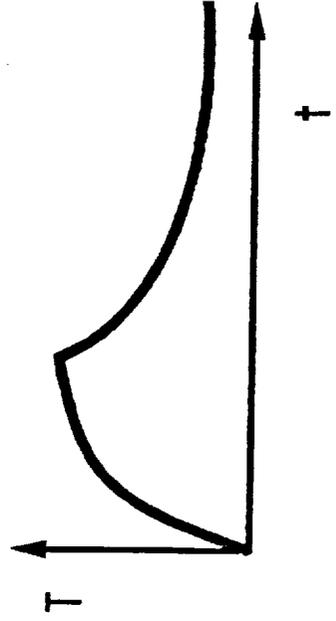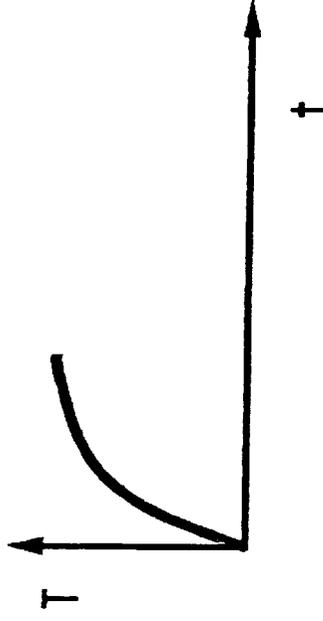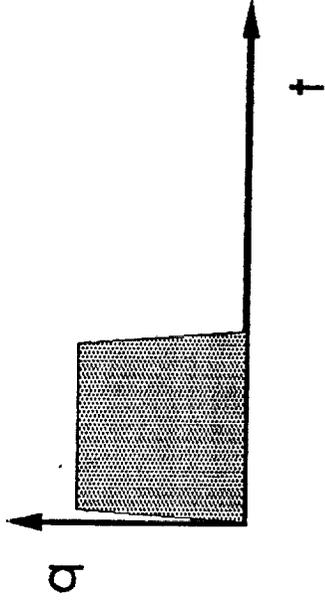
Panel Buckling Tests

Test	P (%)	Max. Temp (°F)	Behavior
1	5	250	Elastic
2*	15	375	Elastic
3	15	500	Possibly Plastic
4	30	700	Plastic
5*	70	1000	Plastic

* Results Presented

TEST 2 - Panel Temperature Distributions
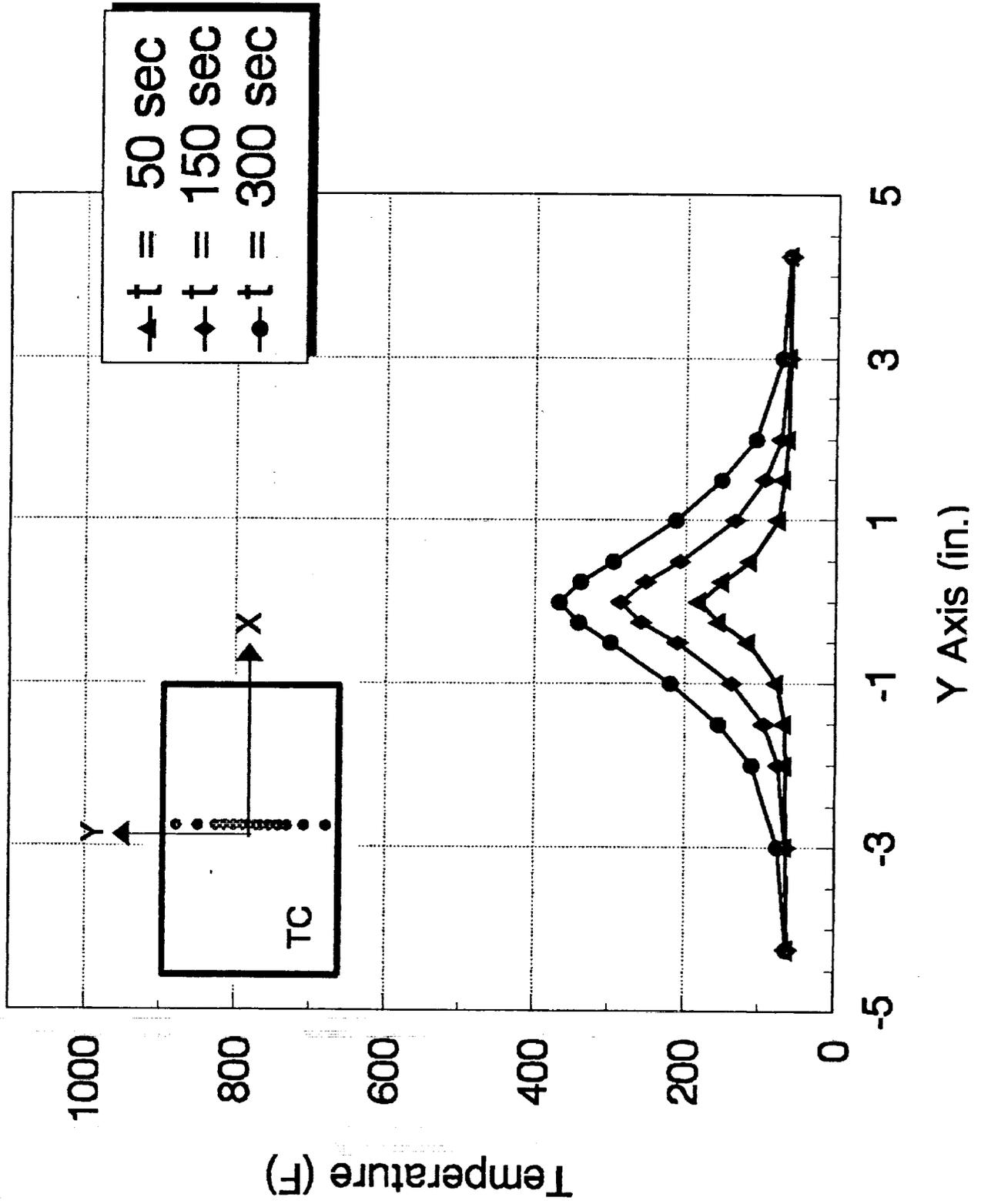
TEST 2 - Panel Temperature Histories
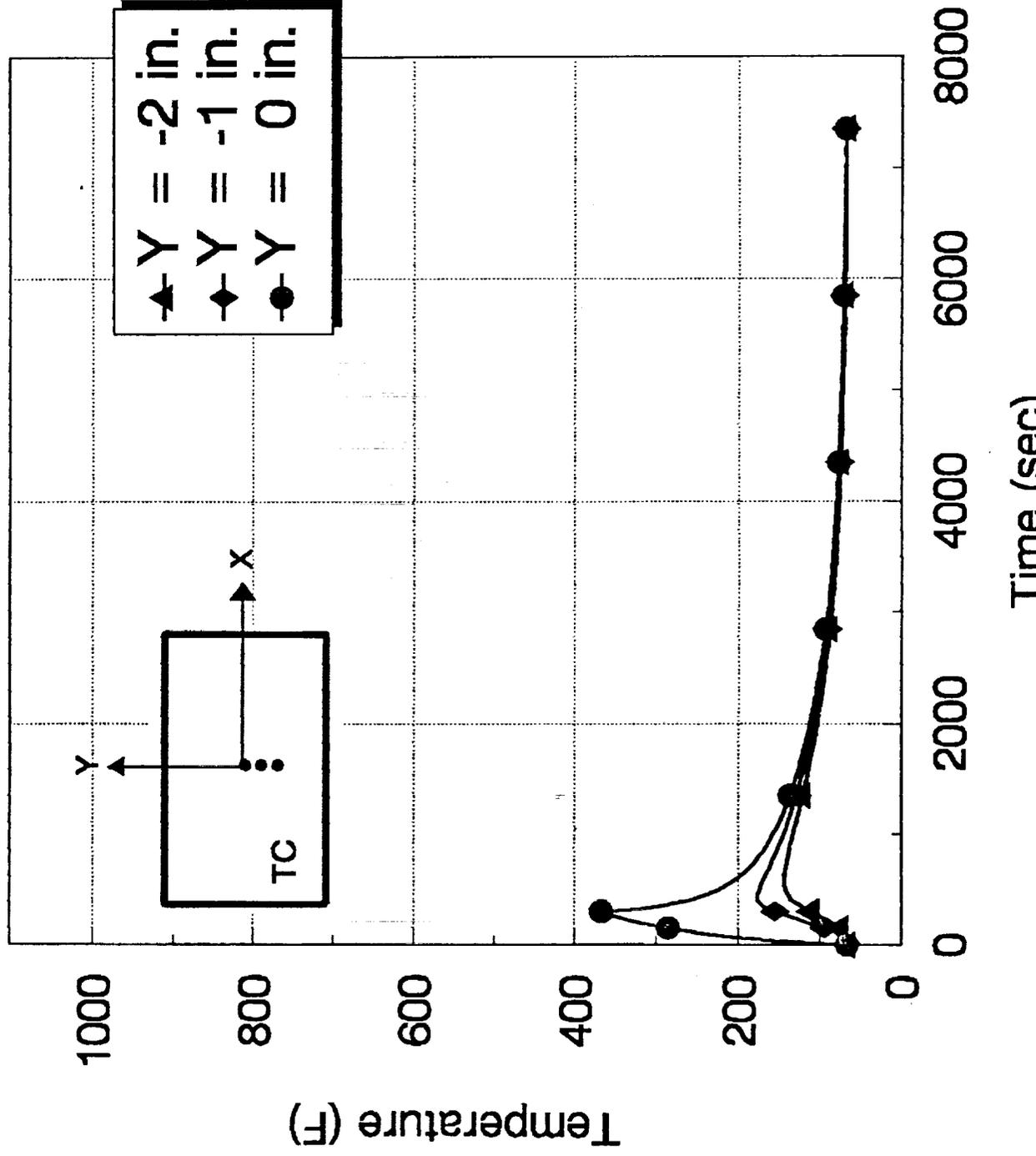
TEST 2 - Panel Displacement Distributions

TEST 2 - Panel Displacement Distributions

Legend:
- t = 0 sec
- t = 150 sec
- t = 300 sec

Displacement (in.)

Y Axis (in.)
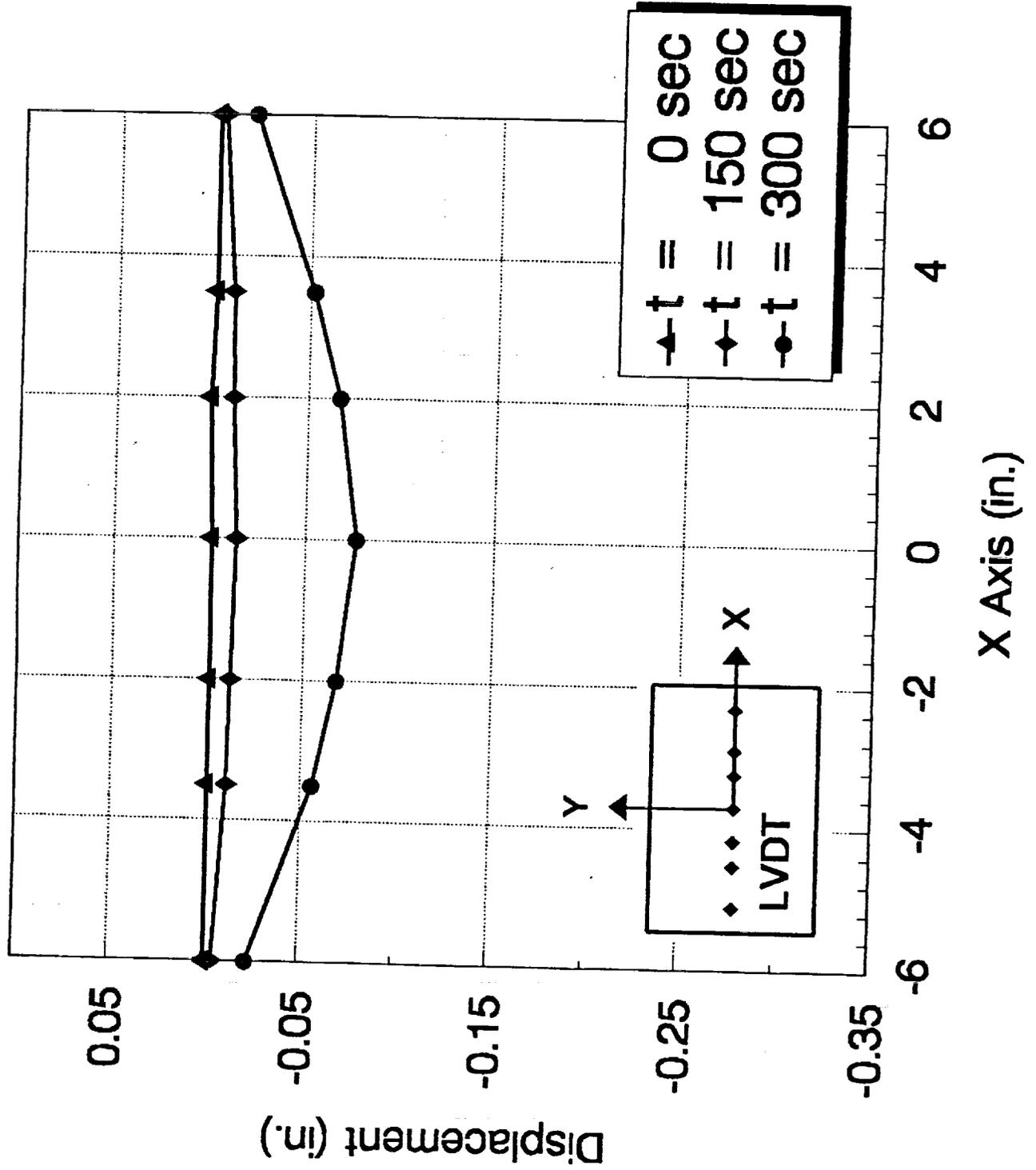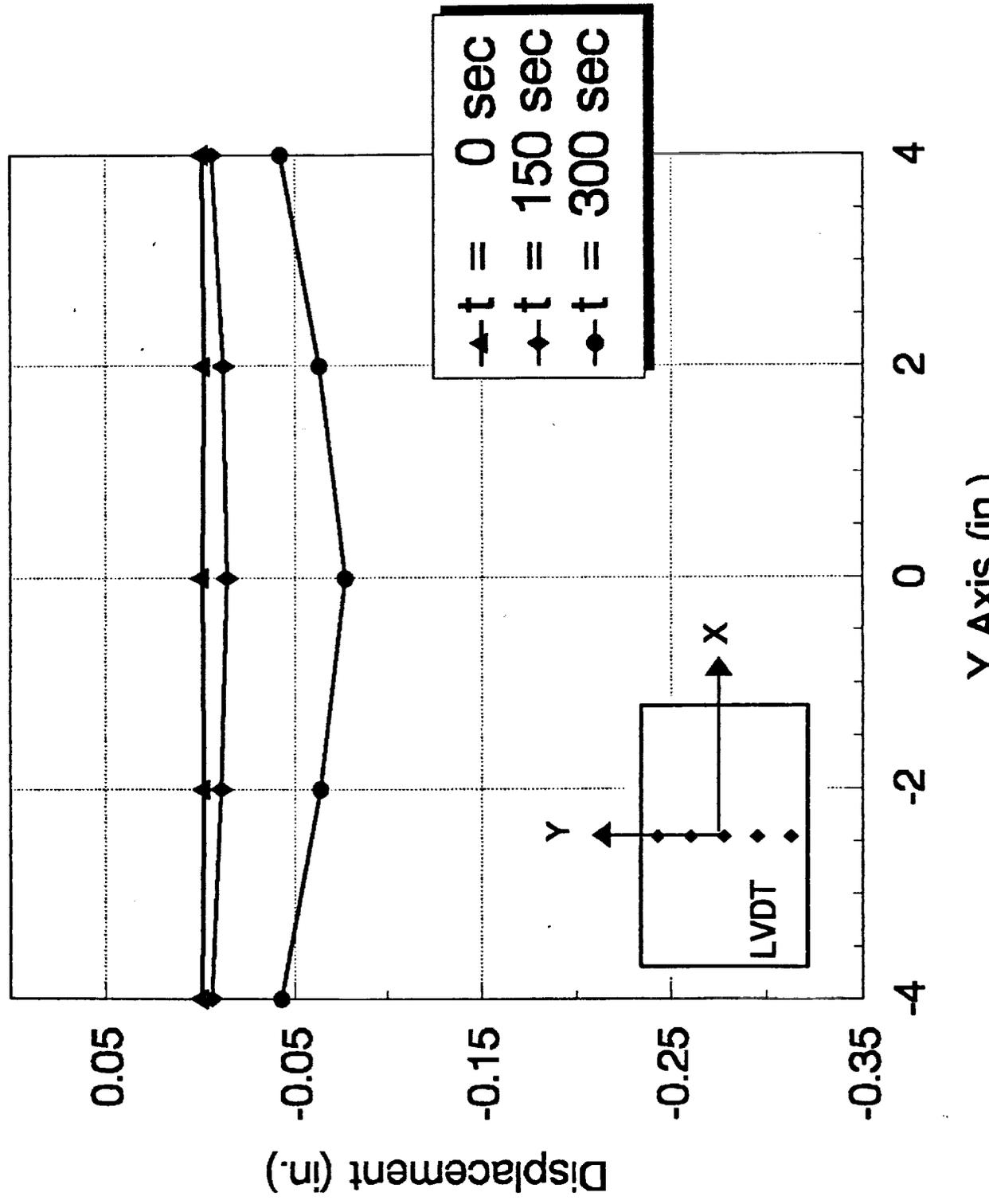
TEST 2 - Deformed Panel
at Selected Times

$w_{max}/h = 0.00$
$t = 0$ sec.

$w_{max}/h = 0.05$
$t = 100$ sec.

$w_{max}/h = 0.22$
$t = 200$ sec.
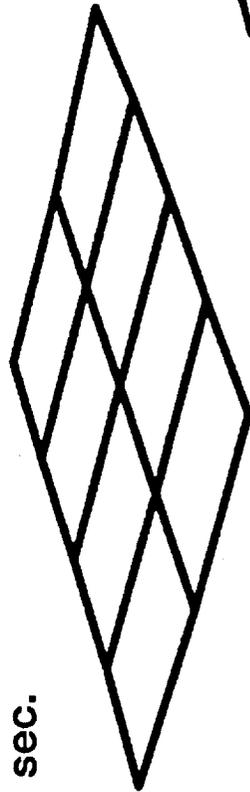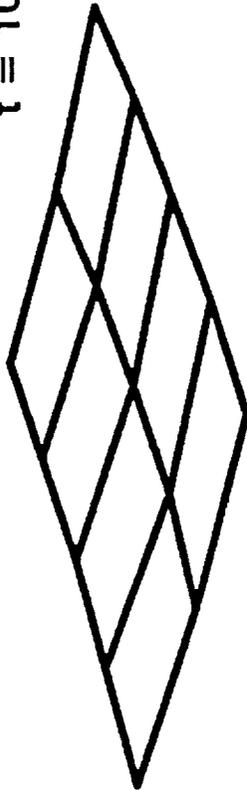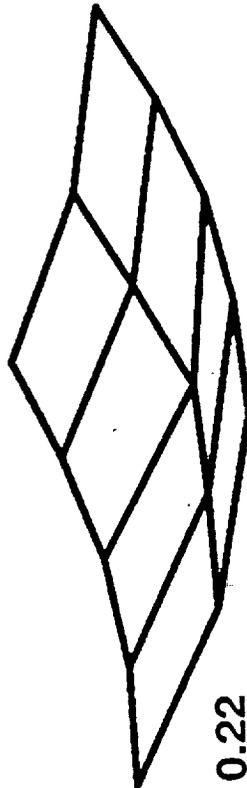
$w_{max}/h = 0.62$
$t = 300$ sec.
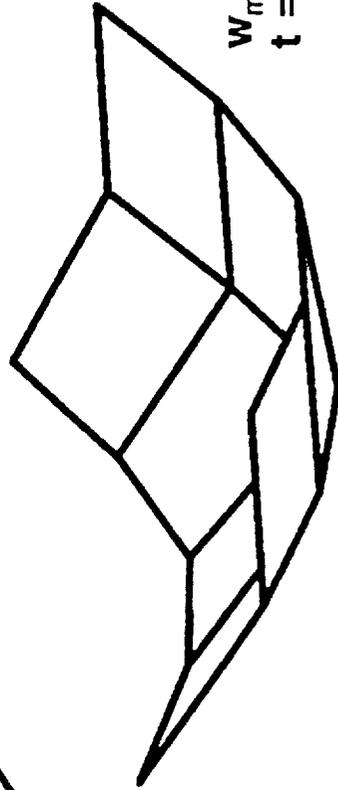
TEST 2 - Panel Center Temperature Versus Displacement
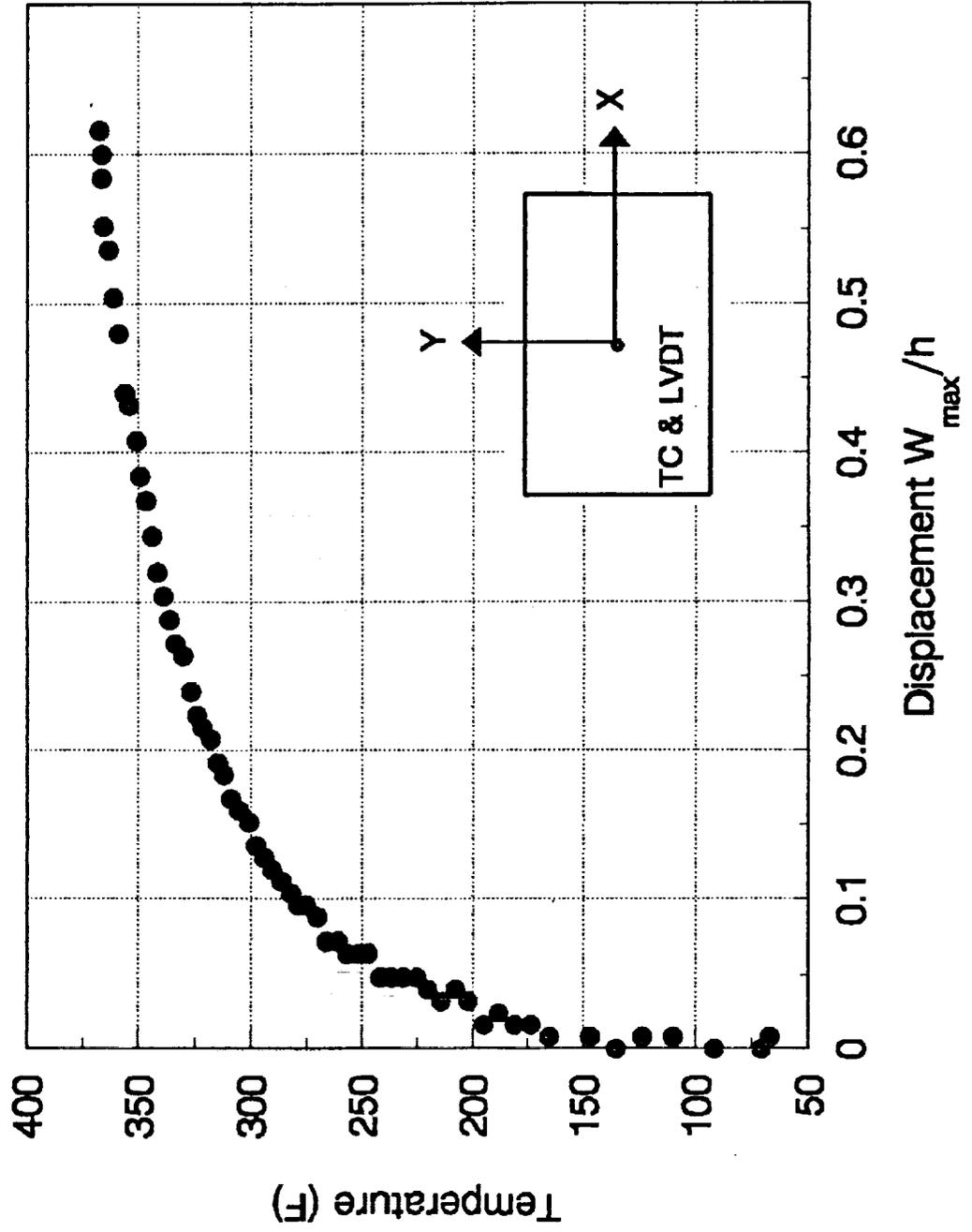
TEST 2 - Analytical Temperature Distributions Lamp at 15% Power

TEST 5 - Panel Temperature Distributions

Legend:
- t = 8 sec
- t = 40 sec
- t = 88 sec

X-axis: Y Axis (in.)

Y-axis: Temperature (F)
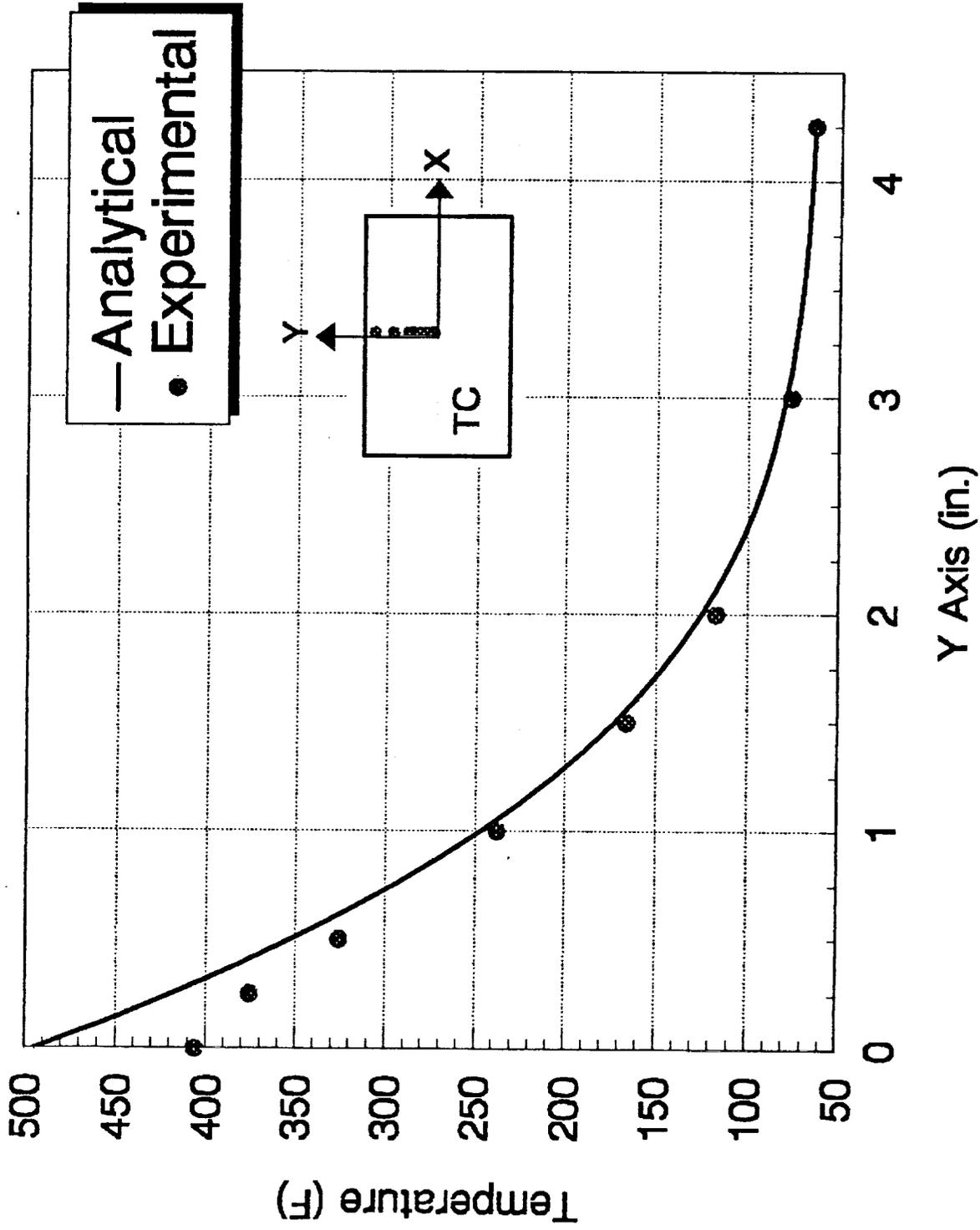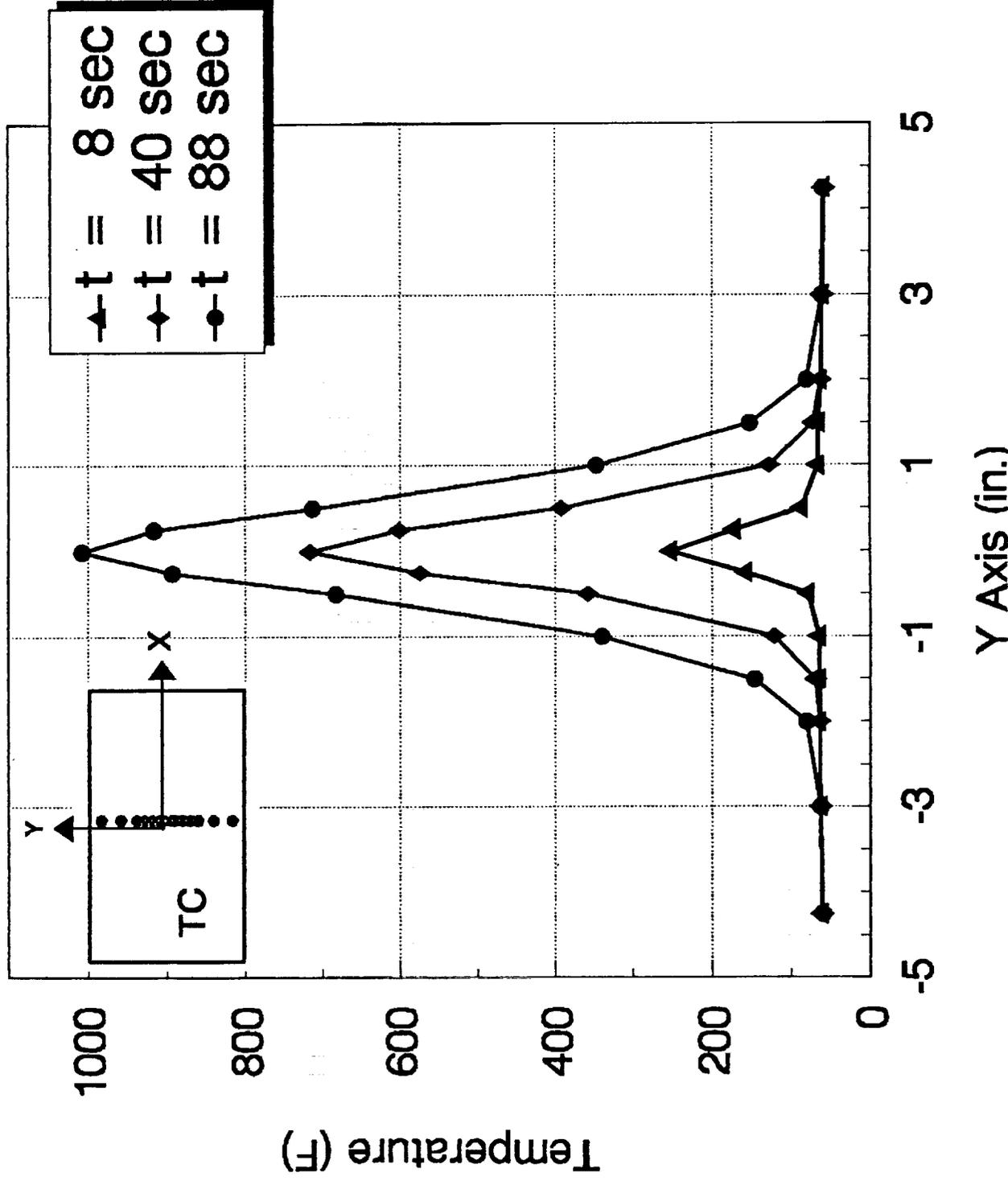
TEST 5 - Panel Temperature Histories

TEST 5 - Panel Displacement Distributions

Legend:
- t = 0 sec
- t = 40 sec
- t = 88 sec
- Final

X Axis (in.)
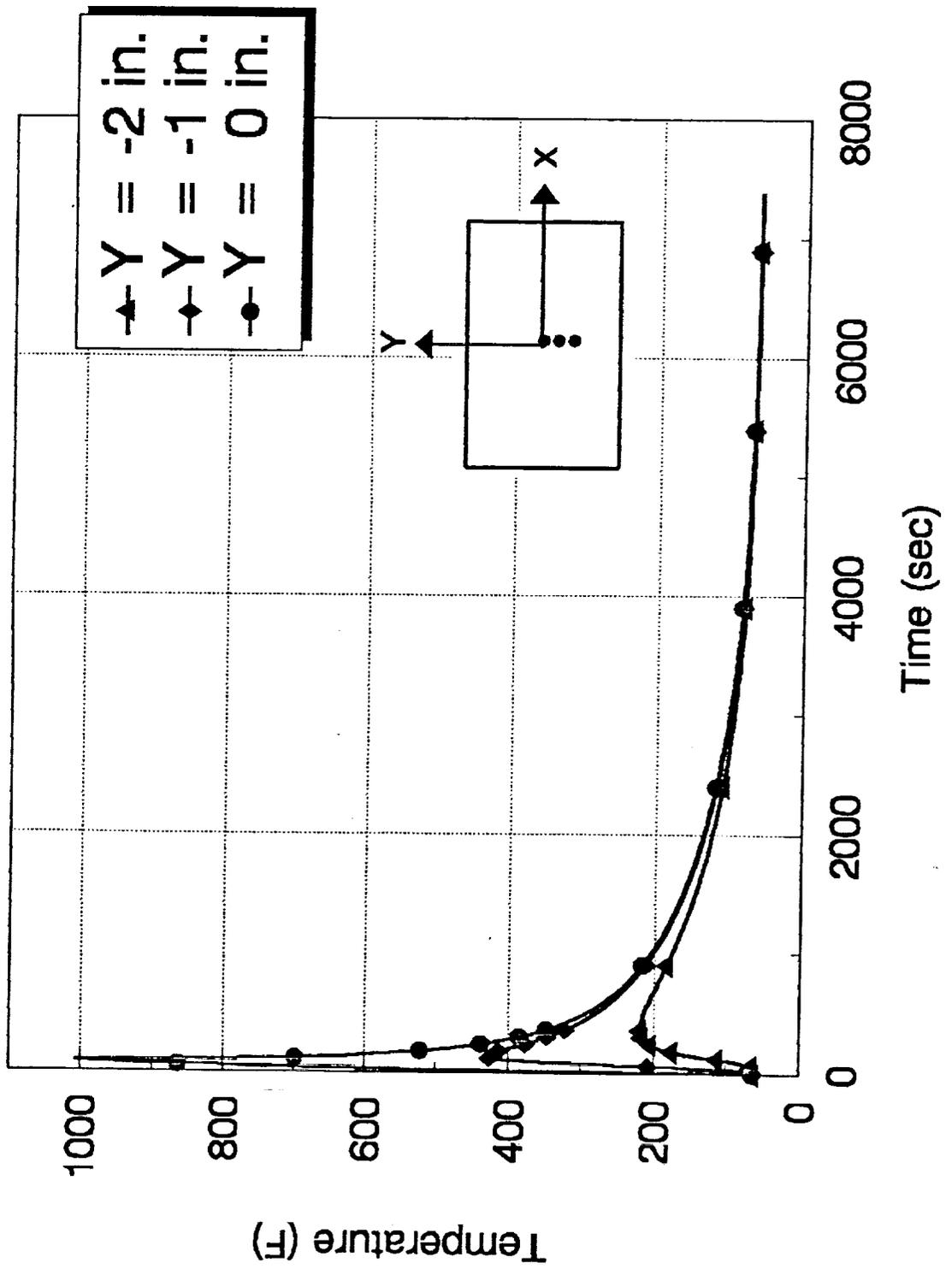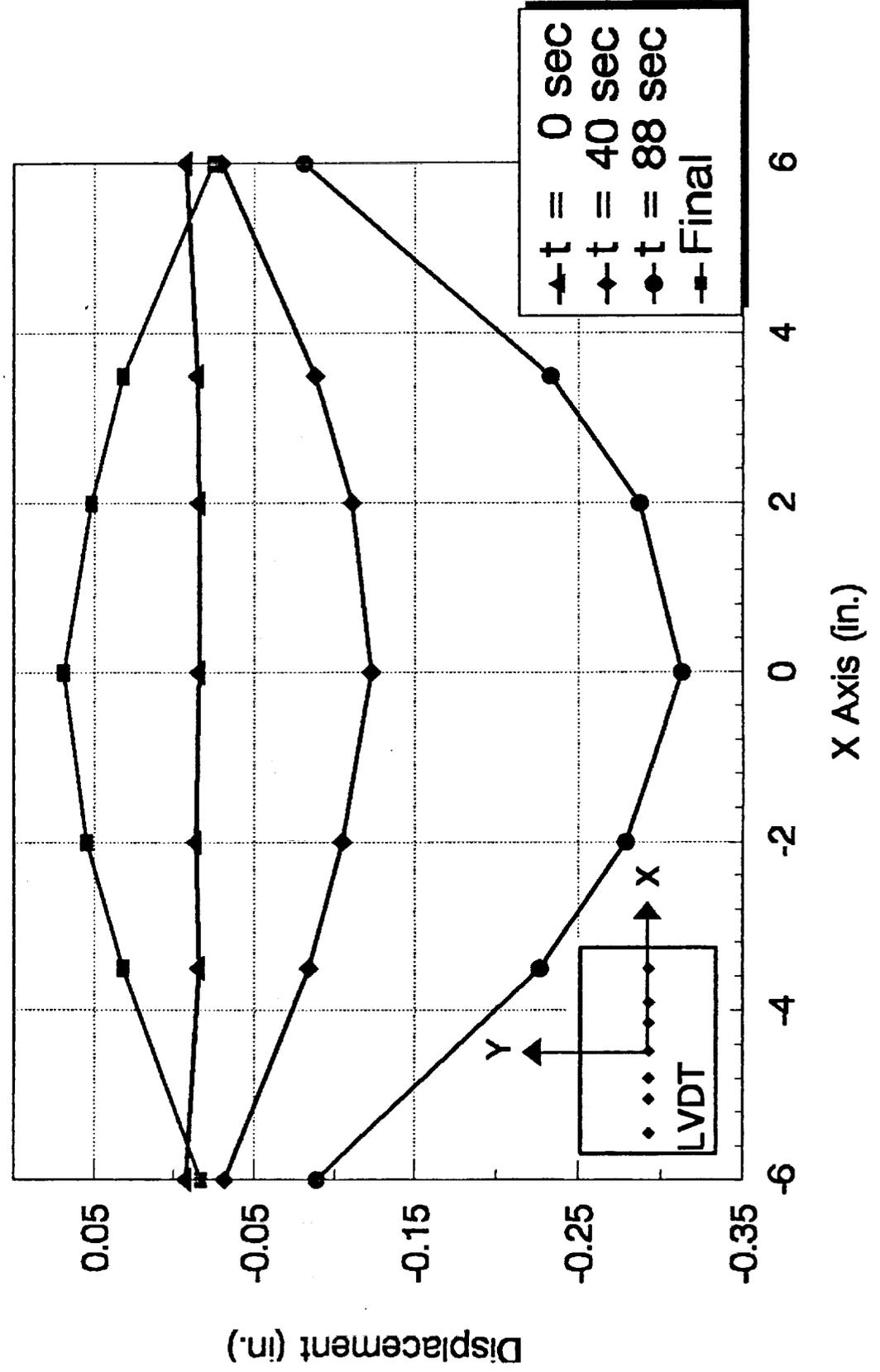
Displacement (in.)

TEST 5 - Panel Displacement Distributions
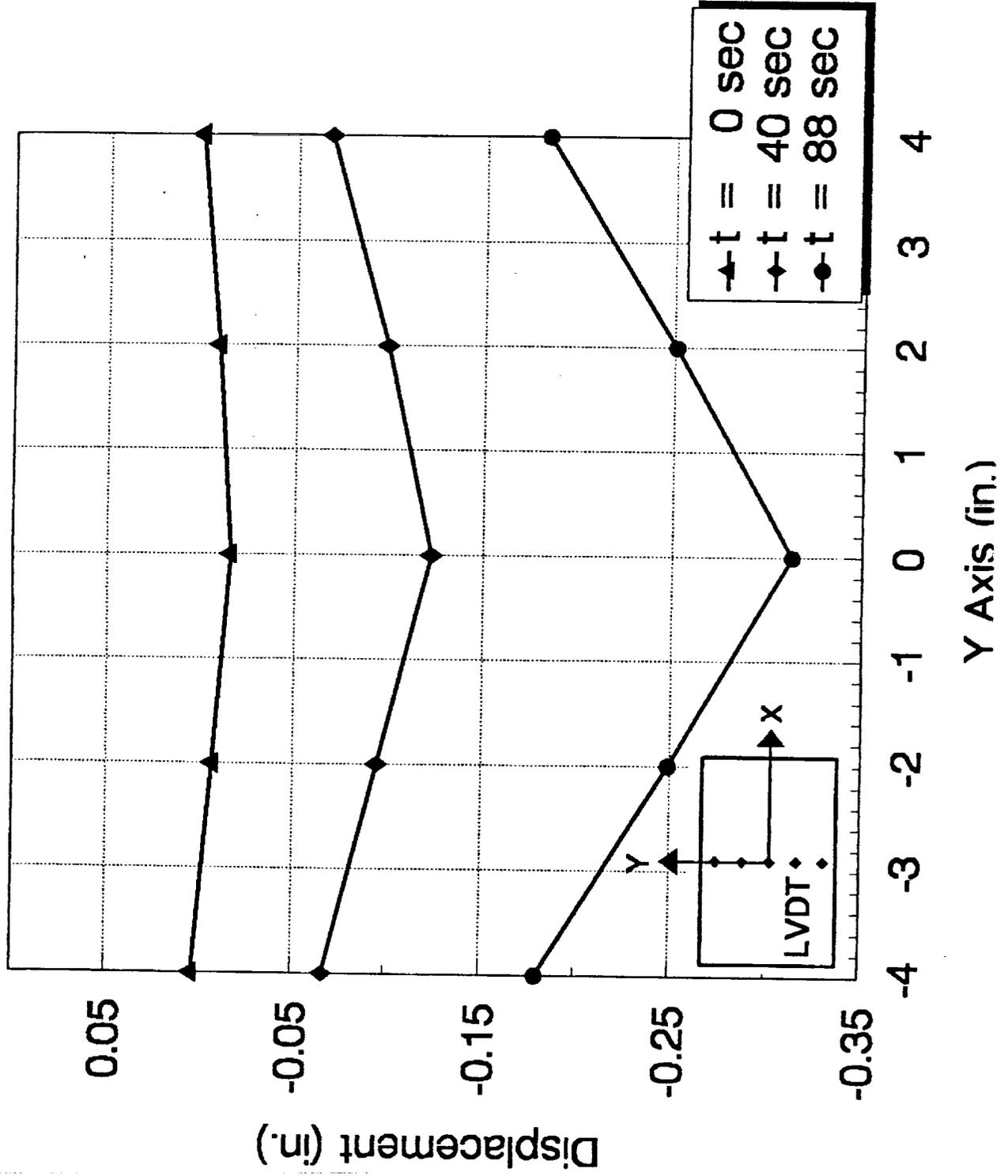
TEST 5 - Deformed Panel
at Selected Times

$w_{max}/h = 1.1$
$t = 44$ sec.

$w_{max}/h = 0.4$
$t = 750$ sec.

$w_{max}/h = 0.1$
$t = 0$ sec.
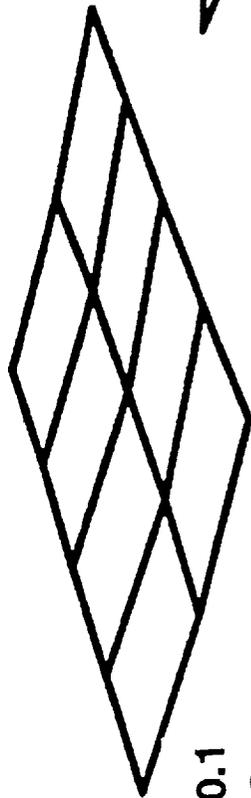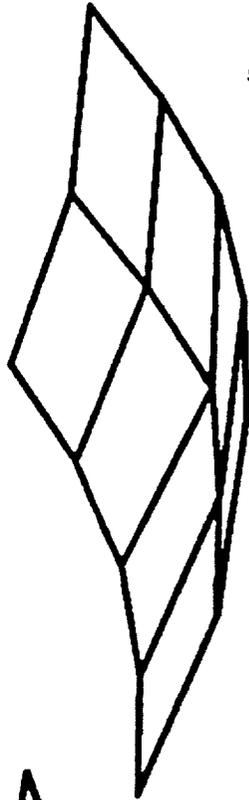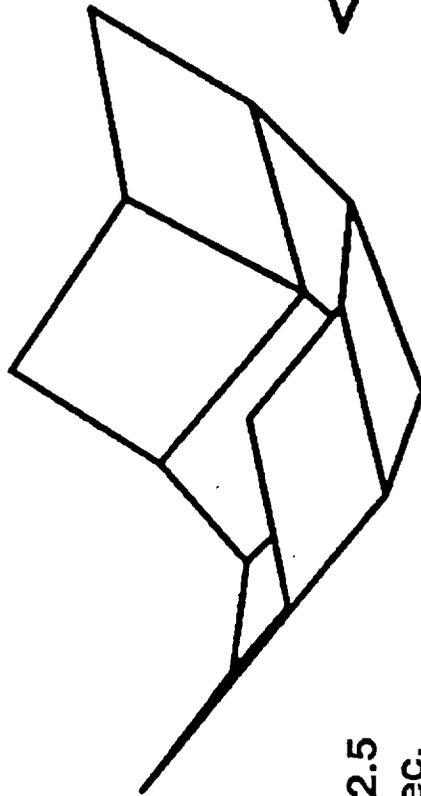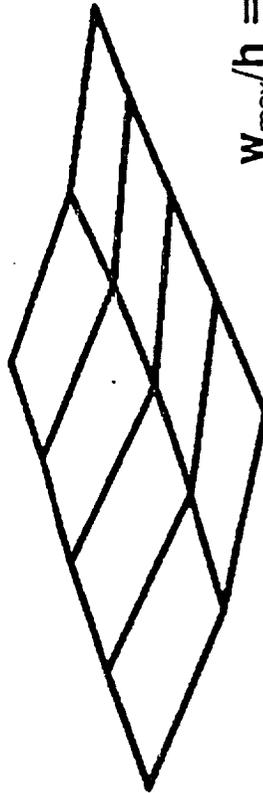
$w_{max}/h = 2.5$
$t = 88$ sec.

TEST 5 - Panel Center Temperature Versus Displacement
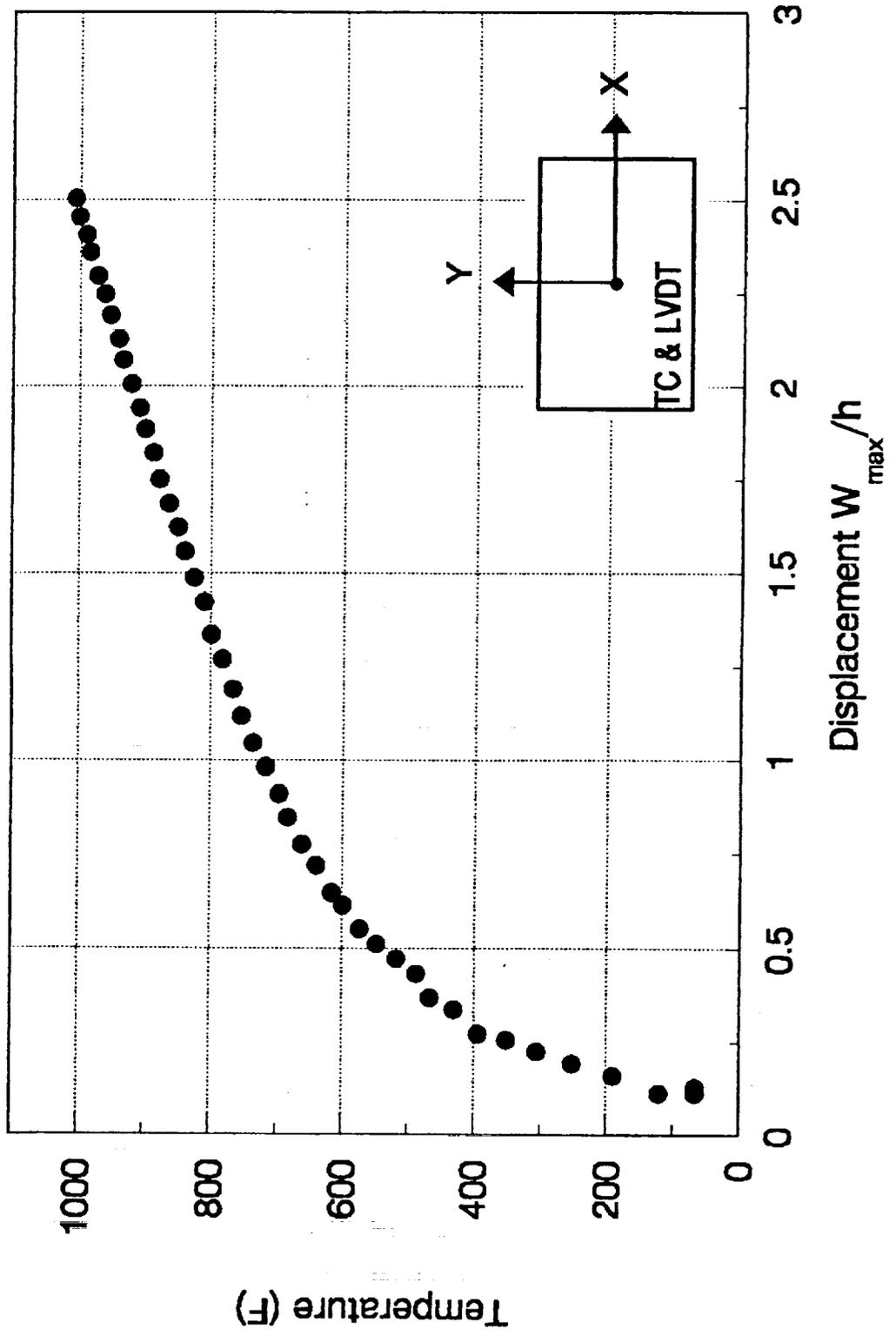
TEST 5 - Analytical Temperature Distributions
Lamp at 70% Power
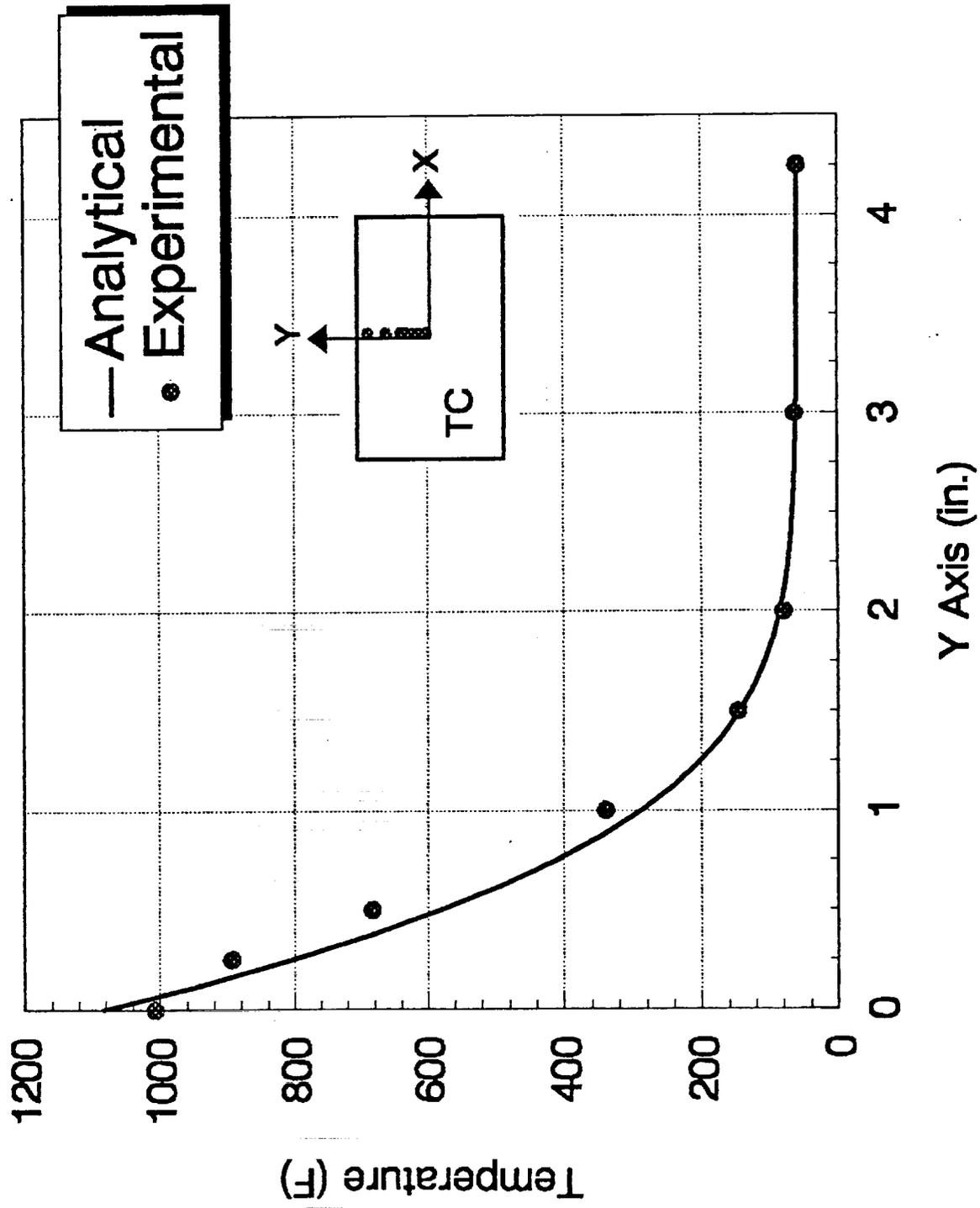
FUTURE RESEARCH PLANS

- CONTINUE LAMP CHARACTERIZATION TESTS IN Z DIRECTION

- CONCLUDE TESTS OF HASTELLOY-X PANELS WITH STRAIN GAGES

- INITIATE TESTS OF ALUMINUM ALLOY PANELS

- BEGIN CORRELATION WITH STRUCTURAL ANALYSIS

APPENDIX I: GRANT PUBLICATIONS (January 1 to June 30, 1992)

1. J.A. Wagner and R.P. Gangloff, "Fracture Toughness of Al-Li-Cu-In Alloys", Scripta Metallurgica et Materialia, Vol. 26, pp. 1779-1784 (1992).

2. R.S. Piascik and R.P. Gangloff, "Environmental Fatigue of an Al-Li-Cu Alloy: Part III - Modeling of Crack Tip Hydrogen Damage", Metall. Trans. A, in review (1992).

3. R.S. Piascik and R.P. Gangloff, "Environmental Fatigue of an Al-Li-Cu Alloy: Part II - Microscopic Hydrogen Cracking Processes", Metall. Trans. A, in review (1992).

4. W.C. Porr, Jr. and R.P. Gangloff, "Elevated Temperature Fracture of RS/PM Alloy 8009: Part I - Fracture Mechanics Behavior", Metall. Trans. A, in review (1992).

5. J.B. Parse and J.A. Wert, "A Geometrical Description of Particle Distributions in Materials", Modeling and Simulation in Materials Science and Engineering, in review, 1992.

6. J.B. Parse and J.A. Wert, "Effects of Deformation Processing in the Oxide Particle Distribution in PM Al Alloy Sheet", Metallurgical Transactions, in review, 1992.

7. E.A. Thornton, M.F. Coyle and R.N. McLeod, "Experimental Study of Plate Buckling Induced by Spatial Temperature Gradients", AIAA Paper No. 92-2540, AIAA/ASME/ASCE/AHS/ASC 33rd Structures, Structural Dynamics and Materials Conference, Dallas, TX, April, 1992.
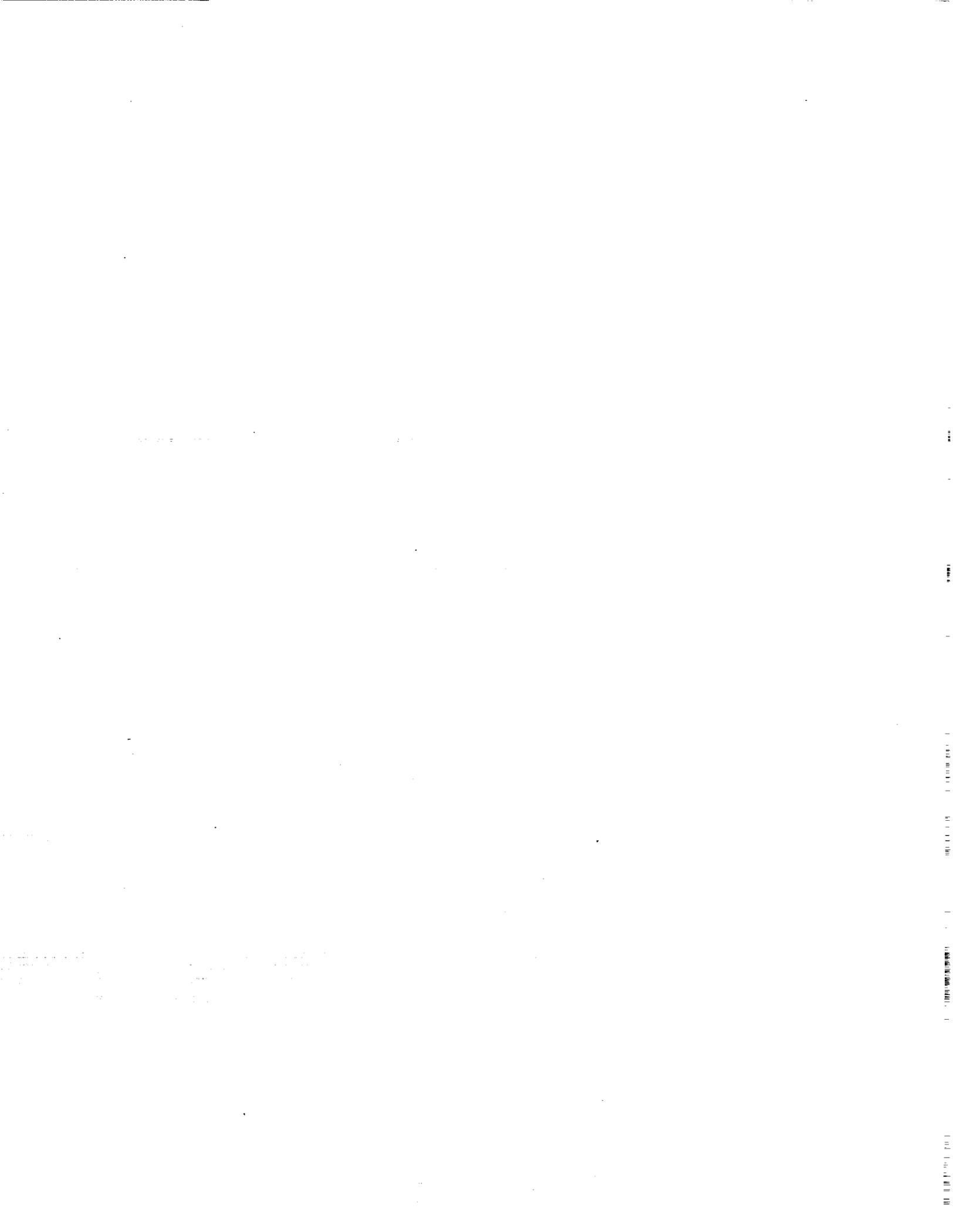
APPENDIX II: GRANT PRESENTATIONS (January 1 to June 30, 1992)

1. R.P. Gangloff, "Environmental Effects on Fatigue Crack Propagation: The Life Prediction Challenge", NASA-LaRC Fracture Control Panel, Hampton, VA, April, 1992.

2. R.P. Gangloff and J.R. Scully, "Plastic Strain and Strain Rate Effects in Hydrogen Embrittlement", ASTM Symposium on Slow Strain Rate Techniques for Evaluating Environmental Cracking, Pittsburgh, PA, May, 1992.

3. R.P. Gangloff and W.C. Porr, "Elevated Temperature Fracture of PM Aluminum Alloys", General Electric Corporate Research and Development Center, Schenectady, NY, June, 1992.

4. R.P. Gangloff, "Crack Tip Micromechanical and Chemical Processes", Gordon Conference on Physical Metallurgy, Plymouth, NH, June, 1992.

5. R.J. Kilmer and G.E. Stoner, "Correlations of Microstructure and Stress Corrosion Cracking Behavior in Al-Li-Cu-Mg and Al-Li-Cu-Mg-Zn Alloys", Corrosion 92, NACE, Poster Session, Nashville, TN, May, 1992.

6. S. Pride and J. Scully, "Metastable Pitting of Al and Al Alloy Thin Films: Analysis using Methods from Nonlinear Dynamics and Phenomenological Modelling," CORROSION-92, NACE, Student Poster Session, Nashville, May, 1992. *(4th place award)*.

7. S. Pride and J. Scully, "Analysis of Metastable Pitting Transients from Al and Al-Cu Alloys in Halide Solutions," Extended Abstracts of the 182nd Meeting of the Electrochemical Society, May, 1992.

8. S. Smith and J. Scully, "Hydrogen Interactions in Al-Li Alloys," CORROSION-92, NACE Student Poster Session, Nashville, May 1992.

9. J.B. Parse and J.A. Wert, "A geometrical Description of Microstructure with Applications to Al PM Processing", TMS Annual Meeting, San Diego, March, 1992.

10. C.J. Lissenden, C.T. Herakovich, "Comparison of Micromechanical Models for Elastic Properties," ASCE SPACE92, Denver Tech Center, Denver, CO, May, 1992.

11. C.T. Herakovich, "Issues in Mechanics of Composites," University of Illinois, June, 1992.

12. C.J. Lissenden, M.-J. Pindera and C.T. Herakovich, "Damage Induced Plasticity in MMC Tubes Subjected to Biaxial Loading," Accepted for presentation at SES-UCSD, September, 1992.

13. F. Mirzadeh and C.T. Herakovich, "Room and Elevated Temperature Response of SCS-6/β 21S", ASTM Committee D10 on Composites, Pittsburgh, PA, May, 1992.
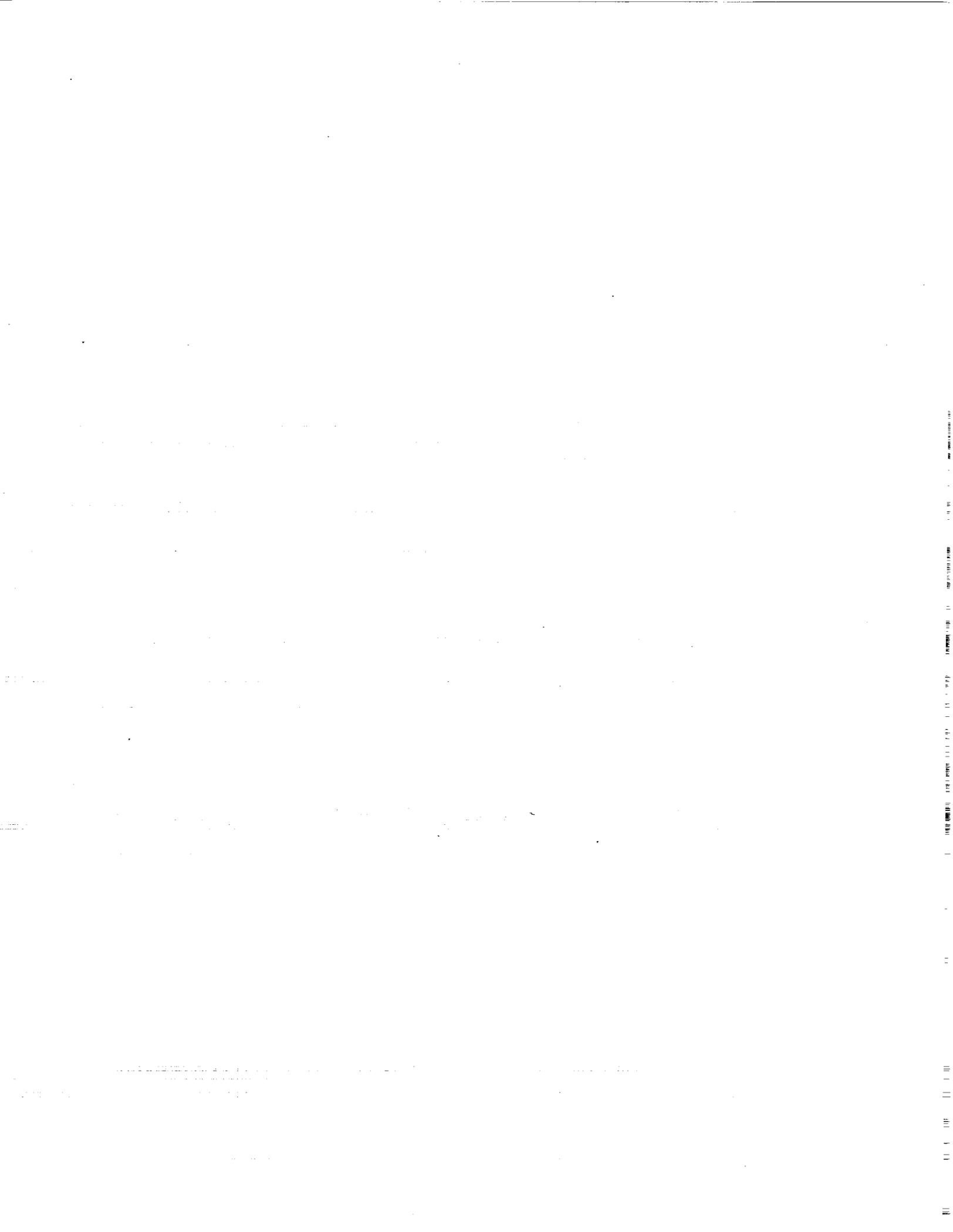
FATIGUE RESPONSE OF SCS-6/β-21S MMC LAMINATES AT ROOM & ELEVATED TEMPERATURE

by

F. Mirzadeh and C. T. Herakovich

University of Virginia
Charlottesville, VA 22903

ABSTRACT

Experimental results are presented for the tension-tension fatigue response of SCS-6/β21-S laminates at room temperature and 480°C. Tests were conducted on straight-sided and dog bone specimens from three laminates, [0]₃, [0/90/0], and [0/+—45/90/—+45/0].

1. INTRODUCTION

This investigation was undertaken as part of the ASTM D-30 MMC Round Robin test program to evaluate the fatigue test procedure for metal matrix composites at room and elevated (480°C) temperatures. The material used in the test is SCS-6/β21-S metal matrix composite. This report documents the results of fatigue tests conducted in the Composite Mechanics Laboratory at the University of Virginia. Large scatter was observed in the fatigue life, failure location and stiffness of the specimens.

2. SPECIMENS

The composite specimens used in this investigation were made of SCS-6 silicon carbide fibers and β21-S titanium alloy matrix. Twenty-four specimens, 150 mm in length and machined per ASTM standard D 3552-77, were supplied by NASA Langly Research Center. The specimens were of three different laminate configurations [0]₃, [0/90/0], and [0/+-45/90/-+45/0]. Twelve of the specimens were straight-sided and the other twelve were dog bone. Details of specimen geometry, dimensions and test conditions are provided in Table 1 (room temperature) and Table 2 (elevated temperature).

3. TEST METHODS

Tests were performed under load control at a frequency of 1 Hz. on a 22 Kip capacity MTS 810 servo-hydraulic load frame at room temperature and 480°C. Hydraulic grips with water cooled wedges were used to introduce load to the specimens, and emory cloth was used in the grips to protect the specimens from surface damage and provide additional friction. A fatigue load ratio ($\sigma^{min}/\sigma^{max}$) of R=0.1 was applied. Maximum stress levels are presented in Tables 3 and 4. A data acquisition and reduction software package called MATPAC was employed along with an ORION datalogger to read and store stress, strain and temperature data during the tests. Data were acquired at a rate of five data points per cycle.

3.1. Room Temperature Tests

Four specimens from each laminate were tested, two straight-sided and two dog bone. For the room temperature tests, strain was measured at mid-length using a MTS extensometer (Model 632.11 B-20) with 25.4 mm gage length as shown in Fig. 1. Some problems were encountered with the use of this extensometer at very low stress levels due to bending of the specimen.

The axial modulus of each specimen was first obtained by quasi-static loading to 20% of maximum fatigue load prior to the actual fatigue test. The results of these tests are shown in Figs. 2-4 where it is evident that the measured response generally exhibited some initial nonlinearity. This nonlinearity was associated with bending of the specimen because of the manner in which the extensometer was mounted on one side of the specimen (Fig. 1). Because of these bending problems, the RT modulus values reported in Table 3 were taken from either a straight line fitted to the linear portion of the quasi-static test or from the initial unloading portion of the first fatigue cycle, as indicated in the table.

The room temperature stiffness values were also obtained during the first cycle (N_1), at mid-life ($N_f/2$) and during a cycle just prior to the failure of the specimen (N_f-1). The stiffness values during cycle N_1 of the fatigue tests were obtained by fitting a straight line to the initial linear portion of the stress-strain data. Stiffness at cycles $N_f/2$ and N_f-1 were obtained by fitting a straight line to the data obtained during the during the full cycle. This difference in procedure was necessary because the first cycle typically exhibited nonlinearity, but subsequent cycles did not because there was no additional matrix plasticity.

3.2. Elevated Temperature Tests

As in the case of the room temperature tests, four specimens of each laminate were tested at 480°C, two straight-sided and two dog bone. However, for the high temperature tests, strain was measured using a water cooled MTS high temperature extensometer (Model 632.51 B-01) at mid-length along the specimen edge (Fig. 1). The extensometer was maintained at 22 °C using a constant temperature water circulator. The Young's modulus of each specimen was first obtained at room temperature (using the same high temperature extensometer) prior to the elevated temperature fatigue test. This was accomplished by loading the specimen to 20% of maximum fatigue load. The stress-strain curves of these tests are shown in Figs. 5-7. It is evident from the linearity of these curves that no bending problems were encountered with the use of the extensometer mounted off the specimen. The high temperature stiffness of each specimen was obtained at N_1, $N_f/2$ and N_f-1 by the same method used for the room temperature tests.

A quartz heater with six quartz lamps, three on each side, in a water cooled fixture was used to heat the specimen to 480°C. The fixture was covered on the top and bottom with aluminum plates and insulating material to form a closed oven and to reduce the chimney effect. Temperature was measured with three type K thermocouples equally spaced along the 25 mm gage length of the specimen. The thermocouples were spring loaded on the specimen by their own bending stiffness. Unlike tack welding which can cause damage to the specimen, this method results in the measurement of the temperature on the surface of the specimen without possibility of causing damage to the specimen.

The temperature of the specimens was increased to 480°C at the rate of 10°C/sec. Specimens were soaked at this temperature for 20 minutes before the fatigue test started. The temperature in the gage section was maintained within ±4°C of the specified temperature throughout the tests.

4. RESULTS

4.1. Room Temperature Results

The results of the room temperature fatigue tests are summarized in Table 3 and the degradation in stiffness with loading cycles is shown in Fig. 8. The fatigue life of the different specimen types and laminate configurations are compared in Fig. 9. Because of the problems associated with specimen bending at the very low load levels,

some room temperature modulus values reported in Table 3 were taken from the initial unloading portion of the first cycle. They are so indicated.

As indicated in Fig. 8, two of the [0]₃ specimens (one dog bone and one straight-sided coupon) exhibited nearly constant stiffness for the first two-thirds of life, and then decreased only slightly thereafter prior to failure. One specimen (a straight-sided coupon) failed in the grips, prematurely, and the fourth specimen (a dog bone) exhibited a small, continuous degradation in stiffness after approximately 25% of life. The largest decrease in stiffness of all [0]₃ specimens was 6%.

The [0/90/0] specimens exhibited behavior that was quite different from the [0]₃ laminate. These specimens generally exhibited variable stiffness during the fatigue life. Several specimens actually exhibited slightly high stiffness at mid-life and three of the four specimens exhibited stiffness degradation prior to failure. The largest decrease in stiffness for any of these specimens was 13.7%. The variations in stiffness during the fatigue test are believed to be associated with measurement accuracy rather than actual material response. It can be said that the dog bone specimens exhibited longer fatigue life than the straight-sided coupons, 42% longer on average.

Specimens from the [0/+-45/90/-+45/0] laminate showed steady reduction in stiffness during the tests. The reduction in stiffness ranged from 19% to 32%, by far the largest stiffness degradation of the three laminates considered. One of the straight-sided coupon specimens (# 271) exhibited unusually high, unexplained, stiffness both during the quasi-static and the fatigue tests. The [0/+-45/90/-+45/0] specimens exhibited the longest and most consistent fatigue life of all three laminates.

4.2. Elevated Temperature Results

The elevated temperature fatigue test results are summarized in Table 4 and Figs. 10 and 11. Figure 10 shows the variation in stiffness with cycles and Fig. 11 shows a comparison of fatigue life for the different specimen geometries and laminate stacking sequences. As indicated in Table 4, the stiffness values during the first cycle of the elevated temperature fatigue tests were, as expected, well below the room temperature stiffness for all laminates with the [0]₃ specimens exhibiting the smallest change in stiffness and the [0/+-45/90/-+45/0] specimens exhibiting the largest decrease (typically 60%).

As indicated in Figs. 10 and 11, the [0]₃ specimens exhibited behavior that was quite variable. The two dog bone specimens exhibited very little degradation in stiffness, but one of the dog bones specimens had a fatigue life

that was almost twice that of all other [0]$_3$ specimens. The two straight-sided coupons exhibited surprising stiffness changes during the last 10% of fatigue life. One exhibited a sharp increase in stiffness (more than 10%) and the second showed a sharp decrease (7%) in stiffness. The increase in stiffness is certainly believed to be associated with measurement accuracy rather than material response.

The [0/90/0] specimens showed relatively small changes in stiffness during the elevated temperature fatigue tests with the largest reduction being only 6%. The fatigue life was variable with one dog bone specimen exhibiting a very short life relative to the three other specimens.

The stiffness of the [0/+-45/90/-+45/0] specimens varied over a small range during the fatigue tests. One specimen (a dog bone) exhibited a 7% increase prior to failure. Two specimens exhibited degradation of 11% and 14% and the fourth specimen did not exhibit any significant change in stiffness. The most surprising aspect of the [0/+-45/90/-+45/0] specimens is that one of the dog bone specimens exhibited a fatigue life that was more than double that of the other specimens.

4.3. Failure Locations

Only one of the twelve room temperature specimens failed within the 1" (25mm) gage section and only three of the elevated temperature specimens failed within the gage section. Thus, failure of the elevated temperature specimens generally occurred in a region of temperature gradient rather than in a region of uniform temperature.

5. SUMMARY

The most significant results of this very limited test program can be summarized as follows:

- Mounting an extensometer on the face of these specimen introduces significant bending and is not recommended.

- The [0]$_3$ specimens exhibited relatively little stiffness degradation at both room and elevated temperature

- The [0/90/0] and [0+-45/90/-+45/0] specimens exhibited relatively little stiffness degradation at elevated temperature, but significant degradation at room temperature.

- The room temperature [0/+-45/90/-+45/0] specimens exhibited the largest stiffness degradation.

- There was significant scatter in fatigue life at both room and elevated temperature, except for the room temperature tests on [0/+-45/90/-+45/0] specimens.

Table 1. Specimen and Test Details - Room Temperature SCS-6/β-21S Specimens

	Tension-Tension Room Temperature Fatigue Tests						
Specimen #	Laminate	Type	t (mm)	W (mm)	Humidity (%)	Lab Temp. (°C)	Test Temp. (°C)
22	[0]₃	Straight	0.813	10.10	80	23	23
64	[0]₃	Straight	0.825	10.00	75	24	24
38	[0]₃	Dog Bone	0.825	10.06	76	24	24
43	[0]₃	Dog Bone	0.813	10.16	80	23	23
152	[0/90/0]	Straight	0.838	10.06	72	24	24
156	[0/90/0]	Straight	0.825	10.08	70	24	24
144	[0/90/0]	Dog Bone	0.838	10.11	72	24	24
177	[0/90/0]	Dog Bone	0.825	10.13	72	24	24
271	[0/±45/90/-+45/0]	Straight	1.65	15.14	70	23	23
274	[0/±45/90/-+45/0]	Straight	1.65	15.16	70	23	23
237	[0/±45/90/-+45/0]	Dog Bone	1.66	15.16	70	22	22
282	[0/±45/90/-+45/0]	Dog Bone	1.65	15.08	70	24	24

Table 2. Specimen and Test Details - Elevated Temperature SCS-6/β-21S Specimens

Tension-Tension Room Temperature Fatigue Tests							
Specimen #	Layup	Geometry	T mm	W mm	Humidity %	Lab Temp. °C	Test Temp. °C
17	$[0]_3$	Straight	0.813	10.09	80	24	480
10	$[0]_3$	Straight	0.812	9.98	70	24	480
8	$[0]_3$	Dog Bone	0.813	10.13	70	24	480
34	$[0]_3$	Dog Bone	0.825	9.97	70	24	480
148	[0/90/0]	Straight	0.838	10.03	75	24	480
98	[0/90/0]	Straight	0.838	10.06	75	24	480
145	[0/90/0]	Dog Bone	0.838	10.11	73	24	480
175	[0/90/0]	Dog Bone	0.825	10.13	72	24	480
255	[0/±45/90/-+45/0]	Straight	1.68	15.14	72	24	480
202	[0/±45/90/-+45/0]	Straight	1.66	15.07	70	24	480
246	[0/±45/90/-+45/0]	Dog Bone	1.66	15.16	70	22	480
234	[0/±45/90/-+45/0]	Dog Bone	1.65	15.08	70	24	480

Table 3. Room Temperature Fatigue Test Results - SCS-6/β-21S Specimens

Tension-Tension Room Temperature Fatigue Tests								
Laminate (Specimen #)	Specimen Type	RT E_x (GPa)	N_1 E_x (GPa)	$N_f/2$ E_x (GPa)	N_f-1 E_x (GPa)	Stress σ_{max} (MPa)	Cycles N_f	Failure Distance From Bottom End (mm)
[0]$_3$ (22)	Straight	177.9*	177.9	---	178.7	625	24,071	130
[0]$_3$ (64)	Straight	178.2	181.3	181.2	177.4	625	59,520	60
[0]$_3$ (38)	Dog Bone	181.7	181.7	179.6	169.9	625	49,023	50
[0]$_3$ (43)	Dog Bone	184.8	187.9	188.3	184.7	625	54,613	52
[0/90/0] (152)	Straight	153.7*	153.7	135.6	132.9	525	12,380	105
[0/90/0] (156)	Straight	141.6	139.9	146.2	142.0	525	16,081	130
[0/90/0] (144)	Dog Bone	147.4	139.4	143.1	131.5	525	22,576	47
[0/90/0] (177)	Dog Bone	149.3	155.5	144.1	138.9	525	26,378	100
[0/±45/90/-+45/0] (271)	Straight	142.5*	142.5	121.1	115.7	325	66,788	90
[0/±45/90/-+45/0] (274)	Straight	124.9	119.9	102.4	88.4	325	69,140	52
[0/±45/90/-+45/0] (237)	Dog Bone	121.8*	120.7	104.8	91.5	325	69,085	96
[0/±45/90/-+45/0] (282)	Dog Bone	120.0	117.9	103.3	81.2	325	70,031	80

* Unloading modulus of the first cycle.

Table 4. Elevated Temperature Fatigue Test Results - SCS-6/β-21S Specimens

Tension-Tension Elevated Temperature Fatigue Tests								
Laminate (Specimen #)	Specimen Type	RT E_x (GPa)	N_1 E_x (GPa)	$N_f/2$ E_x (GPa)	N_f-1 E_x (GPa)	Stress σ_{max} (MPa)	Cycles N_f	Failure Distance From Bottom End (mm) O=Outside Heated Zone I=Inside Heated Zone
[0]₃ (17)	Straight	185	165.00	165.4	154.8	600	64,437	52-O
[0]₃ (10)	Straight	186.5	175.5	177.4	197.0	600	72,434	54-O
[0]₃ (8)	Dog Bone	182.8	173.9	175.7	178	600	121,915	103-O
[0]₃ (34)	Dog Bone	196.7	173.4	173.0	170.7	600	73,990	101-I
[0/90/0] (148)	Straight	161.7	128.7	133.4	134.8	460	50,509	120-O
[0/90/0] (98)	Straight	162.6	131.7	136.2	132.7	460	66,918	21-O
[0/90/0] (145)	Dog Bone	166.1	128.3	128.0	122.9	460	50,843	94-I
[0/90/0] (175)	Dog Bone	161.3	132.2	133.8	123.7	460	19,996	59-O
[0/±45/90/-+45/0] (255)	Straight	153	95.5	98.6	93.3	280	63,785	100-O
[0/±45/90/-+45/0] (202)	Straight	154.2	93.7	95.8	83.9	280	69,731	107-O
[0/±45/90/-+45/0] (246)	Dog Bone	150.4	92.8	94.5	99.4	280	175,100	---
[0/±45/90/-+45/0] (234)	Dog Bone	156.8	93.9	98.0	80.1	280	88,010	102-I

SCS6/β 21S
Round Robin Specimens

26 mm

10.0 to 15.16 mm

0.81 to 1.66 mm

MTS

Doge Bone

Straight-Sided

15 mm

Room Temperature

Heated Zone

Thermocouple

MTS

150 mm

High Temperatue
(480 C)
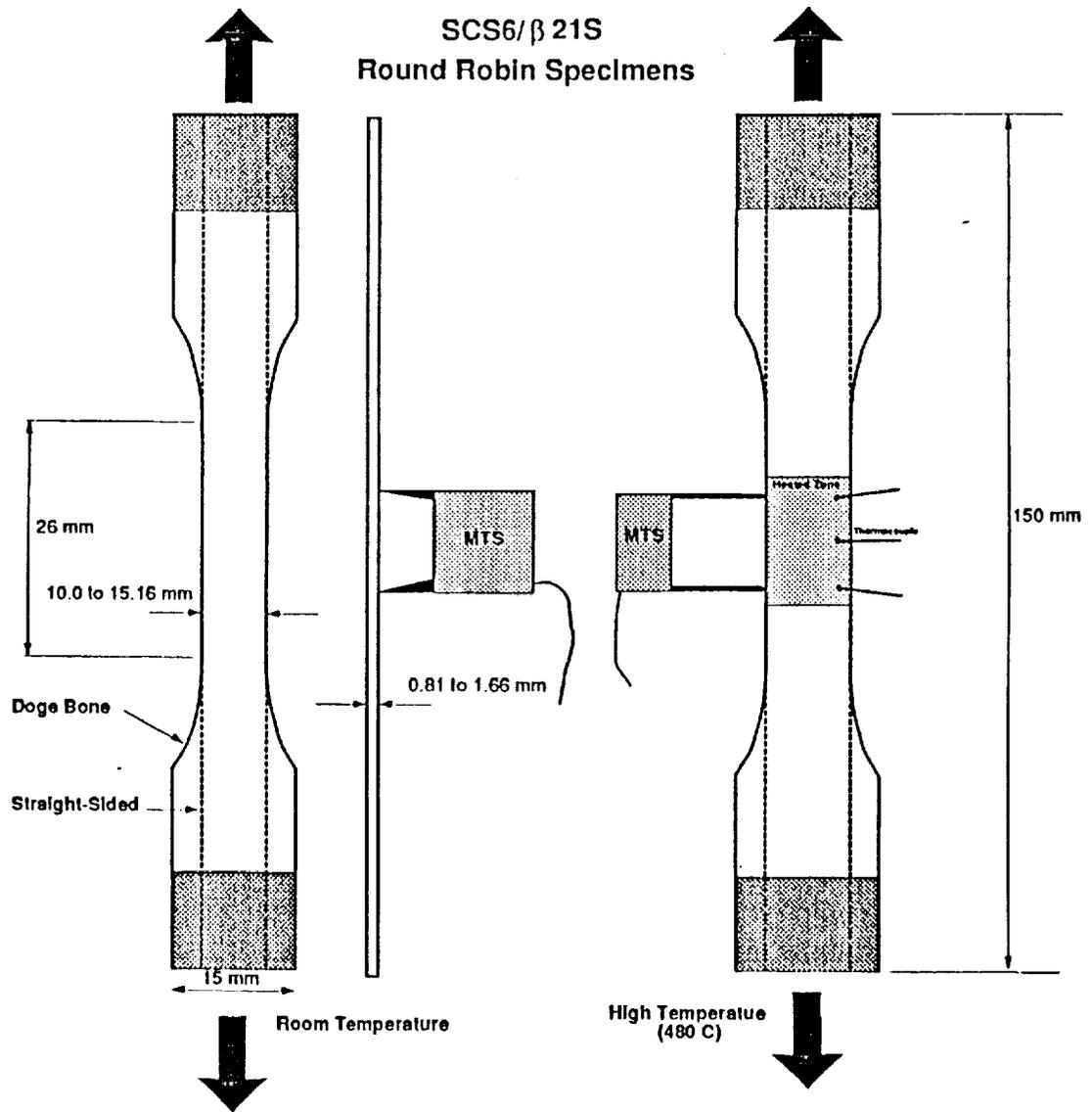
Fig. 1. Specimen Geometries and Strain Gages

SCS-6/β 21S

Room Temperature Static Test
of Room Temperature Fatigue Specimens

|	
—×—	[0]$_3$ DB #38
....▽....	[0]$_3$ DB #43
–□–	[0]$_3$ SS #22
—O—	[0]$_3$ SS #64
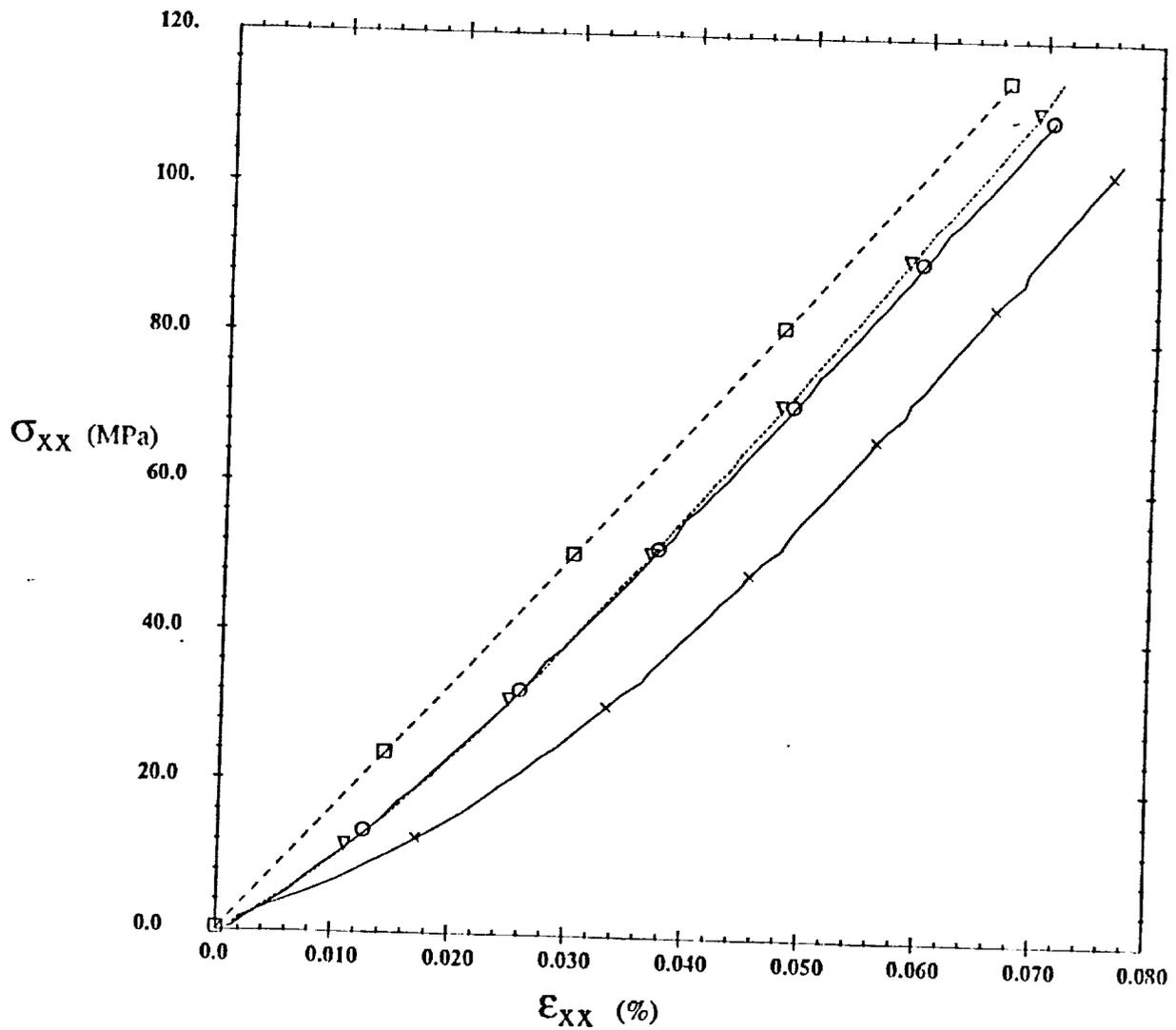
Fig. 2. RT Response of RT [0]$_3$ SCS-6/β-21S Specimens
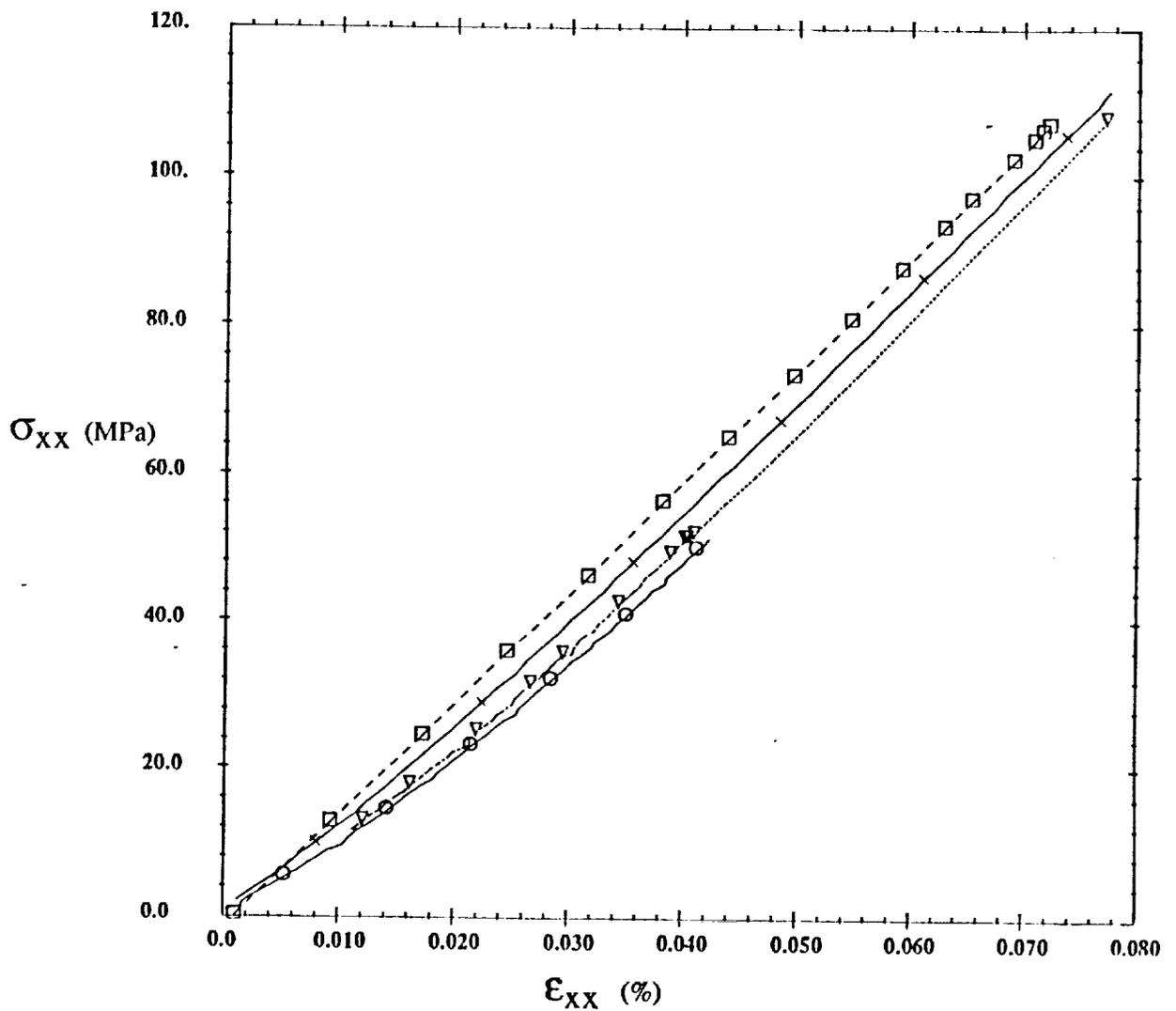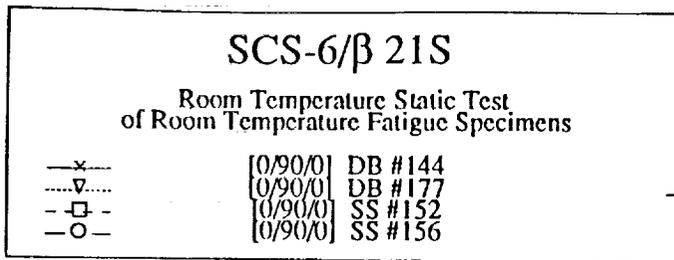
Fig. 3. RT Response of RT [0/90/0] SCS-6/β-21S Specimens

SCS-6/β 21S

Room Temperature Static Test
of Room Temperature Fatigue Specimens

—×—	[0/+—45/90/—+45/0]	DB #237
....▽....	[0/+—45/90/—+45/0]	DB #282
- □ -	[0/+—45/90/—+45/0]	SS #271
—○—	[0/+—45/90/—+45/0]	SS #274

σ_{xx} (MPa)

ε_{xx} (%)
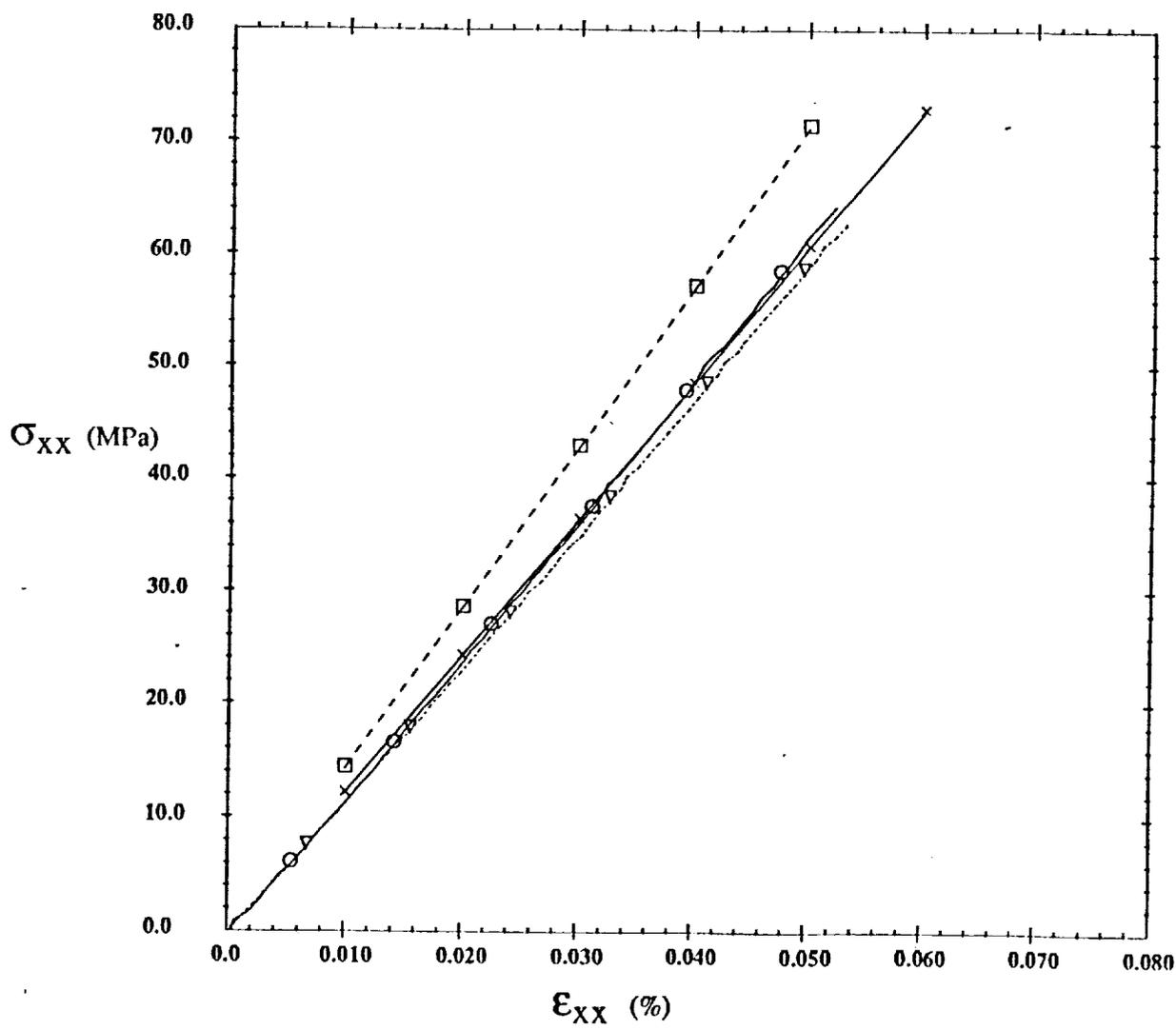
Fig. 4. RT Response of RT [0/+—45/90/—+45/0] SCS-6/β-21S Specimens

Q-6

Fig. 5. RT Response of ET [0]₃ SCS-6/β-21S Specimens

SCS-6/β 21S

Room Temp. Static Test
of High Temperature Fatigue Specimens

—×—	[0/90/0] DB #145
⋯▽⋯	[0/90/0] DB #175
–□–	[0/90/0] SS #98
—○—	[0/90/0] SS #148
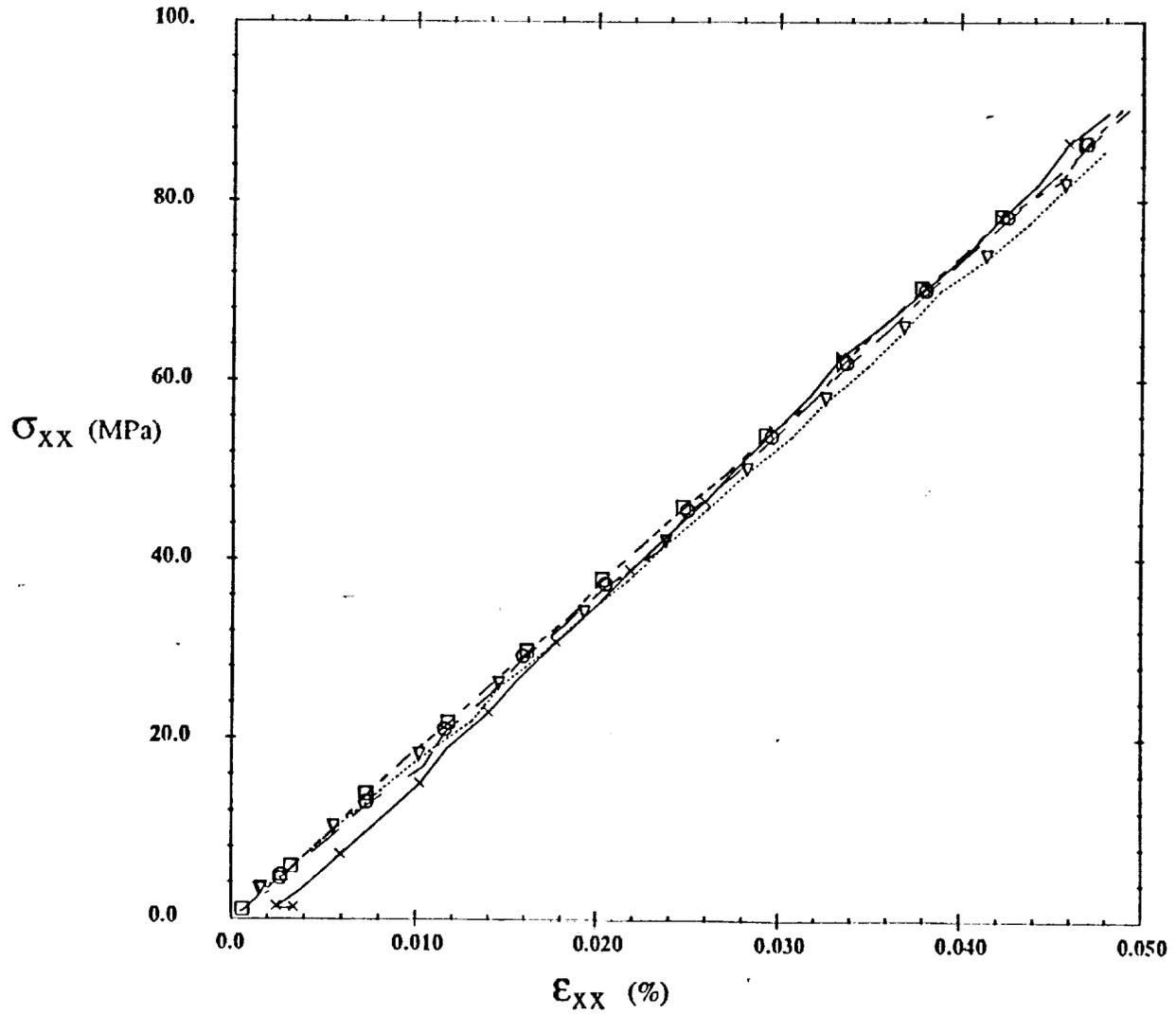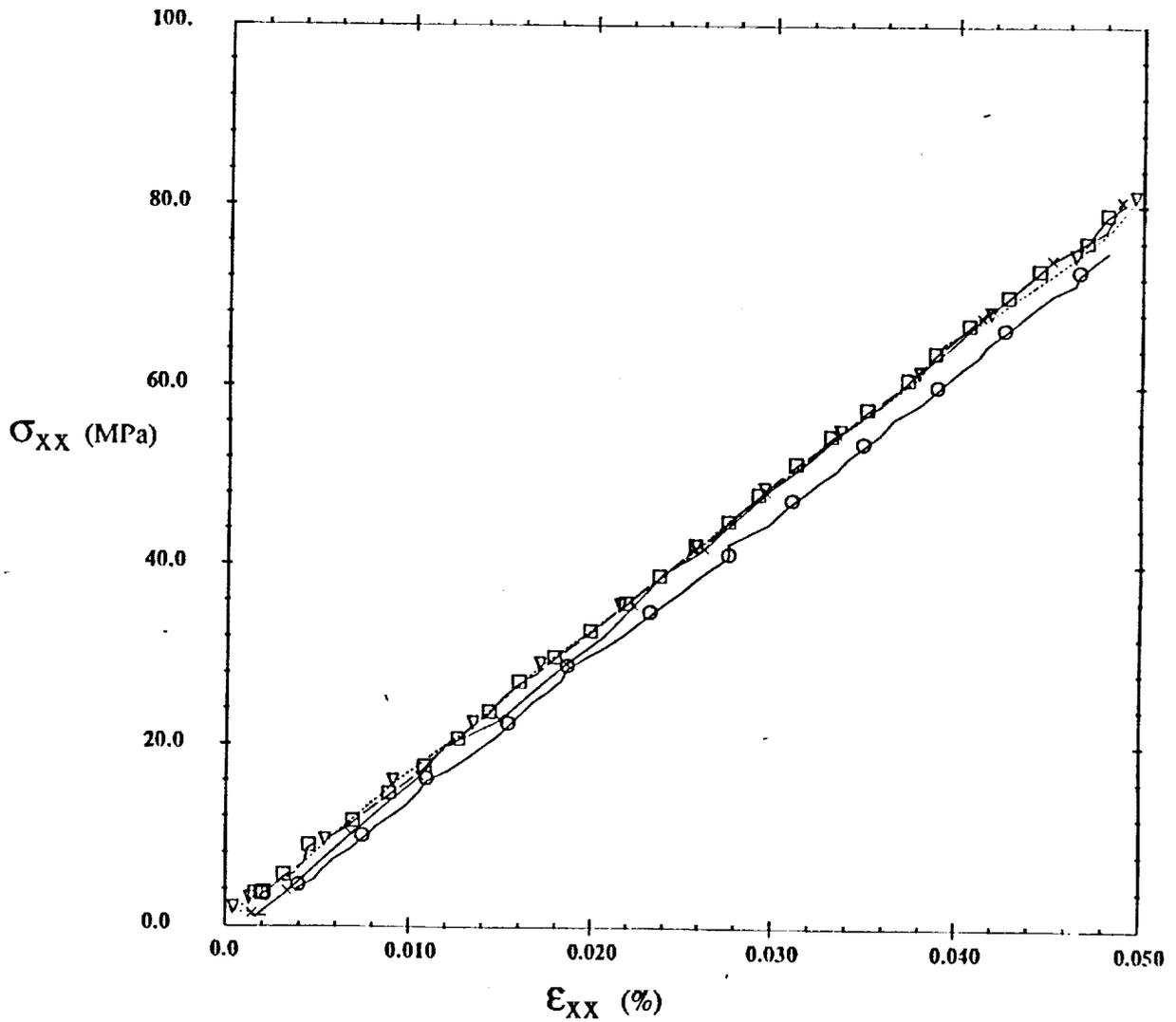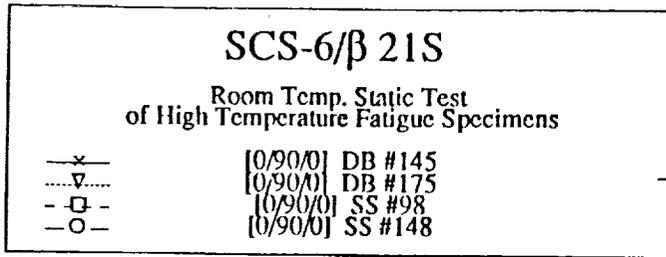
Fig. 6. RT Response of ET [0/90/0] SCS-6/β-21S Specimens
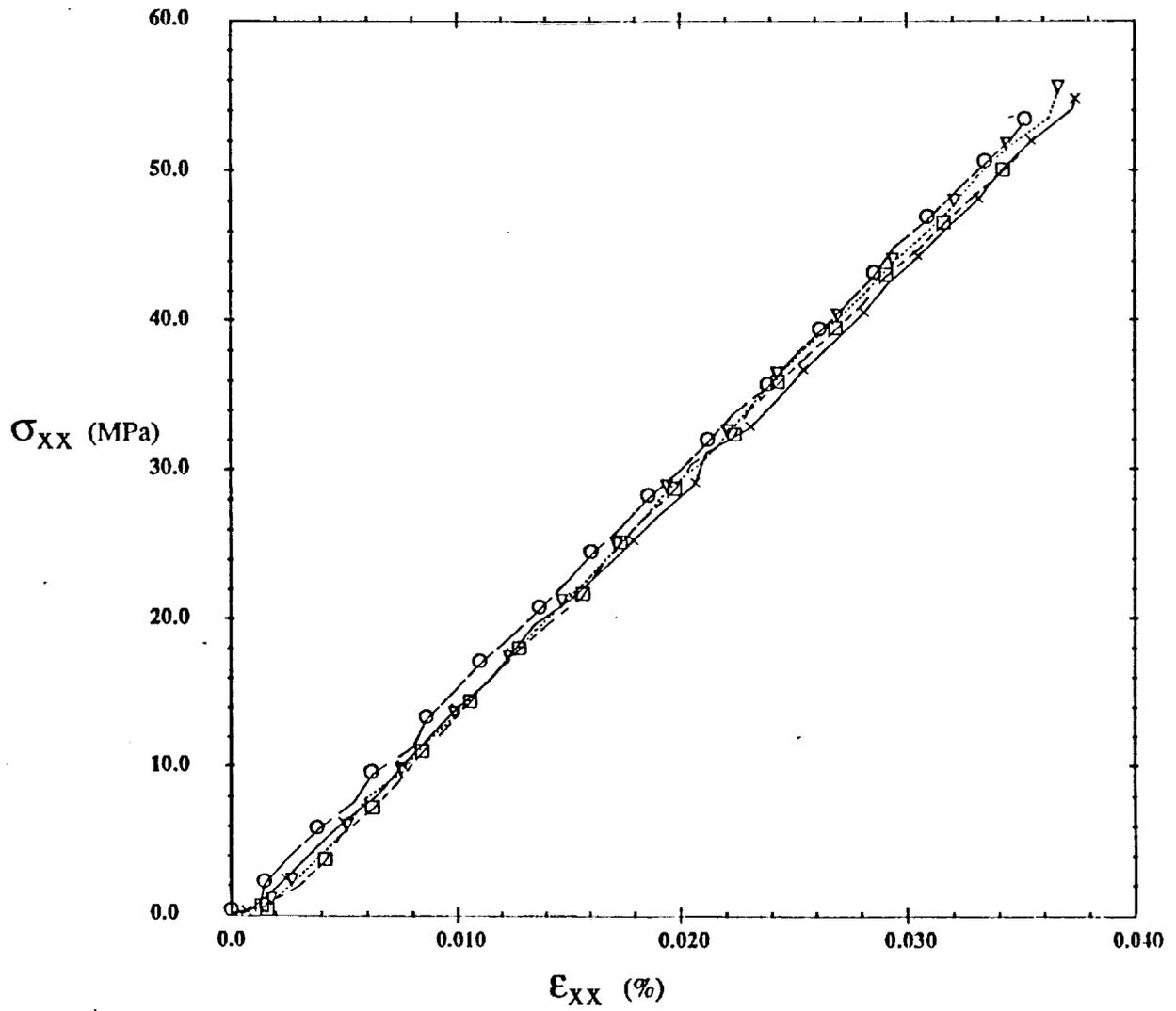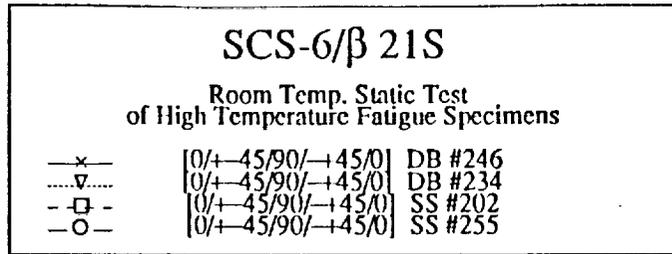
Fig. 7. RT Response of ET [0/+—45/90/—+45/0] SCS-6/β-21S Specimens
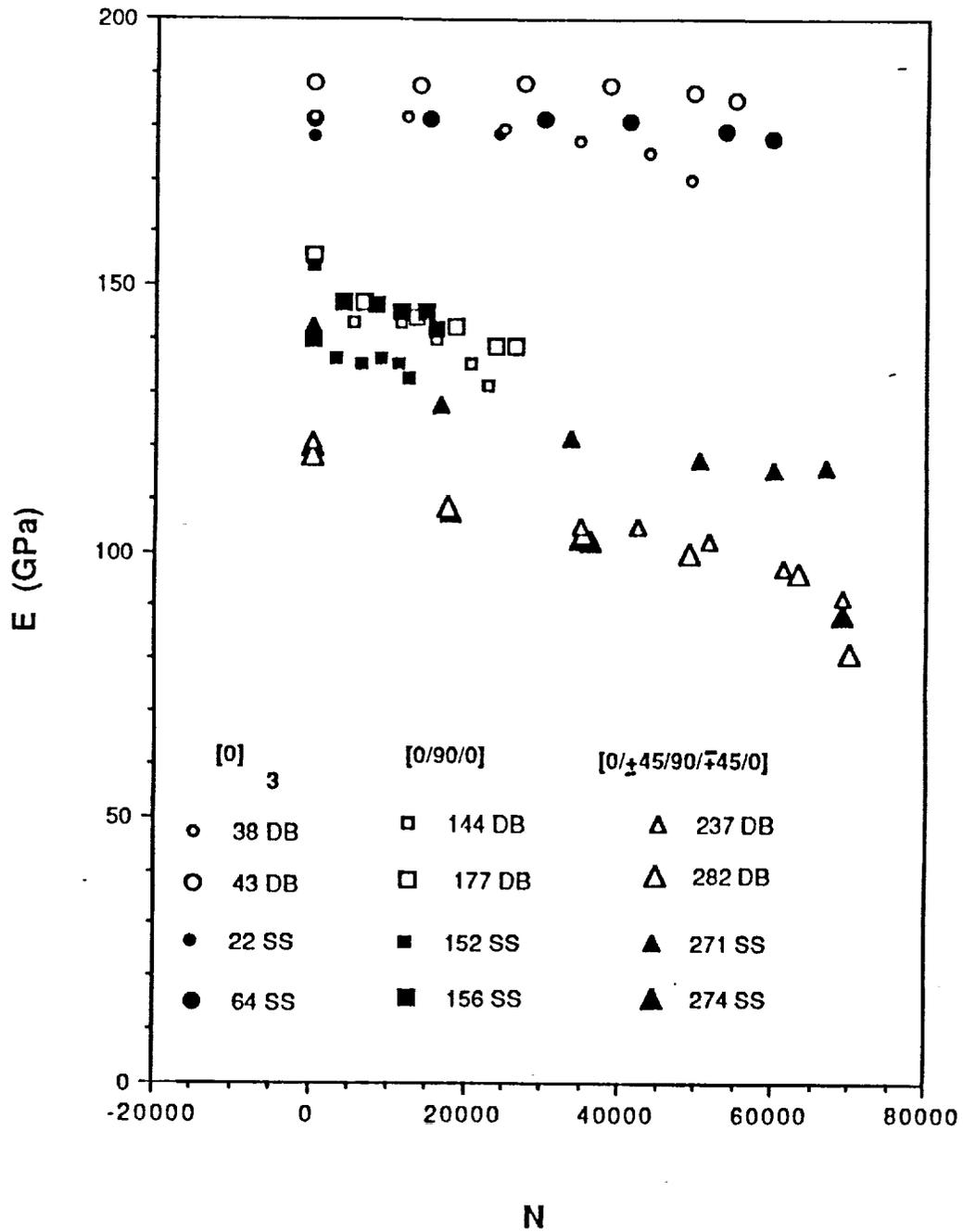
Fig. 8. Room Temperature Stiffness Degradation
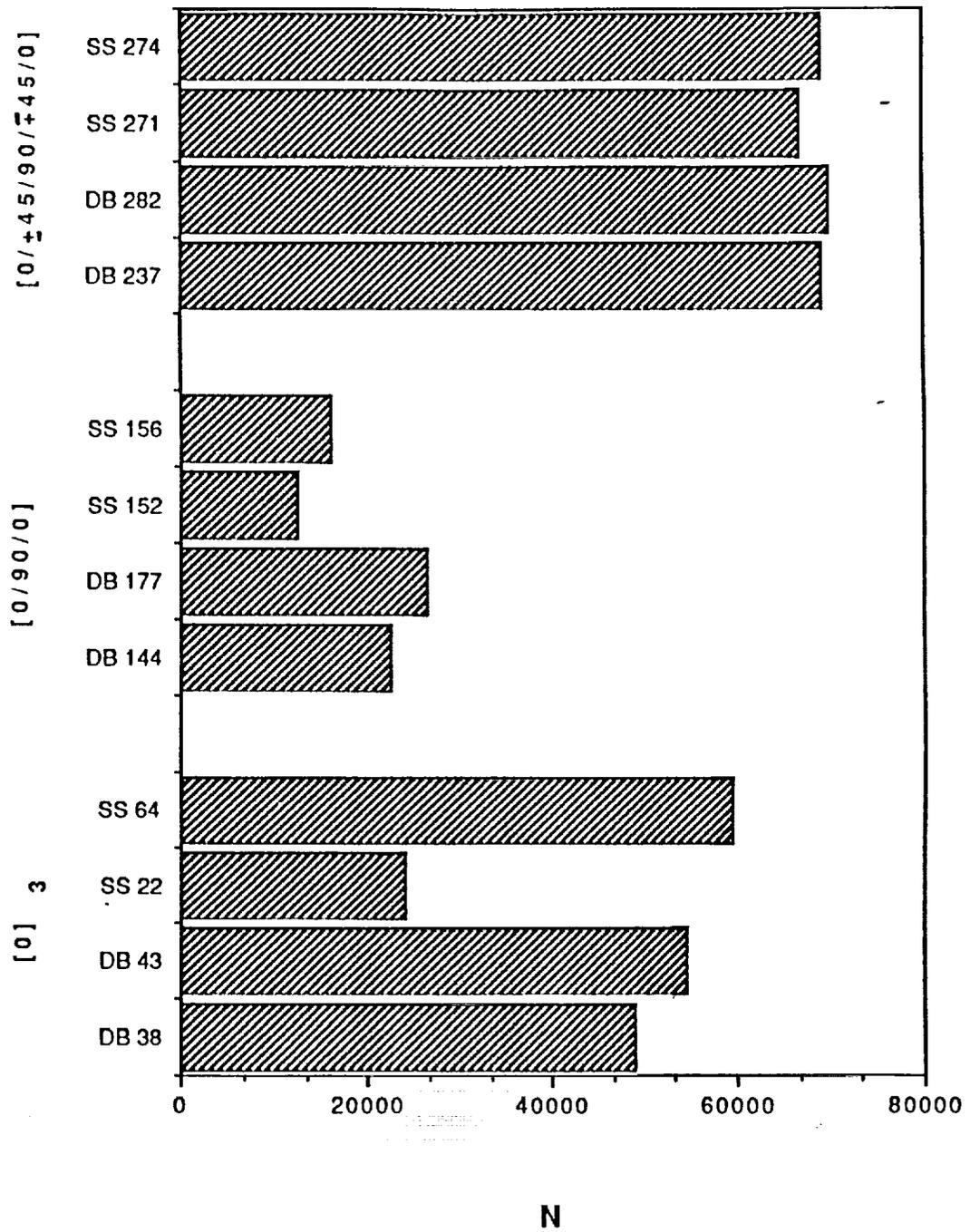
Fig. 9. Room Temperature Fatigue Life
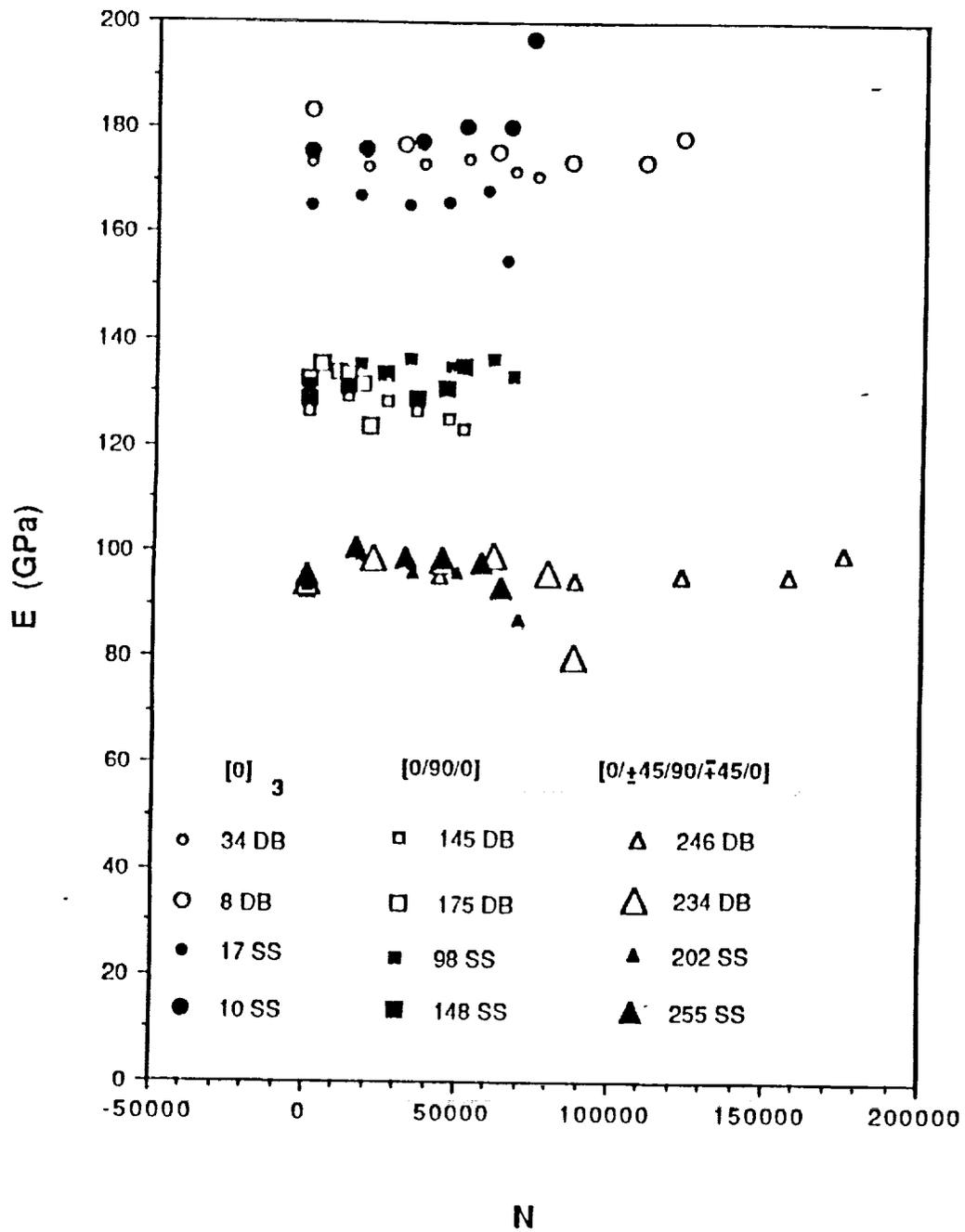
Fig. 10. Elevated Temperature Stiffness Degradation
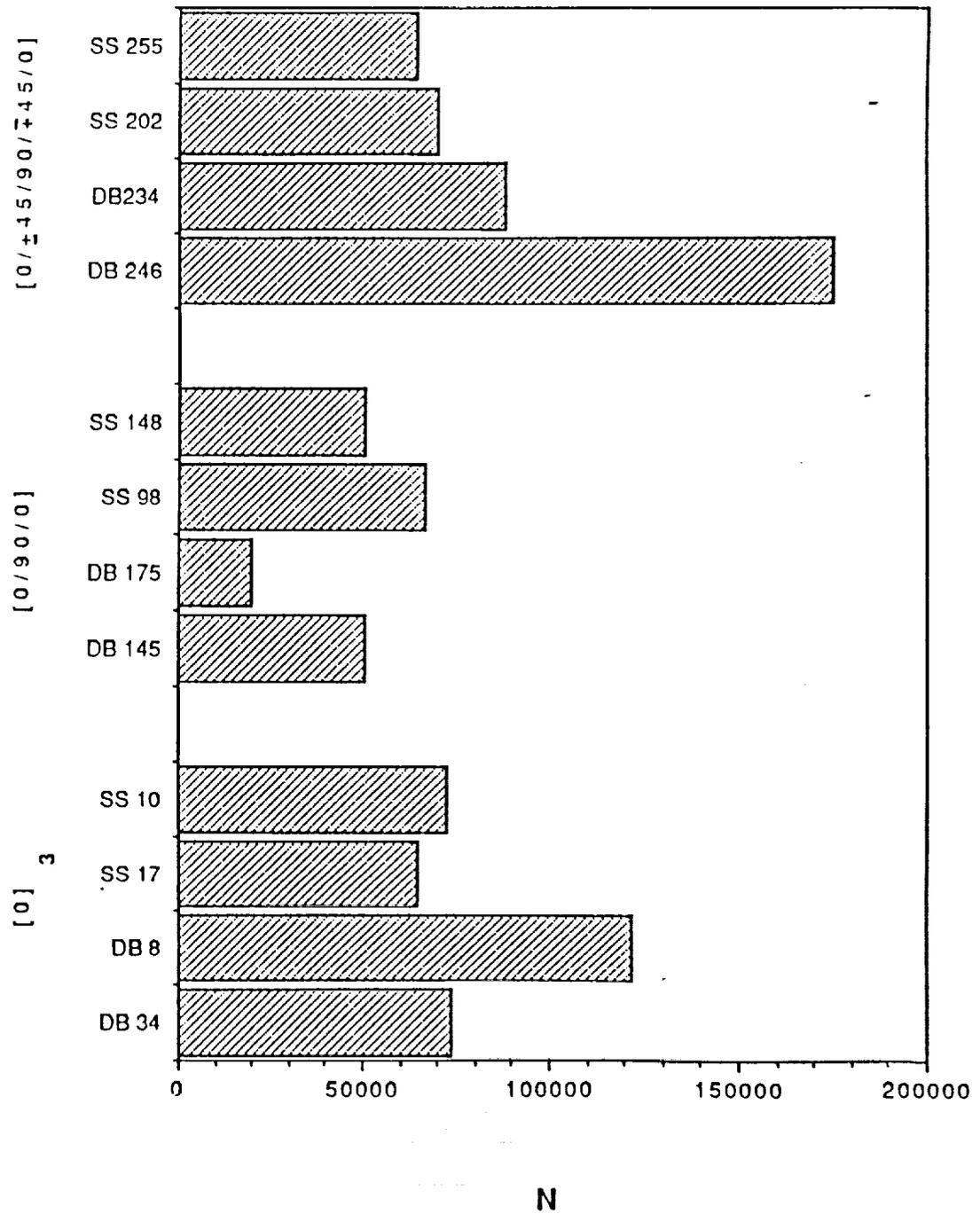
Fig. 11. Elevated Temperature Fatigue Life
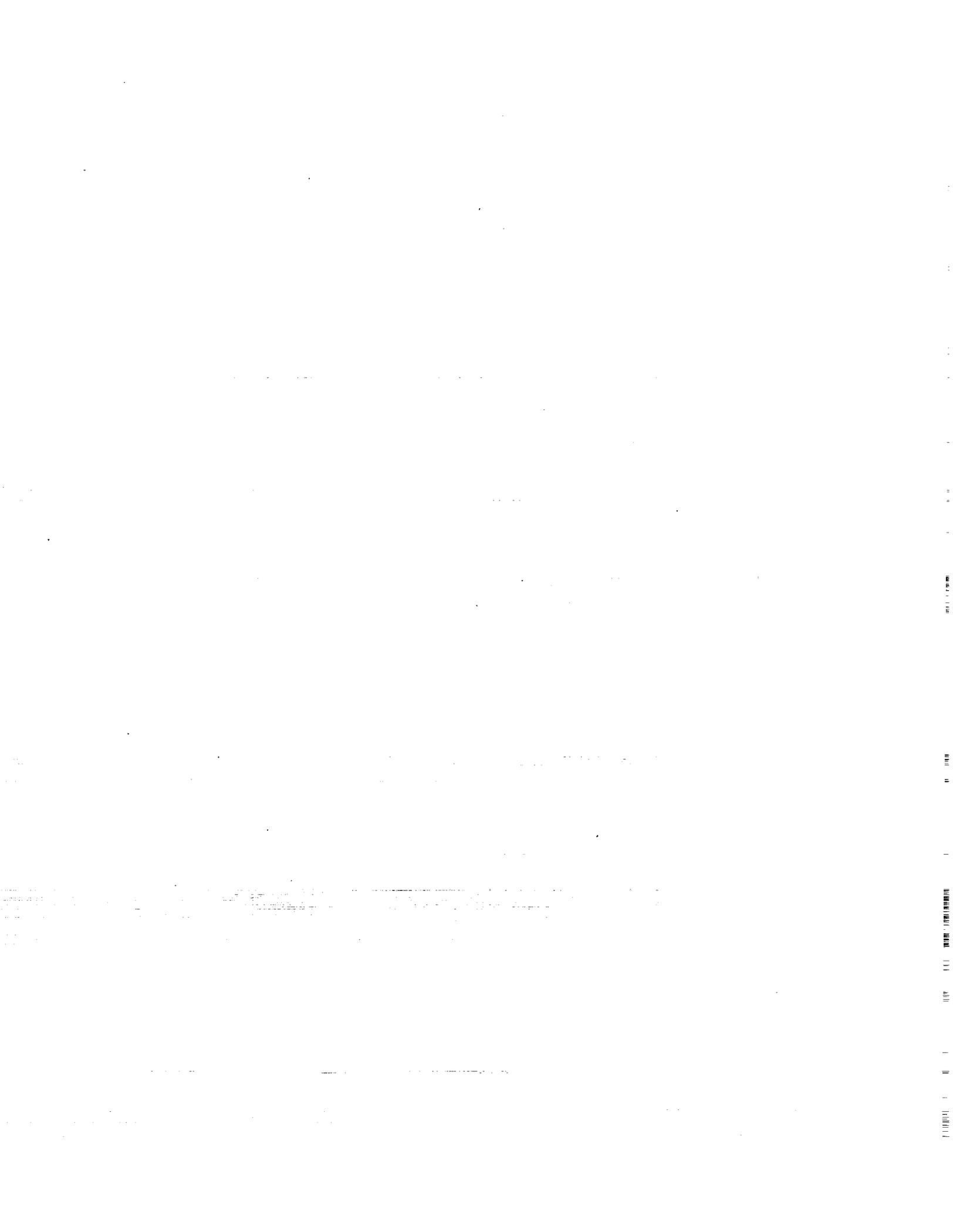
APPENDIX IV: GRANT PROGRESS REPORTS   (January, 1988 to July, 1992)

1.   R.P. Gangloff, G.E. Stoner and R.E. Swanson, "Environment Assisted Degradation Mechanisms in Al-Li Alloys", University of Virginia, Report No. UVA/528266/MS88/101, January, 1988.

2.   R.P. Gangloff, G.E. Stoner and R.E. Swanson, "Environment Assisted Degradation Mechanisms in Advanced Light Metals", University of Virginia, Report No. UVA/528266/MS88/102, June, 1988.

3.   R.P. Gangloff, G.E. Stoner and R.E. Swanson, "Environment Assisted Degradation Mechanisms in Advanced Light Metals", University of Virginia, Report No. UVA/528266/MS89/103, January, 1989.

4.   R.P. Gangloff, "NASA-UVa Light Aerospace Alloy and Structures Technology Program", UVa Report No. UVA/528266/MS90/104, August, 1989.

5.   R.P. Gangloff, "NASA-UVa Light Aerospace Alloy and Structures Technology Program", UVa Report No. UVA/528266/MS90/105, December, 1989.

6.   R.P. Gangloff, "NASA-UVa Light Aerospace Alloy and Structures Technology Program", UVa Report No. UVA/528266/MS90/106, June, 1990.

7.   R.P. Gangloff, "NASA-UVa Light Aerospace Alloy and Structures Technology Program", UVa Report No. UVA/528266/MS91/107, January, 1991.

8.   R.P. Gangloff, "NASA-UVa Light Aerospace Alloy and Structures Technology Program", UVa Report No. UVA/528266/MS91/108, July, 1991.

9.   R.P. Gangloff, "NASA-UVa Light Aerospace Alloy and Structures Technology Program", UVa Report No. UVA/528266/MS92/109, January, 1992.

10.   R.P. Gangloff, "NASA-UVa Light Aerospace Alloy and Structures Technology Program", UVa Report No. UVA/528266/MS93/110, July, 1992.
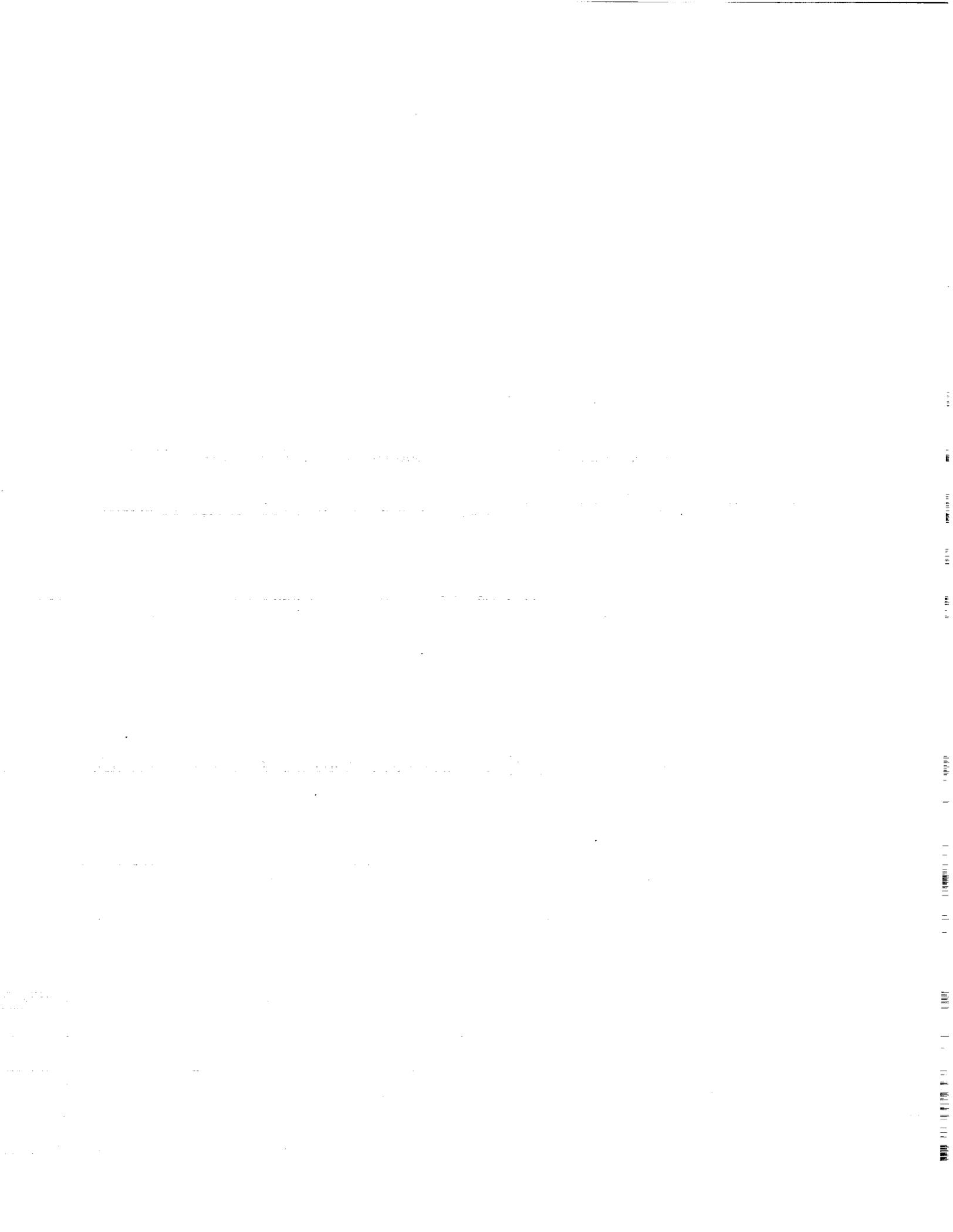
AGENDA FOR THIRD ANNUAL NASA-UVa LA^{2}ST MEETING

NASA-Langley Research Center
Hampton, Virginia

Day 1: July 15, 1992 (Building 1293A, Room 222)

1:00-1:15pm   D.L. Dicus and R.P. Gangloff on LA^{2}ST Program overview; Introductions of graduate and undergraduate participants.

1:15-1:45   "The Effects of Zn Additions on the Microstructure and SCC Performance of Alloy 8090"; R.J. Kilmer and G.E. Stoner; Department Materials Science and Engineering.

1:45-2:15   "Mechanisms of Localized Corrosion in Alloys 2090, X2094 and X2095"; F.D. Wall and G.E. Stoner; Department of Materials Science and Engineering.

2:15-2:45   "Hydrogen Interactions in Aluminum-Lithium Alloys"; S. Smith and J.R. Scully; Department of Materials Science and Engineering.

2:45-3:00   Break

3:00-3:20   "Metastable Pitting of Aluminum-Copper Alloys", Sheldon Pride and J.R. Scully; Department of Chemical Engineering and Department of Materials Science and Engineering.

3:20-3:40   "Incorporating Environmental Effects in Fatigue Life Prediction", Sang-Shik Kim and R.P. Gangloff, Department of Materials Science and Engineering.

3:40-4:10   "Environmental Fatigue Crack Growth in Alloy 2090 Sheet and Plate"; D.C. Slavik and R.P. Gangloff; Department of Materials Science and Engineering.

4:10-4:40   "Superplasticity in Weldalite", M. Lyttle and J.A. Wert; Department of Materials Science and Engineering.

4:40-5:15   "Effects of Cryogenic Temperature and Microstructure on the Fracture Toughness of Alloys 2090, 2090+In and 2095"; J.A. Wagner and C.L. Lach; Metallic Materials Branch, and R.P. Gangloff; Department of Materials Science and Engineering.

6:30   Dinner

8:15-8:45am   "Effect of Thermal Treatment on the Mechanical Properties of Ti-1100/SCS-6 Composites"; D.B. Gundel and F.E. Wawner; Department of Materials Science and Engineering.

8:45-9:00   "Static and Fatigue Response of SCS-6/Beta 21S MMC"; F. Mirzadeh and C.T. Herakovich; Department of Civil Engineering, Applied Mechanics Program.

9:00-9:30   "Inelastic Deformation of Metal Matrix Composites"; C. Lissenden, C.T. Herakovich and Marek-Jerzy Pindera; Department of Civil Engineering, Applied Mechanics Program.

9:30-10:00   "A Geometrical Description of Microstructure: Applications to Aluminum PM Processing"; J.B. Parse and J.A. Wert; Department of Materials Science and Engineering.

10:00-10:15   Break

10:15-10:40   "Elevated Temperature Fracture of RS/PM Aluminum Alloy 8009"; W.C. Porr, Jr., Sang-Shik Kim and R.P. Gangloff; Department of Materials Science and Engineering.

10:40-11:15   "Experimental Study of the Nonlinear Viscoplastic Response of High Temperature Structures"; M.F. Coyle and E.A. Thornton; Department of Mechanical and Aerospace Engineering.

11:15-12:00pm   "Studies in Thermal Structure Analysis"; J.K. Haviland, K. McCarthy, T. Johnson, C. Copper and W.D. Pilkey; Department of Mechanical and Aerospace Engineering.

12:00-1:30   Lunch

1:30-2:15   Group discussion between UVa and LaRC participants on the health and direction of the LA^{2}ST Program; general input to guide the 1993 renewal.

2:15   Individual discussions between UVa investigators and LaRC technical contacts on the 1993 renewal; scheduled as needed.

DISTRIBUTION LIST

1 - 2   Mr. D. L. Dicus
Contract Monitor
Metallic Materials Branch, MS 188A
NASA Langley Research Center
Hampton, VA 23665

3 - 4*   NASA Scientific and Technical Information Facility
P. O. Box 8757
Baltimore/Washington International Airport
Baltimore, MD 21240

5   Mr. Richard J. Siebels
Grants Officer, M/S 126
NASA Langley Research Center
Hampton, VA 23665

6   Dr. Darrel R. Tenney
Materials Division
NASA Langley Research Center
Hampton, VA 23665

7   Dr. Charles E. Harris
Mechanics of Materials Branch
NASA Langley Research Center
Hampton, VA 23665

8   Mr. W. Barry Lisagor
Metallic Materials Branch
NASA Langley Research Center
Hampton, VA 23665

9   Mr. T.W. Crooker
Code RM
NASA Headquarters
Washington, DC 20546

10   Dr. Robert S. Piascik
Mechanics of Materials Branch
NASA Langley Research Center
Hampton, VA 23665

11   Mr. W. Brewer
Metallic Materials Branch, MS 188A
NASA Langley Research Center
Hampton, VA 23665

12   Mr. Thomas Bayles
     Metallic Materials Branch, MS 188A
     NASA Langley Research Center
     Hampton, VA 23665

13   Dr. W.S. Johnson
     Mechanics of Materials Branch
     NASA Langley Research Center
     Hampton, VA 23665

14   Dr. M.J. Shuart
     Aircraft Structures Branch
     NASA Langley Research Center
     Hampton, VA 23665

15   Dr. James H. Starnes, Jr.
     Aircraft Structures Branch
     NASA Langley Research Center
     Hampton, VA 23665

16   Mr. Dana Ward
     Northrop Corporation
     1 Northrop Avenue
     Mail Zone 3872562
     Hawthorne, CA 90250-3277

17   Dr. Santosh K. Das
     Senior Manager
     Metals and Ceramics Laboratory
     Allied-Signal, Inc.
     P. O. Box 1021
     Morristown, NJ 07960

18   Dr. Michael Zedalis
     Metals and Ceramics Laboratory
     Allied-Signal, Inc.
     P. O. Box 1021
     Morristown, NJ 07960

19-20 Mr. E.A. Colvin
     Alcoa Technical Center
     Route 780, 7th Street Road
     Alcoa Center, PA 15069

21   Mr. Fred Casey
Space Transportation Systems Division
Rockwell International
Dept. 289 MC/AC56
12214 Lakewood Blvd.
Downey, CA 90241

22   Mr. Stephen G. Moran
Lockheed Aeronautical Systems Company
Georgia Division; Dept. 73-71
Zone 0160
86 South Cobb Dr.
Marietta, GA 30063

23   Dr. J. Andrew Walker
Advanced Composite Materials Corporation
1525 South Buncombe Road
Greer, SC 29651

24   E.A. Starke, Jr.; UVA

25-27   R.P. Gangloff; MS&E

28   G.E. Stoner; MS&E

29   J.A. Wert; MS&E

30   F.E. Wawner; MS&E

31   W.A. Jesser; MS&E

32   J.R. Scully; MS&E

33   W.D. Pilkey; MAE

34   E.A. Thornton; MAE

35   C.T. Herakovich; CE/Applied Mechanics

36   W.A. Jesser; MS&E

37-38   E.H. Pancake; Clark Hall

39   SEAS Preaward Administration Files

40   Mr. Gwyn Faile
Code ED 24
Marshall Space Flight Center
Huntsville, AL 35812

41   Mr. Brian McPherson
        Code ED 24
        Marshall Space Flight Center
        Huntsville, AL   35812

42   Dr. Ken Garr
        Rocketdyne Division, Rockwell International
        6633 Canoga Ave.
        Canoga Park, CA   91303

43   Mr. Michael Falugi
        WRDC/FIBAA
        Wright Patterson Air Force Base, OH   45433-6553

44   Mr. Peter Rimbos
        Boeing Aerospace and Electronics
        Aerospace Group
        Seattle, WA   98124

45   Mr. James Learned
        Boeing Military Aircraft
        Organization L-7109
        Aerospace Group
        Seattle, WA   98124

46   Dr. Howard G. Nelson
        NASA-Ames Research Center
        EEM: 213-3
        Moffett Field, CA   94035

47   Dr. R.G. Forman
        Mail Code ES-5
        NASA-L.B. Johnson Space Flight Center
        Houston, TX   77058

48   Professor A.K. Noor
        Center for Computational Structures Technology
        NASA Langley Research Center
        Hampton, VA   23665

49   Dr. M.J. Luton
        Exxon Research and Engineering Company
        Clinton Township, Route 22 East
        Annandale, NJ   08801